Hydro-mechanical coupling in numerical analysis of geotechnical structures under multi-directional seismic loading

A thesis submitted in partial fulfilment of the requirements of

the Doctor of Philosophy (PhD) degree

and the Diploma of Imperial College (DIC)

By

Bo Han

Department of Civil and Environmental Engineering

Imperial College London

London SW7 2AZ

October 2014

Declaration

The work presented in this thesis was carried out in the Department of Civil and Environmental Engineering at Imperial College London. This thesis is the result of my own work and any quotation from, or description of the work of others is acknowledged herein by reference to the sources, whether published or unpublished. This thesis is not the same as any that I have submitted for any degree, diploma or other qualification at any other university. No part of this thesis has been or is being concurrently submitted for any such degree, diploma or other qualification.

This document is available online at www.imperial.ac.uk. The copyright of this thesis rests with the author and is made available under a Creative Commons Attribution Non-Commercial No Derivatives licence. Researchers are free to copy, distribute or transmit the thesis on the condition that they attribute it, that they do not use it for commercial purposes and that they do not alter, transform or build upon it. For any reuse or redistribution, researchers must make clear to others the licence terms of this work.

Bo Han

London, October 2014

Abstract

This thesis numerically investigates the seismic behaviour of geotechnical structures under multi-directional loading by employing the coupled hydro-mechanical (HM) formulation of the Imperial College Finite Element Program (ICFEP). The scope of the research work can be summarised as follows:

Firstly, the stability of the generalised-α method (CH method) for the coupled consolidation formulation, is analytically investigated for the first time and the corresponding theoretical stability conditions are derived. The analytically derived stability conditions are validated by finite element (FE) analyses considering a range of loading conditions and soil permeability values.

Secondly, the site response due to the vertical component of the ground motion is systematically investigated by employing analytical and numerical methods. The compressional wave propagation mechanism in saturated porous soils is investigated by the coupled HM formulation. Furthermore, the undertaken coupled FE analyses explore the effects of the parameters characterising the hydraulic phase, i.e. the soil permeability and soil state conditions, on the vertical site response.

Thirdly, three-directional (3-D) site response analyses are conducted for the HINO site of the Japanese KiK-net down-hole array earthquake monitoring system. Different aspects of the numerical modelling for the site response analysis, such as the constitutive model, the use of 3-D input motion and the coupled consolidation formulation, are investigated and validated by the recordings from the KiK-net system. Further parametric studies investigate the impact of the variation of the water table, the soil permeability and the 3-D input motion on the multi-directional site response.

Finally, the seismic response of a well-documented Chinese rockfill dam, the Yele dam, is investigated with the dynamic plane-strain FE analysis, accounting for the HM coupling and nonlinear soil response. The numerical predictions are compared against the available static and dynamic monitoring data, which allows for a rigorous validation of the developed numerical model. Furthermore, parametric studies of the Yele dam are conducted to explore the effects of several critical factors on the seismic response of rockfill dams, i.e. the reservoir simulation method, the permeability of materials

comprising the dam body, the vertical ground motion and the reservoir water level.

Acknowledgements

Firstly and most importantly, I would like to express my sincere gratitude to my supervisors Professor Lidija Zdravković and Dr Stavroula Kontoe. Their broad and deep geotechnical knowledge and practical engineering experience guided me smoothly from hydraulics to geotechnics and from statics to dynamics. Without their guidance this would not have been possible. I need to express my appreciation to them for providing this research opportunity, for their professional and patient supervision and support, for helping me enrich academic experience and for inspiring figures both for my academic and personal life.

This research was funded by the China Scholarship Council (CSC). Great appreciation is expressed to the China government and HoHai University. I want to thank my previous supervisors Professors Xiaoqing Liu and Lanhao Zhao at HoHai University for their help, Professors Shucai Li and Chao Jia at Shandong University for their encouragement and Dr Kun Xiong in Chendu Engineering Corporation for providing the monitoring data on the Yele dam discussed in Chapter 5.

Being part of the Geotechnics Section at Imperial College is considered as an honour and a precious opportunity to learn from the greatest geotechnical professors and experts. I would like to thank all the members in the Section and especially Professor David M. Potts for his valuable advice on numerical analysis, his amazing personality and amusing talks in the pub. Further acknowledgement is attributed to Dr Jamie R. Standing and Dr Clark H. Fenton for expanding my horizons on field monitoring techniques and engineering geology. Many thanks to Dr David M. G. Taborda, Dr Katerina Tsiampousi and Dr Antonio M. G. Pedro for being helpful throughout my research work. Of course, I need to take this opportunity to thank all my close friends, who made my life in London warm and enjoyable. It was a memorable and terrific period of discussing and communicating with my best friends Vasilis, Loizos, Wenjie, George, Giuseppe, Siya and Vasia. Special thanks are due to Ms Fionnuala Ni Dhonnabhain and Mr Stephen J Hullock for their assistance and also to my flatmates Hua and Jiaying.

The deepest gratitude is preserved for my beloved family, my wife Haiying, my parents Xisheng and Guiling and my parents in law. Without their love and support, this thesis could not have been possible. I sincerely wish my entire family can stay close in the future, which I do believe is more important than anything else.

Table of contents

DECLARATION **2**

ABSTRACT **3**

ACKNOWLEDGEMENTS **5**

TABLE OF CONTENTS **7**

LIST OF FIGURES **11**

LIST OF TABLES **25**

LIST OF SYMBOLS **27**

CHAPTER 1 INTRODUCTION **34**

1.1 Background 34

1.2 Scope of research and layout of thesis 35

CHAPTER 2 THE STABILITY OF THE GENERALISED-A TIME INTEGRATION METHOD IN SOLID-PORE FLUID COUPLED FORMULATION **38**

2.1 Introduction 38

2.2 One-phase static and dynamic FE formulations 40

2.3 Two-phase coupled dynamic FE formulation 41

2.4 Direct time integration methods 45

2.4.1 Numerical characteristics of time integration methods 46

2.4.2 Newmark method 50

2.4.3 Generalised-α method 52

2.4.4 Implementation of the CH method to the coupled dynamic formulation 56

2.5 Stability investigation of the CH method for the coupled formulation 59

2.5.1 Scalar form of the coupled dynamic FE formulation 61

2.5.2 Application of the expressions of the Newmark method 61

2.5.3 Application of the CH method 62

2.5.4 Derivation of the unconditional stability conditions 63

2.5.5 Comparison with existing stability investigations 67

2.6 Numerical investigation of the stability characteristics of the CH method 68

2.6.1 1-D column subjected to step loading 69

2.6.2 1-D column subjected to harmonic loading 76

2.6.3 1-D column subjected to impulse loading 82

2.6.4 Elastic foundation subjected to step loading 85

2.6.5 Elasto-plastic foundation subjected to step loading 92

2.7 Summary 96

CHAPTER 3 ANALYTICAL AND NUMERICAL INVESTIGATION OF SITE RESPONSE DUE TO VERTICAL GROUND MOTION **98**

3.1 Introduction 98

3.2 Field evidence of strong vertical motion and empirical design methods 100

3.2.1 Field evidence of strong vertical ground motion and associated compression damage 100

3.2.2 Empirical design models for vertical ground motion 102
3.3 One-phase investigation of vertical site response 105
3.3.1 Frequency domain analytical solution for vertical site response 106
3.3.2 Previous one-phase studies for vertical site response 112
3.3.3 Comparison with time domain FE analysis 113
3.4 Two-phase investigation of compressional wave propagation in saturated porous material 123
3.4.1 Previous two-phase coupled investigation of compressional wave propagation 123
3.4.2 Two-phase analytical solution for compressional wave propagation in saturated porous soils 126
3.4.3 Two-phase compressional wave propagation mechanism in saturated porous soils 134
3.5 Two-phase coupled numerical investigation of vertical site response 143
3.5.1 Two-phase coupled vertical site response analysis 143
3.5.2 Quantitative study of the variation of compressional wave velocity 149
3.5.3 Quantitative study of the variation of viscous damping 152
3.6 Summary 155
CHAPTER 4 NUMERICAL INVESTIGATION OF MULTI-DIRECTIONAL SITE RESPONSE BASED ON KIK-NET DOWN-HOLE ARRAY MONITORING DATA 157
4.1 Introduction 157
4.2 Literature review 158
4.2.1 Site amplification effects based on down-hole array data 159
4.2.2 Site response analyses 165
4.3 Constitutive models for dynamic analysis 173
4.3.1 Cyclic nonlinear models 176
4.3.2 Elasto-plastic models 184
4.4 KiK-net down-hole array observations 185
4.5 Multi-directional site response analysis subjected to two weak earthquake motions 192
4.5.1 Linear analysis 192
4.5.2 Nonlinear analysis 205
4.5.2.1 Logarithmic model 205
4.5.2.2 ICG3S-1 model 212
4.5.2.3 ICG3S-2 model 216
4.5.2.4 Comments 220
4.6 Multi-directional site response analysis subjected to strong earthquake motions 221
4.6.1 Logarithmic model 221
4.6.2 ICG3S-1 model 224
4.6.3 ICG3S-2 model 227
4.6.4 Comments 233
4.7 Parametric investigation on the multi-directional site response 234
4.7.1 Effect of water table location on site response 234
4.7.1.1 Linear site response analysis - parametric study 1 235
4.7.1.2 Nonlinear site response analysis - parametric study 2 236
4.7.1.3 Drained nonlinear site response analysis - parametric study 3 242
4.7.1.4 Realistic soil stiffness profile for high water table - parametric study 4 245

4.7.2 Effect of permeability on site response - parametric study 5 247
4.7.3 Effect of 3-D ground motions on site response analysis - parametric study 6 250
4.8 Summary 253
CHAPTER 5 STATIC AND DYNAMIC FE ANALYSES OF THE YELE DAM 257
5.1 Introduction 257
5.2 Earth and rockfill dams 259
5.2.1 Dam types 259
5.2.2 Seismic damage of earth and rockfill dams 261
5.2.3 Seismic analysis methods for earth and rockfill dams 264
5.3 Introduction of the Yele dam 275
5.3.1 Dam geometry, construction sequence and seismic event 275
5.3.2 Material properties 279
5.3.3 Monitored data 282
5.4 Description of the numerical model 290
5.4.1 Element size 290
5.4.2 Location of the lateral boundaries 294
5.4.3 Calibration of constitutive models 297
5.5 Static analysis of the Yele dam 298
5.5.1 Description of the static analysis 299
5.5.2 Static analysis results 302
5.6 Dynamic analysis of the Yele dam 309
5.6.1 Acceleration time histories and response spectra 310
5.6.2 Seismic deformation of the Yele dam 313
5.6.3 Crest settlements 319
5.6.4 Acceleration distributions within dam body 320
5.6.5 Safety assessment based on seismic design method 321
5.6.6 Stress-strain and pore water pressure response 324
5.7 Summary 328
CHAPTER 6 PARAMETRIC STUDIES OF THE YELE DAM 331
6.1 Introduction 331
6.2 Effect of reservoir simulation 331
6.3 Effect of dam material permeabilities 340
6.4 Effect of vertical ground motion 345
6.5 Effect of reservoir water level 348
6.6 Summary 355
CHAPTER 7 CONCLUSIONS AND RECOMMENDATIONS 357
7.1 Introduction 357
7.2 Conclusions 359
7.2.1 The stability investigation of the CH time integration method in HM coupled formulation 359
7.2.2 Analytical and numerical investigation of site response due to vertical ground motion 360
7.2.3 Numerical investigation of multi-directional site response based on KiK-net data 361

7.2.4 Static and dynamic FE analyses of the Yele dam 364
7.2.5 Parametric studies of the Yele dam 367
7.3 Recommendations for future work 368
7.3.1 The stability investigation of the CH time integration method in HM coupled formulation 368
7.3.2 Analytical and numerical investigation of site response due to vertical ground motion 369
7.3.3 Numerical investigation of multi-directional site response based on KiK-net data 370
7.3.4 Static, dynamic and parametric FE studies of the Yele dam 370
REFERENCES 372

List of figures

Figure 2-1: Approximation of pore water pressure integral (after Potts and Zdravković (1999)) 45

Figure 2-2: Illustration of PE and AD in numerical solution (after Kontoe (2006)) 49

Figure 2-3: Spectral radii for four time integration methods (after Kontoe (2006)) 50

Figure 2-4: Schematic graph of the evaluation of acceleration, velocity and displacement terms for the HHT method (after Kontoe (2006)) 52

Figure 2-5: Schematic graph of the evaluation of acceleration, velocity and displacement terms for the WBZ method (after Kontoe (2006)) 53

Figure 2-6: Schematic graph of the evaluation of acceleration, velocity and displacement terms for the CH method (after Kontoe (2006)) 55

Figure 2-7: Unconditional stability conditions for the CH method (after Chung and Hulbert (1993)) 56

Figure 2-8: FE model for 1-D column analysis subjected to step loading 70

Figure 2-9: The loading history for 1-D column analysis subjected to step loading 70

Figure 2-10: Comparison of ICFEP results and the closed form solution of de Boer et al. (1993) 71

Figure 2-11: Displacement and excess pore water pressure time histories at point A for various β values by using the CH method 74

Figure 2-12: Displacement and excess pore water pressure time histories at point A for various β values by using the Newmark method 75

Figure 2-13: FE model for 1-D column analysis subjected to harmonic loading 76

Figure 2-14: The loading history for 1-D column analysis subjected to harmonic loading 76

Figure 2-15: Comparison of the excess pore water pressure time history at point D 77

Figure 2-16: Excess pore water pressure time history of analyses with high permeabilities at point D 78

Figure 2-17: Displacement (at point C) and excess pore water pressure (at point D) time histories for various β values by using the CH method 80

Figure 2-18: Displacement (at point C) and excess pore water pressure (at point D) time histories for various β values by using the Newmark method 81

Figure 2-19: The loading history for 1-D column analysis subjected to impulse loading 82

Figure 2-20: Spectral radii for the CH3, CH2, CH1, NMK2 and NMK1 method (after Kontoe (2006)) 83

Figure 2-21: Comparison of the acceleration time histories (at point A) by using five time integration methods 84

Figure 2-22: Comparison of displacement time histories (at point A) by using five time integration methods 85

Figure 2-23: Comparison of pore pressure time histories (at point B) by using five time integration methods 85

Figure 2-24: FE model for the elastic foundation analysis 86

Figure 2-25: The loading history for the elastic foundation analysis 86

Figure 2-26: Comparison of the contour of the total pore water pressure at t=1.0s (Pa) 87

Figure 2-27: Comparison of the time history of the displacement at point E 88

Figure 2-28: Displacement (at point E) and excess pore water pressure (at point F) time histories of various β values by using CH method 90

Figure 2-29: Displacement and excess pore water pressure contours at t=1.0s of various β values 91

Figure 2-30: The loading history for the elasto-plastic foundation analysis 92

Figure 2-31: Schematic graph for the PB bounding surface sand model (after Taborda (2011)) 93

Figure 2-32: Displacement (at point E) and excess pore water pressure (at point F) time histories of various β values by using CH method 94

Figure 2-33: Displacement and excess pore water pressure contours at t=1.0s of various β values 95

Figure 3-1: Collapse of the car park building in California State University in the Northridge earthquake (after Papazoglou and Elnashai (1996)) 101

Figure 3-2: A damaged building in the Kobe Earthquake (after Papazoglou and Elnashai (1996)) 102

Figure 3-3: Empirical models of vertical response spectra for near-field and far-field sites (ξ=2%) 103

Figure 3-4: Empirical models of vertical response spectra for near-field and far-field sites (ξ=2%) 104

Figure 3-5: Empirical V/H ratio model. Unless otherwise noted, the V/H ratio model is evaluated for Magnitude (*Mw*)=7.0, Epicentral distance (R)=10 km, strike-slip faulting and firm soil (after Bozorgnia and Campbell (2004)) 105

Figure 3-6: A schematic graph for the principle of the frequency domain method 106

Figure 3-7: Transfer functions for elastic and visco-elastic soil layers subjected to SH waves 107

Figure 3-8: A schematic graph of the compressional wave propagation 108

Figure 3-9: Transfer functions for elastic and visco-elastic soil layers subjected to compressional waves 110

Figure 3-10: Transfer functions for visco-elastic soil layers subjected to compressional waves under drained and undrained conditions 111

Figure 3-11: Comparison of the vertical response spectra between the observed data and the analytical results for Lotung down-hole array (after Elgamal and He (2004)) 112

Figure 3-12: A schematic graph of the 1-D soil columns 114

Figure 3-13: Acceleration time history of the observed vertical ground motion (at the CCCC station) from the Christchurch Earthquake 114

Figure 3-14: Acceleration response spectra of the observed vertical ground motion (at the CCCC station) from the Christchurch Earthquake (5% damping) 115

Figure 3-15: A schematic graph for Rayleigh damping 117

Figure 3-16: Comparison of acceleration time histories at point A between analytical and numerical results 119

Figure 3-17: Comparison of acceleration response amplification spectra at point A between analytical and numerical results 120

Figure 3-18: Comparison of acceleration response amplification spectra at point A between analytical and numerical results (New Rayleigh damping parameters) 122

Figure 3-19: The model test device (after Plona (1980)) 125

Figure 3-20: Observed compressional and shear waves (after Plona (1980)) 125

Figure 3-21: Variations of compressional wave velocity and damping ratio 133

Figure 3-22: Comparison of the wave velocities and damping parameters from the present study and from Bardet and Sayed (1993) results 134

Figure 3-23: A schematic graph for the FE model in coupled analysis 136

Figure 3-24: Illustration of the input vertical motion for the coupled 1-D column FE analysis 136

Figure 3-25: Displacement time histories at monitoring point B for seven cases (χ=0.1) 138

Figure 3-26: Comparison of compressional wave velocity between analytical and numerical results (χ=0.1) 139

Figure 3-27: Comparison of compressional wave velocity between analytical and numerical results (χ=0.1) 140

Figure 3-28: Displacement time histories at monitoring point B for seven cases (χ=1.0) 142

Figure 3-29: Comparison of compressional wave velocity (χ=1.0) 142

Figure 3-30: Displacement time histories at monitoring point B for seven cases (χ=10.0) 142

Figure 3-31: Comparison of compressional wave velocity (χ=10.0) 143

Figure 3-32: A schematic graph of the soil column FE model (Coupled FE analysis) 144

Figure 3-33: Two-phase coupled vertical site response of a soil column considering a wide permeability range (χ=0.1) 147

Figure 3-34: Two-phase coupled vertical site response of a soil column considering a wide permeability range (χ=1.0) 148

Figure 3-35: Two-phase coupled vertical site response of a soil column considering a wide permeability range (χ=10.0) 149

Figure 3-36: Quantitative study for the compressional wave velocity 151

Figure 3-37: A schematic graph for the explanation of the observed different dynamic responses in the parametric study 152

Figure 3-38: Quantitative study of the viscous damping 154

Figure 4-1: A schematic graph for two strong motion monitoring systems 159

Figure 4-2: Shear wave velocity comparison at the SGK site in Hyogo-ken Nanbu earthquake (EW for east-west and NS for north-south) (after Sato et al. (1996)) 160

Figure 4-3: Fourier spectral ratio comparison at the SGK site in the Hyogo-ken Nanbu earthquake (observed data-solid line & analytical simulation-dashed line) (after Sato et al. (1996)) 161

Figure 4-4: Soil profile at the Dahan site (after Huang et al. (2005)) 161

Figure 4-5: Fourier spectral ratio comparison subjected to the main shock and after-shock motions at the Dahan site in the Chi-Chi earthquake (after Huang et al. (2005)) 162

Figure 4-6: Constrained modulus degradation time histories at the PI site in the Hyogo-ken Nanbu earthquake (after Pavlenko and Irikura (2002)) 163

Figure 4-7: Stratigraphy at the PI site in the Hyogo-ken Nanbu earthquake (after Sato et al. (1996)) 163

Figure 4-8: Constrained modulus degradation ratios at three KiK-net sites subjected to strong motions (after Beresnev et al. (2002)) 164

Figure 4-9: Soil profile of the PI site in Hyogo-ken Nanbu earthquake (after Sato et al. (1996)) 166

Figure 4-10: Comparison of acceleration time histories between numerical results and monitored data at the PI site in the Hyogo-ken Nanbu earthquake (after Aguirre and Irikura (1997)) 166

Figure 4-11: Acceleration time history comparison in the NS direction between numerical results and monitored data at the Dahan site (numerical results-grey line; observed data-black line) (after Huang et al. (2005)) 167

Figure 4-12: The applicability ranges of the linear-elastic and equivalent-linear site response analyses (after Kaklamanos et al. (2013)) 168

Figure 4-13: Comparison of site response predicted by the linear elasto-plastic FE and EERA analyses (after Amorosi et al. (2010)) 169

Figure 4-14: Soil properties at the Lotung site (after Li et al. (1998)) 170

Figure 4-15: Comparison of the acceleration response spectra at the ground surface of the Lotung site (left: July 31, 1986 earthquake; right: November 15, 1986 earthquake) (after Li et al. (1998)) 171

Figure 4-16: Soil properties at the Lotung site (after Borja and Chao (1999)) 172

Figure 4-17: Comparison of the acceleration time histories in the UD direction at two depths of the Lotung site (upper plot: ground surface; lower plot: GL. -11.0m) (after Borja and Chao (1999)) 172

Figure 4-18: A typical hysteretic loop of soil behaviour under cyclic loading (after Ishihara (1996)) 175

Figure 4-19: Categorisation of cyclic shear strains subjected to cyclic loads (λ_N indicates the material damping, which is the same as ξ adopted in the thesis) (after Vucetic (1994)) 175

Figure 4-20: Shear stress-strain curves following Masing rules and extended Masing rules ... 177

Figure 4-21: A schematic graph for the backbone curve simulated by the Logarithmic model (after Taborda (2011)) 179

Figure 4-22: A schematic graph for the effect of the parameter *c* on damping curve (after Taborda (2011)) 180

Figure 4-23: Damping curves predicted by Darendeli (2001) empirical models (after Guerreiro et al. (2012)) 180

Figure 4-24: Location of the epicentre of 2000 Western Tottori earthquake and location of the HINO site (after Matsunami et al. (2002)) 186

Figure 4-25: 3-D acceleration time histories at the base layer of HINO site in 2000 Western Tottori earthquake 188

Figure 4-26: 3-D acceleration time histories at the base layer of HINO site in 2001 weak motion 1 189

Figure 4-27: 3-D acceleration time histories at the base layer of HINO site in 2002 weak motion 2 189

Figure 4-28: Acceleration response spectra of the observed response at the base layer of HINO site in three earthquake events (5% damping) 190

Figure 4-29: Soil profile at the HINO site (NIED database) 191

Figure 4-30: Soil profile at the HINO site employed in FE analyses 191

Figure 4-31: FE model for HINO site 194

Figure 4-32: Linear analysis results under weak earthquake motion 1 (response amplification spectra) 197

Figure 4-33: Linear analysis results under weak earthquake motion 2 (response amplification spectra) 197

Figure 4-34: Linear analysis results under weak earthquake motion 1 (acceleration time histories) 198

Figure 4-35: Linear analysis results under weak earthquake motion 2 (acceleration time histories) 199

Figure 4-36: Linear analysis results under weak earthquake motion 1 (response amplification spectra) (adjusted Rayleigh damping parameter) 202

Figure 4-37: Comparison of Rayleigh damping 203

Figure 4-38: Linear analysis results under weak earthquake motion 1 (acceleration time histories) 203

Figure 4-39: Linear analysis results under weak earthquake motion 1 (response amplification spectra) 204

Figure 4-40: Linear analysis results under weak earthquake motion 1 (acceleration time histories) 204

Figure 4-41: Constrained modulus degradation curves (after LeBlanc et al. (2012)) 207

Figure 4-42: Calibration of the Logarithmic model for nonlinear analyses 208

Figure 4-43: Nonlinear analysis results under weak earthquake motion 1 (response amplification spectra) 210

Figure 4-44: Nonlinear analysis results under weak earthquake motion 1 (acceleration time histories) 210

Figure 4-45: Nonlinear analysis results under weak earthquake motion 2 (response amplification spectra) 211

Figure 4-46: Nonlinear analysis results under weak earthquake motion 2 (acceleration time histories) 211

Figure 4-47: Calibration of the ICG3S-1 model for nonlinear analysis 213

Figure 4-48: Nonlinear analysis results under weak earthquake motion 1 (response amplification spectra) 214

Figure 4-49: Nonlinear analysis results under weak earthquake motion 1 (acceleration time histories) 214

Figure 4-50: Nonlinear analysis results under weak earthquake motion 2 (response amplification spectra) 215

Figure 4-51: Nonlinear analysis results under weak earthquake motion 2 (acceleration time histories) 215

Figure 4-52: Calibration of the ICG3S-2 model for the nonlinear analysis 217

Figure 4-53: Nonlinear analysis results under weak earthquake motion 1 (response amplification spectra) 218

Figure 4-54: Nonlinear analysis results under weak earthquake motion 1 (acceleration time histories) 218

Figure 4-55: Nonlinear analysis results under weak earthquake motion 2 (response amplification spectra)..... 219

Figure 4-56: Nonlinear analysis results under weak earthquake motion 2 (acceleration time histories) 219

Figure 4-57: Nonlinear analysis results under Western Tottori earthquake (response amplification spectra) 222

Figure 4-58: Nonlinear analysis results under Western Tottori earthquake (acceleration time histories) 223

Figure 4-59: Nonlinear analysis results under Western Tottori earthquake (response amplification spectra) 226

Figure 4-60: Nonlinear analysis results under Western Tottori earthquake (acceleration time histories) 226

Figure 4-61: Calibration of the ICG3S-2 model for the nonlinear analysis of the main earthquake motion 228

Figure 4-62: Nonlinear analysis results under Western Tottori earthquake (response amplification spectra) 229

Figure 4-63: Nonlinear analysis results under Western Tottori earthquake (acceleration time histories) 229

Figure 4-64: Average modulus degradation ratio variation 231

Figure 4-65: Stress-strain response simulated by the nonlinear analysis 232

Figure 4-66: Plastic strain time histories at element C simulated by the nonlinear analysis 233

Figure 4-67: Soil profiles for parametric studies of the water table location 235

Figure 4-68: Acceleration response amplification spectra of the HINO site from parametric study 1..... 236

Figure 4-69: Acceleration response spectra of the HINO site from the parametric study 2 240

Figure 4-70: Acceleration response amplification spectra of the HINO site from the parametric study 2..... 240

Figure 4-71: Variations of the average stiffness degradation ratio from the parametric study 2 241

Figure 4-72: Plastic strain time histories from the parametric study 2..... 241

Figure 4-73: Shear/constrained modulus degradation and damping curves..... 241

Figure 4-74: Comparison of site response predictions considering two pore fluid bulk modulus values (after Yang and Sato (2000))..... 242

Figure 4-75: Variations of the peak acceleration from the parametric study 2 242

Figure 4-76: Acceleration response amplification spectra of the HINO site from the parametric study 3..... 244

Figure 4-77: Variations of the average stiffness degradation ratio from the parametric study 3 244

Figure 4-78: Plastic strain time histories from the parametric study 3..... 245

Figure 4-79: Shear modulus variations for the parametric study 4 246

Figure 4-80: Acceleration response amplification spectra of the HINO site from the parametric study 4..... 247

Figure 4-81: Acceleration response spectra of the HINO site from the parametric study 5 249

Figure 4-82: Acceleration response amplification spectra of the HINO site from the parametric study 5..... 249

Figure 4-83: Variations of the average modulus degradation ratio from the parametric study 5 250

Figure 4-84: FE mesh for 2-D plane-strain FE analysis..... 251

Figure 4-85: Comparison of response amplification spectra between 2-D and 3-D nonlinear FE analyses..... 252

Figure 4-86: Comparison of plastic strain time histories between 2-D and 3-D nonlinear FE analyses..... 252

Figure 4-87: Comparison of average stiffness degradation between 2-D and 3-D nonlinear FE analyses..... 253

Figure 5-1: Typical geometry of a uniform earth dam (after Gu (1988)) 259

Figure 5-2: Typical geometry of a zoned earth and rockfill dam (vertical core) (after Gu (1988)) 260

Figure 5-3: Typical geometry of a zoned earth and rockfill dam (inclined core) (after Gu (1988)) 260

Figure 5-4: Typical geometry of a concrete-faced rockfill dam (after Gu (1988)) 261

Figure 5-5: Failure mode of the Nozawa Poe dam in the 1968 Tokachi-oki earthquake (after Gu (1988)) 262

Figure 5-6: Deformation mode of the Douhe earth dam in the 1976 Tangshan earthquake (after Gu (1988)) 263

Figure 5-7: Layout of cracks on Dianju earth dam in 1970 Tonghai earthquake (after Gu (1988)) 263

Figure 5-8: The failure mode of the Shivlakha dam in the 2001 Bhuj earthquake (after Singh (2005)) 264

Figure 5-9: A schematic graph of the shear beam method for earth dams (after Kramer (1996)) 265

Figure 5-10: The FE mesh of a homogeneous triangular dam (after Clough and Chopra (1966)) 267

Figure 5-11: Comparison of seismic response from one-phase and two-phase FE analyses (after Lacy and Prevost (1987)) 269

Figure 5-12: Impact of dam-reservoir interaction on seismic response of the La Villita dam (after Guan and Moore (1997)) 270

Figure 5-13: FE mesh of Marana Capacciotti dam (after Elia et al. (2011)) 271

Figure 5-14: The FE mesh of La Villita dam (after Pelecanos (2013)) 272

Figure 5-15: Prediction accuracy of k_{hmax} (after Papadimitriou et al. (2014)) 274

Figure 5-16: The plan view of the Yele dam (after He et al. (2006)) 276

Figure 5-17: The axial longitudinal section 1-1 of the Yele dam (after Wang et al. (2008)) 276

Figure 5-18: The maximum transverse section D-D of the Yele dam 276

Figure 5-19: Simplified construction and reservoir impounding sequences in FE analyses of the Yele dam 278

Figure 5-20: Effects of canyon geometry on the fundamental natural period of a dam (after Dakoulas and Gazetas (1987). 281

Figure 5-21: Dynamic soil properties of the Yele dam rockfill materials (after Xiong (2009)) 281

Figure 5-22: Monitored dam settlements (after Wang et al. (2008)) 282

Figure 5-23: Monitored horizontal core displacements (after Wang et al. (2008)) 283

Figure 5-24: Monitoring periods of different observations 283

Figure 5-25: The layout of seismometers on the maximum transverse section 286

Figure 5-26: The layout of seismometers on the Yele dam in plan view 286

Figure 5-27: Seismic monitored data (acceleration time histories) 287

Figure 5-28: Seismic monitored data (acceleration response spectra) 288

Figure 5-29: Seismic monitored data (acceleration response amplification spectra) 289

Figure 5-30: Fourier amplitude spectra of the horizontal bedrock excitation 291

Figure 5-31: FE model for parametric studies of element size limit 292

Figure 5-32: Comparison of Fourier amplitude spectra for different horizontal element dimensions 293

Figure 5-33: Comparison of Fourier amplitude spectra for different vertical element dimensions 293

Figure 5-34: FE mesh of the Yele dam 296

Figure 5-35: Acceleration response spectra from the parametric study for lateral boundary location 296

Figure 5-36: Calibration of the ICG3S-2 model for the Yele dam materials 298

Figure 5-37: FE mesh of the Yele dam and boundary conditions for the static analysis 302

Figure 5-38: Horizontal displacement distribution along the concrete core (scenario 1) 303

Figure 5-39: Horizontal displacement distribution along the concrete core (scenario 2) 304

Figure 5-40: Settlements at different locations on the Yele dam 305

Figure 5-41: Accumulated deformed mesh and vectors of accumulated displacement on the Yele dam before the Wenchuan earthquake (displacement scaling factor: 1:50) 306

Figure 5-42: Contour plots of pore water pressure of the Yele dam at different stages (kPa) .. 308

Figure 5-43: FE mesh and boundary conditions for the dynamic analysis of the Yele dam 309

Figure 5-44: Dynamic response of the Yele dam in two directions (acceleration response spectra) 311

Figure 5-45: Dynamic response of the Yele dam in two directions (acceleration time histories) 312

Figure 5-46: Accumulated deformed mesh and vectors of accumulated displacement on the Yele dam after the Wenchuan earthquake (displacement scaling factor: 1:50) 315

Figure 5-47: Sub-accumulated deformed mesh and vectors of sub-accumulated displacement on the Yele dam due to the Wenchuan earthquake (displacement scaling factor: 1:600) 316

Figure 5-48: Contours of sub-accumulated shear strain and vertical strain on the Yele dam due to the Wenchuan earthquake..... 317

Figure 5-49: Contours of sub-accumulated shear strain and vertical strain on the Yele dam due to the Wenchuan earthquake..... 318

Figure 5-50: Monitoring points on the Yele dam..... 319

Figure 5-51: Sub-accumulated crest vertical displacement time histories at two locations on the dam crest due to the Wenchuan earthquake..... 319

Figure 5-52: Peak acceleration variation on the Yele dam..... 320

Figure 5-53: Peak acceleration variation on the largest section of the Yele dam recorded in the 23/10/2007 earthquake (after Xiong et al. (2008)) 321

Figure 5-54: Schematic graph for the seismic design method of Papadimitriou et al. (2014) .. 323

Figure 5-55: Variations of the parameter $k_{hmax}/(\ PGA_{crest}/g)$ and k_{hmax} 323

Figure 5-56: Stability analysis for the Yele dam..... 324

Figure 5-57: Sub-accumulated stress-stain loops at four locations on the Yele dam due to the Wenchuan earthquake..... 326

Figure 5-58: Sub-accumulated pore water pressure time histories at two locations on the Yele dam due to the Wenchuan earthquake 327

Figure 5-59: Vertical acceleration time histories at element 9 and 10 327

Figure 5-60: Sub-accumulated pore water pressure contour plot on the Yele dam due to the Wenchuan earthquake (kPa) 328

Figure 5-61: Final accumulated pore water pressure contour plot on the Yele dam after the Wenchuan earthquake (kPa) 328

Figure 6-1: FE mesh and dynamic boundary conditions for the parametric study 1..... 332

Figure 6-2: Accumulated deformed mesh and vectors of accumulated displacement on the Yele dam employing solid elements for reservoir simulation before the Wenchuan earthquake (displacement scaling factor: 1:50) 333

Figure 6-3: Contours of pore water pressure in the Yele dam at the end of the static analysis from the parametric study 1 (kPa) 334

Figure 6-4: Dynamic response of the Yele dam from the parametric study 1 (acceleration response spectra)..... 336

Figure 6-5: Dynamic response of the Yele dam from the parametric study 1 (acceleration time histories) 337

Figure 6-6: Sub-accumulated deformed mesh and vectors of sub-accumulated displacement on the Yele dam due to the Wenchuan earthquake from the parametric study 1 (displacement scaling factor: 1:600)..... 338

Figure 6-7: Sub-accumulated crest vertical displacement time histories at three locations on the Yele dam due to the Wenchuan earthquake from the parametric study 1 339

Figure 6-8: Dynamic response of the Yele dam from the parametric study 2 (acceleration response spectra)..... 342

Figure 6-9: Dynamic response of the Yele dam from the parametric study 2 (acceleration time histories) 343

Figure 6-10: Tangent shear modulus time histories at element 7 on the Yele dam due to the Wenchuan earthquake from the parametric study 2 343

Figure 6-11: Sub-accumulated deformed mesh and vectors of sub-accumulated displacement on the Yele dam due to the Wenchuan earthquake from the parametric study 2 (displacement scaling factor: 1:600)..... 344

Figure 6-12: Sub-accumulated crest vertical displacement time histories at two locations on the Yele dam due to the Wenchuan earthquake from the parametric study 2 345

Figure 6-13: Dynamic response of the Yele dam from the parametric study 3 (acceleration response spectra)..... 346

Figure 6-14: Dynamic response of the Yele dam from the parametric study 3 (acceleration time histories) 347

Figure 6-15: Sub-accumulated crest vertical displacement time histories at two locations on the Yele dam due to the Wenchuan earthquake from the parametric study 3 347

Figure 6-16: Accumulated deformed mesh and vectors of accumulated displacement on the Yele dam subjected to high reservoir water level before the Wenchuan earthquake (displacement scaling factor: 1:50)..... 349

Figure 6-17: Contour lines of pore water pressure on the Yele dam subjected to high reservoir water level at the end of the static analysis (kPa) 350

Figure 6-18: Dynamic response of the Yele dam from the parametric study 4 (acceleration response spectra)..... 352

Figure 6-19: Dynamic response of the Yele dam from the parametric study 4 (acceleration time histories) 353

Figure 6-20: Sub-accumulated deformed mesh and vectors of sub-accumulated displacement on the Yele dam due to the Wenchuan earthquake from the parametric study 4 (displacement scaling factor: 1:600)..... 354

Figure 6-21: Sub-accumulated crest vertical displacement time histories at two locations on the Yele dam due to the Wenchuan earthquake from the parametric study 4 355

List of tables

Table 2-1: Newmark method family 51

Table 2-2: Unconditional stability conditions of the CH method for the coupled formulation .. 67

Table 2-3: Soil properties for 1-D column analysis subjected to step loading..... 70

Table 2-4: Integration parameters for the CH method 70

Table 2-5: Integration parameters for the CH and Newmark methods 72

Table 2-6: Soil properties for 1-D column analysis subjected to harmonic loading 77

Table 2-7: Soil properties for 1-D column analysis subjected to impulse loading..... 82

Table 2-8: Parameters for the CH and Newmark method 83

Table 2-9: Soil properties for the elastic foundation analysis 87

Table 2-10: Soil properties for the elasto-plastic foundation analysis 93

Table 3-1: Soil parameters for the 1-D soil column 115

Table 3-2: Fundamental frequencies calculated based on Zienkiewicz et al.'s theory (1980b) 117

Table 3-3: Soil properties of the coupled 1-D column FE analysis 136

Table 3-4: Detailed soil properties for seven cases (χ=0.1) 137

Table 3-5: Soil parameters for the coupled 1-D soil column analysis 144

Table 3-6: Permeability values for parametric studies (coupled FE analysis) 145

Table 4-1: Earthquake data and site information 188

Table 4-2: Earthquake data for HINO site in three earthquake events..... 188

Table 4-3: Soil properties at the HINO site..... 192

Table 4-4: The integration parameters for CH method employed in site response analyses 194

Table 4-5: Parameters of the Logarithmic model for the nonlinear analysis 207

Table 4-6: Parameters of the ICG3S-1 model for the nonlinear analysis..... 213

Table 4-7: Parameters of the ICG3S-2 model for the nonlinear analysis..... 217

Table 4-8: Parameters of the ICG3S-2 model for the nonlinear analysis..... 228

Table 4-9: PGAs in three directions from parametric study 2..... 239

Table 4-10: Parameters for the shear modulus calibration..... 246

Table 4-11: PGA in three directions from the parametric study 5 248

Table 5-1: Soil properties for materials of Yele project..... 280

Table 5-2: Summaries of the seismic monitoring data..... 289

Table 5-3: The integration parameters for the CH method 292

Table 5-4: Parameters for the Yele dam materials by using the ICG3S-2 model 297

Table 5-5: Stages of the static analysis of the Yele dam..... 302

List of symbols

a, b, …q	Parameters composing the polynomial function of complex number z in Routh-Hurwitz conditions
a, b, c, d_1, d_2, d_3 and d_4	Model parameters for shear deformation simulation in Imperial College Generalised Small Strain Stiffness model
$a_0, a_1, a_2 .... a_n$	Multipliers in the polynomial function of complex number z in Routh-Hurwitz conditions
a_h and a_v	Horizontal and vertical accelerations in the pseudostatic method
A and B	Amplitudes of the one-dimensional harmonic waves propagating in upward direction and downward directions
A and B	Parameters controlling the variation of the Rayleigh damping
A, B, C and D	Four representing parameters in the polynomial function of complex number z in Routh-Hurwitz conditions
$[A]$	Amplification matrix of a time integration method
$[B]$	Matrix of derivatives of the shape function
c	Constant representing the damping characteristics of the material
c	Scalar form of the damping matrix
c	Compressional wave velocity employed in two-phase coupled formulations
c'	Soil material cohesion
c_o, c_d, δ_o and δ_d	Normalising parameters for the fast wave velocity, slow wave velocity, fast wave amplitude decay and slow wave amplitude decay respectively in Bardet and Sayed (1993)
c_1 and c_2	Fast and slow wave velocities
c_w	Wave velocity in the fluid
$[C]$	Global damping matrix

C_l, C_b, C_f and C_g	Four correction parameters representing respectively the effects of the sliding mass location, the stabilising berm, the foundation material stiffness and the sliding mass geometry in the seismic design method of Papadimitriou et al. (2014)
$\ddot{d}$, $\dot{d}$ and d	Acceleration, velocity and displacement of soil particles
D	Soil constrained modulus
$[D]$	Constitutive relation matrix
$D_{Undrained}$ and $D_{Drained}$	Soil constrained modulus under the undrained and drained conditions
e	Void ratio
E	Young's modulus
$[E]$	Vectors containing the derivatives of the pore fluid shape functions
f	Loading frequency
$f_{\max}$	Highest frequency of the input motion to be modelled
$f_{Undrained}$ and $f_{Drained}$	Fundamental frequency of a soil layer subjected to vertical motions under the undrained and drained conditions
$F_0(\omega)$ and $F_1(\omega)$	Transfer functions for undamped and damped soil layers
$F_{bb}(\gamma)$	Backbone curve function
F_h and F_v	Horizontal and vertical inertial forces applied in the pseudostatic method
g	Gravitational acceleration
$g(\theta)$	Function defining the shape of the yield surface on the deviatoric plane
$[G]$	Global pore fluid inertia matrix
G_0, p'_{ref} and m_G	Parameters prescribing the empirical expression for maximum shear modulus in Hardin and Black (1968)
G_s	Specific gravity
$G_{\sec}$, $G_{\tan}$ and $G_{\max}$	Secant, tangent and maximum shear modulus
h	Hydraulic head

H	Depth of a soil layer
$\{i_G\}$	The unit vector
J and E_d	3-D stress and strain invariants
J^* and E_d^*	Modified 3-D stress and strain invariants
J_r^* and $E_{d,r}^*$	Modified stress and strain invariants at the reversal point
J_L, $E_{d,\mathrm{L}}$ and c	Model parameters for the Logarithmic model
k	Permeability
k	Scalar form of the stiffness matrix
k	Wave number
$[k]$	Permeability matrix
k^*	Complex wave number
k_0	Coefficient of earth pressure at rest
k_h and k_v	Horizontal and vertical seismic coefficients in the pseudostatic method
k_{hmax}	Peak horizontal coefficients in seismic design methods
$[K]$	Global stiffness matrix
K_f	Bulk modulus of the pore fluid
K_{sec}, $K_{\tan}$ and $K_{\max}$	Secant, tangent and maximum bulk modulus
l	Scalar form of the consolidation stiffness matrix
l	Element size limit
$[L]$	Global off diagonal sub-matrix in consolidation stiffness matrix
m	Scalar form of the mass matrix
$\{m\}^T$	Multiplying vector equal to $\{1 \quad 1 \quad 1 \quad 0 \quad 0 \quad 0\}$
$[M]$	Global mass matrix
n	Material porosity
$[N]$	Shape function matrix
$[N_P]$	Shape function matrix for the pore fluid
OCR	Over consolidation ratio
p	Pore water pressure
p'	Mean effective stress

Q	Sink or/and sources
r, s, t, d_5, d_6, d_7 and d_8	Model parameters for volumetric deformation simulation in Imperial College Generalised Small Strain Stiffness model
R( ) and I( )	Real and imaginary parts of a complex number
$\mathrm{Re}(z)$	Real part of the complex number z in Routh-Hurwitz conditions
s	Scalar form of the compressibility matrix
$[S]$	Global pore fluid compressibility matrix
t	Current time in any analysis
t_k and t_{k+1}	The kth and k+1th time increment
$t_{k+1-\alpha_m}$ and $t_{k+1-\alpha_f}$	Time instant at $k+1-\alpha_m$ and $k+1-\alpha_f$
T	Loading period
T	Undamped natural period of a single degree of freedom system
T	The nonlinear fundamental period of the foundation vibration in the seismic design method of Papadimitriou et al. (2014)
T'	Undamped natural period of a single degree of freedom system obtained by the numerical solution
T_o	The nonlinear fundamental period of the dam vibration in the seismic design method of Papadimitriou et al. (2014)
T_{oe}	The elastic fundamental period of the dam vibration in the seismic design method of Papadimitriou et al. (2014)
T_e	The predominant period of the input excitation in the seismic design method of Papadimitriou et al. (2014)
T_1 and $T_{1\infty}$	Fundamental periods of a dam in a narrow canyon and in an infinitely wide canyon
u, v and w	One-directional solid skeleton displacement, pore fluid displacement and their relative displacement
$\ddot{u}$	Relative acceleration of shear beams to bases in the shear beam method

$\ddot{u}_b$	Absolute acceleration of rigid bases in the shear beam method
u_x and u_y	Horizontal and vertical displacement
$\{v\}$	Fluid velocity vector
v_x, v_y and v_z	Three components of the pore fluid seepage velocity in the coordinate directions
v_b	The shear wave velocity of the foundation material in the seismic design method of Papadimitriou et al. (2014)
v_s	Shear wave velocity
$v_{s\min}$	Minimum shear wave velocity
v_p	Compressional wave velocity
$v_{pUndrained}$ and $v_{pDrained}$	Compressional wave velocity under the undrained and drained conditions
W	Weight of a potential sliding mass in the pseudostatic method
W	Maximum strain energy of soil materials
z	A complex number in Routh-Hurwitz conditions
z	Vertical distance in a soil layer from the coordinate origin
α and R	Model parameters for the Logarithmic model
α and δ	Integration parameters for the Newmark method
α_m and α_f	Integration parameters for the CH method
β	Integration parameter of the time marching scheme in the consolidation equation
β_1 and β_2	Newmark integration parameters in finite element program SWANDYNE (Chan, 1988)
$\overline{\beta}_1$	Integration parameter for consolidation equation in finite element program SWANDYNE (Chan, 1988)
γ_f	Bulk unit weight for the pore fluid
δ	Amplitude decay employed by to quantify the wave attenuation in Bardet and Sayed (1993)
$\Delta\ddot{d}$, $\Delta\dot{d}$ and Δd	Incremental acceleration, velocity and displacement of soil

	particles
$\{\Delta\ddot{d}\}$, $\{\Delta\dot{d}\}$ and $\{\Delta d\}$	Incremental acceleration, velocity, displacement vector
$\{\Delta F\}$	Incremental right hand side flow vector
$\{\Delta F\}_{t_k}$	Out-of-balance flow at the previous time increment
Δp	Incremental pore water pressure
$\{\Delta p\}$	Incremental pore water pressure vector
$\{\Delta R\}$	Incremental right hand side load vector
$\{\Delta R\}_{t_k}$	Out-of-balance force at the previous time increment
Δt	Time step
Δt_{cr}	Critical time step
ΔW	Loop area of the hysteretic stress-strain curve
ε	Order of the accuracy of a time integration method
ε_1, ε_2 and ε_3	Principle strains
ε_v, ε_h and ε_{vol}	Vertical, horizontal and volumetric strains
θ	Lode's angle
λ_1, λ_2 and λ_3	Eigenvalues of the amplification matrix $[A]$
$\lambda_{\min}$	Minimum wave length
ν	Poisson's ratio
ξ	Material damping ratio
ξ_1 and ξ_2	Damping ratios for fast and slow waves
ρ	Material density
ρ	Spectral radius of the amplification matrix $[A]$
ρ_s and ρ_f	Densities of the solid skeleton and pore fluid
ρ_∞	Spectral radius at infinity of a time integration method
σ_1', σ_2' and σ_3'	Principle effective stresses
σ_z and ε_z	Normal stress and normal strain
τ and γ	Shear stress and shear strain
τ_r and γ_r	Shear stress and shear strain at the reversal point
τ_{ref}	Reference shear stress for the Logarithmic model
ϕ	Scalar forms of the permeability matrix

ϕ	A complex number representing different types of compressional waves
ϕ'	Angle of shearing resistance
$[\Phi]$	Global permeability matrix
χ	Ratio between the effective soil constrained modulus and pore fluid bulk modulus
ω	Circular frequency of an input motion
ω_1 and ω_2	Frequencies defining the concerned frequency range over which the variation of Rayleigh damping is approximately constant

CHAPTER 1
Introduction

1.1 Background

The safety of geotechnical structures under earthquake loading is of vital importance. Seismically induced destruction of large-scale geotechnical structures, such as dams, slopes and building foundations, can significantly threaten human lives. Furthermore, failures of geotechnical structures in railway embankments, airports and tunnels may also affect the quick response for post-earthquake rescue operations. Therefore, there is a need to conduct in-depth investigation of the seismic response of geotechnical structures, in order to better understand their seismic behaviour, predict and mitigate potential failure mechanisms.

Among the available methodologies for the dynamic analysis of geotechnical structures, the finite element (FE) method is probably the only one capable of including realistic modelling of complete boundary value problems. This is achieved through the implementation of appropriate constitutive models, boundary conditions, time integration schemes and hydro-mechanical (HM) coupling. The development of soil constitutive models improves the simulation accuracy of real dynamic soil behaviour. The implementation of the HM coupled formulation realistically simulates two-phase state of soil materials. Furthermore, boundary conditions assist dynamic FE analyses to reduce computational cost and accurately simulate the wave propagation mechanism in

the far-field. Finally, time integration methods are employed to achieve stable, accurate and realistic solutions for dynamic analyses.

The seismic response of geotechnical structures has been studied by researchers by employing different analysis methods. However, difficulties still exist in developing advanced numerical analysis methods to accurately simulate real dynamic soil behaviour, in terms of soil constitutive models, HM coupled methods, consideration of three-directional (3-D) input motions, etc. For instance, the undrained condition has been widely assumed in dynamic analyses of geotechnical structures because of the short duration of dynamic loading. However, if the dynamic loading duration is relatively long or/and the soil permeability is relatively high, consolidation can occur during the loading. Consequently, the undrained assumption is inappropriate and the two-phase coupled formulation should be employed to more accurately simulate the soil-pore water interaction effects in saturated porous materials. Furthermore, the multi-directional ground motions have been increasingly considered in the earthquake-resistance design of critical structures, such as large-scale dams and nuclear power plants. However, the dynamic response of geotechnical structures subjected to multi-directional loading and their coupling effects have not been investigated in great detail.

1.2 Scope of research and layout of thesis

This research aims to numerically simulate and investigate the seismic behaviour of geotechnical structures under multi-directional loading by employing the coupled HM formulation of the Imperial College Finite Element Program (ICFEP) (Potts and Zdravković, 1999). The scope of the research work can be summarised as follows:

In order to achieve stable solutions for dynamic coupled consolidation analyses, the first task is to investigate the stability of the generalised-α method (CH method) for the coupled consolidation formulation. The CH method satisfies the main requirements for an efficient time marching algorithm, which include unconditional stability for linear problems, second order accuracy and controllable numerical dissipation in the high frequency range (Hilber and Hughes, 1978). A stability analysis was conducted for the CH method based on an analytical framework and the corresponding stability conditions were derived. The proposed stability conditions were validated by FE analyses

considering a range of loading conditions and soil permeability values. Since the CH method is a generalisation of the Newmark, HHT and WBZ methods, the stability investigation of the CH method for the two-phase coupled formulation is relevant for most of the commonly utilised time integration methods. This part of work is presented in Chapter 2, following a discussion of some commonly used time integration methods and an introduction of the implementation of the CH method for the HM coupled formulation in ICFEP.

The second objective is to explore the site response due to the vertical component of the ground motion. For this purpose, Chapter 3 first reviews the evidence of strong vertical ground motions observed in earthquake events and spectral design methods for the vertical site response. Subsequently, the vertical site response was simulated by employing a one-phase total-stress analytical solution in frequency domain. The compressional wave propagation mechanism in saturated porous soils was further investigated by the coupled consolidation formulation accounting for HM coupling. Finally, the undertaken coupled FE analyses explored the effects of the parameters characterising the hydraulic phase, i.e. soil permeability and soil state conditions, on the vertical site response, both in terms of frequency content and amplification. Correspondingly, the respective associated parameters, i.e. the predicted wave velocities and damping ratios, are qualitatively assessed.

The third aim of this study is to simulate and investigate the multi-directional site response employing the coupled HM formulation. The HINO site of the Japanese KiK-net down-hole array earthquake monitoring system was considered for the analyses. Through the FE simulations, different aspects of the numerical modelling for the site response analysis, such as the constitutive model, the use of 3-D input motion and the coupled consolidation formulation, were investigated and validated by the recordings from the KiK-net system. Further parametric studies investigated the impact of the variation of the water table, the soil permeability and the 3-D input motion on the multi-directional site response. The investigation of the multi-directional site response is presented in Chapter 4, following a discussion of the existing investigations for site response analyses.

The fourth objective is to employ the developed numerical model to investigate a more complicated boundary value problem. The seismic response of a well-documented Chinese rockfill dam, the Yele dam, was investigated with the dynamic plane-strain FE

analysis, accounting for HM coupling and nonlinear soil response. A static analysis was first undertaken aiming to simulate the geological history of the dam foundation, the dam construction, the reservoir impounding and the dam operation. The subsequent dynamic analysis computed the seismic behaviour of the Yele dam under the 2008 Wenchuan earthquake loading. The numerical predictions were compared against the available static and dynamic monitoring data, which allowed for a rigorous validation of the developed numerical model. Furthermore, the simulated seismic behaviour of the Yele dam was analysed, which led to a seismic safety assessment. The static and dynamic analyses of the Yele dam are presented in Chapter 5, following a discussion concerning the development of the dynamic FE method associated with applications for the earth and rockfill dams.

Furthermore, parametric studies of the Yele dam were conducted to explore the effects of several critical factors on the seismic response of rockfill dams, i.e. the reservoir simulation method, the permeability of materials comprising the dam body, the vertical ground motion and the reservoir water level. The influence of these factors was interpreted in terms of the dam deformed shape, acceleration time histories and crest settlements. This part of work is presented in Chapter 6.

Finally, Chapter 7 summarises the findings of the research and gives recommendations for related future studies.

CHAPTER 2

The stability of the Generalised-α time integration method in solid-pore fluid coupled formulation

2.1 Introduction

In dynamic FE analysis, the governing equation of motion is a second order differential equation. Generally, there are three categories of methods available to solve this second order equation. These are the frequency domain analysis, the modal analysis and the direct time integration method. The direct time integration method has a distinct advantage over the two other approaches in that it reproduces both material and geometric nonlinearities. Since 1950s, various time integration methods have been proposed, such as the Newmark method (Newmark, 1959) and the Generalised-α method (CH method) of Chung and Hulbert (1993), which have been widely implemented into FE programs and successfully utilised to solve numerically the equation of motion for one-phase materials. The main requirements of an efficient time marching algorithm are unconditional stability for linear problems, second order accuracy and controllable numerical dissipation in the high frequency range (Hilber and Hughes, 1978). The role of numerical damping is to eliminate spurious high-frequency oscillations that are introduced into the solution due to poor spatial representation of the

high-frequency modes. The CH method is an implicit, unconditionally stable, second order accurate integration scheme that allows such controllable numerical dissipation.

Depending on the soil permeability, the rate of loading and the hydraulic boundary conditions, it is often necessary to employ coupled analysis to accurately model the two-phase behaviour of the soil. Dynamic analyses are further complicated by the presence of the inertia forces of the different phases (i.e. solid skeleton and pore fluid) and the coupling between them. Hence, the formulation of the CH method was extended by Kontoe (2006) and Kontoe et al. (2008b) to enable the solution of dynamic coupled consolidation problems and was then implemented in the FE program ICFEP (Imperial College Finite Element Program) (Potts and Zdravković, 1999). The key feature of unconditional stability of this method has been comprehensively investigated by previous studies, both analytically and numerically, but only for the one-phase formulation (Chung and Hulbert, 1993). The two-phase coupled FE formulation requires an additional equation (the dynamic consolidation equation) and an additional unknown (pore fluid pressure). Aiming to solve two dynamic coupled equations (i.e. the equation of motion and the consolidation equation), the time integration method is applied to both equations. This not only increases the complexity of the implementation, but it also changes the numerical features of the time integration method. Therefore, the numerical stability of the CH method needs to be investigated rigorously for two-phase coupled problems.

In this chapter, the stability of the CH method for the coupled formulation is analytically investigated for the first time and the corresponding theoretical stability conditions are derived. The analytically derived stability conditions are validated by FE analyses considering a range of loading conditions and for various soil permeability values, showing that the numerical results are in agreement with the theoretical investigation. Then, the stability characteristics of the CH method are explored beyond the limits of the theoretical investigation, assuming elasto-plastic soil behaviour which is prescribed with a bounding surface plasticity constitutive model. Furthermore, since the CH method is a generalisation of the Newmark (Newmark, 1959), HHT (Hilber et al., 1977) and WBZ (Wood et al., 1981) methods, the stability investigation of the CH method for the two-phase coupled formulation is relevant for most of the commonly utilised time integration methods.

2.2 One-phase static and dynamic FE formulations

All the analyses conducted in this research are based on the ICFEP formulation, which employs the displacement-based FE method. The characteristics of soil behaviour, such as nonlinearity, plasticity and hysteretic response, can be realistically simulated by various advanced elasto-plastic constitutive models in ICFEP. Furthermore, the existing formulation of ICFEP allows the modelling of two-phase materials and the performance of dynamic analysis. For the latter, various time integration schemes and boundary conditions are available in the program. A brief description of the static and dynamic formulations is presented in this chapter. However, the finer details of the FE theory are beyond the scope of this thesis. Further information and detailed description of the FE method in geotechnical engineering can be found in Potts and Zdravković (1999).

The FE method considers the geometry of the problem as a continuum composed of an assemblage of discrete elements, which are defined by nodes at element boundaries. Since the FE method satisfies the requirements of a true theoretical solution, the FE formulation can be obtained by employing the four requirements, which are equilibrium, compatibility, material constitutive relations and boundary conditions. As a result, the global FE equation, obtained from the principle of minimum potential energy, is shown in Equation 2-1, where the displacement is the only degree of freedom (DOF). It should be noted that the sign convention of tension positive is employed in this thesis to present the FE formulation.

$$[K]\{\Delta d\} = \{\Delta R\} \qquad 2\text{-}1$$

where

$$[K] = \sum_{i=1}^{N}\left(\int_{Vol} [B]^T [D][B] dVol \right)$$

where $[K]$ is the global stiffness matrix, $[D]$ is the constitutive relation matrix, $[B]$ is the matrix of derivatives of the shape function, $\{\Delta d\}$ is the incremental nodal displacement vector and $\{\Delta R\}$ is the incremental right hand side load vector.

Similarly, the dynamic equation of motion for the one-phase FE formulation can be obtained by satisfying the same conditions as that for the static formulation, namely,

equilibrium, material constitutive relations, compatibility and boundary conditions. In the dynamic equation of motion, inertial forces, damping forces and internal forces (stresses) are balanced by external loads, as described by the equation below.

$$[M]\{\Delta\ddot{d}\}+[C]\{\Delta\dot{d}\}+[K]\{\Delta d\}=\{\Delta R\} \qquad 2\text{-}2$$

where

$$[M]=\sum_{i=1}^{N}\left(\int_{Vol}[N]^T\rho[N]dVol\right)$$

$$[C]=\sum_{i=1}^{N}\left(\int_{Vol}[N]^T c[N]dVol\right)$$

$$[K]=\sum_{i=1}^{N}\left(\int_{Vol}[B]^T[D][B]dVol\right)$$

where $[M]$ is the global mass matrix, $[C]$ is the global damping matrix, $[K]$ is the global stiffness matrix, $[N]$ is the shape function matrix, $[B]$ is the matrix of derivatives of the shape function, $[D]$ is the constitutive relation matrix, ρ and c are the material density and damping ratio of the material, $\{\Delta\ddot{d}\}$, $\{\Delta\dot{d}\}$ and $\{\Delta d\}$ are the incremental acceleration vector, the incremental velocity vector and the incremental displacement vector respectively, and $\{\Delta R\}$ is the incremental external load vector.

2.3 Two-phase coupled dynamic FE formulation

The one-phase dynamic formulation presented in the previous section allows the simulation of either purely drained or purely undrained condition. The assumption of undrained behaviour is of acceptable accuracy for relatively impermeable materials or/and under loading of relatively short duration. Therefore, the undrained condition is widely used in dynamic analysis because of the short duration of dynamic loading. However, for geotechnical earthquake engineering problems, if the dynamic loading duration is relatively long or/and the soil permeability is relatively high, consolidation can occur during the loading. Consequently, the undrained assumption is inappropriate and the two-phase coupled formulation should be employed to more accurately simulate the soil-pore water interaction effects in saturated porous materials.

In order to precisely simulate the static and dynamic behaviour of saturated porous materials, the static coupled consolidation formulation was implemented into ICFEP (Potts and Zdravković, 1999) and was later extended to deal with dynamic loading by Hardy (2003) and Kontoe (2006). The coupled consolidation FE formulation is based on Biot's consolidation theory, proposed in 1956 and 1962, which was firstly implemented numerically by Ghaboussi and Wilson (1973). Zienkiewicz and Shiomi (1984) identified three categories of dynamic coupled formulations, namely the u-p formulation, the u-p-w formulation and the u-U formulation, where u, w, U and p denote the solid displacement, the fluid velocity relative to the solid component, the fluid displacement and the pore water pressure respectively. Among these three formulations, the u-p-w formulation is the most rigorous one and fully satisfies Biot's theory. However, according to Zienkiewicz and Shiomi (1984), the effects of the fluid acceleration relative to the solid and its convective terms are insignificant in the frequency range that is of concern in earthquake engineering problems. Therefore, by ignoring the relative fluid acceleration and its convective terms, Biot's theory can be simplified to the u-p formulation. Furthermore, the u-U formulation is another simplified form of the Biot's theory, which utilises U to represent the fluid deformation instead of using p in the u-p formulation. However, there is no obvious predominance between the u-p and u-U formulations according to Smith (1994). Since one less DOF (relative fluid velocity) is involved in the u-p and u-U formulations, both formulations are more computationally efficient than the u-p-w formulation. Therefore, the u-p formulation was adopted and implemented in ICFEP, which considers u and p as the main unknowns.

In the coupled consolidation formulation of ICFEP, the dynamic equation of motion can be obtained by employing equilibrium, material constitutive relations, compatibility and boundary conditions, in terms of effective stresses and pore fluid pressure, as shown by the following expressions (Hardy, 2003; Kontoe, 2006).

$$[M]\{\Delta\ddot{d}\}+[C]\{\Delta\dot{d}\}+[K]\{\Delta d\}+[L]\{\Delta p\}=\{\Delta R\} \qquad 2\text{-}3$$

where

$$[L]=\sum_{i=1}^{N}\left(\int_{Vol}\{m\}[B]^{T}[N_p]dVol\right)$$

$$\{m\}^{T}=\{1 \quad 1 \quad 1 \quad 0 \quad 0 \quad 0\}$$

where $[K]$ is the effective stiffness matrix, $[L]$ is the coupling matrix, $[N_P]$ is the shape function matrix for the pore fluid, and $\{\Delta p\}$ is the incremental pore water pressure vector.

In addition to the dynamic equation of motion, the consolidation equation for the coupled formulation is derived from the water flow continuity equation given by Equation 2-4.

$$\frac{\partial v_x}{\partial x}+\frac{\partial v_y}{\partial y}+\frac{\partial v_z}{\partial z}+\frac{n}{K_f}\cdot\frac{\partial p}{\partial t}-Q=\frac{\partial \varepsilon_{vol}}{\partial t} \qquad 2\text{-}4$$

where v_x, v_y and v_z represent three components of the pore fluid seepage velocity in the coordinate directions, Q is any sink or/and sources (the sign of outflow is positive), and ε_{vol} is the volumetric strain for the solid skeleton. The continuity equation expresses the flow of pore fluid in and out of a soil element of unit dimensions. It should be noted that the term $\frac{n}{K_f}\cdot\frac{\partial p}{\partial t}$ denotes the volume stored in the solid element because of the fluid compressibility, where n and K_f are the porosity of the soil and the bulk modulus of the pore fluid. In addition, Darcy's law (Equation 2-5) is applied to express the pore fluid seepage velocity.

$$\{v\}=-[k]\cdot\left(\{\nabla h\}+\frac{1}{g}\{\ddot{d}\}\right) \qquad 2\text{-}5$$

$$h=\frac{-p}{\gamma_f}+\left(x\cdot i_{Gx}+y\cdot i_{Gy}+z\cdot i_{Gz}\right) \qquad 2\text{-}6$$

where $\{v\}$ is the fluid velocity vector, $[k]$ is the permeability matrix, h is the hydraulic head expressed by Equation 2-6, g is the gravity and $\{\ddot{d}\}$ is the acceleration vector of the soil particles, which represents the impact of the soil particles' acceleration to the pore fluid pressure. Furthermore, $\{i_G\}=\{i_{Gx}\quad i_{Gy}\quad i_{Gz}\}^T$ is the unit vector parallel, but in the opposite direction, to the gravity and γ_f is the bulk unit weight for the pore fluid.

The principle of virtual work is applied to the continuity equation (Equation 2-4), which leads to the equation below.

$$\int_{Vol}\left[\{v\}^T\{\nabla\{\Delta p\}\}+\frac{n}{K_f}\cdot\frac{\partial p}{\partial t}\{\Delta p\}-\frac{\partial \varepsilon_{vol}}{\partial t}\{\Delta p\}\right]dVol=\{Q\}\{\Delta p\} \qquad 2\text{-}7$$

Substituting Equations 2-5 and 2-6 into Equation 2-7 and also approximating terms $\frac{\partial p}{\partial t}$ and $\frac{\partial \varepsilon_{vol}}{\partial t}$ as $\frac{\Delta p}{\Delta t}$ and $\frac{\Delta \varepsilon_{vol}}{\Delta t}$ respectively, the consolidation equation is upgraded to Equation 2-8:

$$\int_{Vol}\left[\int_{t_k}^{t_k+\Delta t}\left[-[k]\left(\frac{-\{\nabla p\}}{\gamma_f}+\{i_G\}+\frac{1}{g}\{\ddot{d}\}\right)^T\{\nabla\{\Delta p\}\}\right]dt+\frac{n}{K_f}\{\Delta p\}\{\Delta p\}-\Delta\varepsilon_{vol}\{\Delta p\}\right]dVol=\{Q\}\{\Delta p\}\Delta t \qquad 2\text{-}8$$

Moreover, the FE form of Equation 2-8 is given as:

$$\int_{t_k}^{t_k+\Delta t}[\Phi]\{p\}dt-\int_{t_k}^{t_k+\Delta t}[G]\{\ddot{d}\}dt+[S]\{\Delta p\}-[L]^T\{\Delta d\}=([n]+\{Q\})\Delta t \qquad 2\text{-}9$$

where

$$[\Phi]=\sum_{i=1}^{N}\left(\int_{Vol}\frac{1}{\gamma_f}[E]^T[k][E]dVol\right)$$

$$[G]=\sum_{i=1}^{N}\left(\int_{Vol}\frac{1}{g}[N]^T[k][E]dVol\right)$$

$$[S]=\sum_{i=1}^{N}\left(\int_{Vol}\frac{n}{K_f}[N_p]^T[N_p]dVol\right)$$

$$[n]=\sum_{i=1}^{N}\left(\int_{Vol}[E]^T[k]\{i_G\}dVol\right)$$

$$[E]=\begin{bmatrix}\frac{\partial N_p}{\partial x} & \frac{\partial N_p}{\partial y} & \frac{\partial N_p}{\partial z}\end{bmatrix}^T$$

In order to solve the integrals in Equation 2-9, a time marching scheme is applied, which is shown in Equation 2-10, where β is the integration parameter of the applied time marching scheme. As illustrated in Figure 2-1, the pore fluid integral on the left hand side of Equation 2-10 is represented by the grey area, which can be approximated by the shaded area through adopting the time marching scheme. Based on the principle of this time marching scheme, the β values should be bounded between 0 and 1.

$$\int_{t_k}^{t_k+\Delta t}\{p\}dt = \left[\{p_{t_k}\}+\beta\{\Delta p\}\right]\Delta t$$
$$\int_{t_k}^{t_k+\Delta t}\{\ddot{d}\}dt = \left[\{\ddot{d}_{t_k}\}+\beta\{\Delta \ddot{d}\}\right]\Delta t \qquad 2\text{-}10$$

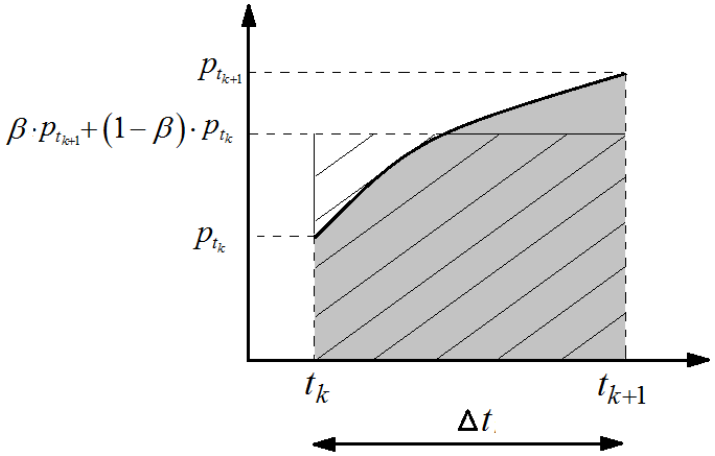


Figure 2-1: Approximation of pore water pressure integral (after Potts and Zdravković (1999))

By substituting Equation 2-10 into Equation 2-9, the FE form of the consolidation equation is shown in Equation 2-11.

$$-[\Phi]\left(\{p_{t_k}\}+\beta\{\Delta p\}\right)+[G]\left(\{\ddot{d}_{t_k}\}+\beta\{\Delta \ddot{d}\}\right)-[S]\frac{\{\Delta p\}}{\Delta t}+[L]^T\frac{\{\Delta d\}}{\Delta t}=-[n]-\{Q\} \qquad 2\text{-}11$$

The incremental FE form of the consolidation equation can be rearranged from the previous equation, shown as:

$$\left(-\beta\cdot\Delta t[\Phi]-[S]\right)\{\Delta p\}+\beta\cdot\Delta t[G]\{\Delta \ddot{d}\}+[L]^T\{\Delta d\}=\left(-[n]-\{Q\}+[\Phi]\{p_{t_k}\}-[G]\{\ddot{d}_{t_k}\}\right)\Delta t \qquad 2\text{-}12$$

2.4 Direct time integration methods

The main principle of the direct time integration method is that the dynamic equation is discretised into a number of small time increments Δt and the governing equation is satisfied at discrete time intervals. Furthermore, variations for two of the three variables (i.e. acceleration, velocity and displacement) within each increment are assumed. What distinguishes the various time integration methods is the adopted variation of the variables within each increment. Since 1950s, various direct time

integration methods have been proposed. Among all of these methods, the Newmark method and the CH method are probably the most representative as they have been widely implemented in FE programs. Therefore, the basic theories of these two methods are introduced briefly in this section, as well as their numerical features, i.e. stability and numerical damping.

2.4.1 Numerical characteristics of time integration methods

The main requirements of an efficient time marching algorithm are unconditional stability for linear problems, second order accuracy, controllable numerical dissipation in the high frequency range, self-starting and no tendency for pathological overshooting (Hilber and Hughes, 1978). However, herein three of them, the unconditional stability, second order accuracy and controllable numerical dissipation are examined in this section.

Stability

A time integration method is considered stable when it produces a numerical solution which remains always bounded (Bathe, 1996). In order to investigate the stability of a time integration method, the scalar form of the dynamic equilibrium equation of a single degree-of-freedom (SDOF) system subjected to free vibration is considered, given by Equation 2-13.

$$m \cdot \ddot{d} + c \cdot \dot{d} + k \cdot d = 0 \qquad \text{2-13}$$

where m, c and k are the mass, damping and stiffness of a SDOF model, d, $\dot{d}$ and $\ddot{d}$ denote the displacement, velocity and acceleration respectively.

The fundamental assumption of a time integration method is that the acceleration, velocity and displacement at a specific increment can be expressed as a function of these variables at previous increments, as follows:

$$\begin{Bmatrix} \ddot{d}_{t_{k+1}} \\ \dot{d}_{t_{k+1}} \\ d_{t_{k+1}} \end{Bmatrix} = [A] \begin{Bmatrix} \ddot{d}_{t_k} \\ \dot{d}_{t_k} \\ d_{t_k} \end{Bmatrix} \qquad \text{2-14}$$

where $\ddot{d}_{t_{k+1}}$, $\dot{d}_{t_{k+1}}$ and $d_{t_{k+1}}$ are the acceleration, velocity and displacement at time increment t_{k+1}. Similarly $\ddot{d}_{t_k}$, $\dot{d}_{t_k}$ and d_{t_k} are the acceleration, velocity and displacement at time increment t_k, and $[A]$ is the amplification matrix controlling the stability, accuracy and other numerical features of the considered time integration method. Based on the definition of numerical stability, for a time integration method to be stable, the matrix $[A]$ should be bounded. Namely, it should satisfy the following condition:

$$\|A\kappa\| \leq Constant \qquad 2\text{-}15$$

where κ is a real number. To fulfil Equation 2-15, the modulus of the eigenvalues of matrix $[A]$ should be less than one, expressed by the following equation.

$$\rho(A) = \max\{|\lambda_1|, |\lambda_2|, |\lambda_3|\} \leq 1 \qquad 2\text{-}16$$

where ρ is the spectral radius of the matrix $[A]$, and λ_1, λ_2 and λ_3 are the eigenvalues of the matrix $[A]$.

Based on their stability characteristics, time integration schemes can be divided into two categories: unconditionally stable methods and conditionally stable methods. For unconditionally stable methods, the stability of the numerical solution is independent of the size of the time step Δt, while for conditionally stable methods, the stability of the numerical solution depends on the size of the time step Δt, where the values of Δt should be less than a critical value Δt_{cr}. This critical value is a fraction of the natural period of a SDOF system. For a multi DOF system, i.e. a FE model, the critical value Δt_{cr} is a fraction of the smallest natural period of all vibration modes, which results in severe restriction on the size of the time step and usually leads to high computational cost. Therefore, unconditionally stable methods are generally preferable in FE analysis, without limiting the size of the time step by stability requirements.

Moreover, time integration schemes can also be categorised as explicit and implicit schemes. The advantage of explicit schemes is that the inversion of the stiffness matrix is not involved in the solution process. However, based on Dahlquist (1963), the explicit schemes are all conditionally stable, which on the other hand increases the computational cost.

Accuracy

After satisfying the stability condition, accuracy is the second critical numerical feature for a time integration method. Generally, the accuracy depends on the size of the time step. The numerical solution approaches the exact solution when the time step tends to zero. Two kinds of numerical error control the accuracy of a time integration method; the period elongation (PE) and the amplitude decay (AD). In order to illustrate these two numerical errors, the dynamic response of an undamped SDOF oscillator subjected to free vibration is shown in Figure 2-2, in terms of the time history of displacement (d) normalised by the initial displacement (d_0). The dash and the solid lines represent the numerical solution and the closed form solution respectively. Firstly, the period elongation is given by the following expression.

$$PE = \left(T' - T\right)/T \tag{2-17}$$

where T' is the natural period of the system obtained by the numerical solution and T is the actual natural period of the system. Secondly, the amplitude decay at time t_k is expressed by the following equation.

$$AD = 1 - \frac{d_{t_k + T'}}{d_{t_k}} \tag{2-18}$$

It should be noted that the magnitude of the numerical error is proportional to $\left(\Delta t / T\right)^{\varepsilon}$, where ε denotes the order of the accuracy. Hilber and Hughes (1978) suggested that the second order accurate time integration methods are superior to the first order accurate methods. In addition, Dahlquist theorem (1963) stated that third order accurate linear multi-step methods are only conditionally stable. Consequently, second order accuracy is the optimum level of accuracy for a time integration method (Kontoe, 2006).

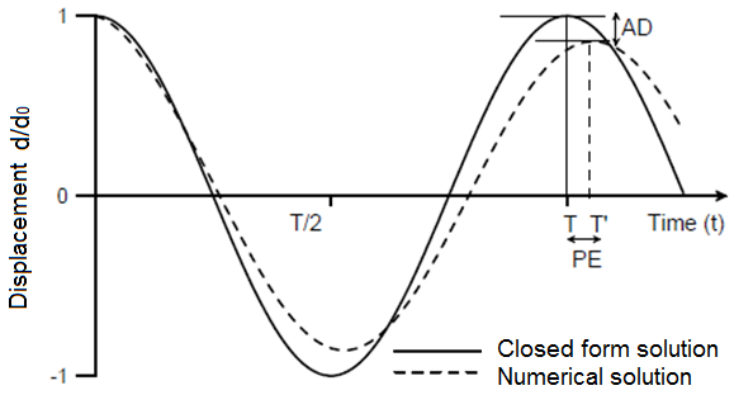


Figure 2-2: Illustration of PE and AD in numerical solution (after Kontoe (2006))

Controllable numerical dissipation

Numerical damping is another critical numerical feature for a time integration method. In FE analysis, the high frequency modes involve propagating waves of short wave length. Due to the poor discretisation of the FE mesh, the response of a FE system in the high frequency range cannot be simulated accurately, which can lead to spurious high frequency vibrations. In order to eliminate these spurious high frequency oscillations, numerical damping needs to be introduced to generate algorithmic dissipation for the high frequency vibrations. However, in geotechnical earthquake engineering, the seismic response of geotechnical structures is usually restricted to a relatively low frequency range (up to 15-20 Hz). Therefore, even though the high frequency vibrations are dissipated by the introduced numerical damping, the accuracy of the dynamic analysis can be well retained. Furthermore, controllable numerical dissipation is a desirable characteristic of time integration methods, because optimum of high frequency dissipation can be achieved without affecting the low frequency response.

The spectral radius (ρ) can be considered as a measure for the numerical damping. The characteristics of the algorithmic dissipation of a time integration scheme can be investigated by plotting the spectral radius (ρ) against $\Delta t / T$, where T is the natural period of an undamped SDOF system and Δt is the time step. The variations of spectral radii of four time integration schemes are shown in Figure 2-3, where $\rho = 1$ means no numerical damping and $\rho = 0$ means that the maximum numerical damping is obtained. It is suggested by Wood (1990) that the optimum algorithm dissipation is

obtained when ρ stays close to 1 for as long as possible and decreases to approximately 0.5-0.8 as $\Delta t / T$ reaches infinity. However, the four time integration methods are introduced in detail in Section 2.6.3.

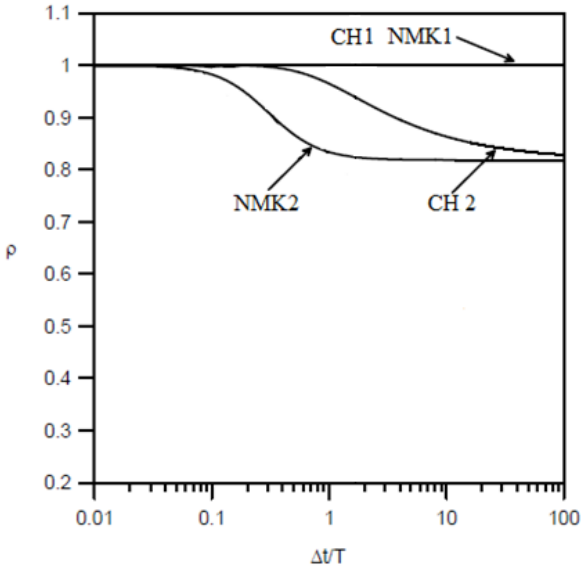


Figure 2-3: Spectral radii for four time integration methods (after Kontoe (2006))

2.4.2 Newmark method

The Newmark method, proposed by Newmark in 1959, is a family of time integration algorithms implemented widely in numerical analysis. It utilises a truncated Taylor's expansion to approximate the variations of acceleration, velocity and displacement between t_k and t_{k+1}, and to finally calculate the variables at increment t_{k+1}, by using the known variables at increment t_k. The basic equations of the Newmark method are shown in Equations 2-19 and 2-20.

$$d_{t_{k+1}} = d_{t_k} + \dot{d}_{t_k} \cdot \Delta t + (0.5 - \alpha) \cdot \ddot{d}_{t_k} \cdot \Delta t^2 + \alpha \cdot \ddot{d}_{t_{k+1}} \cdot \Delta t^2 \qquad 2\text{-}19$$

$$\dot{d}_{t_{k+1}} = \dot{d}_{t_k} + (1 - \delta) \cdot \ddot{d}_{t_k} \cdot \Delta t + \delta \cdot \ddot{d}_{t_{k+1}} \cdot \Delta t \qquad 2\text{-}20$$

where α and δ are the integration parameters approximating the variations of the velocity and displacement between t_k and t_{k+1}, which also control the numerical features of the Newmark method, such as stability, accuracy, etc. By substituting $\ddot{d}_{t_{k+1}} = \ddot{d}_{t_k} + \Delta \ddot{d}$, $\dot{d}_{t_{k+1}} = \dot{d}_{t_k} + \Delta \dot{d}$ and $d_{t_{k+1}} = d_{t_k} + \Delta d$ into Equations 2-19 and 2-20, the incremental form of the Newmark method can be expressed as:

$$\Delta d = \dot{d}_{t_k} \cdot \Delta t + 0.5\ddot{d}_{t_k} \cdot \Delta t^2 + \alpha \cdot \Delta\ddot{d} \cdot \Delta t^2 \quad \text{2-21}$$

$$\Delta\dot{d} = \ddot{d}_{t_k} \cdot \Delta t + \delta \cdot \Delta\ddot{d} \cdot \Delta t \quad \text{2-22}$$

After rearranging Equations 2-21 and 2-22, the Newmark method can also be expressed as in Equations 2-23 and 2-24:

$$\Delta\dot{d} = \frac{\delta}{\alpha \cdot \Delta t} \cdot \Delta d - \frac{\delta}{\alpha} \cdot \dot{d}_{t_k} + \left(1 - \frac{\delta}{2\alpha}\right) \cdot \Delta t \cdot \ddot{d}_{t_k} \quad \text{2-23}$$

$$\Delta\ddot{d} = \frac{1}{\alpha \cdot \Delta t^2} \cdot \Delta d - \frac{1}{\alpha \cdot \Delta t} \cdot \dot{d}_{t_k} - \frac{1}{2\alpha} \cdot \ddot{d}_{t_k} \quad \text{2-24}$$

By varying α and δ, various time integration schemes can be obtained, which possess different numerical features. Table 2-1 gives a summary of various time integration schemes of Newmark's family of methods. Based on Newmark (1959), unconditional stability can be obtained when Equations 2-25 and 2-26 are satisfied.

$$\delta \geq 0.5 \quad \text{2-25}$$

$$\alpha \geq 0.25(0.5 + \delta) \quad \text{2-26}$$

Table 2-1: Newmark method family

Parameter / Name of the scheme	α	δ	Stability
Central difference method (CDM)	0	1/2	Conditionally stable
Linear acceleration method	1/6	1/2	Conditionally stable
Constant average acceleration method (denoted as NMK1)	1/4	1/2	Unconditionally stable
Dissipative Newmark method (denoted as NMK2)	0.3025	0.6	Unconditionally stable

Among all the integration schemes shown in Table 2-1, the two unconditionally stable methods, NMK1 and NMK2, are widely employed in numerical analysis. It was proved by Dahlquist (1963) that NMK1 is the most accurate unconditionally stable time integration scheme, while the disadvantage of NMK1 is that it does not possess numerical damping. However, selecting values of δ greater than 0.5 could introduce numerical damping into the time integration schemes, such as the NMK2 method, which is widely used due to the existence of numerical damping.

2.4.3 Generalised-α method

HHT method

Following the Newmark method, various time integration methods were proposed, adopting different assumptions for the variations of acceleration, velocity and displacement. The HHT method, proposed by Hilber et al. (1977), is probably the first time integration method possessing controllable numerical damping. The basic principle of the HHT method is that the velocity and displacement are evaluated at an instant within the time step and the acceleration is evaluated at the end of the time step, as shown in Equation 2-27 and Figure 2-4. It should be noted that the variations of velocity and displacement are still approximated by using the expressions of the Newmark method. Therefore, the HHT method is considered as an extension of the Newmark method, but with an additional integration parameter α_f.

$$[M]\{\ddot{d}_{t_{k+1}}\}+[C]\{\dot{d}_{t_{k+1-\alpha_f}}\}+[K]\{d_{t_{k+1-\alpha_f}}\}=\{R_{t_{k+1-\alpha_f}}\} \qquad 2\text{-}27$$

where

$$t_{k+1-\alpha_f}=(1-\alpha_f)\cdot t_{k+1}+\alpha_f\cdot t_k$$

$$d_{t_{k+1-\alpha_f}}=(1-\alpha_f)\cdot d_{t_{k+1}}+\alpha_f\cdot d_{t_k}$$

$$\dot{d}_{t_{k+1-\alpha_f}}=(1-\alpha_f)\cdot \dot{d}_{t_{k+1}}+\alpha_f\cdot \dot{d}_{t_k}$$

$$R_{t_{k+1-\alpha_f}}=(1-\alpha_f)\cdot R_{t_{k+1}}+\alpha_f\cdot R_{t_k}$$

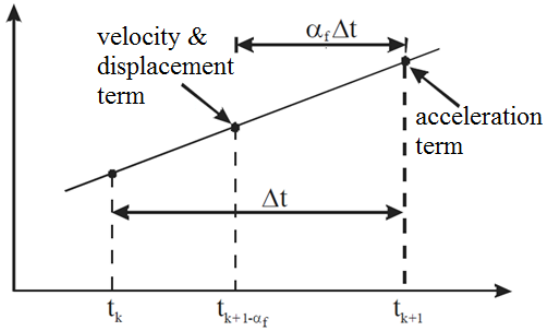


Figure 2-4: Schematic graph of the evaluation of acceleration, velocity and displacement terms for the HHT method (after Kontoe (2006))

Based on Equation 2-27, it is obvious that the acceleration term is evaluated at the end of the time step t_{k+1} and that the velocity and displacement terms are evaluated within the time step at $t_{k+1-\alpha_f}$.

WBZ method

Another extension of the Newmark method is the WBZ method (Wood et al., 1981). The principle of the WBZ method is similar to that of the HHT method. However, for the WBZ method, the acceleration term is evaluated at the instant $t_{k+1-\alpha_m}$ within the time step and the velocity and displacement terms are evaluated at the end of the time step t_{k+1}, as shown in Figure 2-5. The governing equation for the WBZ method is given by Equation 2-28.

$$[M]\{\ddot{d}_{t_{k+1-\alpha_m}}\}+[C]\{\dot{d}_{t_{k+1}}\}+[K]\{d_{t_{k+1}}\}=\{R_{t_{k+1}}\} \qquad 2\text{-}28$$

where

$$t_{k+1-\alpha_m}=(1-\alpha_m)\cdot t_{k+1}+\alpha_m\cdot t_k$$

$$\ddot{d}_{t_{k+1-\alpha_m}}=(1-\alpha_m)\cdot \ddot{d}_{t_{k+1}}+\alpha_m\cdot \ddot{d}_{t_k}$$

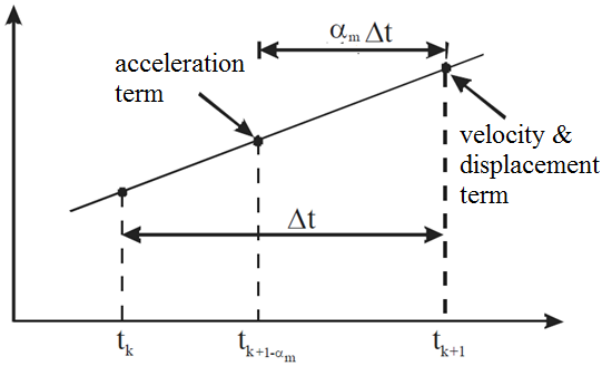


Figure 2-5: Schematic graph of the evaluation of acceleration, velocity and displacement terms for the WBZ method (after Kontoe (2006))

It should be noted that both the HHT and WBZ method collapse to the Newmark method when α_f and α_m become zero respectively.

CH method

The CH method, proposed by Chung and Hulbert in 1993, is a combination of the HHT and the WBZ methods. According to the principle of the CH method, the acceleration term is evaluated at the time instant $t_{k+1-\alpha_m}$ and the velocity and displacement terms are evaluated at the time instant $t_{k+1-\alpha_f}$, as shown in Figure 2-6. Furthermore, the expressions of the Newmark method are employed as well to approximate the variations of velocity and displacement. The equation of motion for the CH method is shown in Equation 2-29. There are totally four integration parameters involved in the CH method, where α and δ originate from the Newmark method expressions, and α_m and α_f are employed to evaluate different terms in dynamic equilibrium equation within a time step. It should be noted that the CH method, which is often called the generalised-α method, collapses to the HHT, WBZ and Newmark methods with the conditions of $\alpha_m = 0$, $\alpha_f = 0$ and $\alpha_m = \alpha_f = 0$ respectively.

$$[M]\{\ddot{d}_{t_{k+1-\alpha_m}}\}+[C]\{\dot{d}_{t_{k+1-\alpha_f}}\}+[K]\{d_{t_{k+1-\alpha_f}}\}=\{R_{t_{k+1-\alpha_f}}\} \qquad 2\text{-}29$$

where

$$t_{k+1-\alpha_m} = (1-\alpha_m)\cdot t_{k+1} + \alpha_m \cdot t_k$$

$$t_{k+1-\alpha_f} = (1-\alpha_f)\cdot t_{k+1} + \alpha_f \cdot t_k$$

$$\ddot{d}_{t_{k+1-\alpha_m}} = (1-\alpha_m)\cdot \ddot{d}_{t_{k+1}} + \alpha_m \cdot \ddot{d}_{t_k}$$

$$\dot{d}_{t_{k+1-\alpha_f}} = (1-\alpha_f)\cdot \dot{d}_{t_{k+1}} + \alpha_f \cdot \dot{d}_{t_k}$$

$$d_{t_{k+1-\alpha_f}} = (1-\alpha_f)\cdot d_{t_{k+1}} + \alpha_f \cdot d_{t_k}$$

$$R_{t_{k+1-\alpha_f}} = (1-\alpha_f)\cdot R_{t_{k+1}} + \alpha_f \cdot R_{t_k}$$

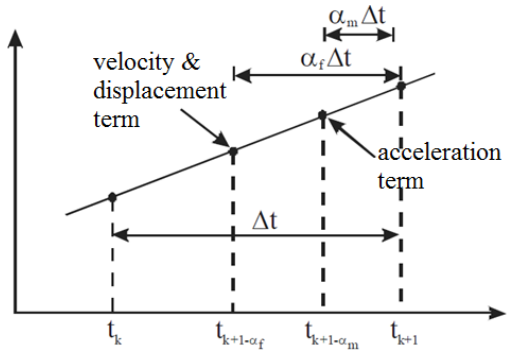


Figure 2-6: Schematic graph of the evaluation of acceleration, velocity and displacement terms for the CH method (after Kontoe (2006))

According to Chung and Hulbert (1993), firstly, second order accuracy can be achieved for the CH method by applying Equations 2-30.

$$\delta = \frac{1}{2} - \alpha_m + \alpha_f \qquad 2\text{-}30$$

Secondly, the maximum high frequency dissipation can be attained when:

$$\alpha = \frac{1}{4}\left(1 - \alpha_m + \alpha_f\right)^2 \qquad 2\text{-}31$$

Thirdly, the minimum low frequency dissipation can be obtained when:

$$\alpha_m = \frac{2\rho_\infty - 1}{\rho_\infty + 1} \quad and \quad \alpha_f = \frac{\rho_\infty}{\rho_\infty + 1} \qquad 2\text{-}32$$

where ρ_∞ is the spectral radius when the ratio $\Delta t / T$ tends to infinity, where T is the natural period of an undamped SDOF system and Δt is the time step.

Based on the Equation 2-32, it is obvious that, for the CH method, the numerical damping is controllable by conveniently varying the integration parameters α_m and α_f. Furthermore, based on Equations 2-31 and 2-32, by employing the CH method, the optimum of high frequency dissipation can be achieved without affecting the low frequency vibrations, which is a distinctive merit of the CH method.

The stability of the CH method for the one-phase formulation was investigated by Chung and Hulbert in 1993. The proposed stability conditions of the CH method are expressed as a function of two integration parameters, α_m and α_f, as shown in Equation 2-33. However, in the stability analysis for the CH method, the other two

integration parameters, α and δ were substituted by α_m and α_f (based on Equations 2-30 and 2-31), in order to achieve second order accuracy and maximum dissipation effect on the high-frequency spurious vibration. Furthermore, the proposed unconditional stability conditions can also be illustrated by the shaded area in Figure 2-7.

$$\alpha_m \leq \alpha_f \leq 0.5 \qquad 2\text{-}33$$

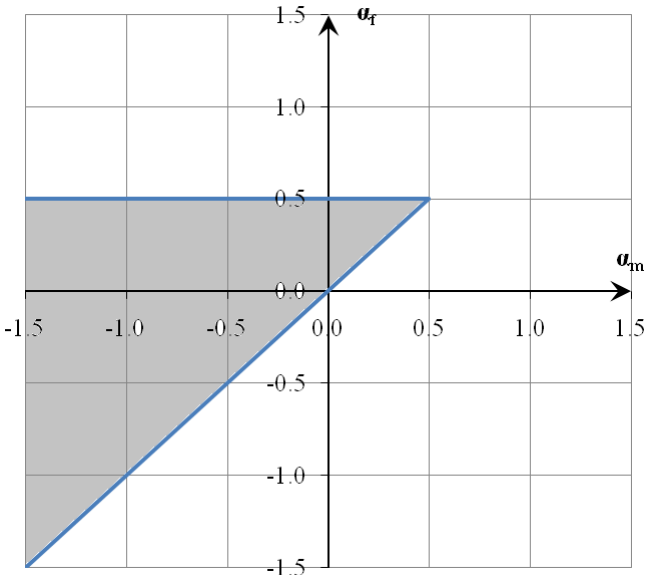


Figure 2-7: Unconditional stability conditions for the CH method (after Chung and Hulbert (1993))

2.4.4 Implementation of the CH method to the coupled dynamic formulation

There are two main categories of time integration methods for two-phase coupled formulation, the monolithic schemes, in which the different unknowns of the FE formulation are solved simultaneously, and the staggered schemes, in which different unknowns are solved iteratively. Generally, monolithic schemes can be more simply and directly implemented into FE programs and are more computationally efficient (Wood, 1990). Therefore, monolithic schemes are implemented in ICFEP, where the same integration method is applied to both the equation of motion and the consolidation equation.

Based on the advantages of the CH method discussed in the previous section, the CH method was extended in Kontoe (2006) and Kontoe et al. (2008b) to enable the solution

of dynamic coupled consolidation problems, which involves two-phase materials, and was then implemented in the FE program ICFEP. Herein the implementation of the CH method for the coupled dynamic formulation is introduced.

By applying the CH method, the accumulated form of the FE equation of motion can be written as:

$$[M]\{\ddot{d}_{t_{k+1-\alpha_m}}\}+[C]\{\dot{d}_{t_{k+1-\alpha_f}}\}+[K]\{d_{t_{k+1-\alpha_f}}\}+[L]\{p_{t_{k+1-\alpha_f}}\}=\{R_{t_{k+1-\alpha_f}}\} \qquad 2\text{-}34$$

where the pore fluid pressure term is evaluated at time increment $t_{k+1-\alpha_f}$. After substituting Equation 2-29, Equation 2-34 can be expressed as:

$$\begin{aligned}&(1-\alpha_m)[M]\{\ddot{d}_{t_{k+1}}\}+\alpha_m[M]\{\ddot{d}_{t_k}\}+(1-\alpha_f)[C]\{\dot{d}_{t_{k+1}}\}+\alpha_f[C]\{\dot{d}_{t_k}\}+(1-\alpha_f)[K]\{d_{t_{k+1}}\}\\&+\alpha_f[K]\{d_{t_k}\}+(1-\alpha_f)[L]\{p_{t_{k+1}}\}+\alpha_f[L]\{p_{t_k}\}=(1-\alpha_f)\{R_{t_{k+1}}\}+\alpha_f\{R_{t_k}\}\end{aligned} \qquad 2\text{-}35$$

Equation 2-35 can be converted to the incremental form, which is shown in Equation 2-36.

$$(1-\alpha_m)[M]\{\Delta\ddot{d}\}+(1-\alpha_f)[C]\{\Delta\dot{d}\}+(1-\alpha_f)[K]\{\Delta d\}+(1-\alpha_f)[L]\{\Delta p\}=(1-\alpha_f)\{\Delta R\}+\{\Delta R\}_{t_k} \qquad 2\text{-}36$$

where

$$\{\Delta R\}_{t_k}=\{R_{t_k}\}-[M]\{\ddot{d}_{t_k}\}-[C]\{\dot{d}_{t_k}\}-[K]\{d_{t_k}\}-[L]\{p_{t_k}\}$$

and $\{\Delta R\}_{t_k}$ is the out-of-balance force at the previous time increment, which ideally should be zero.

By utilising the expressions of the Newmark method (Equations 2-23 and 2-24), the final FE form of the consolidation equation after the implementation of the CH method is shown in Equation 2-37.

$$\begin{aligned}&\left[\left(\frac{1-\alpha_m}{\alpha\cdot\Delta t^2}\right)[M]+\left(\frac{(1-\alpha_f)\cdot\delta}{\alpha\cdot\Delta t}\right)[C]+(1-\alpha_f)[K]\right]\{\Delta d\}+(1-\alpha_f)[L]\{\Delta p\}\\&=(1-\alpha_f)\{\Delta R\}+(1-\alpha_m)[M]\left(\frac{1}{\alpha\cdot\Delta t}\{\dot{d}_{t_k}\}+\frac{1}{2\alpha}\{\ddot{d}_{t_k}\}\right)+(1-\alpha_f)[C]\left(\frac{\delta}{\alpha}\{\dot{d}_{t_k}\}-\left(1-\frac{\delta}{2\alpha}\right)\cdot\Delta t\{\ddot{d}_{t_k}\}\right)+\{\Delta R\}_{t_k}\end{aligned} \qquad 2\text{-}37$$

With regard to the consolidation equation, as suggested in Kontoe (2006), the CH

method is applied directly to the incremental form of the consolidation equation (Equation 2-12) resulting in the following:

$$\left(1-\alpha_f\right)\cdot\left(-\beta\cdot\Delta t\left[\Phi\right]-\left[S\right]\right)\left\{\Delta p\right\}+\left(1-\alpha_m\right)\cdot\beta\cdot\Delta t\left[G\right]\left\{\Delta\ddot{d}\right\}+\left(1-\alpha_f\right)\left[L\right]^T\left\{\Delta d\right\}=\left(1-\alpha_f\right)\left\{\Delta F\right\}+\left\{\Delta F\right\}_{t_k}$$

2-38

where

$$\left\{\Delta F\right\}=\left(-\left[n\right]-\left\{Q\right\}+\left[\Phi\right]\left\{p_{t_k}\right\}-\left[G\right]\left\{\ddot{d}_{t_k}\right\}\right)\Delta t$$

with $\left\{\Delta F\right\}$ being the incremental right hand flow vector and $\left\{\Delta F\right\}_{t_k}$ being the out-of-balance flow at the previous time increment, which ideally should be zero.

By utilising the expressions of the Newmark method (Equation 2-24), the final FE form of the consolidation equation is shown in Equation 2-39.

$$\left[\frac{\left(1-\alpha_m\right)\cdot\beta}{\alpha\cdot\Delta t}\left[G\right]+\left(1-\alpha_f\right)\left[L\right]^T\right]\left\{\Delta d\right\}+\left(1-\alpha_f\right)\left(-\beta\cdot\Delta t\left[\Phi\right]-\left[S\right]\right)\left\{\Delta p\right\}$$

$$=\left(1-\alpha_f\right)\cdot\Delta t\cdot\left(-\left[n\right]-\left\{Q\right\}+\left[\Phi\right]\left\{p_{t_k}\right\}-\left[G\right]\left\{\ddot{d}_{t_k}\right\}\right)+\left(1-\alpha_m\right)\cdot\beta\cdot\Delta t\left[G\right]\left(\frac{1}{\alpha\cdot\Delta t}\left\{\dot{d}_{t_k}\right\}+\frac{1}{2\alpha}\left\{\ddot{d}_{t_k}\right\}\right)+\left\{\Delta F\right\}_{t_k}$$

2-39

Consequently, the final FE formulation for coupled analysis after the implementation of the CH method is shown in Equation 2-40.

$$\begin{bmatrix}\left(\frac{1-\alpha_m}{\alpha\cdot\Delta t^2}\right)\left[M\right]+\left(\frac{\left(1-\alpha_f\right)\cdot\delta}{\alpha\cdot\Delta t}\right)\left[C\right]+\left(1-\alpha_f\right)\left[K\right] & \left(1-\alpha_f\right)\left[L\right] \\ \frac{\left(1-\alpha_m\right)\cdot\beta}{\alpha\cdot\Delta t}\left[G\right]+\left(1-\alpha_f\right)\left[L\right]^T & \left(1-\alpha_f\right)\cdot\left(-\beta\cdot\Delta t\left[\Phi\right]-\left[S\right]\right)\end{bmatrix}\begin{bmatrix}\left\{\Delta d\right\} \\ \left\{\Delta p\right\}\end{bmatrix}=\begin{bmatrix}\Delta\overline{R} \\ \Delta\overline{F}\end{bmatrix}$$

2-40

where

$$\Delta\overline{R}=\left(1-\alpha_f\right)\left\{\Delta R\right\}+\left(1-\alpha_m\right)\left[M\right]\left(\frac{1}{\alpha\cdot\Delta t}\left\{\dot{d}_{t_k}\right\}+\frac{1}{2\alpha}\left\{\ddot{d}_{t_k}\right\}\right)$$

$$+\left(1-\alpha_f\right)\left[C\right]\left(\frac{\delta}{\alpha}\left\{\dot{d}_{t_k}\right\}-\left(1-\frac{\delta}{2\alpha}\right)\cdot\Delta t\left\{\ddot{d}_{t_k}\right\}\right)+\left\{\Delta R\right\}_{t_k}$$

$$\Delta\overline{F} = (1-\alpha_f)\cdot\Delta t\cdot\left(-[n]-\{Q\}+[\Phi]\{p_{t_k}\}-[G]\{\ddot{d}_{t_k}\}\right)+(1-\alpha_m)\cdot\beta\cdot\Delta t[G]\left(\frac{1}{\alpha\cdot\Delta t}\{\dot{d}_{t_k}\}+\frac{1}{2\alpha}\{\ddot{d}_{t_k}\}\right)$$
$$+\{\Delta F\}_{t_k}$$

It should be noted that the matrix $[G]$ in the above equation represents the impact of the inertia of the solid particles on the pore fluid pressure. It has been suggested though that the influence of the matrix $[G]$ on the dynamic response is insignificant for the frequency range within which the "u-p" formulation is valid (Chan, 1988). Therefore, the matrix $[G]$ will not be included in the dynamic coupled consolidation formulation for the following work.

2.5 Stability investigation of the CH method for the coupled formulation

Since the stability of a time integration method is a key numerical feature, researchers have extensively investigated the stability of the widely used time integration methods. In particular, Newmark (1959) analysed the numerical stability for the Newmark Method and proposed the unconditional stability conditions. Hilber et al. (1977) and Wood et al. (1981) theoretically studied the stability of the HHT and WBZ methods respectively. Furthermore, Chan (1988) investigated the stability for the SSpj (single step time stepping scheme) and GNpj (generalised Newmark stepping scheme) methods in coupled consolidation formulation and proposed the unconditional stability conditions for two methods. It should be noted that the SSpj and GNpj methods are two families of monolithic time integration schemes, proposed by Zienkiewicz et al. (1980a and 1984) and Katona and Zienkiewicz (1985) respectively, where p denotes the order for the interpolation and s denotes the order of the differential equations.

However, as an increasingly widely employed time integration method, the stability of the CH method was also studied by Chung and Hulbert (1993), but just for the one-phase formulation. The stability of the CH method for the coupled formulation has not been systematically investigated before. Due to its features of unconditional stability and controllable numerical damping, the CH method is considered as one of the most advanced time integration methods. Therefore, the stability of the CH method in the

coupled formulation is critical and needs to be thoroughly studied. Furthermore, as mentioned before, since the CH method is a generalisation of the Newmark, HHT and WBZ methods, the stability conditions for the CH method are relevant to most of the commonly used time integration methods. In this part, the stability of the CH method for a fully coupled dynamic consolidation formulation is systematically investigated for the first time and unconditional stability conditions are proposed.

The stability investigation presented in this section follows a four-step procedure. First, the accumulated scalar form of the coupled dynamic formulation is derived based on the FE formulation presented in the previous section. Second, the expressions of the Newmark method for the variation of velocity and displacement within a time step are utilised in the accumulated scalar form of the coupled dynamic formulation. Third, the approximations of the CH method for the various variables are employed in the formulation. Last, the stability of the CH method is investigated based on the derived formulation which includes only two variables: the incremental acceleration and pore fluid pressure.

The Routh-Hurwitz condition, which has been widely employed in the stability analysis of various time integration methods (Wood, 1990), is adopted in this study. As mentioned before, a time integration method is stable when the modulus of the eigenvalue, λ, of the amplification matrix $[A]$ is less or equal to one (Equation 2-16 in Section 2.4.1). Routh (1877) and Hurwitz (1895) suggested that, if λ is substituted by a function of a complex number z (as shown in Equation 2-41), the condition of $|\lambda| \le 1$ can be converted to the condition of $\mathrm{Re}(z) \le 0$, indicating that the real part of z should be less or equal to zero in order to satisfy the stability conditions.

$$\lambda = \frac{1+z}{1-z} \qquad 2\text{-}41$$

Furthermore, for a general polynomials of the form shown in Equation 2-42 to satisfy the condition of $\mathrm{Re}(z) \le 0$, the conditions of Equation 2-43 should be satisfied. Therefore, the stability condition of $|\lambda| \le 1$ is finally converted to the conditions given by Equation 2-43, which will be used for the following stability analysis of the CH method.

$$a_0 \cdot z^n + a_1 \cdot z^{n-1} + a_2 \cdot z^{n-2} + ...a_n = 0 \qquad 2\text{-}42$$

$$\begin{aligned} &a_0 > 0 \quad and \quad a_i \geq 0 \quad for \quad i > 0 \\ &a_1 \cdot a_2 \cdot a_3 - a_0 \cdot a_3{}^2 - a_4 \cdot a_1{}^2 > 0 \end{aligned} \qquad 2\text{-}43$$

2.5.1 Scalar form of the coupled dynamic FE formulation

In order to analyse the stability of the CH method, it is simpler to use the accumulated scalar form of the coupled dynamic formulation. Firstly, for the equation of motion, based on Equation 2-34, the accumulated scalar form after utilising the CH method is shown in Equations 2-44 and 2-45.

$$m \cdot \ddot{d}_{t_{k+1-\alpha_m}} + c \cdot \dot{d}_{t_{k+1-\alpha_f}} + k \cdot d_{t_{k+1-\alpha_f}} + l \cdot p_{t_{k+1-\alpha_f}} = 0 \qquad 2\text{-}44$$

$$\begin{Bmatrix} \ddot{d}_{t_{k+1-\alpha_m}} \\ \dot{d}_{t_{k+1-\alpha_f}} \\ d_{t_{k+1-\alpha_f}} \\ p_{t_{k+1-\alpha_f}} \end{Bmatrix} = \begin{Bmatrix} (1-\alpha_m) \cdot \ddot{d}_{t_{k+1}} + \alpha_m \cdot \ddot{d}_{t_k} \\ (1-\alpha_f) \cdot \dot{d}_{t_{k+1}} + \alpha_f \cdot \dot{d}_{t_k} \\ (1-\alpha_f) \cdot d_{t_{k+1}} + \alpha_f \cdot d_{t_k} \\ (1-\alpha_f) \cdot p_{t_{k+1}} + \alpha_f \cdot p_{t_k} \end{Bmatrix} \qquad 2\text{-}45$$

where m, c, k and l are the scalar forms of the matrices $[M]$, $[C]$, $[K]$ and $[L]$ respectively.

Secondly, the scalar form of the consolidation equation, obtained from Equation 2-38, is shown in Equation 2-46.

$$-(1-\alpha_f) \cdot \phi \cdot (p_k + \beta \cdot \Delta p) - (1-\alpha_f) \cdot s \cdot \frac{\Delta p}{\Delta t} + (1-\alpha_f) \cdot l^T \cdot \frac{\Delta d}{\Delta t} = 0 \qquad 2\text{-}46$$

where ϕ and s are the scalar forms of the matrices $[\Phi]$ and $[S]$.

2.5.2 Application of the expressions of the Newmark method

Based on the basic principle of the time integration method, the acceleration, velocity and displacement at time increment t_{k+1} can be expressed as a function of their historic values, as shown in Equation 2-47.

$$\begin{Bmatrix} \ddot{d}_{t_{k+1}} \\ \dot{d}_{t_{k+1}} \\ d_{t_{k+1}} \\ p_{t_{k+1}} \end{Bmatrix} = \lambda \begin{Bmatrix} \ddot{d}_{t_k} \\ \dot{d}_{t_k} \\ d_{t_k} \\ p_{t_k} \end{Bmatrix} \tag{2-47}$$

Substituting the Routh-Hurwitz condition into Equation 2-47 results to Equation 2-48.

$$\begin{Bmatrix} \ddot{d}_{t_{k+1}} \\ \dot{d}_{t_{k+1}} \\ d_{t_{k+1}} \\ p_{t_{k+1}} \end{Bmatrix} = \frac{1+z}{1-z} \begin{Bmatrix} \ddot{d}_{t_k} \\ \dot{d}_{t_k} \\ d_{t_k} \\ p_{t_k} \end{Bmatrix} \tag{2-48}$$

The left hand side of Equation 2-48 is rewritten in incremental form employing the expressions of the Newmark method (Equations 2-21 and 2-22) for displacement and velocity.

$$\begin{Bmatrix} \ddot{d}_{t_{k+1}} \\ \dot{d}_{t_{k+1}} \\ d_{t_{k+1}} \\ p_{t_{k+1}} \end{Bmatrix} = \begin{Bmatrix} \ddot{d}_{t_k} + \Delta\ddot{d} \\ \dot{d}_{t_k} + \ddot{d}_{t_k} \cdot \Delta t + \delta \cdot \Delta\ddot{d} \cdot \Delta t \\ d_{t_k} + \dot{d}_{t_k} \cdot \Delta t + 0.5\ddot{d}_{t_k} \cdot \Delta t^2 + \alpha \cdot \Delta\ddot{d} \cdot \Delta t \\ p_{t_k} + \Delta p \end{Bmatrix} \tag{2-49}$$

By substituting Equation 2-48 into Equation 2-49, the acceleration, velocity, displacement and pore water pressure at the time instant t_k can be expressed as follows.

$$\begin{Bmatrix} \ddot{d}_{t_k} \\ \dot{d}_{t_k} \\ d_{t_k} \\ p_{t_k} \end{Bmatrix} = \begin{Bmatrix} \frac{1-z}{2z} \cdot \Delta\ddot{d} \\ \frac{(1-z)\cdot\left[1+(2\delta-1)\cdot z\right]}{4z^2} \cdot \Delta\ddot{d} \cdot \Delta t \\ \frac{(1-z)\cdot\left[1+(2\delta-1)\cdot z+(4\alpha-2\delta)\cdot z^2\right]}{8z^3} \cdot \Delta\ddot{d} \cdot \Delta t^2 \\ \frac{1-z}{2z} \cdot \Delta p \end{Bmatrix} \tag{2-50}$$

2.5.3 Application of the CH method

In order to perform the stability analysis of the CH method, Equations 2-48 and 2-50 are substituted into the equations for the CH method (Equation 2-45), giving the final expressions of the acceleration, velocity, displacement and pore water pressure:

$$\begin{Bmatrix} \ddot{d}_{t_{k+1-\alpha_m}} \\ \dot{d}_{t_{k+1-\alpha_f}} \\ d_{t_{k+1-\alpha_f}} \\ p_{t_{k+1-\alpha_f}} \end{Bmatrix} = \begin{Bmatrix} \dfrac{(1-2\alpha_m)\cdot z+1}{2z}\cdot\Delta\ddot{d} \\ \dfrac{(2\delta-1)\cdot(1-2\alpha_f)\cdot z^2+(2\delta-2\alpha_f)\cdot z+1}{4z^2}\cdot\Delta\ddot{d}\cdot\Delta t \\ \dfrac{(4\alpha-2\delta)\cdot(1-2\alpha_f)\cdot z^3+(4\alpha-4\delta\alpha_f+2\alpha_f-1)\cdot z^2+(2\delta-2\alpha_f)\cdot z+1}{8z^3}\cdot\Delta\ddot{d}\cdot\Delta t^2 \\ \dfrac{(1-2\alpha_f)\cdot z+1}{2z}\cdot\Delta p \end{Bmatrix}$$

2-51

In addition, based on Equations 2-48 and 2-50, Δd in Equation 2-46 can be expressed by Equation 2-52.

$$\Delta d = \frac{(4\alpha-2\delta)\cdot z^2+(2\delta-1)\cdot z+1}{4z^2}\cdot\Delta\ddot{d}\cdot\Delta t^2 \qquad 2\text{-}52$$

2.5.4 Derivation of the unconditional stability conditions

The expressions for the acceleration, velocity, displacement and pore water pressure in the form of Equations 2-51 and 2-52 can be then substituted into the scalar forms of the coupled FE formulation (Equations 2-44 and 2-46). This allows the equation of motion and the dynamic consolidation equation to be expressed in terms of only two unknowns ($\Delta\ddot{d}$ and Δp) as shown in Equations 2-53 and 2-54.

$$\begin{aligned} &m\cdot\frac{(1-2\alpha_m)\cdot z+1}{2z}\cdot\Delta\ddot{d}+c\cdot\frac{(2\delta-1)\cdot(1-2\alpha_f)\cdot z^2+(2\delta-2\alpha_f)\cdot z+1}{4z^2}\cdot\Delta\ddot{d}\cdot\Delta t \\ &+k\cdot\frac{(4\alpha-2\delta)\cdot(1-2\alpha_f)\cdot z^3+(4\alpha-4\delta\cdot\alpha_f+2\alpha_f-1)\cdot z^2+(2\delta-2\alpha_f)\cdot z+1}{8z^3}\cdot\Delta\ddot{d}\cdot\Delta t^2 \\ &+l\cdot\frac{(1-2\alpha_f)\cdot z+1}{2z}\cdot\Delta p=0 \end{aligned}$$

2-53

$$-\phi\cdot\left(1-\alpha_f\right)\cdot\left(\frac{1-z}{2z}\cdot\Delta p+\beta\cdot\Delta p\right)-s\cdot\left(1-\alpha_f\right)\cdot\frac{\Delta p}{\Delta t}$$
$$+l^T\cdot\left(1-\alpha_f\right)\cdot\frac{\left(4\alpha-2\delta\right)\cdot z^2+\left(2\delta-1\right)\cdot z+1}{4z^2}\cdot\Delta\ddot{d}\cdot\Delta t=0 \qquad 2\text{-}54$$

After rearrangement, Equations 2-53 and 2-54 become Equations 2-55 and 2-56 respectively:

$$m\cdot\left[4\left(1-2\alpha_m\right)\cdot z^3+4z^2\right]\cdot\Delta\ddot{d}+c\cdot\Delta t\cdot\left[2\left(2\delta-1\right)\cdot\left(1-2\alpha_f\right)\cdot z^3+2\left(2\delta-2\alpha_f\right)\cdot z^2+2z\right]\cdot\Delta\dot{d}$$
$$+k\cdot\Delta t^2\cdot\left[\left(4\alpha-2\delta\right)\cdot\left(1-2\alpha_f\right)\cdot z^3+\left(4\alpha-4\delta\cdot\alpha_f+2\alpha_f-1\right)\cdot z^2+\left(2\delta-2\alpha_f\right)\cdot z+1\right]\cdot\Delta\ddot{d}$$
$$+l\cdot\left[4\left(1-2\alpha_f\right)\cdot z^3+4z^2\right]\cdot\Delta p=0 \qquad 2\text{-}55$$

$$-\phi\cdot\left(1-\alpha_f\right)\cdot\left[2z+\left(4\beta-2\right)\cdot z^2\right]\cdot\Delta p-4s\cdot\left(1-\alpha_f\right)\cdot z^2\cdot\frac{\Delta p}{\Delta t}$$
$$+l^T\cdot\Delta t\cdot\left(1-\alpha_f\right)\cdot\left[\left(4\alpha-2\delta\right)\cdot z^2+\left(2\delta-1\right)\cdot z+1\right]\cdot\Delta\dot{d}=0 \qquad 2\text{-}56$$

In order to separate the main unknowns $\Delta\ddot{d}$ and Δp, another form of Equations 2-55 and 2-56 is obtained after algebraic rearrangement, which is expressed as follows:

$$\left\{\begin{array}{c}\left[4m\cdot\left(1-2\alpha_m\right)+2c\cdot\Delta t\cdot\left(2\delta-1\right)\cdot\left(1-2\alpha_f\right)+k\cdot\Delta t^2\cdot\left(4\alpha-2\delta\right)\cdot\left(1-2\alpha_f\right)\right]\cdot z^3\\+\left[4m+2c\cdot\Delta t\cdot\left(2\delta-2\alpha_f\right)+k\cdot\Delta t^2\cdot\left(4\alpha-4\delta\cdot\alpha_f+2\alpha_f-1\right)\right]\cdot z^2\\+\left[2c\cdot\Delta t+k\cdot\Delta t^2\cdot\left(2\delta-2\alpha_f\right)\right]\cdot z\\+k\cdot\Delta t^2\end{array}\right\}\cdot\Delta\ddot{d}$$
$$+\left\{\begin{array}{c}4l\cdot\left(1-2\alpha_f\right)\cdot z^3\\+\left(4l\right)\cdot z^2\end{array}\right\}\cdot\Delta p=0 \qquad 2\text{-}57$$

$$\left\{\begin{array}{c}l^T\cdot\Delta t\cdot\left(4\alpha-2\delta\right)\cdot\left(1-\alpha_f\right)\cdot z^2\\+l^T\cdot\Delta t\cdot\left(2\delta-1\right)\cdot\left(1-\alpha_f\right)\cdot z\\+l^T\cdot\Delta t\cdot\left(1-\alpha_f\right)\end{array}\right\}\cdot\Delta\ddot{d}-\left\{\begin{array}{c}\phi\cdot\left(4\beta-2\right)\cdot\left(1-\alpha_f\right)+4\frac{s}{\Delta t}\cdot\left(1-\alpha_f\right)\cdot z^2\\+2\phi\cdot\left(1-\alpha_f\right)\cdot z\end{array}\right\}\cdot\Delta p=0 \qquad 2\text{-}58$$

For convenience A and B are set to represent the multipliers in front of $\Delta\ddot{d}$ and Δp respectively in Equation 2-57, whereas C and D are used for the same purpose in Equation 2-58. The two equations are then written as:

$$\begin{bmatrix} A & B \\ C & -D \end{bmatrix} \begin{Bmatrix} \Delta\ddot{d} \\ \Delta p \end{Bmatrix} = 0 \qquad \text{2-59}$$

For a non-trivial solution, the determinant of the matrix $\begin{bmatrix} A & B \\ C & -D \end{bmatrix}$ must be zero. The determinant of this matrix is a polynomial of z, which leads to the following:

$$F(z) = \begin{vmatrix} A & B \\ C & -D \end{vmatrix} = A \cdot (-D) - B \cdot C = 0 \qquad \text{2-60}$$

where $F(z)$ is the polynomial of z. After substituting the original forms of A, B, C and D into Equation 2-60, $F(z)$ is expressed as the following equation:

$$F(z) = a_0 \cdot z^5 + a_1 \cdot z^4 + a_2 \cdot z^3 + a_3 \cdot z^2 + a_4 \cdot z = 0 \qquad \text{2-61}$$

where

$$a_0 = (a+b+c) \cdot (o+p) + l \cdot j$$
$$a_1 = (a+b+c) \cdot q + (d+e+f) \cdot (o+p) + l \cdot k + m \cdot j$$
$$a_2 = (d+e+f) \cdot q + (g+h) \cdot (o+p) + m \cdot k + n \cdot j$$
$$a_3 = (g+h) \cdot q + i \cdot (o+p) + n \cdot k$$
$$a_4 = i \cdot q$$

and a, b, …,q are illustrated in Equation 2-62.

$$\begin{Bmatrix} \underset{a}{} \\ \left[4m \cdot (1-2\alpha_m) + 2c \cdot \Delta t \cdot (2\delta - 1) \cdot (1-2\alpha_f) + k \cdot \Delta t^2 \cdot (4\alpha - 2\delta) \cdot (1-2\alpha_f)\right] \cdot z^3 \\ \underset{d}{} \qquad \underset{e}{} \qquad \underset{f}{} \\ +\left[4m + 2c \cdot \Delta t \cdot (2\delta - 2\alpha_f) + k \cdot \Delta t^2 \cdot (4\alpha - 4\delta \cdot \alpha_f + 2\alpha_f - 1)\right] \cdot z^2 \\ \underset{g}{} \qquad \underset{h}{} \\ +\left[2c \cdot \Delta t + k \cdot \Delta t^2 \cdot (2\delta - 2\alpha_f)\right] \cdot z \\ \underset{i}{} \\ +k \cdot \Delta t^2 \end{Bmatrix} \Delta\ddot{d} + \begin{Bmatrix} \underset{j}{} \\ 4l \cdot (1-2\alpha_f) \cdot z^3 \\ \underset{k}{} \\ +(4l) \cdot z^2 \end{Bmatrix} \Delta p = 0 \qquad \text{2-62}$$

$$\begin{Bmatrix} \underset{l}{} \\ l^T \cdot \Delta t \cdot (4\alpha - 2\delta) \cdot (1-\alpha_f) \cdot z^2 \\ \underset{m}{} \\ +l^T \cdot \Delta t \cdot (2\delta - 1) \cdot (1-\alpha_f) \cdot z \\ \underset{n}{} \\ +l^T \cdot \Delta t \cdot (1-\alpha_f) \end{Bmatrix} \Delta\ddot{d} - \begin{Bmatrix} \underset{o}{} \qquad \underset{p}{} \\ \varphi \cdot (4\beta - 2) \cdot (1-\alpha_f) + 4\frac{s}{\Delta t} \cdot (1-\alpha_f) \cdot z^2 \\ \underset{q}{} \\ +2\varphi \cdot (1-\alpha_f) \cdot z \end{Bmatrix} \Delta p = 0$$

Based on the Routh-Hurwitz condition for stability, in order for the CH method to be stable, the coefficients in Equation 2-61 should firstly obey the conditions of $a_0 > 0 \quad and \quad a_i \geq 0 \quad for \quad i > 0$. However, based on the expressions of a_0 to a_4, the time step Δt is included in the terms a_0 to a_4, which means that the stability conditions depend on the time step and therefore the CH method is only conditionally stable. Considering that Δt is always greater than zero, the unconditional stability conditions for the CH method can be obtained by setting every single term within a_0 to a_4, (i.e. a, b,…,q) to be equal or larger than zero, which leads to the following conditions:

$$a, b, ..., q \geq 0 \qquad 2\text{-}63$$

Based on Chung and Hulbert (1993), the CH method achieves second order accuracy and maximum high frequency dissipation when $\delta = 0.5 - \alpha_m + \alpha_f$ and $\alpha = 0.25(1 - \alpha_m + \alpha_f)^2$. These two expressions for δ and α are employed herein to derive the unconditional stability conditions only in terms of α_m, α_f and β. Hence, after substituting the two expressions, based on Equation 2-63, the final unconditional stability conditions of the CH method for the coupled formulation are summarised in Table 2-2. The overall unconditional stability conditions are expressed by parameters α_m, α_f and β, which are $\alpha_m \leq \alpha_f \leq 0.5$ and $\beta \geq 0.5$.

However, the second determinant inequality in Equation 2-43 is difficult to algebraically evaluate. Based on the investigation strategy in Chan (1988), random values for parameters α_m, α_f and β within the stable range are employed in this determinant condition to check the stability condition, where no violating case has been observed. This procedure empirically ensures the satisfaction of the second determinant inequality in Equation 2-43.

The stability conditions derived by employing the Routh-Hurwitz conditions cannot guarantee the L-stability of the CH method. A time integration method is said to be L-stable if it is A-stable and the numerical solution tends to be zero when the real part of $\lambda \Delta t$ approaches infinity, where λ is the eigenvalue of the amplification matrix and Δt is the time step (Wood, 1990). L-stability is critical for stiff systems of equations originating from FE discretisation and it can help FE analysis to dissipate the high-frequency spurious vibrations for stiff problems. However, for geotechnical earthquake engineering problems, soil stiffness is relatively low compared to the stiffness of structural materials, such as concrete and steel, and therefore the A-stability

is reasonably sufficient for the dynamic FE analysis of geotechnical problems.

Table 2-2: Unconditional stability conditions of the CH method for the coupled formulation

	Terms in the polynomial F(z)	Unconditional stability conditions
For the one-phase formulation	$a: 4m \cdot (1-2\alpha_m) \geq 0$	$\alpha_m \leq 0.5$
	$b: 2c \cdot \Delta t \cdot (2\delta - 1) \cdot (1-2\alpha_f) \geq 0$	$\alpha_m \leq \alpha_f, \alpha_f \leq 0.5$
	$c: k \cdot \Delta t^2 \cdot (4\alpha - 2\delta) \cdot (1-2\alpha_f) \geq 0$	$\alpha_f \leq 0.5$
	$d: 4m \geq 0$	
	$e: 2c \cdot \Delta t \cdot (2\delta - 2\alpha_f) \geq 0$	$\alpha_m \leq 0.5$
	$f: k \cdot \Delta t^2 \cdot (4\alpha - 4\delta \cdot \alpha_f + 2\alpha_f - 1) \geq 0$	$\alpha_m \leq \alpha_f, \alpha_m + 3\alpha_f - 2 \leq 0$
	$g: 2c \cdot \Delta t \geq 0$	
	$h: k \cdot \Delta t^2 \cdot (2\delta - 2\alpha_f) \geq 0$	$\alpha_m \leq 0.5$
	$i: k \cdot \Delta t^2 \geq 0$	
Additional conditions for the two-phase coupled formulation	$j: 4l \cdot (1-2\alpha_f) \geq 0$	$\alpha_f \leq 0.5$
	$k: 4l \geq 0$	
	$l: l^T \cdot \Delta t \cdot (4\alpha - 2\delta) \cdot (1-\alpha_f) \geq 0$	$\alpha_f \leq 1.0$
	$m: l^T \cdot \Delta t \cdot (2\delta - 1) \cdot (1-\alpha_f) \geq 0$	$\alpha_m \leq \alpha_f, \alpha_f \leq 1.0$
	$n: l^T \cdot \Delta t \cdot (1-\alpha_f) \geq 0$	$\alpha_f \leq 1.0$
	$o: \phi \cdot (4\beta - 2) \cdot (1-\alpha_f) \geq 0$	$\beta \geq 0.5, \alpha_f \leq 1.0$
	$p: 4s / \Delta t \cdot (1-\alpha_f) \geq 0$	$\alpha_f \leq 1.0$
	$q: 2\phi \cdot (1-\alpha_f) \geq 0$	$\alpha_f \leq 1.0$
Overall		$\alpha_m \leq \alpha_f \leq 0.5$ and $\beta \geq 0.5$

2.5.5 Comparison with existing stability investigations

Chung and Hulbert investigated the stability of the CH method for the one-phase formulation in 1993 and proposed the stability conditions as a function of α_m and α_f, as shown in Equation 2-64.

$$\alpha_m \leq \alpha_f \leq 0.5 \qquad 2\text{-}64$$

Based on the derived unconditional stability conditions of the CH method for the coupled formulation, i.e. $\alpha_m \leq \alpha_f \leq 0.5$ and $\beta \geq 0.5$, the former condition is based on the equation of motion and the latter on the dynamic consolidation equation. It is obvious that the stability conditions can reduce to $\alpha_m \leq \alpha_f \leq 0.5$ by ignoring the hydraulic coupling, which is identical to the unconditional stability conditions of the CH method for the one-phase formulation proposed by Chung and Hulbert (1993).

As discussed before, the CH method collapses to the Newmark method by applying $\alpha_m = \alpha_f = 0$. In Table 2-2, if $\alpha_m = \alpha_f = 0$ is adopted in the relevant terms of the polynomial $F(z)$, the unconditional stability conditions of the Newmark method for the coupled formulation can be obtained, which is $2\alpha \geq \delta \geq 0.5$ and $\beta \geq 0.5$. It is worthy to mention that the stability of the Newmark method for the coupled formulation was investigated by Chan (1988) and the unconditional stability conditions for GN22-GN11 method was proposed as Equation 2-65.

$$\beta_2 \geq \beta_1 \geq 0.5 \quad and \quad \overline{\beta}_1 \geq 0.5 \tag{2-65}$$

where β_2 represents 2α, β_1 represents δ and $\overline{\beta}_1$ is the integration parameter for the pore fluid pressure in the consolidation equation. For GN22-GN11 method, the variation of pore fluid pressure within a time increment is assumed by $\overline{\beta}_1$, as shown in Equation 2-66. It should be noted that the parameter $\overline{\beta}_1$ is similar to the integration parameter β which is adopted in the present study, suggesting that the proposed conditions for unconditional stability for the Newmark method are in agreement with the ones given by Chan (1988).

$$p_{k+1} = p_k + \dot{p}_k \cdot \Delta t + \overline{\beta}_1 \cdot \Delta \dot{p} \cdot \Delta t \tag{2-66}$$

2.6 Numerical investigation of the stability characteristics of the CH method

In this part, the analytically derived stability conditions of the CH method are firstly validated with dynamic coupled consolidation FE analyses and then the stability performance of the CH method is examined beyond the limits of the theoretical investigation assuming elasto-plastic soil behaviour. For the validation part, a one-dimensional (1-D) soil column, assuming linear elastic soil behaviour and plane-strain conditions, is analysed considering a range of dynamic loading conditions for various soil permeability values. The numerical results are firstly compared with previously published numerical investigations to further verify the implementation of the CH method for dynamic coupled consolidation analysis. It should be noted that zero material damping is employed for all the linear elastic numerical simulations for

consistency with the assumptions of the theoretical stability analysis. The last numerical exercise involves plane-strain analyses of a foundation subjected to dynamic surface loading, assuming both linear elastic and elasto-plastic soil behaviour prescribed with a bounding surface plasticity constitutive model.

2.6.1 1-D column subjected to step loading

The first example concerns a soil column subjected to step loading. The FE mesh (consisting of 500 8-noded quadrilateral isoparameteric elements) and the boundary conditions are shown in Figure 2-8. For the hydraulic boundary conditions, pore water pressure is prescribed as zero at the top of the mesh and is not allowed to change throughout the analysis (i.e. Δp=0). The remaining boundaries are considered to be impermeable (i.e. no flow across the boundaries). Hydrostatic pore water pressure and static self-weight are prescribed as the initial stresses for all the numerical analyses in this chapter, where the coefficient of earth pressure at rest (K_0) is applied to be 0.5. Furthermore, a uniformly distributed load is applied on the top boundary as illustrated in Figure 2-9. The soil properties are shown in Table 2-3. It should be noted that high permeability is employed for the present FE analysis, in order to trigger the numerical instability, which can represent the permeability for coarse gravel in the geotechnical point of view. In all the presented examples, the values of the time integration parameters for the CH method are obtained by complying with the previously discussed conditions for unconditional stability, second order accuracy and optimum high-frequency dissipation with minimum low frequency impact. In this example, the adopted parameters of the CH method, shown in Table 2-4, correspond to a spectral radius at the high frequency limit of ρ_∞ =0.818. It should be noted that the spectral radius is a measure of numerical damping; ρ =1.0 corresponds to zero numerical damping and descending values below that limit indicate an increasing presence of numerical damping. This set of parameters is denoted as CH2 in order to distinguish it from the sets of parameters which are adopted in the subsequent examples. It should be noted that a value of β=0.8 is initially adopted as an example for the unconditional stable range for this parameter.

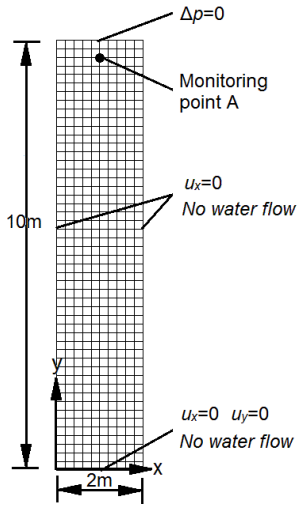


Figure 2-8: FE model for 1-D column analysis subjected to step loading

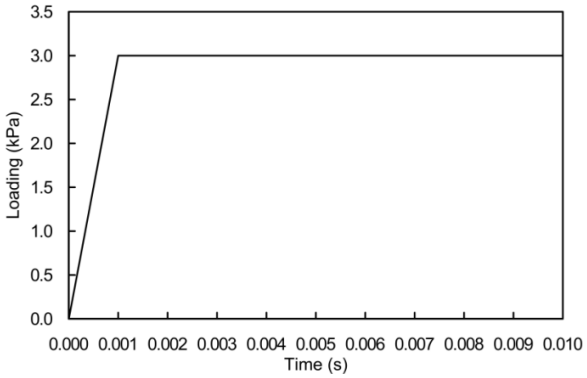


Figure 2-9: The loading history for 1-D column analysis subjected to step loading

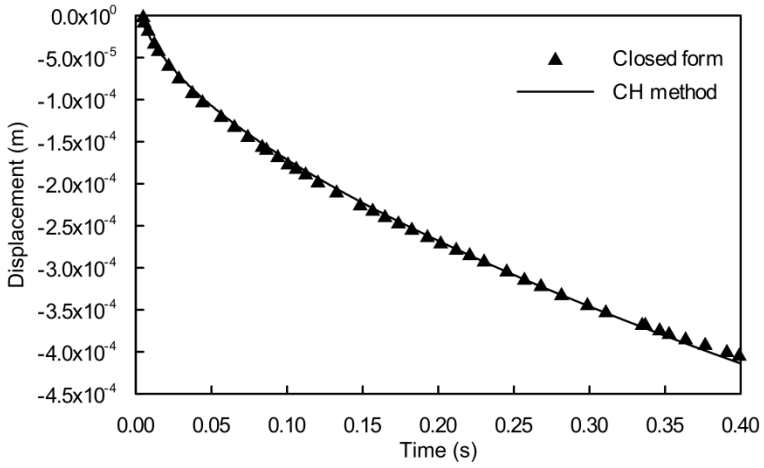
Table 2-3: Soil properties for 1-D column analysis subjected to step loading

Parameter	**Value**
Young's modulus E (kPa)	3.0E+04
Density ρ (g/cm^3)	1.67
Poisson's ratio ν	0.2
Void ratio e	0.5
Permeability k (m/s)	1.0E-02
Time step Δt (s)	1.0E-03

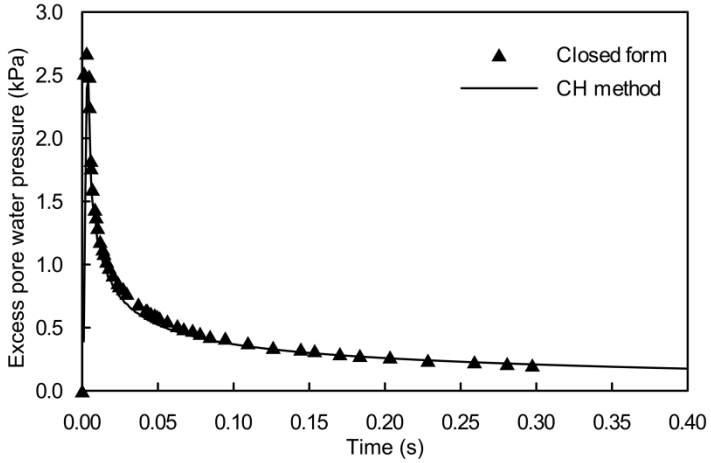
Table 2-4: Integration parameters for the CH method

Parameter	δ	α	α_m	α_f	ρ_∞	β
CH method (CH2)	0.6	0.3025	0.35	0.45	0.818	0.8

The displacement and compressive excess pore water pressure time histories are calculated at a monitoring point A (0.4m below the top boundary as shown in Figure 2-8). These two sets of results are compared in Figure 2-10 with a closed form solution, which was proposed by de Boer et al. (1993) to simulate the dynamic response of saturated porous media. It can be seen from Figure 2-10 that both the displacement and excess pore water pressure time histories are accurately predicted by the numerical analysis. Although not shown here for brevity and clarity of the graphs, the same response is obtained for all β values between 0.5 and 1.0 inclusive.



(a): Displacement time history at point A



(b): Excess pore water pressure time history at point A

Figure 2-10: Comparison of ICFEP results and the closed form solution of de Boer et al. (1993)

In the following analyses, the integration parameter β is varied parametrically in order to validate the stability conditions for the coupled formulation introduced in the

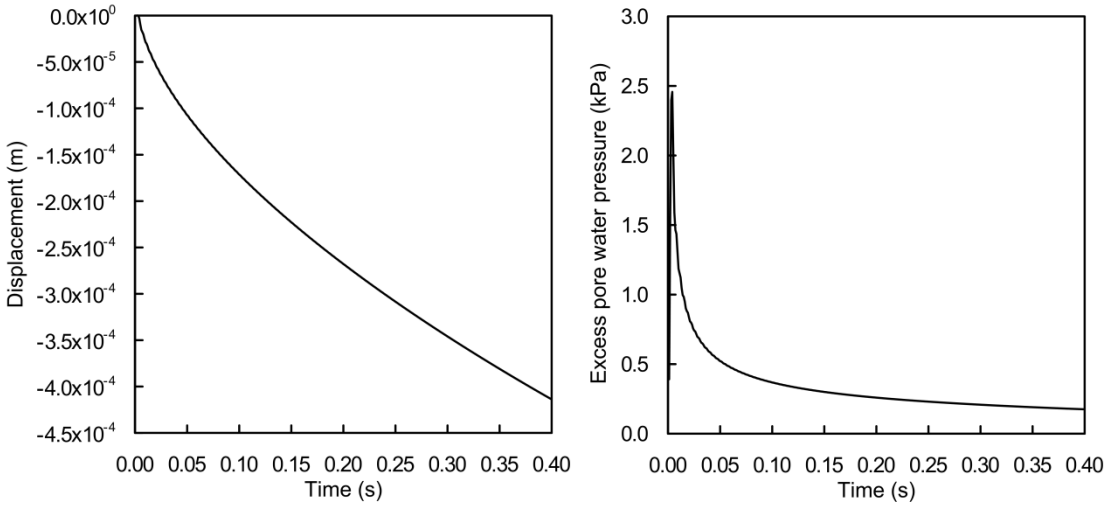
previous section. Both the CH and Newmark methods are employed for the numerical simulations and the integration parameters for these two integration methods are shown in Table 2-5. As mentioned before, the parameters α_m, α_f and β govern the stability conditions for the CH method, which are $\alpha_m \le \alpha_f \le 0.5$ and $\beta \ge 0.5$. Since the stability of the CH method for the one-phase formulation has been previously thoroughly checked by other studies, the focus of the present investigation is only on the stability for the coupled formulation. Therefore, for the following validation analyses, only the effect of parameter β is examined (all other parameters are set to the values shown in Table 2-5). In particular, β is gradually reduced below 0.5 in order to reach numerically the stability limit for both the CH and Newmark methods.

Table 2-5: Integration parameters for the CH and Newmark methods

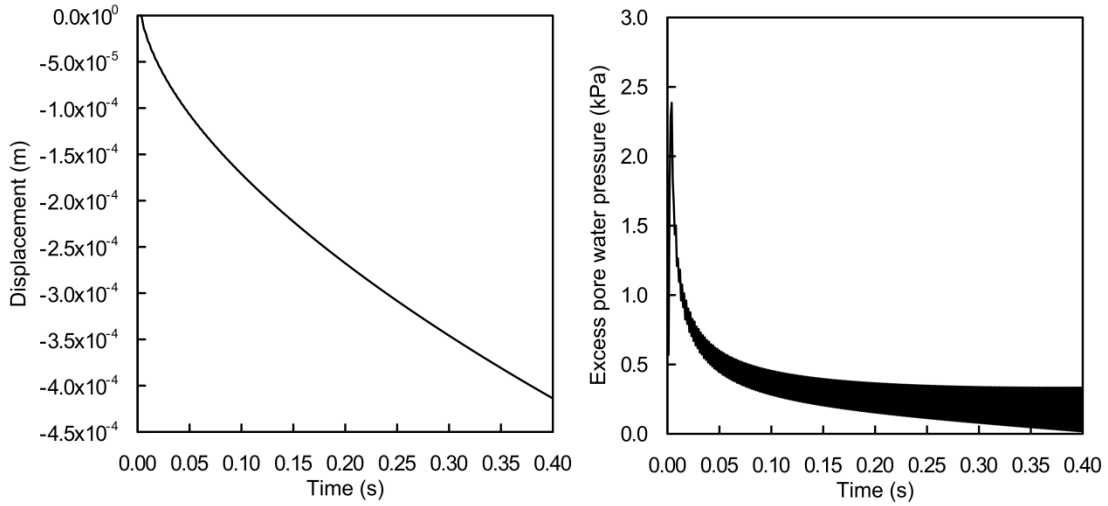
Parameter / Time integration method	Integration scheme	δ	α	α_m	α_f
CH method	CH2	0.6	0.3025	0.35	0.45
Newmark method	NMK2	0.6	0.3025		

Figure 2-11 shows the displacement and excess pore water pressure time histories recorded at the monitoring point A for various values of β by using the CH method. Clearly, when β=0.5-1.0 (taking β=0.8 as an example in Figure 2-11 (a)), both the displacement and pore water pressure responses are stable. When, however, β is reduced to a value slightly less than 0.5 (0.499), an instability in the pore water pressure response is observed immediately. In particular, the oscillation in terms of pore water pressure gradually increases, indicating that the numerical error is increasingly amplified by the unstable solution. Nevertheless, the evolution of displacement with time remains stable (Figure 2-11 (b)). Finally, when β is reduced further to 0.492, the instability in terms of excess pore water pressure aggravates, while the displacement response also starts to be unstable (Figure 2-11 (c)). Consequently, this example confirms that, to ensure stability of the numerical solution when using the CH method, β should be equal or larger than 0.5, which is in agreement with the proposed theoretical condition for unconditional stability. Furthermore, the pore water pressure response seems to be slightly more sensitive to the β value than the displacement response.

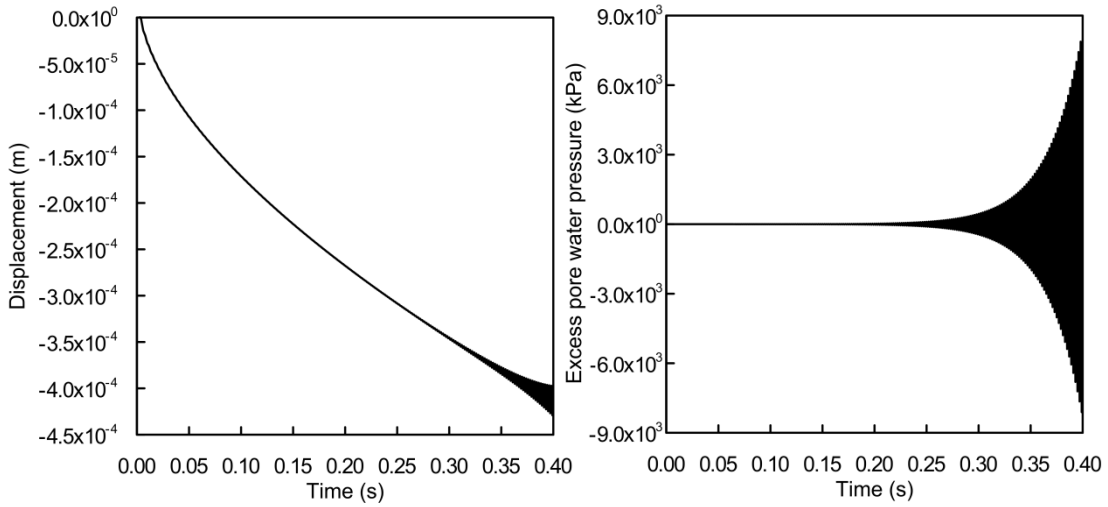
The Newmark method is also used in the numerical analyses to validate the stability conditions. As mentioned before, when the CH method collapses to the Newmark method, the unconditional stability conditions are $2\alpha \geq \delta \geq 0.5$ and $\beta \geq 0.5$. Similarly, herein only the effect of parameter β on the stability is checked and the results are shown in Figure 2-12. Similar results and trends are observed when using the Newmark method to the ones obtained with the CH method. It should be noted that the displacement and excess pore water pressure computed with the Newmark method are slightly more stable than the CH method results. This phenomenon probably results from the different numerical damping introduced by the two methods, which is discussed in detail in Section 2.6.3.



(a): Displacement and excess pore water pressure time histories (CH method and β=0.8)

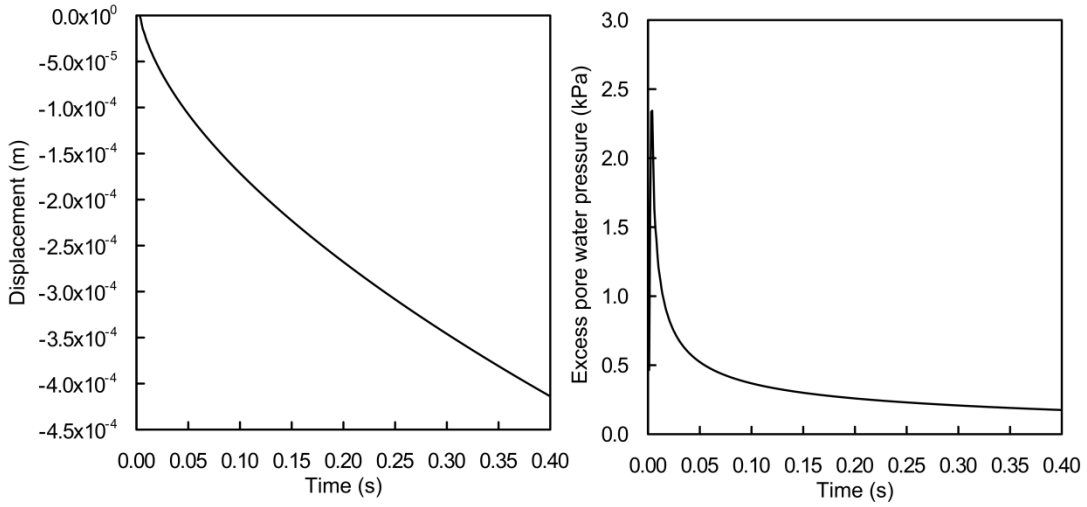


(b): Displacement and excess pore water pressure time histories (CH method and β=0.499)

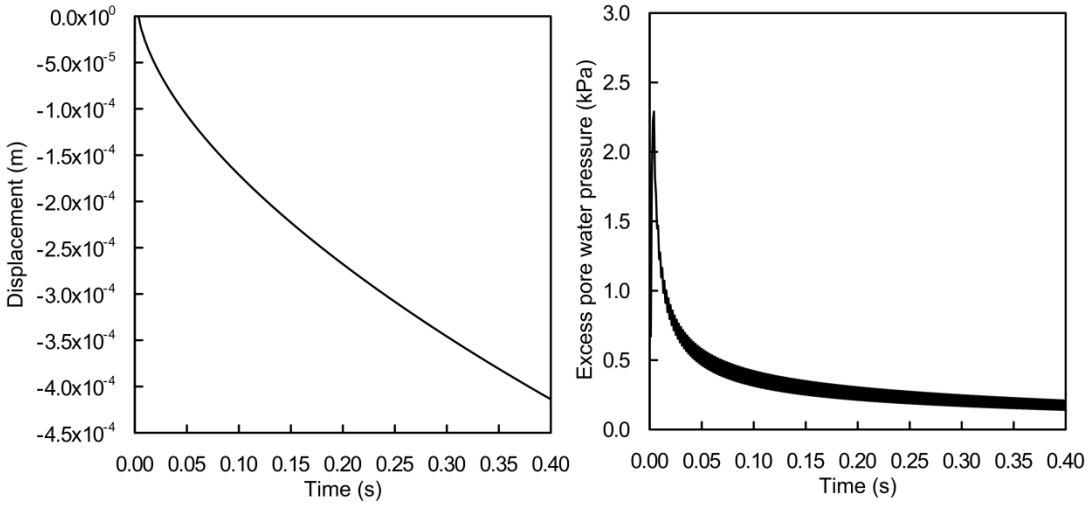


(c): Displacement and excess pore water pressure time histories (CH method and β=0.492)

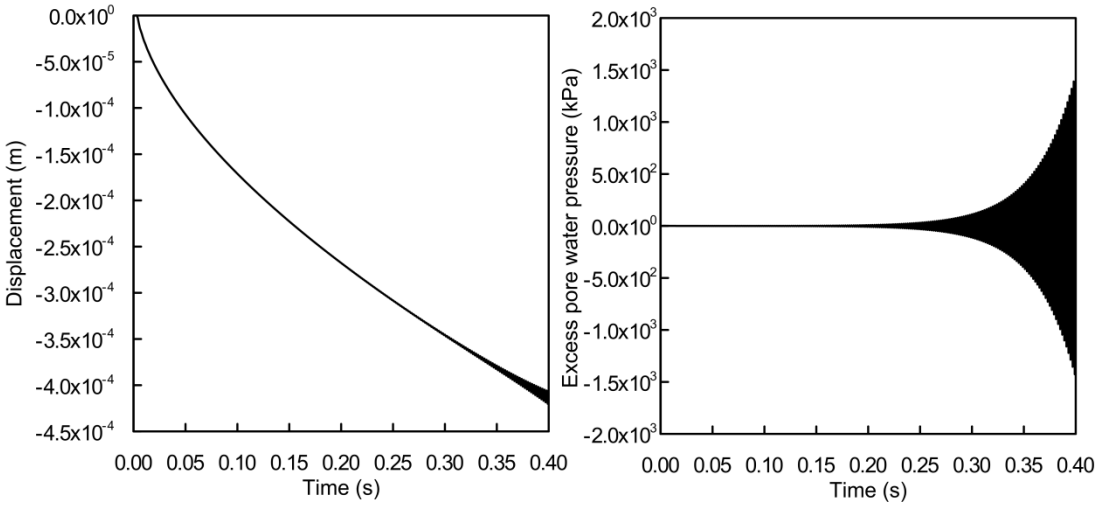
Figure 2-11: Displacement and excess pore water pressure time histories at point A for various β values by using the CH method



(a): Displacement and excess pore water pressure time histories (Newmark method and β=0.8)



(b): Displacement and excess pore water pressure time histories (Newmark method and β=0.499)



(c): Displacement and excess pore water pressure time histories (Newmark method and β=0.492)

Figure 2-12: Displacement and excess pore water pressure time histories at point A for various β values by using the Newmark method

2.6.2 1-D column subjected to harmonic loading

To validate the stability conditions of the CH method when subjected to more complicated loading, 1-D soil column analyses under harmonic loading are carried out in this part. The FE mesh (consisting of 80 8-noded quadrilateral isoparameteric elements) and the boundary conditions are shown in Figure 2-13. The displacement and hydraulic boundary conditions are identical to the ones used in the previous section. Furthermore, a uniformly distributed sinusoidal load is applied on the top boundary of the model, which is described by Equation 2-67 and is illustrated in Figure 2-14. Lastly, the soil properties of the model are listed in Table 2-6.

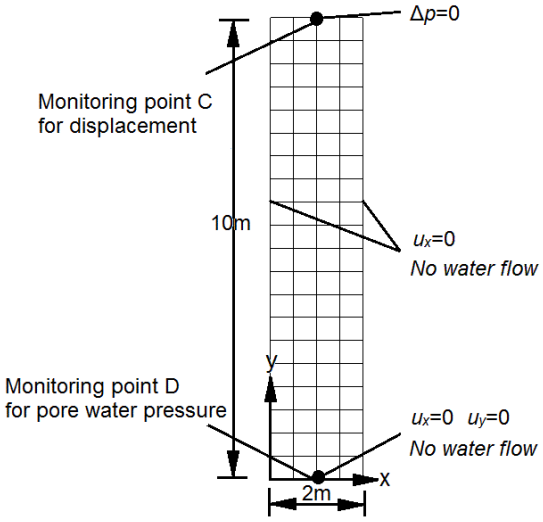


Figure 2-13: FE model for 1-D column analysis subjected to harmonic loading

$$q = \begin{cases} t/0.02 & 0 \le t \le 0.02s \\ 1+0.25\sin\left[20\pi\cdot\left(t-0.02\right)\right] & t > 0.02s \end{cases} \qquad 2\text{-}67$$

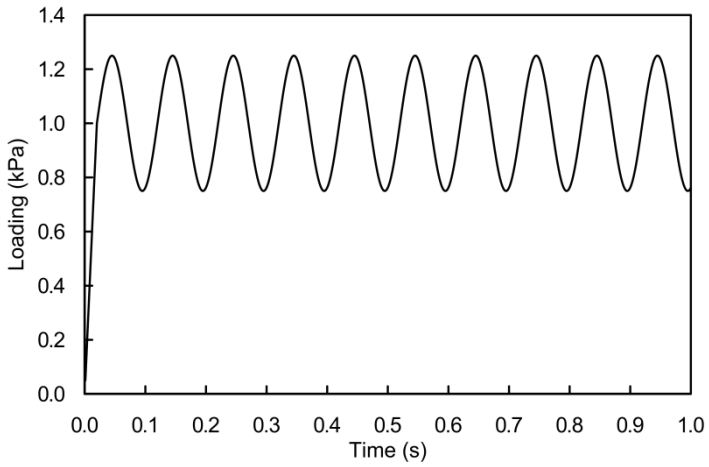


Figure 2-14: The loading history for 1-D column analysis subjected to harmonic loading

Table 2-6: Soil properties for 1-D column analysis subjected to harmonic loading

Parameter	Case1
Young's modulus E (kPa)	1.0E+04
Density ρ (g/cm^3)	2.0
Poisson's ratio ν	0.2
Void ratio e	0.538
Permeability k (m/s)	1.0E-15
Time step Δt (s)	1.0E-03

The numerical predictions of this study are first compared with the results presented by Li et al. (2003), where a similar FE analysis was conducted and an "iterative stabilised fractional step" time integration algorithm was used. It should be noted that an impermeable soil column was simulated by Li et al. (2003). However, in the present study, a very low permeability value (1.0E-15 m/s) is adopted to represent an impermeable material, utilising the two-phase coupled formulation. The CH method is utilised for the numerical simulation and the employed parameters are shown Table 2-4. Figure 2-15 shows the comparison of the compressive excess pore water pressure time history at the point D, which shows good agreement between the numerical prediction and Li et al. (2003). Although not shown here for brevity and clarity of the graphs, the same response is obtained for all β values between 0.5 and 1.0 inclusive.

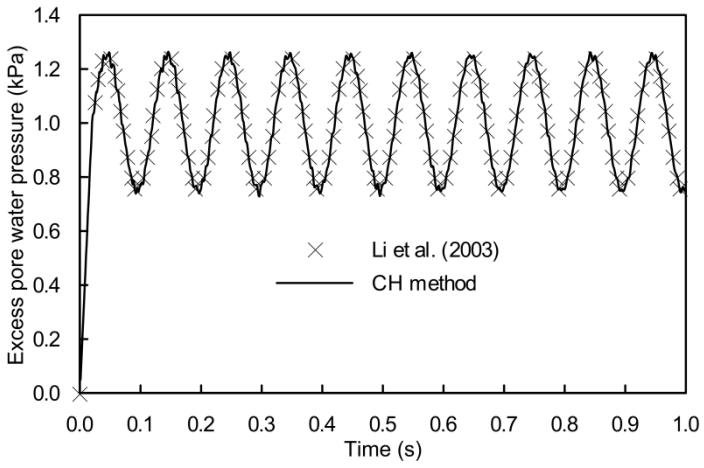


Figure 2-15: Comparison of the excess pore water pressure time history at point D

Further analyses are then performed in which β is reduced below 0.5 in order to check numerically the stability limit for the CH method. The results show the same

stable pore water pressure response as shown in Figure 2-15, even for β values as low as 0.2. This is attributed to the employed extremely low permeability for the soil column. In particular, the multiplier in front of β in the dynamic coupled formulation (Equation 2-58) is ϕ, which is the scalar form of the matrix $[\Phi]$. For the analysis with low permeability, $[\Phi]$ is close to zero, and therefore the effect of β on the stability is insignificant. However, when high permeability (k=1.0E-2 m/s) is adopted for the numerical simulation, the impact of β becomes significant. This is confirmed by the results presented in Figure 2-16, where high permeability is used and instability is observed.

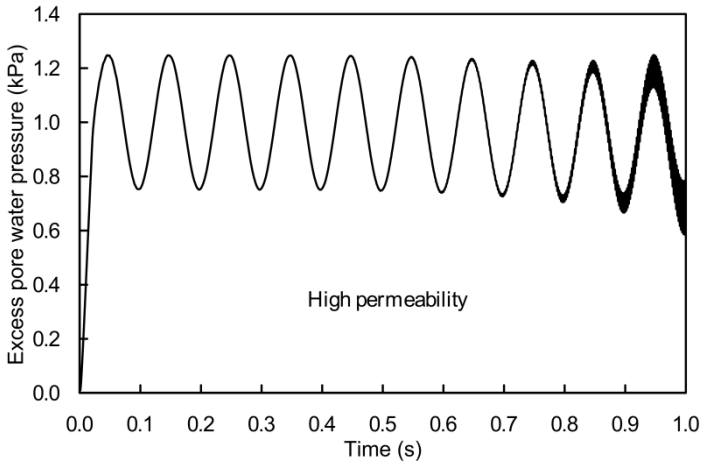
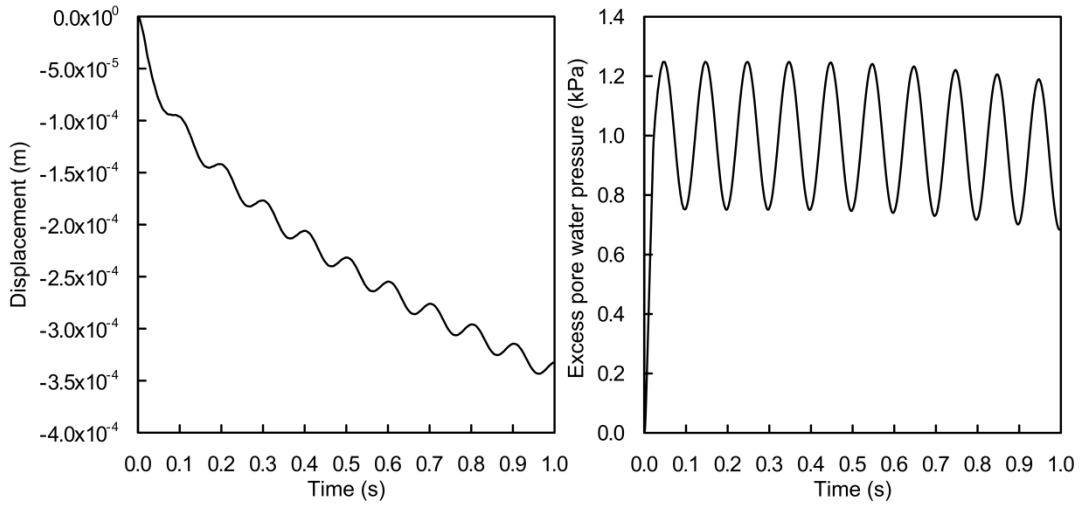


Figure 2-16: Excess pore water pressure time history of analyses with high permeabilities at point D

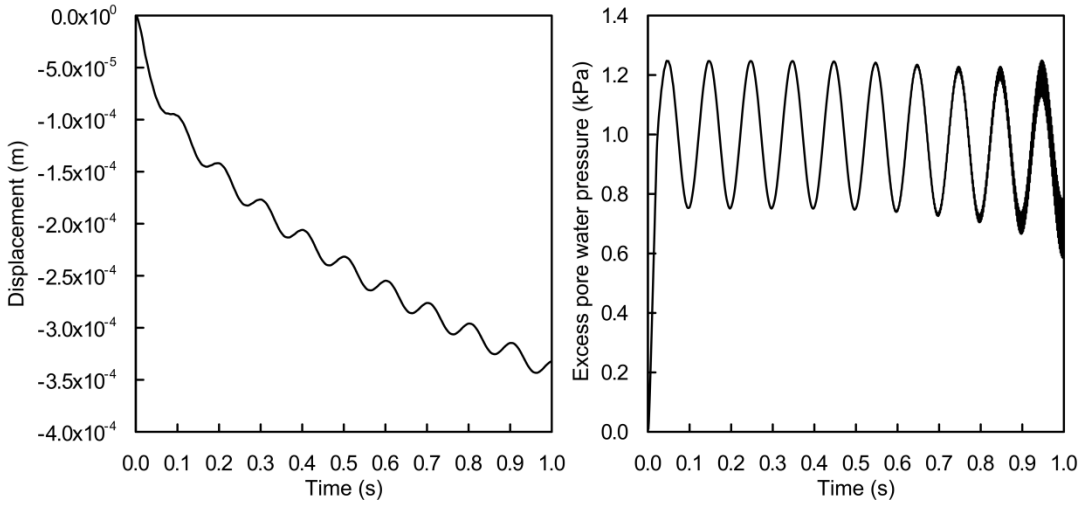
(CH method, β=0.497 and high permeability: 1.0E-2m/s)

However, the effect of the parameter β on the stability of the analysis becomes more significant when higher soil permeability is employed. In the following analysis, a higher permeability value (k=1.0E-2m/s) is adopted for the soil column, where β is again gradually reduced below 0.5 to reach numerically the stability limit. Two integration methods (CH and Newmark methods) are used to validate the stability conditions and the analysis results by using two methods in terms of displacement (at point C) and excess pore water pressure (at point D) time histories are shown in Figures 2-17 and 2-18. Clearly, when β=0.5-1.0 (taking β=0.8 as an example in Figures 2-17 (a) and 2-18 (a)), both the displacement and excess pore water pressure responses are stable and the same results are obtained for values of $0.5 \le \beta \le 1.0$. When, however, β is reduced to a same slightly smaller value of 0.497, the pore water pressure response starts to be unstable immediately, while the displacement response is still stable

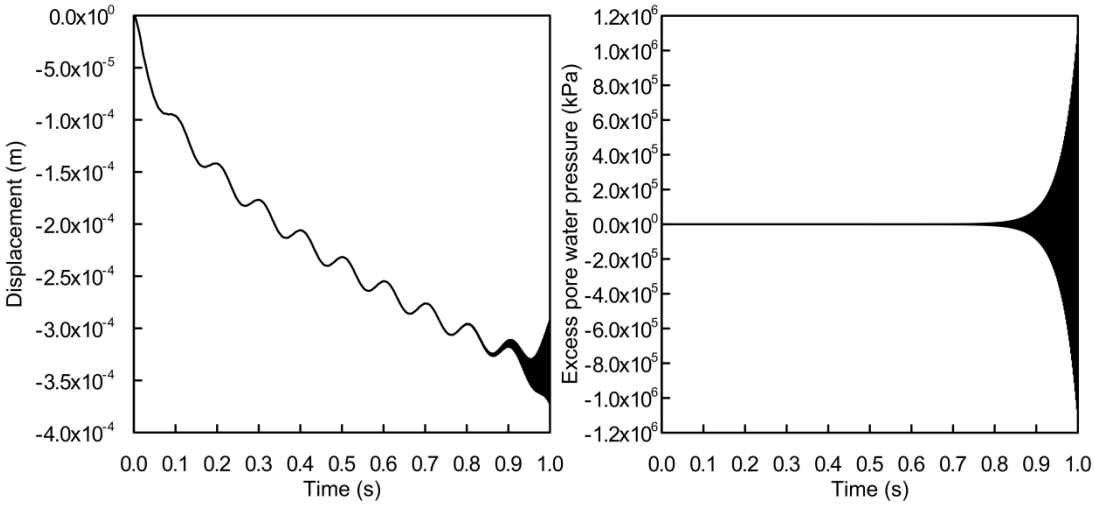
(Figures 2-17 (b) and 2-18 (b)). Furthermore, when β is reduced to 0.493, the instability of the excess pore water pressure aggravates and this triggers the instability of the displacement response (Figures 2-17 (c) and 2-18 (c)). Therefore, good agreement is observed between the numerical results and the theoretical stability conditions for the 1-D column analysis subjected to harmonic loading. Moreover, same as the phenomenon observed in the previous section, the results of the analysis using the Newmark method seem to be more stable than those using the CH method, which is explained in detail in Section 2.6.3.



(a): Displacement and excess pore water pressure time histories (CH method and β=0.8)

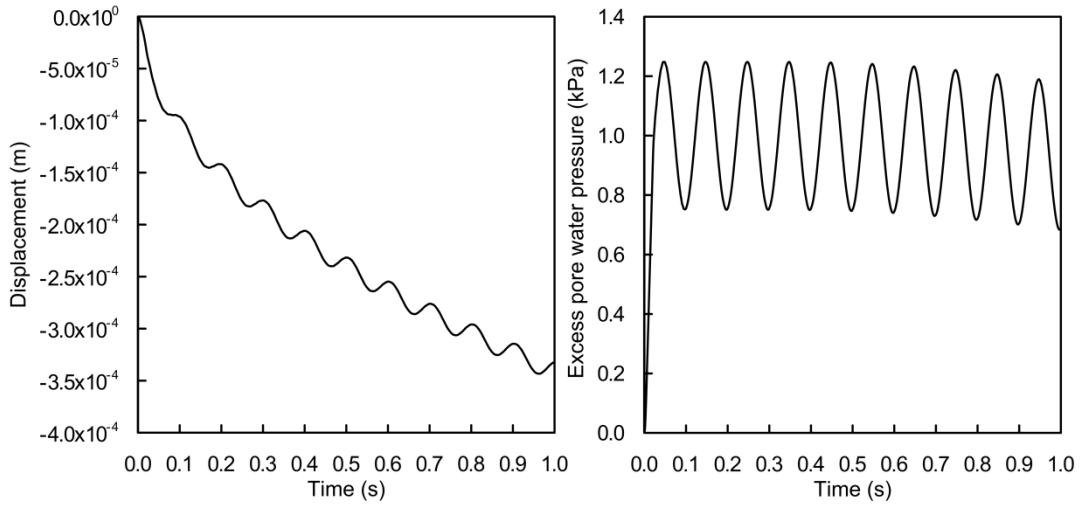


(b): Displacement and excess pore water pressure time histories (CH method and β=0.497)

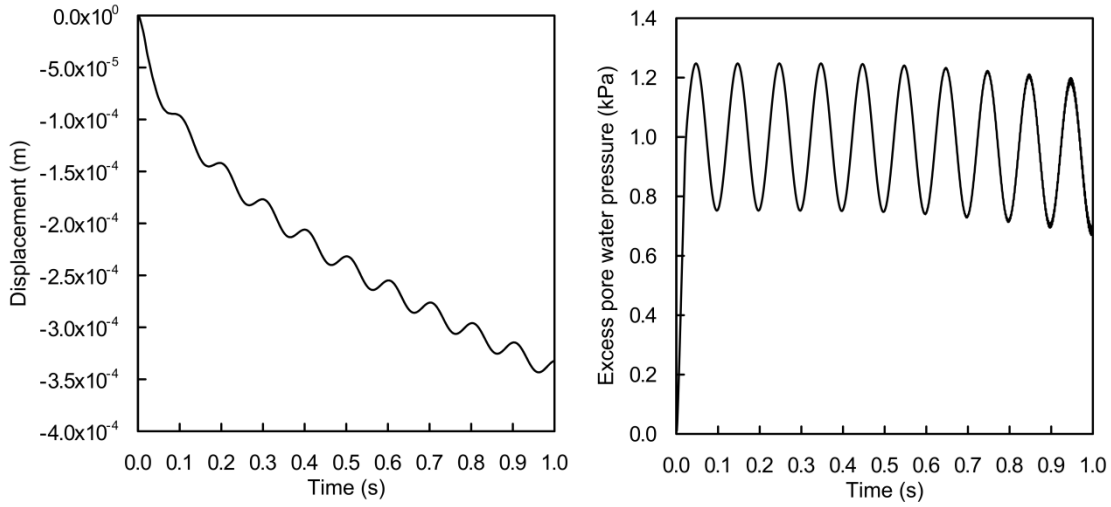


(c): Displacement and excess pore water pressure time histories (CH method and β=0.493)

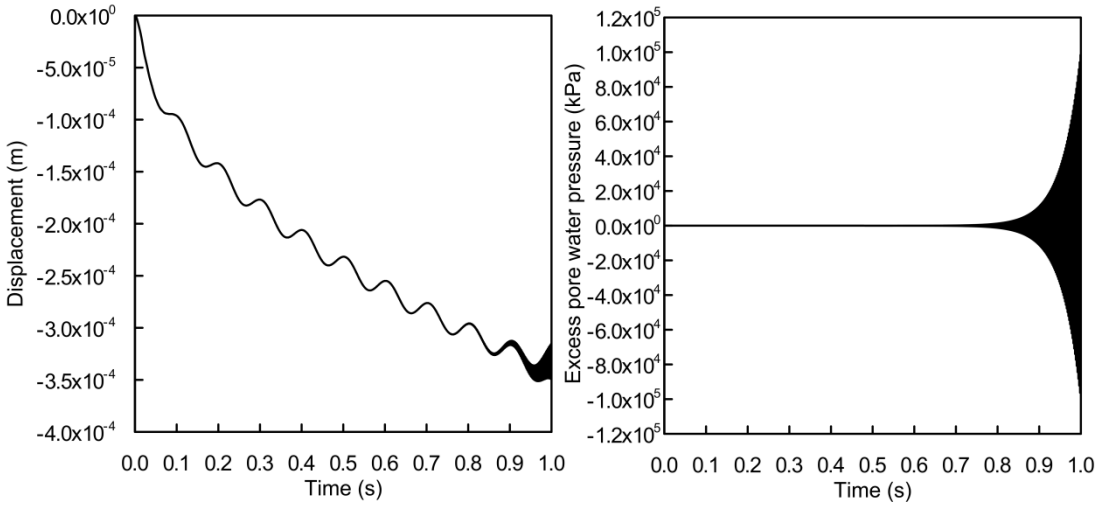
Figure 2-17: Displacement (at point C) and excess pore water pressure (at point D) time histories for various β values by using the CH method



(a): Displacement and excess pore water pressure time histories (Newmark method and β=0.8)



(b): Displacement and excess pore water pressure time histories (Newmark method and β=0.497)



(c): Displacement and excess pore water pressure time histories (Newmark method and β=0.493)

Figure 2-18: Displacement (at point C) and excess pore water pressure (at point D) time histories for various β values by using the Newmark method

2.6.3 1-D column subjected to impulse loading

As mentioned before, the main advantage of the CH method is that the numerical damping is controllable by the user allowing the dissipation of spurious high-frequency noise without affecting low-frequency response. For the one-phase formulation, this feature of the CH method has been thoroughly investigated in Kontoe (2006) and Kontoe et al. (2008a). However, for the two-phase coupled formulation, the numerical damping does not only affect the displacement response, but also the predicted pore water pressure. Therefore, in order to explore the effects of numerical damping on the predicted response, 1-D FE analyses subjected to impulse loading are carried out herein. The FE mesh and the boundary conditions are the same as the model used in the previous section, shown in Figure 2-13. Furthermore, the loading applied on the top boundary of the soil column is illustrated in Figure 2-19 and the soil properties are shown in Table 2-7.

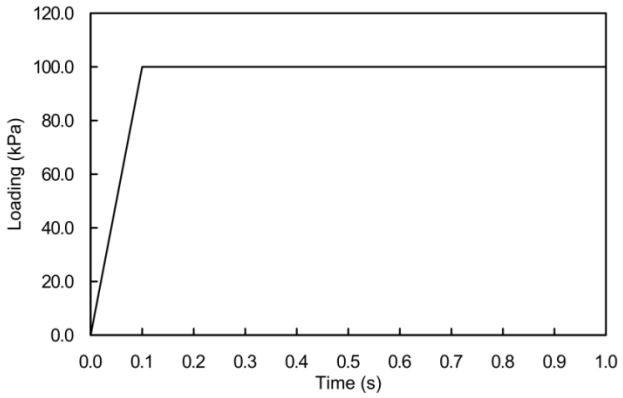


Figure 2-19: The loading history for 1-D column analysis subjected to impulse loading

Table 2-7: Soil properties for 1-D column analysis subjected to impulse loading

Parameter	Value
Young's modulus E (kPa)	1.0E+06
Density ρ (g/cm^3)	2.0
Poisson's ratio ν	0.2
Void ratio e	0.538
Permeability k (m/s)	1.0E-02
Time step Δt (s)	1.0E-01

Two time integration methods are used in the analyses, the CH and the Newmark methods, adopting in total 5 sets of parameters, which are shown in Table 2-8. The spectral radius (ρ) variations against $\Delta t / T$ for the five sets of parameters are shown in Figure 2-20, where $\rho = 1$ corresponds to zero numerical damping and $\rho = 0$ corresponds to the maximum attained numerical damping. Furthermore, T is the natural period of an undamped SDOF system and Δt is the time step. For the examined soil column this corresponds to an equivalent SDOF $\Delta t/T$ of 1.8. Therefore, based on Figure 2-20, it can be seen that, when $\Delta t/T$ is equal to 1.8, the order of the numerical damping obtained by the five integration methods is CH3>NMK2>CH2>CH1=NMK1.

Table 2-8: Parameters for the CH and Newmark method

Time integration method	**Integration scheme**	δ	α	α_m	α_f	β
CH method	CH2	0.6	0.3025	0.35	0.45	0.8
CH method	CH1	0.5	0.25	0.5	0.5	0.8
Newmark method	NMK2	0.6	0.3025			0.8
Newmark method	NMK1	0.5	0.25			0.8
CH method	CH3	0.9286	0.5102	-0.1429	0.2857	0.8

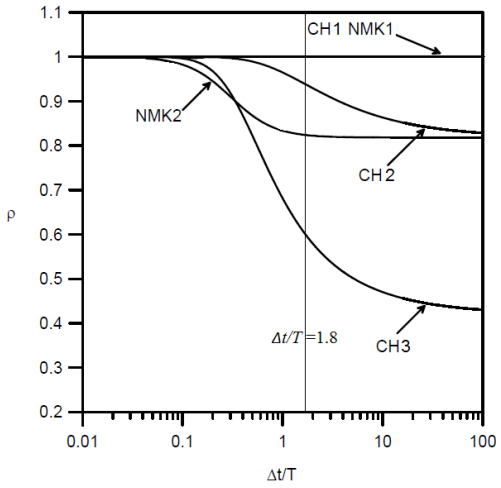


Figure 2-20: Spectral radii for the CH3, CH2, CH1, NMK2 and NMK1 method (after Kontoe (2006))

The acceleration and displacement time histories at the monitoring point C and the excess pore water pressure time history at the monitoring point D are computed with the five time integration methods. To investigate the impact of numerical damping on the

predicted response, the analysis results using the five methods are compared in Figures 2-21, 2-22 and 2-23, in terms of acceleration, displacement and excess pore water pressure time histories respectively, in both original and zoom-in scales. From the three figures, it can be seen that the predicted oscillations in different responses by the five methods vary significantly. In particular, based on the comparison of acceleration time histories, undamped oscillations are observed for the dynamic response predicted by CH1 and NMK1 methods, while for those analyses involving numerical damping (CH2, NMK2 and CH3), oscillations are more significantly damped as larger numerical damping is employed. Furthermore, for the displacement and pore water pressure response, it can be seen that with a larger numerical damping, the oscillation magnitude reduces more dramatically, approaching faster the steady state. However, for more general recommendations for the selection of numerical damping, a wider study is necessary on a range of real engineering problems. Finally, this explains the observations of the previous two sections, that the analyses using the NMK2 method are more stable than those using the CH2 method, due to the higher numerical damping of the NMK2 method.

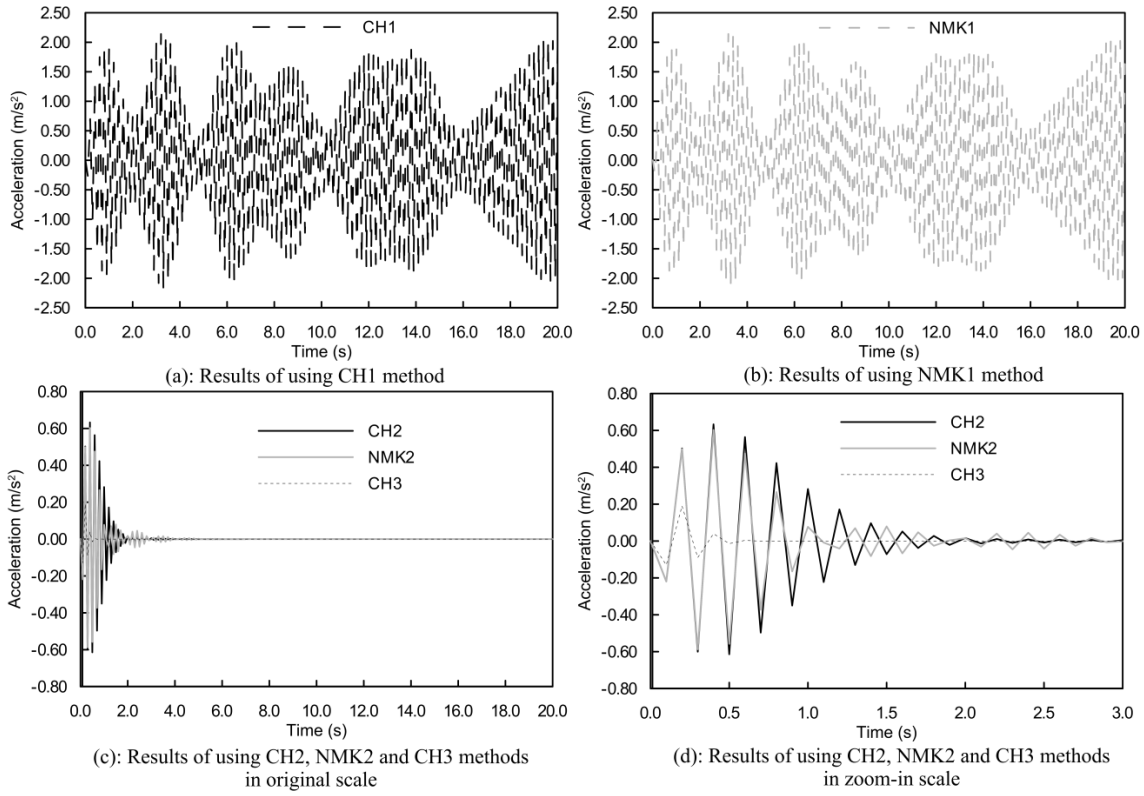
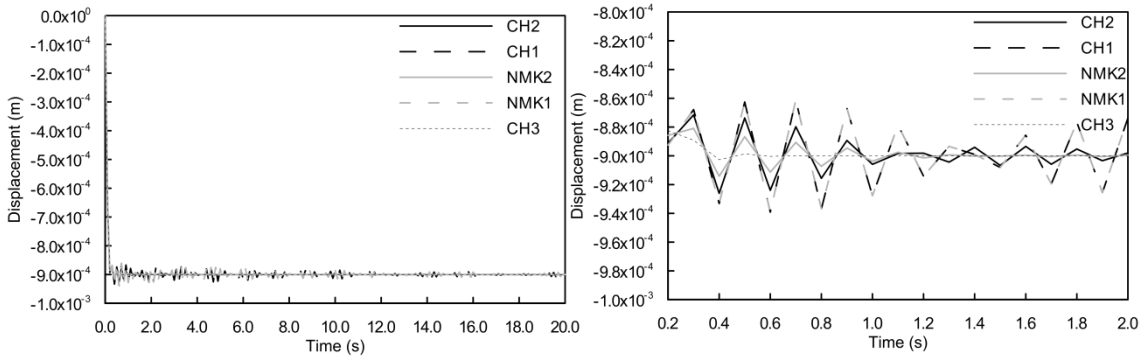
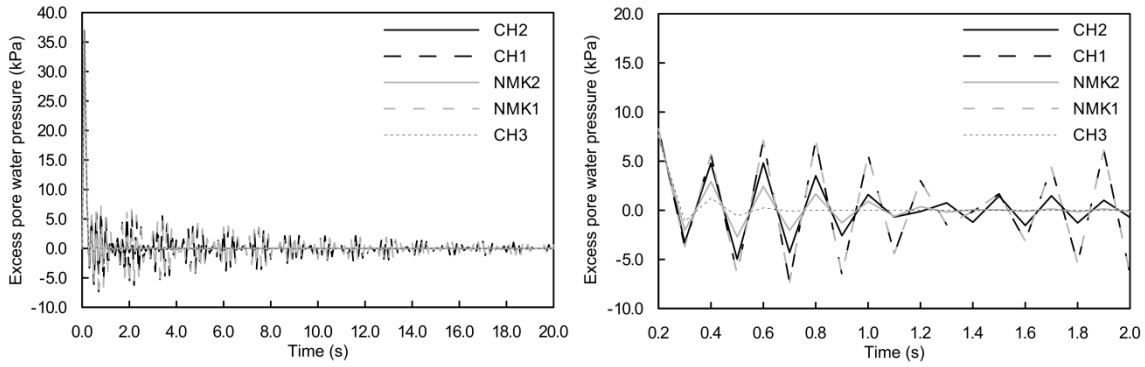


Figure 2-21: Comparison of the acceleration time histories (at point A) by using five time integration methods



(a): Results in original scale (b): Results in zoom-in scale

Figure 2-22: Comparison of displacement time histories (at point A) by using five time integration methods



(a): Results in original scale (b): Results in zoom-in scale

Figure 2-23: Comparison of pore pressure time histories (at point B) by using five time integration methods

2.6.4 Elastic foundation subjected to step loading

In this part, the stability conditions are validated in a more complicated boundary value problem, where coupled FE analyses of a foundation assuming linear elastic behaviour are conducted. The FE mesh and boundary conditions of the elastic foundation analysis are shown in Figure 2-24, where only a half of the model is discretised because of the symmetry and 100 8-noded quadrilateral isoparameteric elements are generated. For the displacement boundary conditions, both horizontal and vertical displacements are restricted at the bottom boundary and only horizontal displacements are restricted at the lateral boundaries. It should be noted that advanced absorbing boundary conditions could be used to avoid the reflection of waves for the dynamic analysis. However, since the purpose of this analysis is to investigate the stability conditions for the CH method, only elementary boundary conditions are

utilised. Furthermore, for the hydraulic boundary conditions, pore water pressure is prescribed as zero at the ground surface (outside the footing) and is not allowed to change. The remaining boundaries are considered to be impermeable (i.e. no flow across the boundaries). Finally, a uniformly distributed load is applied on the top boundary, as illustrated in Figure 2-25.

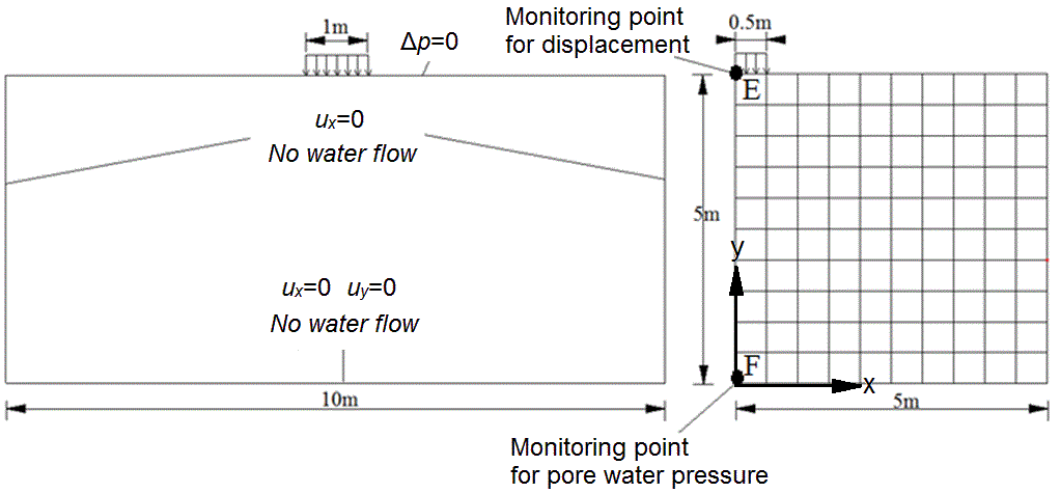


Figure 2-24: FE model for the elastic foundation analysis

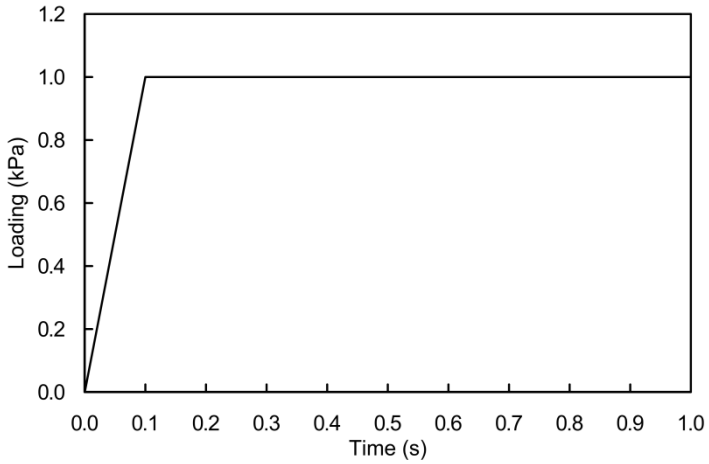
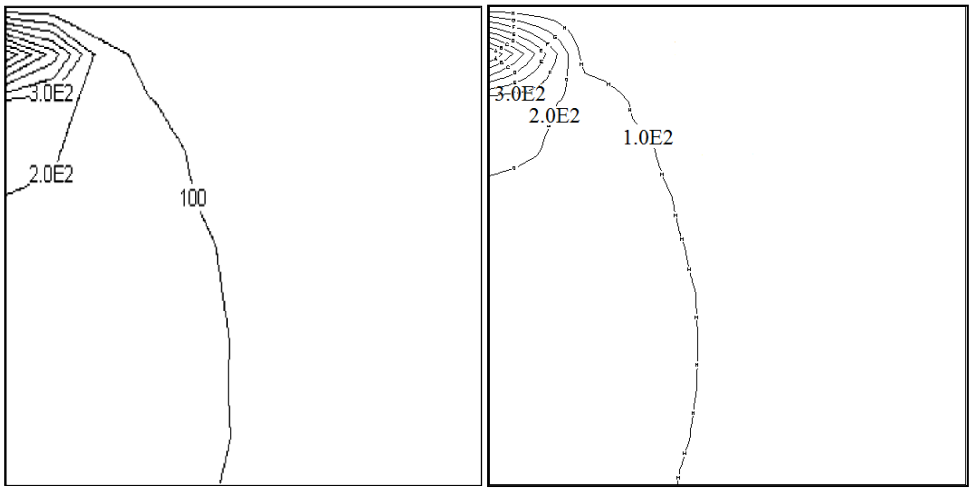


Figure 2-25: The loading history for the elastic foundation analysis

Table 2-9: Soil properties for the elastic foundation analysis

Parameter	Case1	Case2
Young's modulus E (kPa)	1.0E+04	1.0E+04
Density ρ (g/cm^3)	2.0	2.0
Poisson's ratio ν	0.2	0.2
Void ratio e	0.538	0.538
Permeability k (m/s)	1.0E-15	1.0E-03
Time step Δt (s)	1.0E-03	1.0E-03

For the elastic foundation analysis, the two sets of parameters (case1 and case2) shown in Table 2-9 are examined, which have the same soil properties as that of the analyses carried out by Li et al. (2003) and Soares (2008) respectively. The CH method is utilised for the numerical simulation and the employed parameters are shown in Table 2-4. Firstly, the contours of the excess pore water pressure for case1 at the end of the analysis are shown in Figure 2-26, where the results from numerical analysis are compared with the results given by Li et al. (2003). Secondly, the time history of the displacement at the monitoring point for case2 is shown in Figure 2-27 and is compared with the results provided by Soares (2008). As shown in both figures, the numerical results compare favourably with the results from previous researchers.



(a): Results of Li et al. (2003) (b): Results from ICFEP using the CH method

Figure 2-26: Comparison of the contour of the total pore water pressure at t=1.0s (Pa)

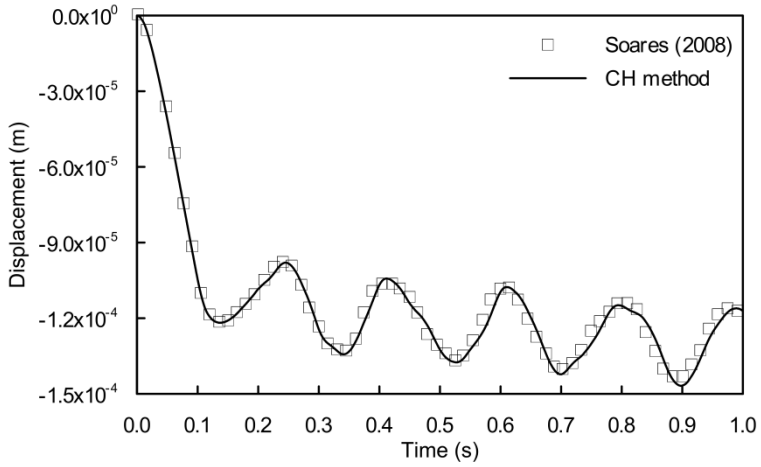


Figure 2-27: Comparison of the time history of the displacement at point E

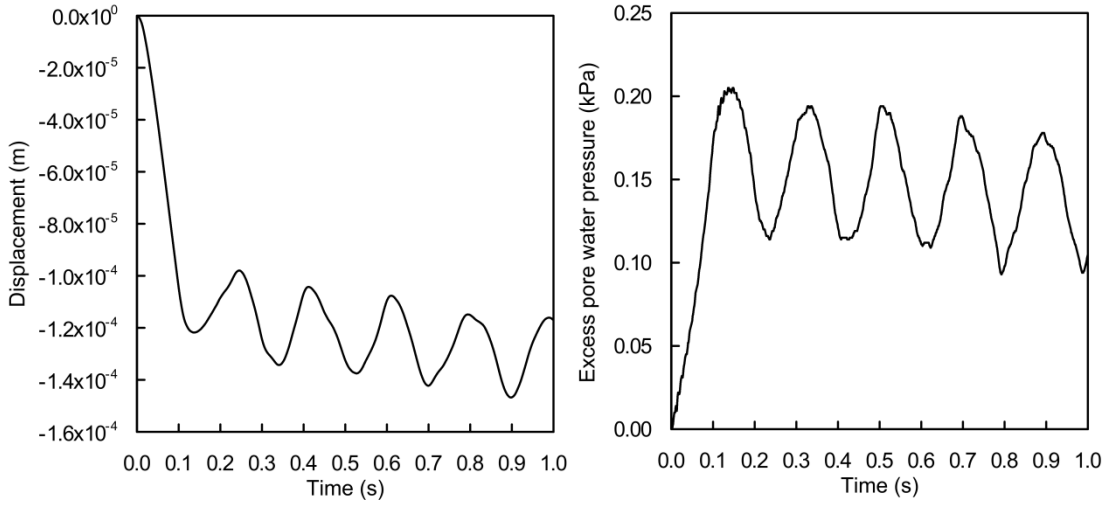
In the following analyses, β is gradually reduced below 0.5 to reach numerically the stability limit for the coupled analysis using the CH method. The FE analyses conducted here are based on the Case2 of the elastic foundation analysis, which involves higher permeability in order to highlight the effect of β on the stability.

The displacement (at point E) and excess pore water pressure (at point F) time histories are presented in Figure 2-28. When β=0.5-1.0, both displacement and pore water pressure responses are stable, as shown in Figure 2-28 (a) of taking β=0.8 for example. However, based on Figure 2-28 (b), when β is reduced to 0.480, the pore water pressure response starts to be unstable. Nevertheless, the displacement response remains stable. Lastly, when β is reduced further to 0.474, the instability of excess pore water pressure deteriorates, which triggers the instability of displacement response (Figure 2-28 (c)).

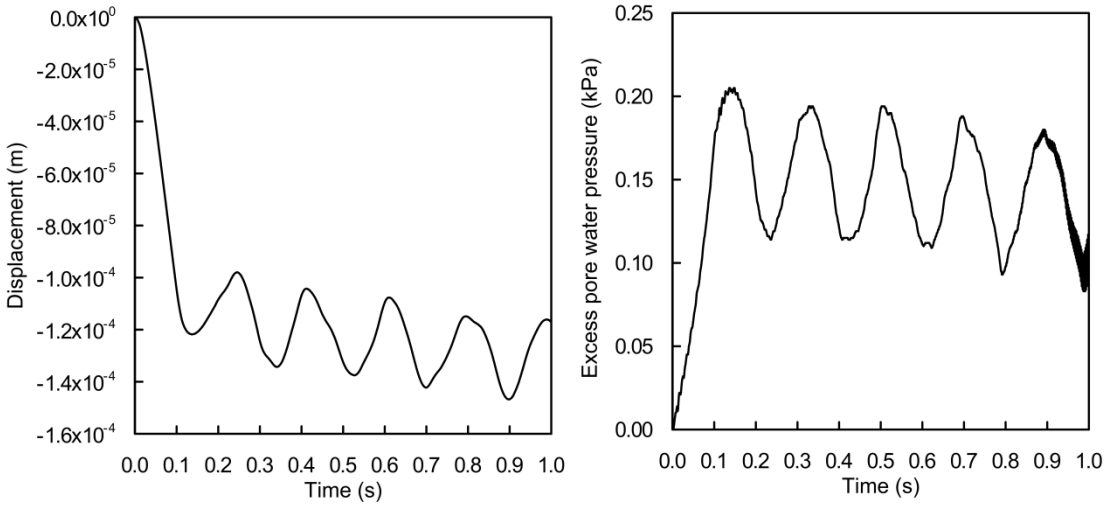
Furthermore, the contours of the displacement and excess pore water pressure at the end of the analyses (at t=1.0s) are presented in Figure 2-29. It should be noted hat for each analysis the contours show a range of displacement and excess pore water pressure between the maximum and the minimum respective values in the mesh. Firstly, when β=0.8, stable displacement and pore pressure responses are observed in the contours (Figure 2-29 (a)). The excess pore water pressure is negligible at this stage. Secondly, when β is reduced to 0.480, the excess pore water pressure starts to be unstable from the bottom of the numerical model, creating unusual contour patterns, while the displacement response remains stable along the whole model (Figure 2-29 (b)). Thirdly, when β is reduced further to 0.474, the instability of excess pore water pressure

worsens, which triggers the instability of displacement response (Figure 2-29 (c)). Furthermore, for both displacement and excess pore water pressure, the response at the bottom of the numerical model is more unstable than the response at the top.

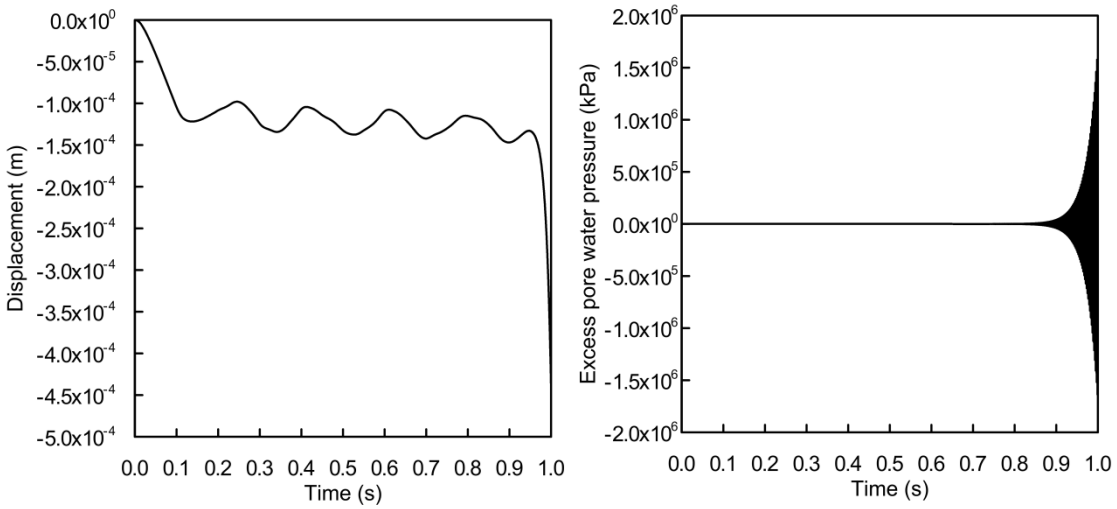
Consequently, based on the results shown for the elastic foundation analysis, in order to obtain stable dynamic results with the CH method, β should be equal or larger than 0.5. Furthermore, the pore water pressure response is slightly more sensitive to the values of β than the displacement response. Therefore, good agreement is observed between FE analysis results and the theoretical stability conditions.



(a): Displacement and excess pore water pressure time histories (CH method and β=0.800)

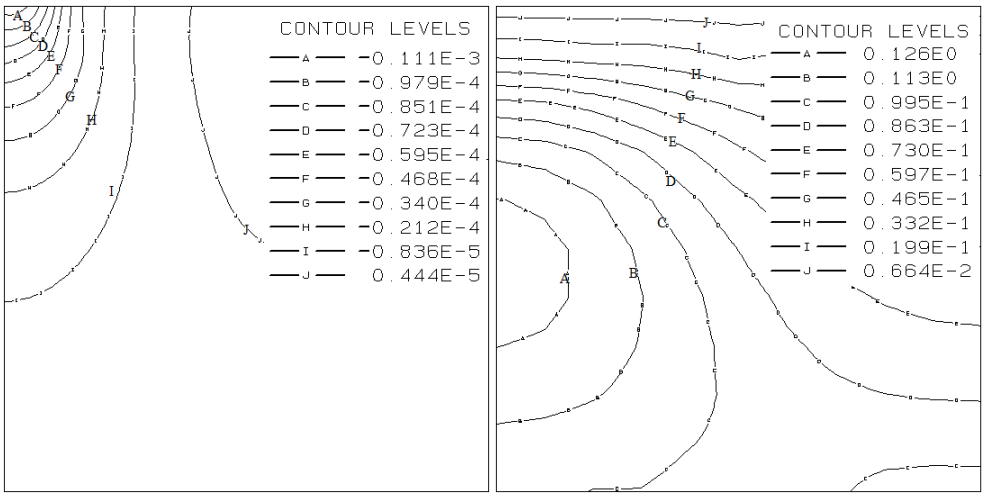


(b): Displacement and excess pore water pressure time histories (CH method and β=0.480)

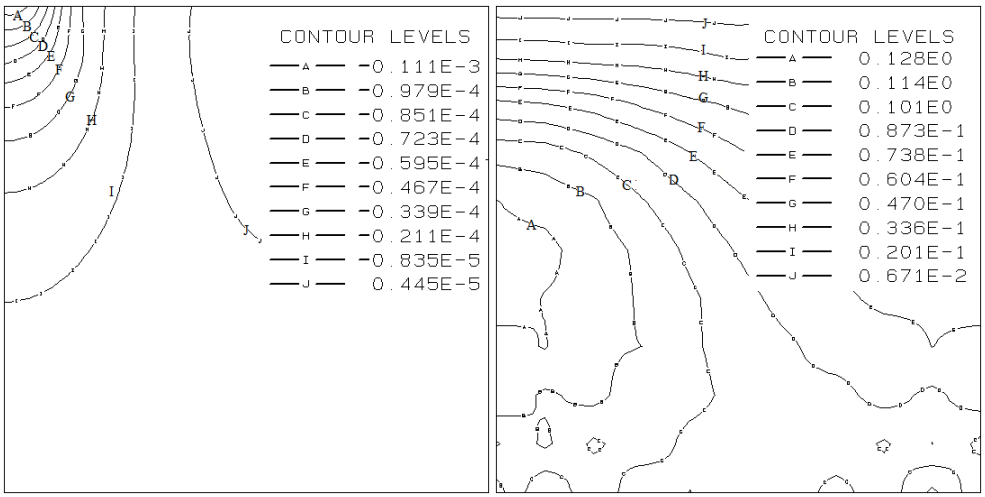


(c): Displacement and excess pore water pressure time histories (CH method and β=0.474)

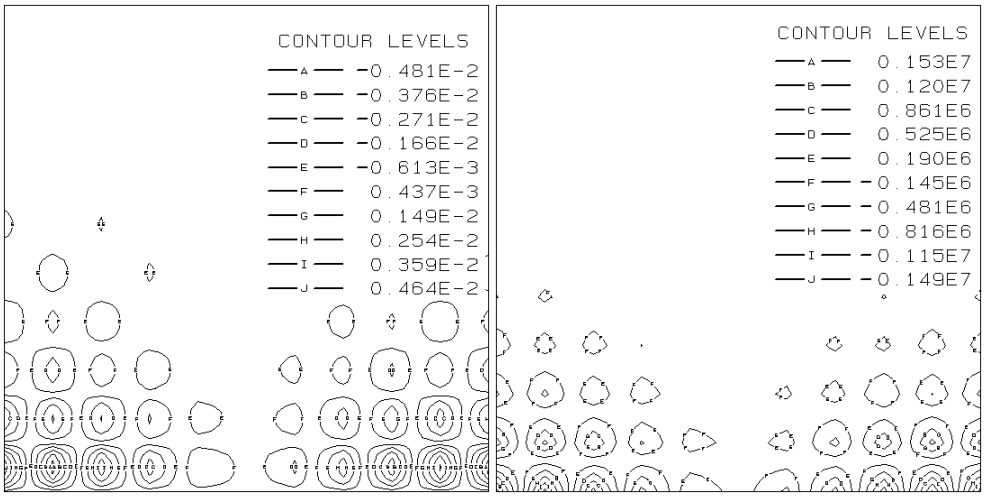
Figure 2-28: Displacement (at point E) and excess pore water pressure (at point F) time histories of various β values by using CH method



(a): Displacement and excess pore water pressure contours (CH method and β=0.800)



(b): Displacement and excess pore water pressure contours (CH method and β=0.480)



(c): Displacement and excess pore water pressure contours (CH method and β=0.474)

Figure 2-29: Displacement and excess pore water pressure contours at t=1.0s of various β values

(displacement: m and excess pore water pressure: kPa)

2.6.5 Elasto-plastic foundation subjected to step loading

In order to explore the stability performance of the CH method beyond the assumptions of the theoretical investigation, a strip footing resting on the ground surface is analysed, assuming elasto-plastic soil constitutive behaviour. The foundation mesh and the boundary conditions are the same as that of the elastic foundation presented in the previous section. Identically, uniformly distributed step load is applied on the top boundary, as shown in Figure 2-30. However, the magnitude of this step loading is larger in order to trigger the plasticity of the soil material of the foundation.

A variant of the bounding surface plasticity model of Papadimitriou and Bouckovalas (2002) (Taborda, 2011; Taborda et al. 2014), is utilised for this foundation analysis, which is capable of simulating elasto-plastic cyclic behaviour of granular materials subjected to dynamic loading. For this constitutive model, a kinematic yield surface, bounding surface, dilatancy surface and critical state surface (illustrated in Figure 2-31) are utilised to simulate the plastic deformation, hardening and softening behaviour and failure criterion. 29 model parameters are required to describe the soil behaviour and various surfaces for this model. The input parameters for the soil properties are based on the calibration of Taborda (2011) and Taborda et al. (2014) for the Nevada sand. However, herein only the basic soil properties are given in Table 2-10 and the reader is directed to Taborda et al. (2014) for detailed description of model parameters and their calibration.

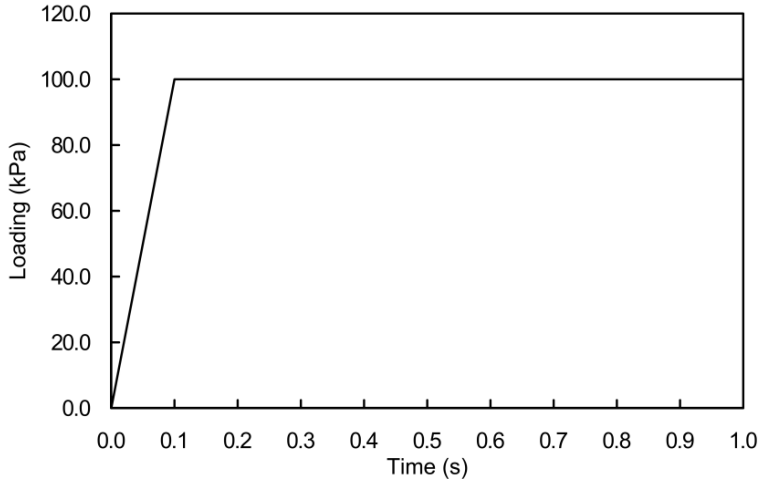


Figure 2-30: The loading history for the elasto-plastic foundation analysis

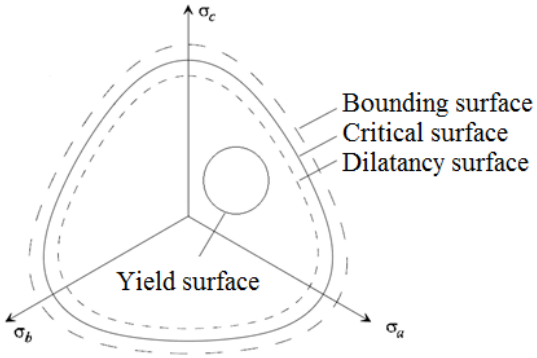
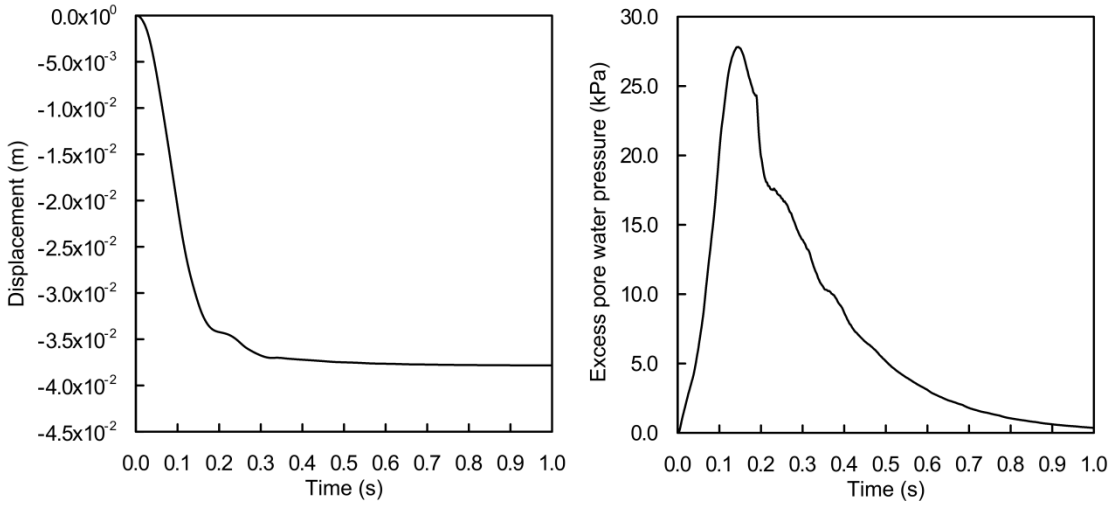


Figure 2-31: Schematic graph for the PB bounding surface sand model (after Taborda (2011))

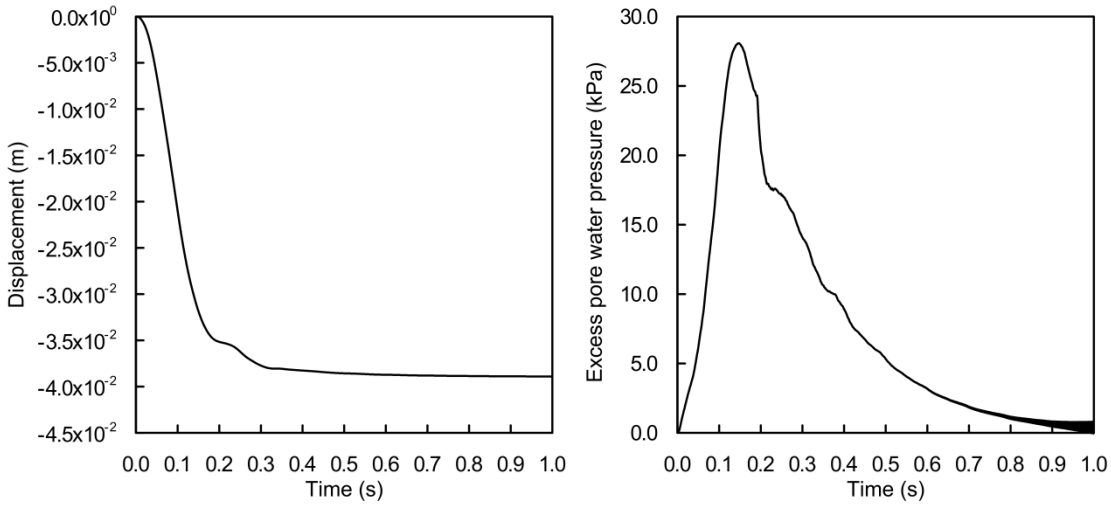
Table 2-10: Soil properties for the elasto-plastic foundation analysis

Parameter	Soil properties
Shear modulus G (kPa)	164.0
Density ρ (g/cm^3)	2.0
Poisson's ratio ν	0.20
Void ratio e	0.724
Permeability k (m/s)	1.0E-02
Time step Δt (s)	1.0E-03

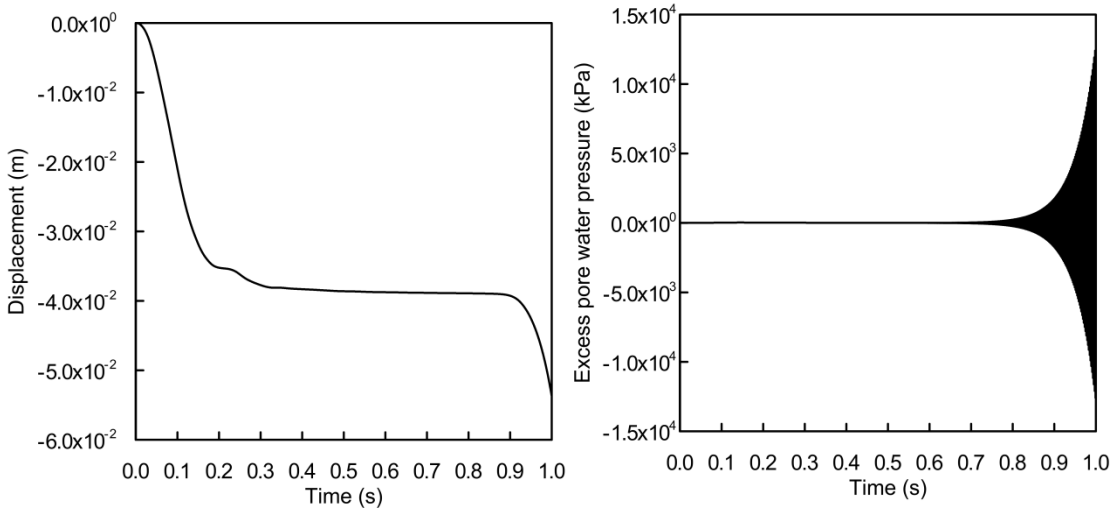
The stability condition of the CH method is investigated for the elasto-plastic foundation using the same procedure as in the previous examples. Namely, the CH method is adopted and β is gradually reduced below 0.5 in order to reach numerically the stability limit for the coupled analysis. Concerning the results for both the displacement and excess pore water pressure, in terms of the time history (Figure 2-32) and the contour plots (Figure 2-33), similar trends are observed for the elasto-plastic foundation analysis, compared with that of the elastic foundation analysis. It indicates that, in order to obtain stable dynamic results by using the CH method, β should be equal or larger than 0.5. However, it should be noted that, when β is reduced to 0.496, the displacement response is observed to be stable, but its magnitude at the end of analysis is slightly greater than that with β=0.8. This indicates that the numerical error has been slightly amplified through the FE analysis although no obvious unstable displacement response is observed. Based on the results of the elasto-plastic foundation analysis, despite that the theoretical stability conditions for the CH method is only valid for the linear problem, it could also be relevant for the nonlinear elasto-plastic problem.



(a): Displacement and excess pore water pressure time histories (CH method and β=0.800)

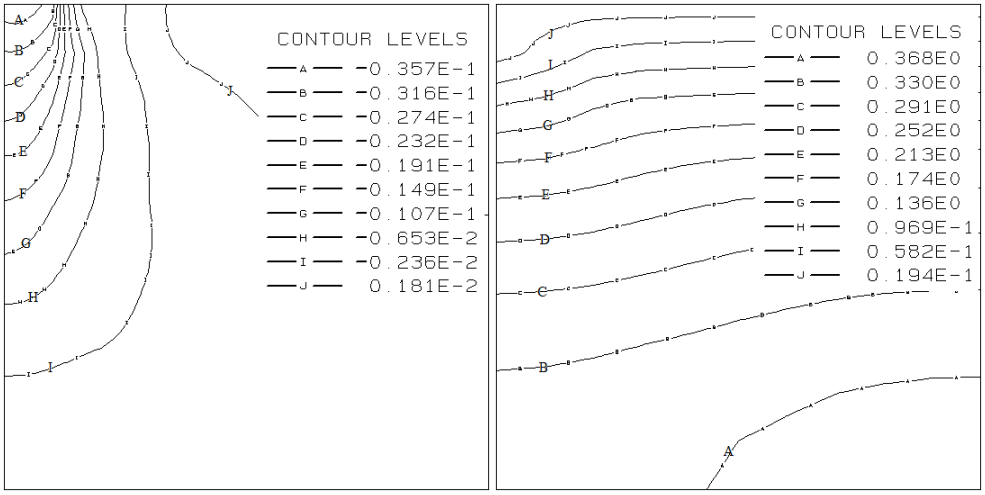


(b): Displacement and excess pore water pressure time histories (CH method and β=0.496)

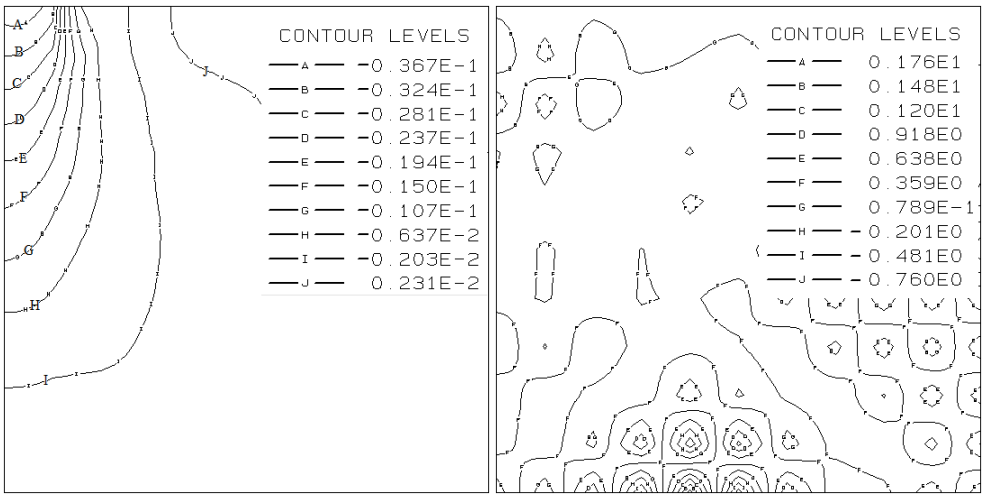


(c): Displacement and excess pore water pressure time histories (CH method and β=0.493)

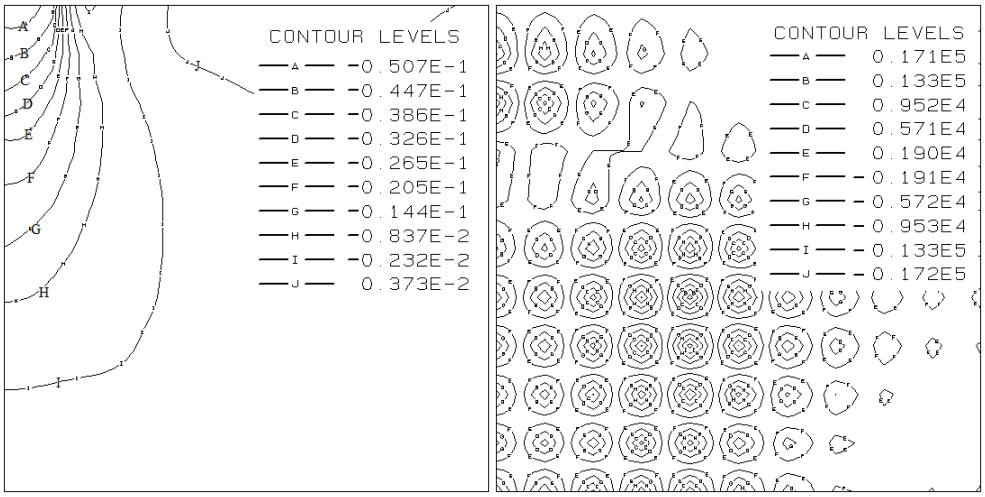
Figure 2-32: Displacement (at point E) and excess pore water pressure (at point F) time histories of various β values by using CH method



(a): Displacement and excess pore water pressure contours (CH method and β=0.800)



(b): Displacement and excess pore water pressure contours (CH method and β=0.496)



(c): Displacement and excess pore water pressure contours (CH method and β=0.493)

Figure 2-33: Displacement and excess pore water pressure contours at t=1.0s of various β values

(displacement: m and excess pore water pressure: kPa)

2.7 Summary

The first part of this chapter introduces the fundamental static and dynamic formulations of ICFEP, presenting both the one-phase and the two-phase coupled formulations. For the coupled formulation, Darcy's law is utilised to derive the consolidation equation, in order to take into account the effects of consolidation. Therefore, the two-phase behaviour can be simulated in dynamic analysis, which is significant for geotechnical structures of high permeabilities or/and long duration loading.

The second part of this chapter involves the description of several widely used time integration methods, which are the Newmark, HHT, WBZ and CH methods. The basic principles and advantages of the different methods were briefly discussed. Furthermore, the numerical features, such as the stability, accuracy and numerical damping were introduced. Lastly, the merits of the CH method were emphasised and the implementation of the CH method in ICFEP was presented.

In the third part of this chapter, the stability of the CH method for the HM coupled formulation was examined following an analytical procedure of employing the Routh-Hurwitz conditions and the unconditional stability conditions were derived. It was shown that the proposed stability conditions can simplify to the stability conditions of the CH method for the one-phase formulation (i.e. without hydraulic coupling). Furthermore, by degrading the CH method to the Newmark method, the stability conditions were in agreement with those proposed in previous stability investigations for the Newmark method based on coupled formulation. Since the CH method is a generalisation of the Newmark, HHT and WBZ methods, the proposed stability conditions are relevant for most of the commonly used time integration methods for the two-phase coupled formulation.

The analytically derived stability conditions were explored with FE analyses considering a range of loading conditions, model geometries and constitutive models. Firstly, analyses considering a 1-D linear elastic soil column subjected to a step and harmonic loads were carried out showing a good agreement between the derived stability condition and the back-calculated one with the aid of numerical analysis. This set of analyses also showed that the stability of the solution depended on the adopted soil permeability value, with the instability being more pronounced for the high

permeability soil column. The next set of analyses considered the impact of numerical damping on the predicted response of a soil column subjected to impulse loading. The parametric variation of the numerical damping showed that the predicted response was significantly affected in terms of acceleration, displacement and pore water pressure. In particular, oscillations in terms of the acceleration, displacement and pore water pressure were more significantly damped as larger numerical damping was employed, but without affecting the response and finally approaching the same steady state. Finally, the stability characteristics of the CH method were investigated more stringently with an elastic and elasto-plastic analysis of a foundation subjected to dynamic loading. Satisfactory agreement was observed between the FE analysis results and the theoretical stability conditions for the linear elastic analysis. Furthermore, the investigated stability conditions with an advanced elasto-plastic constitutive model were also in agreement with the theoretical conditions, indicating that the proposed stability conditions may be also applicable to more complicated nonlinear problems.

CHAPTER 3

Analytical and numerical investigation of site response due to vertical ground motion

3.1 Introduction

During an earthquake, the ground is subjected to simultaneous shaking in both the horizontal and vertical direction. However, common practice for geotechnical earthquake engineering problems is to assess the site response to the horizontal component of the ground motion only. This is attributed to the assumption that the effect of the vertical ground motion component is less significant, due to its smaller magnitude and higher frequency content compared to the horizontal ground motion component (Yang and Yan, 2009a). When the effect of the vertical ground motion is taken into account for earthquake-resistant design, either simple empirical models for the vertical response spectra, or empirical ratios between the vertical and horizontal response spectra (V/H), are usually employed to estimate the earthquake loading imposed on engineering structures due to the vertical ground motion. Furthermore, the V/H ratios are commonly assumed to be less than 2/3 over the concerned frequency range (UBC, 1997). However, since 1990s, strong vertical ground motions have been repeatedly observed, leading to significant damage of engineering structures in the form of vertical compression (Papazoglou and Elnashai, 1996; Yang and Sato, 2000; Bradley, 2011). Moreover, for the earthquake-resistant design of critical structures (e.g. nuclear power plants, high dams), the ground motion effects due to a wide-range of frequency

components need to be taken into account and it is the high frequency components that are usually generated by the vertical ground motion. It is also noteworthy that according to the earthquake-resistant design standards in highly seismic regions, such as the China Earthquake-resistant Design Standard for Civil Engineering Structures (Ministry of Housing and Urban-Rural Development of the People's Republic of China, 2010), it is compulsory to investigate the three-directional dynamic response of critical engineering structures. Therefore, there is a need for a more systematic and rigorous analysis of soil response that can account for the vertical component of the ground motion. Consequently, in this chapter the site response to vertical ground motion is investigated by employing both analytical and numerical methods.

This chapter first presents an overview of field evidence concerning strong vertical ground motion and corresponding compression damage of engineering structures. Furthermore, the empirical methods for assessing vertical ground motions in earthquake-resistant design are briefly introduced, where their shortcomings are also discussed.

Subsequent to this, in order to explain the shortcomings of the above empirical methods and to more accurately investigate the site response to the vertical component of the ground motion, a 1-D total-stress analytical solution is studied in frequency domain and compared with the numerical solution obtained from FE time domain analyses.

In the final two parts of this chapter, the vertical site response is further investigated by considering the solid-fluid interaction. Since the site response due to the vertical component of the ground motion mainly involves compressional waves, the compressional wave propagation mechanism in saturated porous soils is investigated, by employing a hydro-mechanical (HM) coupled analytical solution and an HM coupled FE method. In this, an analytical solution for the compressional wave propagation is studied based on Biot's theory (1956a, b), showing the existence of two types of compressional waves (a fast and a slow wave). Their characteristics (i.e. the wave dispersion and attenuation) are shown to be highly dependent on soil and dynamic parameters (i.e. the permeability, loading frequency and soil stiffness). Subsequently, the compressional wave propagation problems are rigorously simulated and investigated by the coupled FE analysis.

Based on the coupled HM two-phase investigation of the compressional wave

propagation mechanism, the site response to the vertical ground motion is investigated by considering the solid-fluid interaction with fully coupled FE analysis. The undertaken parametric studies show that the predicted dynamic response is strongly affected by the parameters characterising the hydraulic phase, i.e. the soil permeability and soil state conditions, both in terms of frequency content and amplification.

3.2 Field evidence of strong vertical motion and empirical design methods

For geotechnical earthquake engineering problems, the effects of the vertical component of the ground motion are usually assumed to be insignificant due to the small magnitude and high frequency content (Yang and Yan, 2009a). Therefore, when the effect of vertical ground motion is taken into account for earthquake-resistant design, usually simple empirical models, such as V/H response spectra ratio models, are employed. The V/H ratios are commonly assumed to be less than 2/3 over the concerned frequency range (UBC, 1997). However, in recent earthquake events, strong vertical ground motions and significant vertical compression damage have been repeatedly observed, where the limit of 2/3 has been exceeded (Yang and Yan, 2009a). In this part of the chapter, field evidence of strong vertical ground motions and compression damage are presented. Furthermore, typical empirical methods for assessing vertical ground motions in earthquake-resistant design are also briefly introduced and their drawbacks are discussed.

3.2.1 Field evidence of strong vertical ground motion and associated compression damage

A representative investigation of field evidence of strong vertical ground motion is perhaps that of Papazoglou and Elnashai (1996), who collected and analysed monitoring data from three earthquakes; the Kalamata (Greece, 1986), Northridge (California, 1994) and Kobe (Japan, 1995) earthquakes. Based on the post earthquake reports, the V/H ratios were calculated for all strong-motion sites in these three events and the maximum values of 1.26, 1.79 and 1.63 were reported for the Kalamata, Northridge and Kobe earthquake respectively. However, these maximum V/H ratios were only observed

at near-field sites (less than 15km from the hypocentre), while at far-field sites (more than 15km from the hypocentre), the V/H ratios were still within the 2/3 limit. The evidence from one of recent large-magnitude earthquake events, the Christchurch earthquake (New Zealand, 2011) (Bradley, 2012), showed that the V/H ratios for most near-field sites were considerably higher than 2/3, reaching a ratio of 4.8 at HVSC station (with peak vertical acceleration of 2.21g), while at far-field sites V/H ratios fluctuated at around 2/3. Based on these field observations, the maximum V/H ratio can clearly significantly exceed the limit of 2/3 at near-field sites.

According to Papazoglou and Elnashai (1996), strong vertical motion can directly result in structural failure due to vertical compression/extension. Furthermore, the shear resistance of a structure can be reduced due to the loss of axial structural forces caused by the vertical motion, which can potentially lead to shear failure. The vertical compression damage of engineering structures due to strong vertical ground motion was evident after the Northridge earthquake (Papazoglou and Elnashai, 1996) on numerous concrete buildings and concrete bridges. One example is a 3-storey car park building in California State University, which collapsed during the Northridge earthquake (Figure 3-1). The failure of this building was attributed to the collapse of the interior columns due to axial loading increase caused by strong vertical ground motion, while the external walls, which were designed to resist shearing, only experienced minor damage. More evidence of vertical compression damage was detected in the Kobe earthquake, mainly in the Chuo Ward area of Kobe where the highest vertical acceleration was recorded. One example in Figure 3-2 shows the vertical compression of the fifth floor of a 12-storey building in the Chuo Ward area of Kobe.



Figure 3-1: Collapse of the car park building in California State University in the Northridge earthquake (after Papazoglou and Elnashai (1996))



Figure 3-2: A damaged building in the Kobe Earthquake (after Papazoglou and Elnashai (1996))

3.2.2 Empirical design models for vertical ground motion

Two methods are usually employed to estimate the earthquake loading imposed on engineering structures due to vertical ground motion; the empirical models and the empirical ratio models. For both methods, a database of a sufficient number of records is required in order to represent realistically the vertical ground motion of a site. In the first method, representative empirical models for the vertical response spectra are proposed to represent the vertical ground motion. In the second method, empirical ratios between the vertical and horizontal response spectra (V/H) are proposed, based on which the vertical response spectra can be obtained by multiplying the V/H ratios with the selected horizontal response spectra. The following section presents an overview of some widely used models for the assessment of the vertical ground motion in earthquake-resistant design.

Empirical models

Since 1990s, numerous empirical models for predicting the vertical ground motion have been proposed (Elnashai and Papazoglou, 1997; Campbell and Bozorgnia, 2003; Elgamal and He, 2004). Among these, the most representative work is probably from Elgamal and He (2004). In particular, empirical models for normalised vertical response spectra for both near-field and far-field sites were proposed, after analysing a strong-motion database consisting of 50 near-field and 61 far-field records, which were

obtained from 6 earthquake events in California with peak vertical accelerations greater than 0.1g. The proposed empirical models for both near-field and far-field sites are shown in Figure 3-3, where a damping ratio of ξ=2% is employed. It is observed that the predominant period of the normalised vertical response spectra for near-field sites is slightly smaller than that for far-field sites. Furthermore, the spectral accelerations normalised by peak vertical accelerations for near-field sites are slightly smaller than these for far-field sites.

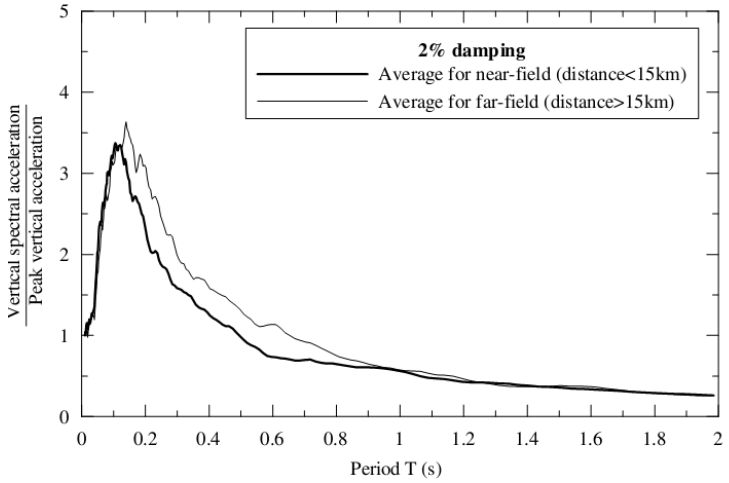


Figure 3-3: Empirical models of vertical response spectra for near-field and far-field sites (ξ=2%)

(after Elgamal and He (2004))

By developing the work of Elgamal and He (2004), Elnashai et al. (2004) proposed design spectra for vertical motion at both near-field and far-field sites, which are shown in Figure 3-4. It should be noted that the influence of the Chi-Chi earthquake data (Taiwan, 1999) on the proposed design spectra was also investigated. This is due to that the response spectra of vertical ground motions in the Chi-Chi earthquake contain significant long period magnitudes, which is different from earlier observations (Wang et al., 2001). It is shown that including the Chi-Chi earthquake data leads to considerable *bias* compared with the original vertical response spectra, although the latter already involves a large number of earthquake records (more than 100 records in 6 earthquake events). Consideration of the Chi-Chi earthquake data results in more significant differences in larger period range in terms of higher normalised spectral accelerations, whereas in the lower period range the differences are negligible. However, the induced deviations by including the Chi-chi earthquake data were only investigated for the design spectra of vertical ground motion without exploring its effect

on the horizontal component. According to Elnashai et al. (2004), in order to develop an appropriate empirical model for assessing the vertical ground motion, it is critical to consider sufficient amount of monitoring data from different typical earthquake events.

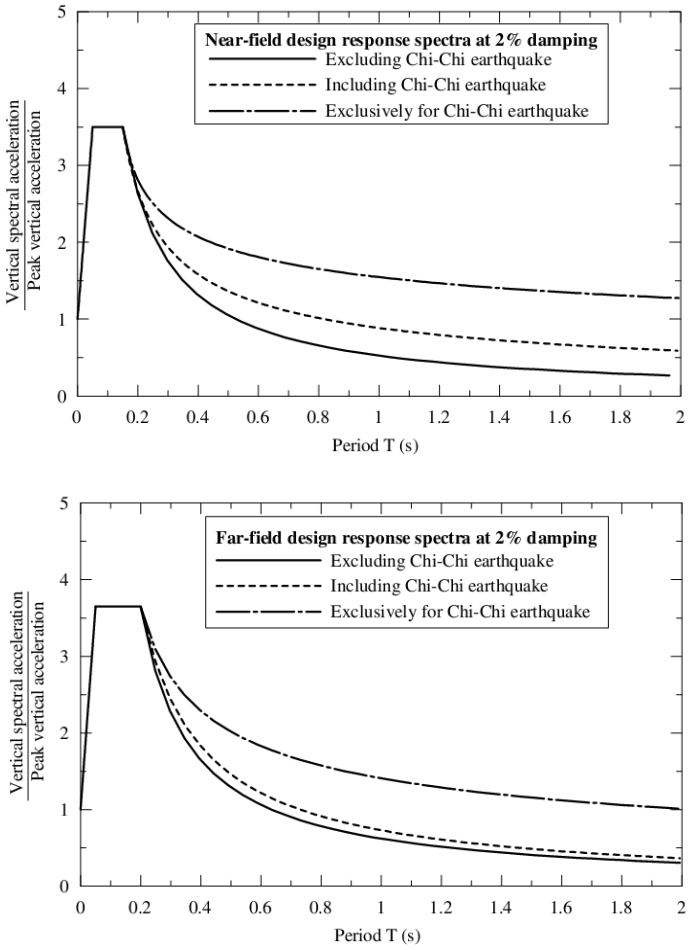


Figure 3-4: Empirical models of vertical response spectra for near-field and far-field sites (ξ=2%)

(after Elnashai et al. (2004))

Empirical V/H ratio models

Another commonly used method is the empirical V/H ratio models, where the vertical design response spectra can be obtained by multiplying the proposed empirical V/H ratios with the horizontal design response spectra over a given frequency range. One of the most commonly used empirical V/H ratio models was proposed by Bozorgnia and Campbell (2004). The authors investigated 443 near-field strong motions from 36 earthquake events and proposed an empirical V/H ratio model shown in Figure 3-5, which takes into account the effects of the earthquake magnitude, epicentral distance, site conditions and fault type on V/H ratio design models. Based on the work

carried out by Bozorgnia and Campbell (2004), it can be observed that the empirical V/H ratio model is highly dependent on the different earthquake characteristics. The proposed model clearly does not exhaust the potential effects of other earthquake characteristics on the V/H ratio design models, introducing therefore a degree of *uncertainty* in the assessment of the vertical ground motion.

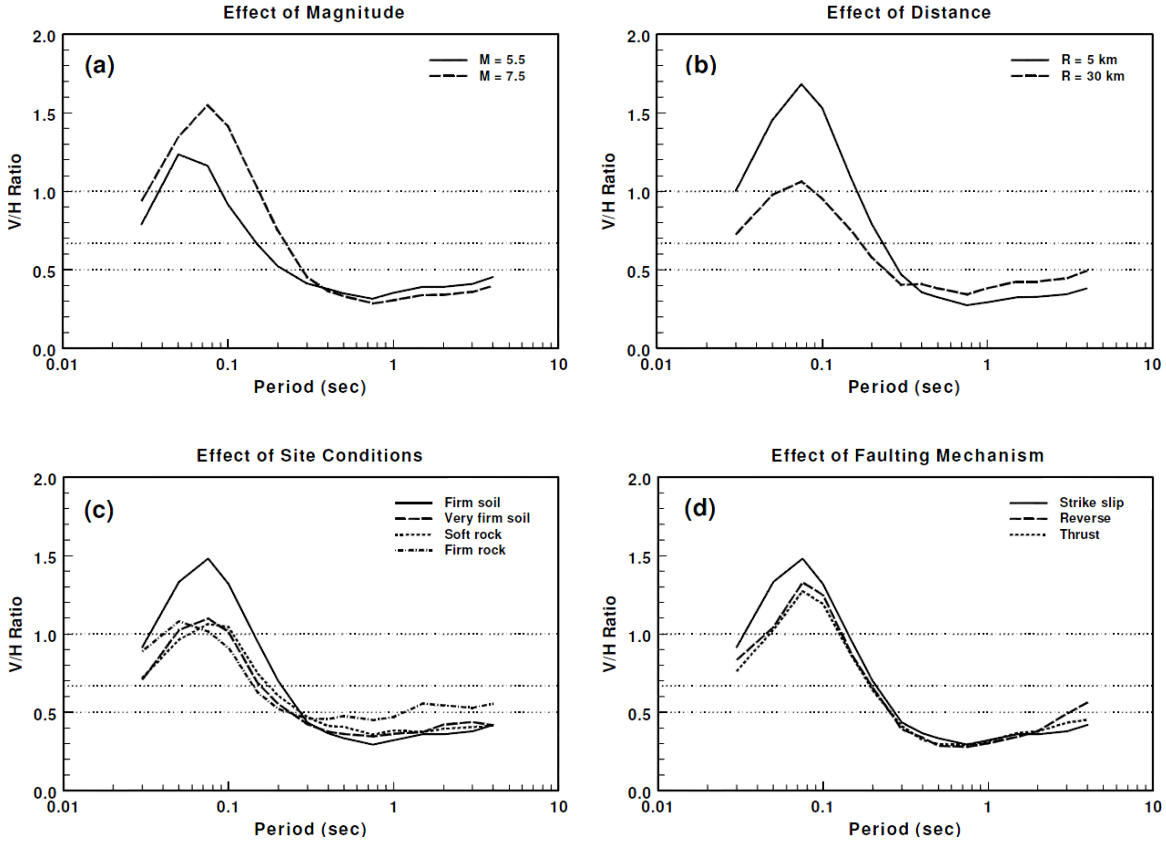


Figure 3-5: Empirical V/H ratio model. Unless otherwise noted, the V/H ratio model is evaluated for Magnitude (*Mw*)=7.0, Epicentral distance (R)=10 km, strike-slip faulting and firm soil (after Bozorgnia and Campbell (2004))

3.3 One-phase investigation of vertical site response

Due to the *bias* and *uncertainty* characteristics of empirical design models, there is a need for more advanced site response analyses, aiming to more accurately estimate the earthquake loading imposed on engineering structures subjected to vertical ground motion. Therefore, a 1-D total-stress analytical solution in frequency domain is firstly discussed in this part to investigate fundamental aspects of site response due to the vertical component of the ground motion.

3.3.1 Frequency domain analytical solution for vertical site response

Since the 1970s, analytical solutions have been proposed and developed to investigate the dynamic response of the ground, most of which are derived in the frequency domain. These solutions form the basis of the so called shake-type programs, such as SHAKE (Schnabel et al., 1972) and EERA (Bardet et al., 2000). However, the majority of these programs only consider vertical propagation of SH waves and therefore limited investigation has been performed on the site response due to vertical ground motion.

The basic principles of the frequency domain analytical solutions employed in site response analysis can be found in Kramer (1996) and are only briefly discussed herein. As it is shown in Figure 3-6, considering a uniform soil layer of isotropic and linear elastic behaviour overlying rigid bedrock, the input motion of a harmonic pulse imposed at the bottom boundary is firstly decomposed into a Fourier frequency series, usually using a Fast Fourier Transform (FFT). Each term of the frequency series is then amplified by the transfer function, to obtain the response of the ground surface. The transfer function determines how much the input motion is amplified by the soil layer at each frequency. Furthermore, by employing the inverse FFT, the frequency series of the surface motion is converted to the time domain response. According to Kramer (1996), the transfer functions of a homogeneous soil layer subjected to vertical propagating harmonic SH waves are described in Equations 3-1 and 3-2 and illustrated in Figures 3-7 (a) and (b), respectively for undamped ($F_0(\omega)$) and damped ($F_1(\omega)$) soil materials, where ω, v_s, ξ and H are the circular frequency of the input motion, shear wave velocity, material damping and depth for the soil layer respectively.

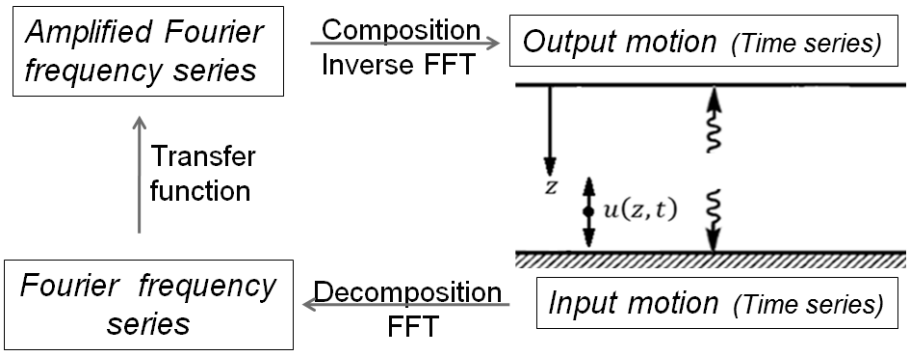
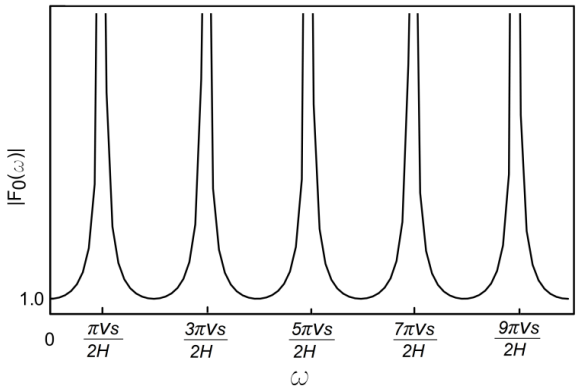


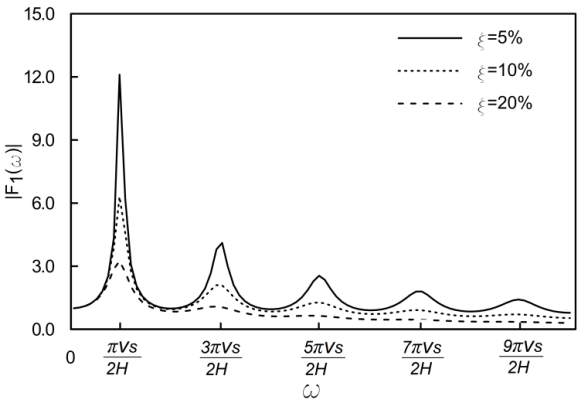
Figure 3-6: A schematic graph for the principle of the frequency domain method

$$\left|F_0(\omega)\right| = \frac{1}{\left|\cos\frac{\omega \cdot H}{v_s}\right|} \qquad 3\text{-}1$$

$$\left|F_1(\omega)\right| = \frac{1}{\sqrt{\cos^2\left(\frac{\omega \cdot H}{v_s}\right) + \left(\frac{\omega \cdot H}{v_s} \cdot \xi\right)^2}} \qquad 3\text{-}2$$



(a): Transfer function between the top and bottom boundaries for an elastic soil layer



(b): Transfer function between the top and bottom boundaries for a visco-elastic soil layer

Figure 3-7: Transfer functions for elastic and visco-elastic soil layers subjected to SH waves

By following a similar procedure of Kramer (1996), the transfer function for the 1-D dynamic response of a homogeneous layer subjected to harmonic compressional waves is derived. In particular, a uniform soil layer of isotropic and linear visco-elastic behaviour overlying rigid bedrock, which is subjected to harmonic vertical motion imposed at the bottom boundary, can generate vertical propagating compressional waves in two directions (shown in Figure 3-8). The corresponding elastic wave propagation equation for steady state response is shown in Equation 3-3.

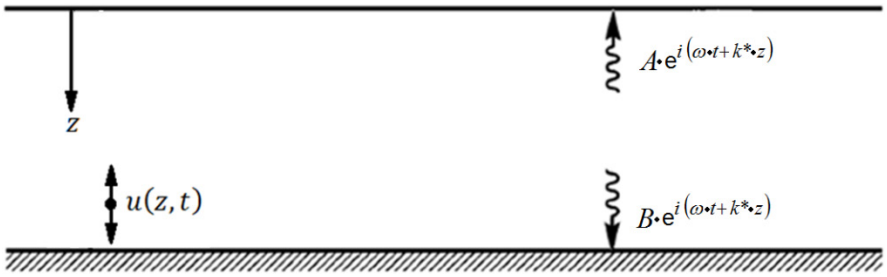


Figure 3-8: A schematic graph of the compressional wave propagation

$$u(z,t) = A \cdot e^{i\cdot(\omega\cdot t + k^*\cdot z)} + B \cdot e^{i\cdot(\omega\cdot t - k^*\cdot z)} \qquad 3\text{-}3$$

where $u(z,t)$ is the vertical displacement of the soil layer at depth z and time t, ω is the circular frequency of the input motion, A and B are the amplitudes of the waves propagating in $-z$ direction (upward) and $+z$ direction (downward) and k^* is the complex wave number. According to Kramer (1996), k^* can be expressed by the wave number k and damping ratio ξ, as shown in Equation 3-4. It should be noted that the wave number k is expressed by $k = \omega / v_p$, where v_p is the compressional wave velocity.

$$k^* = k \cdot (1 - i \cdot \xi) \qquad 3\text{-}4$$

The normal stress can be determined by the soil constrained modulus and normal strain as shown in Equation 3-5. Furthermore, due to the zero stress boundary condition at the surface of the soil layer, the normal stress and the normal strain must vanish, leading to Equation 3-6.

$$\sigma_z(z,t) = D \cdot \varepsilon_z(z,t) \qquad 3\text{-}5$$

$$\sigma_z(0,t) = D \cdot \varepsilon_z(0,t) = D \cdot \frac{\partial u(0,t)}{\partial z} = 0 \qquad 3\text{-}6$$

where D is the soil constrained modulus, σ_z is the normal stress and ε_z is the normal strain. By substituting Equation 3-6 into Equation 3-3, the new relation can be expressed as:

$$D \cdot i \cdot k^* \cdot (A - B) \cdot e^{i\cdot\omega\cdot t} = 0 \qquad 3\text{-}7$$

For a nontrivial solution, the condition of $A=B$ should be satisfied for Equation 3-7, based on which Equation 3-3 can be rearranged to the following equation:

$$u(z,t) = 2A \cdot \frac{e^{i \cdot k^* \cdot z} + e^{-i \cdot k^* \cdot z}}{2} \cdot e^{i \cdot \omega \cdot t} = 2A \cdot \cos(k^* \cdot z) \cdot e^{i \omega t} \qquad 3\text{-}8$$

Equation 3-8 can be then employed to produce the transfer function between any two depths in the soil layer. Taking the bottom and top boundaries for example, the transfer function is given by Equation 3-9, where H is the depth of the soil layer.

$$F_1(\omega) = \frac{u(0,t)}{u(H,t)} = \frac{2A \cdot e^{i \cdot \omega \cdot t}}{2A \cdot \cos(k^* \cdot H) \cdot e^{i \cdot \omega \cdot t}} = \frac{1}{\cos(k^* \cdot H)} = \frac{1}{\cos\left[k \cdot (1 - i \cdot \xi) \cdot H\right]} = \frac{1}{\cos\left[\frac{\omega \cdot H}{v_p} \cdot (1 - i \cdot \xi)\right]} \qquad 3\text{-}9$$

Considering the identity $\cos(x + i \cdot y) = \sqrt{\cos^2 x + \sinh^2 y}$, the amplitude of the transfer function can be expressed by Equation 3-10.

$$\left|F_1(\omega)\right| = \frac{1}{\sqrt{\cos^2\left(\frac{\omega \cdot H}{v_p}\right) + \sinh^2\left(-\frac{\omega \cdot H}{v_p} \cdot \xi\right)}} = \frac{1}{\sqrt{\cos^2\left(\frac{\omega \cdot H}{v_p}\right) + \sinh^2\left(\frac{\omega \cdot H}{v_p} \cdot \xi\right)}} \qquad 3\text{-}10$$

Assuming $\sinh^2 y \approx y^2$ for small vales of y, Equation 3-10 can be simplified to Equation 3-11, as the final transfer function between the top and bottom boundaries of a visco-elastic soil layer:

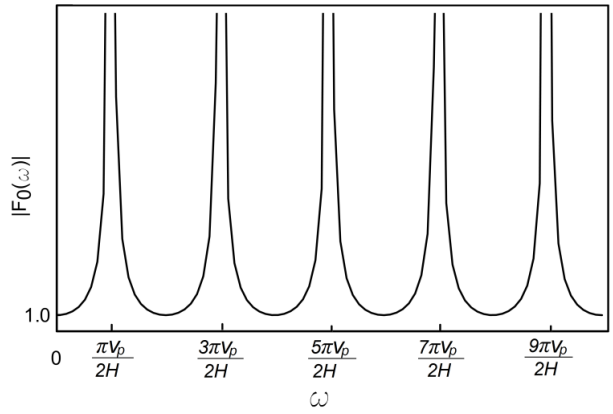
$$\left|F_1(\omega)\right| = \frac{1}{\sqrt{\cos^2\left(\frac{\omega \cdot H}{v_p}\right) + \left(\frac{\omega \cdot H}{v_p} \cdot \xi\right)^2}} \qquad 3\text{-}11$$

It should be noted that when $\xi = 0$ in Equation 3-11, the resulting Equation 3-12 can represent the transfer function between the top and bottom boundaries of an elastic soil layer:

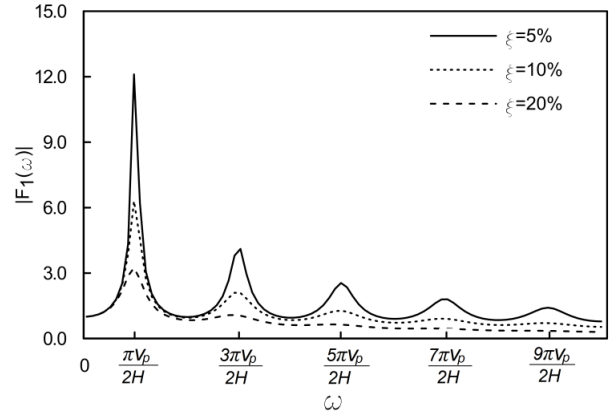
$$\left|F_0(\omega)\right| = \frac{1}{\left|\cos\frac{\omega \cdot H}{v_p}\right|} \qquad 3\text{-}12$$

The transfer functions obtained above are illustrated in Figures 3-9 (a) and (b), for an elastic soil layer and a visco-elastic soil layer respectively. For the transfer function related to an elastic soil layer, infinite amplification factors are observed at the fundamental frequencies of the soil layer. However, for the transfer function involving a visco-elastic soil layer, finite amplification factors are obtained due to the existence of

the material damping, but they still peak at the fundamental frequencies of the soil layer.



(a): Transfer function between the top and bottom boundaries for an elastic soil layer



(b): Transfer function between the top and bottom boundaries for a visco-elastic soil layer

Figure 3-9: Transfer functions for elastic and visco-elastic soil layers subjected to compressional waves

By comparing the transfer functions of the analytical solution for vertical site response (Equations 3-11 and 3-12) to those for horizontal site response (Equations 3-1 and 3-2), it can be clearly seen that the expressions are similar. The differences are in the employment of different soil stiffness, with the constrained modulus *D* applied in the transfer function for vertical site response analysis, compared to the shear modulus *G* which is used in horizontal site response analysis. Therefore, the existing shake-type programs, such as SHAKE and EERA can be directly utilised for vertical site response analysis, by employing the appropriate soil constrained modulus in the analysis. However, according to Zienkiewicz et al. (1980b), the compressional deformation of saturated porous soil media is highly dependent on the conditions of the soil state (i.e. undrained, drained and transient conditions). The soil constrained modulus under the undrained condition is composed of both the constrained modulus of the soil skeleton

and the pore water bulk modulus, while under the drained condition, it is only affected by the constrained modulus of the soil skeleton (as shown in Equation 3-13). It should be noted that the above transfer functions for vertical site response analysis shown in Figure 3-9 only considers the drained soil behaviour, which are compared with the transfer functions under the undrained condition in Figure 3-10. It can be observed that larger fundamental frequencies are observed for the transfer functions under the undrained condition, due to the larger compressional wave velocity ($v_{p\ \mathrm{Undrained}}$) induced by larger constrained modulus of the soil layer under the undrained condition. Therefore more attention should be given to the appropriate employment of soil constrained modulus values in the analytical solution for vertical site response. Overall, the existing shake-type programs are capable of simulating the vertical site response of a soil layer by prescribing two parameters into the analytical solution (compressional wave velocity and damping ratio). However, only two extreme soil state conditions, undrained and drained, can be reproduced, since the analytical solution is based on the total-stress method, i.e. no distinction between the effective stresses and pore pressures.

$$D_{Undrained} = \frac{E \cdot (1-\nu)}{(1+\nu)\cdot(1-2\nu)} + \frac{K_f}{n}$$

$$D_{Drained} = \frac{E \cdot (1-\nu)}{(1+\nu)\cdot(1-2\nu)} \qquad \text{3-13}$$

where D and E are the soil constrained modulus and Young's modulus respectively, ν is the Poisson's ratio, K_f is the bulk modulus for the pore water and n is the porosity.

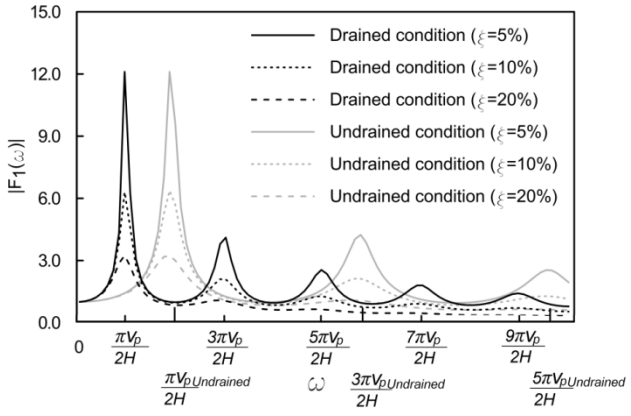


Figure 3-10: Transfer functions for visco-elastic soil layers subjected to compressional waves under drained and undrained conditions

3.3.2 Previous one-phase studies for vertical site response

It has been proved in the previous section that the existing shake-type programs can be directly utilised for vertical site response analysis, by employing the appropriate soil properties in the analysis. However, only limited investigation has been performed on this, where the representative works are attributed to Elgamal and He (2004) and Yang and Yan (2009b).

Elgamal and He (2004) presented an investigation of the vertical site response, using the Lotung (Taiwan) down-hole array and applying a 1-D analytical solution in frequency domain through SHAKE analysis. The analytical results were compared with the observed data from the 1986 Hualien earthquake, in terms of vertical acceleration response spectra at different depths, where a satisfying agreement was obtained (shown in Figure 3-11). The soil properties employed in their work (i.e. the compressional wave velocity and damping ratio) were back-analysed by reproducing the observed data, through which, a high damping ratio (15%) and low compressional wave velocity (3/4 of original) were assumed. However, the principles for the analytical solution of vertical site response were not described in detail, which may lead to inappropriate execution for vertical site response analysis of soil layers under different soil state conditions. The applicability of the frequency domain analytical solution on the vertical site response needs to be rigorously verified.

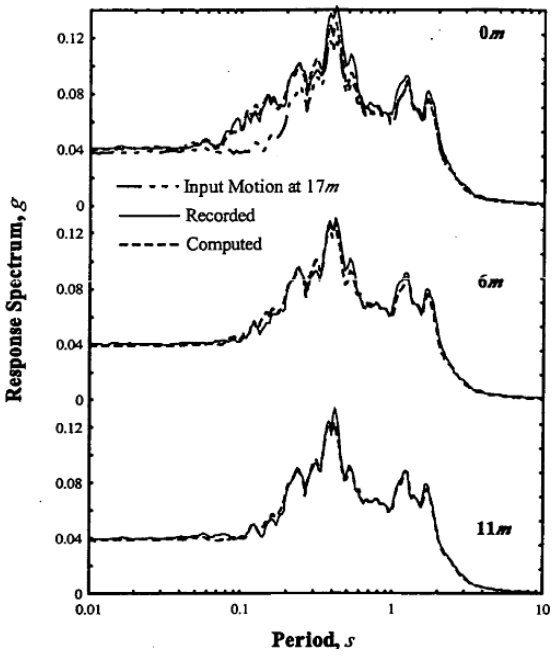


Figure 3-11: Comparison of the vertical response spectra between the observed data and the analytical results for Lotung down-hole array (after Elgamal and He (2004))

Yang and Yan (2009b) developed an analytical program named PASS, which can address both horizontal and vertical dynamic analysis of 1-D homogeneous soil columns, but with uncoupled analysis, i.e. no coupling effects between the two-directional motions. The soil constrained modulus was employed in the stress-strain constitutive relation of the formulation, which is a function of the Young's modulus and Poisson's ratio as shown in Equation 3-14. It should be noted again that the soil constrained modulus is highly affected by the soil state conditions (i.e. drained and undrained conditions). Therefore, the soil constrained modulus used by Yang and Yan (2009b) can only represent the soil stiffness under the drained condition. The appropriate employment of soil constrained modulus values needs to be further investigated for the frequency domain analytical solution, in order to account for the vertical site response under different soil state conditions.

$$D = \frac{E \cdot (1-\nu)}{(1+\nu) \cdot (1-2\nu)} \qquad 3\text{-}14$$

3.3.3 Comparison with time domain FE analysis

In this section the analytical solution for the vertical site response is compared against the FE analyses performed in time domain. More specifically, the dynamic response of a soil column subjected to vertical ground motion is simulated by using both an analytical solution and FE analysis, assuming linear visco-elastic soil behaviour and plane-strain geometry. The numerical analyses are carried out using ICFEP and the FE mesh (consisting of 20 8-noded isoparametric quadrilateral elements) and boundary conditions are shown in Figure 3-12. The horizontal displacements are restricted at the bottom boundary and the horizontal and vertical displacements at corresponding nodes of same height along the two lateral boundaries are tied to be identical. Hydrostatic pore water pressure and static self-weight are prescribed as the initial stress for all the numerical analyses in this chapter, where the coefficient of earth pressure at rest (K_0) is applied to be 0.5. The constant average acceleration time integration method from the Newmark's family of algorithms (Newmark, 1956), is employed for the FE analysis. No numerical damping is produced by using this time integration method, in order to keep the assumptions of numerical analyses consistent with that of the analytical solution. Vertical accelerations are uniformly prescribed at the bottom boundary of the mesh as

the input motion. The strong vertical ground motion observed at the Christchurch Cathedral College station (the CCCC station) from the Christchurch Earthquake (New Zealand, 2011), shown in Figures 3-13 and 3-14, is chosen for this purpose. The parameters used in the FE analysis and analytical solution are listed in Table 3-1. As mentioned before, the compressional deformation of saturated porous soil media is highly dependent on the conditions of the soil state (i.e. undrained, drained and transient conditions) (Zienkiewicz et al., 1980b). This influence can be accurately simulated by the two-phase coupled FE formulation by considering the consolidation process. However, herein only the one-phase FE formulation of ICFEP is employed in order to be consistent with the total-stress analytical solution. Therefore, different pore water bulk moduli (2.20E+06 kPa and 0.0 kPa) are employed in the one-phase FE analysis to account for the undrained and drained soil behaviour respectively. Moreover, compressional wave velocities of the soil layer under undrained and drained conditions are calculated based on Equations 3-13, 3-15 and 3-16, and implemented in the site response software EERA.

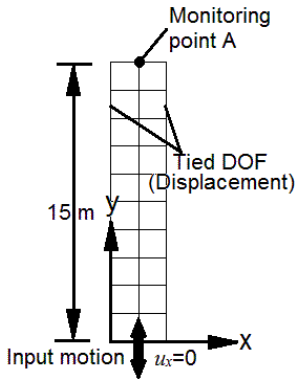


Figure 3-12: A schematic graph of the 1-D soil columns

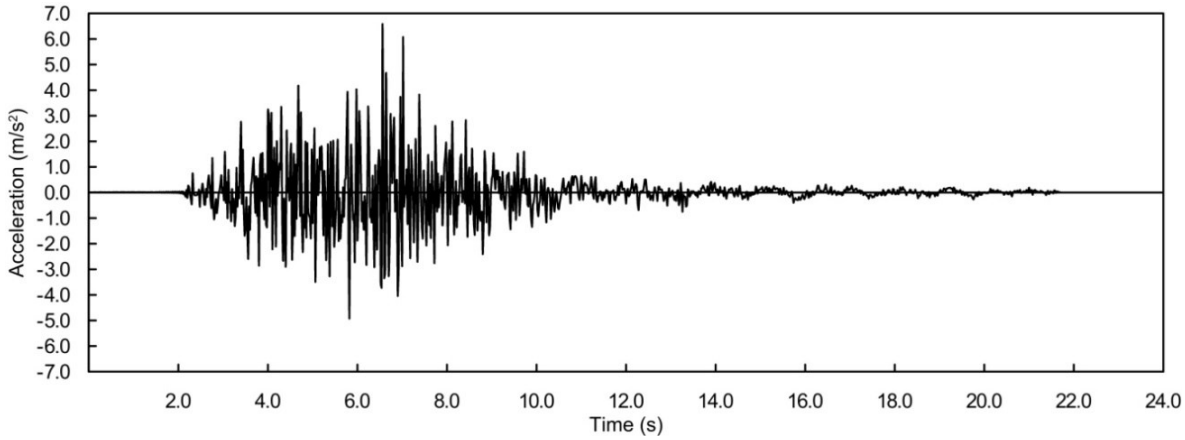


Figure 3-13: Acceleration time history of the observed vertical ground motion (at the CCCC station) from the Christchurch Earthquake

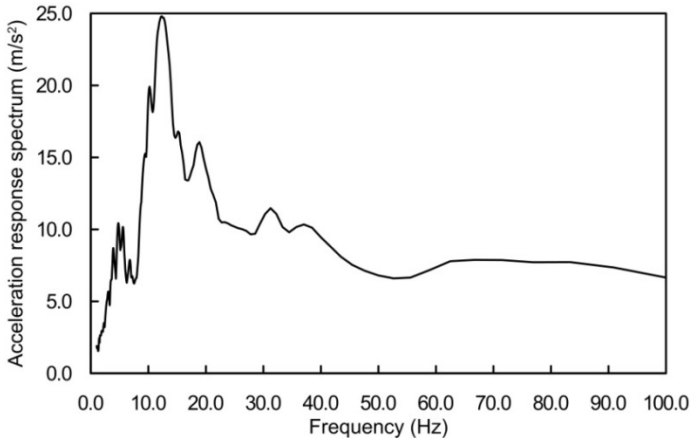


Figure 3-14: Acceleration response spectra of the observed vertical ground motion (at the CCCC station) from the Christchurch Earthquake (5% damping)

Table 3-1: Soil parameters for the 1-D soil column

	Parameter	**Value**
FE analysis	Young's modulus E (kPa)	1.98E+06
	Bulk modulus for pore water K_f (kPa)	2.20E+06/Undrained
		0.0/Drained
	Density ρ (g/cm^3)	2.0
	Poisson's ratio ν	0.2
	Time step Δt (s)	0.003
	Height H (m)	15.0
Analytical solution	Compressional wave velocity v_p(m/s)	2018.2/Undrained
		1048.8/Drained
	Height H (m)	15.0

$$v_{p\,Undrained} = \sqrt{D_{Undrained}/\rho}$$
$$v_{p\,Drained} = \sqrt{D_{Drained}/\rho} \qquad 3\text{-}15$$

$$f_{Undrained} = v_{p\,Undrained}/4H$$
$$f_{Drained} = v_{p\,Drained}/4H \qquad 3\text{-}16$$

where $v_{p\ Undrained}$ and $v_{p\ Drained}$ and $f_{Undrained}$ and $f_{Drained}$ are the compressional wave velocities and fundamental frequencies for a soil layer under undrained and drained conditions respectively.

For the analytical investigation, 1.0% and 5.0% material damping ratios are applied under both soil state conditions, while for the numerical analysis, Rayleigh damping, an idealised equivalent viscous damping, is employed with the same target damping ratios as the ones used in analytical solution. The damping values employed in both analytical solution and numerical analysis are assumed to be constant with depth. According to Bathe (1996), the Rayleigh damping for a single mode of a multiple DOF system is given by Equation 3-17.

$$\xi_i = \frac{A}{2\omega_i} + \frac{B\omega_i}{2}$$

where ξ_i and ω_i are the Rayleigh damping ratio and circular frequency at the ith mode of the considered vibration system respectively, and A and B are two parameters controlling the variation of the Rayleigh damping against the circular frequency. It should be noted that the first and second terms of the Rayleigh damping are called mass damping and stiffness damping respectively. The variation of the Rayleigh damping formulations is illustrated in Figure 3-15. It can be seen that the mass damping ratio is inverse-proportional to the frequency and dominates the low frequency range, while the stiffness damping ratio increases proportionally with the frequency and dominates the high frequency range. Nevertheless, in reality the material damping is almost independent of the frequency. However, based on Figure 3-15, it can be seen that a reasonably constant variation of Rayleigh damping can be achieved over the concerned frequency range (between ω_1 and ω_2) when appropriate values for A and B are selected. According to Bathe (1996), the parameters A and B can be calculated based on Equation 3-18. In this equation, ω_1 and ω_2 are the two frequencies defining the concerned frequency range over which the variation of Rayleigh damping is approximately constant. Thus the target damping ξ_t can be represented by the Rayleigh damping at desired frequency range (between ω_1 and ω_2), as illustrated in Figure 3-15. According to Zerwer et al. (2002), ω_1 can be taken as the first fundamental frequency of the system and ω_2 can be taken as the concerned highest fundamental frequency of the system. In these analyses, the third fundamental frequency of the system is employed as ω_2. Based on Zienkiewicz et al.'s theory (Equations 3-15 and 3-16), the

fundamental frequencies of the investigated soil column under undrained and drained conditions are calculated and shown in Table 3-2, which also gives the employed values for Rayleigh parameters ω_1 and ω_2 in numerical analyses.

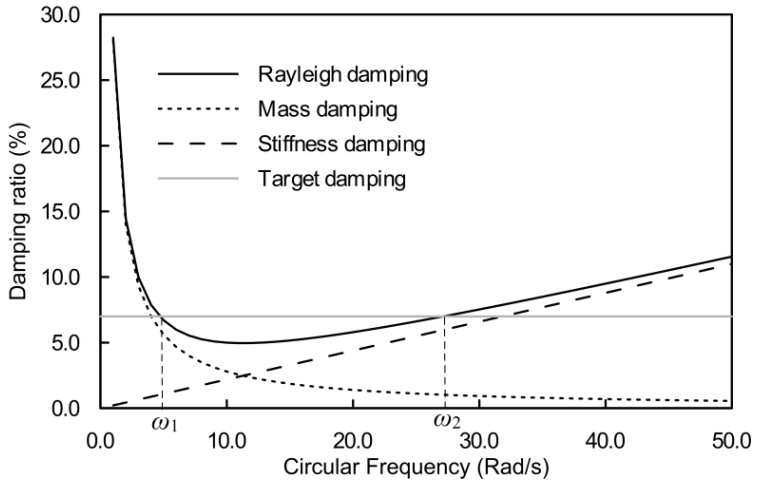


Figure 3-15: A schematic graph for Rayleigh damping

$$A = \frac{2\omega_1\omega_2\xi_t}{\omega_1 + \omega_2}$$

$$B = \frac{2\xi_t}{\omega_1 + \omega_2}$$

Table 3-2: Fundamental frequencies calculated based on Zienkiewicz et al.'s theory (1980b)

Parameter / Scenarios	Constrained modulus (kPa)	Compressional wave velocity (m/s)	First fundamental frequency (ω_1) (Hz)	Third fundamental frequency (ω_2) (Hz)
Undrained	8.10E+06	2018.2	33.6	168.2
Drained	2.20E+06	1048.8	17.5	87.4

Comparison between the analytical and numerical results

The comparison of analytical and numerical results is shown in Figures 3-16 and 3-17, in terms of acceleration time histories and acceleration response amplification spectra respectively at the monitoring point A (see Figure 3-12). It should be noted that the response spectra amplification factors are calculated by dividing the response spectra obtained at a point at the top boundary by the spectra at a corresponding point at the bottom boundary over the frequency range. It should be noted that the acceleration

response spectra in this thesis are all calculated by assuming 5% damping for single DOF system.

Based on Figure 3-17, it can been seen that the vertical site response predicted by the analytical solution compares reasonably well with the numerical results, in terms of the acceleration response amplification spectra. In particular, identical fundamental frequencies are predicted by the analytical and numerical simulations and they are in good agreement with the numerically calculated values based on Zienkiewicz's theory (Table 3-2). However, the response spectra amplification factors are slightly underestimated by the numerical analysis. This is also in agreement with the smaller acceleration values predicted by the numerical analysis in Figure 3-16. This phenomenon can be probably attributed to the inaccurate representation of material damping by the Rayleigh formulation in the FE analysis, which is further investigated in the following part.

It is worthy to mention that different dynamic responses are observed between analyses under the two considered extreme conditions, in terms of both the fundamental frequency and amplification factor. This reflects the influence of soil state conditions on the vertical site response for saturated porous material. In particular, a larger fundamental frequency is observed for the analysis performed under undrained condition. Furthermore, larger amplification factors at fundamental frequency are observed for the vertical site response subjected to the drained condition. However, according to the derived analytical transfer functions, peak amplification factors are found to be identical under two soil states (see Figure 3-10). This is due to the assumption of steady state response in the frequency domain analytical solution, whereas the FE analysis can account for the transient effect of non-periodical input motion on dynamic simulations. The observed differences in vertical site response under the two extreme conditions essentially imply that the total-stress analytical solution is not sufficient for predicting the vertical site response of a soil layer at any intermediate transient state, when consolidation occurs during the dynamic loading (depending on soil permeability and loading duration). Consequently, it is necessary to investigate the vertical site response by using the two-phase coupled FE analysis, in order to consider the solid-fluid interaction effects.

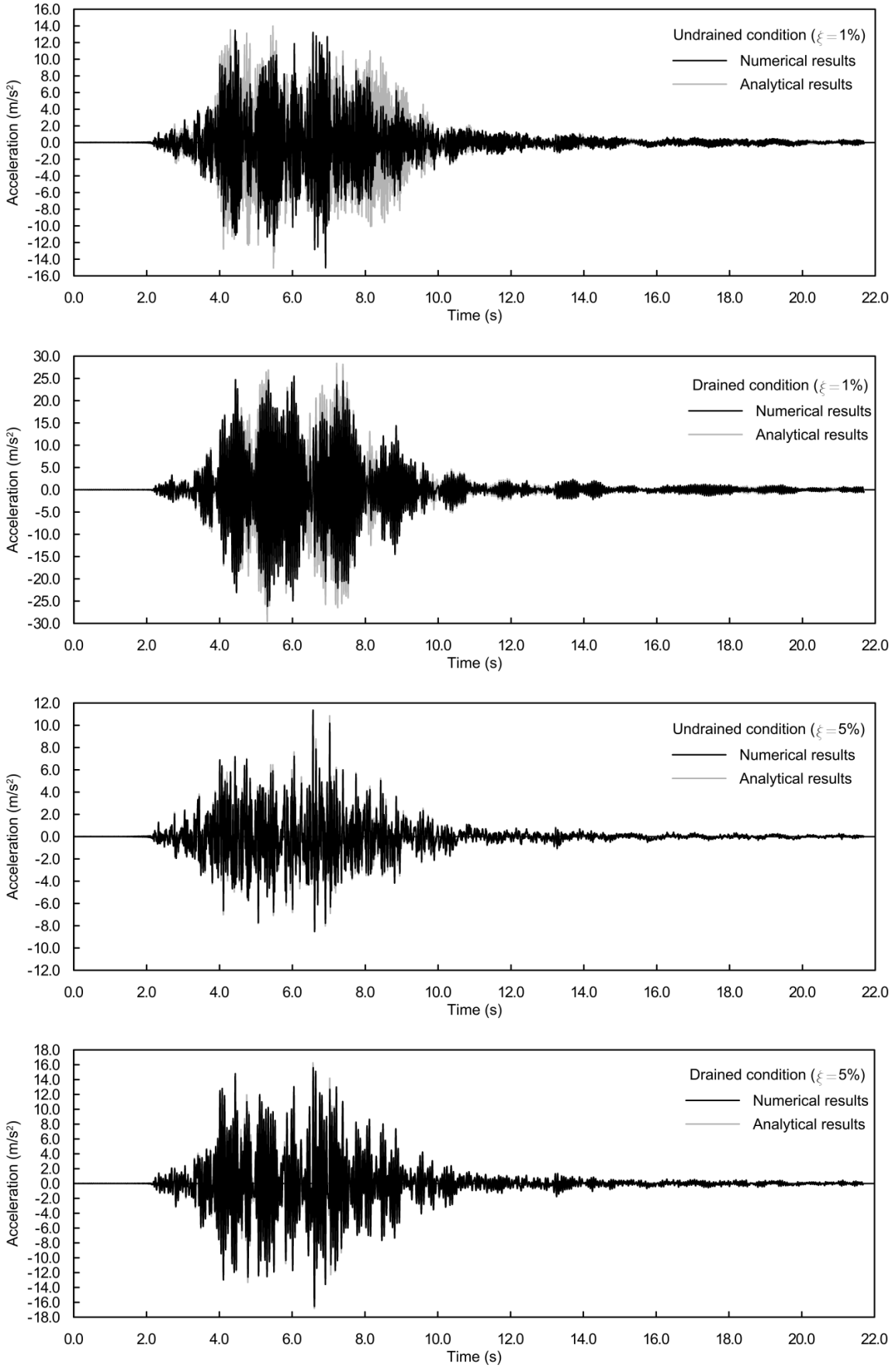


Figure 3-16: Comparison of acceleration time histories at point A between analytical and numerical results

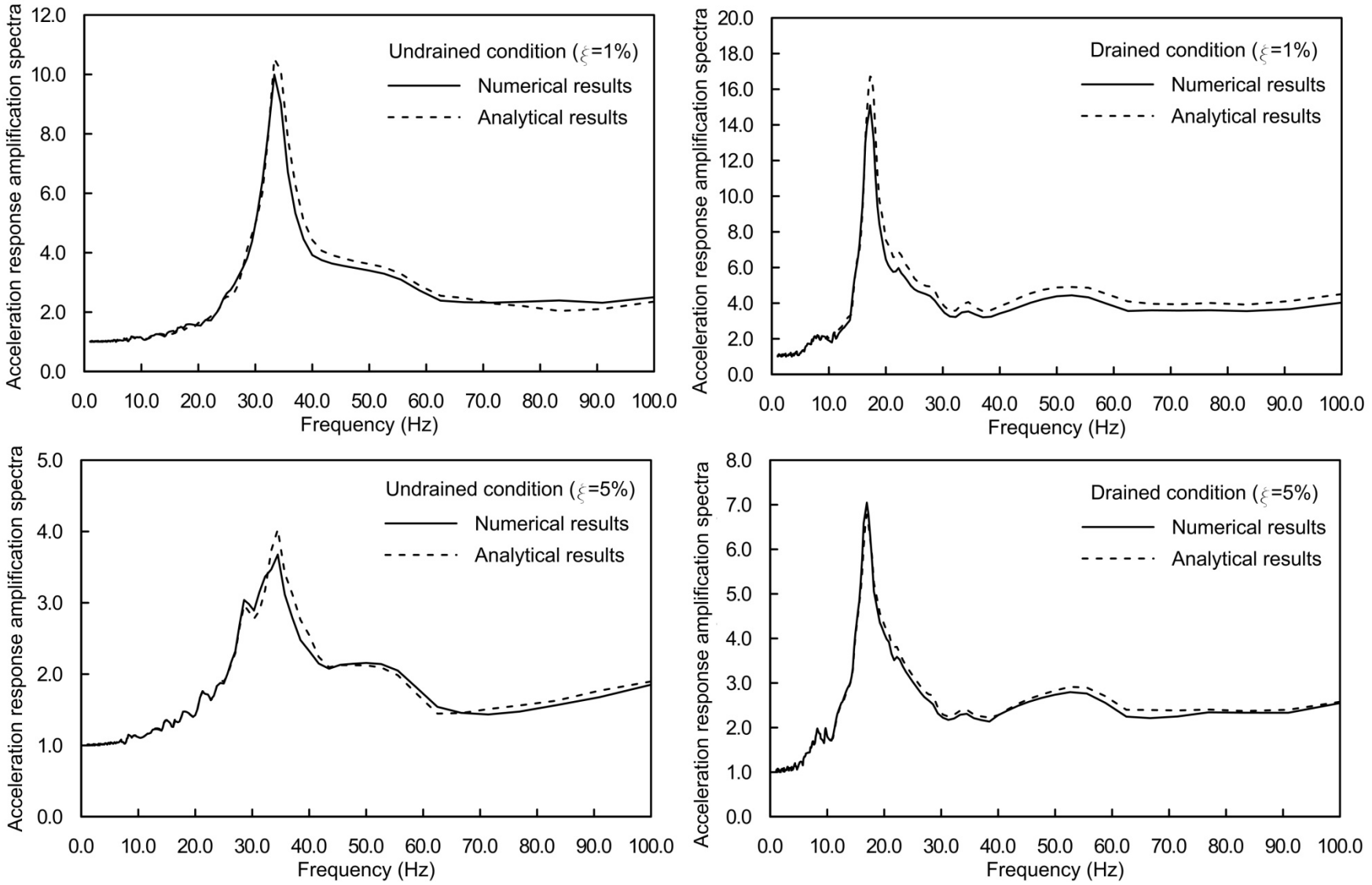


Figure 3-17: Comparison of acceleration response amplification spectra at point A between analytical and numerical results

Calibration of Rayleigh damping parameters

As mentioned in the previous section, the vertical site response is slightly underestimated by the numerical analysis compared to the analytical solution. This is probably due to the inaccurate representation of the material damping by the Rayleigh formulation employed in the FE analysis. Based on the expressions of the Rayleigh damping parameters (Equation 3-18), ω_1 and ω_2 are the two frequencies defining the concerned range over which the variation of Rayleigh damping is approximately constant (shown in Figure 3-15). If the system frequency simulated in the numerical analysis is not within the frequency range defined by ω_1 and ω_2, the damping can be overestimated and therefore the dynamic response would be underestimated, as observed in the previous section. Hence, in order to achieve a more accurate representation of the response, appropriate values of ω_1 are calibrated through a parametric study. Namely, the value of ω_1 is decreased gradually until the system frequency lies within the concerned range between ω_1 and ω_2. When a fractional value of the first fundamental frequency of the studied system is employed as ω_1, more accurate response is predicted by the numerical analysis, as shown in Figure 3-18, in terms of the acceleration response amplification spectra. It should be noted that 90% of the original fundamental frequency is employed as ω_1 for the analysis presented in Figure 3-18. Therefore, it is suggested that a fractional value of the first fundamental frequency of the system should be employed as the Rayleigh damping parameter ω_1 in the numerical analysis for vertical site response, in order to achieve a more accurate prediction.

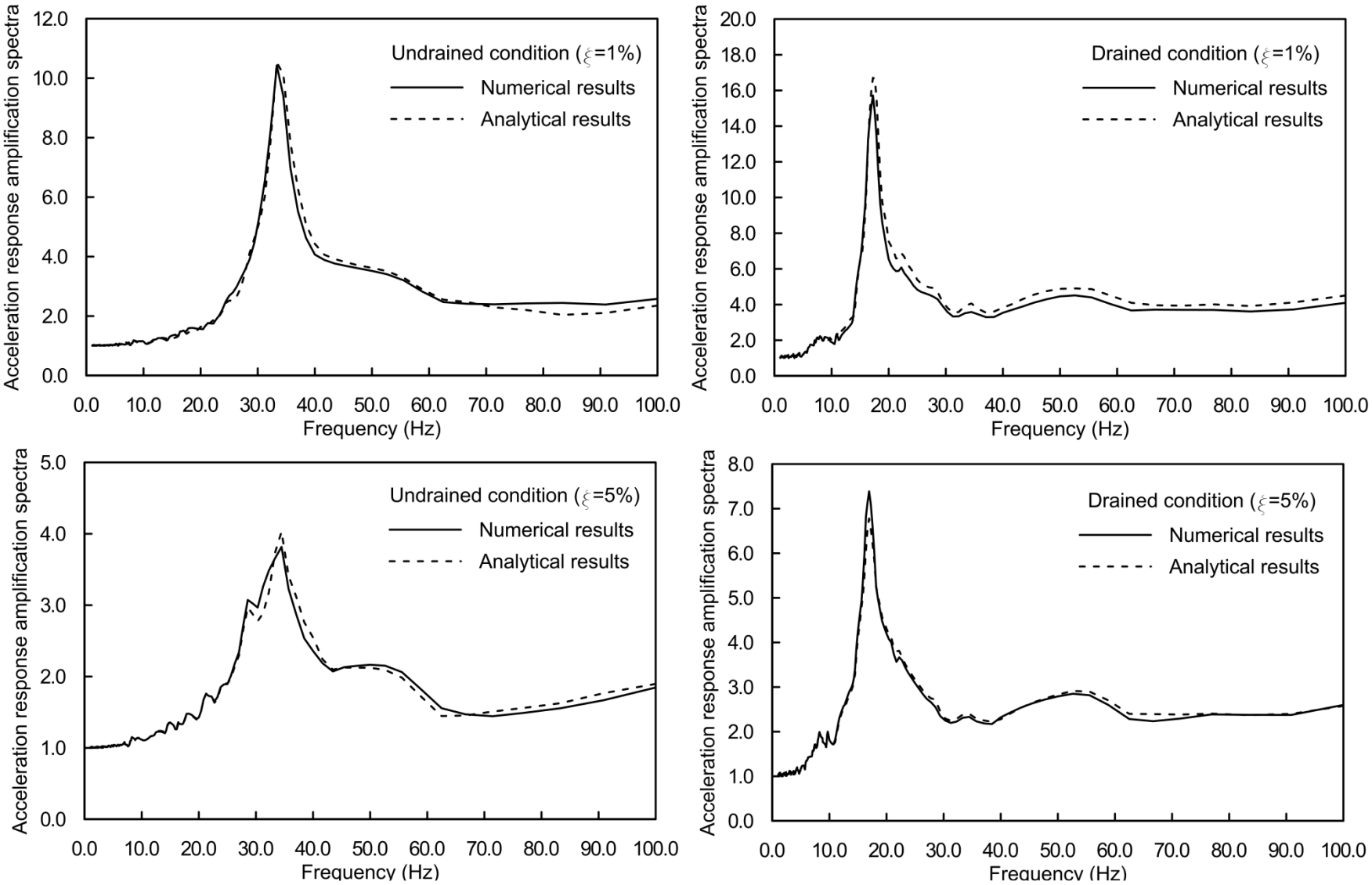


Figure 3-18: Comparison of acceleration response amplification spectra at point A between analytical and numerical results (New Rayleigh damping parameters)

3.4 Two-phase investigation of compressional wave propagation in saturated porous material

The vertical site response is investigated by using one-phase frequency domain analytical solution in the previous section. However, due to the complexity of dynamic soil behaviour and earthquake loading conditions, consolidation can occur in a soil profile during earthquake loading, depending on the range of the dynamic loading duration and soil permeability. In that case, the one-phase analytical solution is insufficient for the accurate simulation of vertical site response at any intermediate transient states. Therefore, two-phase coupled analysis is required to investigate the site response to vertical ground motion which accounts for soil-pore fluid interaction effects. Since the site response subjected to vertical ground motion mainly involves propagation of compressional waves, the compressional wave propagation mechanism in saturated porous soil is initially studied in this part, by employing a two-phase coupled analytical solution and the FE method.

3.4.1 Previous two-phase coupled investigation of compressional wave propagation

The two-phase coupled theory concerning the elastic wave propagation in saturated porous materials was initially studied by Biot (1956a, b). Based on the proposed formulation, three types of waves were introduced in saturated porous soil media under dynamic loading; two types of compressional waves and one type of shear wave. The two compressional waves are called the fast wave and slow wave. In particular, the fast wave exists when the pore fluid and solid particles move simultaneously under dynamic loading, while the slow wave is generated when there is a relative movement between pore fluid and solid phase. It was pointed out by Biot (1956a) that the fast wave is the usually observed compressional body wave in earthquake engineering, also called P-wave. Furthermore, the slow wave is highly dispersive and tends to attenuate at low loading frequencies. Therefore the slow wave is difficult to be observed in standard field measurements or experiments.

Since 1956, when the two-phase coupled dynamic theory of elastic wave propagation in saturated porous materials was proposed by Biot, the existence of the slow wave has

been widely doubted by various researchers. It was only in 1980 when Plona (1980) experimentally proved for the first time the existence of the slow wave, 24 years after the proposal of Biot's theory. Plona's (1980) test is shown in Figure 3-19, where a transmitter, a poroelastic slab and a receiver are placed in liquid (water). The slab represents an artificial rock, made of sintered glass spheres saturated with pore water, which is used to refract the incident wave to different types of waves. It should be noted that the slab was vibrated under an ultrasonic-frequency load (greater than 2000Hz), in order to trigger the development of slow waves. Hence, an ultrasonic-frequency impulse was generated by the transmitter, which propagated as an acoustic wave in the liquid until it reached the slab. At the interface between the liquid and the slab, since the slab was made of porous material, the incident wave was refracted to three waves; two compressional waves and one shear wave. These three waves then propagated in the slab with different paths and velocities. When they reached the bottom interface of the slab, respective reflections and refractions occurred again for all three waves. These three refracted waves then propagated in the water and reached the receiver. They were identified by the receiver based on the different monitored arrival times. Plona (1980)'s results are shown in Figure 3-20, where wave A is the primary fast wave, while waves C, E and G are multiply reflected waves of wave A by the surfaces of the slab. Furthermore, wave D is the primary slow wave and wave F is the reflection of the slow wave. It should be noted that the received waves shown in Figure 3-20 were obtained when the slab was oriented perpendicular to the incident wave, so no shear wave could be generated. After Plona (1980), researchers started to dedicate effort to proving the existence of the slow wave. Rasolofosaon (1988) modified Plona's device and observed the slow wave in water-saturated porous plates made of artificially bonded natural sand grains. Nagy (1990) carried out similar experiments and observed the slow wave in natural rocks, which was the first time that the slow wave was experimentally observed in a natural material.

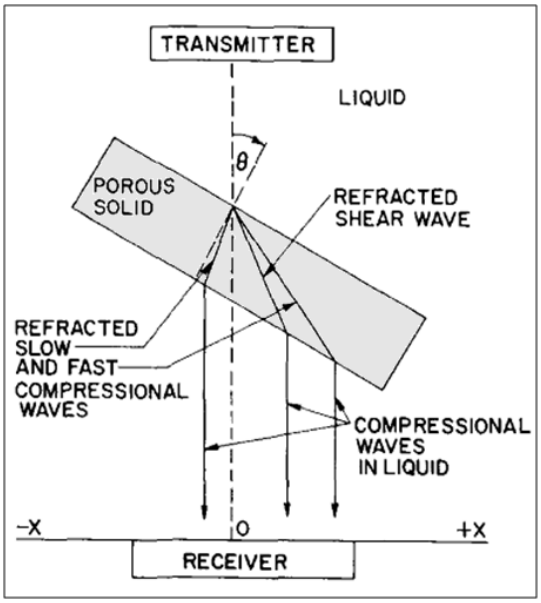
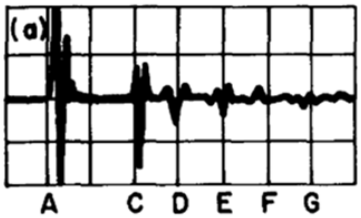


Figure 3-19: The model test device (after Plona (1980))



Fast waves: A, C, E, and G
Slow waves: D and F

Figure 3-20: Observed compressional and shear waves (after Plona (1980))

Apart from the experimental work, efforts were also dedicated to the analytical investigation of the compressional wave propagation. Dutta (1980) and Berryman (1980) compared the observed slow wave velocities from Plona's work (1980) with the analytical expressions of the compressional wave velocities derived from Biot's theory (1956a, b) and showed a good agreement. Boyle and Chotiros (1991) carried out experiments with samples made of river sediments and observed the slow wave under ultrasonic-frequency loading. The observed slow wave velocities were compared with the analytical expressions for the compressional wave velocities proposed by Biot (1956a, b) and showed some discrepancy. This was explained by saying that probably the bulk modulus of the solid skeleton was not accurately obtained.

Teng (1990) probably for the first time employed the FE method to investigate the slow wave propagation in porous materials subjected to ultrasonic-frequency loading,

where Plona (1980) experiment was numerically simulated. Gurevich et al. (1999) also successfully validated Biot's slow wave theory by simulating Plona (1980) experimental work employing his OASES FE modelling code. Furthermore, Arntsen and Carcione (2001) numerically proved the existence of the slow wave in water-saturated Nivelsteiner sandstone under ultrasonic-frequency loading. It was the first time that the slow wave propagation problems were investigated with the finite difference method. The obtained numerical results compared well with the experimental observations presented by Kelder and Smeulders (1997), where a test similar to Plona (1980) work was carried out.

Based on the presented previous studies, it can be seen that most of the work concentrated on the investigation of the existence of the slow wave under the ultrasonic-frequency loading. This is because the slow wave is less dispersive and attenuated under high frequency loading and therefore easier to be observed. Nevertheless, the ultrasonic-frequency loading is beyond the concerned loading frequency range for geotechnical earthquake engineering problems. However, according to Biot (1956a) and Kim et al. (2002), the characteristics of the dispersion and attenuation for the fast and slow waves are also affected by the examined soil permeability range, as the effect of the loading frequency range. More importantly, the effect of the permeability on the characteristics of the compressional waves can be more critical than that of the loading frequency, in the geotechnical point of view. Therefore, the following work concentrates on the investigation of the permeability effect on the compressional wave propagation mechanism, by employing a two-phase coupled analytical theory and numerical analysis.

3.4.2 Two-phase analytical solution for compressional wave propagation in saturated porous soils

In this section, a two-phase coupled analytical solution for the compressional wave propagation is studied. The work follows a similar procedure presented by Bardet and Sayed (1993), where however some developments and extensions have been made. In particular, firstly, the two-phase coupled governing equation of motion for saturated porous materials is reviewed based on Biot's theory (1956a, b). Furthermore, by combining the elastic wave propagation equation, the exact solutions for the dispersion

and attenuation characteristics of compressional waves are extensively derived. Finally, based on the derived solution, the characteristics of the compressional waves are specifically investigated.

Two-phase coupled governing equation of motion

Based on Biot (1956a) and Vardoulakis and Beskos (1986), the one-dimensional dynamic response of saturated porous visco-elastic materials is described by Equation 3-19.

$$\begin{cases} \left(D+\dfrac{1-n}{n}\cdot K_f\right)\cdot\dfrac{\partial^2 u}{\partial z^2}+K_f\cdot\dfrac{\partial^2 v}{\partial z^2}=(1-n)\cdot\rho_s\cdot\dfrac{\partial^2 u}{\partial t^2}+n\cdot\rho_f\cdot\dfrac{\partial^2 v}{\partial t^2} \\ K_f\cdot\left(\dfrac{1-n}{n}\cdot\dfrac{\partial^2 u}{\partial z^2}+\dfrac{\partial^2 v}{\partial z^2}\right)=n\cdot\rho_f\cdot\dfrac{\partial^2 v}{\partial t^2}+\dfrac{n\cdot\rho_f\cdot g}{k}\cdot\left(\dfrac{\partial v}{\partial t}-\dfrac{\partial u}{\partial t}\right) \end{cases} \quad 3\text{-}19$$

where u and v, and ρ_s and ρ_f are the displacements and densities of the solid skeleton and pore fluid respectively, D and K_f are the soil skeleton constrained modulus and pore fluid bulk modulus respectively, n and k are the material porosity and permeability respectively, g is the gravitational acceleration and z is the depth of the soil layer.

After rearrangement, Equation 3-19 becomes:

$$\begin{cases} c_w^2\cdot\left(\left(\dfrac{1}{n}+\chi\right)\cdot\dfrac{\partial^2 u}{\partial z^2}+\dfrac{1}{n}\cdot\dfrac{\partial^2 w}{\partial z^2}\right)=\dfrac{1}{\beta}\cdot\dfrac{\partial^2 u}{\partial t^2}+\dfrac{\partial^2 w}{\partial t^2} \\ c_w^2\cdot\left(\dfrac{1}{n}\cdot\dfrac{\partial^2 u}{\partial z^2}+\dfrac{1}{n}\cdot\dfrac{\partial^2 w}{\partial z^2}\right)=n\cdot\dfrac{\partial^2 u}{\partial t^2}+\dfrac{\partial^2 w}{\partial t^2}+\dfrac{g}{k}\cdot\dfrac{\partial w}{\partial t} \end{cases} \quad 3\text{-}20$$

where $w=n\cdot(v-u)$, $\chi=\dfrac{D}{K_f}$, $\beta=\dfrac{1}{n+(1-n)\cdot G_s}$ and $G_S=\dfrac{\rho_S}{\rho_f}$. Furthermore, c_w is the wave velocity in the fluid, which is equal to $c_w=\sqrt{\dfrac{K_f}{\rho_f}}$.

1-D elastic wave propagation equation

Kramer (1996) considered a uniform soil layer of isotropic and linear visco-elastic behaviour overlying rigid bedrock, which is subjected to harmonic vertical motion imposed at the bottom boundary of the soil layer. Vertically propagating compressional waves are generated and are expressed by Equation 3-21.

$$u(z,t) = A \cdot e^{i\cdot(\omega\cdot t + k^*\cdot z)} \quad 3\text{-}21$$

$$k^* = k\cdot(1 - i\cdot\xi) \quad 3\text{-}22$$

where $u(z,t)$ is the vertical displacement of the soil layer at depth z and time t, ω is the circular frequency of the input motion, A is the amplitude of the propagating wave and k^* is the complex wave number. Based on Kramer (1996), k^* can be expressed by the wave number k ($k = \omega/c$, where c is the compressional wave velocity) and the damping ratio ξ, as shown in Equation 3-22. It should be noted that Bardet and Sayed (1993) employed a different parameter, the amplitude decay δ to quantify the wave attenuation, which is expressed in Equation 3-23. However, the damping ratio ξ is used in the present study to indicate the soil material damping subjected to compressional deformation, which ensures the consistent physical meaning of damping parameters employed for both soil shearing and compressional deformations. Furthermore, parameter c is employed to express the compressional wave velocity, in order to distinguish it from v_p used for the one-phase study of vertical site response.

$$\delta = \frac{c}{\xi} \quad 3\text{-}23$$

After substituting Equation 3-22 in Equation 3-21, the compressional wave propagation equation is expressed by Equation 3-24.

$$u(z,t) = A \cdot e^{i\cdot\omega\cdot t + \frac{i\cdot\omega\cdot z}{c} + \frac{\xi\cdot\omega\cdot z}{c}} \quad 3\text{-}24$$

It is convenient to introduce a complex number ϕ:

$$\phi = \frac{i\cdot c_w}{c} + \frac{\xi\cdot c_w}{c} \quad 3\text{-}25$$

from which, the compressional wave velocity and damping ratio can be expressed as:

$$c = \frac{c_w}{I(\phi)} \quad \text{and} \quad \xi = \frac{R(\phi)\cdot c}{c_w} \quad 3\text{-}26$$

where $R(\phi)$ and $I(\phi)$ are the real and imaginary parts of complex number ϕ respectively.

By substituting Equation 3-25 into Equation 3-24, the compressional wave propagation equation can be expressed as follows:

$$u(z,t) = A \cdot \mathrm{e}^{\mathrm{i}\cdot\omega\cdot t+\phi\cdot\frac{\omega\cdot z}{c_w}} \tag{3-27}$$

In addition, according to Bardet and Sayed (1993), the compressional wave propagation equation for the fluid phase can be expressed in a similar way, but with different amplitude *C*, as shown in Equation 3-28

$$w(z,t) = C \cdot \mathrm{e}^{\mathrm{i}\cdot\omega\cdot t+\phi\cdot\frac{\omega\cdot z}{c_w}} \tag{3-28}$$

After substituting the elastic wave propagation equations (Equations 3-27 and 3-28) into the two-phase governing equation of motion (Equation 3-20), two linear equations with unknowns *A* and *C* are obtained:

$$\begin{cases} A\cdot\left(\phi^2\cdot\left(\chi+\frac{1}{n}\right)+\frac{1}{\beta}\right)+C\cdot\left(1+\frac{\phi^2}{n}\right)=0 \\ A\cdot\left(n+\frac{\phi^2}{n}\right)+C\cdot\left(1+\frac{\phi^2}{n}-\mathrm{i}\cdot\frac{g}{k\cdot\omega}\right)=0 \end{cases} \tag{3-29}$$

For a non-trivial solution, the determinant of the Equation 3-29 should be equal to zero, leading to the following characteristic equation:

$$\frac{\chi}{n}\cdot\phi^4 + a\cdot\phi^2 + b = 0 \tag{3-30}$$

where

$$a = \chi+\frac{1}{n\cdot\beta}-1-\mathrm{i}\cdot\frac{g}{k\cdot\omega}\cdot\left(\chi+\frac{1}{n}\right)$$

$$b = \frac{1}{\beta}-n-\mathrm{i}\cdot\frac{g}{k\cdot\omega}\cdot\frac{1}{\beta}$$

There are four complex roots for the solution of Equation 3-30, as expressed by Equation 3-31. These can account for the characteristics of four compressional waves, where their wave velocities and damping ratios can be calculated based on Equation 3-26. However, among the obtained expressions of four compressional waves, ϕ_1 and ϕ_3 represent the same type of wave with opposite propagation directions. Similarly, ϕ_2 and ϕ_4 represent another type of wave with opposite propagation directions. Therefore, two types of compressional waves (represented by ϕ_1 and ϕ_2) are introduced based on the studied two-phase analytical solution, which are described as the fast and slow waves respectively by Biot (1956a). Finally, the expressions of the wave velocities and

damping ratios for the fast and slow waves are given by Equation 3-32, where subscripts 1 and 2 indicate fast and slow waves.

$$\begin{cases} \phi_{1,3} = \pm\sqrt{\dfrac{-a\cdot n-\sqrt{a^2\cdot n^2-4b\cdot n\cdot\chi}}{2\chi}} \\ \phi_{2,4} = \pm\sqrt{\dfrac{-a\cdot n+\sqrt{a^2\cdot n^2-4b\cdot n\cdot\chi}}{2\chi}} \end{cases} \tag{3-31}$$

$$\begin{cases} c_{1,2} = \dfrac{c_w}{\left|I\left(\phi_{1,2}\right)\right|} \\ \xi_{1,2} = \dfrac{\left|R\left(\phi_{1,2}\right)\right|\cdot c_{1,2}}{c_w} \end{cases} \tag{3-32}$$

It should be noted that the expressions of compressional wave velocities and damping ratios given by Equation 3-32 cannot be directly employed to investigate the characteristics of compressional waves, since they consist of complex parameters. Similar implicit forms of these expressions were also presented by Bardet and Sayed (1993). Therefore, herein these expressions are mathematically solved based on the angular transformation for complex parameters and the explicit exact solutions are derived and given by Equation 3-33, which is believed to provide an easier way to investigate the characteristics of compressional waves.

$$\begin{cases} c_{1,2} = \dfrac{c_w}{\left|I\left(\phi_{1,2}\right)\right|} \\ \xi_{1,2} = \dfrac{\left|R\left(\phi_{1,2}\right)\right|\cdot c_{1,2}}{c_w} \end{cases} \tag{3-33}$$

where

$$\phi_{1,2} = \frac{\sqrt{r_4}\cdot\cos\dfrac{\theta_4}{2}}{\sqrt{2\chi}} + i\cdot\frac{\sqrt{r_4}\cdot\sin\dfrac{\theta_4}{2}}{\sqrt{2\chi}}$$

$$\begin{cases} r_4 = \sqrt{a_4^2+b_4^2} & \theta_4 = \arctan\dfrac{b_4}{a_4} \\ a_4 = -n\cdot a_1\,\mathrm{m}\sqrt{r_3}\cdot\cos\dfrac{\theta_3}{2} & b_4 = -n\cdot b_1\,\mathrm{m}\sqrt{r_3}\cdot\sin\dfrac{\theta_3}{2} \end{cases}$$

$$\begin{cases} r_3 = \sqrt{a_3^2 + b_3^2} & \theta_3 = \arctan\dfrac{b_3}{a_3} \\ a_3 = n^2 \cdot a_1^2 - n^2 \cdot b_1^2 - 4n \cdot \chi \cdot a_2 & b_3 = 2n^2 \cdot a_1 \cdot b_1 - 4n \cdot \chi \cdot b_2 \end{cases}$$

$$\begin{cases} a_1 = \chi + \dfrac{1}{n \cdot \beta} - 1 & b_1 = -\dfrac{g}{k \cdot \omega} \cdot \left(\chi + \dfrac{1}{n} \right) \\ a_2 = \dfrac{1}{\beta} - n & b_2 = -\dfrac{g}{k \cdot \omega} \cdot \dfrac{1}{\beta} \end{cases}$$

Characteristics of the wave velocities and damping ratios for the fast and slow waves

By employing the expressions in Equation 3-33, the compressional wave velocities and damping ratios for the fast and slow waves can be calculated and investigated. The obtained compressional wave velocities and damping ratios are plotted in Figure 3-21 against the dimensionless parameter $k\omega/g$. According to Biot (1956a, b), permeability k and loading frequency ω are the main parameters that affect the characteristics of compressional waves. It should be noted that the results are obtained based on typical values of soil properties, where n=0.36 (soil porosity) and ρ=2.0g/cm^3 (mass density). Furthermore, results of three scenarios are presented in the plots, by employing different values of parameter χ (stiffness ratio between the soil skeleton constrained modulus and pore fluid bulk modulus).

As it can be observed in Figure 3-21, the variations of the fast wave velocity and damping ratio are represented by the three upper lines in Figure 3-21 (a) and three lower lines in Figure 3-21 (b) respectively. In particular, the following observations can be made:

- for the scenario of χ=0.1 (relatively soft soil), the variation of the fast wave velocity is represented by the upper solid line in Figure 3-21 (a). It can be seen that the fast wave velocity is independent of the ratio $k\omega/g$ in its low range (i.e. smaller than 0.1), but is dependent on it in the high range of the ratio $k\omega/g$ (i.e. larger than 0.1). This indicates that the fast wave is dispersive for high value of $k\omega/g$. However, it should be noted that the fast wave is the usually observed P-wave in earthquake engineering, which is always considered as non-dispersive. This apparent contradiction can be explained by the observed damping ratio variation for the fast wave, as shown by the lower solid line in Figure 3-21 (b), where higher damping ratios are observed for the

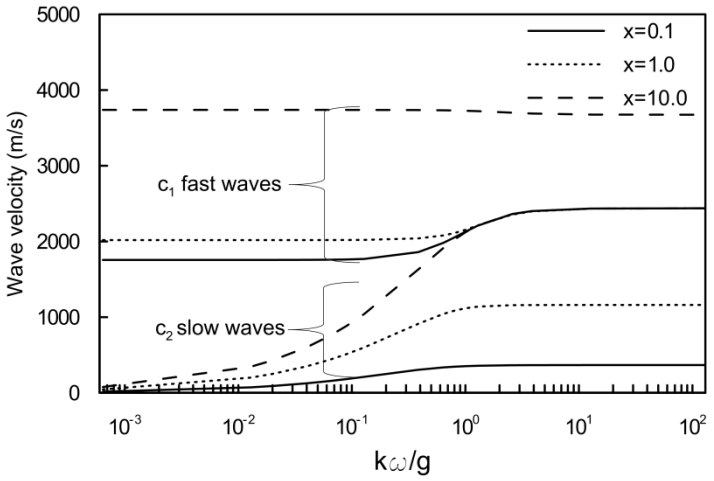
fast wave in the high range of $k\omega/g$, implying that the fast wave has attenuated. Therefore, based on the observed wave characteristics, the dispersion of the fast wave can be practically ignored in the high range of $k\omega/g$, due to its higher attenuation, also as stated by Biot (1956a);

- for the scenario of χ=1.0 (relatively stiff soil), similar trends are observed for the variations of fast wave velocity and damping ratio, compared to the previous scenario. However, larger wave velocities and smaller damping ratios are achieved for this scenario, which is reasonable since stiffer soil is involved;
- for the scenario of χ=10.0 (extremely stiff soil), extremely large wave velocities and almost null damping ratios are obtained, which correspond to the properties of extremely stiff soil.

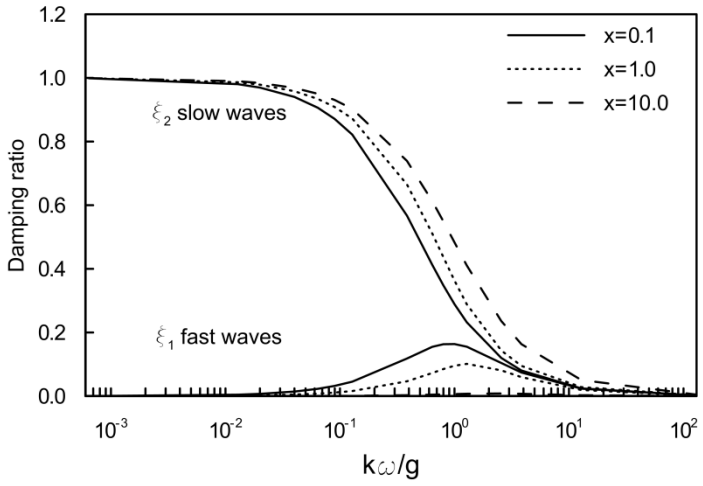
The variations of wave velocity and damping ratio for the slow wave are represented by the three lower lines in Figure 3-21 (a) and the three upper lines in Figure 3-21 (b) respectively. As expected, the slow wave velocities are smaller than the fast wave velocities. Furthermore, larger slow wave velocities are observed for the stiffer soil (higher χ value), which is the same trend as observed for the fast wave velocity variation. Finally, the slow wave velocity increases as the ratio $k\omega/g$ increases in the low range of $k\omega/g$ and stabilises in the high range of $k\omega/g$. This indicates that the slow wave becomes less dispersive as $k\omega/g$ increases. When it comes to the variation of the damping ratio for the slow wave, it can be seen that the damping ratios are considerably higher in the low range of $k\omega/g$ and decrease as $k\omega/g$ increases. This means that the slow wave is highly attenuated at the low range of $k\omega/g$ and becomes less attenuated as $k\omega/g$ increases. These observations explain the fact that the slow wave is difficult to be observed in the low range of loading frequency due to its high attenuation, as stated by Biot (1956a).

Furthermore, the variations of the compressional wave velocity and damping ratio obtained by the examined two-phase analytical solution are also compared with the results presented by Bardet and Sayed (1993), in terms of the normalised wave velocity and damping ratio, as shown in Figure 3-22. The wave velocities and damping ratios are normalised by corresponding parameters independent of the ratio $k\omega/g$ (Bardet and Sayed, 1993), as defined in Equation 3-34. Based on Figure 3-22, it can be seen that, the results from the present study agree well with the results presented by Bardet and Sayed

(1993), in terms of both normalised wave velocity and damping ratio for the fast and slow waves.



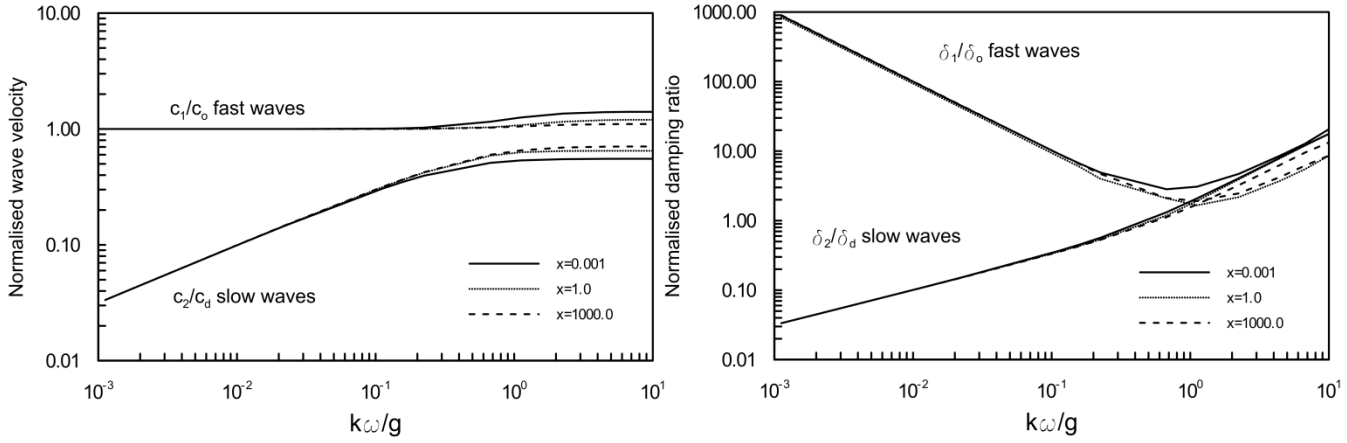
(a): Variation of compressional wave velocity



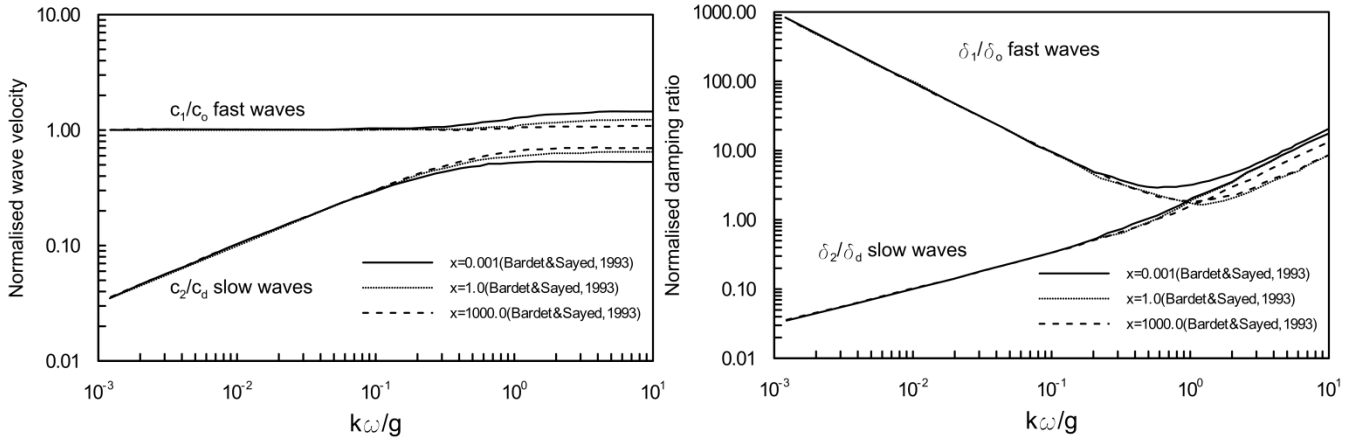
(b): Variation of compressional wave damping ratio

Figure 3-21: Variations of compressional wave velocity and damping ratio

$$\begin{cases} c_o = c_w \cdot \sqrt{\beta \cdot \left(\chi + \dfrac{1}{n}\right)} & c_d = \sqrt{2} c_w \cdot \sqrt{\dfrac{\chi}{n \cdot \chi + 1}} \\ \delta_o = \dfrac{2c_w}{\sqrt{\beta}} \cdot \dfrac{\left(\chi + \dfrac{1}{n}\right)^{2.5}}{n \cdot \chi^2 + \left(1 + n - \dfrac{(1-n)^2}{n} \cdot G_s\right) \cdot \chi + \dfrac{(1-n)^2}{n^2} \cdot G_s \cdot (G_s - 1)} & \delta_d = c_d \end{cases} \quad \text{3-34}$$



(a): Results from the present studied two-phase analytical solution



(b): Results presented by Bardet and Sayed (1993)

Figure 3-22: Comparison of the wave velocities and damping parameters from the present study and from Bardet and Sayed (1993) results

3.4.3 Two-phase compressional wave propagation mechanism in saturated porous soils

The results of the previously studied two-phase analytical solution for compressional wave propagation, showed the existence of two types of compressional waves (fast and slow waves) and indicated that their characteristics (i.e. the wave dispersion and attenuation) are highly dependent on soil and dynamic parameters (i.e. the permeability, loading frequency and soil stiffness). Therefore, in this section, the compressional wave propagation mechanism is further simulated and investigated by employing coupled FE analysis, where the influence of the soil properties (i.e. soil permeability and soil stiffness) is investigated in parametric studies.

For numerical analysis, the compressional wave propagation in a 1-D soil column is simulated by ICFEP, assuming linear elastic soil behaviour and plane-strain geometry. The FE mesh, consisting of 800 8-noded isoparametric quadrilateral elements and the boundary conditions are shown in Figure 3-23. For the boundary conditions, the DOFs of displacement and pore water pressure at corresponding nodes of same height along the two lateral boundaries are tied to be identical. The pore water pressure at the top boundary is prescribed as zero and is not allowed to change throughout the analysis (i.e. Δp=0). The bottom boundary is considered to be impermeable (i.e. no flow across the boundaries). Hydrostatic pore water pressure and static self-weight are prescribed as the initial stress for the numerical analyses, where the coefficient of earth pressure at rest (K_0) is applied to be 0.5. An absorbing viscous boundary condition (Lysmer and Kuhlemeyer, 1969) is employed at the bottom boundary, in order to absorb wave reflections.

A uniformly distributed harmonic vertical motion is applied on the top boundary, as illustrated in Figure 3-24, which can generate compressional waves propagating from the top boundary towards the bottom boundary through the soil column. The displacement response at point B (25.0 m below the surface, as shown in Figure 3-23), is monitored for the purpose of recording the wave arrival time. The soil properties are listed in Table 3-3. The constant average acceleration time integration method from the Newmark's family of algorithms (Newmark, 1956), is employed for the FE analysis. Neither numerical damping nor material damping is employed for this numerical simulation, in order to prevent any dissipation impact on the compressional wave propagation. In order to investigate the impact of the permeability on the compressional wave propagation, a parametric study is conducted for a wide permeability range. The detailed soil parameters are listed in Table 3-4. It should be noted that some of the examined permeability values are extremely high in order to trigger the existence of the slow wave. Furthermore, a relatively short-period loading (20.0Hz) is applied in order to more clearly distinguish the fast and slow wavelets at the monitoring point, which can overlap with each other when long-period loading is imposed. Finally, the u-p formulation is employed for the two-phase consolidation formulation of ICFEP, while the two-phase analytical solution for the compressional wave propagation is studied based on the u-U formulation. However, according to Schanz and Pryl (2004), the u-U formulation is supposed to possess the same roots as the u-p formulation, where as

mentioned before, the roots represent the solutions for the compressional waves.

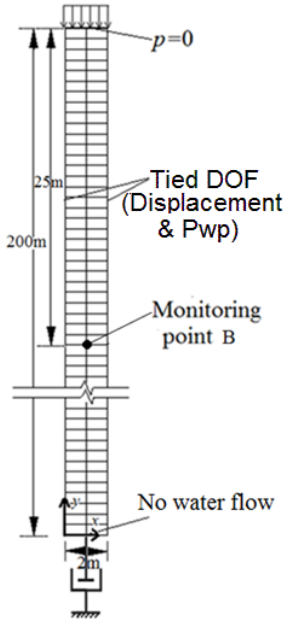


Figure 3-23: A schematic graph for the FE model in coupled analysis

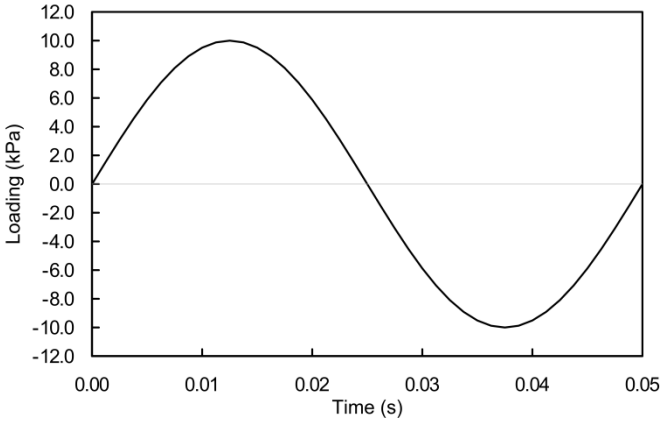


Figure 3-24: Illustration of the input vertical motion for the coupled 1-D column FE analysis

Table 3-3: Soil properties of the coupled 1-D column FE analysis

Parameter	**Value**
Young's modulus E (kPa)	1.98E+05 (χ=0.1)
Bulk modulus of fluid K_f (kPa)	2.20E+06
Stiffness ratio χ	0.1
Density ρ (g/cm^3)	2.0
Poisson's ratio ν	0.2
Void ratio e	0.587

Table 3-4: Detailed soil properties for seven cases (χ=0.1)

Parameter (χ=0.1)	Case1	Case2	Case3	Case4	Case5	Case6	Case7
Loading frequency f (Hz)	20.0	20.0	20.0	20.0	20.0	20.0	20.0
Circular frequency ω (rad/s)	125.7	125.7	125.7	125.7	125.7	125.7	125.7
Loading period T (s)	5.0E-02	5.0E-02	5.0E-02	5.0E-02	5.0E-02	5.0E-02	5.0E-02
Time step Δt=T/160 (s)	3.1E-04	3.1E-04	3.1E-04	3.1E-04	3.1E-04	3.1E-04	3.1E-04
Permeability k (m/s)	1.0E-7	1.0E-3	3.0E-2	5.0E-2	1.0E-1	1.0E+1	1.0E+2
kω/g	***1.0E-6***	***0.01***	***0.38***	***0.64***	***1.28***	***128.0***	***1280.0***

Compressional wave propagation mechanism

The displacement time histories at the monitoring point B for seven studied cases are compared in Figure 3-25, where different dynamic responses are observed. In particular, when a low permeability is employed for the soil column (case1 and case2), identical results are observed, that only one type of compressional wave exists, which is fast waves. For the low permeability soil, the solid and the pore fluid move simultaneously and therefore the fast wave dominates in this scenario. When higher permeability is considered (case3), the fast wave is still the dominant propagating mechanism, but with a lower wave amplitude compared to the previous cases. By further increasing the soil permeability (case4), another compressional wave appears after the fast wave, which is the slow wave. When continuing increasing the permeability (case5), the fast wave amplitude gradually decreases, while the slow wave amplitude increases. However, for the case employing considerably high permeability (case6), the fast wave is highly attenuated and almost disappears and the slow wave becomes the dominant compressional wave. Finally, from case 6 to case 7, the slow wave amplitude stabilises.

As mentioned before, the existence of the slow wave proposed by Biot in 1956 has been both experimentally and numerically proved by researchers, but only for ultrasonic-frequency loading, which is beyond the concerned frequency range in geotechnical earthquake engineering problems. The present work, to the author's knowledge, is the first time to numerically show the existence of the slow wave considering the impact of soil permeability. The present results show a transition from the fast wave to the slow wave when increasingly higher permeability is employed for the two-phase coupled FE analysis of a soil column. Different dominant permeability ranges of the two types of compressional waves can be distinguished, where in

particular the fast wave dominates the low permeability range (i.e. smaller than 5.0E-2 m/s) and the slow wave dominates the high permeability range (i.e. larger than 5.0E-2 m/s).

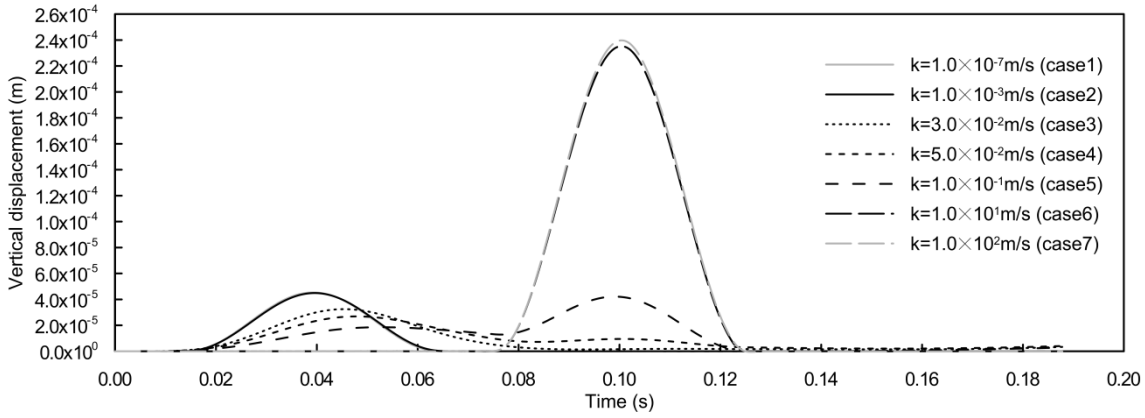


Figure 3-25: Displacement time histories at monitoring point B for seven cases (χ=0.1)

Compressional wave attenuation

The transition from the fast wave to the slow wave can be explained by the characteristics of the damping ratio of the compressional waves. As observed in Figure 3-25, the amplitude of the fast wave gradually decreases as permeability increases and finally it almost vanishes. This proves that the fast wave becomes increasingly attenuated, which corresponds to the fact that the damping ratio for the fast wave is larger in the high permeability range (shown in Figure 3-21). On the other hand, the slow wave is absent in the low permeability range, while its amplitude is gradually raised with increasing permeability. This means that the slow wave becomes less attenuated as permeability increases, which also corresponds to the variation of the damping ratio for the slow wave shown in Figure 3-21.

Compressional wave velocity

The wave velocities monitored at point B from FE analysis are compared to the ones obtained from the analytical solution in Figure 3-26. The numerically obtained wave velocities are calculated by dividing the distance between the monitoring point B and the top boundary by the different wave arrival times. The comparison of the wave velocities shows a good agreement between the numerical and analytical results. It is observed that the wave velocities from low permeability FE analyses match with the

fast wave velocities from the analytical solution and the wave velocities from the high permeability FE analyses agree with the analytically derived slow wave velocities. The wave velocity shift agrees with the transition from the fast wave to the slow wave observed in Figure 3-25. Furthermore, the dispersion of the fast and slow waves can be practically ignored, since they are highly attenuated in the corresponding permeability ranges where the dispersion characteristics are predicted by the analytical solution.

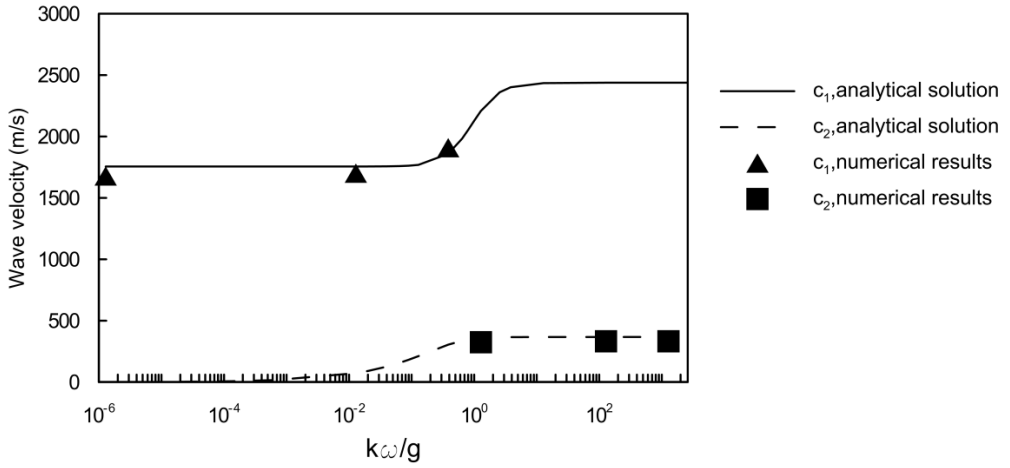


Figure 3-26: Comparison of compressional wave velocity between analytical and numerical results (χ=0.1)

Physical meaning of the compressional waves

Figure 3-27 compares the wave velocities obtained by the FE analysis with the analytically calculated compressional wave velocities under two extreme soil state conditions (undrained and drained conditions), based on Zienkiewicz et al. (1980b) solution shown in Equation 3-35. The calculated wave velocities for the undrained and drained conditions are plotted at the edges of the $k\omega/g$ axis, in order to represent the two extreme conditions. It can be observed that the compressional wave velocities from numerical and analytical solutions for extremely high and low permeability values match with the compressional wave velocities under undrained and drained conditions respectively. Consequently, for the compressional wave propagation in low permeability soils or under undrained condition, the solid and pore fluid move simultaneously and therefore the fast wave dominates the response. For high permeability soils or under drained condition, the slow wave dominates due to the relative movement between the solid and fluid components. Furthermore, these results also highlight the importance of employing two-phase coupled formulation to accurately simulate the compressional

wave propagation at intermediate transient states between undrained and drained conditions.

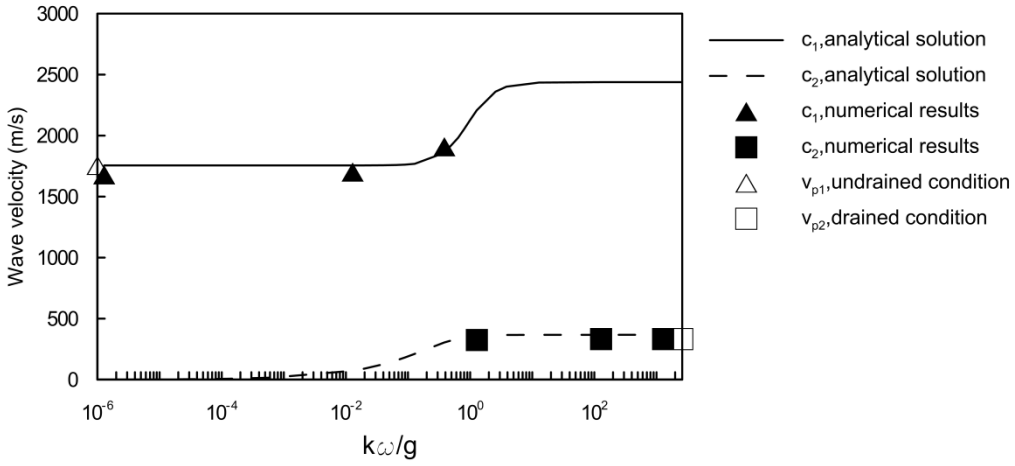


Figure 3-27: Comparison of compressional wave velocity between analytical and numerical results (χ=0.1)

$$v_{p1} = \sqrt{\left(\frac{E(1-\nu)}{(1+\nu)(1-2\nu)} + \frac{K_f}{n} \right) \Big/ \rho}$$
$$v_{p2} = \sqrt{\frac{E(1-\nu)}{(1+\nu)(1-2\nu)} \Big/ \rho} \qquad 3\text{-}35$$

Effect of stiffness ratio on the compressional wave propagation

In order to further investigate the two-phase compressional wave propagation mechanism, a parametric study is conducted in this section to examine the impact of the stiffness ratio between the soil skeleton constrained modulus and pore fluid bulk modulus (χ). Two scenarios are considered, by employing values of χ as 1.0 and 10.0. The remaining soil properties are the same as those used in the previous section (shown in Tables 3-3 and 3-4).

The displacement time histories at monitoring point B for seven cases are compared in Figure 3-28 for the scenario of χ=1.0. From case1 to case7, as increasingly higher permeability is employed, the same trend is observed as the wave propagation mechanism previously observed for the scenario χ=0.1 in Figure 3-25. In particular, a transition from the fast wave to the slow wave is detected since they dominate the response in different permeability ranges. However, the fast and slow wave fronts are

much closer and sometimes overlap with each other, compared to the results for the scenario of χ=0.1. This can be explained by the fact observed in Figure 3-29, that the differences between the fast and slow wave velocities are smaller for the scenario of χ=1.0. In Figure 3-29, compressional wave velocities calculated from the FE analysis are compared with the ones obtained from the analytical solution and of Zienkiewicz et al. (1980b). A good agreement is observed between the numerically and analytically obtained wave velocities. Furthermore, the compressional wave velocities from numerical and analytical solutions at extremely high and low values of permeability can represent the compressional wave velocities under undrained and drained conditions respectively.

For the scenario of χ=10.0, the displacement time histories at the monitoring point B and the corresponding wave velocity comparison are shown in Figures 3-30 and 3-31 respectively. Based on Figure 3-30, only one compressional wave is observed for the different permeability cases, which corresponds to the fact observed in Figure 3-31, that all the numerically derived wave velocities are approximately identical and agree with the fast wave velocities from the analytical solution. Furthermore, the wave velocities under the undrained and drained conditions are also sufficiently close and match with the wave velocities observed in FE analysis, due to the insignificant impact of pore fluid bulk modulus on the wave velocities for the scenario of employing high χ values based on Zienkiewicz et al.'s theory (Equation 3-35). Since the slow wave only exists when the solid and pore fluid move relatively to each other, when a high stiffness ratio is employed for the soil, the interaction effect between the solid and pore fluid is negligible, and therefore the slow wave is highly attenuated and only the fast wave exists.

The parametric study for the stiffness ratio impact on the compressional wave propagation mechanism shows that when relatively low χ values are considered for the soil layer, the fast and slow waves dominate the different permeability ranges and a transition from the fast wave to the slow wave is observed. When relatively high χ values are considered for the soil layer, only the fast wave exists, due to the insignificant interaction effect between the solid and pore fluid components.

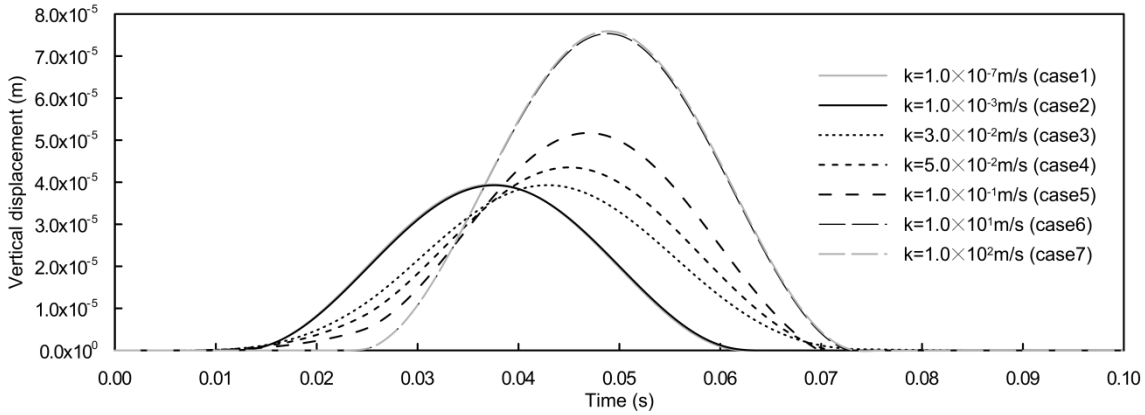


Figure 3-28: Displacement time histories at monitoring point B for seven cases (χ=1.0)

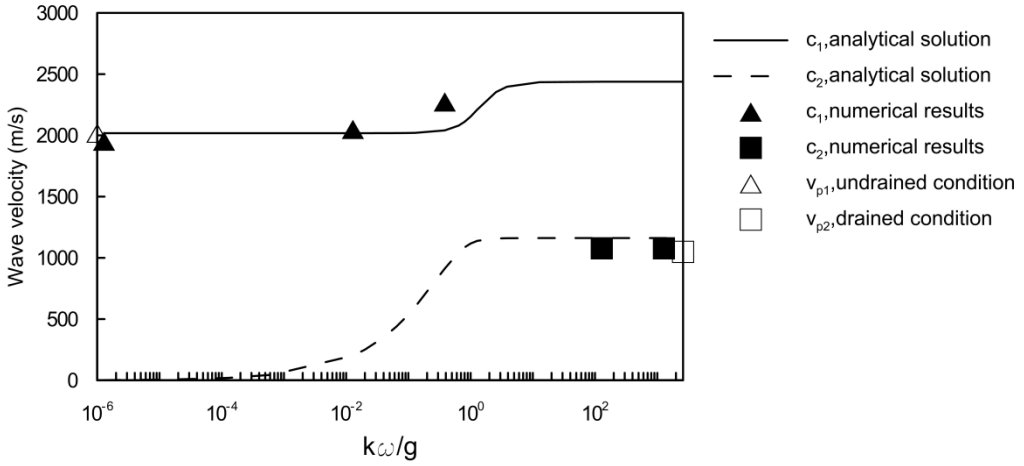


Figure 3-29: Comparison of compressional wave velocity (χ=1.0)

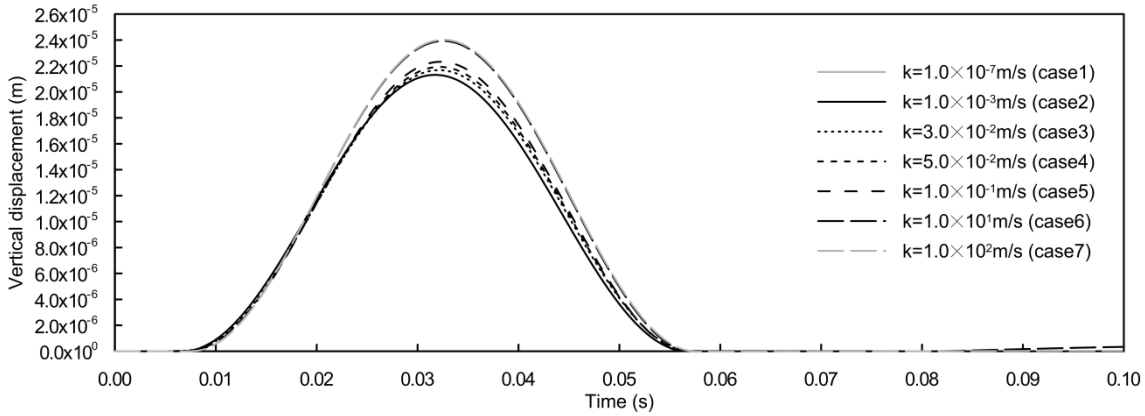


Figure 3-30: Displacement time histories at monitoring point B for seven cases (χ=10.0)

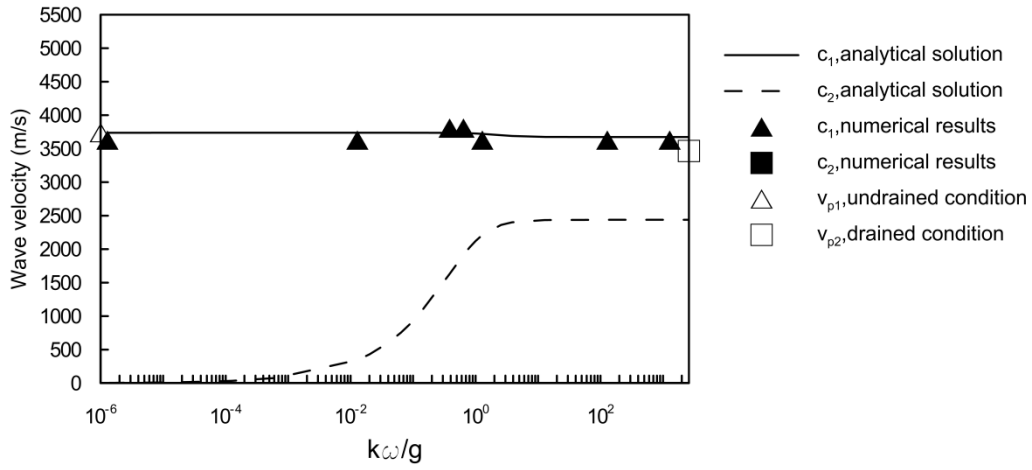


Figure 3-31: Comparison of compressional wave velocity (χ=10.0)

3.5 Two-phase coupled numerical investigation of vertical site response

Based on the coupled two-phase investigation for the compressional wave propagation, in this part the vertical site response is further investigated by considering the solid-fluid interaction, with fully coupled FE analysis (ICFEP), where parametric studies concerning the variation of hydraulic-phase parameters are conducted.

3.5.1 Two-phase coupled vertical site response analysis

For the coupled FE vertical site response analysis, the same FE model, displacement boundary conditions and input motion are employed as the ones used in Section 3.3.3. The parameters for the coupled FE analysis are shown in Table 3-5, where three scenarios of analyses are considered, by employing different values of the stiffness ratio χ. Since the two-phase coupled FE formulation is employed for the present analysis, hydraulic boundary conditions need to be defined. As shown in Figure 3-32, the DOF of pore water pressure at corresponding nodes of the same height along the two lateral boundaries are tied to be identical. The values of pore water pressure at the top boundary are prescribed as zero and are not allowed to change throughout the analysis (i.e. Δp=0). The bottom boundary is considered to be impermeable (i.e. no flow across the boundaries). The employed hydraulic boundary conditions indicate that the pore water pressure due to dynamic loading can only be dissipated at the top boundary of the

mesh. It should be noted that neither Rayleigh damping is employed, nor is numerical damping involved in the time integration method (the constant average acceleration method), in order to avoid their influence on the coupled vertical site response. For the FE analyses of each scenario, a wide range of soil permeability values is parametrically investigated to assess its influence on the vertical site response, as listed in Table 3-6.

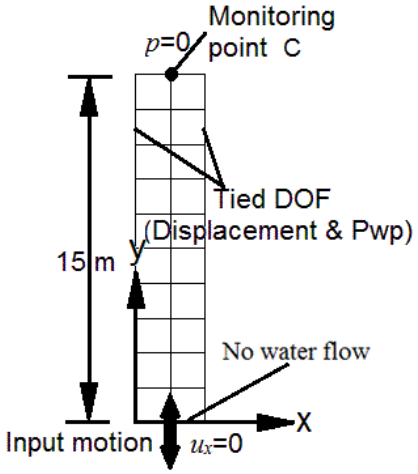


Figure 3-32: A schematic graph of the soil column FE model (Coupled FE analysis)

Table 3-5: Soil parameters for the coupled 1-D soil column analysis

Parameter	Value
Young's modulus E (kPa)	1.98E+05 (Scenario1, χ=0.1)
	1.98E+06 (Scenario1, χ=1.0)
	1.98E+07 (Scenario1, χ=10.0)
Bulk modulus for pore water K_f (kPa)	2.20E+06
Density ρ (g/cm^3)	2.0
Poisson's ratio ν	0.2
Void ratio e	0.587
Time step Δt (s)	0.003
Height H (m)	15.0

Table 3-6: Permeability values for parametric studies (coupled FE analysis)

Scenario	**Case0**	**Case1**	**Case2**	**Case3**	**Case4**
Permeability (m/s)	1.00E-20	1.00E-07	1.00E-05	1.00E-04	1.00E-03
Scenario	**Case5**	**Case6**	**Case7**	**Case8**	
Permeability (m/s)	5.00E-03	1.00E-01	1.00E+00	1.00E+02	

The resulting vertical site response at monitoring point C (Figure 3-32) for the various values of permeability are compared in Figures 3-33 to 3-35, for the scenarios of χ=0.1, χ=1.0 and χ=10.0 respectively, expressed as the acceleration response amplification spectra. Based on the undertaken parametric studies, it is shown that the predicted vertical site response is strongly affected by the parameters characterising the hydraulic phase, i.e. soil permeability and soil state conditions, both in terms of frequency content and amplification. In particular, taking the scenario of χ=0.1 as an example, results are distinguished in two groups: those involving extreme values of permeability and those adopting permeability values within a range encountered in engineering practice. They are shown in Figures 3-33 (a) and (b) respectively. For the numerical results involving extreme permeability conditions (case0 and case8), the dynamic responses match those from the analysis performed under purely undrained and drained conditions respectively using one-phase FE formulation. This agreement between the results is expected, since the definitions of the undrained and drained conditions comply with the employment of extremely low and high permeability values respectively. For the numerical results involving a more realistic permeability range, the influence of permeability is emphasised by the varied dynamic response obtained for the different cases. In particular the following observations can be made:

– when a relatively low permeability is employed (case1 and case2), identical results are obtained and they match with those obtained under the undrained condition;

– as the permeability increases (case3 to case5), the amplification factors gradually decrease, but without a significant change in the frequency content. This means that the soil layer maintains the same constrained modulus, but with more damping introduced;

– when increasingly higher permeability is employed (from case5 to case7), a shift of the fundamental frequency is observed towards the lower frequency range, indicating

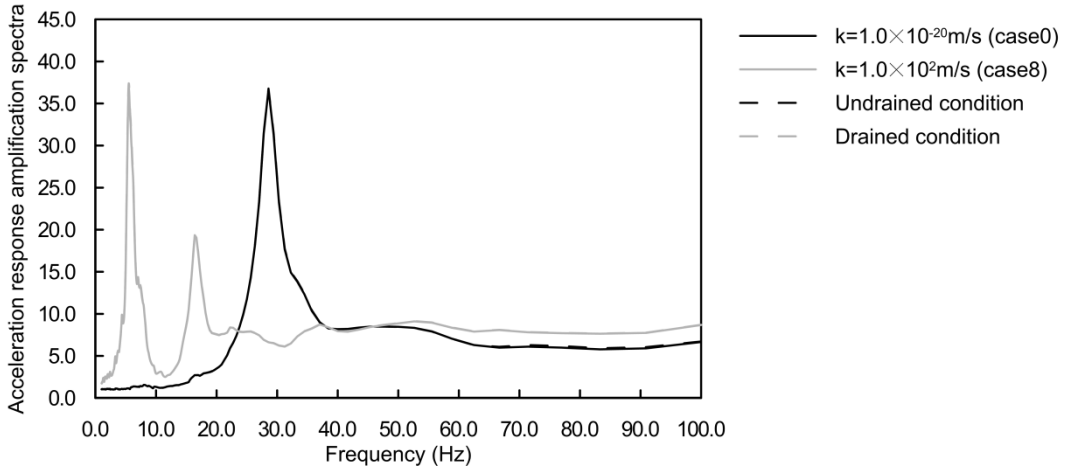
a lower constrained modulus for the soil column. This phenomenon complies with Zienkiewicz's theory (Zienkiewicz et al., 1980b), that the soil constrained modulus is highly affected by the pore water bulk modulus related to different soil state conditions (shown in Equation 3-13);

– by further increasing the permeability (case8 in Figure 3-33 (a)), the amplification factors increase, reaching the peak of the drained dynamic response, indicating less damping involved for the soil column.

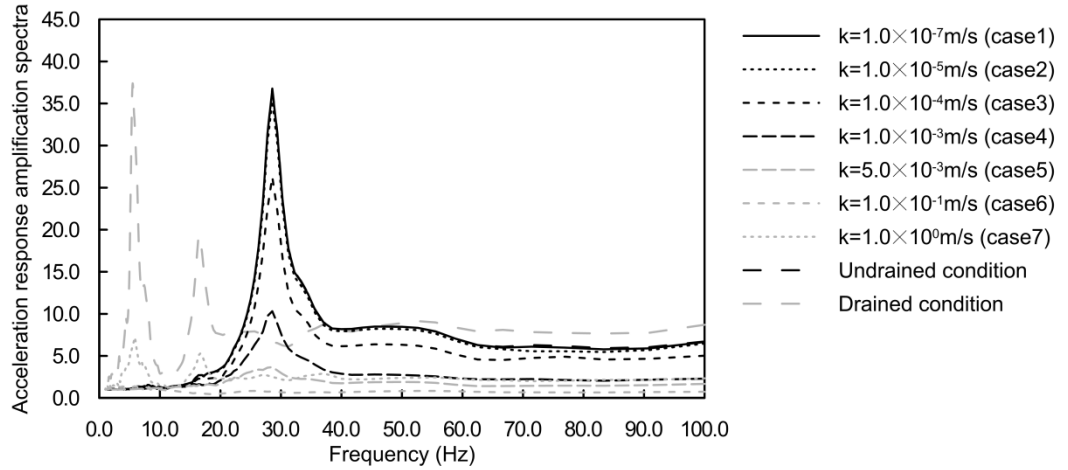
According to Bardet and Sayed (1993), the change in amplification factors is attributed to the impact of the viscous damping, which is due to the interaction between the solid and the pore fluid phases. It should be noted that neither material damping nor numerical damping are employed for the coupled FE analysis and therefore the observed viscous damping effect can be attributed entirely to the solid-pore fluid interaction simulated by the two-phase coupled FE formulation. More specifically, when extremely low permeability is considered for the soil, the pore water cannot flow out of the soil skeleton, leading to no relative movement or viscous damping in the numerical analysis. Therefore the vertical site response for the analysis employing extremely low permeability is identical to the response under the undrained condition (case0, case1 and case2 in Figure 3-33). Furthermore, by increasing the employed soil permeability, the pore fluid starts to move relatively to the soil skeleton, resulting in more relative movement and more viscous damping. Consequently, the amplification factors of the dynamic response gradually decrease when employing higher permeability for the coupled FE analysis, as observed from case3 to case5 in Figure 3-33 (b). Finally, for geotechnical structures involving considerably high permeability, due to the insignificant restriction on the relative movement between two components, the interaction effect between the solid and pore fluid is negligible, leading to less viscous damping involved in the coupled FE simulations. This explains the fact observed in Figure 3-33, that from case7 to case 8, the amplification factors increase and reach the peak of the drained dynamic response, indicating that no viscous damping is involved for the coupled FE analysis employing extremely high permeability.

Similar results are observed for the analysis of scenario χ=1.0 (Figure 3-34), where fundamental frequency shifts and amplification changes are detected for the case considered. It should be noted that larger amplification factors at the fundamental frequency are observed for the vertical site response subjected to drained condition.

However, for the results of the scenario of χ=10.0 (Figure 3-35), no obvious frequency shift or amplification change is observed. This is because, as explained before, that when a high χ value is adopted for the coupled FE analysis, the interaction effect between the pore fluid and solid is insignificant. Therefore, for the analysis employing high χ values, no obvious differences are observed among the dynamic responses from the parametric study involving different permeability values.

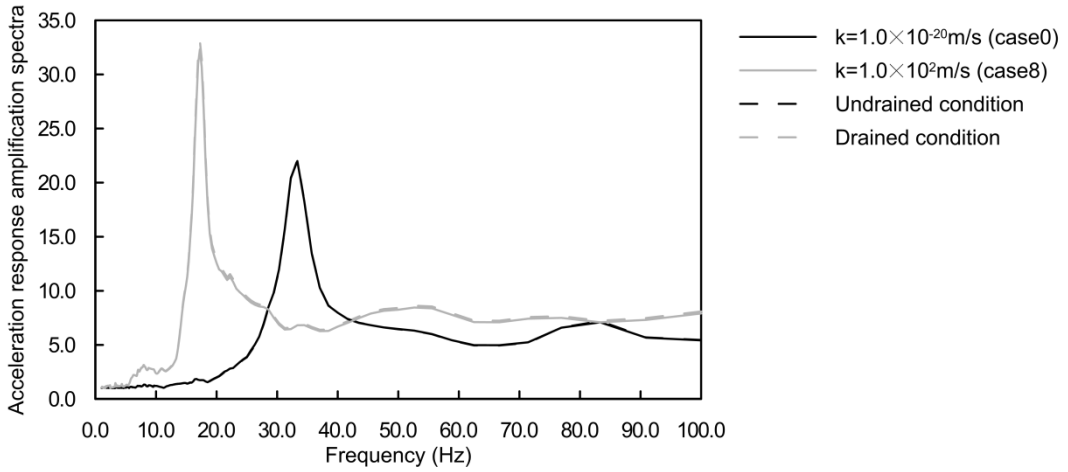


(a): Coupled vertical site response of a soil column for extreme permeability range

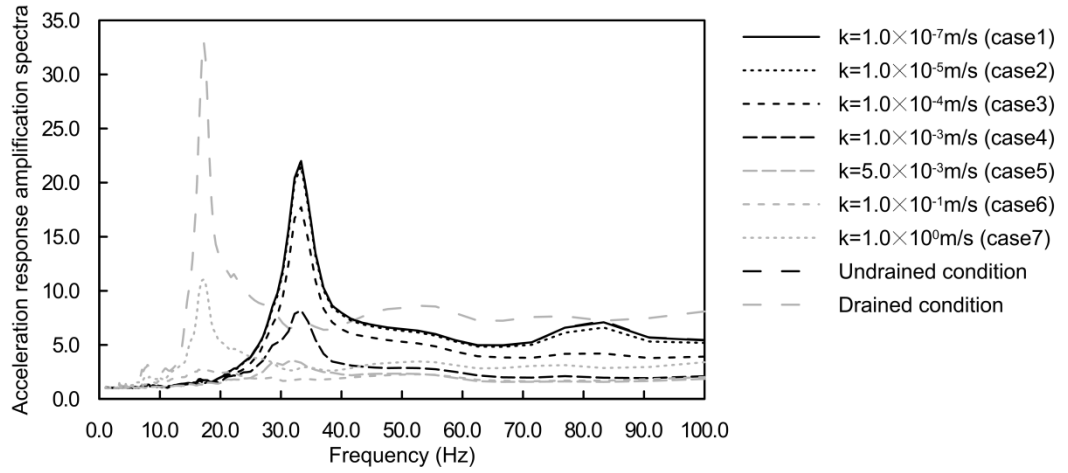


(b): Coupled vertical site response of a soil column for realistic permeability range

Figure 3-33: Two-phase coupled vertical site response of a soil column considering a wide permeability range (χ=0.1)

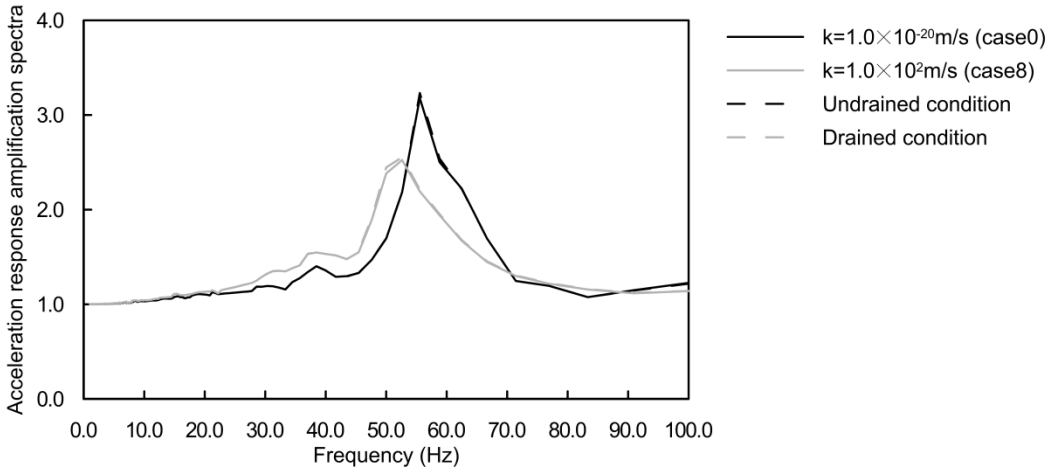


(a): Coupled vertical site response of a soil column for extreme permeability range

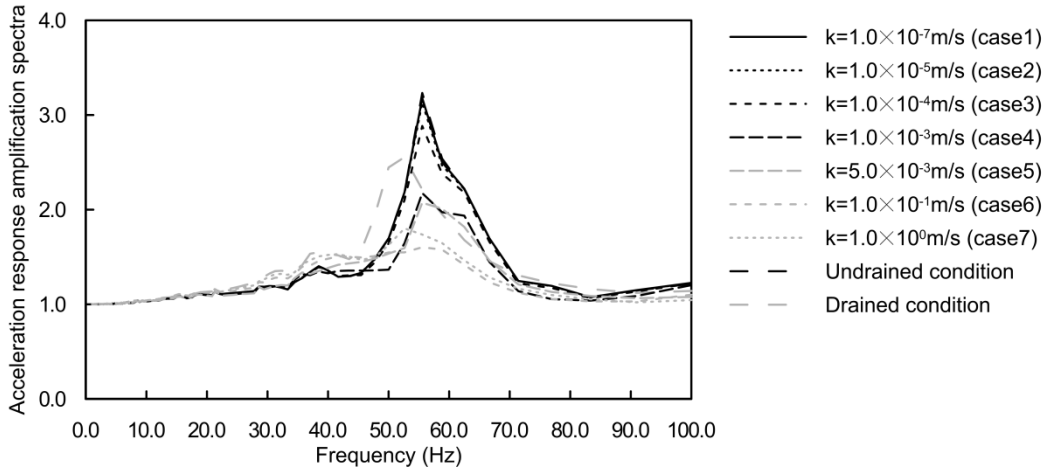


(b): Coupled vertical site response of a soil column for realistic permeability range

Figure 3-34: Two-phase coupled vertical site response of a soil column considering a wide permeability range (χ=1.0)



(a): Coupled vertical site response of a soil column for extreme permeability range



(b): Coupled vertical site response of a soil column for realistic permeability range

Figure 3-35: Two-phase coupled vertical site response of a soil column considering a wide permeability range (χ=10.0)

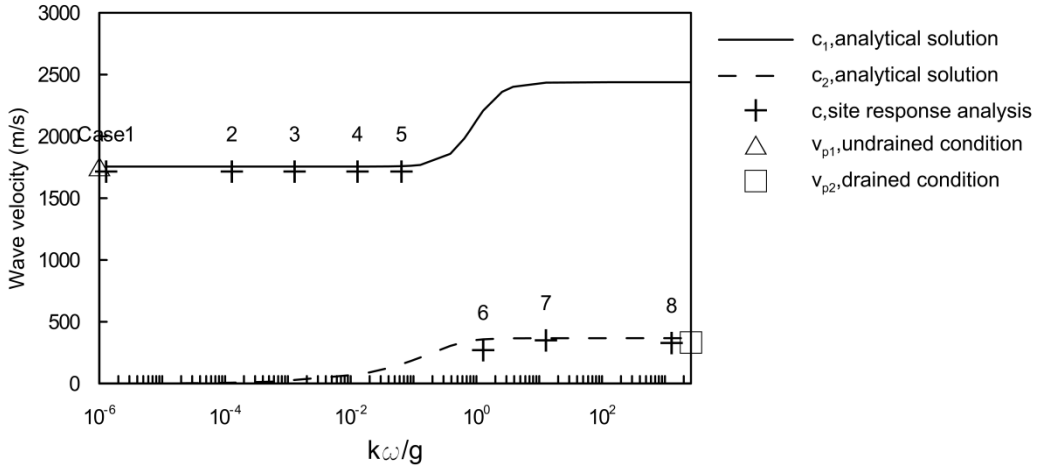
3.5.2 Quantitative study of the variation of compressional wave velocity

The undertaken parametric studies showed that the predicted vertical site response is strongly affected by the parameters characterising the hydraulic phase, i.e. the soil permeability and soil state conditions, both in terms of frequency content and amplification. Therefore, in the next two sections, the variation of the frequency content and amplification components of the dynamic response from the parametric study are quantitatively studied, in terms of the compressional wave velocity and damping ratio respectively.

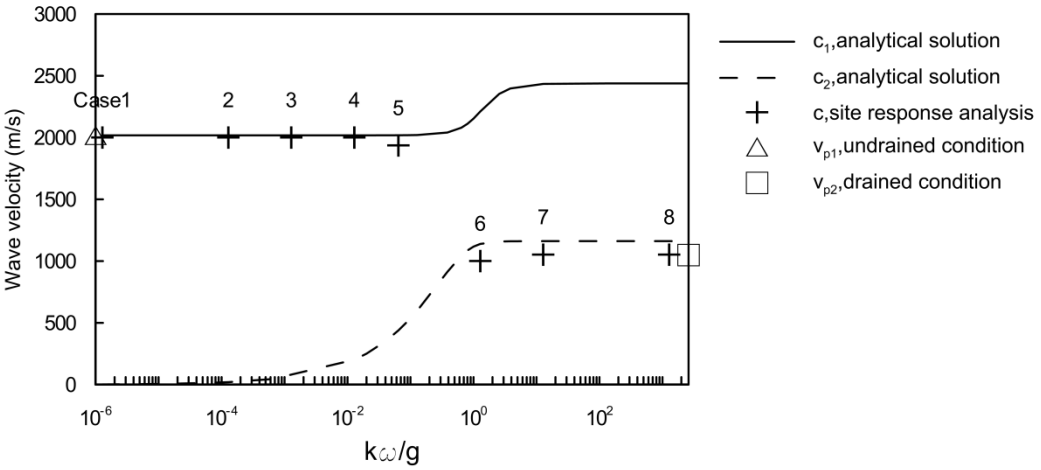
The compressional wave velocities of the studied soil column in the parametric studies can be back-calculated based on the equation of $c=4Hf$, where H is the depth of the soil layer and f is the fundamental frequency of the soil layer as observed in the results of response amplification spectra from the FE parametric studies (Figure 3-33 to Figure 3-35). Hence, the calculated compressional wave velocities from the numerical analysis are compared with the fast and slow wave velocities obtained from the two-phase analytical solution studied in Section 3.4 for three scenarios in Figure 3-36. It should be noted that the compressional wave velocities predicted by the FE analysis are plotted versus the parameter $k\omega/g$, where ω is the circular frequency of the harmonic input loading. However, since a multi-frequency earthquake load is applied for the present FE analysis, the dominant frequency (approximately 17.0Hz based on Figure 3-14) is adopted to plot the variation of compressional wave velocities from the FE analysis versus the parameter $k\omega/g$.

Based on Figure 3-36 (a) (scenario of χ=0.1), it can be observed that the compressional wave velocities obtained from the vertical FE site response analysis match with the fast wave velocities in the low permeability range and agree with the slow wave velocities in the high permeability range from the analytical solution. Furthermore, the compressional wave velocities from the vertical FE site response analysis employing extremely high and low permeability values match with the compressional wave velocities under undrained and drained conditions respectively. This indicates that the predicted different vertical site responses from coupled FE analysis considering a wide permeability range are dominated by different compressional waves. In particular, as illustrated in Figure 3-37, in the low permeability range, the solid and pore fluid move simultaneously and the fast wave dominates the response, resulting in a vertical site response of a larger fundamental frequency. However, at high permeability value, the slow wave dominates due to the relative movement between the solid and the pore fluid, leading to different vertical site responses of a smaller fundamental frequency. Furthermore, a similar comparison is observed for the scenario of χ=1.0, where the compressional wave velocities obtained from the vertical FE site response analysis match with the fast and slow wave velocities in low and high permeability ranges respectively, as shown in Figure 3-36 (b). It should be noted that for the scenario of χ=10.0 (Figure 3-36 (c)), all the wave velocities obtained from the FE analysis match with the fast wave velocities, since as explained

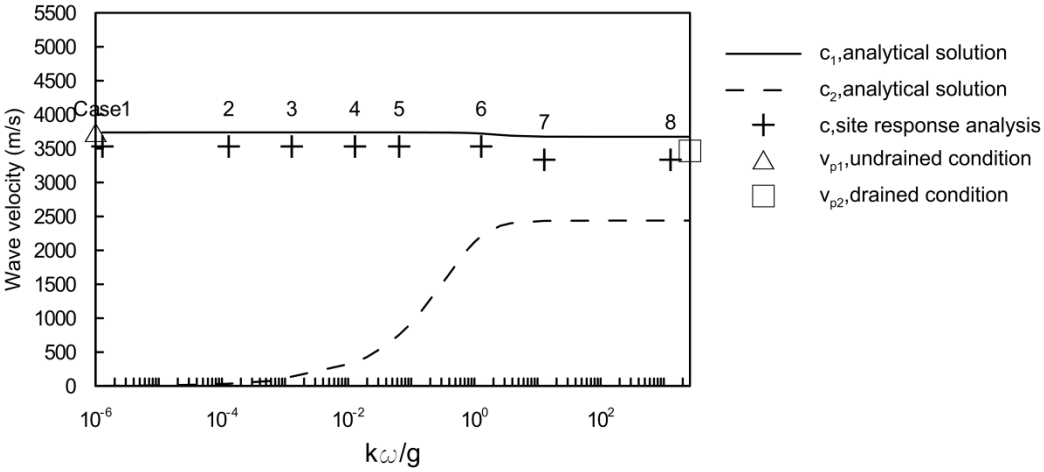
before, only the fast wave exists for the compressional wave propagation in geotechnical structures when employing high values of χ.



(a): Compressional wave velocity variation against permeability (χ=0.1)



(b): Compressional wave velocity variation (χ=1.0)



(c): Compressional wave velocity variation (χ=10.0)

Figure 3-36: Quantitative study for the compressional wave velocity

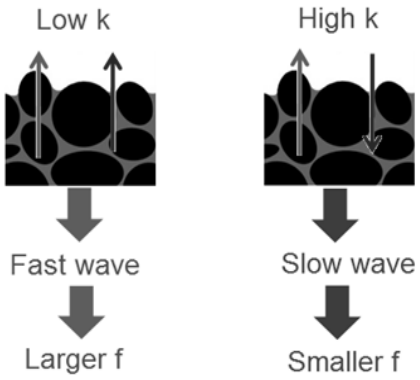


Figure 3-37: A schematic graph for the explanation of the observed different dynamic responses in the parametric study

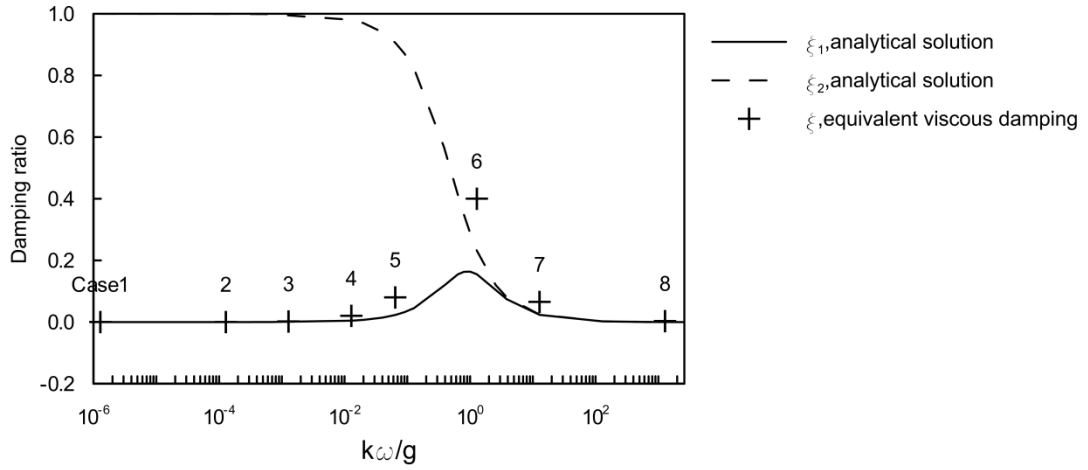
3.5.3 Quantitative study of the variation of viscous damping

The results of response amplification spectra from the FE parametric studies showed that the amplification component is highly affected by the employed soil permeability, which is due to the viscous damping impact introduced by the interaction between the pore fluid and solid. Therefore, in this section, the viscous damping ratios are quantitively assessed. In particular, the same vertical site response analysis is simulated by employing the 1-D total-stress analytical solution (studied in Section 3.3) to reproduce the dynamic response predicted by coupled FE analysis, through which, the calibrated material damping ratios employed in the analytical solution can be used to equivalently represent the viscous damping effect introduced in the coupled FE analysis.

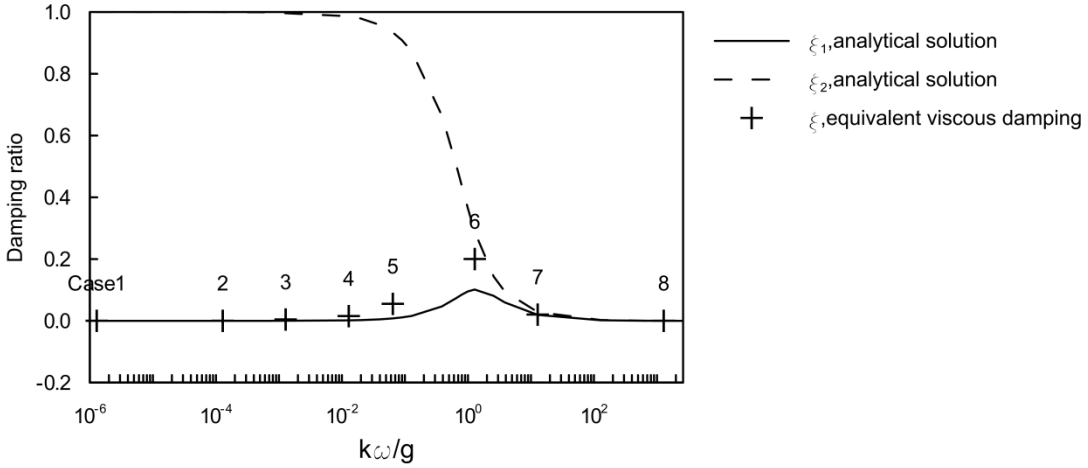
The calibrated equivalent viscous damping ratios are compared with the compressional wave damping ratios obtained from two-phase analytical solution for three scenarios in Figure 3-38. For the scenario of χ=0.1 (Figure 3-38 (a)), it can seen that as the permeability increases, the damping ratio increases in the low permeability range, peaks at the intermediate permeability range and decreases at the high permeability range. This explains the previously observed amplification factor change in the results of response amplification spectra from FE parametric studies, where as permeability increases, the amplification factors decrease and increase (Figure 3-33). Furthermore, similar trends are also observed for the variations of damping ratios for the scenarios of χ=1.0 and χ=10.0, as shown in Figure 3-38 (b) and (c) respectively.

The maximum viscous damping ratios for three scenarios are 40%, 20% and 10%

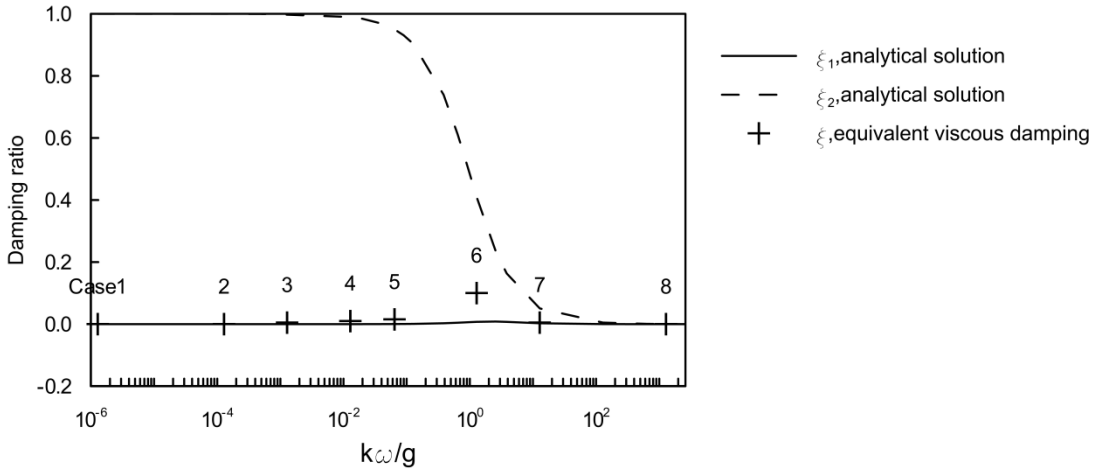
respectively, indicating the significant effect of the viscous damping on the vertical site response. It is therefore suggested that coupled consolidation analysis is necessary for the accurate simulation of vertical site response, in order to account for the solid-pore water interaction effect. Nevertheless, in engineering practice the use of advanced coupled consolidation FE programs is limited. However, as introduced before, the shake-type programs are capable of simulating the vertical site response, but only for two extreme soil state conditions. If the shake-type programs are employed for this purpose, it is suggested that appropriate amount of viscous damping needs to be employed in the analysis in addition to the material damping, in order to take into account the interaction effect between the solid and pore fluid phases. The variation curve of the viscous damping ratios presented in Figure 3-38 provides an empirical reference to select appropriate viscous damping ratios for the vertical site response analysis by employing a total-stress analytical solution.



(a): Equivalent viscous damping ratio variation (χ=0.1)



(b): Equivalent viscous damping ratio variation (χ=1.0)



(c): Equivalent viscous damping ratio variation (χ=10.0)

Figure 3-38: Quantitative study of the viscous damping

3.6 Summary

In this chapter, the site response due to the vertical component of the ground motion was investigated by employing analytical and numerical methods.

Firstly, a 1-D total-stress analytical solution for vertical site response was studied and compared against time domain FE analyses, for two extreme soil state conditions. It was shown that the vertical site response was significantly affected by the assumed conditions (i.e. undrained or drained), highlighting the importance of adopting a coupled consolidation formulation for simulating the vertical site response of a soil layer at any intermediate transient state (i.e. when consolidation occurs during the dynamic loading, depending on the range of soil permeability and loading duration).

Furthermore, a two-phase analytical solution for the compressional wave propagation was studied based on Biot's theory (1956a, b), showing the existence of two types of compressional waves (fast and slow waves) and indicating that their characteristics (i.e. wave dispersion and attenuation) were highly dependent on soil and dynamic parameters (i.e. the permeability, soil stiffness and loading frequency). The compressional wave propagation mechanism was then rigorously investigated by coupled FE analysis, highlighting the different dominant ranges of the two types of compressional waves in terms of soil permeability. Finally, based on the FE parametric study, the geotechnical representation of two types of compressional waves was related with different soil state conditions.

The vertical site response was further investigated with fully coupled FE analysis, considering solid-fluid interaction. The parametric studies showed that the predicted response was strongly affected by the parameters characterising the hydraulic phase, i.e. soil permeability and soil state conditions, both in terms of frequency content and amplification. In particular, a reduction of the soil constrained modulus was induced by employing higher permeability, which was depicted as a shift in the fundamental frequency of the response. Furthermore, the observed changes in the amplification function indicated the effect of viscous damping due to the interaction between the solid and the pore fluid phases. Moreover, the quantitative investigation of the frequency content and the amplification function of the vertical site response, showed that the response was dominated by the different wave velocity and damping characteristics of two types of compressional waves affected by soil hydraulic-phase parameters. It is

therefore suggested that coupled consolidation analysis is necessary to accurately simulate vertical site response at any intermediate transient state, when consolidation occurs during the dynamic loading (depending on soil permeability and loading duration).

The work presented in this chapter can also be a useful reference for simple site response analysis in the vertical direction. It was shown that the methodology adopted by the widely used program SHAKE and its modern variations can be employed for the vertical site response analysis in terms of total stresses, but only for two extreme conditions (i.e. undrained and drained conditions). If the SHAKE approach is employed for the vertical site response analysis of a soil layer at any intermediate transient state, it is suggested that appropriate amount of viscous damping needs to be employed in the analysis, additional to any considered material damping, to take into account the interaction effects between the solid and pore fluid phases. The appropriate viscous damping ratios can be decided based on the empirical curves of the investigated viscous damping ratio proposed in Section 3.5.3.

CHAPTER 4
Numerical investigation of multi-directional site response based on KiK-net down-hole array monitoring data

4.1 Introduction

In this chapter, the multi-directional site response of a well-documented case, the HINO site in Japan, is investigated by employing the 3-D dynamic HM formulation in ICFEP, against monitored data from the KiK-net down-hole array monitoring system (Okada et al., 2004). Different features of the numerical modelling for site response analysis, such as the constitutive models, the use of 3-D input motion and the coupled consolidation formulation, are investigated through the FE simulations and parametric studies.

This chapter first reviews existing investigations of site response based on down-hole array monitoring data. The site amplification effects are investigated through the back-analysis of earthquake recordings. Furthermore, studies of site response analyses employing analytical and numerical methods are briefly reviewed, addressing some critical aspects and drawbacks of the simulations.

Subsequent to this, two soil cyclic nonlinear constitutive models employed in this work are introduced and discussed. Some critical features of cyclic nonlinear models,

such as the independent formulation of shear and volumetric behaviour, the inadequate simulation of material damping at very small strain levels and the simulation of plastic deformations, are briefly discussed.

The following part involves the basic introduction of the KiK-net down-hole array monitoring system. This part presents the monitored earthquake data of the selected case, HINO site, in terms of acceleration time histories recorded at the HINO down-hole array for two weak and one strong earthquake motions. Furthermore, the soil properties for the HINO site are also introduced.

In the subsequent two parts, the multi-directional site response of the HINO site subjected to the weak and strong earthquake motions is simulated by employing the linear and nonlinear 3-D dynamic HM formulation in ICFEP. Different critical aspects of the numerical simulation are employed to enable the accurate prediction of the site response, such as Rayleigh damping, soil constitutive models, 3-D tied DOF boundary condition, use of 3-D input motion and coupled consolidation formulation. The developed FE model is validated by comparing the predicted site response against the monitored motions at the HINO site.

Finally, the effects of three critical factors on site response, i.e. the variation of water table, the soil permeability and the 3-D ground motions, are studied through the parametric studies of the selected case.

4.2 Literature review

Site amplification effects are usually investigated by analysing the spectral ratios between the dynamic response at the ground surface and at the bedrock level. Two types of earthquake monitoring systems have been established for this purpose: the *strong ground motion monitoring system* and the *down-hole array monitoring system*. For the strong ground motion monitoring system, the ground motions at different surface geologies are monitored in a relatively small area, lying on the same bedrock, as shown in Figure 4-1. In particular, ground motions A_a and A_b are monitored at two sites located on the same bedrock, where the former is the surface ground motion and the latter represents the outcrop motion. Furthermore, the outcrop motion A_b can be converted to the bedrock motion at the interface of soil layers and bedrock depending on the

impedance ratio between the deepest soil layer and the bedrock, by assuming the same geological conditions at the bedrock and outcrop sites. Therefore, the spectral response ratios can be evaluated based on the ground motion A_a and the converted bedrock motion. The accuracy of this evaluation method is sensitive to the geological conditions around the outcrop station, which can be considerably complicated and are not always identical to the geological conditions at the bedrock (Aguirre and Irikura, 1997). Therefore, an additional earthquake monitoring system has been established to overcome the above-mentioned disadvantage, which is the down-hole array monitoring system. The earthquake motions at different depths at the same site are monitored by a vertical array of seismometers in a borehole. As shown in Figure 4-1, A_a and A_c are the earthquake motions monitored at the ground surface and at the bedrock respectively in a down-hole. In this case, the site amplification effects can be directly assessed by the spectral response ratios between motions at any two depths whenever an earthquake is recorded. Therefore, the evaluation method based on the down-hole array monitoring system is more straightforward and accurate for investigating site amplification effects, compared to the strong ground motion monitoring system.

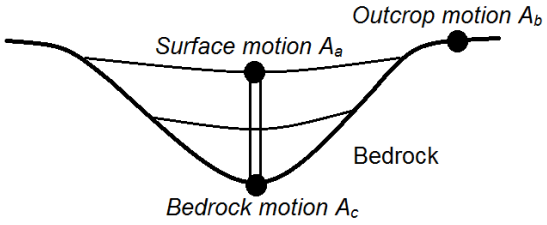


Figure 4-1: A schematic graph for two strong motion monitoring systems

4.2.1 Site amplification effects based on down-hole array data

An important application of the down-hole array observations is to investigate the site amplification effects by analysing the spectral ratios in the frequency-domain between the dynamic response at any two soil layers. Material nonlinearity is one of the most critical soil characteristics in such analyses (e.g. Sato et al., 1996; Aguirre and Irikura, 1997; Huang et al., 2005; Pavlenko and Irikura, 2006; Kokusho et al., 2005; Kokusho and Sato, 2008). The degree of nonlinearity is usually evaluated by comparing the back-analysed material stiffness (or fundamental frequency) subjected to strong motions to the reference one, which is calculated based either on the original soil properties or on the weak motion amplifications. Such representative works are

attributed to Sato et al. (1996) and Huang et al. (2005), which analysed the site response nonlinearity observed at the down-hole array sites in the Hyogo-ken Nanbu (1995, Japan) and the Dahan site of the Chi-Chi earthquake (1999, Taiwan) respectively.

In Sato et al. (1996), the investigated four sites are the PI, SGK, TKS and KNK sites, which were all equipped with an array of seismometers in a down-hole. The shear wave velocities for the four sites were back-calculated by reproducing the recorded Fourier spectral ratios between the horizontal dynamic response at the ground surface and at the base layer during the main shock, through a shake-type analytical solution developed by Ohta (1975) and Ishida et al. (1985). The calculated shear wave velocities were found to be approximately 30% smaller than the measured shear wave velocities obtained from PS-wave logging tests, indicating the strong soil nonlinearity at all four sites. An example of the shear wave velocity comparison at the SGK site is indicated in Figure 4-2. Furthermore, the authors studied the nonlinearity characteristics of the soil layers by comparing the monitored Fourier spectral ratios with the analytically predicted ones, where the original shear wave velocities from the PS-wave logging tests were employed in the linear analytical solution. Results in Figure 4-3 show the comparison of Fourier spectral ratios between the monitoring data and analytical results at the SGK site, where the fundamental frequencies from the monitored dynamic response are smaller than the predicted results, indicating the shear modulus degradation at the SGK site subjected to the Hyogo-ken Nanbu earthquake.

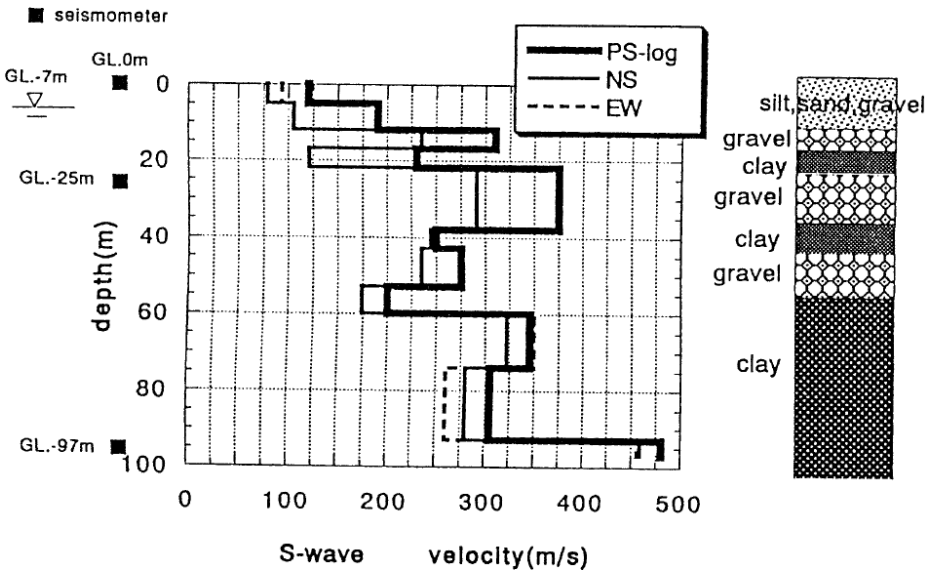


Figure 4-2: Shear wave velocity comparison at the SGK site in Hyogo-ken Nanbu earthquake (EW for east-west and NS for north-south) (after Sato et al. (1996))

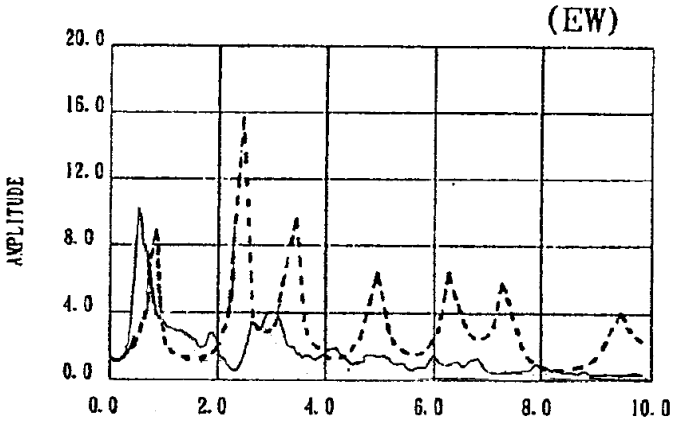


Figure 4-3: Fourier spectral ratio comparison at the SGK site in the Hyogo-ken Nanbu earthquake (observed data-solid line & analytical simulation-dashed line) (after Sato et al. (1996))

Huang et al. (2005) analysed the recorded strong earthquake motions at the Dahan down-hole site (Figure 4-4) during the Chi-Chi earthquake (1999, Taiwan). The nonlinearity characteristics of the soil layers were highlighted by comparing the monitored Fourier spectral ratios in the NS direction from the main shock (the thickest solid line in Figure 4-5), with the ones obtained from 3 after-shock motions (other three lines in Figure 4-5). It can be seen that the fundamental frequencies of the main shock are smaller than those of the after-shock motions, demonstrating the effect of soil nonlinearity induced by strong earthquake motions.

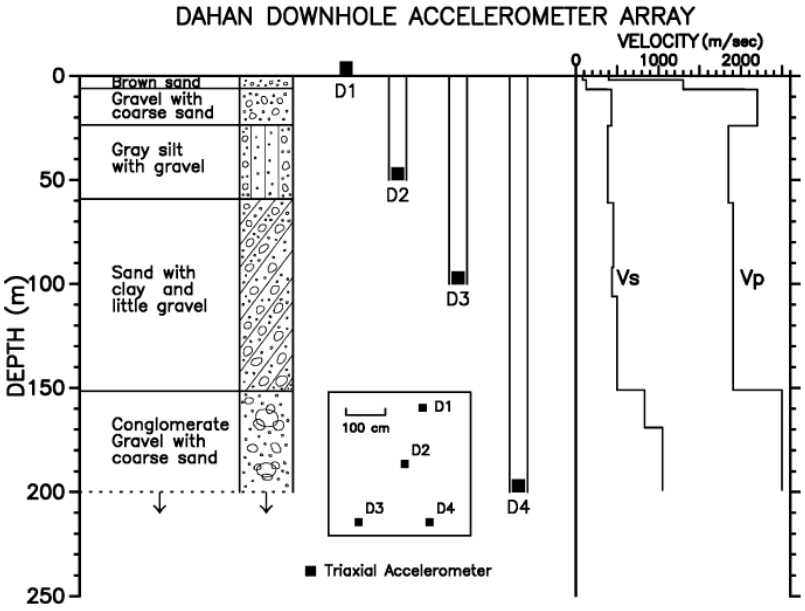


Figure 4-4: Soil profile at the Dahan site (after Huang et al. (2005))

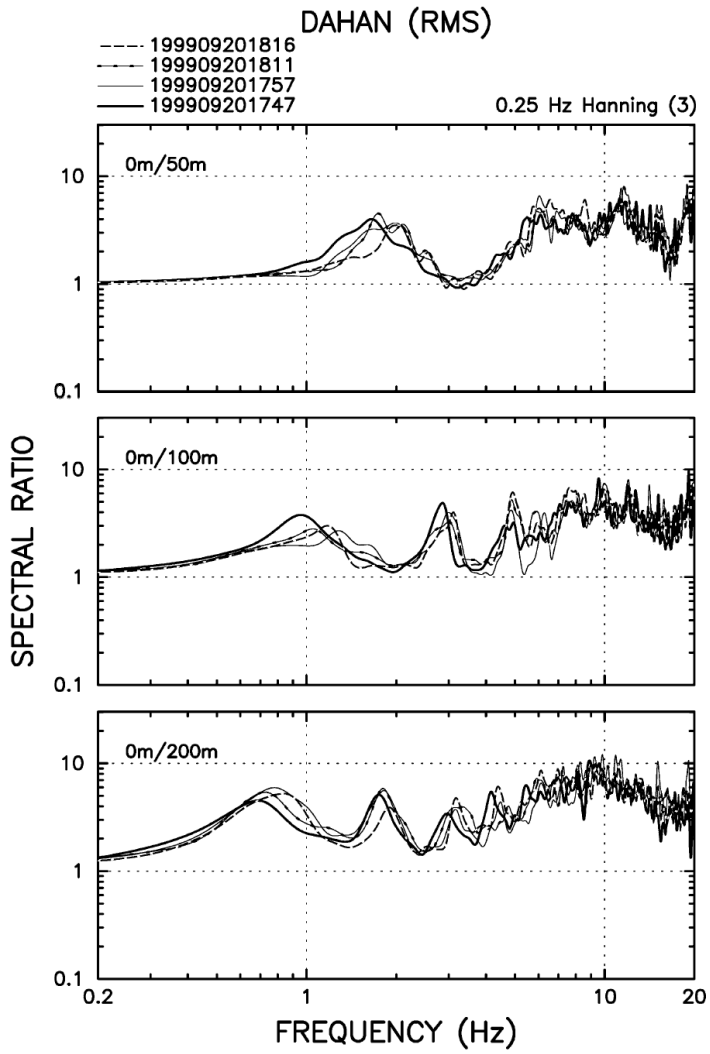


Figure 4-5: Fourier spectral ratio comparison subjected to the main shock and after-shock motions at the Dahan site in the Chi-Chi earthquake (after Huang et al. (2005))

Evidence of strong vertical ground motions and compressional damage of engineering structures have been increasingly observed in recent earthquakes (Papazoglou and Elnashai, 1996; Yang and Sato, 2000; Bradley, 2012). There is therefore a need for systematic and rigorous investigations of the site response subjected to the vertical component of the ground motions. However, there is currently very limited investigation on the site amplification and soil nonlinear effects in the vertical site response. Some studies found that soil nonlinearity due to the vertical ground motion is insignificant (e.g. Ambraseys and Douglas, 2000; Gulerce and Abrahamson, 2011), while others have observed the evidence of vertical nonlinearity, which could be as significant as the horizontal one (e.g. Pavlenko and Irikura, 2002; Beresnev et al., 2002).

In Pavlenko and Irikura (2002), the vertical nonlinearity at three sites, the PI, SGK and TKS sites, in the Hyogo-ken Nanbu earthquake, were investigated by employing the lumped mass method (Joyner and Chen, 1975). For this method, the soil profile was divided into several layers and the mass of each layer was equally lumped at the top and bottom boundaries. The recorded base layer motion was imposed at the bottom boundary as the input motion. Different nonlinear stress-strain behaviour was assumed for different soil layers and at different time intervals. The surface motion could then be calculated by the time integration of the equations of motion. The predictions were compared against the recorded data. Through the "trial and error" procedure, the most appropriate stress-strain behaviour was determined, so that the constrained modulus degradation time histories could be obtained at different depths, as shown in Figure 4-6 for two soil layers at the PI site (stratigraphy shown in Figure 4-7). Considerable constrained modulus reduction was observed, reflecting the significant soil nonlinearity due to strong vertical earthquake motions. It should be noted that, in this result, E is employed to express the soil constrained modulus, which is usually used to denote the soil Young's modulus.

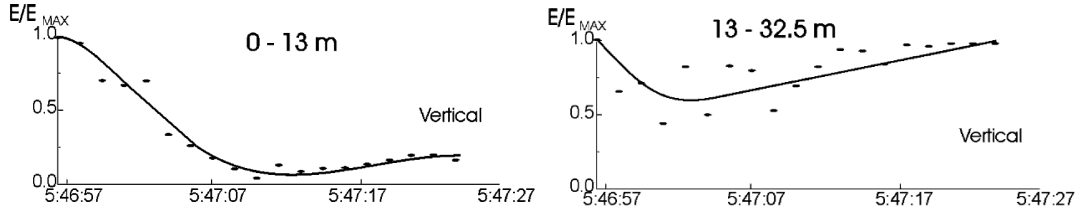


Figure 4-6: Constrained modulus degradation time histories at the PI site in the Hyogo-ken Nanbu earthquake (after Pavlenko and Irikura (2002))

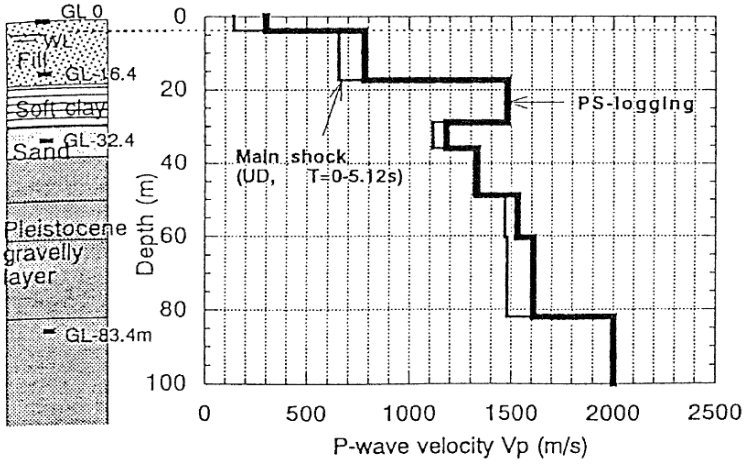


Figure 4-7: Stratigraphy at the PI site in the Hyogo-ken Nanbu earthquake (after Sato et al. (1996))

Vertical nonlinearity was also investigated by Beresnev et al. (2002) by analysing the recorded down-hole array data from the KiK-net system. In particular, the degree of soil vertical nonlinearity was evaluated by comparing the back-analysed fundamental frequency of the soil deposit subjected to strong motions, to the reference one subjected to weak motions. Fundamental frequencies were obtained based on the Fourier spectral ratios between the recorded response at the ground surface and the bottom layer. Seismic data from five sites (i.e. the NARH01, OKYH09, SMNH01, SMNH02 and TTRH02 sites) subjected to several earthquakes were analysed. The vertical nonlinearity in terms of the fundamental shift was observed at the sites subjected to the strong motions with peak acceleration values greater than 0.1g. In order to quantify the vertical nonlinearity, the constrained modulus degradation ratios at three sites, NARH01, SMNH01 and TTRH02, were calculated based on the observed fundamental frequency degradation ratio, and plotted against compressional strains in Figure 4-8. It should be noted that the compressional strains were estimated based on the empirical equation of Beresnev and Wen (1996), which is a function of the observed peak vertical accelerations, predominant frequencies of ground motions and near-surface P-wave velocities. As observed, the constrained modulus (solid circles) degrades in a similar manner to the shear modulus (hollow circles from EPRI (1993)). However, a scatter point was observed in the plot, which suggested that more data should be involved in the investigation to better constrain the degradation curve.

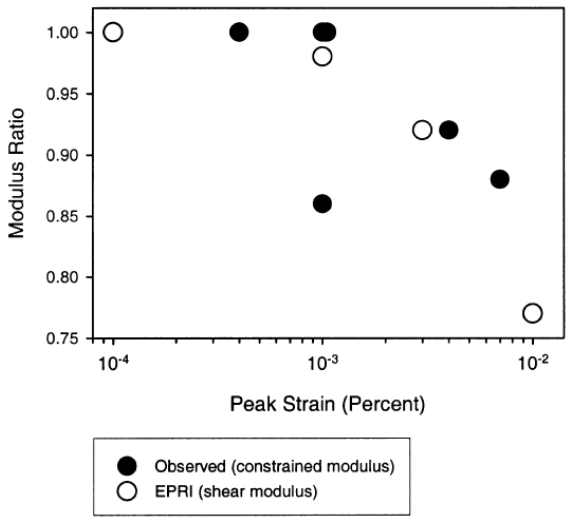


Figure 4-8: Constrained modulus degradation ratios at three KiK-net sites subjected to strong motions (after Beresnev et al. (2002))

4.2.2 Site response analyses

Another important application of down-hole array observations is to validate the analytical or numerical modelling for site response analyses. Recorded bottom motion is usually employed as the input motion for the analyses and the predicted surface motion is compared against the monitored data for the validation of site response modelling. Such analyses have been conducted by numerous researchers, such as Sato et al. (1996), Aguirre and Irikura (1997) and Huang et al. (2005). The following discussions initially concentrate on the site response analyses due to two representative well-documented earthquakes, which are the 1995 Hyogo-ken Nanbu earthquake and the 1999 Chi-Chi earthquake. These two studies are conducted by Aguirre and Irikura (1997) and Huang et al. (2005) respectively.

The site response of the PI site (Figure 4-9) in the Hyogo-ken Nanbu earthquake was simulated by Aguirre and Irikura (1997), employing the finite difference program of Perez-Rocha and Sanchez-Sesma (1992). A cyclic nonlinear model based on Hardin and Drnevich (1972) hyperbolic backbone curve was employed to simulate the hysteretic soil behaviour. By employing the recorded motion at GL. -83.4m as the input motion, the predicted horizontal acceleration time histories were compared with the recorded ground motions in Figure 4-10, at three depths, GL. 0.0m, -16.0m and -32.0m. Based on the comparison, acceleration time histories were reasonably predicted at depths of GL. -16.0m and -32.0m. However, dynamic response was overestimated at the surface station after 15 seconds. It was pointed out that liquefaction only occurred in the layer between the ground surface and 16.0m below, from the 15.0s of the earthquake duration. Therefore, these discrepancies were attributed to the inability for the constitutive model to generate excess pore water pressure. The liquefaction response of the deposit could not be captured by the numerical model. It should be noted that the numerical simulations and observations were plotted in the same graph for comparison. In order to distinguish them, two sets of data were processed with different base lines (i.e. 0.0 cm/s^2 and 1000.0 cm/s^2 for the numerical simulations and observations respectively).

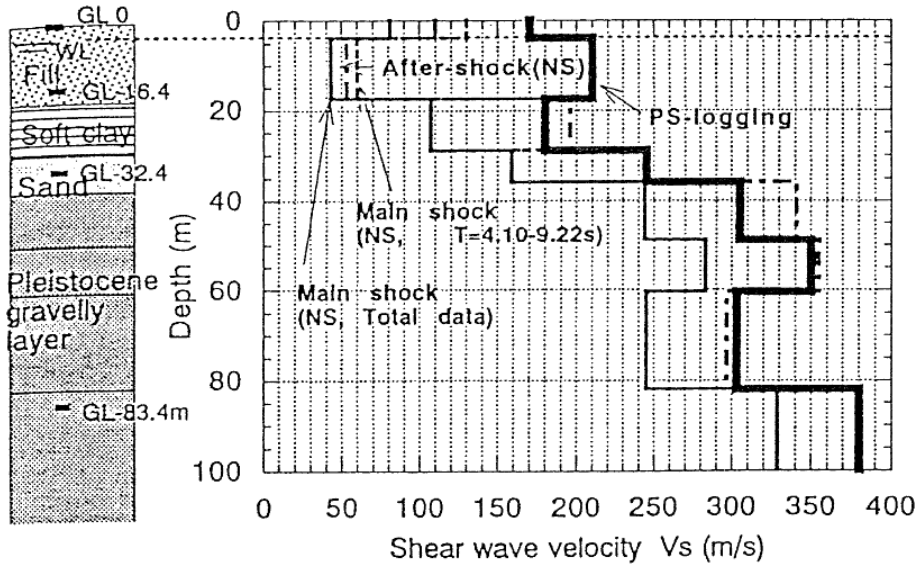
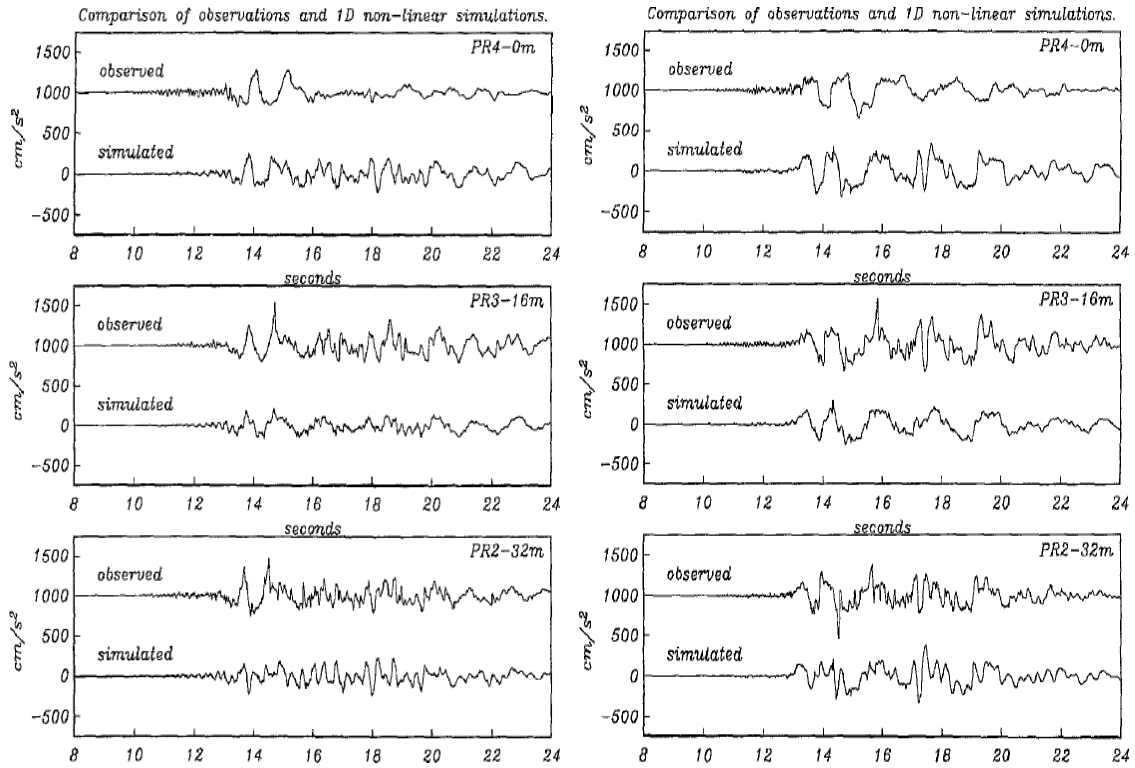


Figure 4-9: Soil profile of the PI site in Hyogo-ken Nanbu earthquake (after Sato et al. (1996))

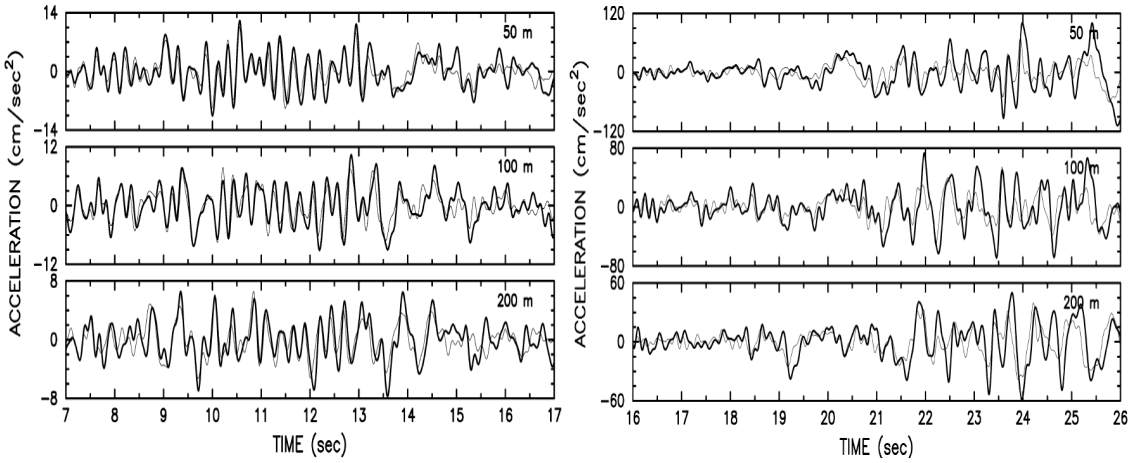


(a): EW direction (b): NS direction

Figure 4-10: Comparison of acceleration time histories between numerical results and monitored data at the PI site in the Hyogo-ken Nanbu earthquake (after Aguirre and Irikura (1997))

The horizontal site response of the Dahan site (Figure 4-4), when subjected to a foreshock weak motion and the main shock of the Chi-Chi earthquake, was numerically

simulated by Huang et al. (2005), by employing the Haskell matrix method (Haskell, 1953). The solution of this method is based on linear elastic shear wave propagation equations in multilayered solid media. The recorded acceleration time histories at the ground surface were employed as the input motion in the numerical analysis. This special simulation way was attributed to its advantage of avoiding the extraction of incident waves from the reflected waves. However, the effects of reflected waves are only significant at the soil material interface where the impedance ratio is large (e.g. the bedrock surface), which is not the case for the Dahan site (Figure 4-4). Therefore, the recorded bottom excitations can be employed as the input motion for the site response analysis (e.g. Christopoulos, 2012). Dynamic response in terms of acceleration time histories at other depths was predicted and compared with the monitored data in Figure 4-11. According to Huang et al. (2005), the horizontal site response at different depths was accurately predicted when the weak motion was considered. However, the dynamic response due to the main shock was not satisfactorily predicted in particular after 20s, due to the employment of a linear elastic model, which is not capable of reproducing nonlinear soil behaviour.



(a): A weak motion before the Chi-Chi earthquake (b): Main shock of the Chi-Chi earthquake

Figure 4-11: Acceleration time history comparison in the NS direction between numerical results and monitored data at the Dahan site (numerical results-grey line; observed data-black line) (after Huang et al. (2005))

Since 1996, after the establishment of the KiK-net system in Japan, more down-hole array monitoring data have become available for numerical site response investigations, e.g. Pavlenko and Irikura (2006), Assimaki and Steidl (2007), Kokusho and Sato (2008)

and Kaklamanos et al. (2013). Among these, a representative work is attributed to Kaklamanos et al. (2013), who performed a large number of site response analyses at 100 KiK-net sites subjected to four earthquakes, including the 2011 Tohoku earthquake (Mw=9.0). Linear-elastic and equivalent-linear analyses were conducted by using the Haskell matrix method (Haskell, 1953) and SHAKE (Schnabel et al., 1972) respectively. Recorded motions at the bottom layer were employed as the input motions. By comparing the predicted acceleration response spectra at the ground surface with the recorded ones, the site response deviations were calculated in the frequency-domain. Sensitivity studies of the response deviations were carried out against the predicted maximum shear strain and the predominant spectral period of the surface ground motion. Based on this work, the applicability ranges of the linear-elastic and equivalent-linear site response analyses were proposed, prescribed by the two aforementioned parameters, as shown in Figure 4-12. In practice, when the predominant spectral period of the surface ground motion is larger than 0.5s, the linear-elastic analysis is sufficiently accurate for site response predictions. When the predominant spectral period is smaller than 0.5s, the linear-elastic analysis only holds its accuracy for maximum shear strains smaller than 0.01%. In the strain range of 0.01%-0.4%, the equivalent-linear analysis can improve the accuracy of the predictions, by accounting for the reduced shear modulus and increased damping due to larger shear deformations. At strain levels beyond 0.4%, the nonlinear time-domain analysis is suggested for accurate site response predictions, through simulating the realistic dynamic soil behaviour.

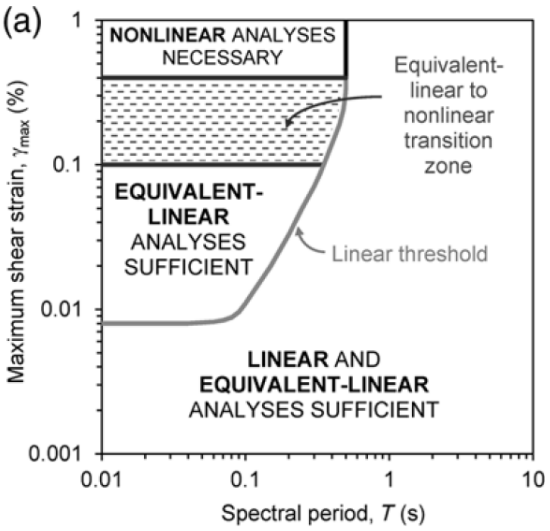


Figure 4-12: The applicability ranges of the linear-elastic and equivalent-linear site response analyses (after Kaklamanos et al. (2013))

Applications of the time-domain method on 1-D site response analyses can be found in Muravskii and Frydman (1998), Lee et al. (2006) and Amorosi et al. (2010). A critical work is attributed to Amorosi et al. (2010), who quantified the effects of the soil plasticity on site response predictions. In particular, the dynamic response of a random clay deposit subjected to four representative earthquakes was predicted by employing the linear elasto-plastic FE formulation in DIANA-SWANDYNE II (Chan, 1988 & 1995). The linear model was coupled with the Mohr–Coulomb yield criterion to account for the soil plasticity. The soil nonlinearity was equivalently simulated by employing the converged reduced shear modulus and damping ratio from corresponding EERA equivalent-linear analyses. Coupled formulation and Rayleigh damping were adopted. One of the critical findings is the significant damping effect of soil plasticity on the site response. It was found that the site response was smaller predicted by the elasto-plastic FE analysis than that from the corresponding EERA reference analysis. An example of the comparison is shown in Figure 4-13, in terms of the acceleration response spectra at the ground surface. Therefore, the plasticity-based time-domain analysis was suggested for more realistic site response predictions, through the simulation of soil plastic deformation and excess pore water pressure build-up under strong earthquake loading. It should be noted that advanced nonlinear models were not employed in the analyses, in order to benefit standard finite element users. Furthermore, numerical results were not compared against down-hole array observations, since this study only focused on some fundamental aspects of the FE site response analysis.

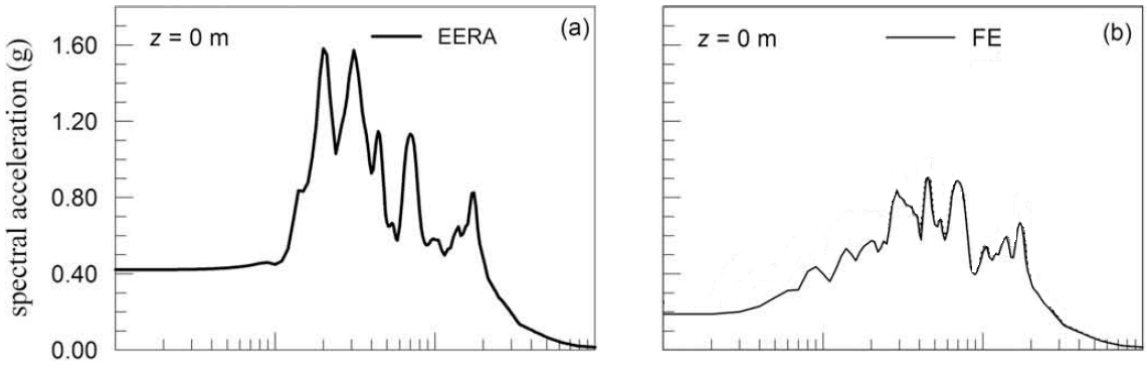


Figure 4-13: Comparison of site response predicted by the linear elasto-plastic FE and EERA analyses (after Amorosi et al. (2010))

The observed evidence of vertical nonlinearity increases the need of vertical site response analyses to achieve more accurate predictions and better understanding of its mechanisms. 3-D nonlinear time-domain analysis is considered to be the most appropriate method for such simulations, which allows the simulation of realistic soil behaviour and coupling effects between shear and compressional deformations. Applications can be found in Li et al. (1998) and Borja and Chao (1999).

In Li et al. (1998), the multi-directional site response at the Lotung site (Taiwan) subjected to two earthquakes (i.e. the July 31, 1986 and November 15, 1986 earthquakes) was numerically simulated by employing the fully coupled inelastic dynamic finite-element program SUMDES (Li et al. 1992). The bounding surface hypoplasticity model of Wang (1990) was employed to simulate the nonlinear elasto-plastic soil behaviour. The soil properties at the Lotung site are shown in Figure 4-14. By employing the recorded motion at GL. -17.0m as the input motion, the predicted 3-D acceleration response spectra at the ground surface were compared against the recorded data, as shown in Figure 4-15. Satisfactory predictions are observed for the horizontal site response, whereas the vertical site response is significantly underestimated by the FE analysis. The under-prediction was attributed to the assumed saturated condition for the upper layers, which might be only partially saturated.

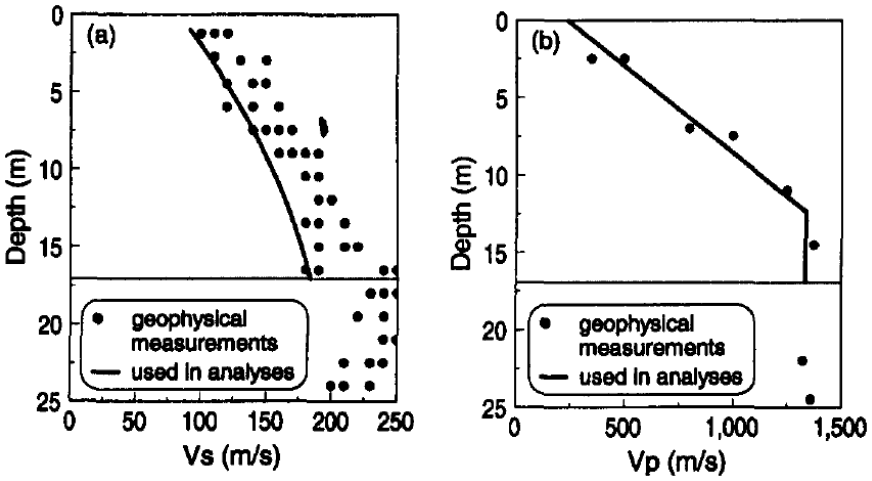


Figure 4-14: Soil properties at the Lotung site (after Li et al. (1998))

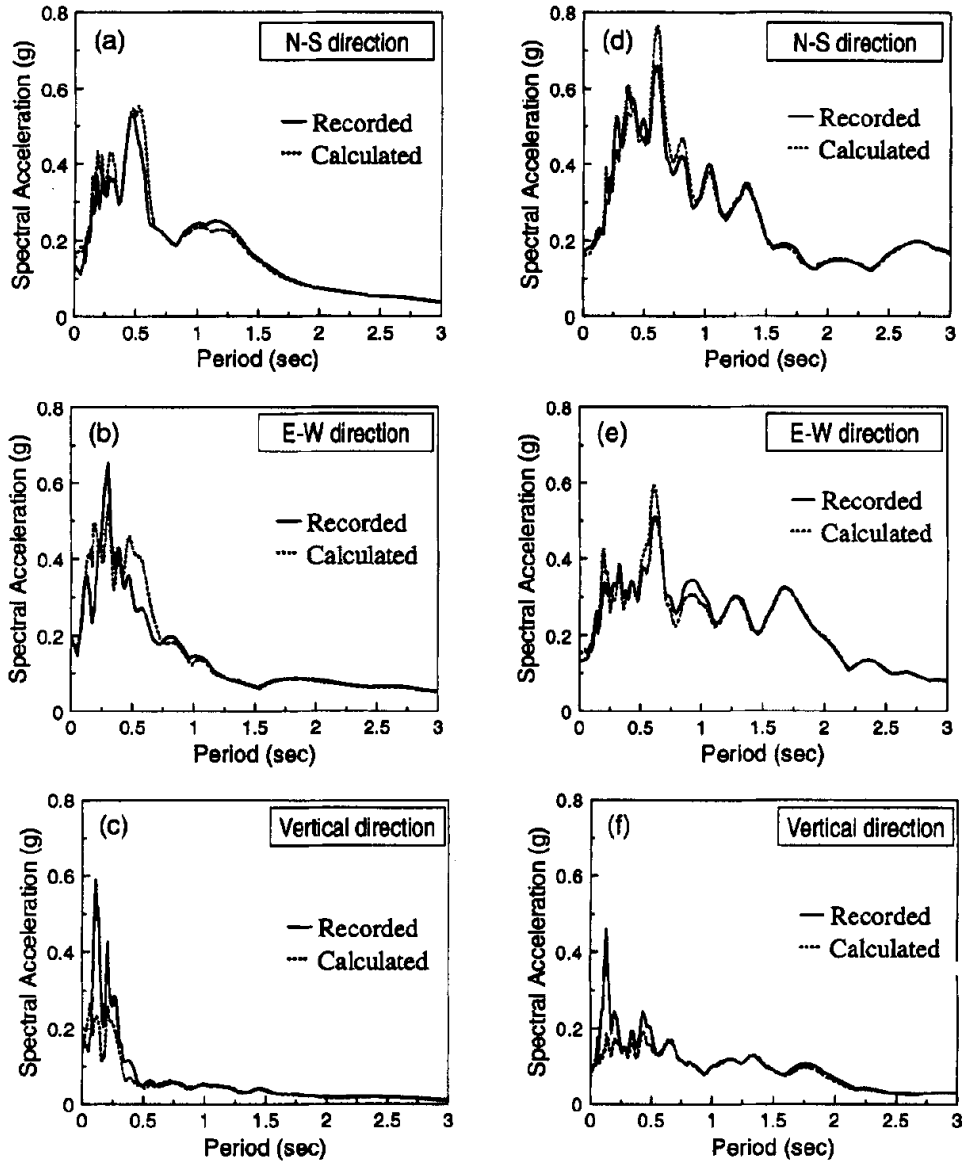


Figure 4-15: Comparison of the acceleration response spectra at the ground surface of the Lotung site (left: July 31, 1986 earthquake; right: November 15, 1986 earthquake) (after Li et al. (1998))

Borja and Chao (1999) employed the 3-D FE program SPECTRA (Borja and Wu 1994) to predict the site response at the Lotung site in the May 20, 1986 earthquake. The bounding surface elasto-plastic model of Chao and Borja (1998) was employed to simulate the nonlinear soil behaviour. The soil properties at the Lotung site are shown in Figure 4-16. By employing the recorded motion at GL. -47.0m as the input motion for the analysis, the predicted acceleration time histories at the ground surface and at the GL. -11.0m were compared against the recorded data. Good agreement was observed for all three directions, as shown for the vertical direction in Figure 4-17. However, only total stress method was employed for the analysis, which cannot simulate the two-phase

soil behaviour, such as the build-up of excess pore pressure, solid-pore fluid interaction effects and liquefaction.

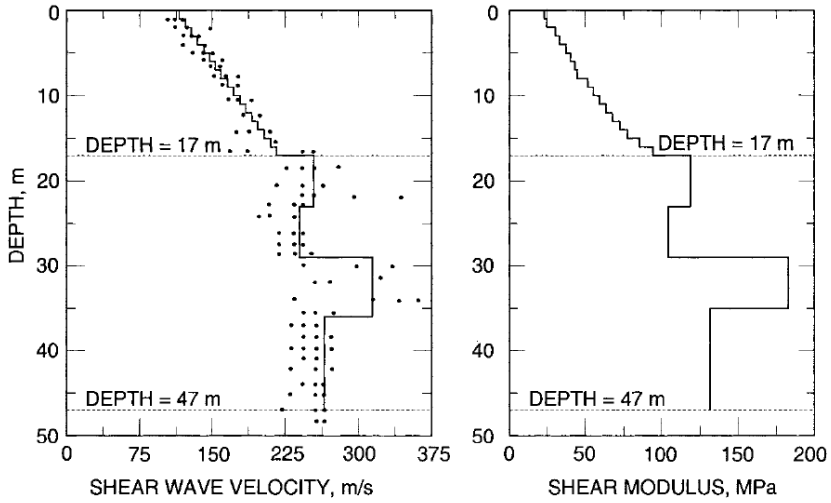


Figure 4-16: Soil properties at the Lotung site (after Borja and Chao (1999))

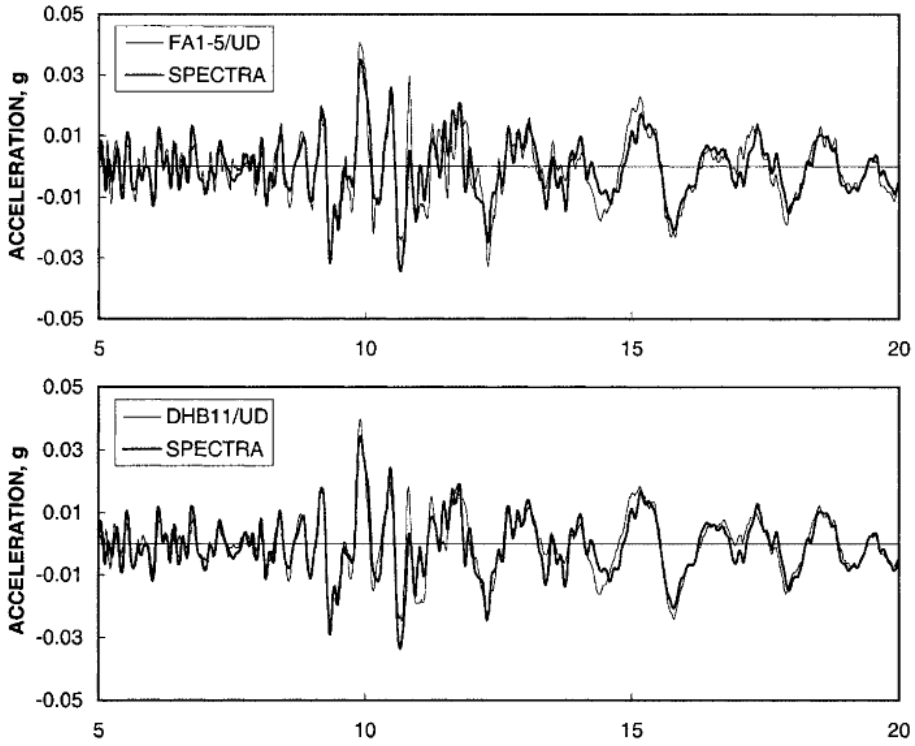


Figure 4-17: Comparison of the acceleration time histories in the UD direction at two depths of the Lotung site (upper plot: ground surface; lower plot: GL. -11.0m) (after Borja and Chao (1999))

It should be noted that in Borja and Chao (1999), 1% Rayleigh damping was employed in the FE analysis in addition to the hysteretic material damping. The application of the Rayleigh damping can approximately simulate the energy loss at very

small strain levels, where nearly linear soil behaviour is simulated by the employed constitutive model in this strain range. This is attributed to the fact that the soil material damping ratio is never zero due to an unclear energy dissipation mechanism even at very smaller strain levels (Kramer 1996). The range of so called "very small strain levels" was suggested to be smaller than 0.0003%-0.003%, where soil behaviour is nearly linear (Vucetic, 1994). The same issue was also addressed in the previously discussed study of Li et al. (1998) and the same technique of additional Rayleigh damping was employed. The employment of the Rayleigh damping in both studies ensures satisfactory site response predictions through FE analyses, which implies the importance of adequate damping simulation at very small strain levels.

However, based on the discussed studies, uncertainties still exist in the vertical site response analysis, mainly due to the sensitivity of the constrained modulus on several factors, such as the pore fluid compressibility, the water table location and the degree of unsaturation. The full 3-D numerical method has been employed for the multi-directional site response analysis, but without rigorously investigating the numerical modelling for the vertical component. Some unsatisfactory predictions of the vertical site response were found (e.g. in Li et al. (1998)), while the reasons have not been investigated in great detail. Therefore, in this chapter, the multi-directional site response is simulated by employing the 3-D dynamic nonlinear HM formulation in ICFEP. Different critical aspects of the numerical modelling for the site response analysis, such as the constitutive models, the use of 3-D input motion and the coupled consolidation formulation, are investigated through the conducted FE simulations. Parametric studies concentrate on the effects of three critical factors on site response, namely the variation of water table, the soil permeability and the 3-D ground motions.

4.3 Constitutive models for dynamic analysis

Soil behaviour subjected to dynamic cyclic loading is acknowledged as strongly inelastic, nonlinear and hysteretic. Figure 4-18 shows a typical hysteretic loop of soil behaviour under cyclic loading. There are two aspects for defining the hysteretic loop: one is the loop path under cyclic loading and the other is the loop shape (Ishihara, 1996). For the loop path, subjected to loading, un-loading and re-loading conditions, the soil behaviour follows the curve OCA, AB and BEA respectively. Concerning the loop

shape, firstly, the inclination of the backbone curve (curve BOA) is expressed by the secant stiffness G_{sec}, as illustrated in Figure 4-18. Furthermore, the breadth of the loop is controlled by the loop area ΔW, representing the dissipated energy of soil materials under cyclic loading. The parameter of damping ratio is introduced in Equation 4-1 to quantitively evaluate the energy dissipation for soil materials under cyclic loading, where W represents the maximum strain energy of soil materials, as illustrated by the triangular area in Figure 4-18. Therefore, the hysteretic loop shape is controlled by two parameters, the secant shear modulus G_{sec} and the damping ratio ξ. The soil hysteretic behaviour is usually studied by investigating the characteristics of these two parameters, in terms of shear modulus degradation curves and damping curves respectively. The ratios between the secant shear modulus and maximum shear modulus (G_{sec}/G_{max}) and the damping ratios are plotted versus cyclic shear strain amplitude, as illustrated in Figure 4-19. In particular, the shear modulus degradation curve represents the change of the backbone curve when the shear strain increases. As observed in Figure 4-19, the G_{sec}/G_{max} ratio initiates at unity at very small strain levels, and gradually reduces as shear strain increases, corresponding to the backbone curve shown in Figure 4-18. Furthermore, the damping curve reflects the energy dissipation within soil materials under cyclic loading, which gradually increases with increasing strain levels.

Figure 4-19 also illustrates the threshold strains for categorising different soil behaviour (i.e. linear, nonlinear and plastic soil behaviour). This work was conducted by Vucetic (1994), through analysing laboratory test results for different types of soils subjected to cyclic loads. As shown in Figure 4-19, the range of very small strain levels was suggested to be smaller than 0.0003%-0.003%, where soil behaviour is nearly linear. At small strain levels, soil behaviour is assumed to be nonlinear but remains largely elastic. At the medium to large strain levels, soil is increasingly nonlinear and plastic, where permanent deformation is generated under cyclic loading.

The described fundamental dynamic soil behaviour can be reproduced by employing numerical or analytical methods, through the implementation of appropriate constitutive models. Three types of dynamic soil constitutive models have been proposed and developed for this purpose, comprising of empirical curves for the equivalent-linear analysis, cyclic nonlinear models and advanced elasto-plastic constitutive models. However, this section only discusses fundamental aspects of dynamic soil behaviour and relevant constitutive models for the analyses presented in the following sections. A

complete review for dynamic soil behaviour is beyond the scope of this thesis, where more specific discussions are attributed to Kramer (1996), Ishihara (1996) and Zienkiewicz et al. (1999).

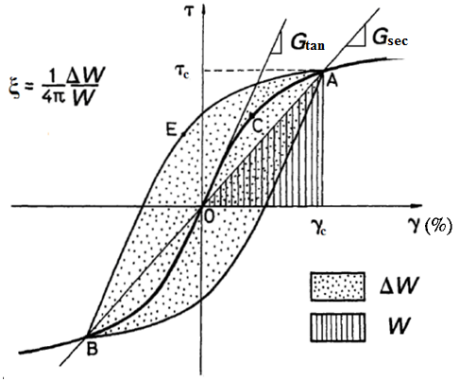


Figure 4-18: A typical hysteretic loop of soil behaviour under cyclic loading (after Ishihara (1996))

$$\xi = \frac{1}{4\pi}\frac{\Delta W}{W} \qquad 4\text{-}1$$

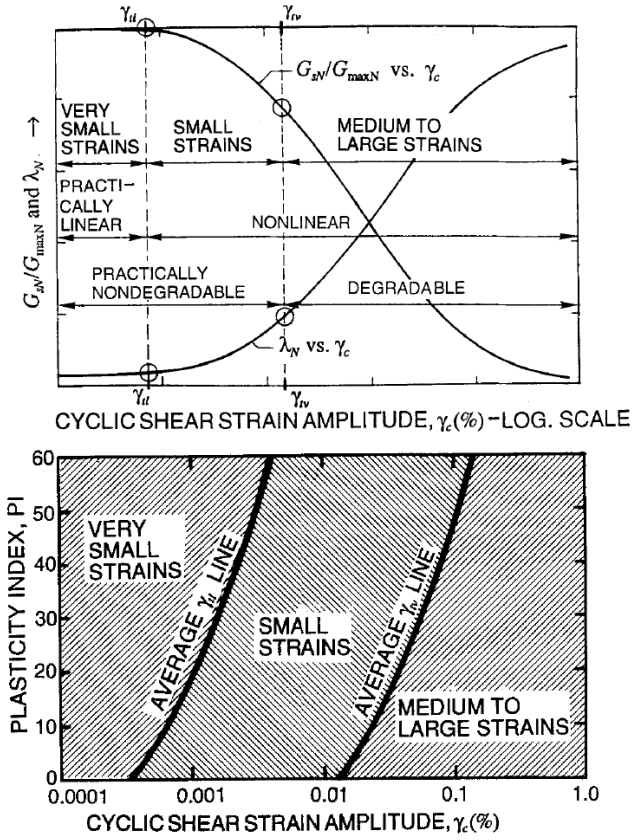


Figure 4-19: Categorisation of cyclic shear strains subjected to cyclic loads (λ_N indicates the material damping, which is the same as ξ adopted in the thesis) (after Vucetic (1994))

4.3.1 Cyclic nonlinear models

In this chapter, cyclic nonlinear models are employed in FE site response analyses to simulate the dynamic soil behaviour under cyclic loading. The main idea for cyclic nonlinear models is to reproduce the actual stress-strain loop path of soils subjected to different deformation levels. Therefore, cyclic nonlinear models can account for the variations of stiffness and material damping at different strain levels. A variety of cyclic nonlinear models have been proposed to simulate the nonlinear and hysteretic soil behaviour, which are all characterised by a backbone curve and several rules controlling loading and unloading. Simple cyclic nonlinear models, such as the Hyperbolic model (Kondner and Zelasko, 1963) and the Logarithmic model (Puzrin and Shiran, 2000), include relatively simple rules which govern the loading-unloading-reloading stress-strain paths. Advanced cyclic nonlinear models can involve more complex rules to account for different soil characteristics, such as soil densification effect, spatial variation of soil stiffness and independent simulation of shear and volumetric deformations (Taborda and Zdravković, 2012). In this chapter, two cyclic nonlinear models are employed in the FE site response analyses, which are the Logarithmic model and the Imperial College Generalised Small Strain Stiffness model (ICG3S model). The fundamental aspects of these two models are briefly discussed in this section. More details about the formulation and implementation of cyclic nonlinear models can be found in Taborda (2011) and Taborda and Zdravković (2012).

The first feature of cyclic nonlinear models is the backbone curve, which describes the initial nonlinear stress-strain behaviour. The backbone curve can be either explicitly expressed as the stress-strain relations $\tau = F_{bb}(\gamma)$, or implicitly expressed as the shear modulus reduction functions $G_{tan}/G_{max} = F_{bb}(\gamma)$, where $\tau, \gamma, G_{tan}, G_{max}$ and $F_{bb}(\gamma)$ are the shear stress, shear strain, tangent shear modulus, maximum shear modulus and backbone curve function respectively.

The second fundamental aspect of cyclic nonlinear models refers to a set of rules governing hysteretic soil behaviour, namely, the unloading and reloading stress-strain path. Masing (1926) proposed the following two rules for this purpose:

– M1: during the initial loading, the stress-strain path follows the backbone curve defined by different models, like the curve A-B shown in Figure 4-20;

– M2: subjected to unloading and reloading condition, the stress-strain curve restarts

from the reversal point (τ_r, γ_r), following the same shape as the backbone curve, but scaled by a scaling factor of 2, illustrated as the curve B-C and D-E.

However, according to Kramer (1996), the original Masing rules are not sufficient to simulate hysteretic soil behaviour under irregular loading conditions, where two additional rules were proposed by Kramer (1996) known as the extended Masing rules:

– M3: subjected to unloading or reloading conditions, if the stress-strain curve exceeds the past maximum strain level and intersects with the backbone curve, it follows the initial backbone curve, like the curve E-F;

– M4: subjected to unloading or reloading conditions, if the stress-strain curve intersects with the previous loop, it follows the previous path (curve G-H).

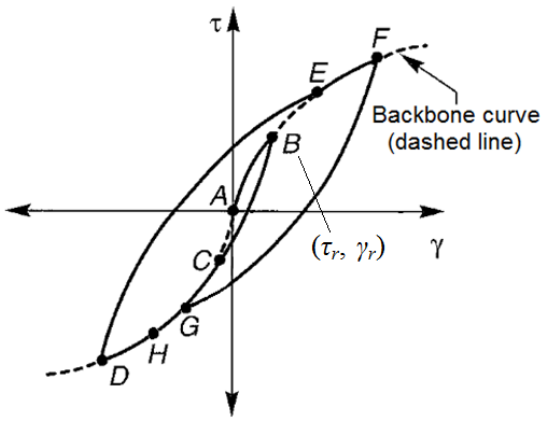


Figure 4-20: Shear stress-strain curves following Masing rules and extended Masing rules (after Kramer (1996))

Logarithmic model

A logarithmic function was initially proposed by Puzrin and Burland (1996) to simulate the pre-yield behaviour of soils subjected to a wide range of strain levels. This formulation was then employed as the backbone curve of the Logarithmic cyclic nonlinear model (Puzrin and Shiran, 2000). The Logarithmic backbone curve is explicitly expressed by Equation 4-2, where α and R are model parameters and τ_{ref} is a reference shear stress.

$$\tau = G_{max}\gamma\left(1-\alpha\left[\ln\left(1+\frac{G_{max}}{\tau_{ref}}\gamma\right)\right]^{R}\right) \qquad 4\text{-}2$$

It should be noted that the backbone curve equation for the Logarithmic model shown above is only based on the 1-D assumptions. In order to account for soil nonlinear behaviour under general loading conditions, the backbone curve equation needs to be expressed in terms of the 3-D stress and strain invariants, which are converted from the corresponding 1-D terms in Equations 4-3 and 4-4 (Potts and Zdravković, 1999).

$$J = \frac{1}{\sqrt{6}}\sqrt{\left(\sigma_1' - \sigma_2'\right)^2 + \left(\sigma_2' - \sigma_3'\right)^2 + \left(\sigma_3' - \sigma_1'\right)^2} = \frac{1}{\sqrt{6}}\sqrt{\left(\sigma_x' - \sigma_y'\right)^2 + \left(\sigma_y' - \sigma_z'\right)^2 + \left(\sigma_x' - \sigma_z'\right)^2 + \tau_{xy}^2 + \tau_{yz}^2 + \tau_{xz}^2} \qquad 4\text{-}3$$

$$E_d = \frac{2}{\sqrt{6}}\sqrt{\left(\varepsilon_1 - \varepsilon_2\right)^2 + \left(\varepsilon_2 - \varepsilon_3\right)^2 + \left(\varepsilon_3 - \varepsilon_1\right)^2} = \frac{2}{\sqrt{6}}\sqrt{\left(\varepsilon_x - \varepsilon_y\right)^2 + \left(\varepsilon_y - \varepsilon_z\right)^2 + \left(\varepsilon_x - \varepsilon_z\right)^2 + \gamma_{xy}^2 + \gamma_{yz}^2 + \gamma_{xz}^2} \qquad 4\text{-}4$$

where J and E_d are the 3-D deviatoric stress and strain invariants respectively, which can be only expressed by positive values, $\sigma_1^{'}, \sigma_2^{'}$ and $\sigma_3^{'}$ are the principal effective stresses, and $\varepsilon_1, \varepsilon_2$ and ε_3 are the principal strains.

By employing the expressions for the 3-D stress and strain invariants into Equation 4-2, the new backbone curve expression for the Logarithmic model is shown in Equation 4-5. It should be noted that J^* and E_d^* are the modified 3-D stress and strain invariants, which are employed to assume both positive and negative stress and strain values, as explained by Taborda (2011).

$$J^* = G_{max} E_d^* \left(1 - \alpha \left[\ln\left(1 + \frac{G_{max}}{J_L} \left| E_d^* \right| \right) \right]^R \right) \qquad 4\text{-}5$$

where

$$R = \frac{c\left(1 + x_L\right)\ln\left(1 + x_L\right)}{x_L\left(x_L - 1\right)}$$

$$\alpha = \frac{x_L - 1}{x_L\left[\ln\left(1 + x_L\right)\right]^R}$$

$$x_L = \frac{E_{d,L}}{J_L} G_{max}$$

Eventually, the backbone curve of the Logarithmic model is controlled by three

model parameters (J_L, $E_{d,L}$ and c) and one soil property parameter (G_{max}), where the meanings of the four parameters are illustrated in Figure 4-21. It can be seen that beyond the strain level of $E_{d,L}$, the stress-strain curve becomes a straight line, where the slope of the straight line (G_{imp}) is controlled by the parameter c. It should be noted that cyclic nonlinear models are usually found to overestimate damping ratio at large strain levels (Puzrin and Shiran, 2000; Phillips and Hashash, 2009; Taborda; 2011). In order to overcome this limitation, the employment of smaller than 1 values for parameter c in the Logarithmic models can avoid overestimating the damping ratio in this range, as illustrated in Figure 4-22. In particular, it can be seen that when employing smaller than 1 values for the parameter c, as deviatoric strain increases, the predicted damping ratio increases at small and intermediate strain levels and decreases at large strain levels. Furthermore, this procedure also avoids the unrealistically significant reduction of the shear modulus (i.e. G_{tan} close to zero) for soils subjected to high nonlinearity under large shear deformations. The soil damping reduction at high strain levels is also observed in the laboratory-based empirical damping curves proposed by Darendeli (2001), as shown in Figure 4-23, particularly for lower plasticity index (I_P) values. However, the strain levels of the damping reduction observation are slightly beyond the recommended applicability range of the proposed model (1%). Apart from this, currently there are limited investigations to support this pattern of soil damping variation at high strain levels.

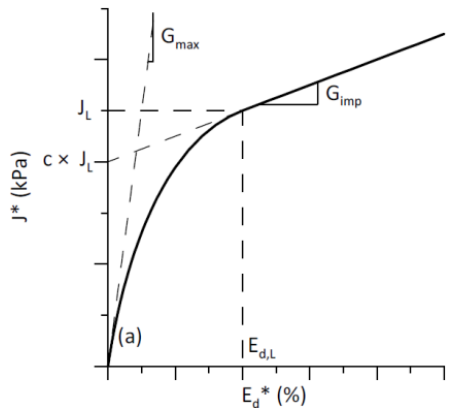


Figure 4-21: A schematic graph for the backbone curve simulated by the Logarithmic model (after Taborda (2011))

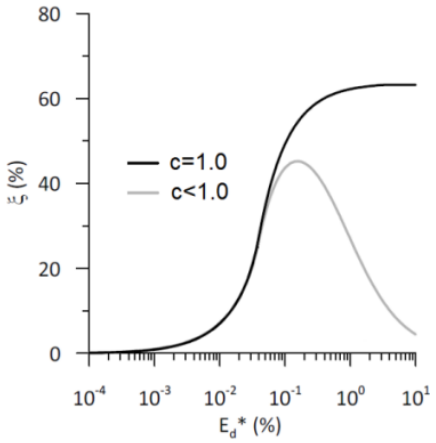


Figure 4-22: A schematic graph for the effect of the parameter *c* on damping curve (after Taborda (2011))

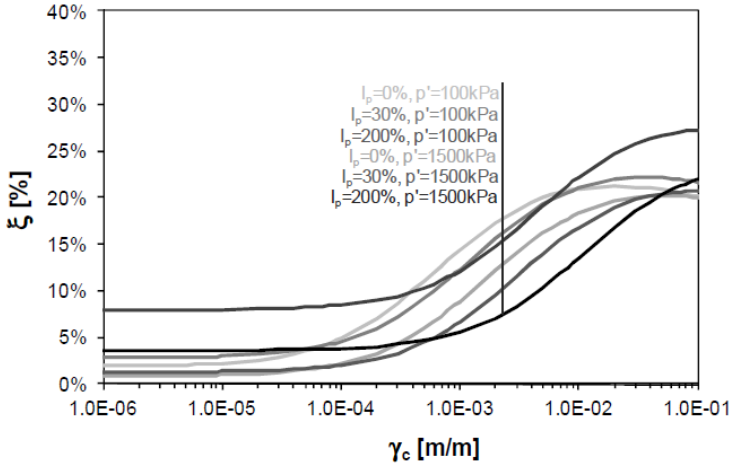


Figure 4-23: Damping curves predicted by Darendeli (2001) empirical models (after Guerreiro et al. (2012))

After employing the Masing rules (M1 and M2 rules), the expression for the Logarithmic model is shown in Equation 4-6, where J_r^* and $E_{d,r}^*$ are the modified stress and strain invariants at the reversal point. *n* is the scaling factor which assumes that the stress-strain curve under the unloading and reloading conditions follows the same shape as the backbone curve, but scaled by the scaling factor *n*. In the Logarithmic model, the values of *n* are taken as 2 and -2 under the unloading and reloading conditions respectively.

$$J^* - J_r^* = G_{max} \cdot \left(E_d^* - E_{d,r}^*\right) \cdot \left(1 - \alpha \cdot \left[\ln\left(1 + \frac{G_{max}}{n \cdot J_L} \cdot \left|E_d^* - E_{d,r}^*\right|\right)\right]^R\right) \qquad 4\text{-}6$$

ICG3S model

As highlighted in previous investigations (discussed in Section 4.2.2), numerical site response analyses employing bounding surface elasto-plastic models tend to underestimate soil material damping at very small strain levels. This essentially results in overprediction of dynamic response for soil profiles. As another widely used type of constitutive models for site response analyses, cyclic nonlinear models are however also found to underestimate soil material damping in this strain range, e.g. in Puzrin and Shiran (2000), Phillips and Hashash (2009) and Taborda and Zdravković (2012). Studies have been conducted to overcome this limitation by mathematically modifying the model formulations. Such effective work can be found in Puzrin and Shiran (2000), Phillips and Hashash (2009), Taborda and Zdravković (2012), etc. Particularly in Taborda and Zdravković (2012), the modified model was rigorously validated against empirical damping curves, showing its satisfactory applicability on adequately simulating soil material damping at very small strain levels. This model is also available in the FE program ICFEP. An advantage of the modified cyclic nonlinear models is to reduce the complexity of employing the additional frequency-dependent Rayleigh damping in FE analyses. Therefore, in this section, the ICG3S model is introduced.

The ICG3S model was proposed by Taborda and Zdravković in 2012 to simulate complex dynamic soil behaviour under cyclic loading. The model was developed based on the Hyperbolic model (Kondner and Zelasko, 1963), but involves complex rules to account for some complicated aspects of soil behaviour, such as the independent simulation of shear and volumetric deformations, spatial variation of soil stiffness and adequate simulation of material damping at very small strain levels. The backbone curve for the ICG3S model after employing the 3-D stress and strain invariants is implicitly expressed by Equation 4-7, where *a, b* and *c* are model parameters. In particular, *a* and *b* control the shift and curvature of the backbone curve respectively, and the employment of smaller than 1 values for the parameter *c* can avoid the overestimation of damping at large strain levels.

$$\frac{G_{tan}}{G_{max}} = c + \frac{(1-c)}{1+\left(\frac{|E_d^*|}{a}\right)^b} \qquad 4\text{-}7$$

Most cyclic nonlinear models simulate hysteretic behaviour considering only the shear stiffness degradation, while bulk and constrained moduli are totally dependent on

the shear modulus, assuming a constant Poisson's ratio, in terms of modulus degradation, material damping and reversal behaviour. However, the ICG3S model was developed to be capable of independently reproducing the shear and volumetric deformations. Therefore, a second backbone curve is implicitly specified for the volumetric deformation, as shown in Equation 4-8, where ε_{vol}^{*} is the volumetric strain, K_{tan} and K_{max} are the tangent and maximum bulk moduli, and *r*, *s* and *t* are another three model parameters, corresponding to parameters *a*, *b* and *c* for the backbone curve of the shear deformation. Furthermore, the reversal behaviour for shear and volumetric deformations are also independently simulated by numerically implementing different reversal control procedures. It should be noted that the material Poisson's ratio simulated by the ICG3S formulation is not constant and depends on the respective nonlinear states of the shear and bulk moduli. Therefore, the simulated Poisson's ratio values should be carefully checked during the numerical analyses in order to avoid unrealistic simulations (i.e. negative Poisson's ratios).

$$\frac{K_{tan}}{K_{max}} = t + \frac{(1-t)}{1+\left(\frac{\left|\varepsilon_{vol}^{*}\right|}{r}\right)^{r}} \qquad 4\text{-}8$$

After employing the Masing rules (M1 and M2 rules), the expressions for the ICG3S model are shown in Equation 4-9, where two scaling factors, n_1 and n_2, are employed for the shear and volumetric stress-strain hysteretic loops respectively. These two scaling factors are independently controlled by the model parameters d_1-d_4 and d_5-d_8. As mentioned in Section 4.2.2, the soil material damping at very small strain levels is generally underestimated by the existing cyclic nonlinear models, which could lead to a non-conservative assessment for dynamic analysis of geotechnical structures and limit the applicability of cyclic nonlinear models (Taborda and Zdravković, 2012). However, the employment of varying scaling factors within the ICG3S model enables the more accurate simulation of material damping in the very small strain range.

$$\begin{cases} \dfrac{G_{tan}}{G_{max}} = c + \dfrac{(1-c)}{1+\left(\dfrac{\left|E_d^{*} - E_{d,r}^{*}\right|}{n_1 a}\right)^{b}} \\ \dfrac{K_{tan}}{K_{max}} = t + \dfrac{(1-t)}{1+\left(\dfrac{\left|\varepsilon_{vol}^{*} - \varepsilon_{vol,r}^{*}\right|}{n_2 r}\right)^{s}} \end{cases} \qquad 4\text{-}9$$

where

$$\begin{cases} n_1 = \left(d_1 + 2\right)^{\left|E_d^* - E_{d,r}^*\right|^{d_2}} \left(\dfrac{\left(d_3 + 1\right)\left|E_d^* - E_{d,r}^*\right|}{1 + \left(d_3 + 1\right)\left|E_d^* - E_{d,r}^*\right|} \right)^{d_4} \\ n_2 = \left(d_5 + 2\right)^{\left|\varepsilon_{vol}^* - \varepsilon_{vol,r}^*\right|^{d_6}} \left(\dfrac{\left(d_7 + 1\right)\left|\varepsilon_{vol}^* - \varepsilon_{vol,r}^*\right|}{1 + \left(d_7 + 1\right)\left|\varepsilon_{vol}^* - \varepsilon_{vol,r}^*\right|} \right)^{d_8} \end{cases}$$

Concerning the calibration for cyclic nonlinear models, usually the reproduced shear modulus degradation and damping curves are compared against corresponding laboratory data or empirical curves. This is sufficient for geotechnical structures subjected only to horizontal earthquake motions. However, for soil profiles subjected to 3-D earthquake motions, the vertical response is dependent on the soil constrained modulus. Therefore, it is also necessary to calibrate the cyclic nonlinear models based on constrained modulus degradation (D/D_{max}) and damping curves. In order to obtain these curves, the vertical stress-strain loops are predicted based on the model formulations. In particular, the incremental vertical stress is calculated based on the incremental vertical strain and tangential constrained modulus. For cyclic nonlinear models that employ only the shear modulus, the tangential constrained modulus can be directly calculated based on the transient tangential shear modulus and Poisson's ratio at each shear strain level. In this case, the modulus degradation and damping curves for shear and compressional deformations are dependent on the same set of model parameters, and therefore the overall calibration of these models should consider an optimum degradation response in both modes of deformation. However, for cyclic nonlinear models that employ both shear and bulk modulus variations, the tangential constrained modulus can be calculated based on the shear and bulk moduli at each shear and volumetric strain levels. In this case, modulus degradation and damping curves for shear and compressional deformations are independently controlled by two sets of model parameters, which can be separately calibrated against the corresponding laboratory data or in-situ observations. Taking the ICG3S model for example, the calibration for modulus degradation and damping curves of shear and compressional deformations are respectively controlled by a, b, c, d_1 to d_4 and r, s, t, d_5 to d_8. Finally, the relationship between the vertical strain and shear strain, and the relationship between the vertical strain and volumetric strain are presented in Equation 4-10, where ε_h and ε_v represent the horizontal and vertical strains respectively. The two relations are derived based on the expression for the deviatoric strain in Equation 4-4 (Potts and

Zdravković, 1999), by referencing the triaxial test conditions of $\varepsilon_x = \varepsilon_y = \varepsilon_h$, $\varepsilon_z = \varepsilon_v$ and $\gamma_{xy} = \gamma_{xz} = \gamma_{yz} = 0$.

$$\begin{cases} E_d = \dfrac{2}{\sqrt{3}}\gamma = \dfrac{2}{\sqrt{3}}\left(\varepsilon_v - \varepsilon_h\right) \overset{\varepsilon_h=0}{=} \dfrac{2}{\sqrt{3}}\varepsilon_v \\ \\ \varepsilon_{vol} = \varepsilon_v + 2\varepsilon_h \overset{\varepsilon_h=0}{=} \varepsilon_v \end{cases} \qquad 4\text{-}10$$

4.3.2 Elasto-plastic models

The previously described cyclic nonlinear models can only simulate the pre-yield elastic soil behaviour. In this chapter, cyclic nonlinear models are coupled with a yield surface defined by a Mohr-Coulomb failure criterion in FE analyses. Plastic deformations can be generated only when the stress state reaches the yield surface. The expression for the Mohr-Coulomb yield function is shown in Equation 4-11.

$$F = J - \left(\frac{c'}{\tan\phi'} + p'\right) g(\theta) = 0 \qquad 4\text{-}11$$

where

$$p' = \frac{1}{3}\left(\sigma_1' + \sigma_2' + \sigma_3'\right)$$

$$\theta = \frac{1}{\sqrt{3}}\left(2\frac{\sigma_2' - \sigma_3'}{\sigma_1' - \sigma_3'} - 1\right)$$

$$g(\theta) = \frac{\sin\phi'}{\cos\theta + \dfrac{\sin\theta\sin\phi'}{\sqrt{3}}}$$

where J is the deviatoric stress invariant, p' is the mean effective stress, c' is the soil material cohesion, ϕ' is the angle of shearing resistance, θ is the Lode's angle and $g(\theta)$ defines the shape of the yield surface on the deviatoric plane.

4.4 KiK-net down-hole array observations

Japan experienced severe economic and life losses due to the 1995 Hyogo-ken Nanbu earthquake. The earthquake and subsequent secondary disasters caused 6300 deaths, 30000 injuries and destruction of 150000 buildings. More than 300000 people were left homeless and the direct economic losses were estimated as US$ 200 billion. After the earthquake, the Japanese National Research Institute for Earth Science and Disaster Prevention (NIED) decided to improve the seismic observation system in Japan by installing a large number of strong-motion, high-sensitivity and broadband seismometers at more than 2000 stations spreading over Japan. These stations are categorised into different systems based on the types of seismometers and their distribution way, i.e. the F-net, Hi-net, KiK-net and K-net systems. In particular, the 71 stations equipped with broadband seismometers comprise the F-net system. 696 stations equipped with high-sensitivity seismometers compose the Hi-net system. For most of the Hi-net stations (659), two 3-D seismometers are placed both at the ground surface and the base layer in a vertical array of a borehole. These 659 stations form the KiK-net down-hole array monitoring system. Furthermore, another 1034 stations are equipped with only one 3-D strong-motion seismometer at the ground surface, which frame the K-net strong ground motion monitoring system. The seismic data monitored by the whole monitoring system are synchronised to research institutions and universities in Japan through satellite communication. These data are also archived in the NIED database system for public use under a fully open policy (Okada et al., 2004). In the following sections, a case is studied based on the data from the KiK-net down-hole array monitoring system. The earthquake motion data of the selected case can be downloaded from the official website: http://www.kyoshin.bosai.go.jp/.

The site response of the HINO site subjected to the 2000 Western Tottori earthquake is chosen for the investigation in this chapter, due to the recorded significant dynamic response at this site. The Western Tottori earthquake occurred at 13:30 JST (04:30 GMT) on 6th October, 2000. The epicentre was located in western Tottori, south-west of Japan, as shown in Figure 4-24. According to the Japan Meteorological Agency seismic intensity scale (JMA scale), the magnitude of the earthquake was M_w 7.3. The earthquake resulted in more than 100 injuries. The HINO site (see Figure 4-24) was the closest to the epicentre (6.0km) among all the monitoring stations and consequently experienced high-intensity shaking, with the absolute peak ground acceleration (PGA)

as 11.42m/s^2. Furthermore, another two after-shock weak motions at the HINO site are also selected for the investigation, where their peak accelerations are below 0.1g in all three directions.

The basic information of the HINO site and the selected three earthquake events are listed in Table 4-1. At the HINO site, two 3-D seismometers are installed at the ground surface and the base layer (100.0m below the ground level) of the down-hole. Earthquake motions were monitored during the three seismic events in three directions, denoted as east-west (EW), north-south (NS) and up-down (UD) directions. The recorded peak accelerations (PA) at the ground surface and the base layer are summarised in Table 4-2. The 3-D acceleration time histories recorded at the base layer during the three earthquakes are shown in Figures 4-25-4-27. These motions are employed as the input motions for the subsequent 3-D numerical site response analyses. Furthermore, the corresponding acceleration response spectra are shown in Figure 4-28. Strong motions are observed in all three directions at the base layer in the Western Tottori earthquake, where the PAs are all larger than 3.0m/s^2. The PAs for both weak motions are found to be smaller than 0.1 m/s^2.

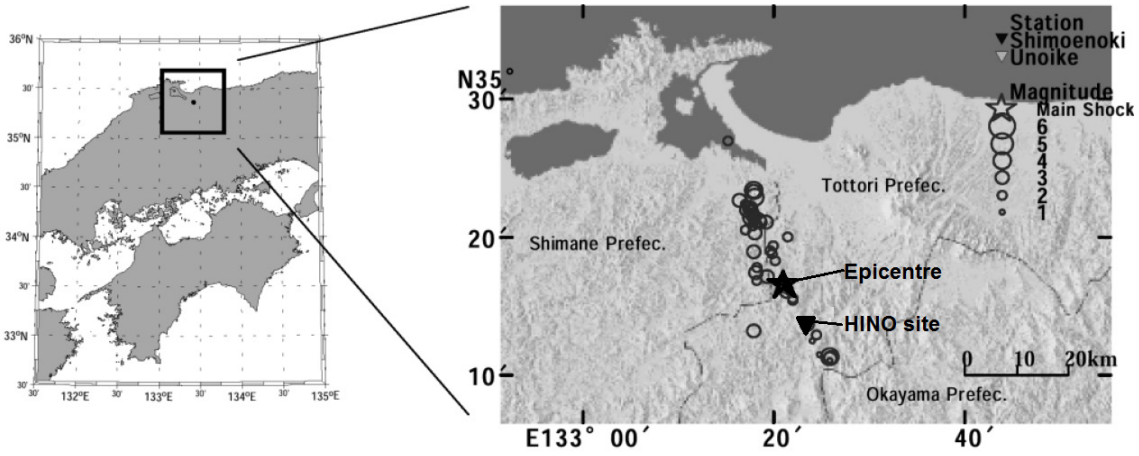


Figure 4-24: Location of the epicentre of 2000 Western Tottori earthquake and location of the HINO site (after Matsunami et al. (2002))

The original soil profile at the HINO site can be found in NIED database based on PS-logging test, in terms of the depth variations of the shear and compressional wave velocities, as shown in Figure 4-29. The water table is assumed at 10.4m below the ground surface in the Western Tottori earthquake due to the significant increase of compressional wave velocity at this depth (Beresnev et al. 2002). The material

porosities are back-calculated based on the constrained modulus equation for saturated soils proposed by Zienkiewicz et al. (1980b), as shown in Equation 4-12. In particular, the constrained and shear moduli can be calculated based on the compressional and shear wave velocities respectively. By assuming the Poisson's ratio as 0.2 for the gravelly soil and weathered granite (Bowles, 1997), the porosities of the soil layers under the water table can be calculated and the porosity for the soil layer above the water table is assumed to be the same as the one in the layer beneath, as shown in Figure 4-29.

$$D = \frac{E \cdot (1-\nu)}{(1+\nu) \cdot (1-2\nu)} + \frac{K_f}{n} = \frac{2G \cdot (1-\nu)}{1-2\nu} + \frac{K_f}{n} \qquad 4\text{-}12$$

An optimum profile for the shear wave velocity at the HINO site was given by Higashi and Abe (2002), where the shear wave velocities were back-calculated by reproducing the recorded Fourier spectral ratios between the horizontal dynamic response at the ground surface and the base layer subjected to the 2000 Western Tottori earthquake, through a shake-type analytical solution. This profile is employed in the subsequent FE analyses due to its accuracy. However, the compressional wave velocities were not investigated in Higashi and Abe (2002). Therefore they are calculated based on Equation 4-12, where it should be noted that the pore fluid bulk modulus only accounts for the soil constrained modulus below the water table. Soil densities at the HINO site can be found in Izutani (2004). The material permeability is employed as 1.0E-7 m/s for the numerical analyses, which was suggested by Domenico and Schwartz (1990) for the weathered granite material. Furthermore, the angle of shearing resistance of soil materials at the HINO site is employed as 35°, suggested by Bowles (1997) for the gravelly materials and the weathered rock. Finally, the material properties at the HINO site are summarised in Figure 4-30 and Table 4-3.

Table 4-1: Earthquake data and site information

	Date	Time	Magnitude	Epicentre position	Site code	Site name	Site position	PA (m/s^2)	Epicentral distance
2000 Western Tottori earthquake	06/10 /2000	13:30 JST	7.3 M_w	35.28°N, 133.35°E	TTRH 02	HINO	35.23°N, 133.39°E	11.42	6.0 km
2001 Weak motion 1	11/02 /2001	09:17 JST	4.3 M_w	35.42°N, 133.29°E				0.43	23.0 km
2002 Weak motion 2	24/01 /2002	16:08 JST	4.5 M_w	35.36°N, 133.32°E				0.79	16.0 km

Table 4-2: Earthquake data for HINO site in three earthquake events

	Seismometer position	Seismometer elevation (m)	EW PA (m/s^2)	NS PA (m/s^2)	UD PA (m/s^2)
2000 Western Tottori earthquake	Ground surface	410	7.53	9.27	7.75
	Base layer	310	5.74	3.57	3.17
2001 Weak motion 1	Ground surface	410	0.39	0.28	0.26
	Base layer	310	0.06	0.04	0.02
2002 Weak motion 2	Ground surface	410	0.48	0.71	0.62
	Base layer	310	0.09	0.07	0.07

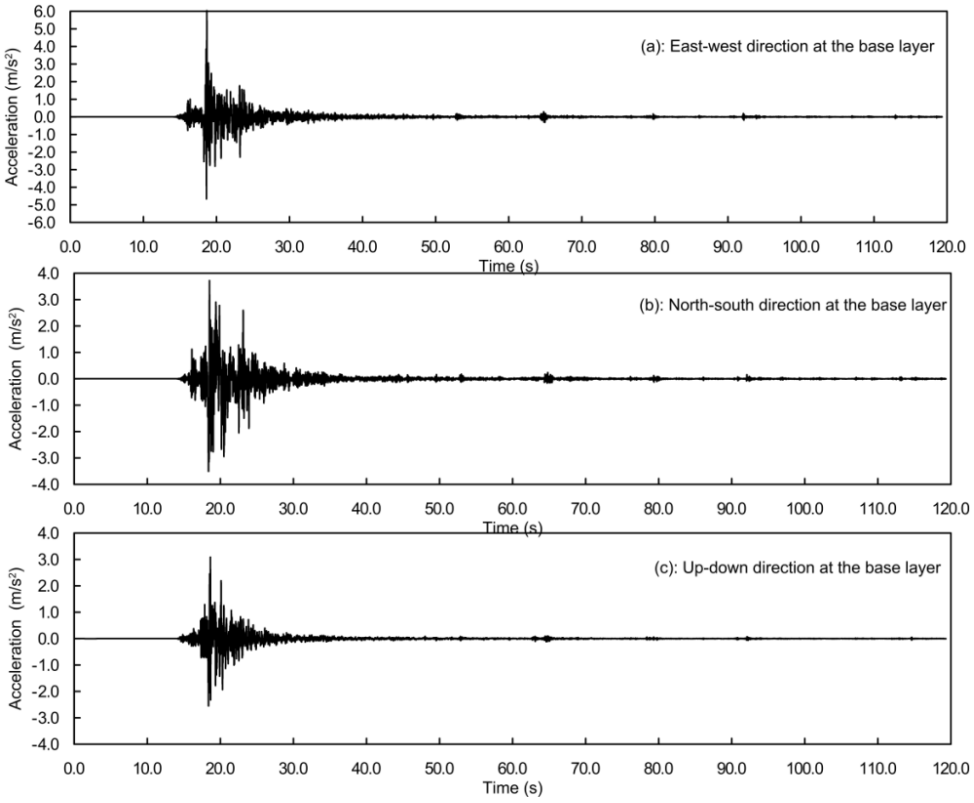


Figure 4-25: 3-D acceleration time histories at the base layer of HINO site in 2000 Western Tottori earthquake

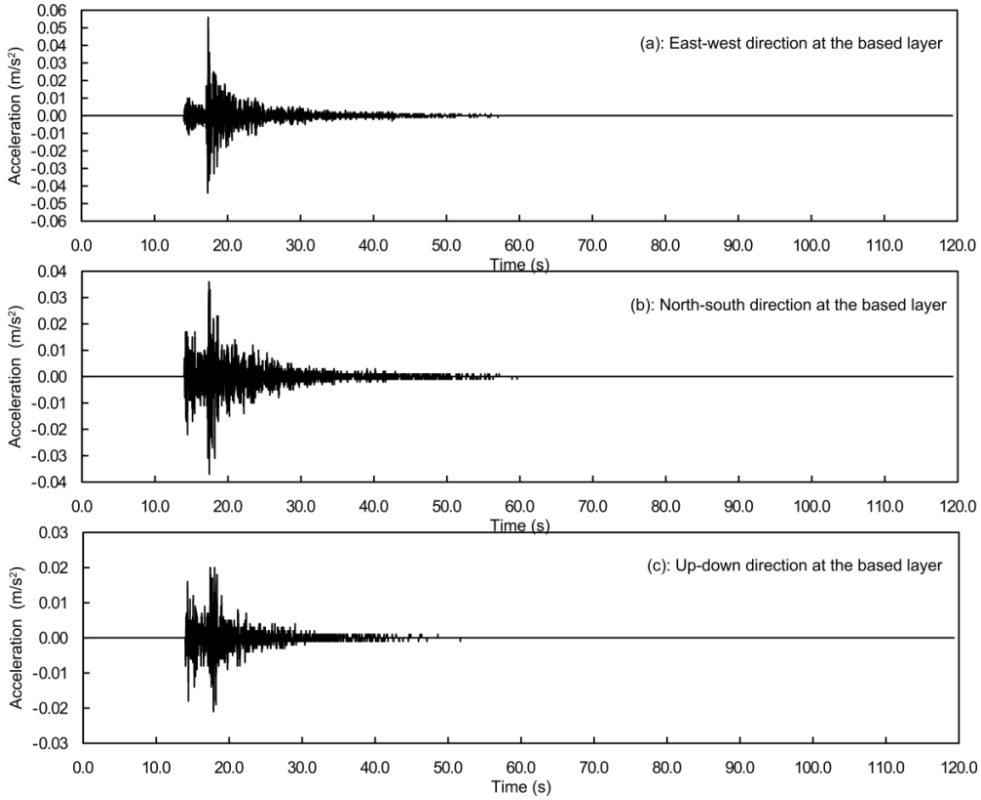


Figure 4-26: 3-D acceleration time histories at the base layer of HINO site in 2001 weak motion 1

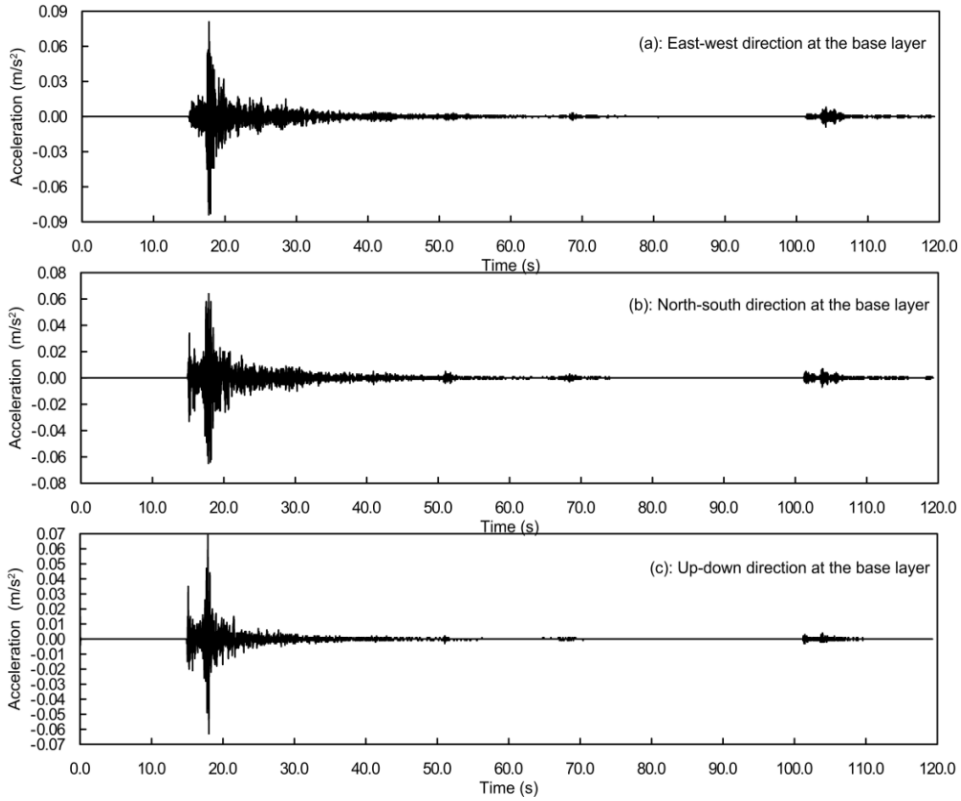
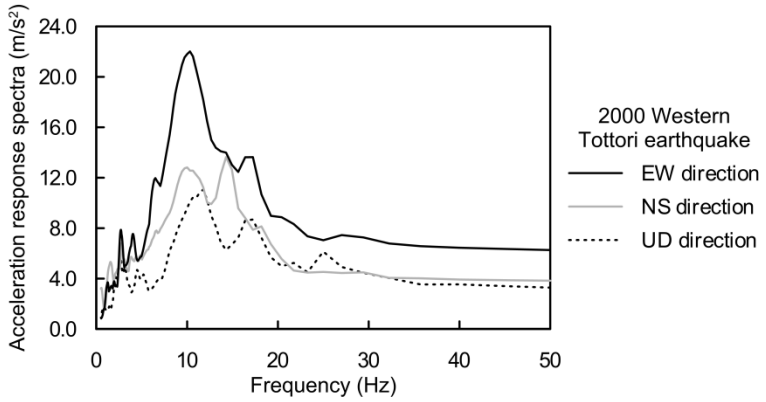
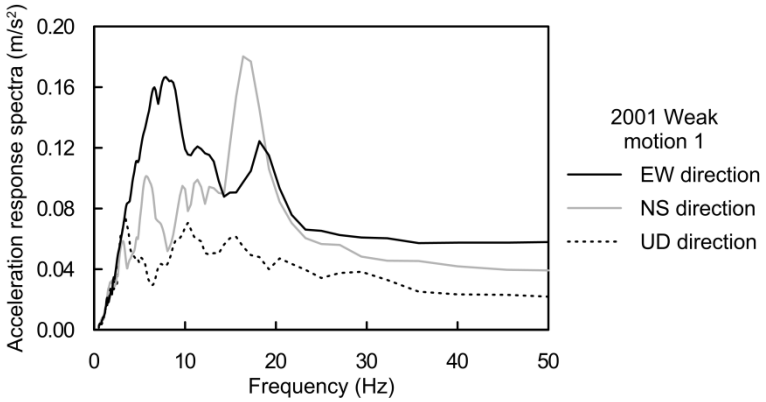


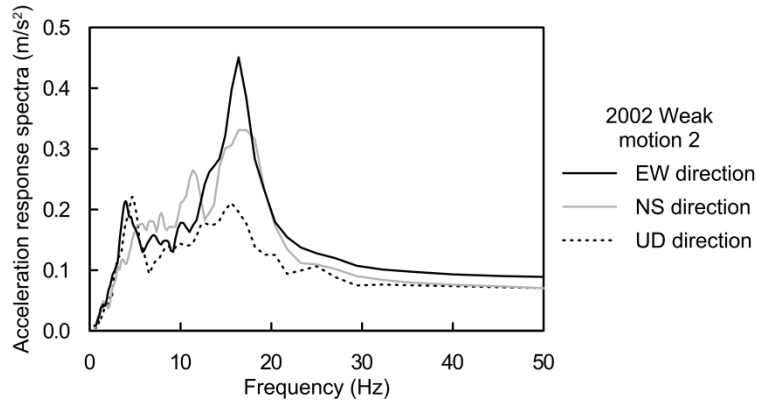
Figure 4-27: 3-D acceleration time histories at the base layer of HINO site in 2002 weak motion 2



(a): 2000 Western Tottori earthquake



(b): 2001 weak motion 1



(c): 2002 weak motion 2

Figure 4-28: Acceleration response spectra of the observed response at the base layer of HINO site in three earthquake events (5% damping)

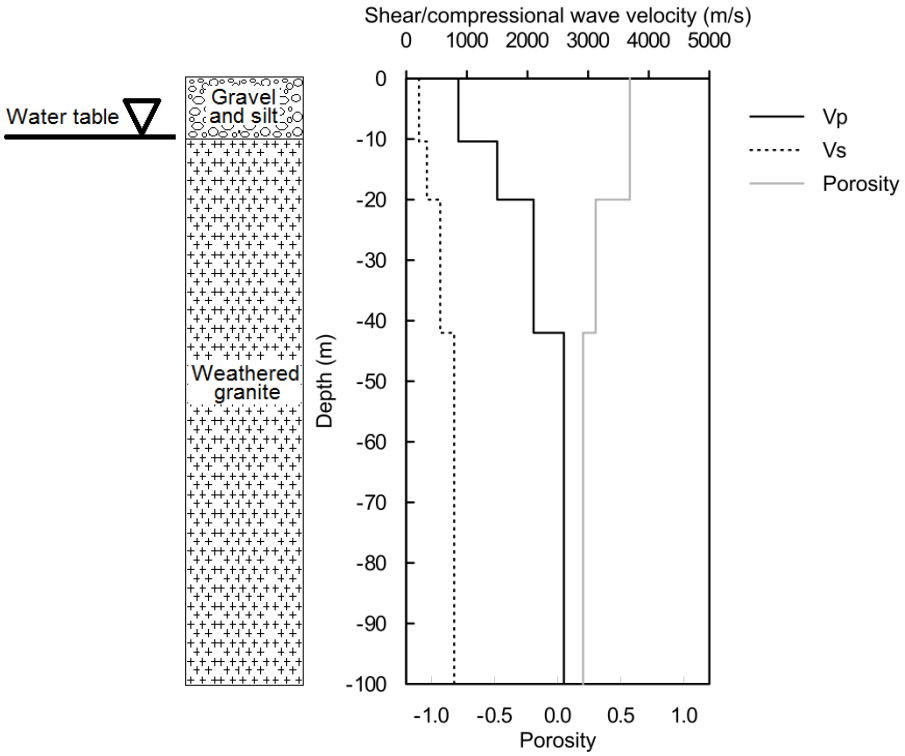


Figure 4-29: Soil profile at the HINO site (NIED database)

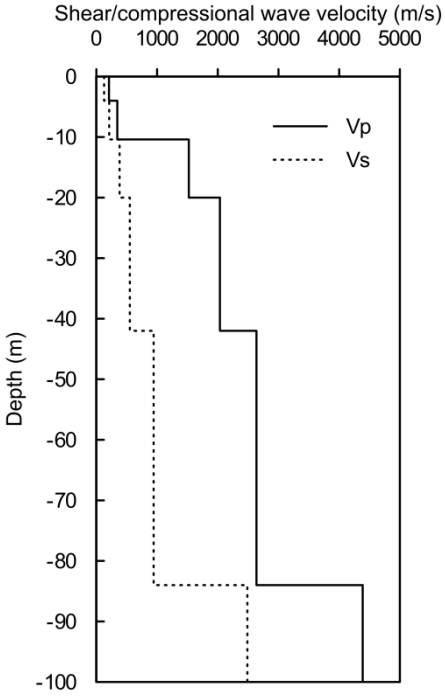


Figure 4-30: Soil profile at the HINO site employed in FE analyses

Table 4-3: Soil properties at the HINO site

Depth (GL. meters)	Porosity n	Poisson's ratio ν	Mass density ρ (g/cm^3)	S-wave velocity v_s (m/s)	P-wave velocity v_p (m/s)	Material type
0.0 ~ -4.0	0.57	0.2	2.0	127	207	Gravel and silt
-4.0 ~ -10.4	0.57	0.2	2.0	211	345	Gravel and silt
-10.4 ~ -20.0	0.57	0.2	2.2	382	1523	Weathered Granite
-20.0 ~ -42.0	0.30	0.2	2.4	551	2035	Weathered Granite
-42.0 ~ -84.0	0.20	0.2	2.6	943	2637	Weathered Granite
-84.0 ~ -100.0	0.20	0.2	2.8	2487	4387	Weathered Granite

4.5 Multi-directional site response analysis subjected to two weak earthquake motions

In this part, the 3-D site response of the HINO site subjected to two weak earthquake motions is simulated by employing the 3-D dynamic HM formulation in ICFEP, using both linear elastic and nonlinear elasto-plastic constitutive models. The predicted site response at the HINO site is compared with the recorded ground motions from the KiK-net down-hole array monitoring system. Different aspects of the numerical modelling of the site response analysis are studied through FE analyses. In particular, the soil behaviour is firstly assumed to be linear elastic due to the small magnitudes of the two weak earthquake motions. Rayleigh damping is employed in the linear FE analysis to account for the material damping, where some critical issues for the employment of Rayleigh damping parameters are addressed. Furthermore, nonlinear FE analyses are carried out employing cyclic nonlinear constitutive models. It should be noted that the frequency domain program (EERA) is also employed as the reference solution. However, the site response in each direction is decoupled and is simulated by separate EERA analyses, i.e. it is not a 3-D simulation.

4.5.1 Linear analysis

In this section, the multi-directional site response at the HINO site subjected to two weak earthquake motions is simulated employing both the linear visco-elastic

time-domain FE analysis and a frequency-domain analytical solution. Firstly, for the FE site response analysis, the FE mesh of the HINO site, consisting of 400 20-noded isoparametric hexahedral elements, and the boundary conditions are shown in Figure 4-31. The dimensions of the FE mesh are 2.0m, 2.0m and 100.0m in the X, Z and Y directions respectively, which represent the corresponding EW, NS and UD directions of the HINO down-hole. 3-D tied DOF boundary conditions are employed on the lateral boundaries in both the EW and NS directions. In particular, the DOFs of displacement and pore water pressure at corresponding nodes of the same elevation along the two opposite lateral boundaries are tied to be identical. The value of pore water pressure at the water table surface boundary is prescribed as zero and is not allowed to change throughout the analysis (i.e. Δp=0). The bottom boundary is considered to be impermeable (i.e. no flow across the boundary). Hydrostatic pore water pressure and static self-weight are prescribed as the initial stresses for all the numerical analyses in this chapter, where the coefficient of earth pressure at rest (K_0) is applied to be 0.5. The CH time integration method is utilised for the FE analyses, where the employed parameters are listed in Table 4-4, which satisfy the stability conditions of the CH method under coupled formulation, proposed in Chapter 2. Furthermore, the 3-D earthquake motions monitored at the base layer of the HINO down-hole, in terms of the acceleration time histories of the two weak motions after the Western Tottori earthquake (Figures 4-26 and 4-27), are uniformly prescribed at the bottom boundary of the mesh as the input motion. The soil properties employed in the numerical analyses are shown in Table 4-3. Coupled consolidation FE analysis is conducted for the soil layers below the water table, while one-phase FE analysis is applied for the soil layers above the water table. For the analytical investigation, three separate analyses are carried out to simulate the site response at the HINO site in the three directions, also adopting the soil properties shown in Table 4-3. Lastly, Rayleigh damping and viscous damping are employed for the FE analysis and the analytical solution respectively, with the same target damping ratio of 1.5% to account for the soil material damping subjected to weak earthquake motions. This value is in accordance with the empirical curves of Vucetic and Dobry (1991) as the proposed damping ratio at very small strain levels (<0.001%).

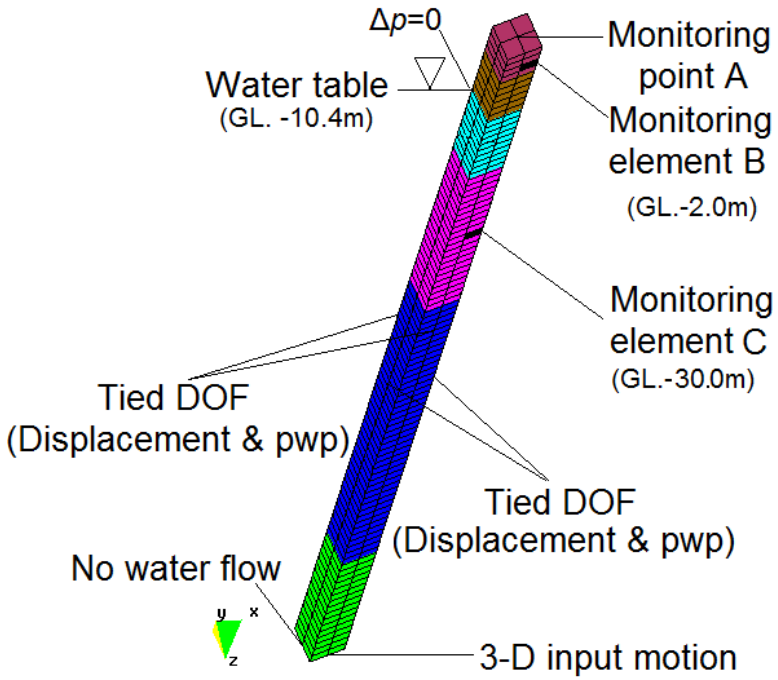


Figure 4-31: FE model for HINO site

Table 4-4: The integration parameters for CH method employed in site response analyses

Parameter	δ	α	α_m	α_f	β	ρ_∞
CH method	0.9286	0.5102	-0.1429	0.2857	0.8	0.6

The 3-D site response at the HINO down-hole predicted by the FE analysis and the analytical solution, are compared against the monitored data in Figures 4-32 and 4-33, for the weak earthquake motion 1 and 2 respectively. The comparison is presented in terms of the acceleration response amplification spectra between the dynamic response at the top (point A) and bottom boundaries. It can be seen that overall both the numerical and the analytical predictions compare reasonably with the monitored data, both in terms of frequency content and amplification. In particular, based on the numerical results for weak motion 1, the fundamental frequencies are estimated to be 2.5 Hz, 2.5 Hz and 6.0 Hz for the EW, NS and UD directions respectively, which are in very good agreement with the ones obtained from the monitored data. This agreement implies that the adopted small strain soil properties for the site response analyses are realistic. Furthermore, the same fundamental frequency is estimated for the site response in both the EW and the NS directions, indicating isotropic soil behaviour in the two horizontal directions. Concerning the site response for weak earthquake motion 2

(Figure 4-33), the fundamental frequencies are estimated as 2.5Hz, 2.5Hz and 6.1Hz for EW, NS and UD directions respectively, which match with the ones predicted for weak motion 1.

However, when compared with the analytical predictions, the amplification factors are slightly overestimated by the FE analysis in the frequency range approximately between 2.5Hz and 12.5Hz for both motions. This overestimation is probably due to the inaccurate representation of the material damping in the FE analysis with the Rayleigh damping formulation. Based on the principles of the Rayleigh damping introduced in Chapter 3 (Figure 3-15), a reasonably constant variation of damping can be achieved in the numerical analysis to represent the material damping, in the range between ω_1 and ω_2, where ω_1 and ω_2 can be taken as the first fundamental frequency and as a higher fundamental frequency respectively of the studied soil layer (Zerwer et al., 2002). In the present numerical studies, the first and the third fundamental frequencies of the soil layer, considering shear modes, are employed for the calibration of the Rayleigh damping parameters, where ω_1 and ω_2 are 2.5Hz and 12.5Hz respectively. This explains the observed overestimation of the amplification factors between 2.5Hz and 12.5Hz, since the Rayleigh damping is slightly underestimated at this range. Theoretically, the amplification of the ground motion at the fundamental frequencies can be significant and therefore it is critical to accurately predict the material damping in the suggested frequency range. While this is the case for the present site response analysis in the horizontal directions, it is not for the vertical direction, since the fundamental frequencies of the soil column when subjected to horizontal and vertical motions are different. In particular, it can be seen in Figures 4-32 (c) that the amplification factors at the vertical fundamental frequency (6.0Hz) are overestimated by the FE analysis compared with the analytical results, while the corresponding amplification factors in the horizontal directions are appropriately predicted (i.e. at the horizontal fundamental frequency (2.5Hz)). Therefore, the vertical fundamental frequency is suggested to be employed as ω_2 for the calibration of the Rayleigh damping parameters in the 3-D linear FE site response analysis. This is expected to allow the accurate prediction of the amplification factors both in the horizontal and vertical directions.

Furthermore, the acceleration time histories of point A (see Figure 4-31) predicted by the FE analysis and the analytical solution are compared with the monitored data in Figures 4-34 and 4-35, for weak earthquake motion 1 and 2 respectively (the response is

plotted only for the significant part of the ground motion). It can be seen that the 3-D site response is reasonably predicted by both the numerical analysis and the analytical solution, both in terms of the acceleration magnitude and phase angles. However, it is observed that the acceleration values are slightly overestimated by the FE analysis after 20.0s, compared with the analytical predictions and the monitored data, for both motions. This observation corresponds to the previously discussed phenomenon of numerical overestimation of amplification factors due to the inaccurate representation of the Rayleigh damping.

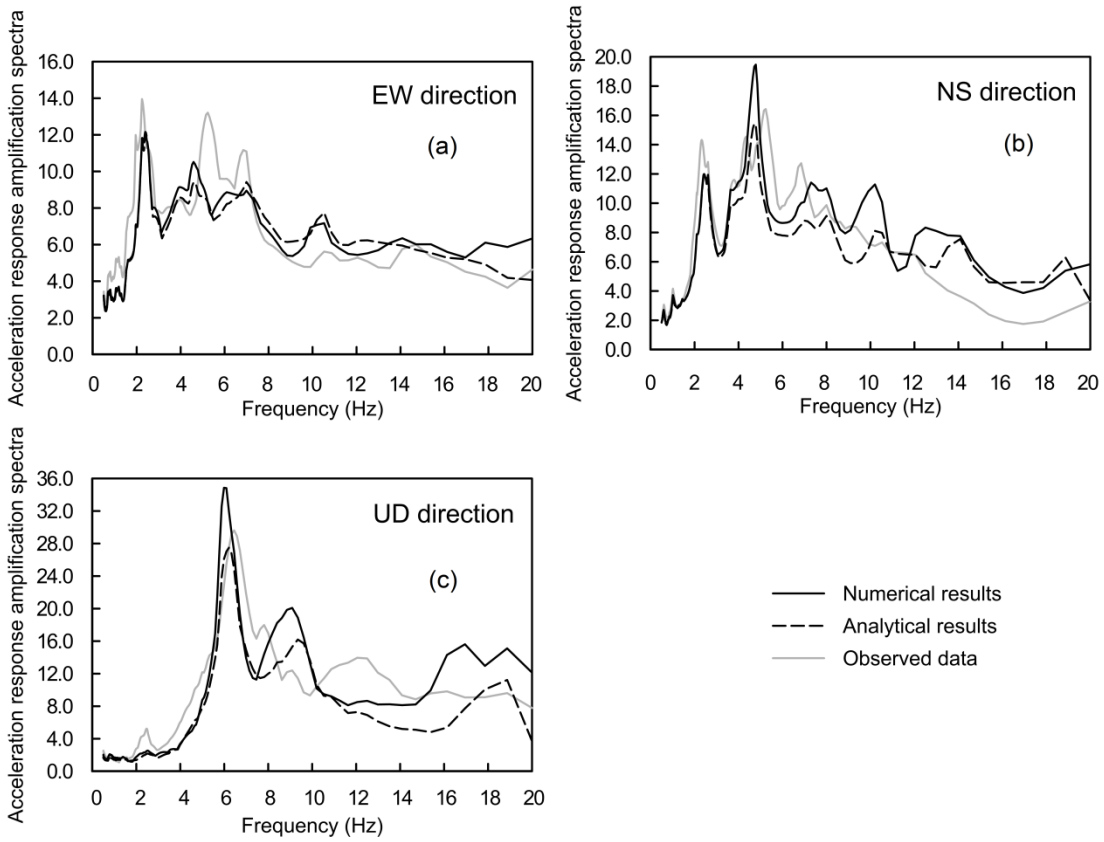


Figure 4-32: Linear analysis results under weak earthquake motion 1 (response amplification spectra)

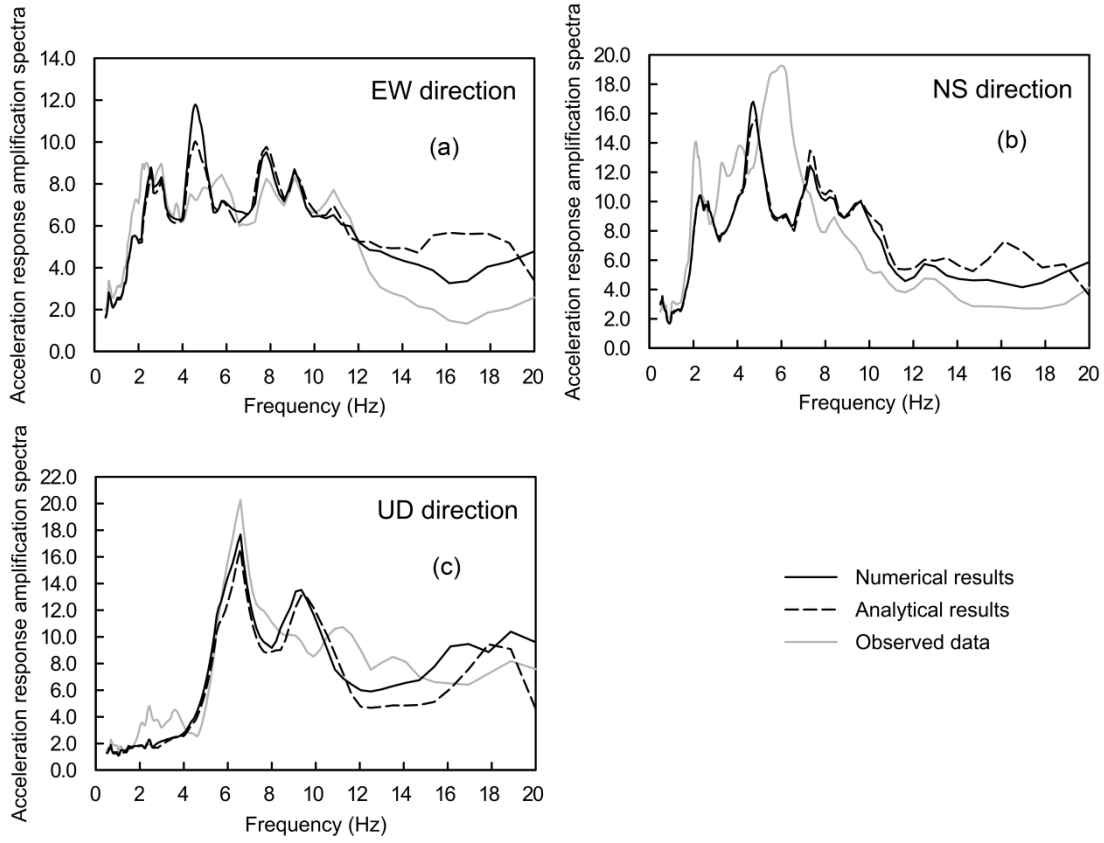


Figure 4-33: Linear analysis results under weak earthquake motion 2 (response amplification spectra)

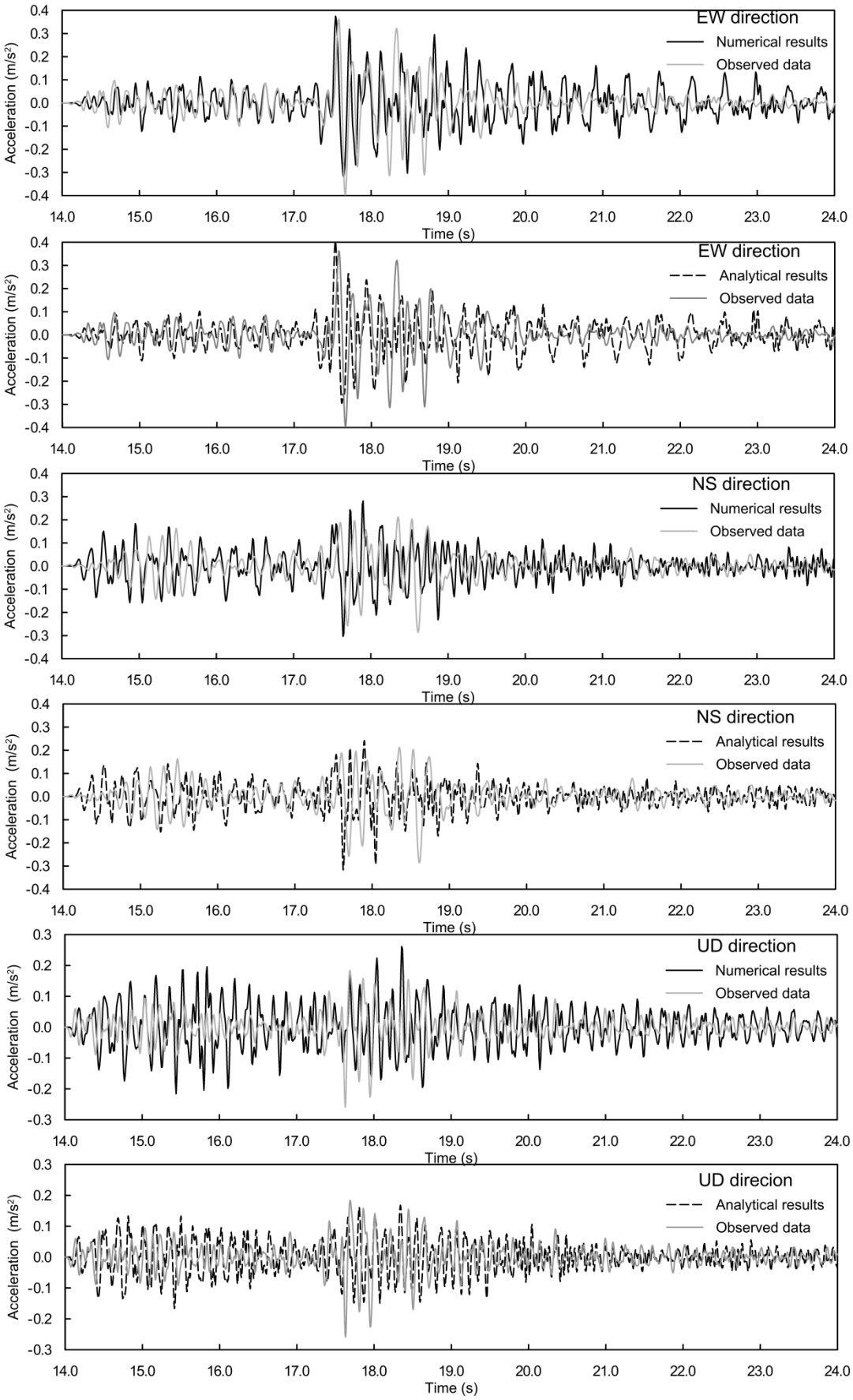


Figure 4-34: Linear analysis results under weak earthquake motion 1 (acceleration time histories)

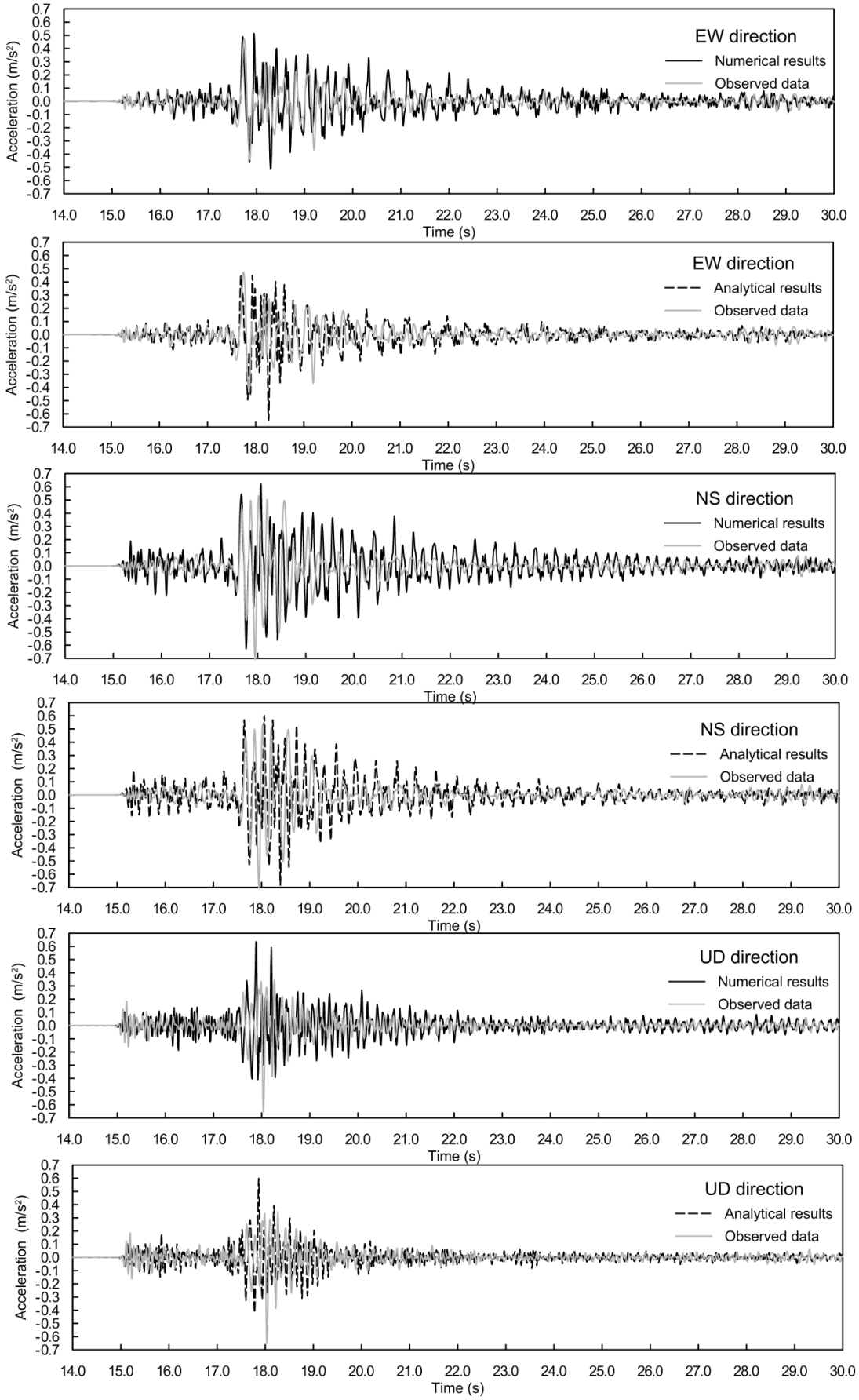


Figure 4-35: Linear analysis results under weak earthquake motion 2 (acceleration time histories)

Investigation of Rayleigh damping parameters for linear 3-D FE site response analysis

In order to investigate the appropriate employment of Rayleigh damping parameters for the linear 3-D FE site response analysis, parametric studies are conducted for the HINO site subjected to the weak earthquake motion 1. As previously discussed, the fundamental frequency in compression of the soil layer at the HINO site is used as ω_2 in the calibration of the Rayleigh damping parameters, while all other aspects of the FE modelling are the same as those used in the original linear FE analysis. The predicted acceleration response amplification spectra in the three directions are compared with the previous results and monitored data in Figure 4-36. It can be seen that the amplification factors of the modified predictions are effectively damped at frequencies larger than 2.5Hz. This is in agreement with the comparison of Rayleigh damping reproduced by the two FE analyses, shown in Figure 4-37. Particularly at approximately 6.0Hz (i.e. the fundamental frequency of the soil layer in the vertical direction), the predicted amplification factors for the vertical site response are closer to the analytical results and the monitored data. Furthermore, the predicted acceleration time histories at point A by employing the adjusted Rayleigh damping parameters are compared with the monitored data in Figure 4-38. It can be seen that the acceleration response is more reasonably predicted by the present FE analysis, compared to the numerical results from the original analysis (Figure 4-34). The acceleration values are effectively damped after t=20.0s due to the employment of the adjusted Rayleigh damping parameters.

Based on the Rayleigh damping variation graph (Figure 4-37), the Rayleigh damping ratios are equal to the target damping ratio at the frequencies ω_1 and ω_2, which are 2.5Hz and 6.0Hz for the present FE analysis. Furthermore, the employed soil permeability in the numerical analysis is considerably low (1.0E-7 m/s). Consequently, additional damping due to solid-pore fluid interaction is expected to be insignificant according to the results of Chapter 3. Therefore, the amplification factors of the numerically predicted site response at these two frequencies are expected to be identical to the ones from the analytical results. However, as observed in Figure 4-36, while this is the case for the horizontal dynamic response, it is not the case for the vertical site response. The amplification factors of the vertical site response at 6.0 Hz predicted by the numerical analysis are larger than the ones from the analytical solution. This could be related to the implementation of Rayleigh damping within the coupled consolidation

formulation. Therefore, in order to investigate this issue, another parametric study is carried out, where the 3-D site response of the HINO site under the weak earthquake motion 1 is simulated by the one-phase undrained FE analysis for the soil column under the water table, but keeping all other aspects of numerical model the same as in the previous FE analysis.

The predicted site response from the one-phase FE analysis is compared with the previous numerical results (employing the adjusted Rayleigh damping parameter) and the monitored data in Figure 4-39, in terms of acceleration response amplification spectra. It can be seen that no differences can be observed between the site response predicted by the one-phase FE analysis and the previous coupled FE analysis in the horizontal directions. However, for the vertical site response, the amplification factors predicted by the one-phase FE analysis are smaller than the ones from the previous coupled FE analysis. This implies that the two FE analyses result in different Rayleigh damping variations despite using identical parameters. Furthermore, the amplification factors for the vertical site response at the vertical fundamental frequency (6.0Hz) predicted by the one-phase FE analysis match with the ones from the one-phase analytical results, which is expected based on the assumed Rayleigh damping variation. The acceleration values predicted by the one-phase FE analysis in the vertical direction (Figure 4-40) are smaller than the previous coupled FE results (Figure 4-38), especially in the ranges of 14.0s-17.0s and 20.0s-24.0s. These observations indicate that the Rayleigh damping formulation should be extended to be compatible with the dynamic consolidation formulation. However, this issue will not be investigated more specifically in this work, since nonlinear FE analysis is able to directly simulate material damping by reproducing hysteretic soil behaviour.

Based on the investigation for Rayleigh damping in the linear FE site response analysis, it is suggested that attention should be paid to the appropriate application of the Rayleigh damping. In particular, firstly, the Rayleigh damping parameters ω_1 and ω_2 are suggested to be taken as the first horizontal and vertical fundamental frequencies of the studied soil profile, in order to more accurately simulate amplification effects at fundamental frequencies in all three directions. Secondly, when conducting the linear coupled FE analysis, the vertical site response is slightly overestimated, due to the fact that the existing Rayleigh damping formulation is not fully compatible with the coupled consolidation formulation. Furthermore, it should be noted that a 1.5% target damping

ratio is employed for the site response analysis in this part, which appropriately represents the material damping of the HINO site under the two weak motions. However, when subjected to stronger seismic motions, the Rayleigh damping ratio should be more carefully selected based on comparisons with corresponding equivalent linear analysis.

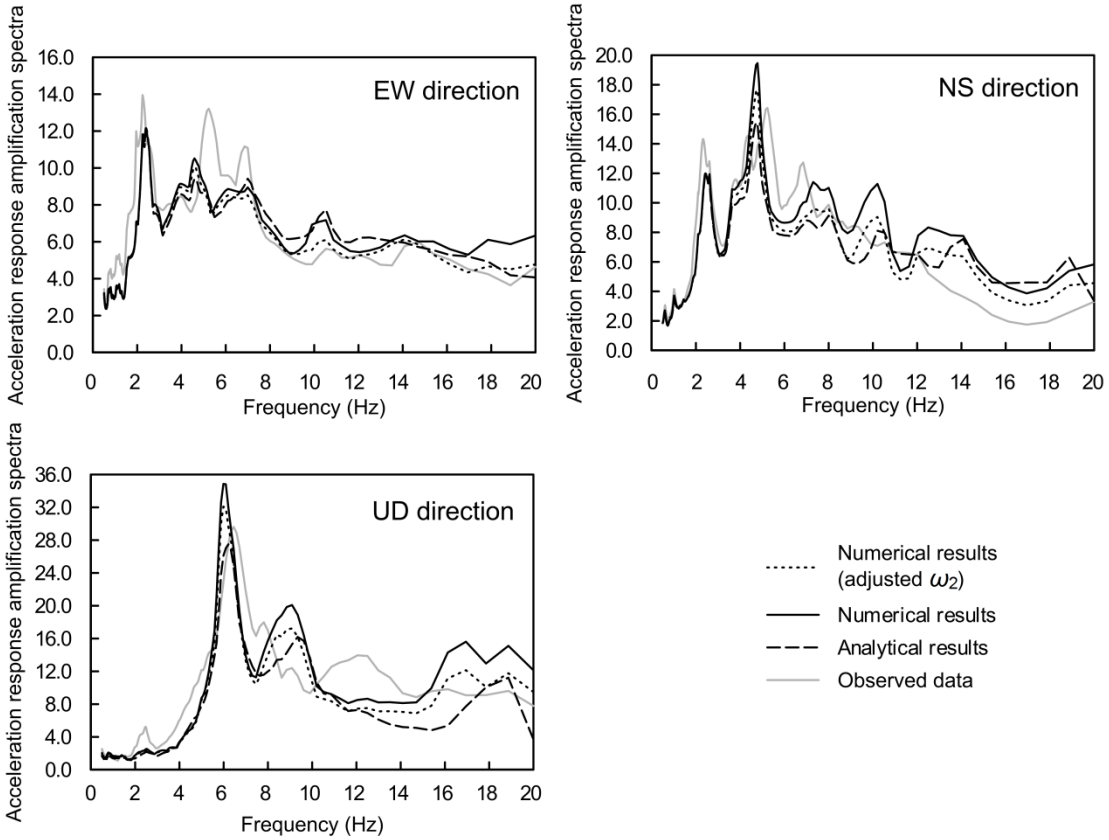


Figure 4-36: Linear analysis results under weak earthquake motion 1 (response amplification spectra) (adjusted Rayleigh damping parameter)

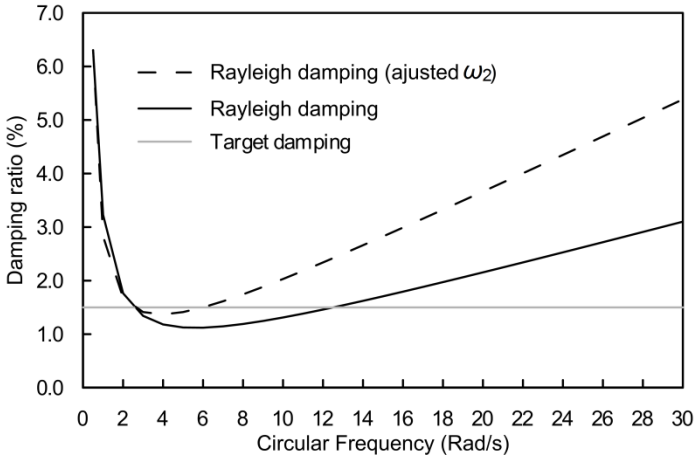


Figure 4-37: Comparison of Rayleigh damping

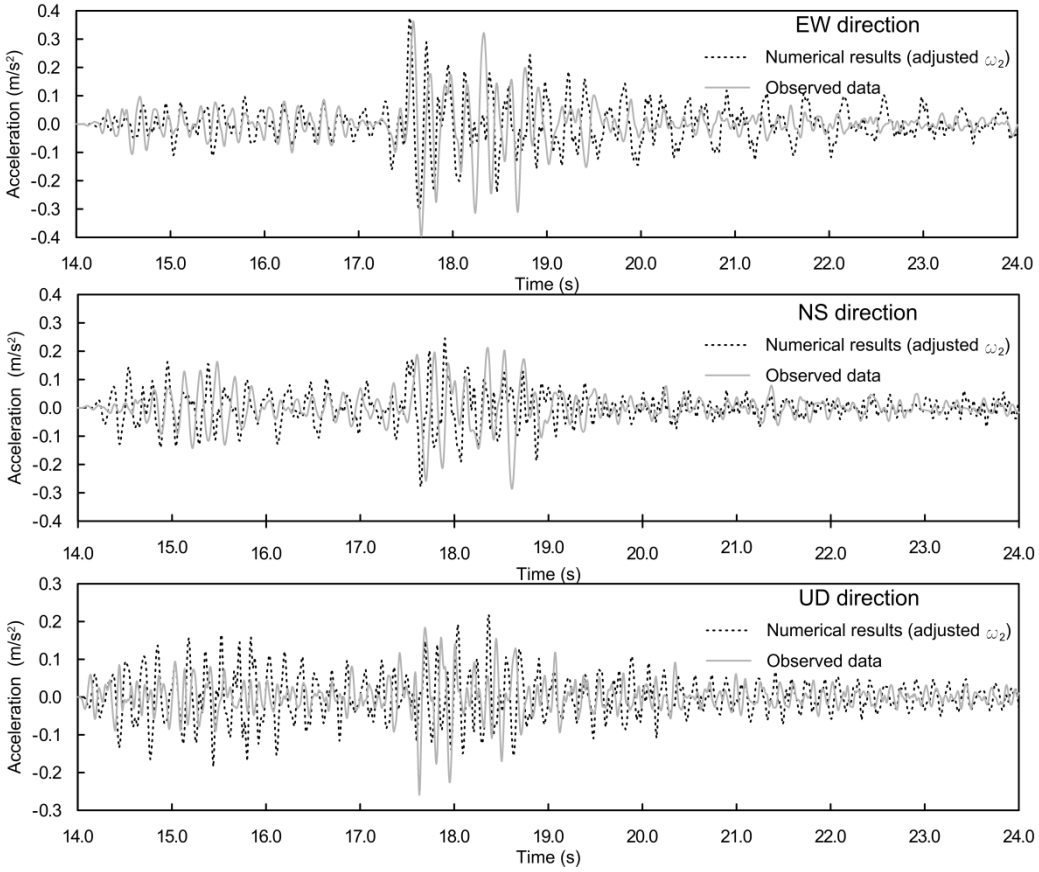


Figure 4-38: Linear analysis results under weak earthquake motion 1 (acceleration time histories) (adjusted Rayleigh damping parameter)

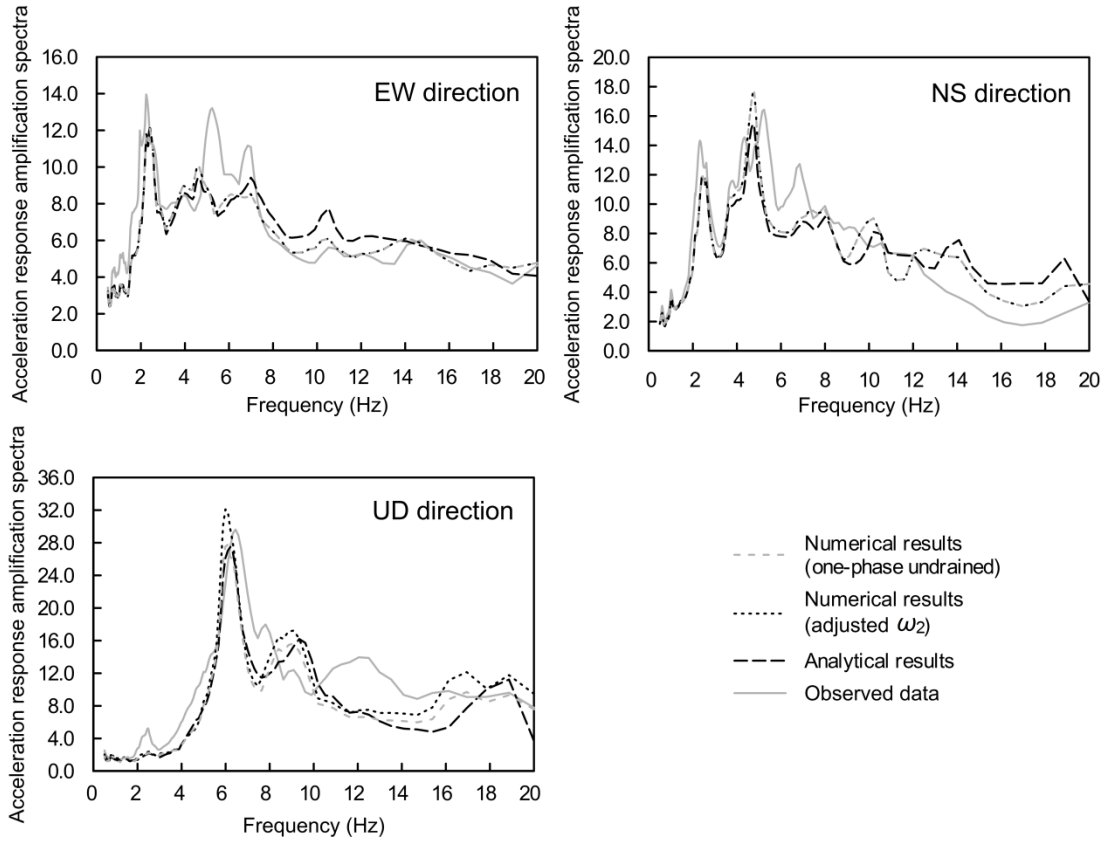


Figure 4-39: Linear analysis results under weak earthquake motion 1 (response amplification spectra) (one-phase undrained FE analysis)

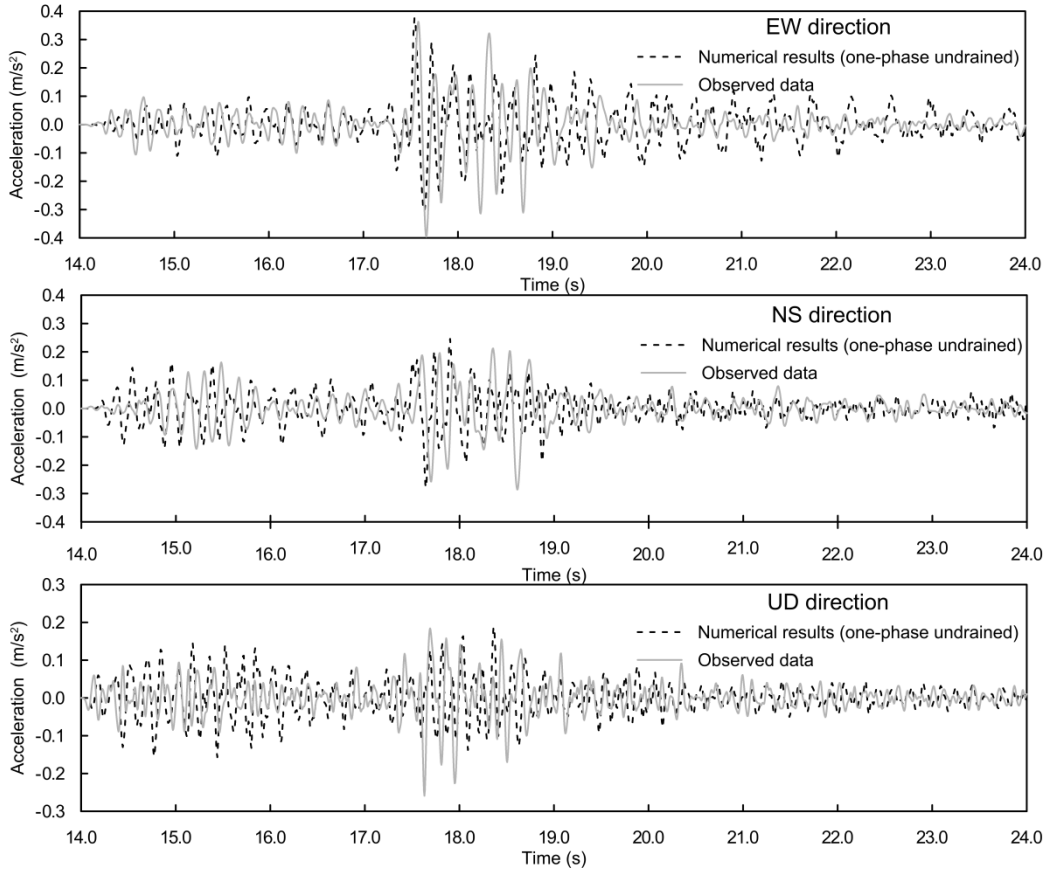


Figure 4-40: Linear analysis results under weak earthquake motion 1 (acceleration time histories) (one-phase undrained FE analysis)

4.5.2 Nonlinear analysis

4.5.2.1 Logarithmic model

Rayleigh damping has been widely used as an approximation of material damping in dynamic numerical analysis, but suffers from several drawbacks. Firstly, Rayleigh damping is frequency dependent, while in reality, soil material damping is nearly independent of frequency. Secondly, Rayleigh damping does not account for the variation of material damping with strain level, which is a fundamental aspect of dynamic soil behaviour. Thirdly, as shown in the previous study, the standard Rayleigh damping formulation is not fully compatible with the coupled consolidation formulation. Therefore, in this section, nonlinear constitutive models are employed for the FE site response analysis, to more accurately simulate material damping under earthquake loading. The logarithmic cyclic nonlinear model is firstly employed for the FE analysis to predict the pre-yield elastic soil behaviour, coupled with Mohr-Coulomb yield function that introduces plasticity in soil behaviour.

In this work, the parameters of the cyclic nonlinear models are calibrated by comparing the reproduced modulus degradation and damping curves against laboratory or in-situ tests. The shear and compressional soil deformations are respectively dependent on the shear and constrained moduli and therefore their characteristics in terms of modulus degradation and material damping are required to be separately calibrated. In particular, the shear modulus degradation and damping curves are compared with the empirical curves proposed by Imazu and Fukutake (1986) for gravelly materials based on laboratory tests. It should be noted that these empirical curves were also utilised by Izutani (2004) to investigate the site response at the HINO site under two earthquake events through 1-D shake-type analytical solution, achieving a reasonable prediction.

However, due to the limited investigation on strain-dependent variation of the constrained modulus, there is a lack of data for the calibration of cyclic nonlinear models concerning the constrained modulus degradation curves. Only recently, such work was attempted by LeBlanc et al. (2012) using in-situ testing apparatuses - the large mobile shaker. Constrained modulus degradation curves were proposed under different vertical confining pressures (σ_v), as shown in Figure 4-41. Under the lowest vertical confining pressure (20kPa), soil constrained modulus shows an increasing trend. This

was attributed to the soil dilatancy behaviour by LeBlanc et al. (2012). However, when subjected to other larger vertical confining pressures (i.e. 28-50kPa), soil constrained modulus exhibits clear degradations as the axial strain increases. It should be noted that the degradation curve under the condition of maximum vertical stress (50kPa) was found to be in agreement with the reduced constrained moduli of the HINO site materials back-analysed from the monitored data in a strong earthquake event (Beresnev et al. 2002). Therefore, this curve is selected for the calibration of cyclic nonlinear models employed in FE analyses. However, there is limited investigation of the material damping related to compressional soil deformation. The calibration for the material damping relating to compressional deformations would only depend on the calibration of constrained modulus. As mentioned before, the Logarithmic model considers only the shear modulus variation with cyclic shear strain. Therefore, the modulus degradation and damping curves for both shear and compressional deformations are determined by the same set of model parameters. This essentially implies that the overall calibration of the model should consider an optimum degradation response in both modes of deformation. The parameters of the Logarithmic model employed in the nonlinear FE site response analyses are listed in Table 4-5 and the calibration results are shown in Figure 4-42, in terms of modulus degradation and damping curves. It should be noted that the Mohr-Coulomb failure criterion is employed in FE analyses to simulate plastic soil behaviour. Therefore, the material damping simulated by the employed elasto-plastic model is also affected by material plasticity at high strain levels. However, this effect is not reflected in the calibration curves presented in Figure 4-42. To do so, single element FE analyses are suggested for a more accurate damping prediction in future research.

The FE mesh, boundary conditions, time integration method, input motions and initial stresses for the nonlinear analysis of the HINO site are the same as employed in the linear FE analysis.

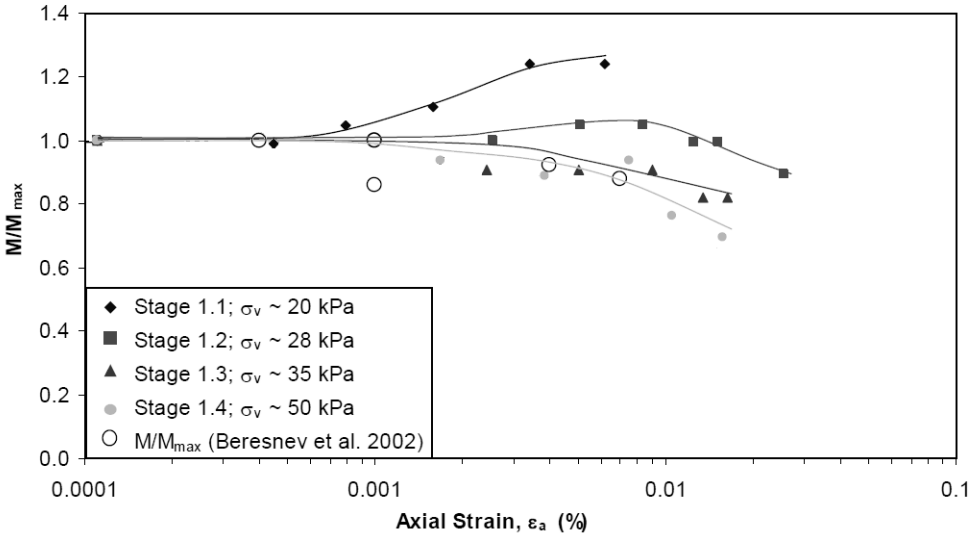


Figure 4-41: Constrained modulus degradation curves (after LeBlanc et al. (2012))

Table 4-5: Parameters of the Logarithmic model for the nonlinear analysis

Depth (GL. meters)	**Shear modulus G (kPa)**	**$E_{d,L}$**	**J_L**	**c**
0.0 ~ -4.0	3.20E+04	4.00E-03	2.50E+01	7.00E-01
-4.0 ~ -10.4	8.84E+04	3.00E-03	5.30E+01	7.00E-01
-10.4 ~ -20.0	3.22E+05	4.00E-03	2.30E+02	7.00E-01
-20.0 ~ -42.0	7.36E+05	3.00E-03	4.60E+02	7.00E-01
-42.0 ~ -84.0	2.35E+06	4.00E-03	1.84E+03	7.00E-01
-84.0 ~ -100.0	1.77E+07	2.40E-03	9.00E+03	7.00E-01

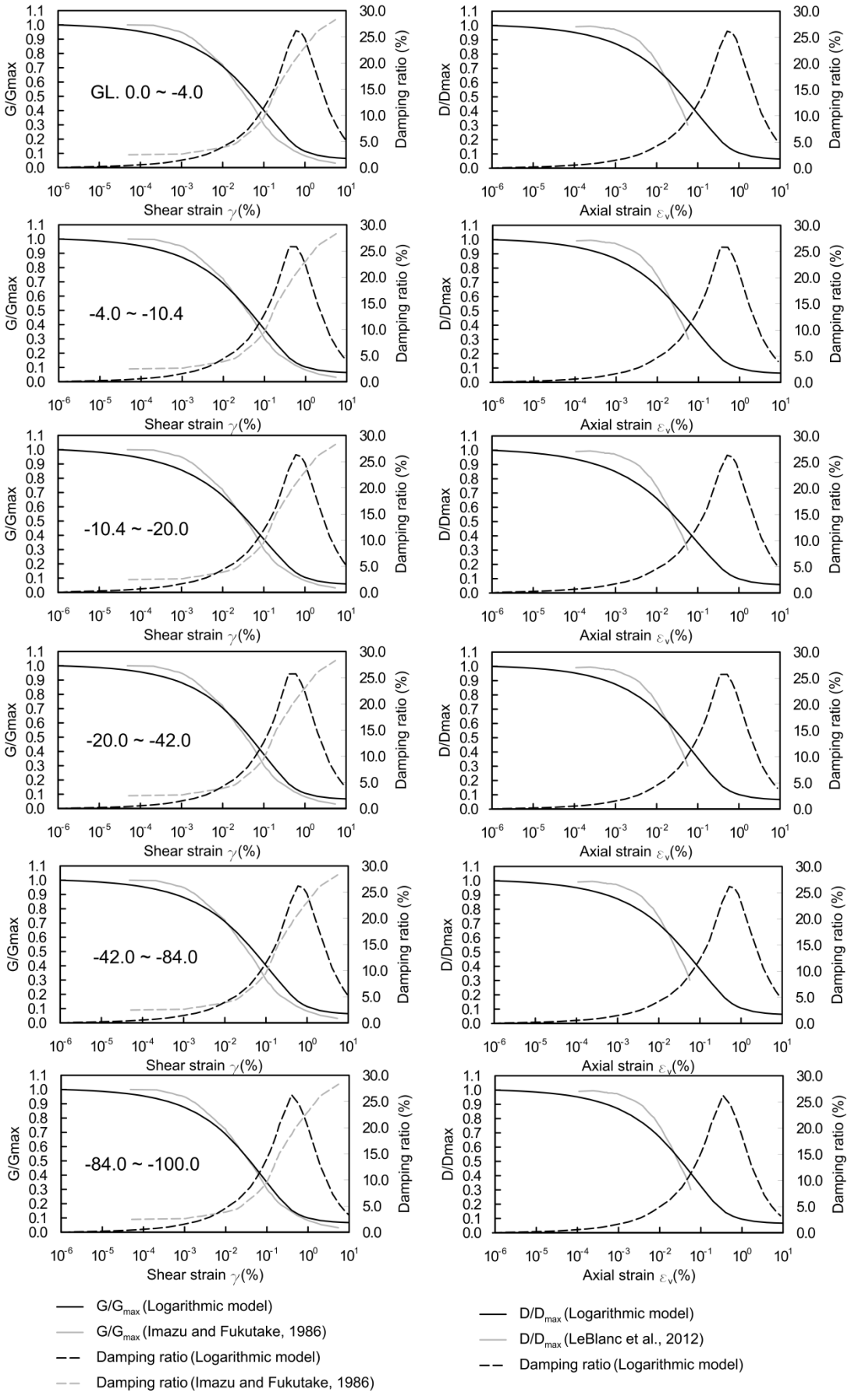


Figure 4-42: Calibration of the Logarithmic model for nonlinear analyses

The predicted site response for the two weak earthquake motions are compared with the monitored data, in terms of the acceleration response amplification spectra between the top (point A) and bottom boundaries in Figures 4-43 and 4-45, and in terms of acceleration time histories at monitoring point A in Figures 4-44 and 4-46. The acceleration response amplification spectra for the weak motion 1 (Figure 4-43) show that the nonlinear FE analysis can accurately predict the fundamental frequencies in the EW and NS directions. These are estimated to be approximately 2.5Hz in accordance with the results obtained from the linear FE analysis and the monitored data. This agreement indicates that the weak motion 1 does not induce any significant nonlinearity in the soil layer. However, the fundamental frequency for the vertical site response is under-predicted by the nonlinear FE analysis. The underestimation is due to the inappropriate calibration for the constrained modulus degradation, which is shown in Figure 4-42. The reproduced constrained modulus starts to degrade at smaller strain levels than the empirical curve. It should be pointed out that the nonlinear analysis is unable to accurately predict the second amplification peak in the NS direction. The reason for this problem is discussed in the subsequent Section 4.5.2.3.

The nonlinear FE analysis generally overestimates the amplification factors in all three directions. This is also reflected in the overprediction of the acceleration time histories shown in Figure 4-44. The overestimated acceleration response is due to the underestimation of material damping at very small strain levels by the Logarithmic model, as shown in Figure 4-42, which is a general problem for cyclic nonlinear models. Concerning the predicted site response for the weak motion 2, similar observations are obtained. The fundamental frequencies for two horizontal directions are accurately predicted, the fundamental frequency for the vertical site response is underestimated and the dynamic response is over-predicted by the nonlinear FE analysis, as shown in Figures 4-45 and 4-46.

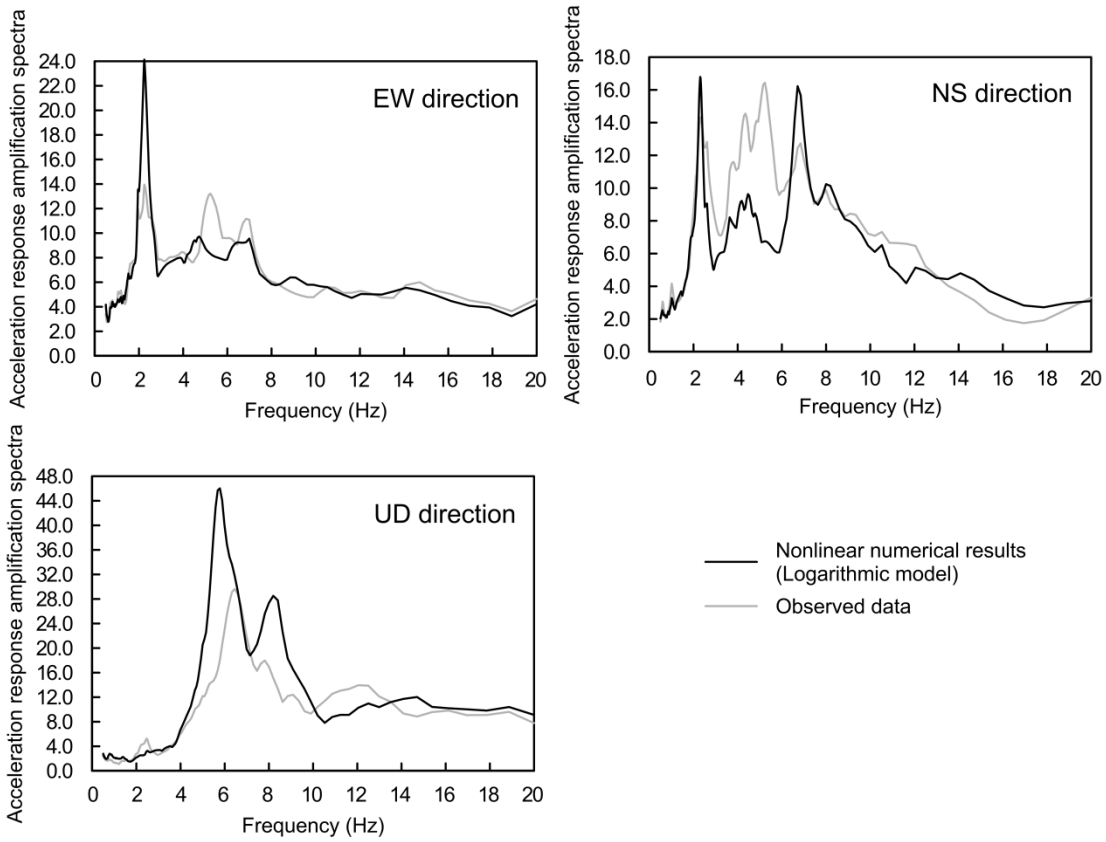


Figure 4-43: Nonlinear analysis results under weak earthquake motion 1 (response amplification spectra) (Logarithmic model)

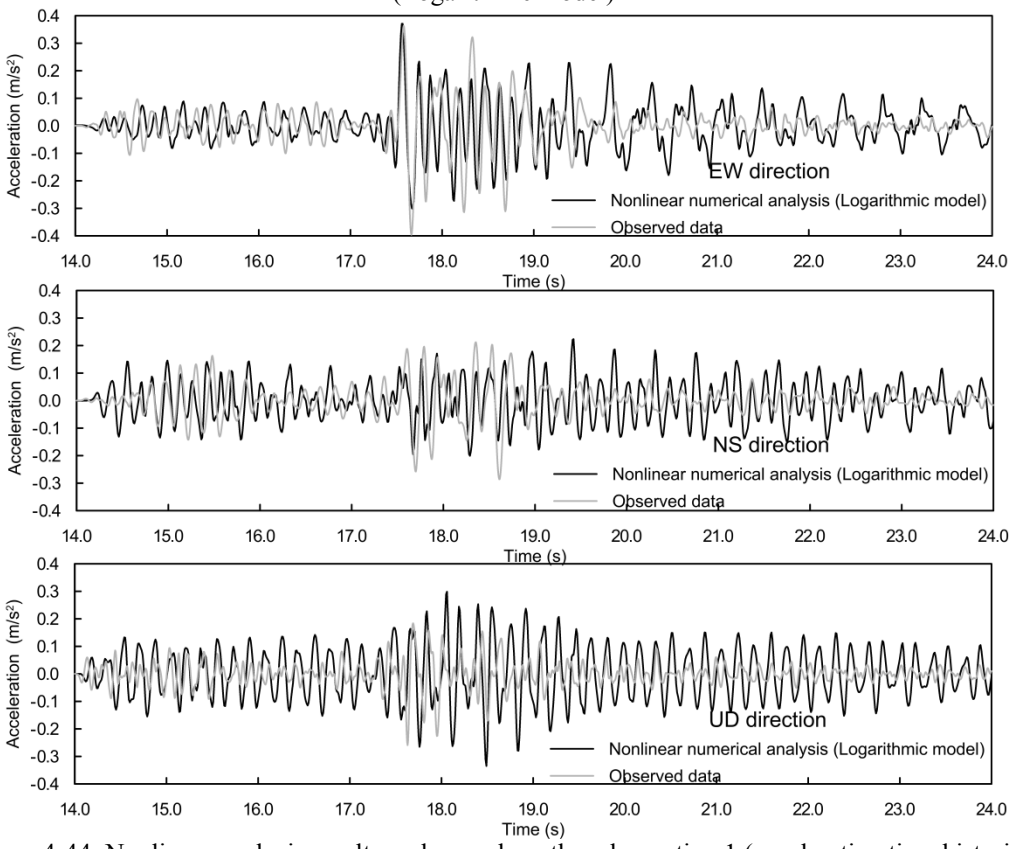


Figure 4-44: Nonlinear analysis results under weak earthquake motion 1 (acceleration time histories) (Logarithmic model)

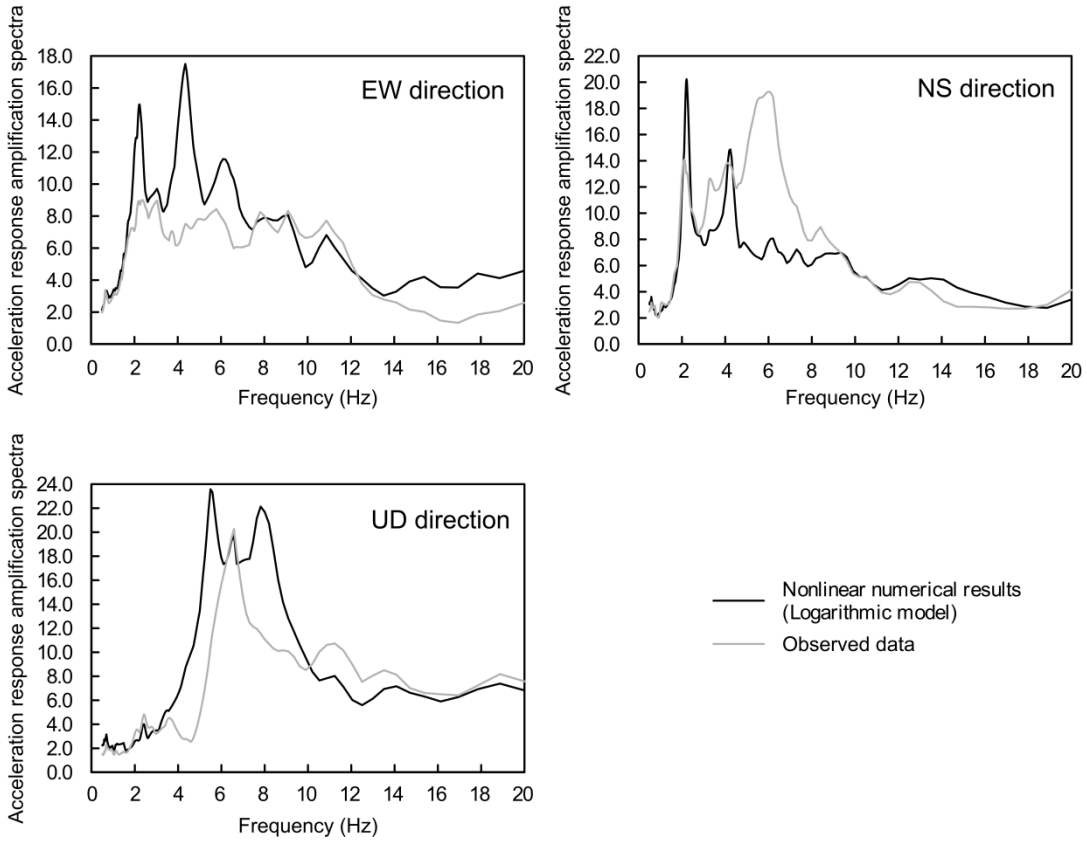


Figure 4-45: Nonlinear analysis results under weak earthquake motion 2 (response amplification spectra) (Logarithmic model)

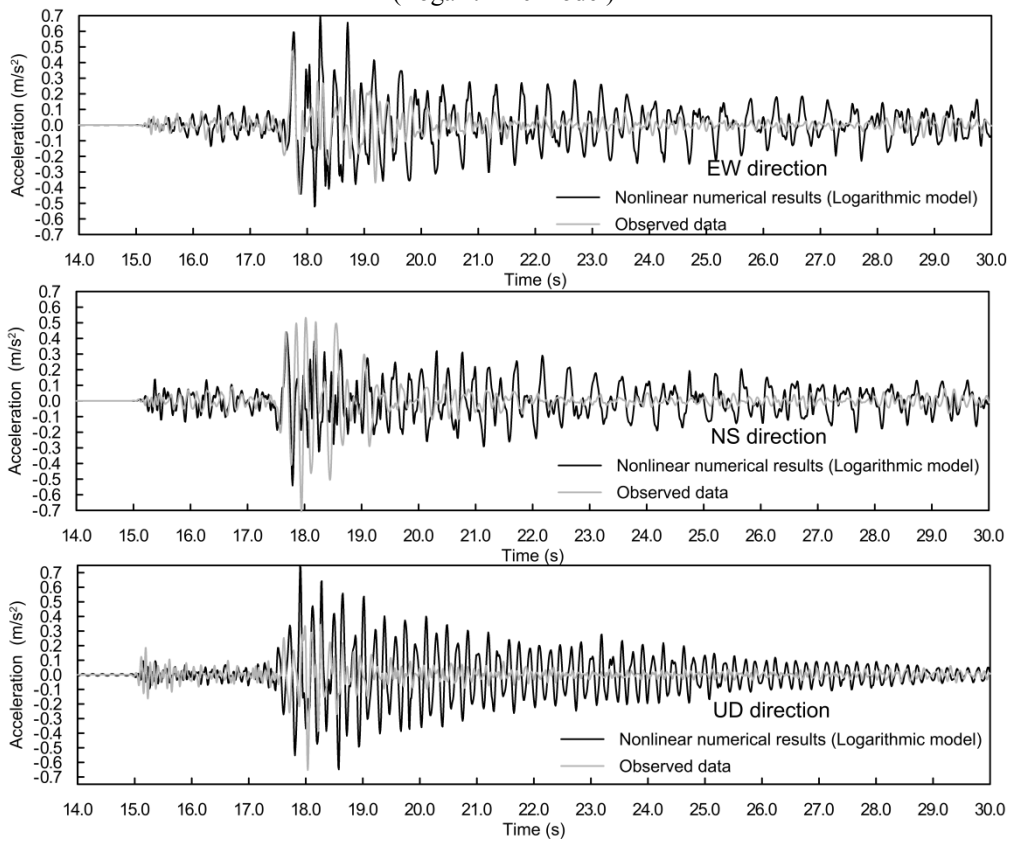


Figure 4-46: Nonlinear analysis results under weak earthquake motion 2 (acceleration time histories) (Logarithmic model)

4.5.2.2 ICG3S-1 model

In order to improve the simulation of material damping at very small strain levels, the ICG3S model is employed for the nonlinear FE analysis of the HINO site for the two weak earthquake motions. The model parameters are listed in Table 4-6 and the calibration curves are shown in Figure 4-47. It should be noted that the simpler version of the ICG3S model is firstly utilised for the nonlinear site response analysis, which employs a variation for the shear modulus with cyclic shear strains and a constant Poisson's ratio. This essentially implies that an identical degradation is adopted for the constrained modulus and this version of the model is denoted herein as the ICG3S-1 model. For the ICG3S-1 model, the material damping at very small strain levels can be increased by employing a varying scaling factor n_1 introduced in Section 4.3.1. Figure 4-47 shows that, compared to the results generated by the Logarithmic model, the material damping reproduced by the ICG3S-1 model is higher at very small strain levels, without significantly affecting the modulus degradation curve. On the other hand, at extremely small strain levels ($<10^{-5}$%), the material damping simulated by the ICG3S-1 model still starts from zero. This under-prediction cannot be mathematically avoided by cyclic nonlinear model formulations. However, the seismic deformation associated with this range is only due to extremely small oscillations, which are beyond the common consideration for geotechnical earthquake engineering problems. It should be noted that the material damping of the shear deformation at higher strain levels is over-estimated by the ICG3S-1 model, compared with the empirical curves. However this can be practically ignored for the analyses for the weak earthquake motions, as high strain levels are not mobilised.

The ICG3S-1 model predictions are compared with the Logarithmic model predictions and the monitored data, in terms of the acceleration response amplification spectra between the top (point A) and bottom boundaries in Figures 4-48 and 4-50, and in terms of acceleration time histories at monitoring point A in Figures 4-49 and 4-51. The ICG3S-1 model results are in better agreement with the recorded data than the Logarithmic model results, in terms of amplification ratios for both weak motions, as shown in Figures 4-48 and 4-50. Furthermore, more accurate acceleration time histories are predicted by the ICG3S-1 model compared with the monitored data for both earthquake events (Figures 4-49 and 4-51) in particular after t=20.0s. Furthermore, the frequency content of the dynamic response predicted by both models is very similar for

both horizontal directions. As previously discussed, the reproduced modulus degradation curves are not significantly affected by employing the ICG3S-1 model.

However, the fundamental frequencies of the vertical site response are still underestimated by the nonlinear analysis employing the ICG3S-1 model (Figures 4-48 and 4-50). As explained before, this can be attributed to the inadequate modelling of the constrained modulus degradation.

Table 4-6: Parameters of the ICG3S-1 model for the nonlinear analysis

Depth (GL. meters)	**a**	**b**	**c**	**d_1**	**d_2**	**d_3**	**d_4**
0.0 ~ -100.0	5.00E-04	4.00E+00	5.00E-02	7.28E+01	2.28E-01	6.77E+02	7.58E-01

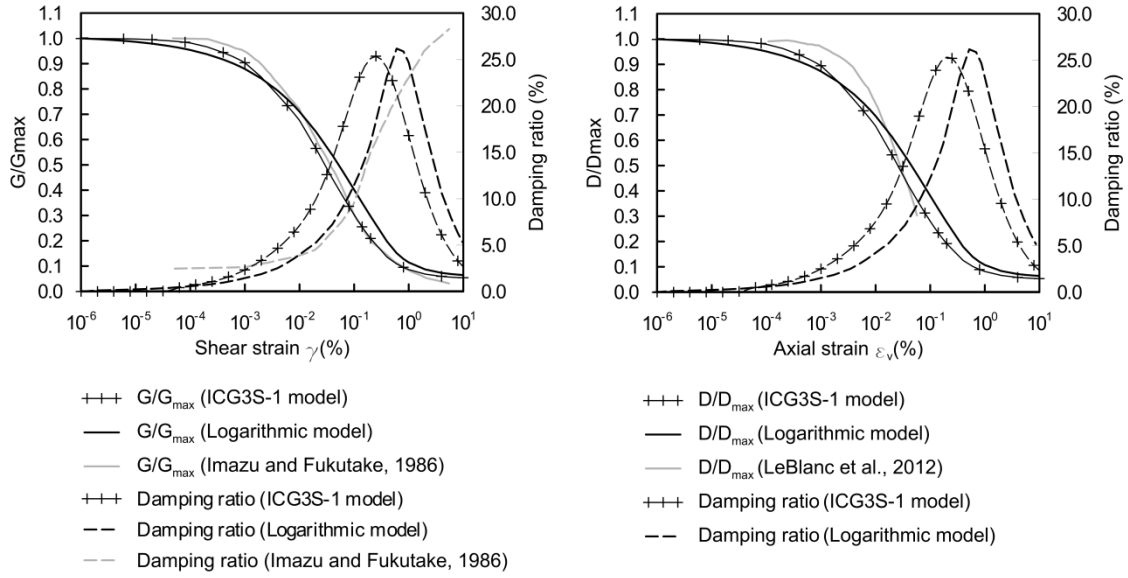


Figure 4-47: Calibration of the ICG3S-1 model for nonlinear analysis

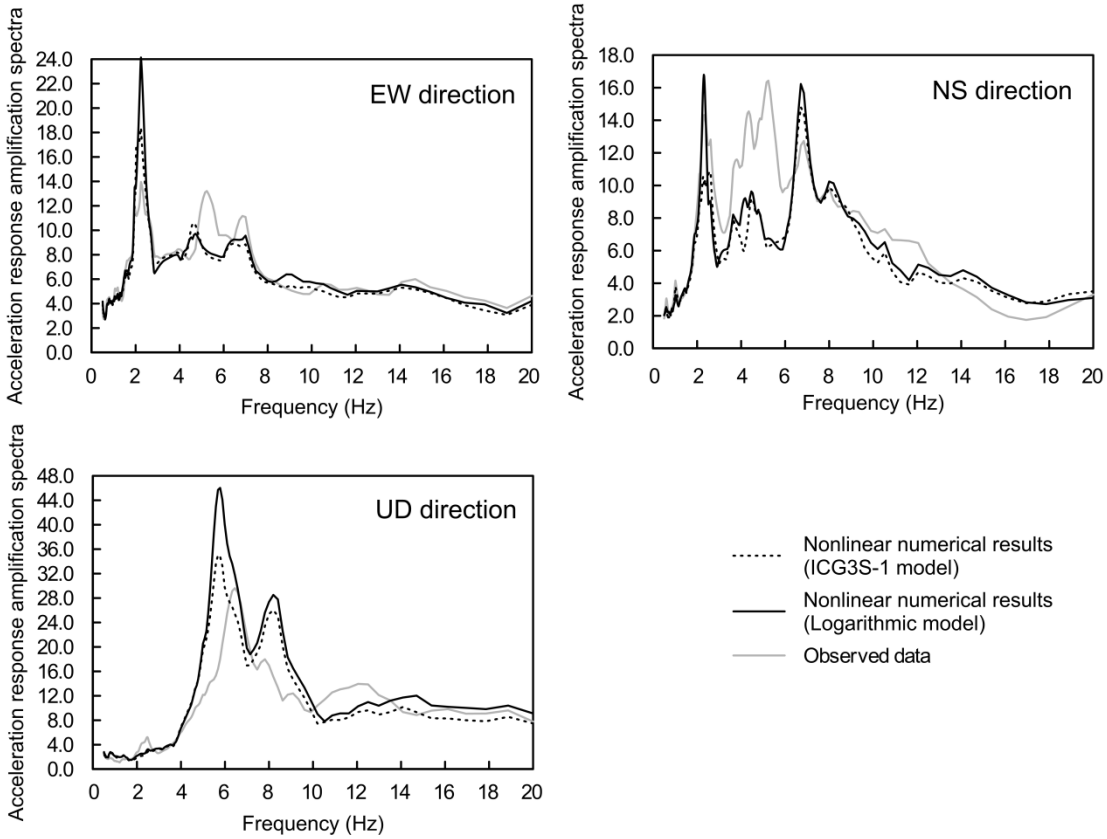


Figure 4-48: Nonlinear analysis results under weak earthquake motion 1 (response amplification spectra) (ICG3S-1 model)

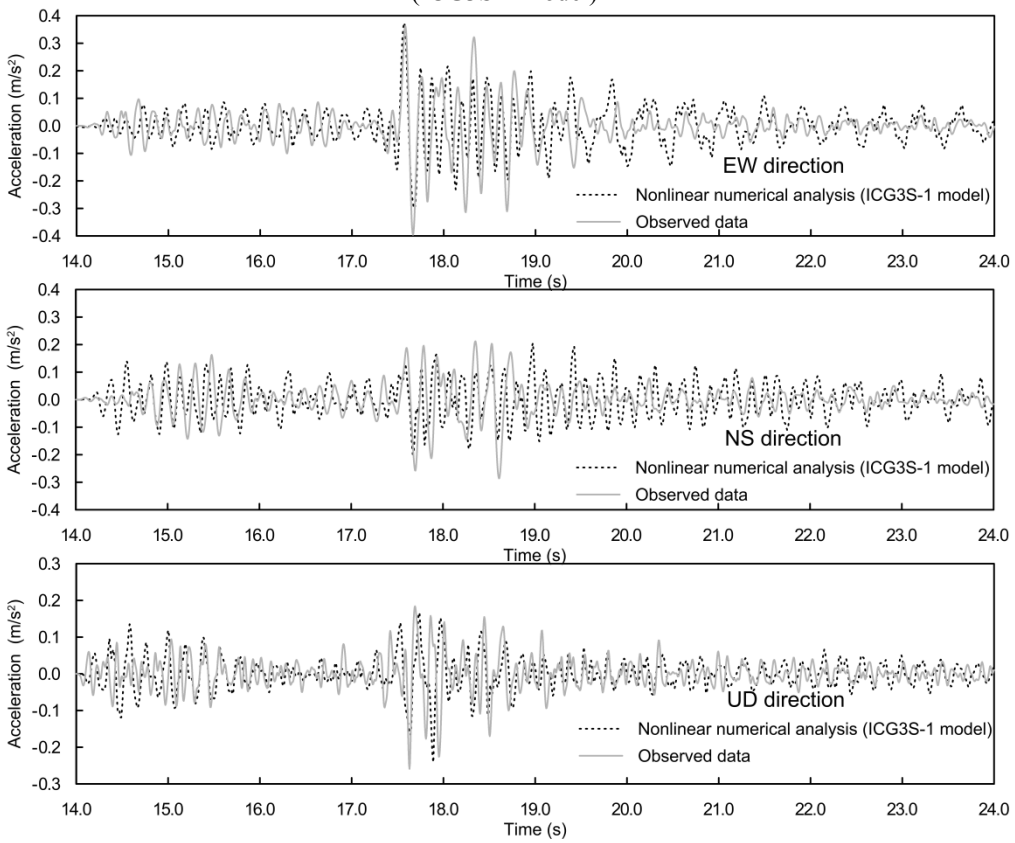


Figure 4-49: Nonlinear analysis results under weak earthquake motion 1 (acceleration time histories) (ICG3S-1 model)

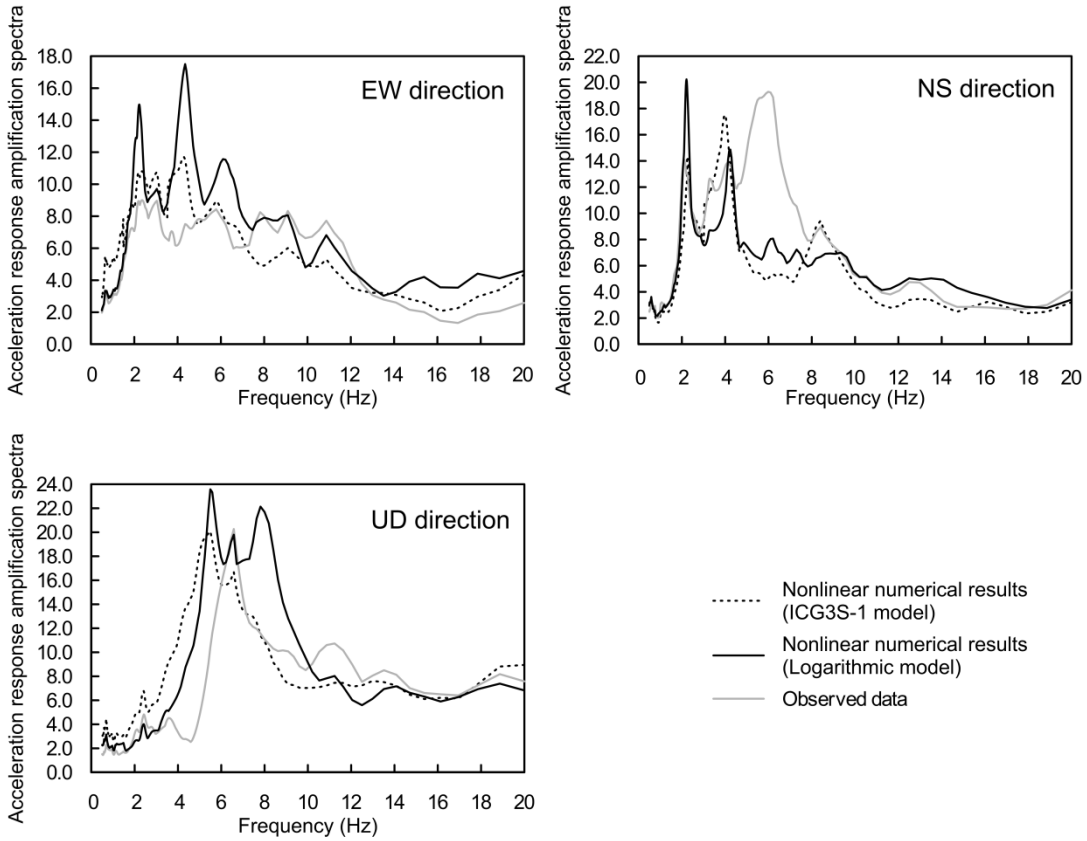


Figure 4-50: Nonlinear analysis results under weak earthquake motion 2 (response amplification spectra) (ICG3S-1 model)

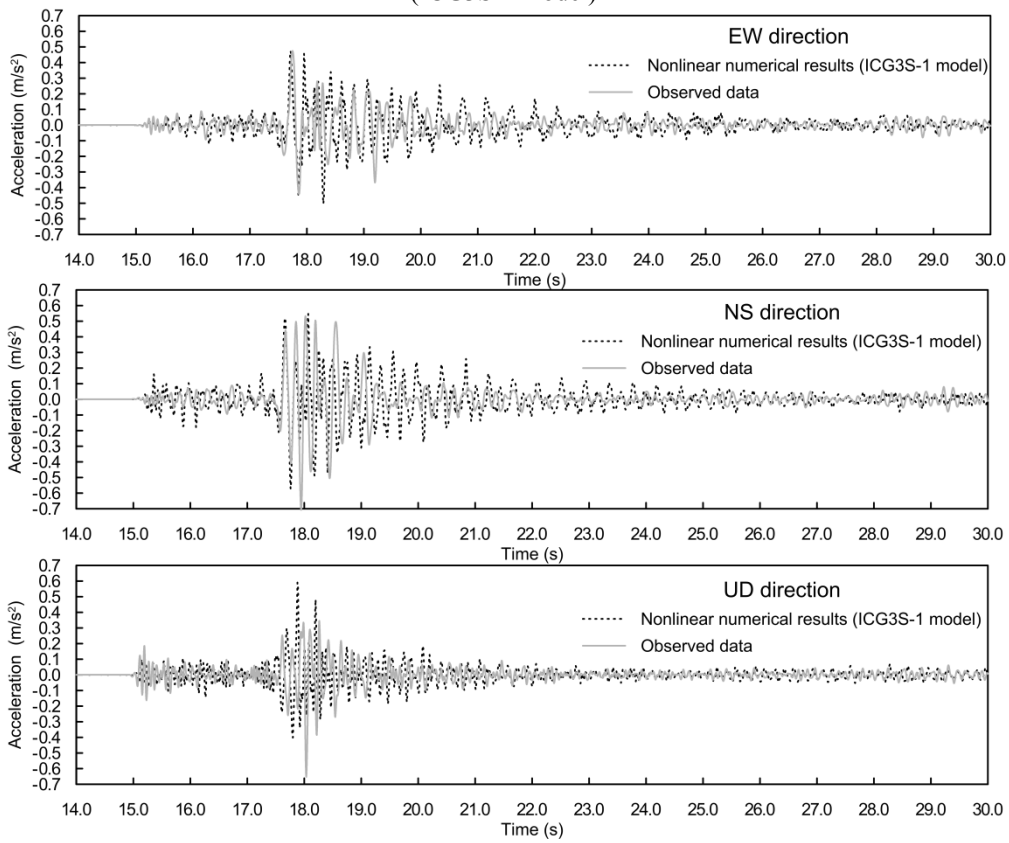


Figure 4-51: Nonlinear analysis results under weak earthquake motion 2 (acceleration time histories) (ICG3S-1 model)

4.5.2.3 ICG3S-2 model

In order to achieve more accurate calibration for the compressional deformation, the ICG3S-2 model is employed for the nonlinear FE site response analysis of the HINO site. In this model the modulus degradation and damping curves for shear and compressional deformations are independently controlled by two sets of model parameters. The ICG3S-2 model parameters for the nonlinear FE analysis are listed in Table 4-7. The calibration curves of the ICG3S-2 model are shown in Figure 4-52 and compared to the ones generated by the previous constitutive models. It should be noted that the model parameters controlling the shear deformation are the same as the ones used for the ICG3S-1 model, hence resulting in identical shear modulus degradation and damping curves. However, a new set of parameters is employed to control the calibration of compressional deformation, based on which the independently reproduced constrained modulus degradation curve matches well with the empirical one.

The ICG3S-2 model predictions are compared with the ICG3S-1 model predictions and the monitored data, in terms of the acceleration response amplification spectra between the top (point A) and bottom boundaries, in Figures 4-53 and 4-55, and in terms of acceleration time histories at monitoring point A in Figures 4-54 and 4-56. More specifically, as shown in Figures 4-53 and 4-55, the response amplification spectra in the two horizontal directions are similar for both ICG3S models. However, at some frequencies, the amplification factors predicted by the ICG3S-2 model are slightly larger than the ones predicted by the ICG3S-1 model. Particularly the ICG3S-2 model achieves a more accurate prediction for the second amplification peak in the NS direction for the weak motion 1. This observation is due to the fact that the reversal behaviour for the shear deformations is independent of the reversal behaviour associated with the volumetric deformation for the ICG3S-2 model and therefore less hysteretic loops are simulated, resulting in smaller material damping. However, the ICG3S-2 model still could not predict the second amplification peak in the NS direction for the weak motion 2, which is found to be at 6.0Hz. However, the numerical predictions for both weak motions and the observed data for the weak motion 1 all show that the second amplification peak is approximately at 4.5Hz. Consequently, it is likely that the observed second amplification peak from weak motion 2 was not real, but has resulted from a potential noise in the record.

For the vertical site response shown in Figures 4-53 and 4-55, the fundamental

frequencies predicted by the ICG3S-2 model are larger than the ones predicted by the ICG3S-1 model and therefore agree better with the monitored data. This is a consequence of the adopted calibration, where the constrained modulus reproduced by the ICG3S-2 model degrades more moderately compared with the one from the ICG3S-1 model (as shown in Figure 4-52). Overall, the ICG3S-2 model achieves satisfactory predictions for the 3-D site response at the HINO site for the two weak motions, both in terms of response amplification spectra and time histories.

Table 4-7: Parameters of the ICG3S-2 model for the nonlinear analysis

	Parameters for the shear deformation						
Depth (GL. meters)	**a**	**b**	**c**	**d_1**	**d_2**	**d_3**	**d_4**
0.0 ~ -100.0	5.00E-04	4.00E+00	5.00E-02	7.28E+01	2.28E-01	6.77E+02	7.58E-01
	Parameters for the compressional deformation						
Depth (GL. meters)	**r**	**s**	**t**	**d_5**	**d_6**	**d_7**	**d_8**
0.0 ~ -100.0	5.00E-04	8.00E+00	5.00E-02	7.28E+01	2.28E-01	6.77E+02	7.58E-01

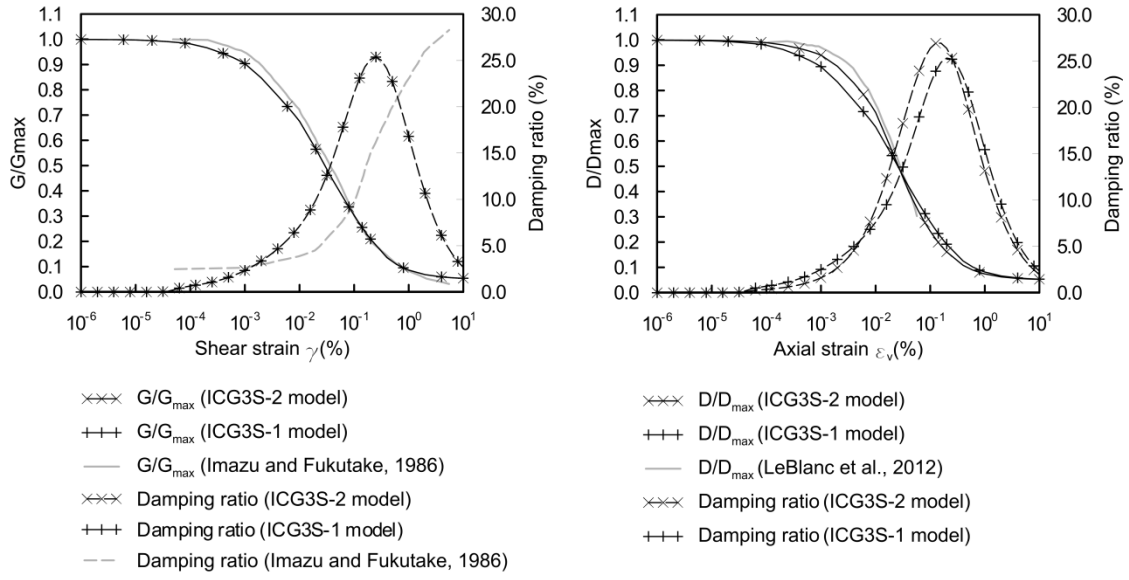


Figure 4-52: Calibration of the ICG3S-2 model for the nonlinear analysis

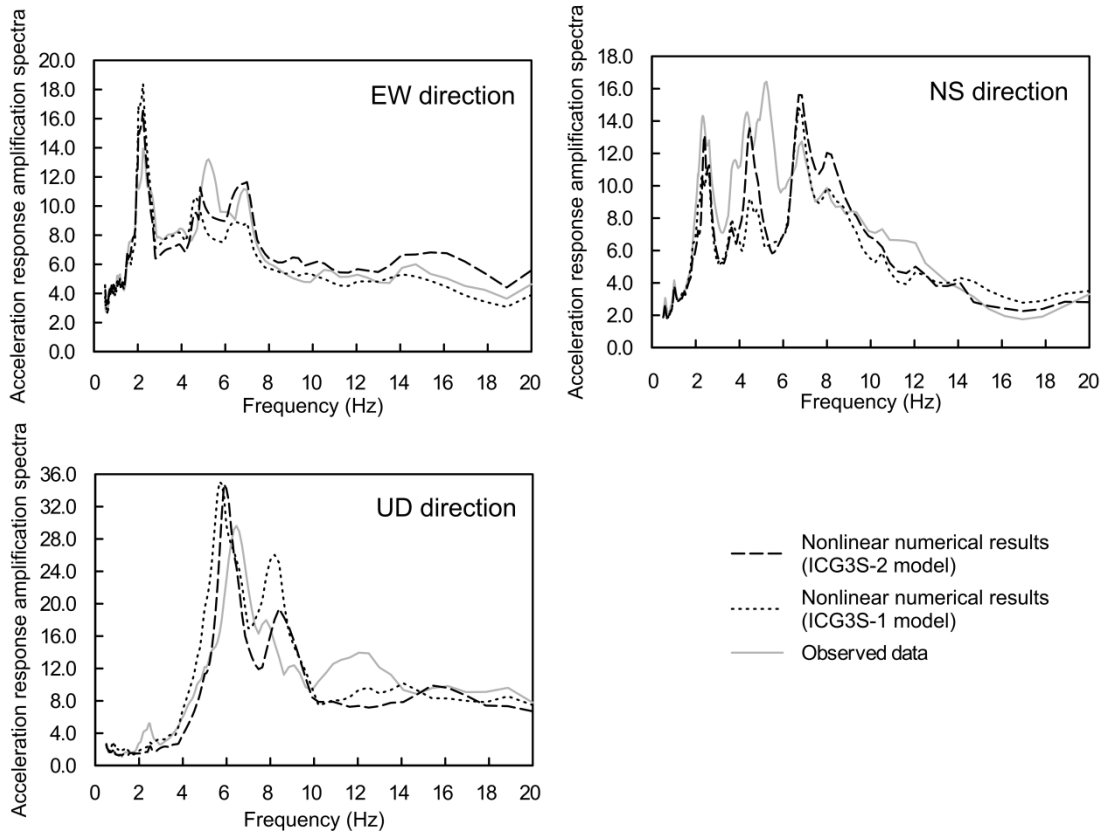


Figure 4-53: Nonlinear analysis results under weak earthquake motion 1 (response amplification spectra) (ICG3S-2 model)

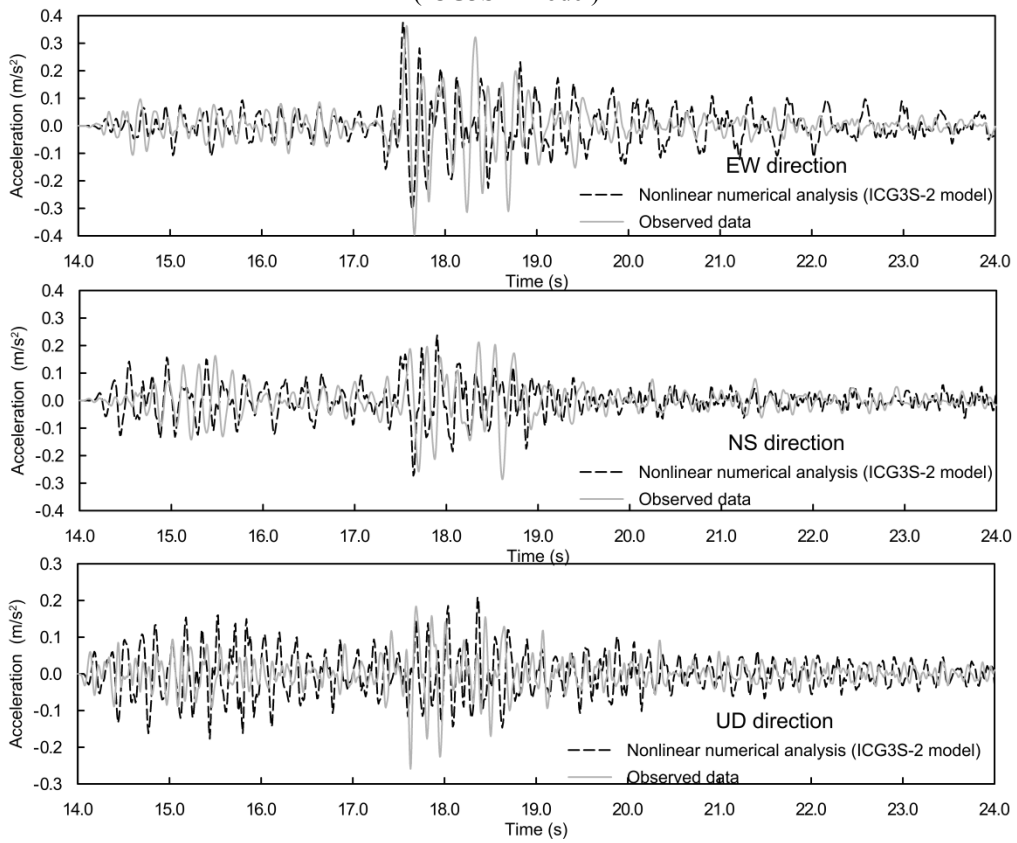


Figure 4-54: Nonlinear analysis results under weak earthquake motion 1 (acceleration time histories) (ICG3S-2 model)

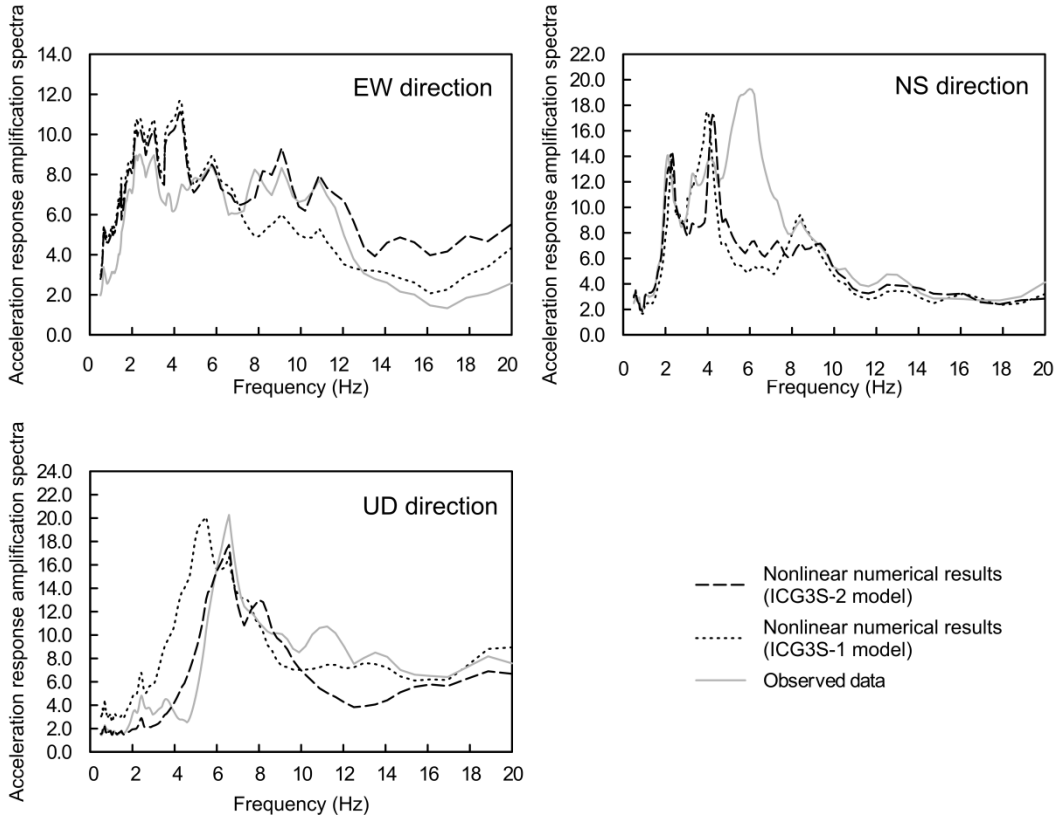


Figure 4-55: Nonlinear analysis results under weak earthquake motion 2 (response amplification spectra) (ICG3S-2 model)

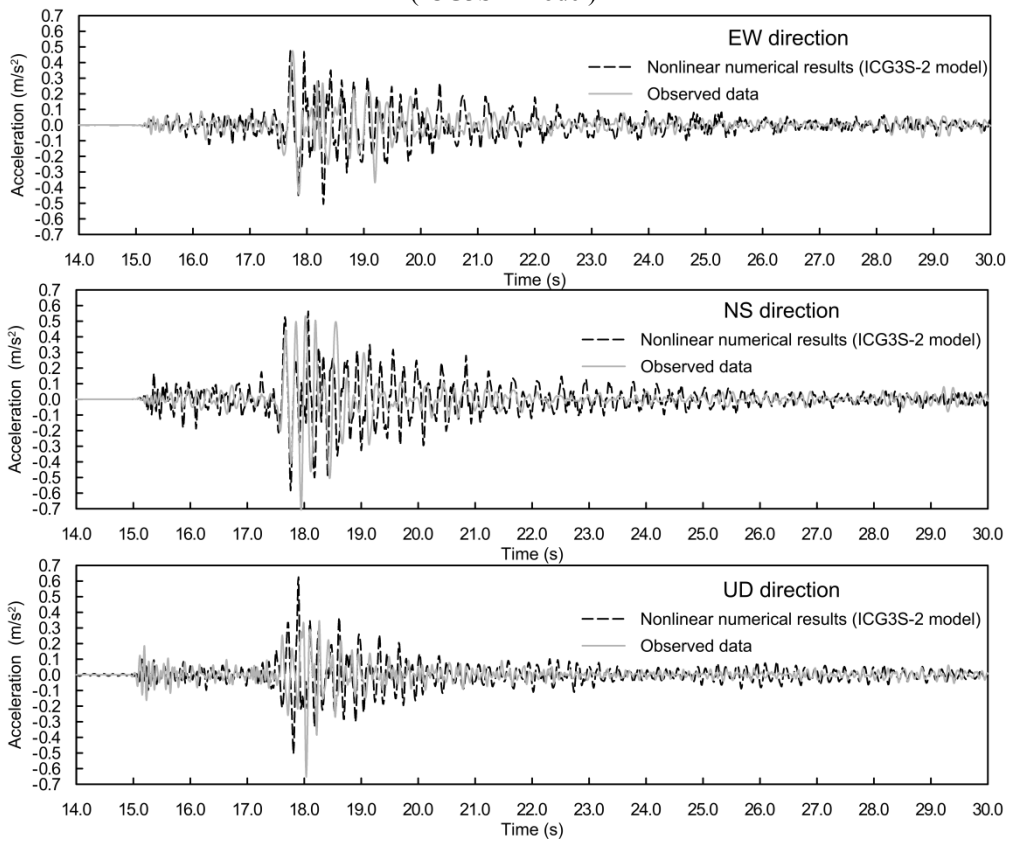


Figure 4-56: Nonlinear analysis results under weak earthquake motion 2 (acceleration time histories) (ICG3S-2 model)

4.5.2.4 Comments

The 3-D site response of the HINO site subjected to two weak earthquake motions is simulated by the nonlinear FE analysis employing three different cyclic nonlinear models, i.e. the Logarithmic, ICG3S-1 and ICG3S-2 models. Based on the presented numerical results, the 3-D site response is reasonably well simulated by the nonlinear FE analysis.

Firstly, based on the site response predicted by the Logarithmic model, the fundamental frequencies of the soil layer in the two horizontal directions are accurately reproduced by the nonlinear FE analysis. However, due to the underestimation of material damping at very small strain levels, the site response is over-predicted, which is a general problem for most cyclic nonlinear models. Furthermore, the fundamental frequency in the vertical direction is underestimated by the Logarithmic model, due to the inadequate modelling of the constrained modulus degradation.

In order to increase the material damping at very small strain levels, the ICG3S-1 model is employed for the nonlinear FE site response analysis. The results show that the site response is effectively damped by the introduced larger material damping. However, the ICG3S-1 model still cannot achieve accurate simulations for the constrained modulus degradation.

Lastly, by employing the ICG3S-2 model, the soil constrained modulus degradation is accurately predicted by the nonlinear FE site response analysis, due to the independent simulation of shear and compressional deformations. The computed site response is found to be in good agreement with the recorded response. Therefore, the ICG3S-2 model is suggested for the nonlinear FE site response analysis subjected to weak earthquake motions. Firstly, the ICG3S-2 model can simulate more accurately the material damping at very small strain levels. Furthermore, by employing the ICG3S-2 model, both the horizontal and the vertical site response can be accurately predicted by independently controlling the degradation of the shear and the constrained moduli.

4.6 Multi-directional site response analysis subjected to strong earthquake motions

4.6.1 Logarithmic model

In this part, the site response of the HINO site subjected to the main earthquake motion of the 2000 Western Tottori earthquake is simulated by the 3-D nonlinear coupled FE analysis. The soil properties, FE mesh, boundary conditions and time integration method are the same as those employed in Section 4.5.2. The strong earthquake motion monitored at the base layer of the HINO down-hole on 06/10/2000 (Figure 4-25) is uniformly prescribed at the bottom boundary of the FE mesh as the input motion for the site response analysis. The Logarithmic model is initially employed to simulate the dynamic soil behaviour. The associated model parameters and calibration are shown in Table 4-5 and Figure 4-42 respectively. The site response at the HINO site is also investigated by employing the frequency-domain analytical solution (EERA), where three separate equivalent-linear analyses are carried out to predict the site response in the three directions. It should be noted that the modulus degradation and damping curves implemented in the analytical solution are based on corresponding reference curves shown in Figure 4-42. However, due to the lack of damping data for the compressional soil deformation, the reproduced damping curve by the Logarithmic model is employed in the vertical site response analysis of EERA.

The numerically and analytically predicted 3-D site response of the HINO site is shown in Figures 4-57 and 4-58, in terms of the acceleration response amplification spectra between the top (point A) and bottom boundaries and acceleration time histories at monitoring point A respectively. In particular, the former show that both horizontal directions are reasonably simulated by the nonlinear FE analysis and the equivalent-linear analytical solution, both in terms of the frequency content and amplification factors. However, a significant discrepancy is observed between the vertical site response predicted by the analytical solution and the monitored data. The fundamental frequency for the vertical response is not accurately predicted and the amplification factors in the frequency range between 5.0Hz and 9.0Hz are significantly overestimated, showing the inadequacy of the one-phase analytical solution. However, the numerically predicted vertical site response is found to agree better with the monitored data. In particular, the fundamental frequency for the vertical site response is

accurately simulated and the amplification factors agree with the monitored data except in the range between 5.0Hz and 9.0Hz, where the amplification factors are overestimated by the FE analysis. The overestimation of the amplification factors for the vertical site response in the high frequency range is probably due to the underestimated material damping at very small strain levels by the Logarithmic model. Furthermore, concerning the numerically and analytically predicted acceleration time histories, based on Figure 4-58, the acceleration time histories in the two horizontal directions are reasonably well predicted by both the FE analysis and the analytical solution. The vertical acceleration values are overestimated by both methods, corresponding to the over-predicted response amplification factors of the vertical site response in Figure 4-57.

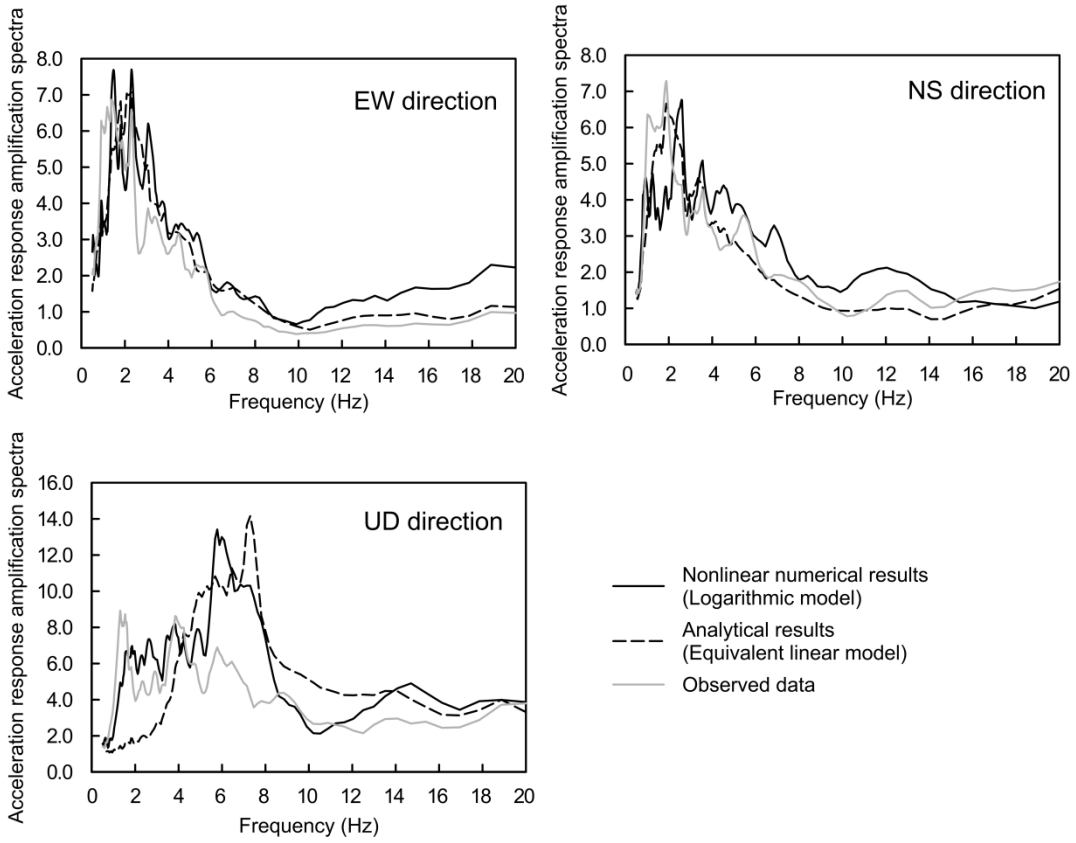


Figure 4-57: Nonlinear analysis results under Western Tottori earthquake (response amplification spectra) (Logarithmic model)

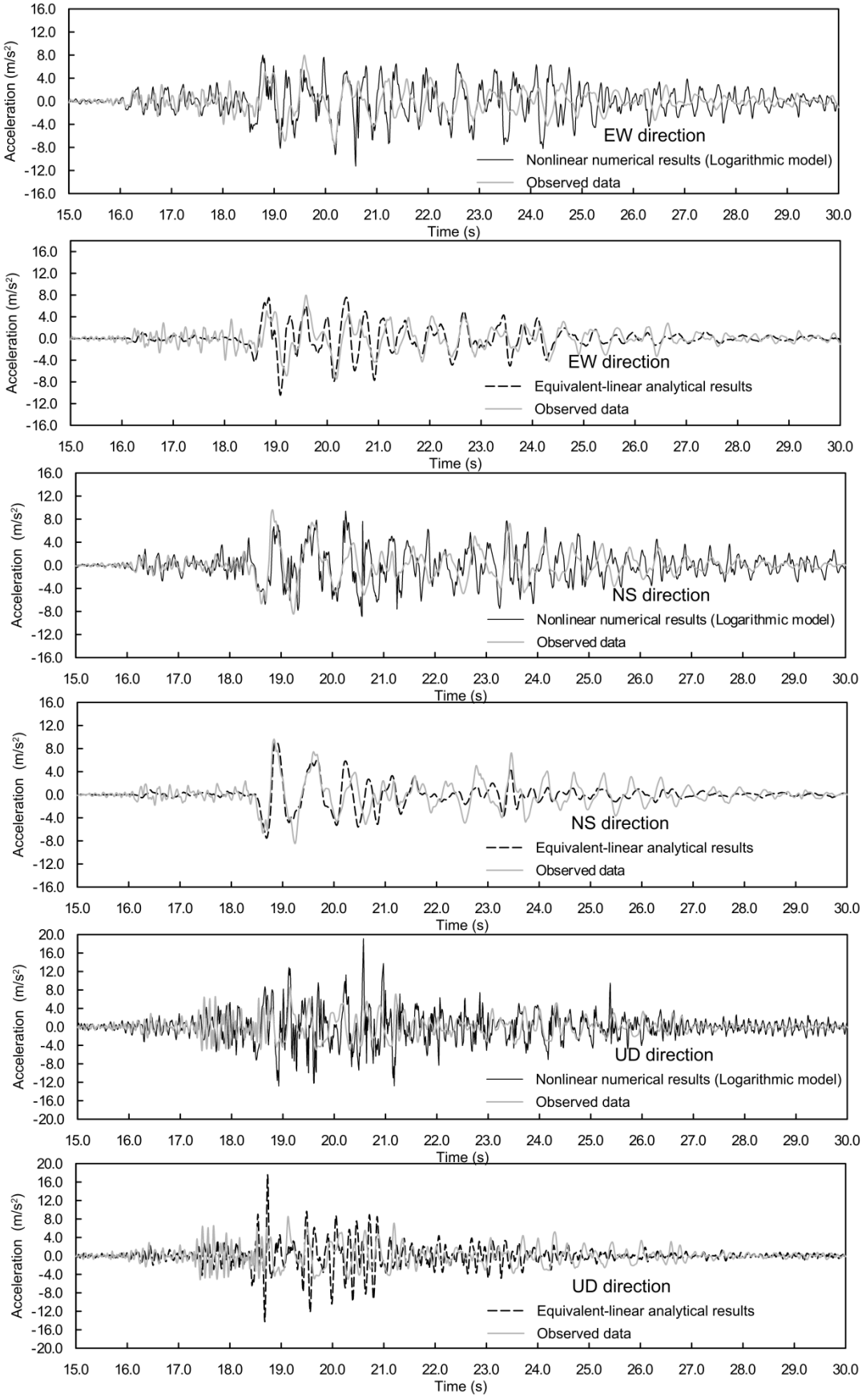


Figure 4-58: Nonlinear analysis results under Western Tottori earthquake (acceleration time histories) (Logarithmic model)

4.6.2 ICG3S-1 model

In this section, the ICG3S-1 model is employed for the nonlinear FE site response analysis of the HINO site subjected to the 2000 Western Tottori earthquake. The model parameters and the calibration curves for the ICG3S-1 model are shown in Table 4-6 and Figure 4-47. As previously explained, in the ICG3S-1 model an identical degradation is adopted for both the shear and constrained moduli. Therefore the ICG3S-1 model can increase the material damping at very small strain levels associated with both the shear and compressional deformations (Figure 4-47).

The resulting 3-D site response is shown in Figures 4-59 and 4-60, in terms of the acceleration response amplification spectra between the top (point A) and bottom boundaries and in terms of acceleration time histories at monitoring point A respectively. Compared to the Logarithmic model predictions, the amplification factors of the vertical site response in the frequency range between 5.0Hz and 9.0Hz are effectively damped for the ICG3S-1 model. Furthermore, the acceleration time histories in the vertical direction are smaller predicted by the ICG3S-1 model and agree better with the monitored data, as shown in Figure 4-60.

However, the amplification factors in the two horizontal directions are simultaneously damped by the ICG3S-1 model. The amplification factors in the frequency range between 1.7Hz and 4.0Hz are considerably smaller than the monitored data (Figure 4-59). Furthermore, the predicted acceleration time histories in the two horizontal directions are over-damped when employing the ICG3S-1 model in comparison to the monitored data (Figure 4-60). Based on this, it can be argued that the accuracy of the site response prediction is reduced when employing the ICG3S-1 model. However, the ICG3S-1 model achieves a better prediction of the vertical site response.

It can be concluded that the increased material damping at very small strain levels of the ICG3S-1 model achieves on one hand a more accurate simulation of the vertical site response, but on the other hand a poorer prediction of the horizontal site response. This is due to the fact that most cyclic nonlinear models cannot fit the damping curves well for the entire strain range. Therefore, the damping curves should be optimally calibrated at respective concerned strain levels when subjected to earthquake motions of different intensities. As shown in Figure 4-47, when γ is smaller than 0.001%, the ICG3S-1 model can increase the damping to account for the material energy dissipation at very

small strain levels. However, at larger strain levels (greater than 0.001%), the material damping related to the shear deformation is overestimated by the ICG3S-1 model compared with the empirical curves. For sites subjected to weak earthquake motions, this over-prediction of the damping can be practically ignored, since only low-magnitude soil deformation is triggered (as shown in Figure 4-53). For sites subjected to strong earthquake motions, larger soil deformation can be generated. Therefore, it is important for the reproduced damping curves related to the shear deformation to match with the empirical curves at the large strain levels (as shown in Figure 4-59). On the other hand, since vertical motions are usually of low intensity compared to the horizontal ones, the vertical soil deformation can be smaller. This requires the model to accurately simulate the damping associated with the compressional deformation at very small strain levels (as shown in Figure 4-57). Therefore, it is necessary for cyclic nonlinear models to independently reproduce the material damping related to the shearing and compressional deformations and achieve optimum calibrations in respective concerned strain ranges. Therefore the ICG3S-2 model is employed for the following nonlinear FE site response analysis.

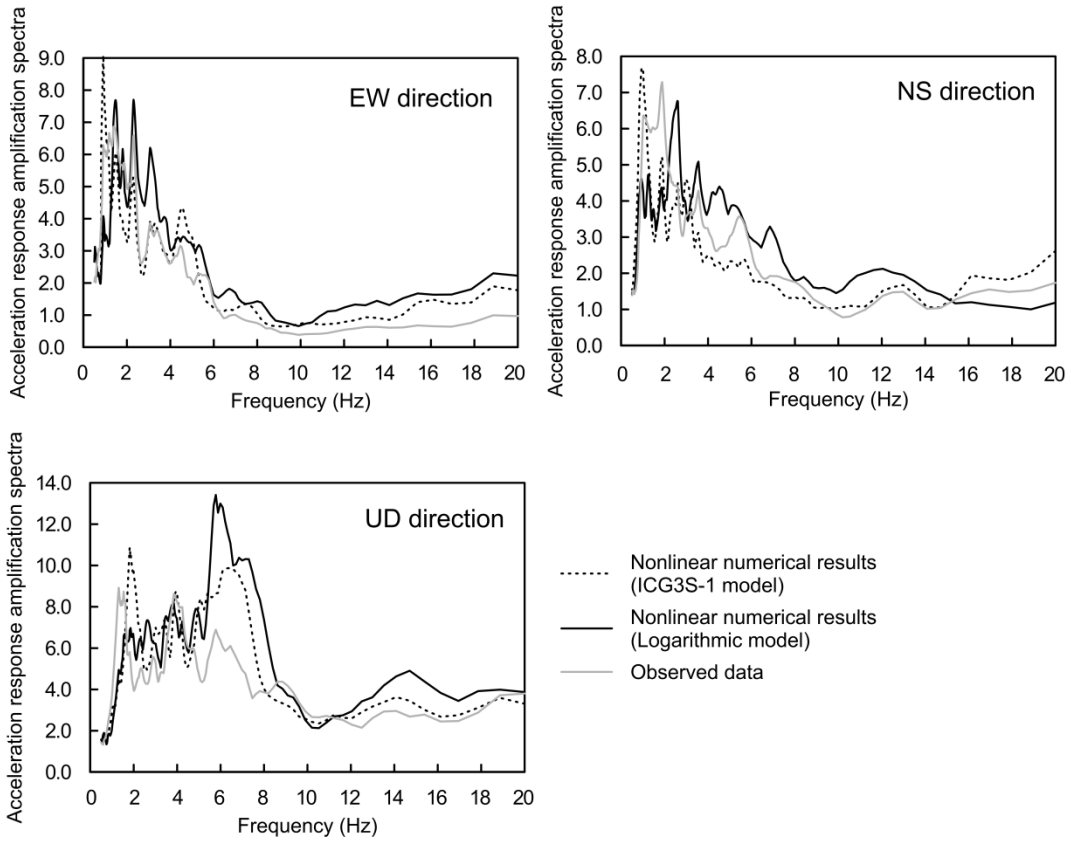


Figure 4-59: Nonlinear analysis results under Western Tottori earthquake (response amplification spectra) (ICG3S-1 model)

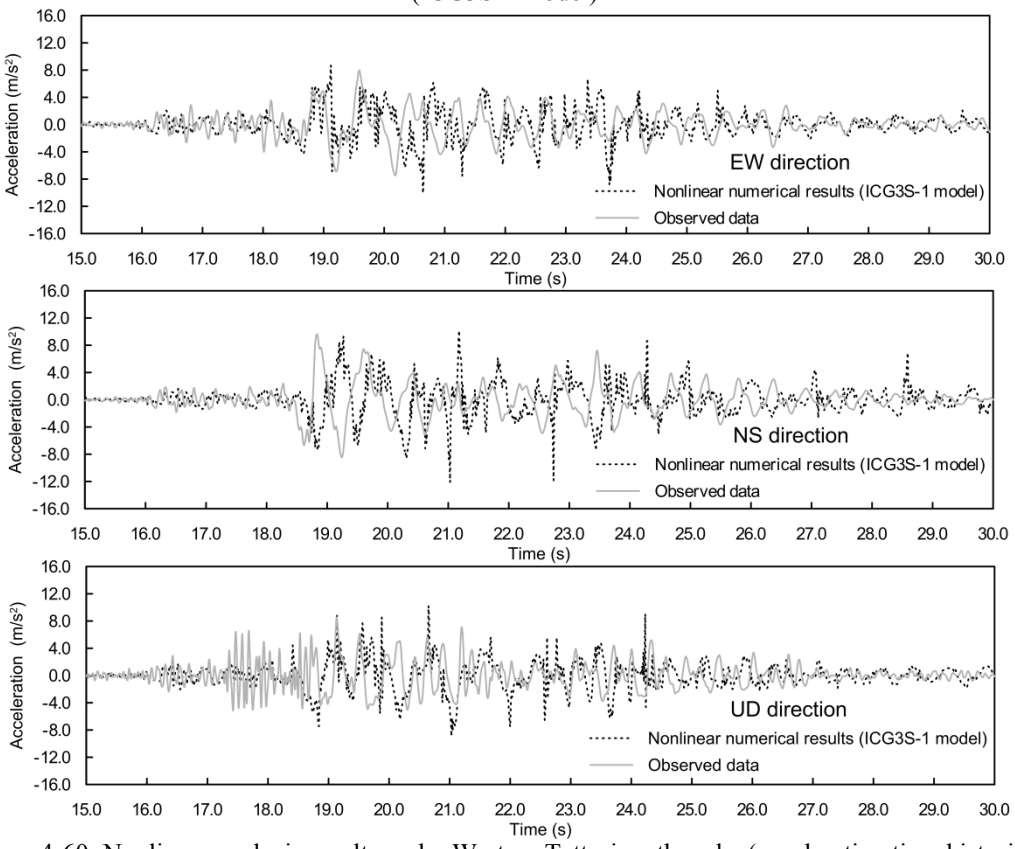


Figure 4-60: Nonlinear analysis results under Western Tottori earthquake (acceleration time histories) (ICG3S-1 model)

4.6.3 ICG3S-2 model

In this section, the ICG3S-2 model is employed for the nonlinear FE site response analysis of the HINO site subjected to the 2000 Western Tottori earthquake, while all other aspects of the numerical model are the same as the ones employed in the previous section. However, the calibration of the ICG3S-2 model is different to the one employed for the nonlinear site response analysis with the two weak earthquake motions (Section 4.5.2.3). As explained in the previous section, this is due to the requirement of optimum calibrations for damping curves at different strain levels when subjected to earthquake motions of different intensities.

The model parameters and calibration of the ICG3S-2 model for the site response analysis of the HINO site subjected to the main earthquake motion are shown in Table 4-8 and Figure 4-61. Based on the calibration curves of the ICG3S-2 model, the material damping related to the shear deformation agrees better with the empirical curves. Furthermore, due to the independent calibration for the two modes of deformation, the reproduced shear and constrained modulus degradation curves match better with the empirical curves.

The computed response with the ICG3S-2 model is shown in Figures 4-62 and 4-63, in terms of the acceleration response amplification spectra between the top (point A) and bottom boundaries and the acceleration time histories at monitoring point A respectively. According to the predicted results, the amplification factors in the two horizontal directions in the frequency range between 1.7Hz and 4.0Hz increase and agree better with the monitored. Furthermore, the vertical site response is more accurately predicted by the ICG3S-2 model, because of the adjusted calibration for the constrained modulus degradation. Considering the predicted acceleration time histories, the under-prediction of the horizontal dynamic response has been avoided by employing the ICG3S-2 model and more reasonable results are obtained for the vertical site response compared with the monitored data.

Table 4-8: Parameters of the ICG3S-2 model for the nonlinear analysis

Depth (GL. meters)	**a**	**b**	**c**	**d_1**	**d_2**	**d_3**	**d_4**
0.0 ~ -100.0	1.00E-04	8.00E-01	5.00E-02	0.00E+00	0.00E+00	0.00E+00	0.00E+00
Depth (GL. meters)	**r**	**s**	**t**	**d_5**	**d_6**	**d_7**	**d_8**
0.0 ~ -100.0	5.00E-04	8.00E+00	5.00E-02	7.28E+01	2.28E-01	6.77E+02	7.58E-01

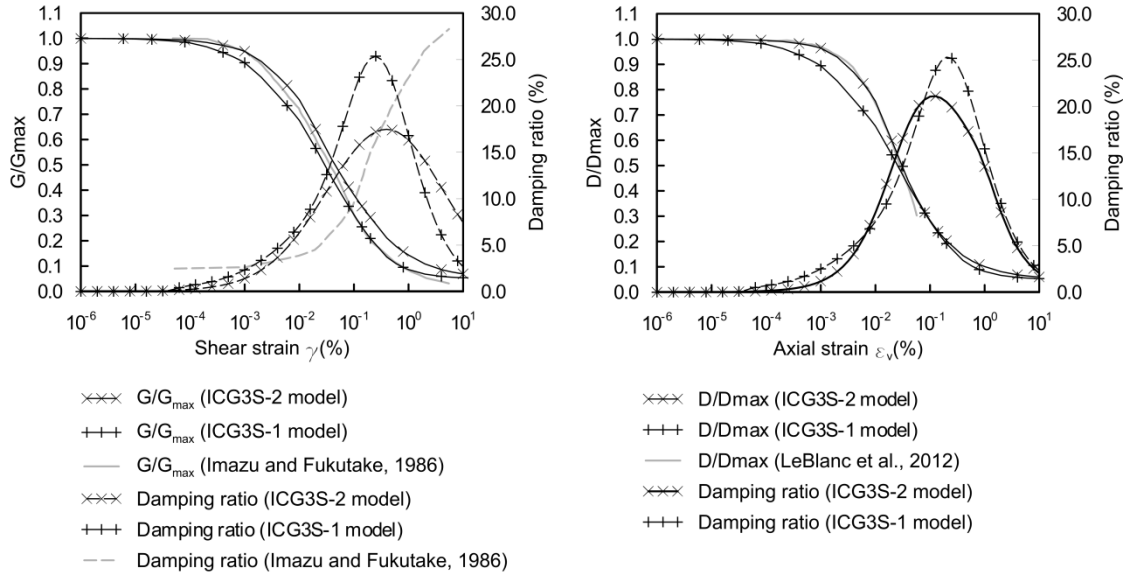


Figure 4-61: Calibration of the ICG3S-2 model for the nonlinear analysis of the main earthquake motion

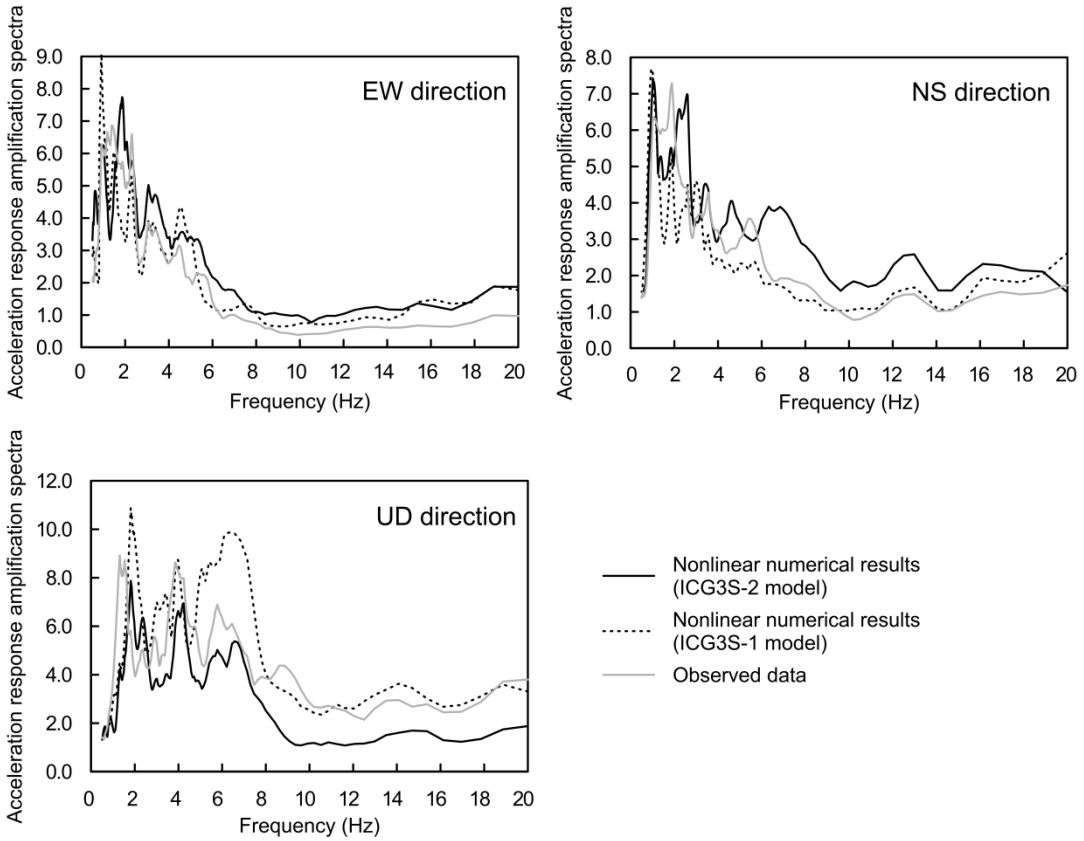


Figure 4-62: Nonlinear analysis results under Western Tottori earthquake (response amplification spectra) (ICG3S-2 model)

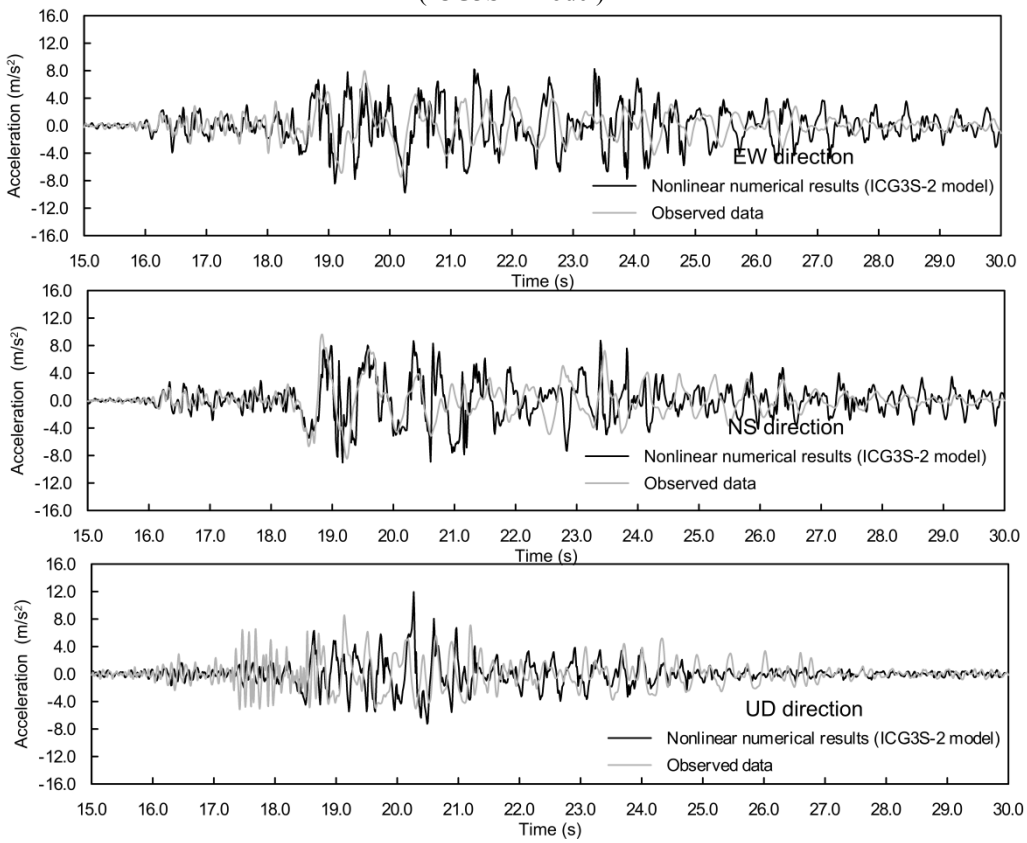


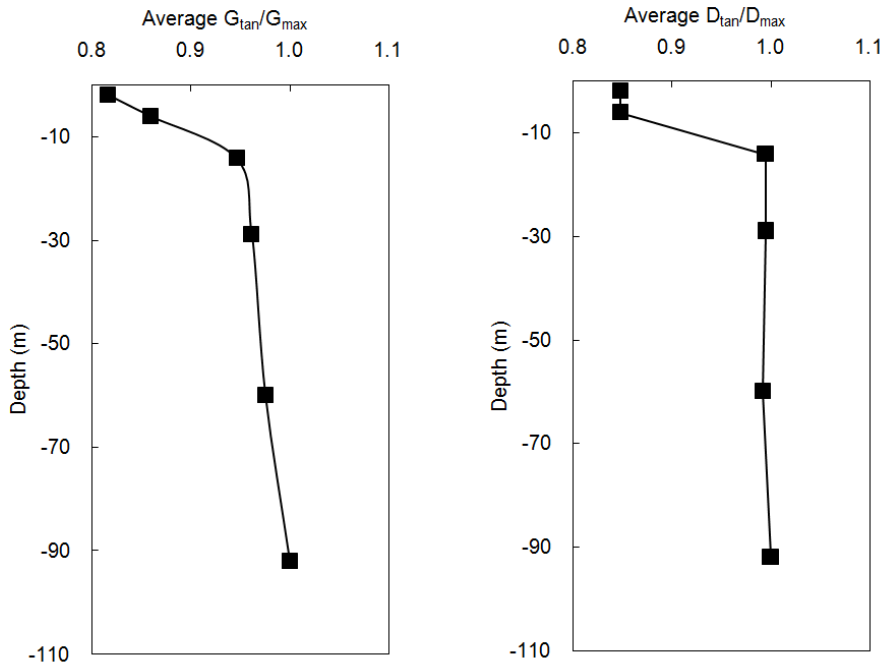
Figure 4-63: Nonlinear analysis results under Western Tottori earthquake (acceleration time histories) (ICG3S-2 model)

By comparing the acceleration response amplification spectra of the strong and weak motions (comparison of Figures 4-62 and 4-53), the effect of soil nonlinearity is observed for all the three directions when subjected to the strong earthquake motion. In particular, the fundamental frequencies in the three directions are observed as 1.0Hz, 1.0Hz and 2.0Hz respectively, which are 40.0%, 40.0% and 33.0% of the ones for the weak motions. This implies the significant degradation for both the shear and constrained moduli of the HINO site. Furthermore, the modulus degradation ratio time histories (G_{tan}/G_{max} and D_{tan}/D_{max}) are calculated for the elements at different depths and the time-average degradation ratios for each element are plotted with depths in Figure 4-64. It can be seen that the shear and constrained moduli degrade more significantly in the top 10 meters, where the ratios gradually increase as depth increases. This is due to the low compressional wave velocities for the layers above the water table, which triggers larger vertical strains and therefore more significant constrained modulus degradation. Based on Equation 4-4, the deviatoric strain is dependent on the strain states of all three directions. Therefore, larger vertical strains can induce larger deviatoric strains and eventually more significant shear modulus degradation in the soil layer above the water table.

The larger deformations in the soil layer above the water table are also reflected by the presented stress-strain response for two monitoring elements (element B and C in Figure 4-31) in Figure 4-65. Elements B and C are located at the depth of GL. -2.0m and -30.0m, which are in the gravel and weathered granite materials respectively. Larger strain levels are predicted at the element B for all three directions, compared with that of the element C, due to its smaller soil stiffness.

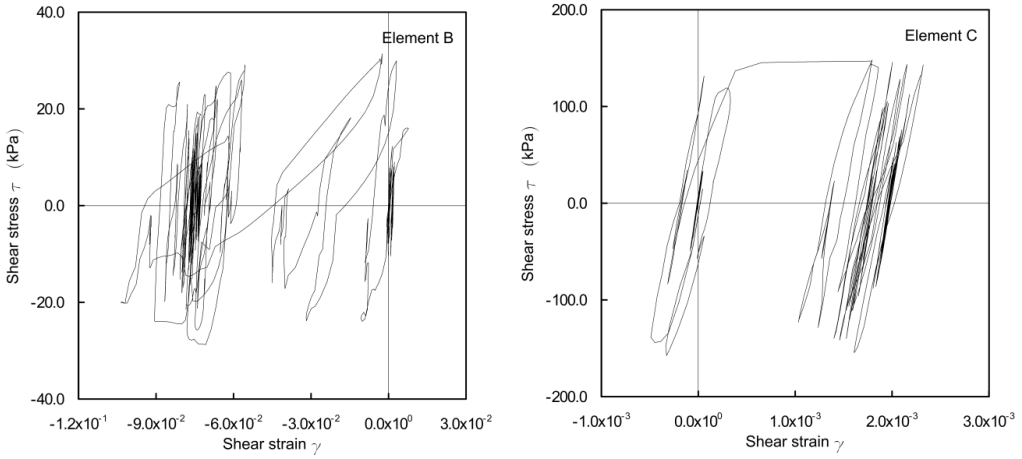
The element C is located in the middle layer of the HINO site and the predicted deformations can approximately represent an average level for the whole layer. The maximum shear strain at the element C is approximately 0.2% (Figure 4-65 (a)). Plastic shear deformation is triggered during the dynamic analysis, indicated by the plastic strain time histories of element C shown in Figure 4-66. This shows that, subjected to strong motions, the damping curves related to the shear deformation require an accurate calibration at large strain levels (i.e. >0.01%-0.1%). Furthermore, the maximum vertical strain at the element C is approximately 0.001% (Figure 4-65 (c)) and no plastic vertical deformation is predicted (Figure 4-66). Hence, the damping curves associated with the compressional deformation need to achieve an accurate calibration at very small strain

levels. These observations are in accordance with the calibration of the ICG3S-2 model in the nonlinear FE analysis.

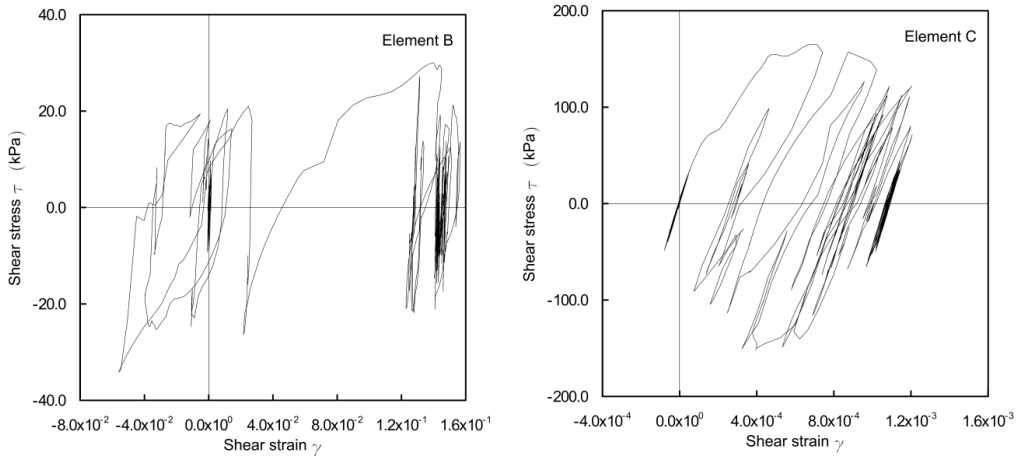


(a): Average shear modulus degradation (b): Average constrained modulus degradation

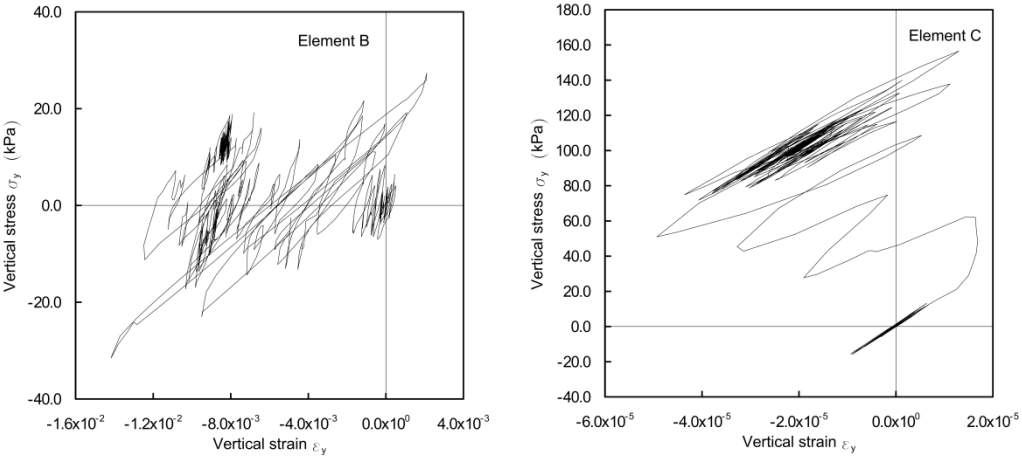
Figure 4-64: Average modulus degradation ratio variation



(a): Shear stress-strain response in EW direction



(b): Shear stress-strain response in NS direction



(c): Vertical stress-strain response in UD direction

Figure 4-65: Stress-strain response simulated by the nonlinear analysis

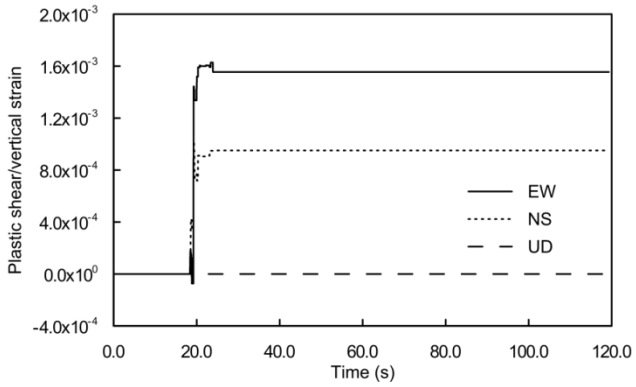


Figure 4-66: Plastic strain time histories at element C simulated by the nonlinear analysis

4.6.4 Comments

The 3-D site response of the HINO site subjected to the Western Tottori earthquake is simulated employing three different cyclic nonlinear models, i.e. the Logarithmic, ICG3S-1 and ICG3S-2 models. Based on the presented numerical results, the site response subjected to the strong earthquake motion is reasonably predicted by the 3-D nonlinear FE analysis.

Firstly, the horizontal site response is appropriately predicted by the Logarithmic model, but the vertical site response is overestimated due to the underestimation of material damping at very small strain levels.

The ICG3S-1 model achieves a better prediction of the vertical site response due to the better representation of the damping at very small strain levels. However the response in the horizontal direction is over-damped in comparison to the recorded data. This implies the need for cyclic nonlinear models to independently simulate material damping related to the shear and compressional deformations and achieve optimum calibrations in respective concerned strain ranges. For this purpose, the ICG3S-2 model is employed, where the results show that the predicted horizontal and vertical site response is both in agreement with the recorded data.

Therefore, the ICG3S-2 model is suggested for the nonlinear FE site response analysis subjected to both weak and strong earthquake motions. Firstly, the ICG3S-2 model can realistically simulate the material damping at very small strain levels. Furthermore, by employing the ICG3S-2 model, soil nonlinear and hysteretic behaviour in different directions, in terms of stiffness degradation and material damping, can be independently simulated, leading to more accurate simulations of multi-directional site

response.

4.7 Parametric investigation on the multi-directional site response

The hydraulic properties of soil profiles, such as the water table location and soil permeability, can be significantly affected by earthquake loading (Rojstaczer et al. 1995). As a consequence, the change of water table location can significantly affect the stiffness of the soil layers in terms of the compressional wave velocity. Furthermore, the soil permeability can strongly influence the vertical site response both in terms of frequency content and amplification. Therefore, in this part, the effects of the variation of the water table and soil permeability on site response are investigated through parametric studies of the selected site (HINO down-hole). Furthermore, the effects of 3-D ground motions are also explored for the multi-directional site response predictions.

4.7.1 Effect of water table location on site response

In this section, the effect of water table location on the site response is investigated through parametric studies. The original water table of the HINO site is raised to the ground surface for the 3-D coupled FE site response analysis. The soil profile of the HINO site, in terms of the variations of shear and compressional wave velocities, is shown in Figure 4-67 by considering the water table at the ground surface and at 10.4m below. It can be seen that the variations of shear wave velocity for the two cases are identical, while the variation of the compressional wave velocity is sensitive to the water table location. In particular, when soil layers are submerged by water, the compressional wave velocity is larger, since the constrained modulus for saturated soil is affected by both the constrained modulus of the soil skeleton and the bulk modulus of the pore water.

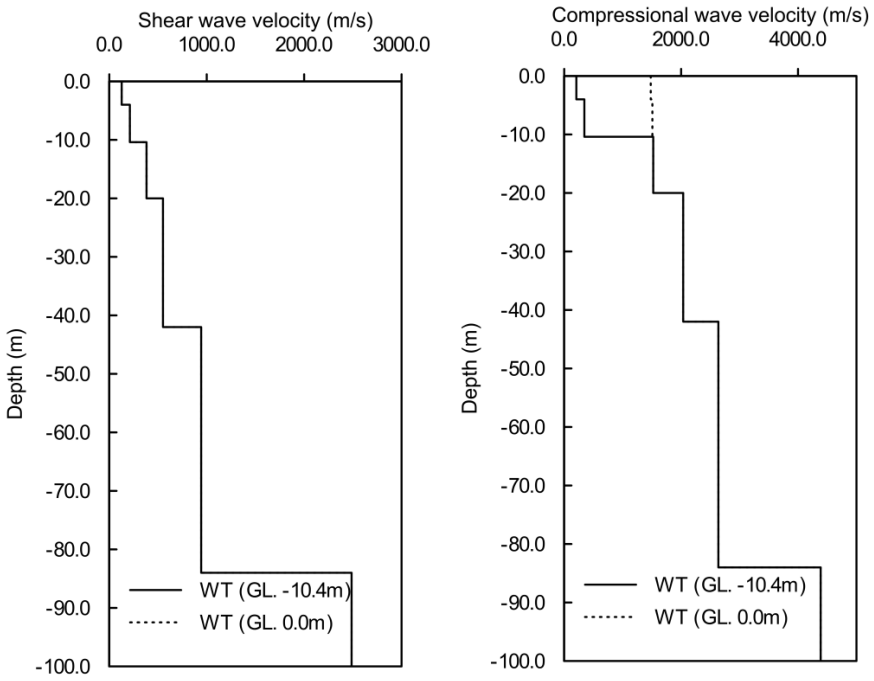


Figure 4-67: Soil profiles for parametric studies of the water table location

4.7.1.1 Linear site response analysis - parametric study 1

Firstly, the effect of the water table location on the site response is investigated through a linear elastic analysis. Two 3-D FE site response analyses are conducted which consider the water table at GL. 0.0m and at GL. -10.4m by employing the corresponding hydrostatic pore water pressure and self-weight as the initial stress profiles, where the coefficient of earth pressure at rest (K_0) is applied to be 0.5. Coupled consolidation analysis is conducted for soil layers under the water table and one-phase drained behaviour is assumed for soil layers above the water table. Linear elastic model and 15.0% Rayleigh damping are employed, where the Rayleigh damping parameters ω_1 and ω_2 are taken as the first fundamental frequency of the soil layer in horizontal and vertical directions respectively. All other aspects of the numerical model are the same as the ones utilised for the previous analyses of the case study. Figure 4-68 shows the comparison of predicted site response in three directions for linear FE analyses considering two water tale locations, in terms of the acceleration response amplification spectra between the top (point A) and bottom boundaries. It can be seen that the response in the horizontal directions is identically predicted by the two analyses, while the vertical site response is affected by the water table location. In particular, a low-frequency shift for the fundamental frequency and higher amplification factors are

observed for the vertical dynamic response of the HINO site with the water table located at GL. -10.4m. This is attributed to the smaller constrained modulus for soil layers with lower water table, since the constrained modulus for soil layers above the water table is not affected by the pore fluid bulk modulus, leading to softer soil behaviour and larger dynamic response.

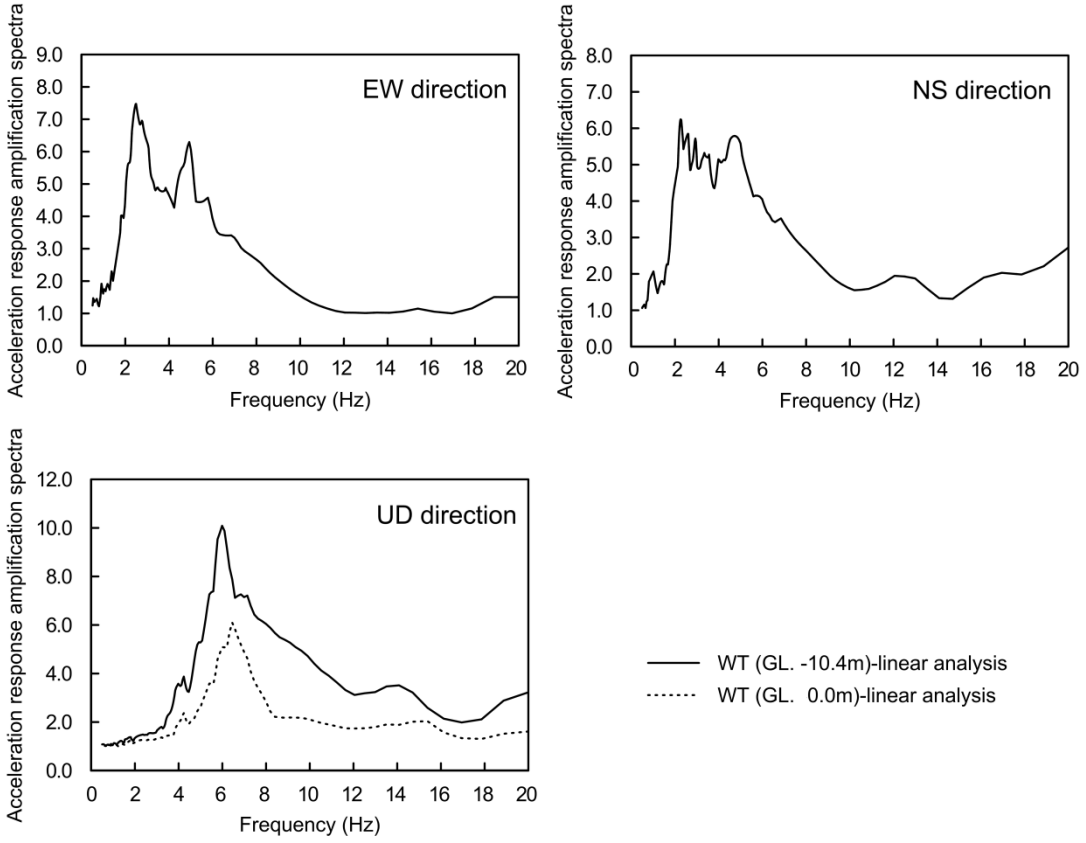


Figure 4-68: Acceleration response amplification spectra of the HINO site from parametric study 1

4.7.1.2 Nonlinear site response analysis - parametric study 2

In order to further explore the effect of the water table location on site response, nonlinear 3-D FE site response analyses are conducted considering the water table located at two different depths, by employing the corresponding initial stresses. The other aspects of the numerical modelling are the same as the ones utilised in the previous analyses. The ICG3S-2 model is employed and the model parameters are listed in Table 4-8. The predicted 3-D site response of the HINO site subjected to the 2000 Western Tottori earthquake with the water table located at the ground surface is compared with the results from the reference case study (water table located at GL. -10.4m), in Table 4-9 and Figures 4-69 and 4-70, in terms of the PGA, acceleration

response spectra at monitoring point A and acceleration response amplification spectra between the ground surface and bottom boundary respectively.

Based on the results from the parametric study 2, by raising the water table from GL. -10.4m to GL. 0.0m, it is observed that the PGAs at the ground surface in the two horizontal directions significantly decrease, by approximately 62.0%, from 9.76m/s^2 and 9.04m/s^2 to 3.79m/s^2 and 3.47m/s^2 in the EW and NS directions, respectively. However, the PGA in the vertical direction slightly increases by 8.1%, from 7.25m/s^2 to 7.84m/s^2. This trend of PGA changes can also be seen in the results of acceleration response spectra at the ground surface for the two cases. By raising the water table from GL. -10.4m to GL. 0.0m, the magnitudes of the predicted response spectra in the two horizontal directions significantly decrease and the magnitude of the vertical response spectra slightly increases. Furthermore, the frequency content of the predicted vertical response is also affected by the water table location, where a high-frequency shift is observed for the dynamic response involving the higher water table. These observations are also reflected in the predicted acceleration response amplification spectra. When raising the water table from GL. -10.4m to GL. 0.0m, in the two horizontal directions, the amplification factors decrease, whereas for the vertical direction, the amplification factors slightly increase and the fundamental frequency changes from 2.0Hz to 6.0Hz.

The observed effects of the water table location on the site response can be further investigated by plotting the variations with depth of average shear and constrained modulus degradation ratios, as shown in Figure 4-71. The lower water table essentially increases the degradation of both the shear and constrained moduli of soil layers at the HINO site. In particular, when the water table is at GL. -10.4m, the soil layers above GL. -10.4m become non-submerged and therefore the constrained moduli of the soil layers above the water table significantly reduce (as shown in Figure 4-67). Furthermore, the reduced constrained moduli trigger larger vertical strains and therefore more significant constrained modulus degradation. This in turn leads to a smaller fundamental frequency for the vertical site response of the profile with the lower water table (Figure 4-70). Based on Equation 4-4, larger vertical strains can induce larger deviatoric strains and eventually more significant shear modulus degradation in the soil layers above the water table, as shown in Figure 4-71.

The plastic shear and vertical stain time histories at element B for both cases are compared in Figure 4-72, showing for both cases high plastic shear strain levels, but

higher for the case with the lower water table. Based on the strain levels monitored at element B, Figure 4-73 schematically indicates the respective damping ratios predicted by the site response analyses involving the two water tables. For both cases, when large deformation is triggered in soil materials, the hysteretic material damping stabilises and the dynamic response is more significantly affected by the resulting deformation magnitude rather than the material damping. In other words, both analyses have reached the same level of damping but not of seismic deformation. Therefore, the horizontal response for the case with lower water table (GL. -10.4m) is much larger than the response with the water table at the ground surface. For the vertical site response, plastic vertical deformation is also predicted for the case with the lower water table, which is smaller in magnitude compared to the horizontal component. However, minor vertical plastic deformation is generated for the case with the higher water table. In this case, the soil layers mostly experience elastic deformation and smaller hysteretic damping is generated. Therefore, although larger vertical deformation levels are induced for the case with the lower water table, its vertical dynamic response is smaller, due to its larger material damping (as illustrated in Figure 4-73 (b)).

The predicted higher horizontal site response of the HINO site with the lower water table is in agreement with the findings in Li et al. (1998) and Yang and Sato (2000). In particular, as introduced in Section 4.2.2, Li et al. (1998) found that the site response in the vertical direction of the Lotung site in both the July 31, 1986 and November 15, 1986 earthquakes was under-predicted by the nonlinear FE analysis, as shown in Figure 4-15. This was attributed to the assumed saturated condition for the upper layers, which might be only partially saturated. This implies that the consideration of smaller pore fluid bulk modulus (essentially smaller soil constrained modulus) can induce larger dynamic response. Furthermore, in Yang and Sato (2000), the effects of the pore fluid bulk modulus on the site response at the Kobe site in 1995 Hyogo-ken Nanbu earthquake were investigated by employing the coupled FE formulation in SUMDES (Li et al. 1992) and the bounding surface hypoplasticity model of Wang (1990). Site response predictions considering two pore fluid bulk modulus values related to the complete and incomplete saturations respectively were compared in Figure 4-74, in terms of the acceleration response spectra at the ground surface. It can be seen that by employing smaller pore fluid bulk modulus (smaller soil constrained modulus), larger dynamic response was predicted by the nonlinear FE analysis. The compressional wave

velocities of both sites are relatively low compared with that of the HINO site. Therefore, when subjected to strong motions, the large vertical deformations can be induced and the vertical response is more significantly affected by the resulted vertical deformation rather than the stabilised hysteretic damping, as explained before. Although the effects of the soil stiffness were only shown on the vertical site response, they can provide an explanation for the higher-predicted horizontal site response of the HINO site for the case with the lower water table.

Finally, the variations of resulting 3-D peak acceleration from the parametric study are plotted versus depth in Figure 4-75. It can be seen that the amplification effect for the HINO site is more significant in the top soil layers (up to 15.0m below the ground surface). The acceleration values in these layers are highly affected by the water table location, where smaller peak accelerations are observed when employing a higher water table.

Table 4-9: PGAs in three directions from parametric study 2

PGA / Water table location	PGA in EW direction (m/s^2)	PGA in NS direction (m/s^2)	PGA in UD direction (m/s^2)
Water table at GL. 0.0m	3.79	3.47	7.84
Water table at GL. -10.4m	9.76	9.04	7.25

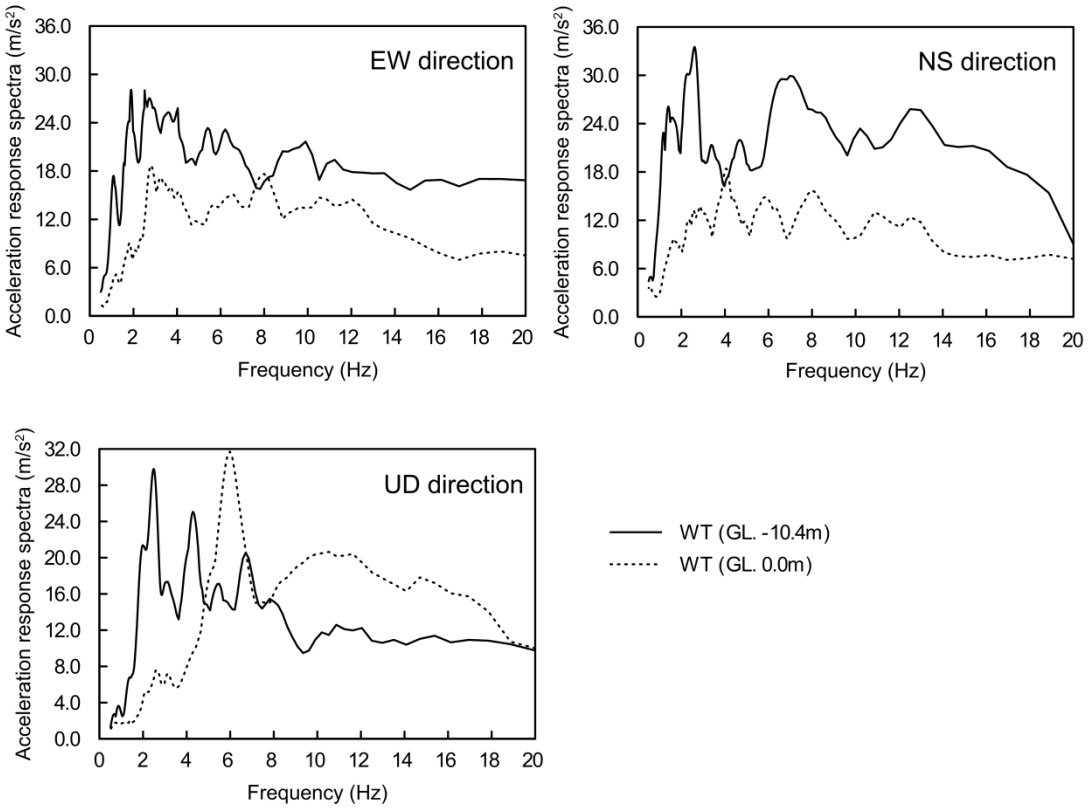


Figure 4-69: Acceleration response spectra of the HINO site from the parametric study 2

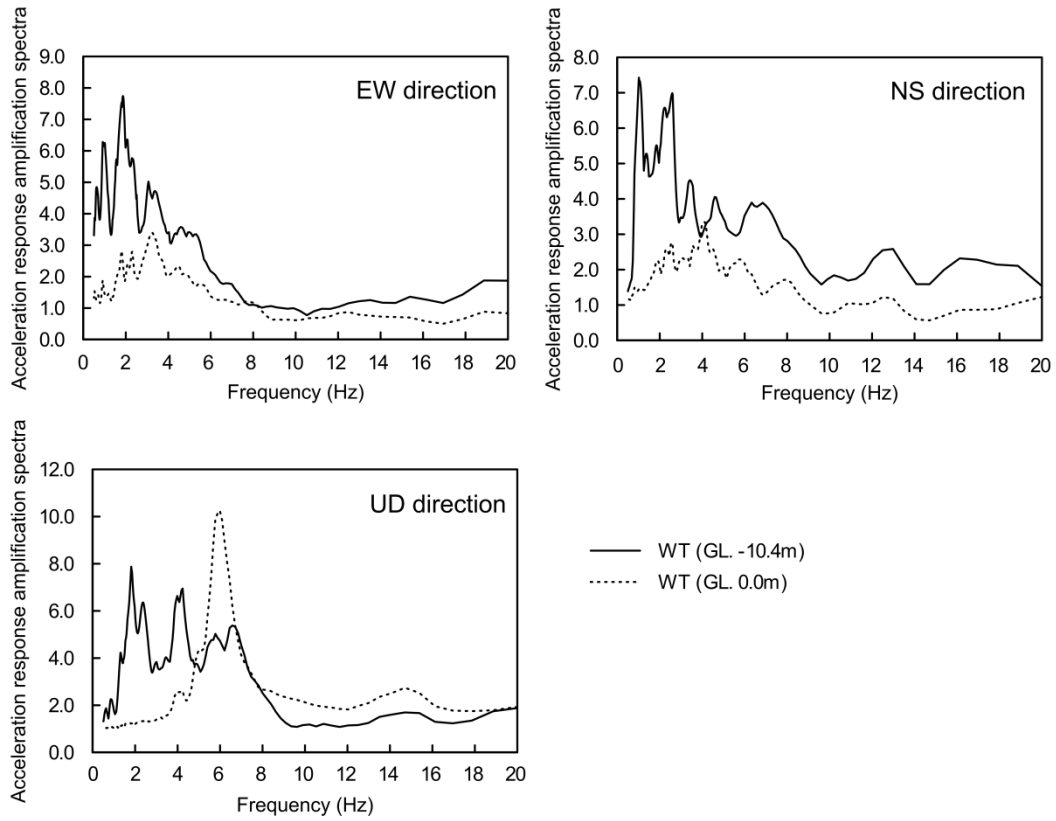


Figure 4-70: Acceleration response amplification spectra of the HINO site from the parametric study 2

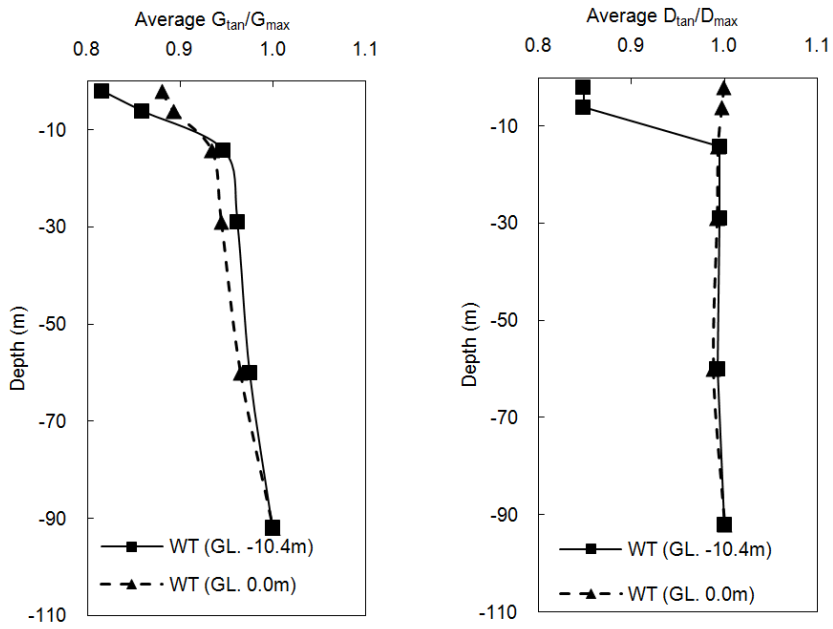


Figure 4-71: Variations of the average stiffness degradation ratio from the parametric study 2

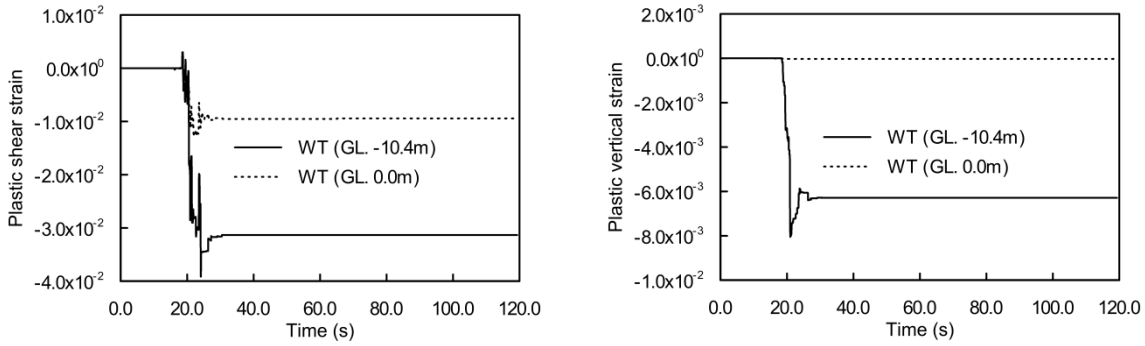
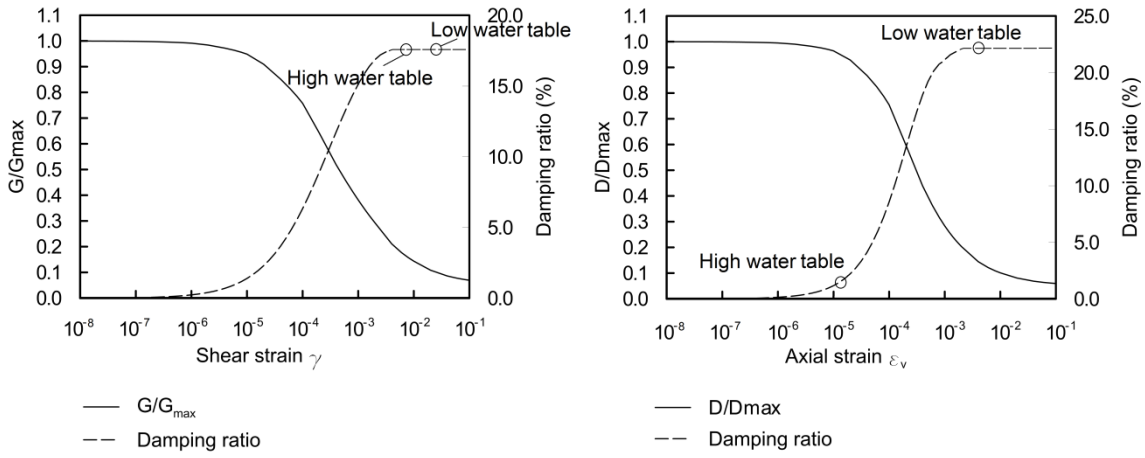


Figure 4-72: Plastic strain time histories from the parametric study 2



(a): Curves related to the shear deformation (b): Curves related to the compressional deformation

Figure 4-73: Shear/constrained modulus degradation and damping curves

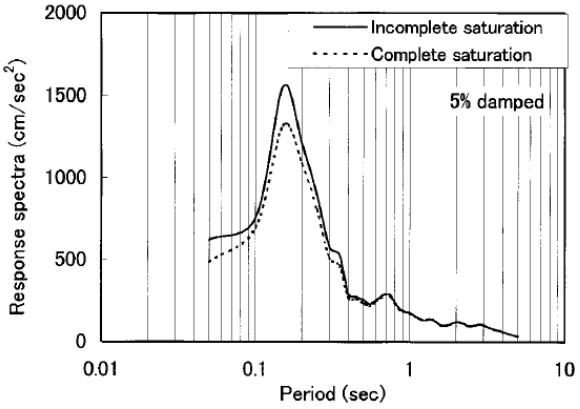


Figure 4-74: Comparison of site response predictions considering two pore fluid bulk modulus values (after Yang and Sato (2000))

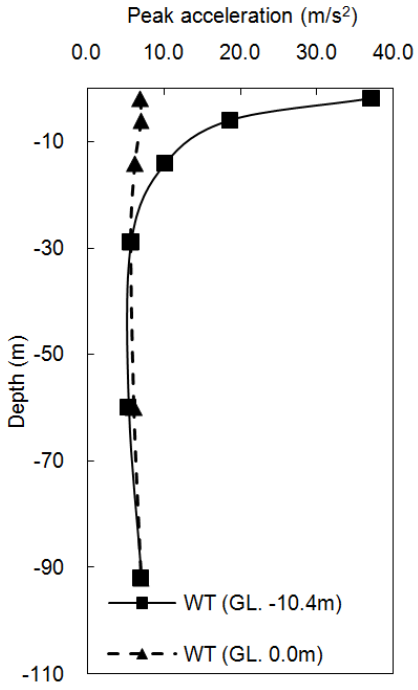


Figure 4-75: Variations of the peak acceleration from the parametric study 2

4.7.1.3 Drained nonlinear site response analysis - parametric study 3

The parametric study 2 highlights the effect of the water table location on both the horizontal and vertical site response. However, the influence of the water table location mainly originates from the pore fluid compressibility. In order to further investigate this effect, a fully drained FE site response analysis is carried out, where all other aspects of the numerical modelling are the same as employed for the reference case study. The predicted 3-D site response is shown in Figure 4-76, in terms of the acceleration

response amplification spectra between the top (point A) and bottom boundaries. It can be seen that the dynamic response in terms of amplification spectra in all three directions increases when ignoring the pore fluid phase, compared to the results from the coupled consolidation analysis. It should be noted that, when conducting the drained analysis, the constrained modulus for the whole profile is not affected by the pore water compressibility and is much smaller than the one employed in coupled consolidation analysis. However, compared with the vertical site response predicted by the coupled consolidation analysis, the fundamental frequency of the vertical response is only slightly smaller predicted by the drained analysis. This is due to the fact that the site response at HINO is more significantly affected by the top soil layers (up to 15.0m below the ground surface), where the constrained modulus for this layer is not highly dependent on the pore water compressibility since the water is located below it.

The effects of the pore fluid compressibility can be further investigated by comparing the depth variations of the average stiffness degradation ratio in Figure 4-77 for the three cases. Based on Figure 4-77 (b), it can be observed that when ignoring the pore water phase, the constrained modulus degradation at different depths of the soil column is more significant, due to the smaller constrained modulus employed for the drained analysis and induced larger vertical strains. Simultaneously, this results in larger deviatoric strains and more significant shear modulus degradation, as shown in Figure 4-77 (a). Larger plastic shear and vertical strain levels are predicted for the drained analysis, as shown in Figure 4-78. As explained in Section 4.7.1.2, in the large strain range, the dynamic response of soils is more significantly affected by the resulting deformation, rather than the stabilised hysteretic material damping and therefore the dynamic response predicted by the drained analysis is larger than the ones resulting from the coupled consolidation analysis.

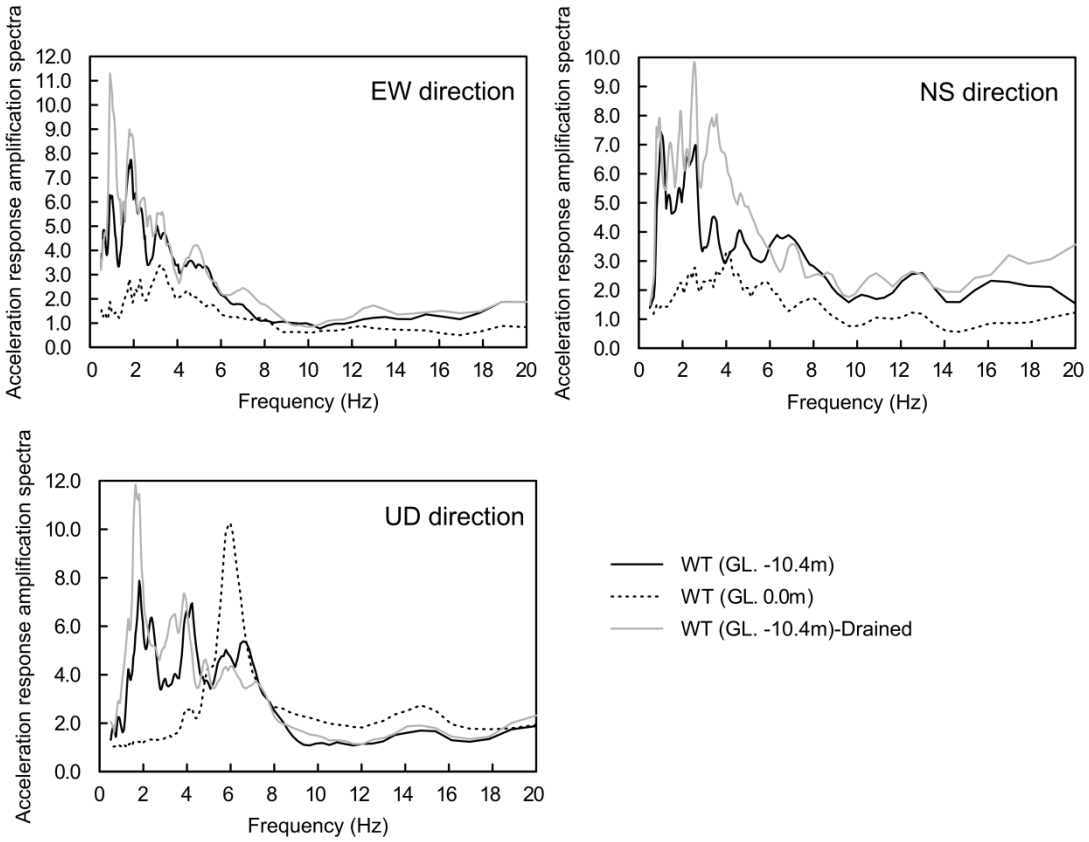


Figure 4-76: Acceleration response amplification spectra of the HINO site from the parametric study 3

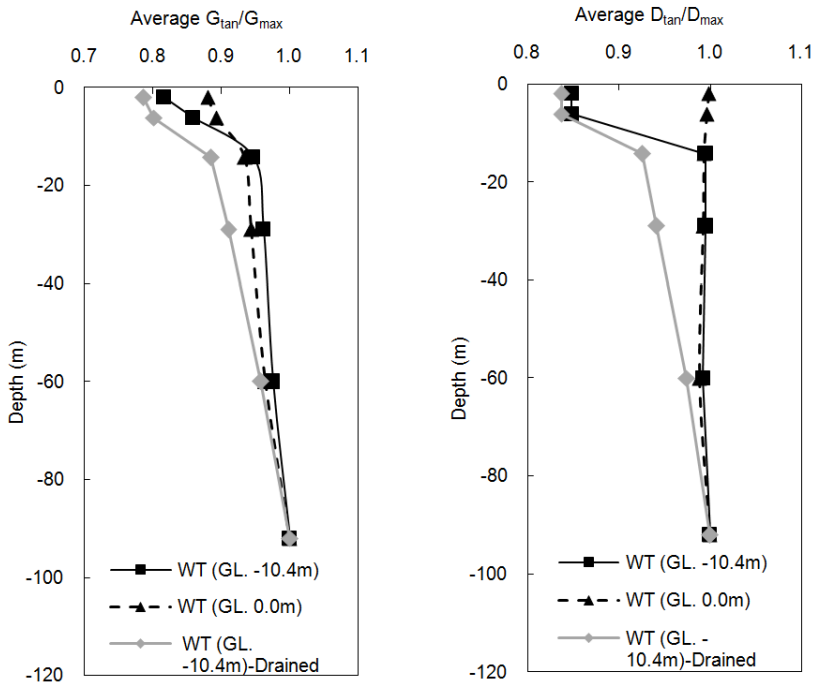


Figure 4-77: Variations of the average stiffness degradation ratio from the parametric study 3

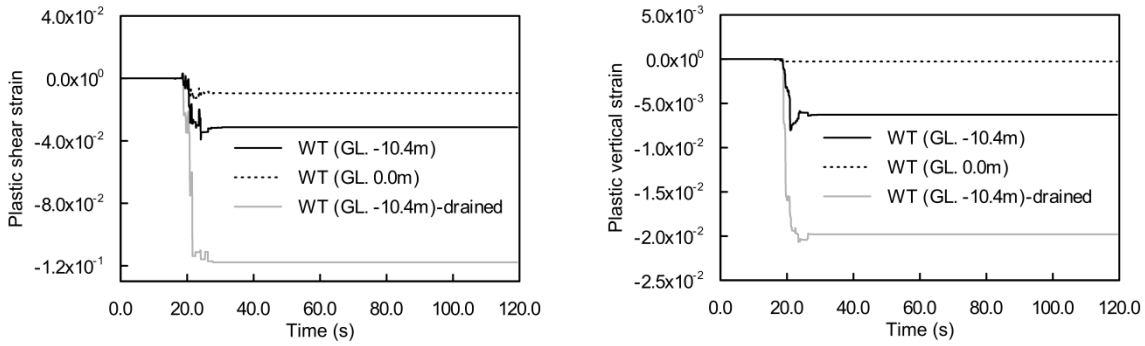


Figure 4-78: Plastic strain time histories from the parametric study 3

4.7.1.4 Realistic soil stiffness profile for high water table - parametric study 4

For the parametric study conducted in previous sections, the same material properties are employed for the site response analysis involving the water table at GL. 0.0m, as the ones for the reference case study (GL. -10.4m). However, increasing the water table level can affect the soil properties in terms of soil stiffness. Therefore, in this section, the effect of the water table location on soil stiffness is considered for the parametric study with the water table located at GL. 0.0m, adopting a more realistic soil stiffness profile through a calibration procedure. In particular, the empirical equation for the maximum shear modulus from Hardin and Black (1968) (Equation 4-13) is employed to reproduce the original shear modulus variation at the HINO site (shown in Figure 4-79), where the parameters for the empirical equation are listed in Table 4-10. It should be noted that the effects of the void ratio and stress history are not taken into account for the calibration of the maximum shear modulus of the HINO site. In order to obtain the shear modulus variation with depth with the water table located at the ground surface, the parameter of effective stress in the empirical equation is correspondingly reduced based on the new water table and the generated shear modulus variation is shown in Figure 4-79. Furthermore, the constrained moduli for this parametric study are calculated based on Equation 4-12. In particular, the constrained modulus for the soil under the water table is dependent on the soil skeleton constrained modulus and pore water bulk modulus, while the constrained modulus for the soil above the water table is only affected by the soil skeleton constrained modulus. It should be noted that Figure 4-79 only shows the shear modulus variation from GL. 0.0m GL. -84.0m, since the deepest layer consists of high-stiffness weathered rock, which is not highly affected by the change of effective stresses. The other aspects of the numerical model are the same

as the ones for the previous parametric study involving the water table at the ground surface in Section 4.7.1.2.

The predicted 3-D site response of the HINO site by the present parametric study considering a more realistic stiffness profile is shown in Figure 4-80, in terms of the acceleration response amplification spectra between the top (point A) and bottom boundaries. Compared with the results from the previous parametric study, larger dynamic response is predicted by the site response analysis considering more realistic soil stiffness. This observation is reasonable, since softer materials are involved for the present parametric study. However, the presently predicted site response is still smaller than the one with the water table at GL. -10.4, indicating the significantly influence of water table location on site response.

$$G_{max} = G_0 \cdot f(e) \cdot OCR^k \left(\frac{p'}{p'_{ref}} \right)^{m_G} \qquad 4\text{-}13$$

Table 4-10: Parameters for the shear modulus calibration

Parameters	**G_0 (kPa)**	**p'_{ref} (kPa)**	**m_G**
Values	3.20E+04	35.32	1.35

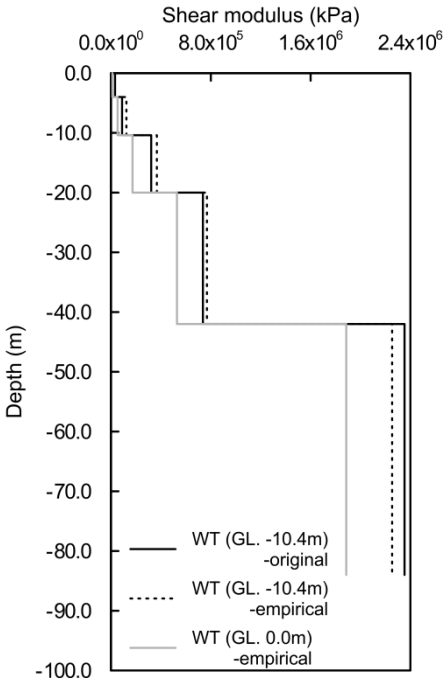


Figure 4-79: Shear modulus variations for the parametric study 4

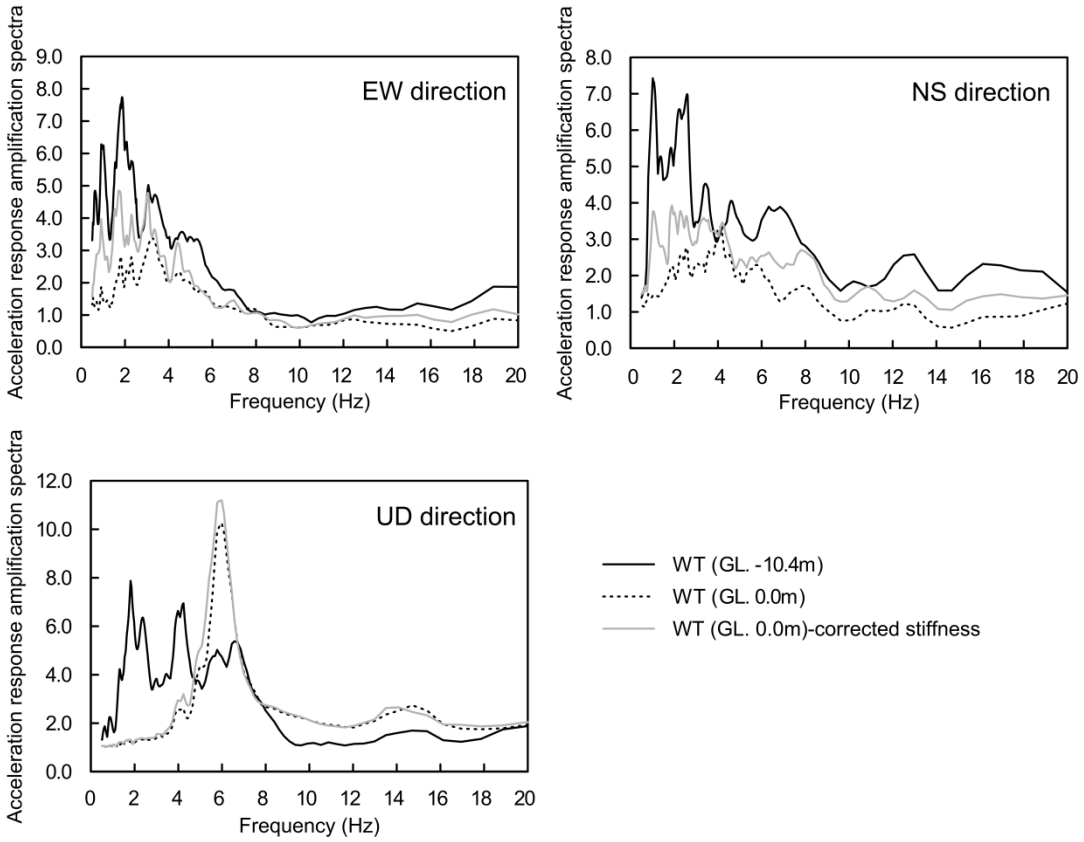


Figure 4-80: Acceleration response amplification spectra of the HINO site from the parametric study 4

4.7.2 Effect of permeability on site response - parametric study 5

In this section, the effect of the soil permeability on the multi-directional site response is investigated through a parametric study of the selected case. The water table is assumed to be at the ground surface, in order to maximise the effect of the soil permeability. Soil permeability is varied in three analyses, adopting values of 1.0E-7m/s, 1.0E-5m/s and 1.0E-3m/s. All other aspects of the numerical model are the same as the ones employed in the nonlinear FE site response analysis of the HINO site with the water table at the ground surface.

The predicted 3-D site response of the HINO site subjected to the 2000 Western Tottori earthquake from the parametric study 5 are demonstrated in Table 4-11 and Figures 4-81 and 4-82, in terms of the PGA, acceleration response spectra at monitoring point A, and acceleration response amplification spectra between the ground surface and bottom boundary respectively. Based on the presented results, when increasing the permeability from 1.0E-7m/s to 1.0E-5m/s, no obvious difference is observed between site response predicted by two FE analyses. When increasing the permeability to

1.0E-3m/s, the horizontal site response slightly decreases, which can be indicated by the smaller PGAs and spectral accelerations. Simultaneously, the vertical site response significantly decreases, in terms of smaller PGAs and spectral accelerations in the vertical direction. These observations can be also depicted in the acceleration response amplification spectra, where for the high permeability slightly smaller amplification factors are observed for the horizontal response and much lower amplification factors are found for the vertical site response. According to the study in Chapter 3, the lower amplification factors for the vertical site response are due to the dissipation effect of the viscous damping, which is introduced by the interaction effects between the solid skeleton and pore fluid phases. In particular, for considerably high values of permeability, the pore water can easier flow out from the solid skeleton and therefore the interaction effects between the solid skeleton and the pore water is more significant, resulting in energy dissipation in the vertical direction.

Furthermore, as shown in Figure 4-83, the smaller vertical dynamic response results in smaller vertical and deviatoric strains and therefore less significant degradation for the soil constrained and shear modulus. This essentially causes slightly smaller shear deformation and smaller horizontal site response, as explained in Section 4.7.1.2. This parametric study demonstrates a noticeable effect of the soil permeability on multi-directional site response and implies the importance of employing coupled consolidation analysis for more accurate simulation of the multi-directional site response at any intermediate transient state (i.e. when consolidation occurs during the dynamic loading, depending on the range of soil permeability and loading duration).

Table 4-11: PGA in three directions from the parametric study 5

PGA / Permeability (m/s)	PGA in EW direction (m/s^2)	PGA in NS direction (m/s^2)	PGA in UD direction (m/s^2)
k=1.0E-7	3.79	3.47	6.84
k=1.0E-5	3.81	3.42	6.77
k=1.0E-3	3.65	3.17	5.60

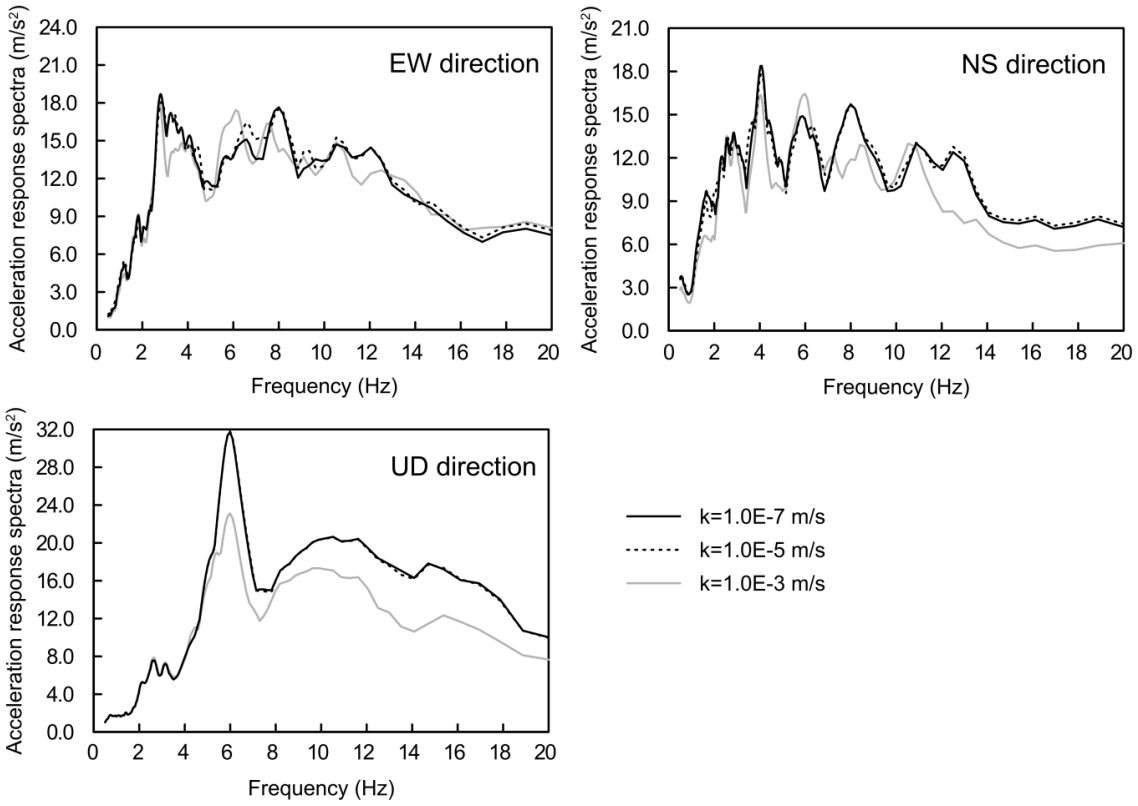


Figure 4-81: Acceleration response spectra of the HINO site from the parametric study 5

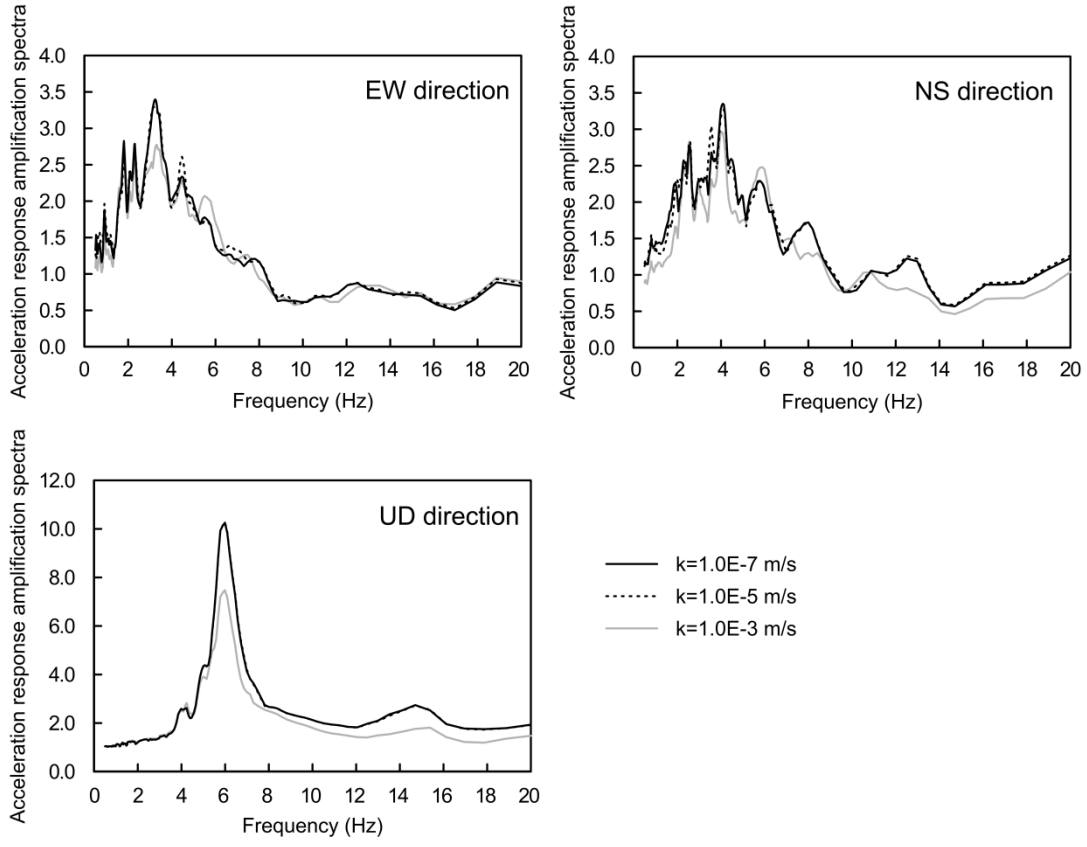


Figure 4-82: Acceleration response amplification spectra of the HINO site from the parametric study 5

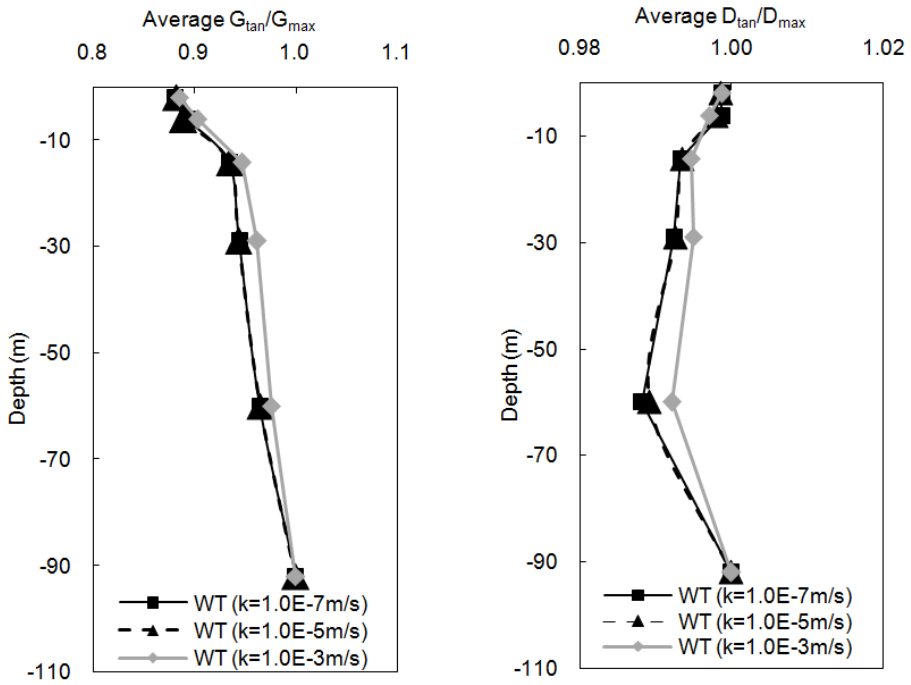


Figure 4-83: Variations of the average modulus degradation ratio from the parametric study 5

4.7.3 Effect of 3-D ground motions on site response analysis - parametric study 6

In this section, the nonlinear site response analysis is simplified to a 2-D plane-strain FE analysis, which can only account for the excitations in one horizontal and vertical directions, namely the EW and UD directions. A 2-D FE mesh is generated based on the plane section of the 3-D mesh, as shown in Figure 4-84, which consists of 200 8-noded isoparametric quadrilateral elements. For the boundary conditions, both displacement and pore water pressure DOFs are tied to be identical for two corresponding nodes at the same height on the two lateral boundaries and the pore water pressure at the water table boundary is prescribed as zero and is not allowed to change throughout the analysis (i.e. Δp=0). The bottom boundary is considered to be impermeable (i.e. no flow across the boundaries). Hydrostatic pore water pressure and static self-weight are prescribed for the 2-D FE analyses as the initial stresses in this section, where the coefficient of earth pressure at rest (K_0) is applied to be 0.5. The EW and UD components of the monitored earthquake motions at the base layer of the HINO down-hole during the 2000 Western Tottori earthquake are uniformly prescribed at the bottom boundary as the input motion. All other aspects of the numerical modelling, such as the time integration parameters and constitutive models, are the same as the reference

case study.

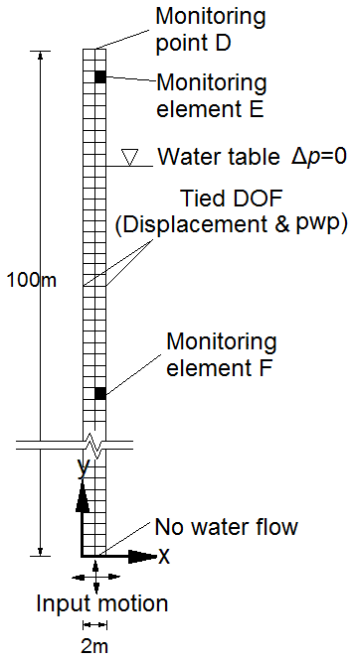


Figure 4-84: FE mesh for 2-D plane-strain FE analysis

The predicted dynamic response of the HINO down-hole by employing the 2-D FE analysis is compared with the 3-D numerical results in Figure 4-85, in terms of the acceleration response amplification spectra in the EW and UD directions. Based on the numerical results, it can be seen that the site response is not significantly affected by the 2-D ground motions. Only at the frequency of approximately 4.2Hz, the amplification factors of the vertical response are underestimated by the 2-D analysis, which are however more accurately predicted by the 3-D analysis.

Figure 4-86 compares the plastic shear and vertical strain time histories predicted by 2-D and 3-D analyses, which are monitored at two corresponding elements at the same height from the 2-D and 3-D FE mesh (elements B and E in Figures 4-31 and 4-84 respectively). It is observed that both plastic shear and vertical strains predicted by the 2-D analysis are smaller. Figure 4-87 plots the depth variations of the average stiffness degradation ratios from two analyses. It can be seen that both the shear and constrained moduli degrade less significantly at all depths when subjected to 2-D excitations. These observations show that the 3-D ground motions can trigger larger soil deformation and therefore more significant soil stiffness degradation than the 2-D ground motions. As explained in Section 4.7.1.2, the larger soil deformation can induce larger site response

in the large strain range. This explains the higher amplification factors of the vertical response at the frequency of 4.2Hz predicted by the 3-D analysis. Therefore, a full 3-D analysis is suggested for a more accurate multi-directional site response prediction.

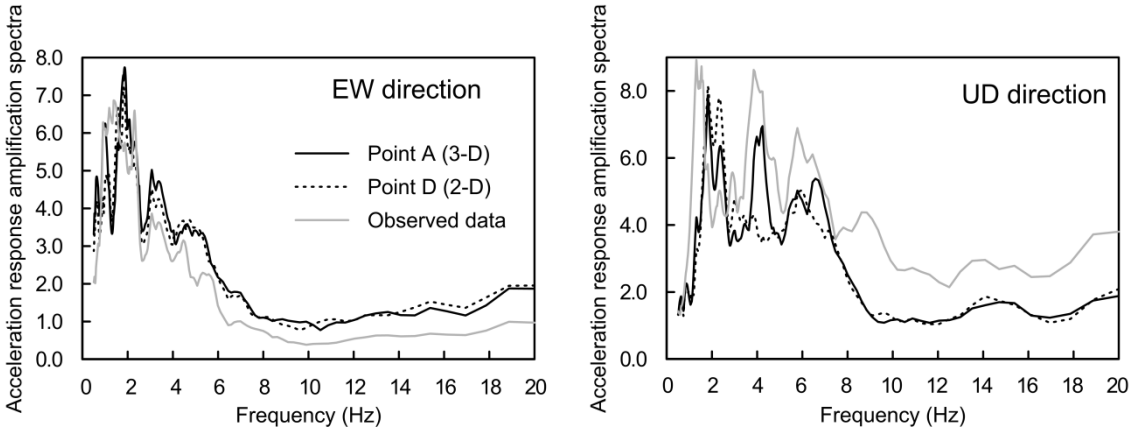
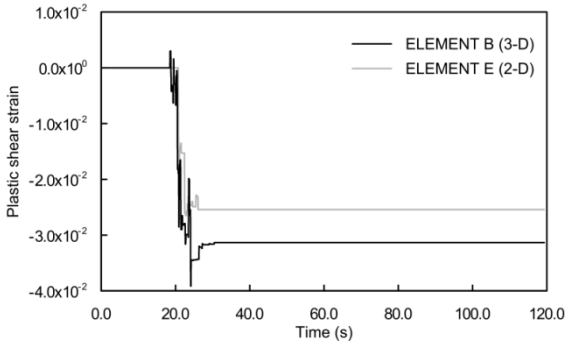
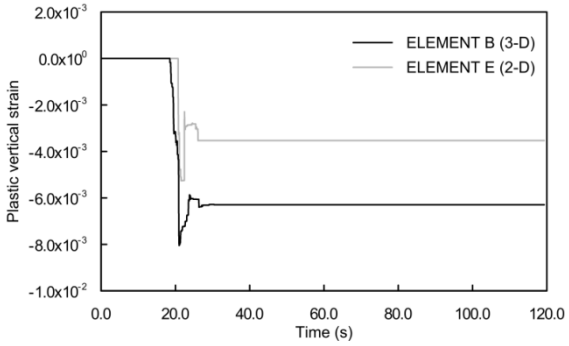


Figure 4-85: Comparison of response amplification spectra between 2-D and 3-D nonlinear FE analyses

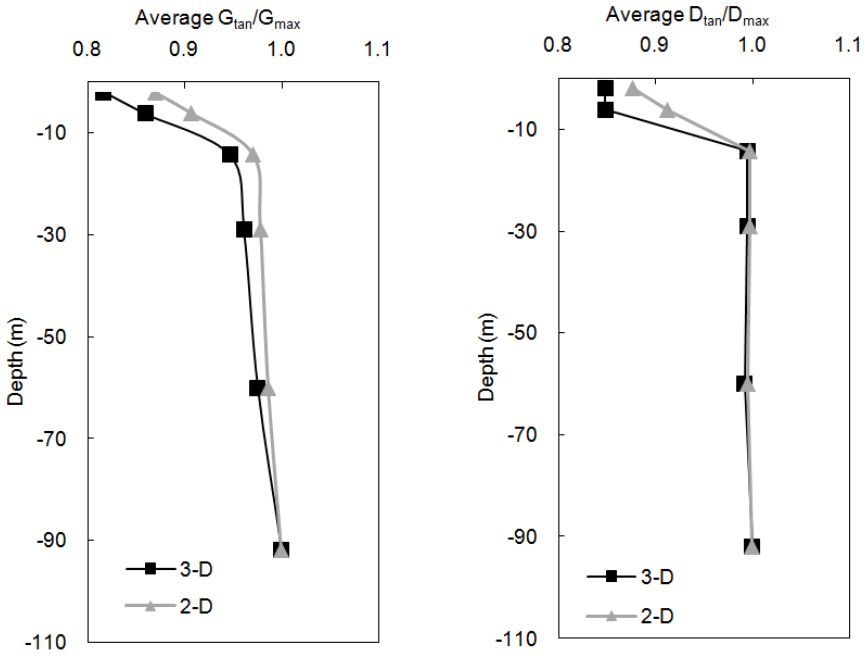


(a): Plastic shear strain time history in EW direction



(b): Plastic vertical strain time history

Figure 4-86: Comparison of plastic strain time histories between 2-D and 3-D nonlinear FE analyses



(a): Average shear modulus degradation (b): Average constrained modulus degradation

Figure 4-87: Comparison of average stiffness degradation between 2-D and 3-D nonlinear FE analyses

4.8 Summary

In this chapter, the multi-directional site response of the HINO site was investigated by employing the 3-D dynamic HM formulation in ICFEP. The computed results were compared with the monitored data from the KiK-net down-hole array system. The 3-D site response of the HINO site, subjected to two weak earthquake motions and the 2000 Western Tottori earthquake, was simulated by linear and nonlinear FE analyses. Different features of the numerical modelling for site response analysis, such as the constitutive models, the use of 3-D input motion and the coupled consolidation formulation, were investigated through the conducted FE simulations and parametric studies.

Firstly, the site response of the HINO site subjected to two weak motions was simulated by linear FE analysis and the analytical solution employed by the software SHAKE. The results showed that the multi-directional site response was reasonably well simulated by both methods, when compared with the monitored response. However, the predicted site response was found to be very sensitive to the employed Rayleigh damping ratio and its associated parameters. A further investigation suggested that, in order to achieve accurate simulations for site response in all three directions, the

Rayleigh damping parameters ω_1 and ω_2 should be taken as the first horizontal and vertical fundamental frequencies of the studied soil profile. Furthermore the numerical investigation revealed that the Rayleigh damping formulation is not fully compatible with the coupled consolidation formulation and this can result in the over-prediction of the vertical site response.

In order to accurately reproduce soil material damping under earthquake loading, cyclic nonlinear models were employed for the FE site response analysis of the HINO site subjected to weak earthquake motions. Three cyclic nonlinear models were utilised, which are the Logarithmic, ICG3S-1 and ICG3S-2 models. These three models distinguish by their abilities of accurately simulating material damping at very small strain levels and realistically simulating the independent shear and volumetric deformations. Numerical results showed that, in order to accurately predict the multi-directional site response, the model of the ICG3S-2 type should be used for the nonlinear FE analysis. Firstly, the ICG3S-2 model can simulate more accurately the material damping at very small strain levels. Furthermore, by employing the ICG3S-2 model, both the horizontal and the vertical site response can be accurately predicted by independently controlling the degradation of the shear and the constrained modulus.

In addition, the 3-D site response of the HINO site subjected to the 2000 Western Tottori earthquake was simulated employing the same three cyclic nonlinear models. Once more, the ICG3S-2 model showed superior performance in terms of more realistic simulation of material damping at very small strain levels and independent simulation of stiffness degradation and material damping related to the shear and compressional deformations. By employing the ICG3S-2 model, a reasonably good agreement was observed between the numerical results and the monitored site response, both in terms of acceleration time histories and response amplification spectra in the three directions. Furthermore, soil nonlinearity was observed for all three directions, but this was more significant in the soil layer above the water table due to the smaller soil constrained modulus. The site response analysis predicted different deformation levels in the horizontal and vertical directions; the deformations were found to be in the large strain range (i.e. >0.01%-0.1%) and in the very small strain range (<0.001%) respectively as defined by Vucetic (1994). This highlighted the importance of independent optimum calibrations for the material damping related to the shear and compressional deformations at the respective relevant strain levels.

In the last part, the effects of three critical factors on the site response, i.e. the variation of water table, the soil permeability and the 3-D ground motions, were investigated through parametric studies for the selected site, where the following conclusions were reached:

– Firstly, results from linear site response analyses considering two water table locations (GL. 0.0m and GL. -10.4m) showed a significant effect of the water table depth on the vertical site response, both in terms of frequency content and amplification, while no influence was identified on the horizontal site response. This effect originates from the change of the soil constrained modulus when the water table level was varied.

– Secondly, the nonlinear site response analysis highlighted the effect of water table location on both the horizontal and vertical site response. Results showed a low-frequency shift for the fundamental frequency and smaller amplification factors for the vertical site response with lower water table. The fundamental frequency shift was attributed to the smaller constrained modulus in the soil layers above the water table and the more significant constrained modulus degradation in these layers. The smaller amplification factors were due to the larger induced material damping compared to that of the analysis involving the higher water table. Simultaneously, larger vertical strains induced larger deviatoric strains and eventually more significant shear modulus degradation. It was observed that the lower water table significantly increased the horizontal site response due to the induced large shear deformation and the stabilised material damping in the large strain range.

– Subsequently, a fully drained site response analysis was conducted, which ignored the pore fluid phase and therefore induced smaller soil constrained modulus. It was observed that larger shear and compressional deformations were induced, which resulted in more significant shear and constrained modulus degradation at all depths than the corresponding coupled analysis. This finally led in larger site response in both horizontal and vertical directions in the large strain range.

– The effect of the water table location on the soil stiffness profile was considered for the site response analysis with the water table at the ground surface. The soil stiffness profile was adjusted by employing the empirical equation for the maximum shear modulus from Hardin and Black (1968), which accounts for the effect of effective

stresses associated with the water table location. This consideration predicted larger site response compared to that employing the original soil stiffness profile, which was, however, still smaller than the one with the water table at GL. -10.4, indicating a significant influence of the water table location on site response.

– Furthermore, based on the parametric study for the soil permeability, both the horizontal and the vertical site response was found to be affected only when considerably high permeability values were assumed for the soil materials (i.e. ≥1.0E-3 m/s). Smaller vertical site response was predicted due to the introduced viscous damping generated by the solid-pore water interaction effects. The smaller vertical dynamic response resulted in smaller vertical and deviatoric strains and therefore less significant degradation for the soil constrained and shear moduli. This essentially caused slightly smaller shear deformation and horizontal site response in the large strain range.

– Finally, the analysis considering 2-D ground motions (i.e. the EW and UD directions) did not generate significant influence on the site response in the EW horizontal direction. However, in the intermediate frequency range (approximately at 4.2Hz), the amplification factors for the vertical response were underestimated by the 2-D analysis. This highlighted the role of the 3-D analysis, which can trigger additional deformations due to the interaction of the third component with other two directions. Therefore, a full 3-D analysis is suggested for more accurate predictions and comprehensive understanding for multi-directional site response analysis.

CHAPTER 5
Static and dynamic FE analyses of the Yele dam

5.1 Introduction

Since 1949, the Chinese government has significantly developed its domestic hydraulic engineering, aiming to adjust the structure of domestic electricity supply, improve the irrigation system and strengthen the flood defences. In the last 60 years, over 87000 dams have been constructed all over China, where there are approximately 400 dams whose reservoir capacities exceed one hundred million cubic metres (Xu, 2009). It should be noted that earth and rockfill dams account for more than 90% of all the constructed dams. Furthermore, 75% of rockfill dams are located in areas of significant seismic activity, greater than class VI according to the Earthquake Intensity Zoning Map of China (China Earthquake Administration, 2011). The safety of the earth and rockfill dams in these seismic regions is critical for millions of people living in the downstream areas. For example, in May 2008, the Wenchuan earthquake (Ms=8.0) occurred in west China causing damage of varying degree in approximately 391 dams, including 4 large-scale rockfill dams (i.e. heights exceeding 100m) (Xu, 2009). Seismic damage such as crest settlement, concrete slab cracks and destruction of crest facilities were widely observed on these dams. Therefore, there is a need to conduct thorough dynamic analyses for these dams, in order to accurately predict their seismic response, analyse potential failure mechanisms and systematically evaluate their seismic

resistance.

The seismic response of earth and rockfill dams has been extensively studied by researchers by employing different analysis methods. However, difficulties still exist in developing advanced numerical analysis methods to accurately simulate real dynamic soil behaviour, in terms of soil constitutive models and HM coupled methods. Therefore, in the following two chapters, the seismic response of a well-documented Chinese rockfill dam, the Yele dam, is investigated by employing the dynamic HM formulation in ICFEP (Potts and Zdravković, 1999). Through the numerical investigation, different aspects of the numerical modelling for static and dynamic analyses of rockfill dams are validated against the available monitored data of the Yele dam before and during the Wenchuan earthquake. Furthermore, the seismic safety of the Yele dam is assessed by analysing the dynamic behaviour predicted by FE analyses.

This chapter first reviews existing dynamic analysis methods for earth and rockfill dams. The discussion is particularly focused on the development of the dynamic FE method. Furthermore, some basic information for earth and rockfill dams, such as different dam types and observed typical seismic dam damage, is also briefly discussed.

Subsequent to this, the basic information about the selected case, the Yele dam, is introduced, including the dam geometry, soil properties and static and dynamic monitored data. The following part presents the establishment of the FE model, involving the spatial discretisation, investigation of boundary locations and calibration of constitutive models.

The following two parts focus on the static and dynamic FE investigations of the Yele dam under construction, impounding, operation and the Wenchuan earthquake loading conditions using ICFEP. Numerical predictions are compared against both the static and dynamic monitored data, through which the applied numerical model is validated. Furthermore, the seismic response of the Yele dam is investigated by analysing the dynamic behaviour predicted by numerical analyses.

Finally, in Chapter 6, parametric studies of the Yele dam are conducted to explore the effects of several critical factors on the seismic response of earth and rockfill dams, i.e. the reservoir simulation method, the permeability of materials comprising the dam body, the vertical ground motion and the reservoir water level.

5.2 Earth and rockfill dams

This part introduces some basic information of earth and rockfill dams, i.e. different dam types and observed typical seismic dam damage. The development of dynamic analysis methods is also reviewed, where the applications of the dynamic FE method are particularly discussed.

5.2.1 Dam types

Earth and rockfill dams are water retaining embankments composed of compacted soil or/and gravel materials. They are the oldest, simplest and most widely used type of dam in existence. According to Zhang (2005), there are approximately 87,000 dams in China of different heights and 90% of them are earth and rockfill dams. Their wide use is attributed to their cost effective construction compared to concrete dams, as local materials such as soil and rock resourced nearby the construction site can be easily transported and used. According to the different materials used, they can be categorised into earthfill dams and rockfill dams. Based on the different types of the dam core, there are uniform earth dams, zoned rockfill dams and upstream membrane rockfill dams.

Uniform earth dams

Uniform earth dams were widely used in ancient times for irrigation, water supply and flood control, which are not very high, approximately 10 meters (Zhang, 2005). Nowadays, they are usually used as coffer dams, which become a part of the upstream dam slope after construction. The materials for uniform earth dams must be impervious to prevent water seepage. The typical geometry of a uniform earth dam is shown in Figure 5-1 (Gu, 1988).

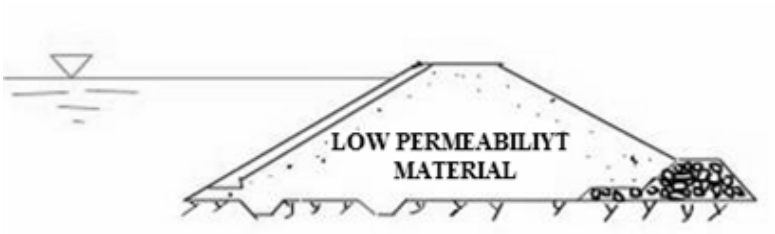


Figure 5-1: Typical geometry of a uniform earth dam (after Gu (1988))

Zoned rockfill dams

Zoned rockfill dams consist of several dam sections of different materials. The core section comprises of low permeability materials such as clay, asphalt or concrete, which can minimise the water seepage from the upstream reservoir. The core can be vertically placed in the centre of the dam or inclined to the upstream slope. Thin filter layers are usually placed adjacent to the downstream side of the core or/and under the downstream rockfill materials, comprising of coarser and higher permeability materials such as sand. This layer aims to discharge the water seeping from reservoirs, in order to prevent internal erosion of core materials. Furthermore, a transition layer next to the upstream side of the core can adjust the different deformations between the core and outer coarse materials. Finally, the outer filling section is composed of very coarse rockfill materials to provide stability for the dam. Two types of zoned rockfill dams (vertical core and inclined core) are shown in Figures 5-2 and 5-3 (Gu, 1988).

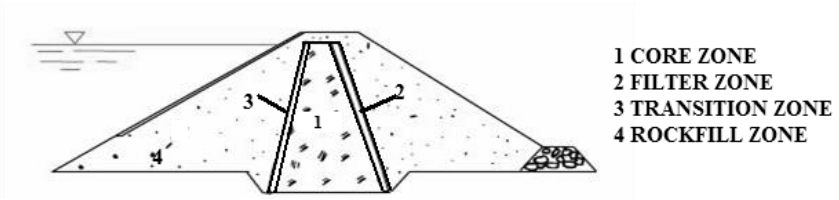


Figure 5-2: Typical geometry of a zoned earth and rockfill dam (vertical core) (after Gu (1988))

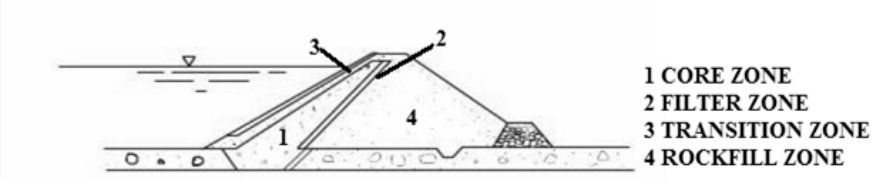


Figure 5-3: Typical geometry of a zoned earth and rockfill dam (inclined core) (after Gu (1988))

Upstream membrane rockfill dams

Upstream membrane rockfill dams are a relatively new type of earth and rockfill dams, which has been widely constructed since 1950s. It should be noted that 50% of the high earth and rockfill dams (higher than 100m) in China belong to this type of dams (Zhang, 2005). Its wide use is due to the fact that upstream membrane rockfill dams contain impervious membranes on the upstream face to prevent seepage, which is thinner and easier to be constructed than the clay core. This membrane is usually made

of concrete or asphalt. Similar to other types of rockfill dams, rockfill is employed as the main construction material to provide stability. The geometry of a concrete-faced rockfill dam is shown in Figure 5-4 (Gu, 1988).

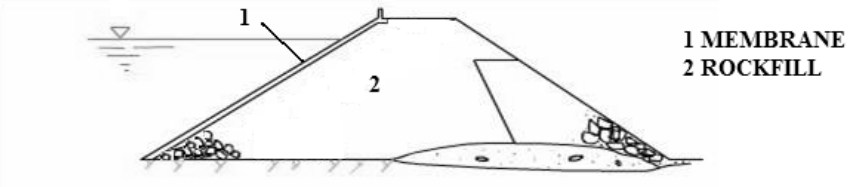


Figure 5-4: Typical geometry of a concrete-faced rockfill dam (after Gu (1988))

5.2.2 Seismic damage of earth and rockfill dams

Seismic loads can induce devastating damage on earth and rockfill dams, in terms of three significant dynamic effects. Firstly, when propagating through earth dams, earthquake waves can be amplified by soil materials, resulting in larger dynamic response at the dam crest. Secondly, earthquake generated accelerations can induce inertial forces on earth dams, whose magnitudes and directions change rapidly and non-periodically. Thirdly, cyclic loading can reduce soil strength due to excess pore pressure generation. These three effects are combined during earthquakes and strongly threaten the safety of earth and rockfill dams.

The seismic damage of earth and rockfill dams can be complicated, where different types can occur due to the complexity of earthquake types, potential failure mechanisms and soil properties (Kramer, 1996). Based on different failure phenomena, two broad classes of seismic damage on earth and rockfill dams are discussed in this section, which are the damage related to inertial deformations and the damage due to liquefaction.

The damage related to inertial deformations on earth and rockfill dams involves large permanent deformations generated by large-magnitude seismic loading. Among all the damage types, slope instability is the most commonly observed one, in terms of large movement or deformation of sliding masses. Other usual damage types related to inertial deformations are listed by Gazetas (1987), including crest settlement, cracking and piping failures.

Slope instability

Slope instability occurs when a large soil mass slides along a slip surface, which are usually induced by two factors. Firstly, earthquake generated accelerations apply inertial forces on slopes, whose magnitudes and directions can change rapidly. Secondly, the shear strength of soil materials can be weakened by excess pore pressure generation under cyclic loading. Slope failures have been widely observed in earthquake events. Examples can be found in the 1968 Tokachi-oki earthquake in Japan (Gu, 1988), where slope failures accounted for 42% of all the observed dam damage. This phenomenon is due to the employment of a particular dam construction material, pozzolanic silty loam. The standard compaction of this material could not be satisfactorily achieved, leading to the poor compaction for most earth dams within 200km from the epicentre (density: 0.90-1.18g/cm^3). Furthermore, dam materials were saturated due to the continuing rainfall before the earthquake, which generated significant excess pore pressures and eventually resulted in slope failures. An example of the failure mode of the Nozawa Poe dam in the Tokachi-oki earthquake is shown in Figure 5-5, which was located 200km from the epicentre (Gu, 1988).

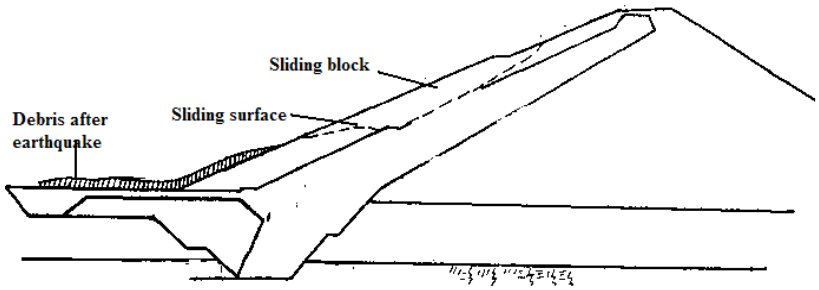


Figure 5-5: Failure mode of the Nozawa Poe dam in the 1968 Tokachi-oki earthquake (after Gu (1988))

Crest settlement

Crest settlement is another type of seismic damage on earth and rockfill dams, which is due to slope failure or/and densification of dam materials. Crest settlement can lead to freeboard loss and may result in overtopping. Furthermore, crest settlement is significantly critical for the safety of structures and equipment placed on dam crests. An example of the crest settlement is shown in Figure 5-6, which was observed on the Douhe earth dam in the 1976 Tangshan earthquake (China). The Douhe earth dam was located 19.0km from the epicentre and is a clay core earth dam. After the earthquake, one-meter settlement was found on the dam crest due to the densification of dam

materials (Gu, 1988).

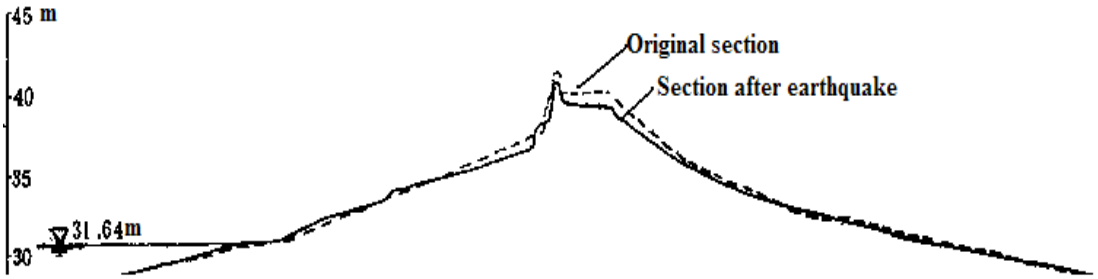


Figure 5-6: Deformation mode of the Douhe earth dam in the 1976 Tangshan earthquake (after Gu (1988))

Cracking

Cracking is another commonly observed seismic damage type for earth and rockfill dams, which includes longitudinal and transverse cracks on dam bodies. The former ones mostly exist on dam crests, due to slope failures or large longitudinal deformations under lateral earthquake excitations. The latter ones are caused by differential deformations between dams and abutments, or between different dam sections, which can occur under transverse excitations. Examples of two types of cracking deformations are shown in Figure 5-7, which were observed on the Dianju earth dam in the 1970 Tonghai earthquake (China). After this earthquake, six longitudinal cracks were found at the upstream slope, downstream slope and on the crest, which were approximately 60.0m long, 6.0cm wide and 5.0m deep. Several transverse cracks were also observed at the right-side of the dam crest, which were nearly 20.0m long and 4.0cm wide (Gu, 1988).

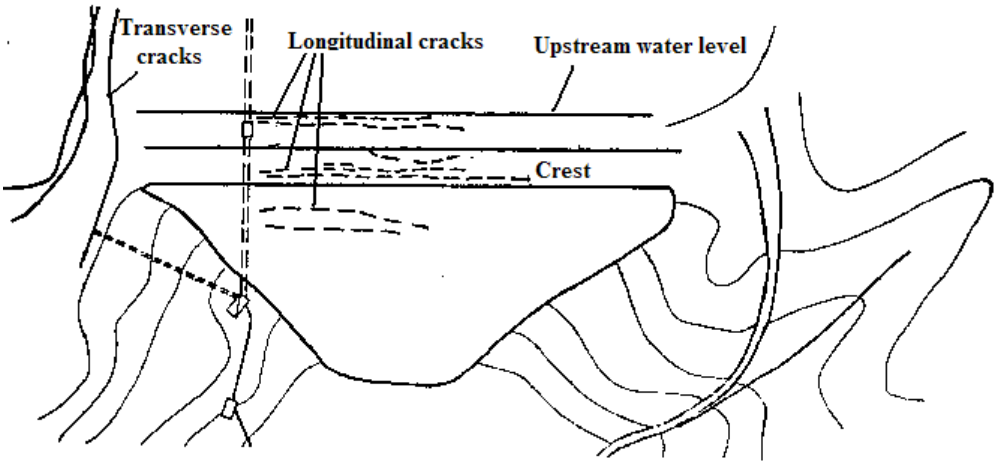


Figure 5-7: Layout of cracks on Dianju earth dam in 1970 Tonghai earthquake (after Gu (1988))

Liquefaction

Liquefaction is a complex and devastating seismic damage type for earth and rockfill dams. Liquefaction involves large deformations due to total or partial shear strength loss, induced by the generation of excess pore pressures. There are two categories of liquefaction, flow liquefaction and cyclic mobility (Kramer, 1996). Generally, the influence of flow liquefaction is more severe although it is less frequently observed. It can occur when the shear stress of the static equilibrium is larger than the shear strength of the liquefied soil (Kramer, 1996). However, cyclic mobility can induce deformations of wider range, from insignificant to severe, where a particular type of the cyclic mobility is sand boils, in the form of upward movement of sand grains (Kramer, 1996).

Flow liquefaction and cyclic mobility have been widely observed on earth dams in earthquake events. For example, flow liquefaction and sand boils were respectively observed on the Shivlakha dam and the Chang dam in the 2001 Bhuj earthquake (India). Both dams were constructed in 1950s, which are approximately 20-meter high and built on mixed layers consisting of sand and silt. After the earthquake, sand boils were observed at the upstream heel of the Chang dam and liquefaction was found underneath the upstream shell of the Shivlakha dam. Moreover, due to the liquefaction effect, slope failures and large cracks were triggered on the upstream slope of the Shivlakha dam, as shown in Figure 5-8 (Singh, 2005).

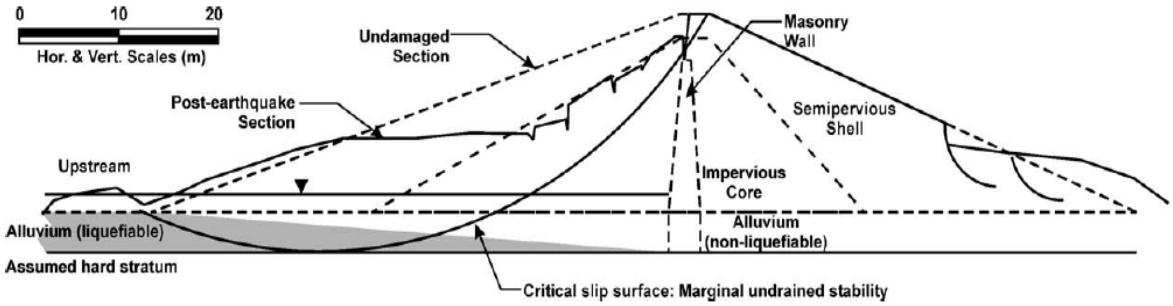


Figure 5-8: The failure mode of the Shivlakha dam in the 2001 Bhuj earthquake (after Singh (2005))

5.2.3 Seismic analysis methods for earth and rockfill dams

Since 1920s, numerous analysis methods have been proposed and developed to investigate the seismic response of earth and rockfill dams. These approaches vary in terms of the different assumptions involved and the accuracy of simulating real dynamic soil behaviour. Based on the different study objectives, these methods can be

categorised into four groups, i.e. the stability analysis methods, the permanent displacement analysis methods, the shear beam method and the FE method.

The stability analysis methods aim to evaluate the stability of geotechnical structures under earthquake loading (such as the pseudostatic method). The permanent displacement analysis methods (such as the sliding block method of Newmark (1965)) concentrate on the prediction of the permanent seismic deformation of earth structures. Both methods are based on the limit equilibrium method and consider the studied geotechnical structures to be rigid and non-deformable. Therefore, the shear beam method predicts more realistic dynamic behaviour of geotechnical structures by considering them as deformable bodies. The shear beam method was proposed by Mononobe (1936) for the dynamic analysis of earth dams. The main idea of the shear beam method is to simulate the deformation of geotechnical structures consisting of a number of thin horizontal soil layers, by applying equilibrium equations on both upper and lower boundaries of the layers (shown in Figure 5-9). The assumptions for the original shear beam method are: (a) there are only horizontal displacements and shearing deformations on shear beams; (b) shear stress and strain are constantly distributed along the upper and lower boundaries; (c) dam materials are assumed to be homogeneous, linear and elastic; (d) dams are long enough compared to the height and are laid on rigid bedrock (Gazetas, 1987).

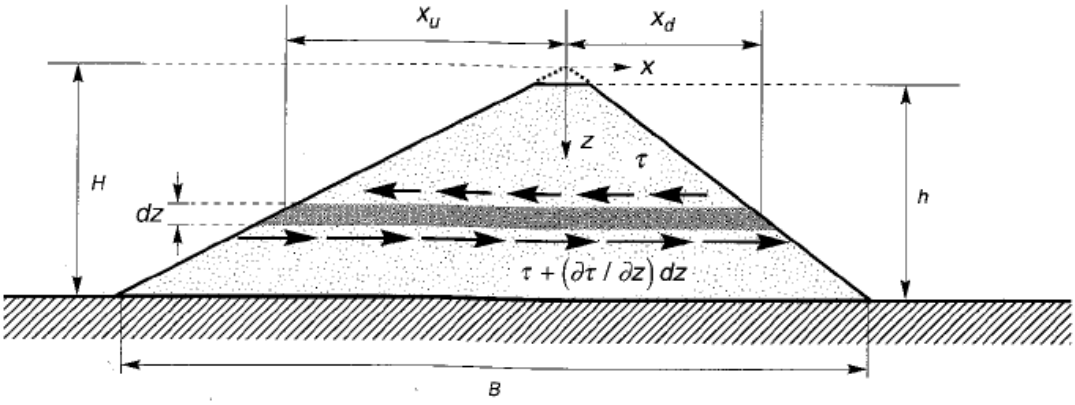


Figure 5-9: A schematic graph of the shear beam method for earth dams (after Kramer (1996))

The seismic analysis of earth and rockfill dams requires the accurate simulation of complex dam geometry, the consideration of structure interaction effects and the reproduction of real soil behaviour. The previous three classes of methods cannot satisfy these requirements and more advanced numerical analysis methods are required for this

purpose. Such numerical methods include the FE method, finite difference method and boundary element method. Among these, the FE method has gained its popularity due to its ability of accurately simulating real dynamic soil behaviour, through the implementation of soil constitutive models, boundary conditions and HM coupled consolidation formulation. Therefore, the FE method has been widely employed to investigate the seismic response of earth and rockfill dams. These numerical investigations are particularly discussed in the following sections, whereas the applications of the other three methods will not be introduced in great detail and can be found in Kramer (1996). However, all the dynamic analysis methods can be utilised as useful analysis tools, providing that their merits and drawbacks are well known to researchers (Gazetas, 1987).

Basic principles of FE method

As mentioned in Chapter 2, the FE method considers the geometry of the problem as a continuum composed of an assemblage of discrete elements, which are defined by nodes at element boundaries. Since the FE method satisfies the requirements of a true theoretical solution, the FE formulation can be obtained by employing the four requirements, which are the equilibrium, compatibility, material constitutive relations and boundary conditions. In order to accurately simulate the dynamic response of geotechnical structures, different critical aspects of the numerical modelling have been investigated and developed in FE programs. Firstly, the development of soil constitutive models ensures the accurate reproduction of real dynamic soil behaviour. Secondly, the implementation of HM coupled formulation interprets of two-phase behaviour of soil materials. Thirdly, boundary conditions assist dynamic FE analyses to reduce computational cost and accurately simulate wave propagation mechanisms. Finally, time integration methods are employed to achieve stable, accurate and realistic solutions for dynamic analyses. Therefore, the FE method can achieve all the objectives of the aforementioned three classes of seismic analysis methods and can overcome their limitations. Namely, the assessment of slope stability and the prediction of permanent displacements can be simultaneously achieved by the FE method by employing appropriate numerical models.

Developments of the dynamic FE analysis for earth and rockfill dams

Clough and Chopra (1966) probably for the first time employed the FE method to analyse the seismic response of earth dams. The dynamic response of a 2-D homogeneous triangular dam (see Figure 5-10) was numerically simulated by assuming linear elastic soil behaviour, where viscous damping was employed to account for the material damping. It should be noted that the limitations of the shear beam method were also highlighted in their works. It was found that the assumption of constant stress distribution on shear beam surfaces is misleading, where stresses are reasonably constant within the middle zone of the dam body, but decrease to zero on the dam surface.

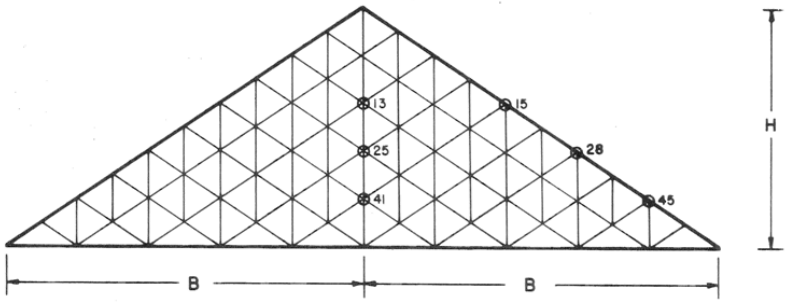


Figure 5-10: The FE mesh of a homogeneous triangular dam (after Clough and Chopra (1966))

Since 1970s, the FE method has been extensively developed to account for material nonlinearity. Due to the complexity of the implementation of nonlinear models and the limited computing development, the equivalent-linear method was firstly employed in the dynamic analysis of earth dams. Equivalent values of shear modulus and damping ratio were iterated and employed in the analysis, to approximately represent the soil nonlinearity in terms of stiffness degradation and hysteretic material damping. Examples can be found in Seed et al. (1969) and Vrymoed (1981).

The first true nonlinear dynamic FE analysis for earth dams is attributed to Prevost et al. (1985) by using DYNAFLOW (Prevost, 1981). 2-D and 3-D dynamic analyses of the Santa Felicia earth dam were conducted by employing a multi-surface plasticity constitutive model (Mroz, 1967). In this model, an 11-piece yield surface linearisation was adopted to approximate the hyperbolic shear stress-strain behaviour. Minor difference was found between the results from 2-D and 3-D dynamic analyses, indicating the insignificant canyon effect for this example.

Lacy and Prevost (1987) conducted a sophisticated investigation of the seismic response of earth dams by employing a two-phase coupled FE method, concentrating on the nonlinear and two-phase soil behaviour. Probably it was the first attempt to utilise the HM coupled formulation to analyse the dynamic response of earth dams. It was pointed out that the numerical model used in the previous study (Prevost, 1985) did not introduce sufficient damping in the dynamic analysis, which caused an overestimation for the seismic response of the Santa Felicia dam compared with the monitored data. Therefore, the HM coupled formulation should be employed to more precisely reproduce the dynamic behaviour of earth dams, by introducing an additional damping generated by the interaction between the soil skeleton and pore water phases (named as viscous damping by Bardet and Sayed (1993)). Multi-surface plasticity theory with kinematic hardening was utilised as the constitutive model in the analysis. Based on Figure 5-11, compared to the results from the one-phase analysis, smaller horizontal response and larger vertical response at the dam crest were predicted by the two-phase analysis. It was the first time to address the viscous damping effect in dynamic analysis of earth dams. However, this observation contradicts the theory of Bardet and Sayed (1993), that the vertical response of saturated porous geotechnical structures is supposed to be more significantly damped by the viscous damping than the horizontal component. This is because pore water in soils does not account for any shear deformation and therefore the interaction effects between the soil skeleton and pore water phases should be less significant on the horizontal dynamic response. Therefore, this implies that the effects of the HM coupled formulation on the seismic response of earth dams require more specific investigations.

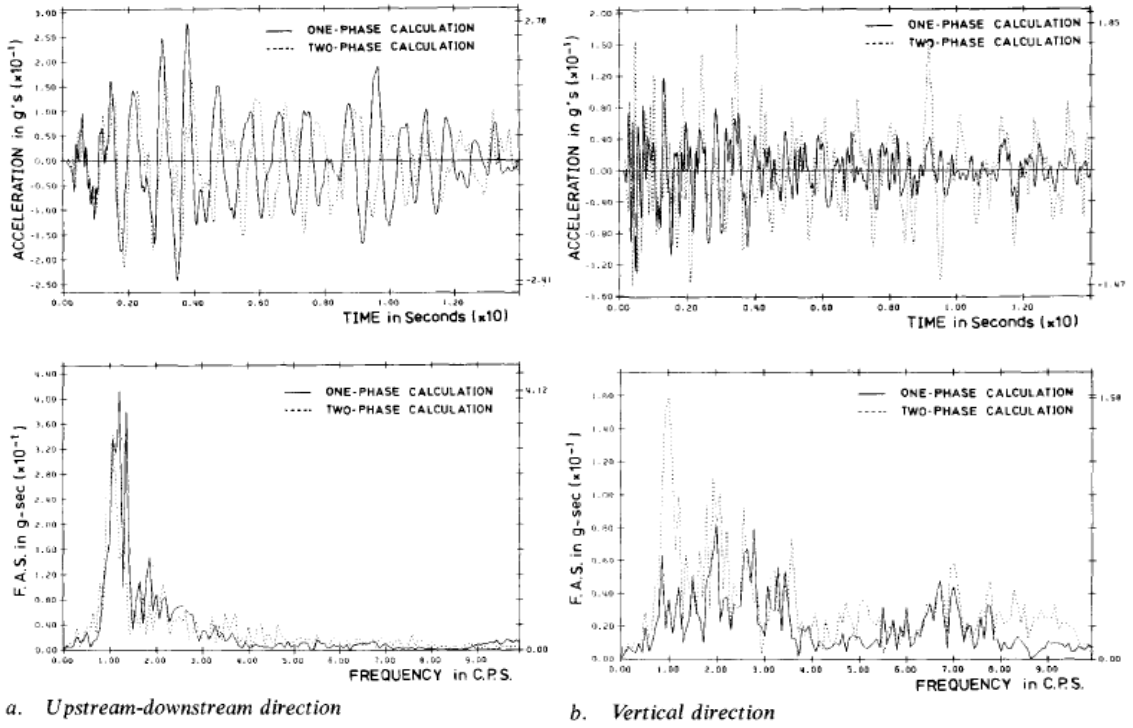


Figure 5-11: Comparison of seismic response from one-phase and two-phase FE analyses (after Lacy and Prevost (1987))

Since 1990s, efforts have been contributed to extensively develop different aspects of the dynamic FE method for earth and rockfill dams. A number of studies have investigated the seismic interaction effects between different dam structures, such as dam-foundation and dam-reservoir interaction. For example, a new technique was proposed by Guan and Moore (1997) to simulate the dam-reservoir interaction in the dynamic FE analysis of the La Villita dam. Frequency-dependent masses and dynamic loading were employed on the dam upstream slope boundary to represent the seismic effects of the reservoir. The predicted dynamic response at the dam crest in terms of the acceleration response spectra, by considering and ignoring the dam-reservoir interaction effects, is compared in Figure 5-12. Minor differences are observed between the seismic response of the La Villita dam under the two considerations.

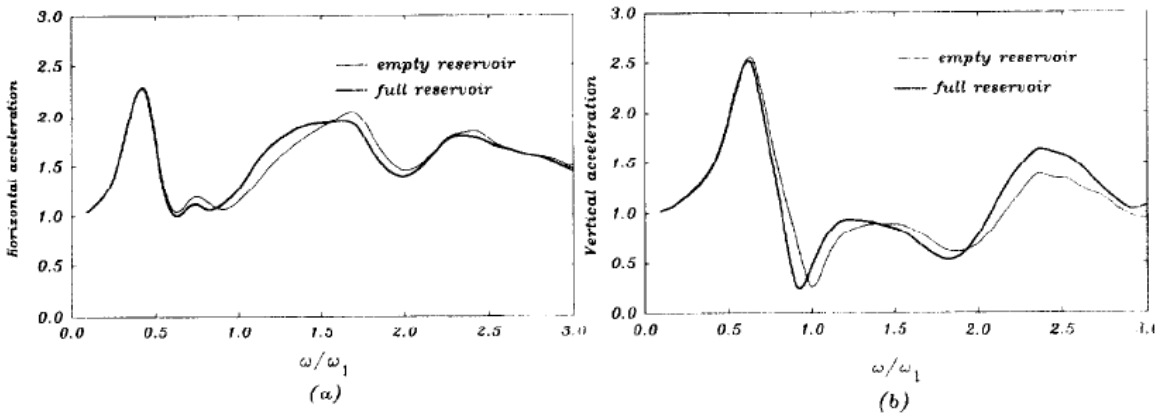


Figure 5-12: Impact of dam-reservoir interaction on seismic response of the La Villita dam (after Guan and Moore (1997))

Moreover, Wu (2005) conducted static and dynamic FE analyses for the Yele rockfill dam to investigate the influence of soil foundations on seismic response of the Yele dam. The Duncan-Chang model (Duncan and Chang, 1970) and the equivalent-linear method were employed in the static and dynamic analyses respectively. The predicted maximum horizontal and vertical seismic displacements on the dam crest were 64.0mm and 23.0mm respectively. Therefore, it was suggested to allow for sufficient freeboard height in earthquake-resistant designs of earth and rockfill dams on soil foundations. Furthermore, it was also pointed out that the stress and strain distribution on the dam body is also strongly affected by the seismic deformation of the soil foundation. However, only one-phase FE formulation and equivalent-linear method were employed in the conducted dynamic analysis for the Yele dam, which were unable to simulate the nonlinear and two-phase soil behaviour.

Lollino et al. (2005) investigated the static behaviour of the Pappadai rockfill dam under construction and impounding conditions using ICFEP. The Modified Cam Clay model was employed to simulate the nonlinear and two-phase behaviour of rockfill materials. A good agreement was achieved between the numerical results and the monitored data. Although this dam was only analysed in static conditions, it is helpful for understanding the application of nonlinear constitutive models and two-phase formulation on the FE analysis of rockfill dams.

Elia et al. (2011) investigated the seismic response of the Marana Capacciotti dam in Italy by employing the coupled FE formulation in DIANA-SWANDYNE II (Chan, 1988 & 1995). A multi-surface elasto-plastic constitutive model was adopted to simulate the static and dynamic soil behaviour of dam materials. The initial stress state of the dynamic analysis was reproduced by simulating the geological history of the dam foundation, the dam construction and the reservoir impounding. The constitutive model was calibrated against the laboratory test results for dam and foundation materials. The FE mesh of the Marana Capacciotti dam is shown in Figure 5-13.

The dynamic response of the Marana Capacciotti dam was parametrically investigated by coupled consolidation FE analyses imposing four earthquake excitations of different return periods. Numerical results showed larger seismic deformation on the downstream dam slope than that on the upstream slope. However, no obvious failure mechanism was observed for the dam subjected to the four earthquake motions. Therefore it was commented that this dam is sufficiently earthquake resistant to future seismic activities. Furthermore, large plastic deformations in the dam body and the foundation layer were found to be further developed due to a post-earthquake consolidation process. Finally, parametric studies highlighted the effects of the excitation magnitude on soil nonlinearity characteristics, in terms of stiffness degradation and material damping. Overall, according to Elia et al. (2011), the fully coupled effective stress non-linear approach is suggested for a more accurate prediction of seismic response of earth and rockfill dams. However, the predicted dynamic response of the Marana Capacciotti dam was not compared against monitored data, since the conducted work originated from a required earthquake-resistant design for the Marana Capacciotti dam.

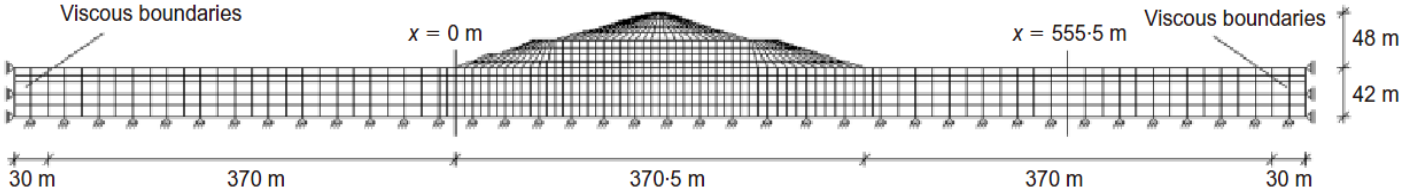


Figure 5-13: FE mesh of Marana Capacciotti dam (after Elia et al. (2011))

Pelecanos (2013) conducted a systematic investigation on the dynamic response of earth dams by employing ICFEP. In particular, different critical aspects of the numerical modelling for dam reservoirs were studied. The guidelines for appropriate application of reservoir boundary conditions, water material stiffness, dam-reservoir interface and water material damping were proposed. The seismic dam-reservoir interaction effects were explored for different types of dams. Based on the conducted work, it was commented that the dam-reservoir interaction effects are less insignificant for dams with inclined upstream slopes, such as earth dams, compared to dams with vertical upstream slopes. Furthermore, FE analyses were conducted to predict the static and dynamic response of the La Villita dam (Figure 5-14) under construction, impounding and a series of earthquake events. A cyclic nonlinear model coupled with the Mohr-Coulomb failure criterion was employed to simulate the elasto-plastic soil behaviour. A good agreement was observed between the dynamic FE results and the monitored seismic response on the dam crest, after considering the stiffening effects of the narrow canyon geometry and ignoring the high frequency vibrations induced by a local failure at the dam crest. Finally, the effects of different factors on the seismic response of earth dams, i.e. the previous loading history, coupled FE analysis, dam-foundation interaction, dam-reservoir interaction and stiffness inhomogeneity, were investigated through parametric studies. It was pointed out that the coupled consolidation analysis did not attribute significant influence on the dynamic response of the La Villita dam. This can be attributed to the fact that only the low permeability clay core and dam foundation were involved in the consolidation analysis, whereas the behaviour of the relatively high permeability rockfill materials was only assumed to be drained. Therefore it was suggested that a full consolidation analysis and appropriate permeability should be employed in the dynamic analysis of rockfill dams for a more accurate prediction of the seismic response.

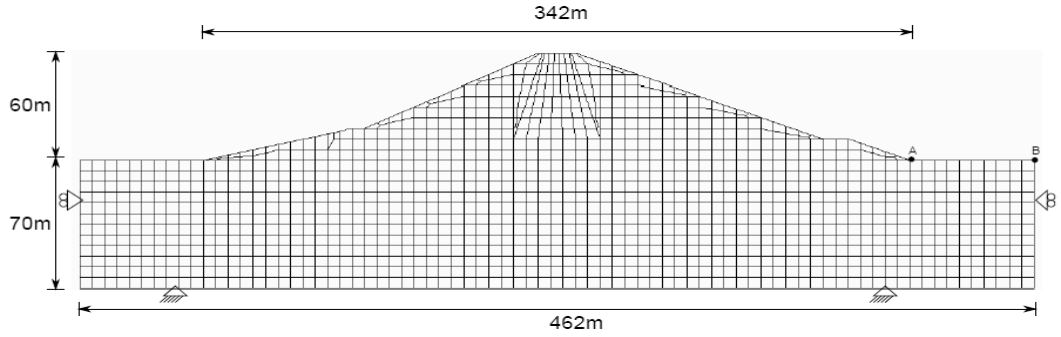


Figure 5-14: The FE mesh of La Villita dam (after Pelecanos (2013))

In engineering practice, the application of the advanced dynamic FE method for the seismic design of earth and rockfill dams is still limited. This is mainly due to the difficulties of employing appropriate numerical models for the accurate prediction of the dynamic response of geotechnical structures. Simple design methods, such as the sliding block method (e.g. Newmark, 1965; Sarma, 1975; Makdisi and Seed, 1978; Ambraseys and Menu, 1988), are still widely used for the earthquake-resistant design for earth and rockfill dams. The sliding block method applies pseudo-static inertial forces on sliding masses to represent the seismic effect, which are calculated by multiplying the seismic coefficient k_h with the weight of a potential sliding mass W (i.e. $F=k_h \cdot W$). This method assumes the sliding mass to obtain permanent displacements whenever the applied acceleration ($k_h \cdot g$) is larger than the critical acceleration ($k_y \cdot g$). The critical seismic coefficient k_y is obtained when achieving the limit equilibrium state of the sliding block. Furthermore, permanent displacements are calculated by the second order integration of the exceedance of the applied accelerations over the critical acceleration. This is a straightforward seismic design method for embankment dams, which however on the other hand restricts its application on more accurate prediction for the seismic response of earth structures subjected to complicated geotechnical and seismic conditions. Therefore, the sliding block method has been extensively developed over the years to account for a variety of parameters: ground motion characteristics, dam geometry, dam and foundation nonlinear material properties, etc. A recent and representative development for such design method can be probably attributed to Papadimitriou et al. (2014) and Andrianopoulos et al. (2014). The main contribution is a proposed methodology for a more rigorous estimation of the peak seismic coefficient k_{hmax} on potential sliding slopes for the performance-based design of embankment dams, based on numerical analysis results from 110 nonlinear dynamic plane-strain analyses for embankment dams with heights ranging from 20-120m. The estimation for k_{hmax} considers the effects of different geotechnical and seismic characteristics, which includes the PGA and predominant period of the bedrock motion, the PGA of the free-field motion, the nonlinear fundamental period of the dam vibration, the foundation and dam material properties, the geometrical characteristics and the location of the potential sliding masses.

In particular, the estimation formulation for k_{hmax} on potential sliding masses is proposed based on the statistical regression of the numerical data. The prediction for

k_{hmax} involves four successive steps, where the first three steps concentrate on estimating the PGA (PGA at free field), T_o (the nonlinear fundamental period of the dam vibration) and PGA_{crest} (PGA at dam crest) respectively. The estimated k_{hmax} can be then employed to predict the seismically induced displacement on potential sliding masses by using the sliding block method (i.e. based on the exceedance of k_{hmax} over k_y). Consequently, the safety of embankments will be assessed based on the predicted displacements on a variety of potential sliding slopes.

These two studies provide a simple seismic design method for embankment dams, but achieve satisfactory accuracy in estimating the seismic coefficient. In Papadimitriou et al. (2014), the estimation of k_{hmax} was compared to results from nonlinear numerical analyses, where a standard deviation of the relative error of ±27% was observed (as shown in Figure 5-15). However, it was suggested that this design method is reliably applicable for embankments with height from 20 to 120 m, with or without typical stabilising berms, under steady state seepage condition, lying on a stiff (v_s≥250 m/s) and thick (thickness≥5 m) soil layer, and subjected to excitations prescribed by specific predominant periods and PGAs. Furthermore, it was pointed out that, in order to simulate complex soil behaviour, such as the excess pore water pressure generation, numerical analysis employing advance constitutive models was required. The detailed formulation of this design method is further discussed in Section 5.6.5.

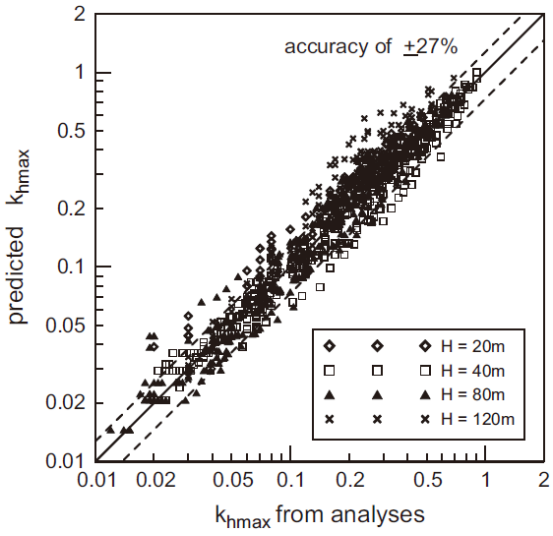


Figure 5-15: Prediction accuracy of k_{hmax} (after Papadimitriou et al. (2014))

5.3 Introduction of the Yele dam

The Yele dam is an asphaltic concrete core rockfill dam located at the Nanya River in Sichuan Province, China. It is the highest asphaltic concrete core rockfill dam among all the same type of dams in China (124.5m high). The Yele dam serves solely as an electricity generation plant. Its reservoir capacity is 298 million cubic metres. On 12th May 2008, the disastrous Wenchuan earthquake (Ms=8.0) occurred in west China. The Yele dam is located 258.0km from the epicentre and experienced strong shaking. During the earthquake, eight seismometers recorded the ground motion at different locations on the dam, providing valuable monitoring data for the dynamic investigation of rockfill dams.

5.3.1 Dam geometry, construction sequence and seismic event

The plan view, axial longitudinal section and maximum transverse section of the Yele dam are shown in Figures 5-16, 5-17 and 5-18 respectively. The maximum height of the Yele dam is 124.5m and the designed normal reservoir water level is 117.0m. The dam axial length is 411.0m and the crest width is 15.0m. The Yele dam body consists of several filling zones, i.e. the asphaltic concrete core, transition layer, filter layer, coffer dam, cap dam and rockfill zone, as shown in Figure 5-18. The gradient of the upstream slope is 1:2.0 (including a 4.0m wide berm). The gradients of the downstream slope are 1:1.8, 1:2.2, 1:2.2 and 1:2.2 respectively for four sections divided by three 4.0m wide berms from the crest to the base. The dam foundation consists of an alluvium layer of varying thickness, where the average depth for the whole foundation layer is approximately 53.0m.

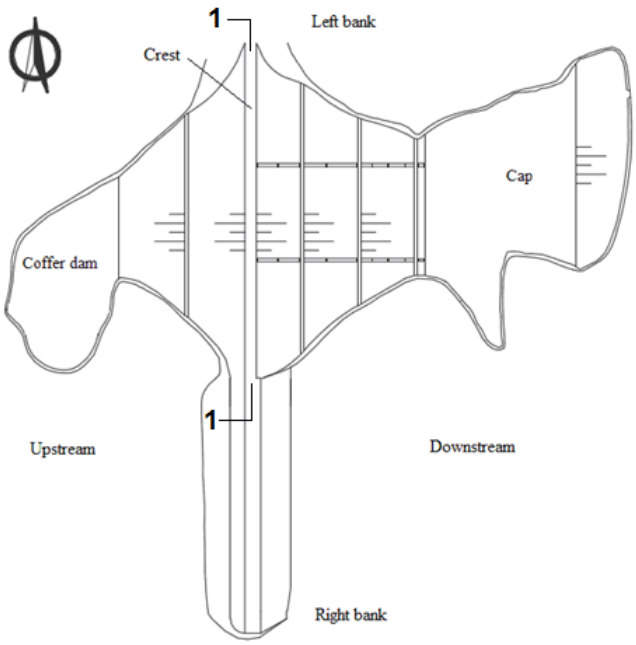


Figure 5-16: The plan view of the Yele dam (after He et al. (2006))

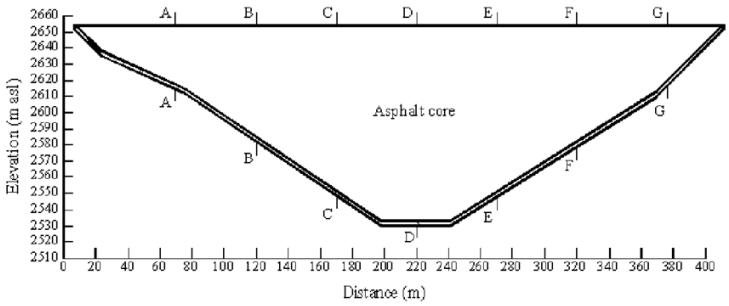


Figure 5-17: The axial longitudinal section 1-1 of the Yele dam (after Wang et al. (2008))

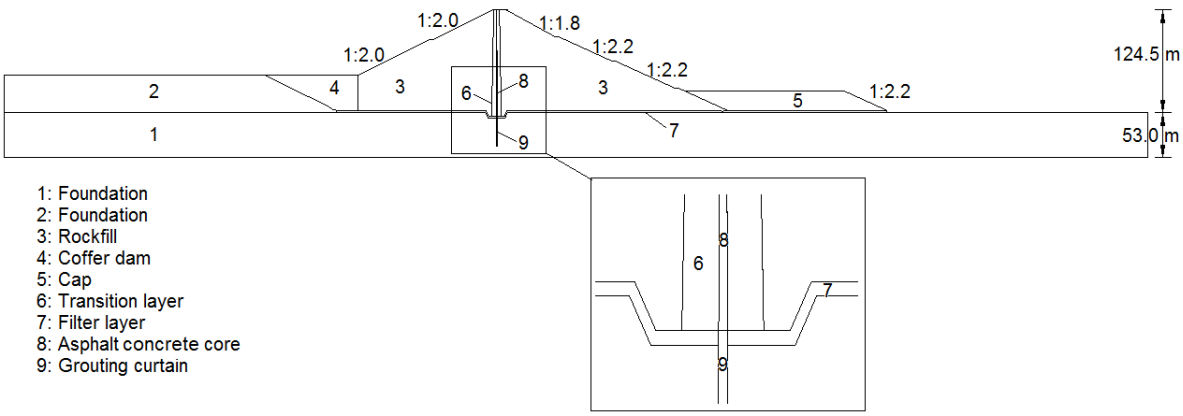
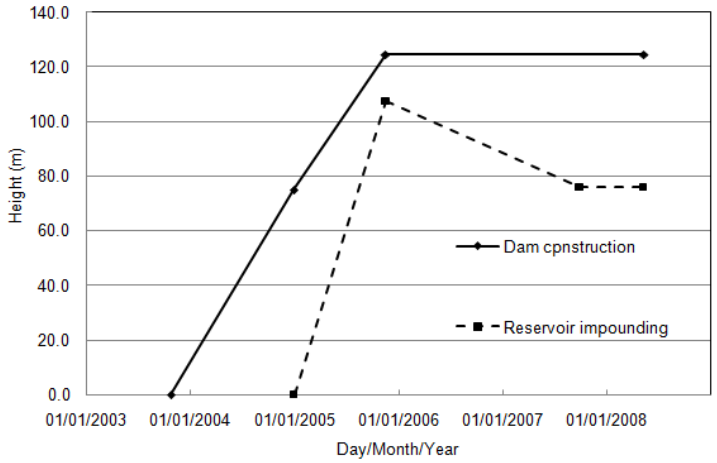
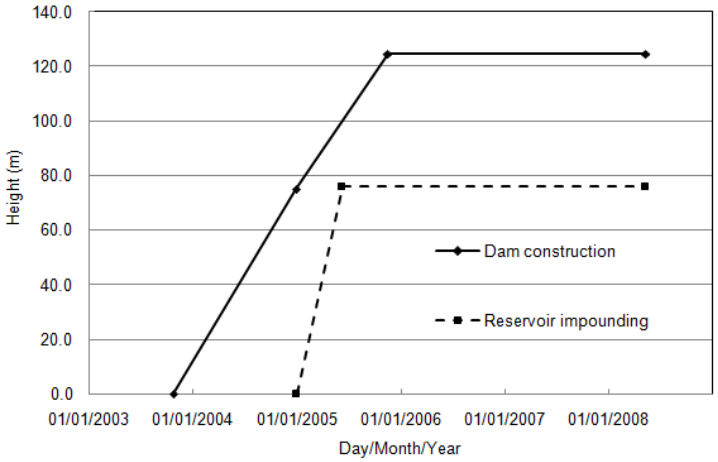


Figure 5-18: The maximum transverse section D-D of the Yele dam

According to He et al. (2006), the Yele water conservancy project commenced in December of 2000. The foundation treatment at the dam shoulders started in April of 2001. The river stream diversion was carried out in September of 2002. Before the construction of the dam body, a 30.0m deep grout curtain was injected under the designed dam longitudinal axis to control the seepage from the upstream area. The construction of the Yele dam started in October of 2003 and reached a height of 75.0m in January of 2005, which is the designed dead water level. The construction of the Yele dam finished in November of 2005, at the maximum dam height of 124.5m. The average construction speed was approximately 0.17m/day. The reservoir impounding of the Yele dam started in January of 2005, just after the completion of 75.0m dam construction, and reached 107.0m in November of 2005, after when the Yele power plant started to generate electricity. During the subsequent 2.5-year operation period, the reservoir experienced annual water level fluctuations due to the seasonal rainfall. Before the occurrence of the Wenchuan earthquake, the reservoir water level decreased to 75.0m, exactly at the dead water level. In order to numerically simulate the dam construction, reservoir impounding and operation processes in the static and dynamic analyses, the construction and reservoir impounding sequence is simplified into two scenarios, as shown in Figure 5-19. For the first scenario, the water level reaches 107.0m after the reservoir impounding and gradually drops to the dead water level of 75.0m during the following operation period. For the second scenario, the water level only reaches the dead water level of 75.0m after the reservoir impounding and remains constant until the occurrence of the Wenchuan earthquake. Both scenarios are employed in the following FE analyses and their effects on the static behaviour of the Yele dam are investigated.



(a): Construction and reservoir impounding sequences-scenario 1



(b): construction and reservoir impounding sequences-scenario 2

Figure 5-19: Simplified construction and reservoir impounding sequences in FE analyses of the Yele dam

On 12th of May 2008, the Wenchuan earthquake (Ms=8.0) occurred in west China, which resulted in 69197 deaths, 374176 injured and 18222 missing. The earthquake left about 4.8 million people homeless. After the earthquake, approximately 391 dams were damaged in varying degrees, including 4 large-scale ones (heights exceeding 100m) (Xu, 2009). It should be noted that among all these dams, only the seismic monitoring equipment of the Yele dam was working in good order and recorded the motions at different locations of the dam. According to Cao et al. (2010), the earthquake did not cause severe damage on the Yele dam. Only some localised damage was observed, which however did not influence the normal operation of the power plant. Furthermore, according to Wu et al. (2009), the low reservoir water level before the Wenchuan earthquake to some extent contributed to the satisfactory seismic performance of the

dam.

It should be noted that before the Wenchuan earthquake, the Yele dam experienced a low-intensity earthquake on 23th October, 2007 (Xiong, 2008). However, this earthquake was not well documented in the literature. Only the acceleration variations on the dam surface at the maximum transverse section can be found in Xiong (2008), which is further discussed in Section 5.6.4. The maximum PGA on the dam surface was recorded to be 0.08m/s^2. Therefore, due to the low-intensity of the earthquake and its insignificant influence on the Yele dam, it is decided here not to simulate this earthquake in the numerical analysis.

5.3.2 Material properties

The design of the Yele dam was briefly discussed by He et al. (2006), where some critical aspects were introduced, such as the geological conditions of the dam site, the dam layout, the dam material properties and the engineering treatment for the dam foundation. As mentioned before, the Yele dam body consists of several filling zones, i.e. the asphaltic concrete core, transition layer, filter layer, coffer dam, cap dam and rockfill zone. Including the dam foundation and grouting curtain, all the materials in the Yele project are described as follows (He et al., 2006)):

- gravelly and silty soils comprise the foundation layer;
- the materials for the core and grouting curtain are asphalt concrete and concrete respectively;
- the filter and transition layers are composed of fine gravel and sand to discharge seeping water and to accommodate any differential deformations between the core and the outer rockfill;
- the rockfill zone, coffer dam and cap dam were constructed with coarse gravel excavated and processed from the site near the dam.

Soil properties for all materials are summarised in Table 5-1 (He et al., 2006), which were obtained based on both in-situ investigations and laboratory tests. In particular, the effective cohesion and angle of shearing resistance were obtained by laboratory direct shear tests. The shear wave velocity was measured by in-situ tests, where however the test type was not reported. The shear and Young's moduli are calculated based on the

shear wave velocity, the density and the Poisson's ratio, where the Poisson's ratio is assumed to be 0.2 for gravelly soils, as suggested by Bowles (1997). The permeability was determined by laboratory permeability tests.

It should be noted that Pelecanos (2013) increased the original soil stiffness of the La Villita dam materials and employed them in the 2-D dynamic analysis, in order to account for the stiffening effects of the 3-D narrow canyon geometry. However, for the Yele dam, the length to height ratio L/H is 3.3, where L and H are the dam axial length and dam height respectively. Based on Dakoulas and Gazetas (1987) (Figure 5-20), the ratio between the fundamental period of a dam in a narrow canyon (T_1) over that in an infinitely wide canyon ($T_{1\infty}$) for the Yele dam is 0.8. This indicates a relatively insignificant canyon stiffening effect on the 2-D plane-strain FE analysis of the Yele dam. Therefore, the original stiffness of the Yele dam is employed for the following static and dynamic analyses.

Table 5-1: Soil properties for materials of Yele project

Parameter / Material	Cohesion c′ (kPa)	Angle of Shearing ϕ′ (degree)	Young's Modulus E (kPa)	Shear Modulus G (kPa)	Poisson's ratio υ	Density ρ (g/cm^3)	S-wave Velocity v_s (m/s)	Permeability k (m/s)
Foundation layer	80.0	38.0	3.53E+06	1.47E+06	0.2	2.3	800.00	1.0E-8
Core			3.00E+09		0.2	2.4		
Grouting curtain			3.00E+09		0.2	2.4		
Transition layer	0.0	45.0	2.78E+05	1.16E+05	0.2	2.3	224.32	1.0E-5
Filter layer	0.0	45.0	2.78E+05	1.16E+05	0.2	2.3	224.32	1.0E-5
Rockfill	0.0	50.0	7.34E+05	3.06E+05	0.2	2.3	364.66	1.0E-3
Coffer dam	0.0	50.0	7.34E+05	3.06E+05	0.2	2.3	364.66	1.0E-3
Cap	0.0	50.0	7.34E+05	3.06E+05	0.2	2.3	364.66	1.0E-3

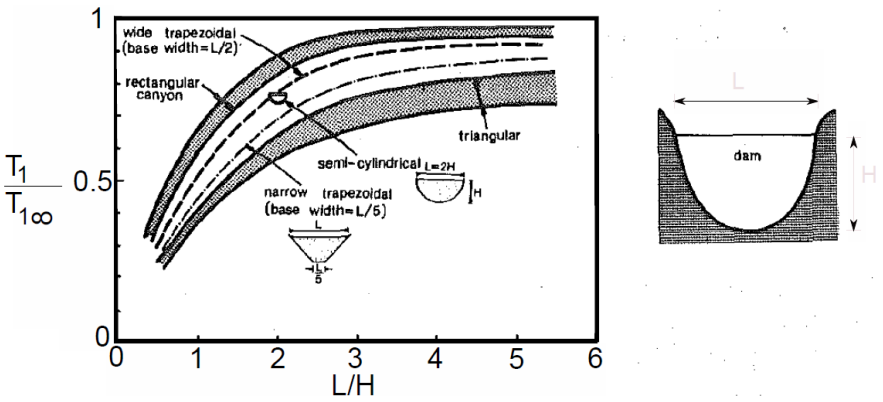


Figure 5-20: Effects of canyon geometry on the fundamental natural period of a dam (after Dakoulas and Gazetas (1987).

The dynamic soil properties for the Yele dam materials were obtained from Xiong (2009) through laboratory tests, in terms of shear modulus degradation and material damping curves, as shown in Figure 5-21. These are also compared with the corresponding curves proposed by Rollins et al. (1998) for the rockfill materials. It can be found that the Yele rockfill materials exhibit a more significant nonlinear behaviour. A more pronounced shear modulus reduction and higher damping ratios are observed for the Yele dam rockfill materials than that from Rollins et al. (1998). However, only the dynamic soil properties for the rockfill materials were available. It should be noted that the rockfill materials were excavated and processed near the dam site and therefore the available dynamic soil properties could also be applicable for the foundation materials. Furthermore, since the volume of the transition and filter layers is relatively small, the employment of the same dynamic soil properties for these two materials is not expected to significantly affect the dynamic deformations of the whole dam.

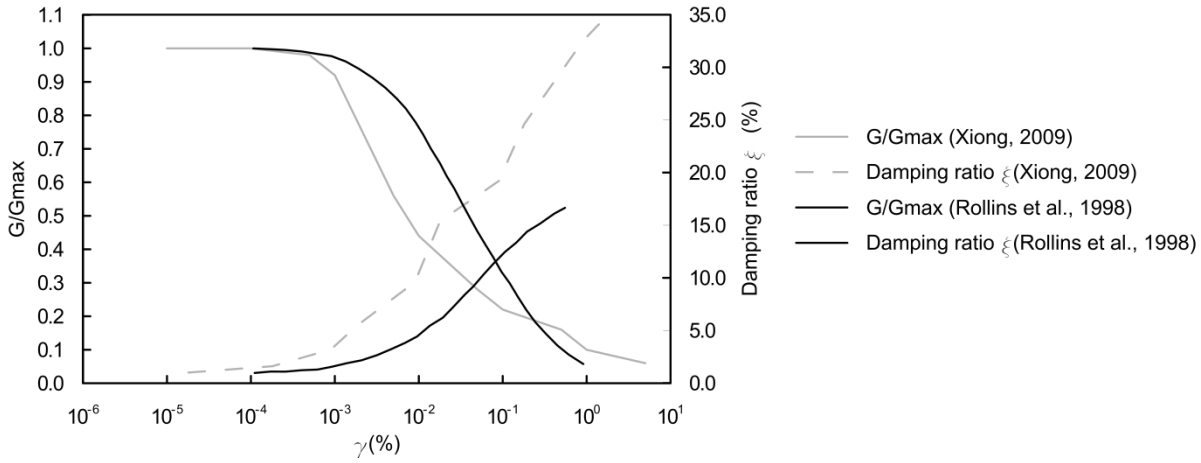


Figure 5-21: Dynamic soil properties of the Yele dam rockfill materials (after Xiong (2009))

5.3.3 Monitored data

Static monitored data

During and after the dam construction, a number of displacement observation bolts were placed at different locations of the Yele dam, in order to monitor the real time deformation at different stages and safe operation of the dam (Wang et al., 2008). In particular, 3 months after the dam construction, two bolts were installed on two downstream berms. At 6 months after the dam construction, three bolts were placed at the upstream side of the crest, at the top of the core and at the downstream side of the crest, to monitor crest settlement. 22 months after the dam construction, the monitored dam settlements at these five locations on the maximum transverse dam section were obtained and shown in Figure 5-22 (Wang et al., 2008). Furthermore, the horizontal displacements of the concrete core were monitored by several bolts installed at different depths of the core, where bolts were placed during the construction of the core section and started to operate immediately after the installation. These measurements at 22 months after the dam construction are shown in Figure 5-23 (Wang et al., 2008). Finally, the monitoring periods for different observations are illustrated in Figure 5-24, by numbering the different monitoring time points. For instance, the settlements at the two downstream berms were measured between the time points 4 and 6, the settlements at the crest were measured between time points 5 and 6, and the horizontal displacements along the core were measured from the instalment of the bolts to time point 6.

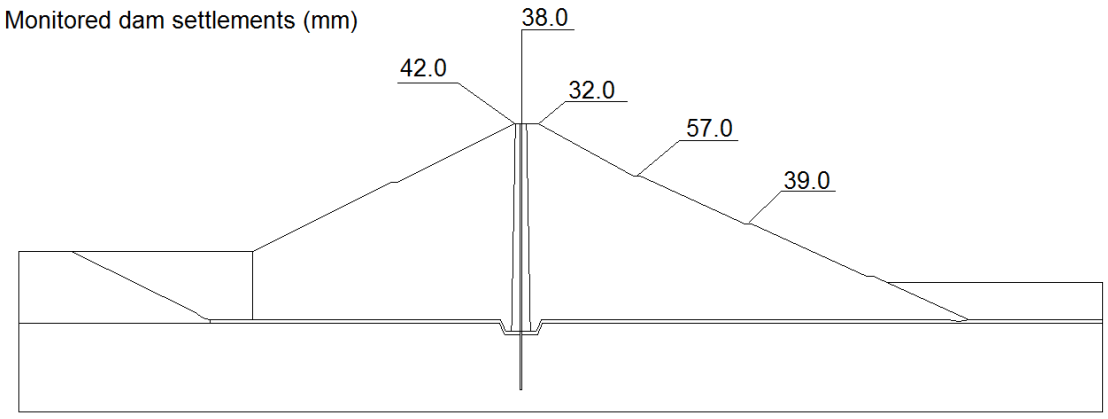


Figure 5-22: Monitored dam settlements (after Wang et al. (2008))

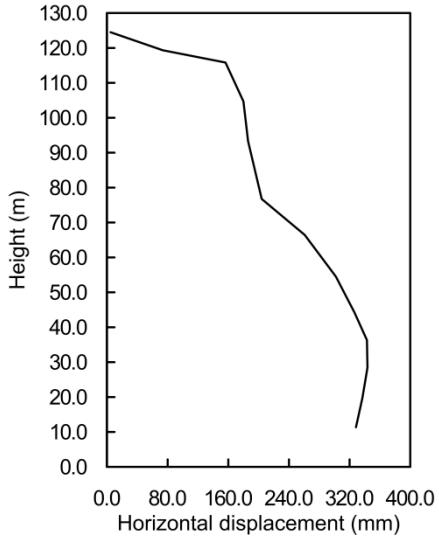


Figure 5-23: Monitored horizontal core displacements (after Wang et al. (2008))

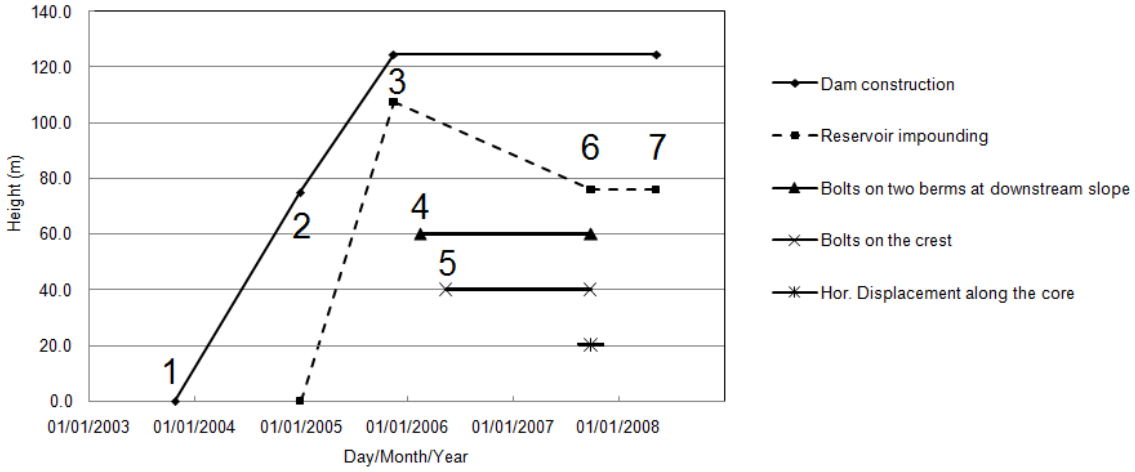


Figure 5-24: Monitoring periods of different observations

Seismic monitored data during the Wenchuan earthquake

Eight seismometers were installed on the Yele dam to capture the dynamic response in the East-West (EW), North-South (NS) and Up-Down (UD) directions. It should be noted that the EW, NS and UD directions denote the transverse, longitudinal and vertical directions respectively. The layout of the eight seismometers is shown in Figures 5-25 and 5-26. In particular, seismometers 4, 5, 6 and 7 were installed from the crest to the base on the downstream slope of the maximum transverse section. Seismometers 1 and 10 were placed at the left and right bank of the main dam. Seismometer 11 was installed at the right bank of the subsidiary dam. Furthermore, there was another seismometer installed in the grouting gallery at the left bank.

However, during the Wenchuan earthquake, only seismometers 4, 7 and the one at the grouting gallery operated. Recorded data from apparatus 4 and 7 reflect the dynamic response on the dam crest and dam base respectively. It should be noted that the grouting gallery was constructed just above the bedrock at the left bank and therefore the data monitored by the seismometer in the grouting gallery could be considered as the bedrock motion.

The recorded dynamic data are shown in Figures 5-27, 5-28 and 5-29, in terms of the acceleration time histories, response spectra and response amplification spectra respectively. It should be noted that the response amplification spectra are calculated by normalising the response at the crest by either the response at the base or at the bedrock, i.e. dam amplification effects corresponding to two different reference locations. Furthermore, based on the results shown in these three figures, the features of the seismic data are also summarised in Table 5-2, in terms of the PGAs and predominant frequencies for the motions at three locations and the dam fundamental frequencies corresponding to two reference locations. In particular, as the dam height increases, the PGA increases from the bedrock to the dam crest, reflecting the amplification effects at different dam locations. The predominant frequencies are found to be larger in the UD direction for the motions at the bedrock and the dam crest than those in the EW direction, while slightly smaller for the motion at the dam base in the UD direction. This reflects the more significant influence of the higher frequency vibrations on the vertical motion. However, the predominant frequencies in both directions are below 5.0 Hz, indicating that the motions are still dominated by low frequency vibrations. The fundamental frequencies of the dam vibration are obtained based on the crest amplifications at two reference locations, i.e. the crest/base and crest/bedrock. For both cases, the fundamental frequencies of the dam are observed to be larger in the vertical direction than those in the horizontal direction, indicating the larger dam material stiffness associated with the vertical motion. It should be noted that the seismic observations show relatively weak bedrock motion and dynamic dam response. However, as this research concentrates on the validation of the numerical modelling for dynamic response of rockfill dams, higher intensity earthquakes may be employed in the future to analyse the dynamic dam behaviour with class-A predictions.

Furthermore, based on the monitored data, the fundamental frequency of the dam vibration is found to be 1.64 Hz ($f_{\text{crest/base}}$) in the horizontal direction (Figure 5-29 and

Table 5-2). It should be noted that the nonlinear fundamental period of the embankment dam vibration can be estimated based on Papadimitriou et al. (2014), as shown in Equation 5-1. In particular, T_o is the nonlinear fundamental period of the dam vibration, T_{oe} is the elastic fundamental period of the dam vibration, T_e is the predominant period of the input excitation, v_b is the shear wave velocity of the foundation material, PGA is the peak ground acceleration at the free field, g is the gravitational acceleration, H is the dam height, v_s is the shear wave velocity of the dam material, $\mathrm{PGA_{rock}}$ is the peak ground acceleration at the bedrock surface, T is the nonlinear fundamental period of the foundation vibration and H_b is the foundation depth. Based on this equation, the nonlinear fundamental period of the Yele dam vibration subjected to the Wenchuan earthquake is calculated as 0.91s, where the corresponding fundamental frequency is 1.09Hz. This is 33% smaller than the monitored one (1.64Hz). However, it should be noted that the monitored fundamental frequency is obtained based on the recorded response amplification between the dam crest and the downstream berm, which only accounts for 78% of the entire dam height and is therefore theoretically larger than the actual fundamental frequency for the Yele dam vibration. Since the dam fundamental frequency is inverse-proportional to the dam height, the actual value for the Yele dam can be estimated by multiplying the observed one (1.64Hz) with the factor 0.78. The estimated value is 1.28 Hz, which is reasonably close to that predicted by the design method (1.09 Hz).

$$\text{Step1: } \mathrm{PGA} = \mathrm{PGA_{rock}} \cdot \frac{1+0.85\left(\mathrm{PGA_{rock}}/g\right)^{-0.17}\cdot\left(T/T_e\right)^2}{\sqrt{\left(1-\left(T/T_e\right)^2\right)^2+1.78\left(T/T_e\right)^2}}$$

$$\text{where } T = \left(\frac{4H_b}{v_b}\right)\cdot\sqrt{1+5330{v_b}^{-1.3}\left(\frac{\mathrm{PGA_{rock}}}{g}\right)^{1.04}}$$

$$\text{Step2: } \frac{T_o}{T_{oe}} = \begin{cases} 1+1.76\left(\dfrac{v_b}{1000}\right)^{0.25}\cdot\left(\dfrac{\mathrm{PGA}}{g}\right)^{0.75}\cdot\left(\dfrac{T_{oe}}{T_e}\right)^{-0.80} & \text{when } T_{oe} > T_e \\ 1+1.76\left(\dfrac{v_b}{1000}\right)^{0.25}\cdot\left(\dfrac{\mathrm{PGA}}{g}\right)^{0.75} & \text{when } T_{oe} \le T_e \end{cases} \quad \text{5-1}$$

$$\text{where } T_{oe} = 2.6\frac{H}{v_s}$$

All the recorded seismic data are provided by the Chendu Engineering Corporation and processed by using the software SeismoSignal (Antoniou and Pinho (2004)), where a linear baseline correction and a 4th order Bandpass Butterworth filtering was employed (frequency range: 0.1-25.0 Hz).

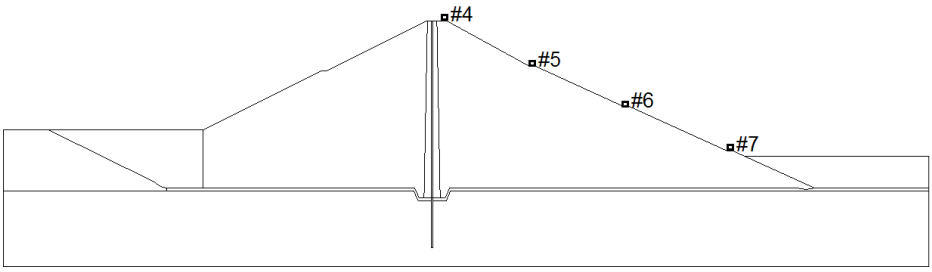


Figure 5-25: The layout of seismometers on the maximum transverse section

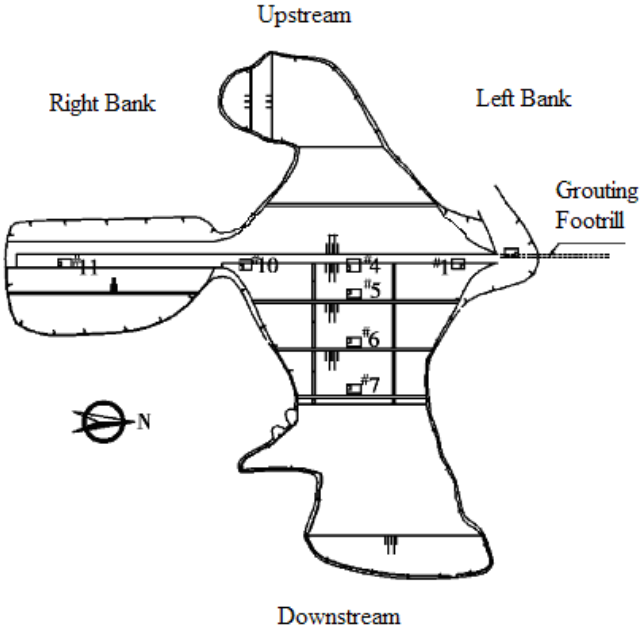
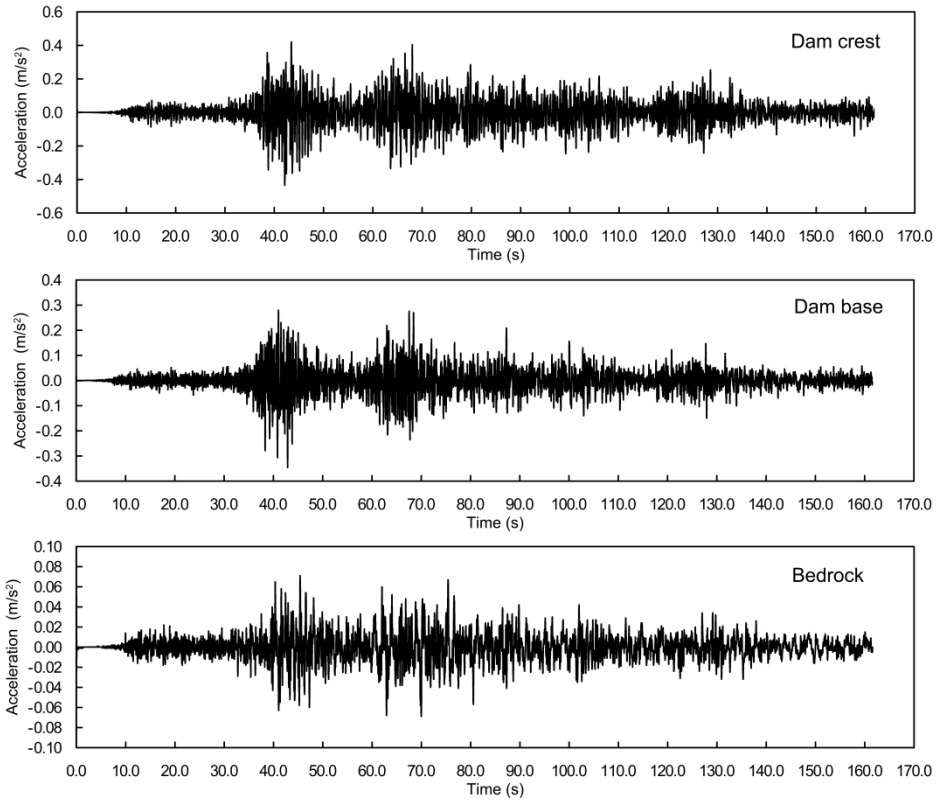
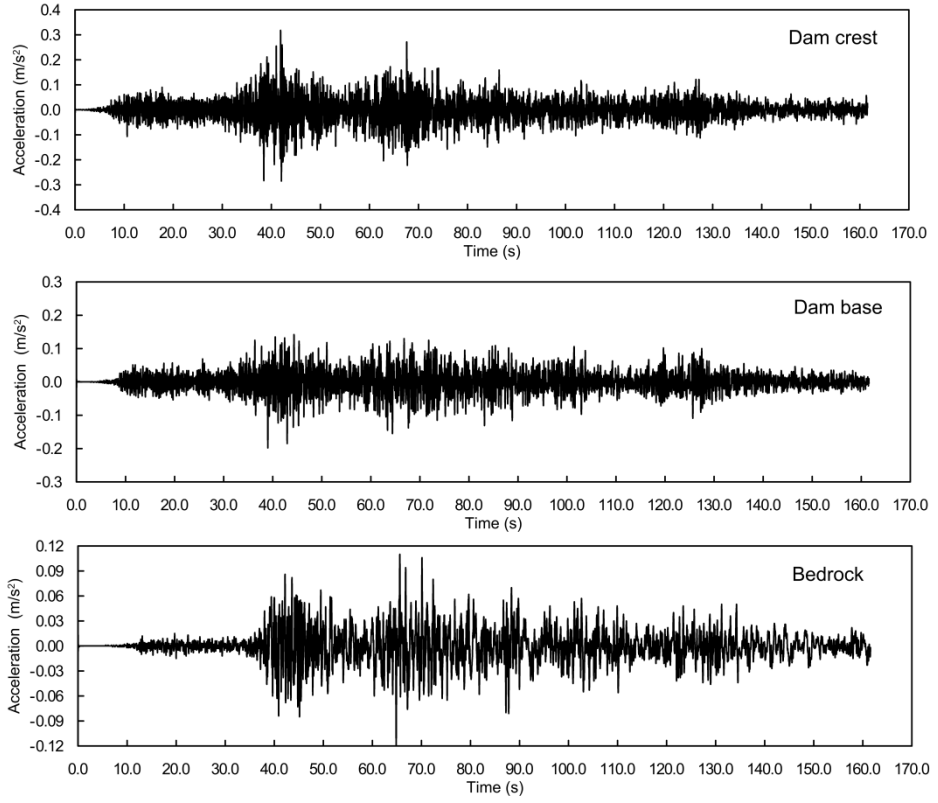


Figure 5-26: The layout of seismometers on the Yele dam in plan view

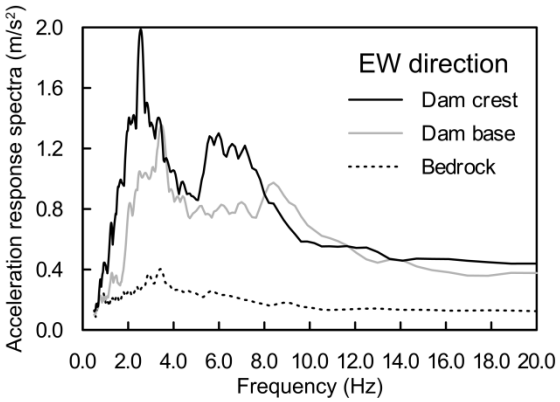


(a): Acceleration time histories in horizontal EW direction

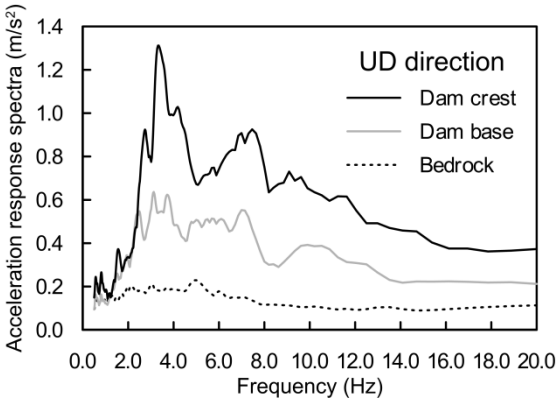


(b): Acceleration time histories in vertical UD direction

Figure 5-27: Seismic monitored data (acceleration time histories)

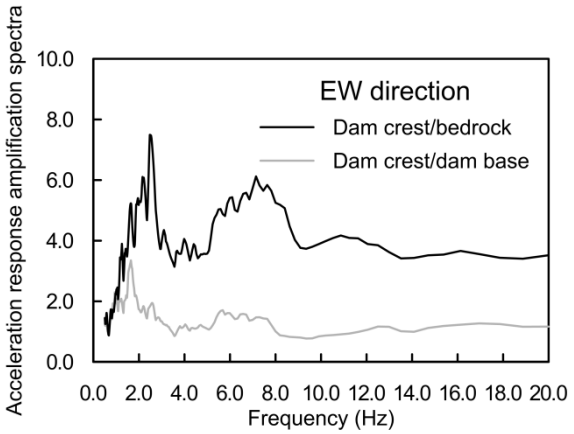


(a): Response spectra in horizontal EW direction

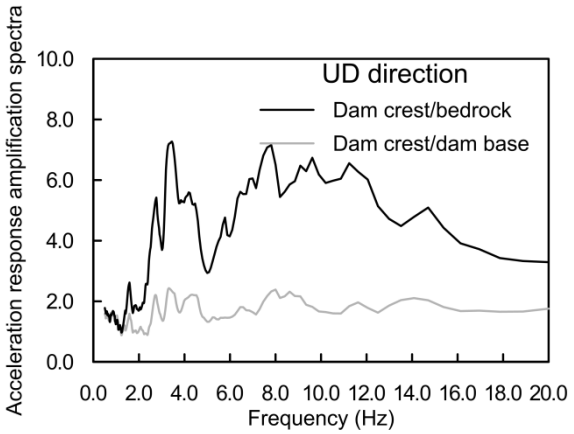


(b): Response spectra in vertical UD direction

Figure 5-28: Seismic monitored data (acceleration response spectra)



(a): Response amplification spectra in horizontal EW direction



(b): Response amplification spectra in vertical UD direction

Figure 5-29: Seismic monitored data (acceleration response amplification spectra)

Table 5-2: Summaries of the seismic monitoring data

Monitoring positions	**EW direction**			**UD direction**		
	Bedrock	**Dam base**	**Dam crest**	**Bedrock**	**Dam base**	**Dam crest**
PGA values (m/s^2)	0.071	0.346	0.435	0.119	0.198	0.318
Predominant frequency (Hz)	3.41	3.48	2.55	5.00	3.13	3.34
Fundamental frequency (Hz)	$f_{crest/bedrock}$= 2.48 $f_{crest/base}$= 1.64			$f_{crest/bedrock}$= 3.45 $f_{crest/base}$= 3.31		

5.4 Description of the numerical model

In this part, different aspects of the numerical model for the static and dynamic analyses are established, including the element size, boundary locations and calibration of the constitutive models.

5.4.1 Element size

A general rule for the element size limit in dynamic FE analysis of geotechnical structures is that it should be fine enough to accurately simulate seismic wave propagation, since a coarse mesh can filter the high frequency components of dynamic excitations. On the other hand, the element size should be as large as possible to reduce the computational cost. The element size limit in the dynamic FE analysis is suggested to be from 1/8 (Kuhlemeyer and Lysmer, 1973) to 1/5 (Lysmer et al., 1975) of the shortest wavelength of all materials for 4-noded elements, whereas for 8-noded elements, the limit is from 1/5 (Kuhlemeyer and Lysmer, 1973) to 1/4 (Bathe, 1996) of the shortest wavelength. As shown in Equations 5-2 and 5-3, l is the element size limit; $\lambda_{\min}$ is the minimum wavelength of all soil materials; $v_{s\min}$ is the minimum shear wave velocity of different soil materials and $f_{\max}$ is the highest frequency of the input motion to be modelled.

$$l = \frac{1}{5}\lambda_{\min} \tag{5-2}$$

$$\lambda_{\min} = \frac{v_{s\min}}{f_{\max}} \tag{5-3}$$

In this work, 8-noded quadrilateral isoparametric elements are employed for the static and dynamic analyses of the Yele dam and therefore 1/5 of the shortest wavelength is chosen as the element size limit. The shear wave velocities for all the materials of the Yele dam are shown in Table 5-1. Based on the geometry of the Yele dam, the volume of the concrete core, transition layer and filter layer is relatively small, so that the element size limit can be easily satisfied in these zones. Therefore, the shear velocity of the rockfill material is chosen, as the minimum velocity to establish the element size limit. Furthermore, 20.0Hz is chosen as the maximum frequency $f_{\max}$ to be

modelled, since the Fourier spectral amplitudes of the horizontal bedrock motion beyond 20.0Hz are sufficiently small to be ignored (as shown in Figure 5-30). Finally, based on the aforementioned parameters, the element size limit for the dynamic FE analysis of the Yele dam was preliminarily calculated as 3.65m.

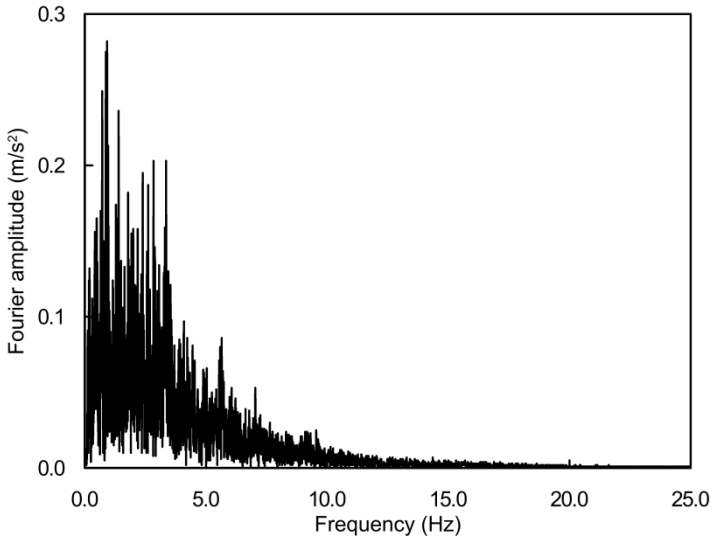


Figure 5-30: Fourier amplitude spectra of the horizontal bedrock excitation

If one employs 3.65m as the maximum element size for the dynamic analysis of the Yele dam, the total element number is estimated to be more than 10000. Clearly, the computational cost of analysis with such a model would be significant. There is therefore scope for investigating further the impact of element size. In particular, a number of FE column analyses (for varying mesh coarseness) subjected to the monitored bedrock motion were carried out, assuming linear elastic undrained soil behaviour. The FE model is shown in Figure 5-31, where vertical displacements are restricted at the bottom boundary, tied DOF boundary conditions are employed at the lateral boundaries and the monitored horizontal bedrock motion is uniformly prescribed at the bottom boundary as the input motion. It should be noted that the vertical input motion is not considered for these analyses. The element size limit for a FE analysis subjected to shear wave vibrations is always stricter due to the shorter wavelengths, than that subjected to compressional wave vibrations. Rayleigh damping is employed to represent the material damping, where a 5.0% target damping is applied. Static self-weight is prescribed as the initial stress, where the coefficient of earth pressure at rest (K_0) is applied to be 0.5. The CH time integration method is utilised, where the employed parameters are listed in Table 5-3, which satisfy the stability conditions of the

CH method under the coupled formulation studied in Chapter 2. The rockfill material is employed in the parametric studies, since it accounts for most of the construction materials of the Yele dam.

Firstly, the element dimension in the horizontal direction is varied in the parametric studies with a very fine element size in the vertical direction of 2.0m. The predicted dynamic response at monitoring point A (see Figure 5-31) is compared in Figure 5-32, in terms of the Fourier spectra. It is observed that the dynamic response employing different horizontal element dimensions is almost identical, indicating the insignificant effects of the horizontal element dimension on the wave propagation in the Yele dam materials. Secondly, seven different vertical element dimensions are employed in FE analyses with the horizontal element dimension as 10.0m. The predicted dynamic response is compared in Figure 5-33. As expected, the vertical element dimension influences more significantly the high-frequency components of the dynamic response than the low-frequency components. The predicted dynamic response in terms of Fourier spectra starts to be sensitive to the vertical element dimension when it is larger than 6.0m. Therefore, 10.0m and 6.0m can be applied as the horizontal and vertical element dimensions for the FE analysis of the Yele dam. However, in order to have more regular element shapes, 8.0m and 6.0m are the dimensions finally adopted for the static and dynamic analyses.

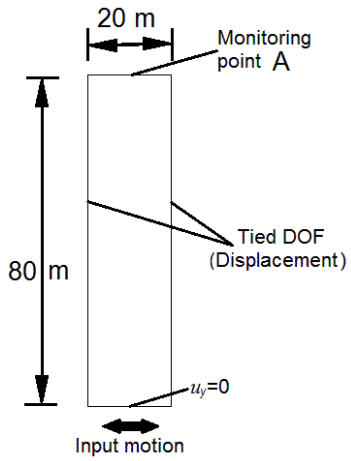


Figure 5-31: FE model for parametric studies of element size limit

Table 5-3: The integration parameters for the CH method

Parameter	δ	α	α_m	α_f	β	ρ_∞
CH method	0.9286	0.5102	-0.1429	0.2857	0.8	0.6

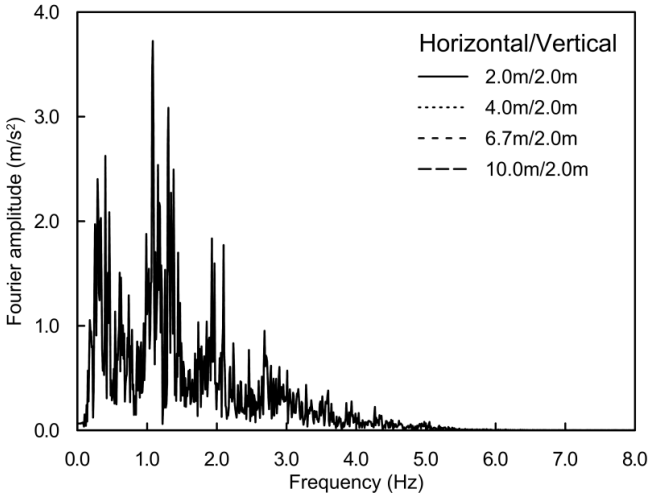
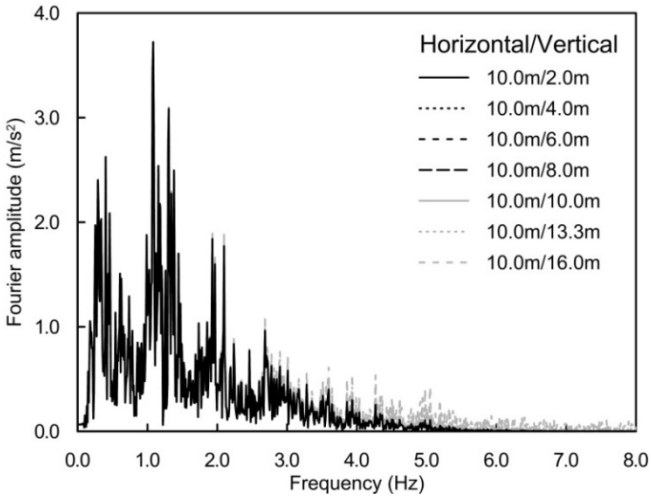
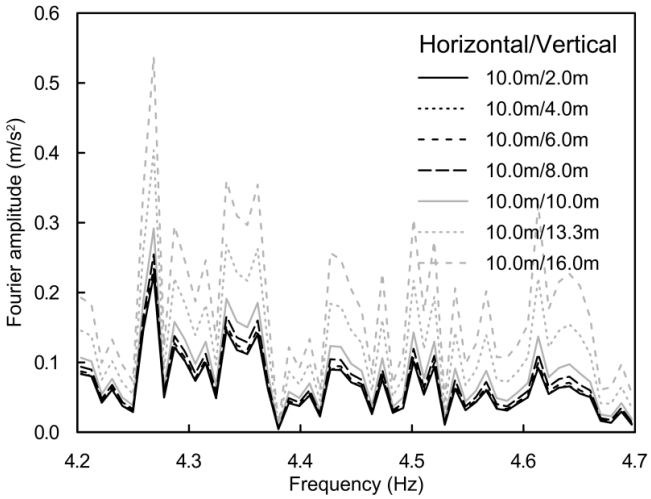


Figure 5-32: Comparison of Fourier amplitude spectra for different horizontal element dimensions



(a): Normal scale



(b): Zoomed-in scale

Figure 5-33: Comparison of Fourier amplitude spectra for different vertical element dimensions

5.4.2 Location of the lateral boundaries

For economical simulations of dynamic soil-structure interaction problems, artificial boundaries are required to restrict the theoretically infinite computational domain to a finite one. At boundaries where the radiation damping effect is insignificant, the typical elementary boundaries can be employed, where either a zero stress or a zero displacement condition is prescribed. However, in most cases, the truncation of the computation domain inevitably results in spurious wave reflections at artificial boundaries and therefore the boundary conditions have been extensively developed to prevent these wave reflection effects. Such boundaries include the tied DOF boundaries applicable only for lateral boundaries (Zienkiewicz et al., 1988), local boundaries (such as the cone boundary conditions (Kellezi, 1998 & 2000)) and consistent boundaries (such as the coupled boundary element method). For the dynamic analysis of the Yele dam, an elementary bottom boundary is placed at the interface between the soil layers and bedrock, where the monitored bedrock excitations are prescribed as the input motion for the dynamic analysis. For the lateral boundaries, appropriate boundary conditions should be employed, in order to minimise the effects of spurious wave reflections on the dynamic response of the Yele dam. It should be noted that the depth of the Yele dam foundation at the upstream and downstream sides is asymmetric (see Figure 5-18), and therefore the tied DOF boundary conditions cannot be employed. On the other hand, consistent boundaries have been rarely used in numerical analyses due to their computational inefficiency, frequency dependency and problematic implementation in FE codes (Kontoe, 2006). Therefore, a type of local boundary, the widely used cone boundary was employed at the lateral boundaries of the FE mesh for the dynamic analysis of the Yele dam. The values of the stiffness of the springs and the viscosities of the dashpots are calculated based on the elastic properties of the materials adjacent to the applied boundaries, where the detailed formulations and implementation of the cone boundary conditions in ICFEP can be found in Kontoe (2006).

Accurate predictions of the dynamic response of soil-structure interaction problems require the lateral boundaries to be sufficiently far from the area of interest to achieve free-field response close to the lateral sides of the mesh. For this purpose, viscous boundaries are always suggested to be placed far from excitation sources, where waves propagate approximately normally to the truncated boundaries (Kellezi, 1998). In that case, prefect absorption can be achieved for wave reflections and therefore free-field

conditions can be easily recovered near the lateral boundaries. However, concerning the dynamic analysis of the Yele dam, the input excitations are prescribed at the entire bottom boundary, which generates waves propagating parallel to the lateral boundaries. Therefore, free-field response is very difficult to be achieved near to the lateral sides. It is necessary to investigate the appropriate location of such viscous boundaries, in order to achieve free-field response at a distance within the lateral boundaries. Therefore, a preliminary dynamic analysis for the Yele dam is conducted by assuming linear-elastic undrained soil behaviour. The FE mesh for the Yele dam is generated by following the established element size, as shown in Figure 5-34, which consists of 2440 8-noded isoparametric quadrilateral solid elements. The lateral boundaries are placed at 300.0m away from the dam toe and the dam heel respectively for the downstream side and the upstream side. The cone boundary conditions are employed at the lateral boundaries and the monitored 2-D bedrock motion is uniformly prescribed at the bottom boundary as the input motion. Rayleigh damping is employed to represent the material damping effect, where a target damping of 5.0% is applied. Static self-weight is prescribed as the initial stress. The CH time integration method is utilised, where the employed parameters are listed in Table 5-3. The material properties employed in the analysis are listed in Table 5-1.

The predicted dynamic response at different monitoring points along the downstream alluvium surface (see Figure 5-34) is compared in Figure 5-35, in terms of two-directional acceleration response spectra. It can be observed that the horizontal dynamic response is highly affected by the viscous boundary condition, which becomes insensitive to it from point 5, at a distance of 81.0m from the lateral boundary. The vertical dynamic response stabilises from point 4, at a distance of 63.0m from the lateral boundary. Furthermore, as shown in Figure 5-35, the stabilised 2-D dynamic response of the Yele dam is identical to the free-field response predicted by the 1D FE column analysis, by employing the same spatial discretisation and material parameters as that of the downstream alluvium section near the lateral boundary. This proves that the adopted lateral extent of the mesh and the boundary condition are sufficient and do not influence the response of the dam. Therefore, this model is employed for the following FE analyses of the Yele dam, as shown in Figure 5-34, which consists of 2440 8-noded isoparametric quadrilateral solid elements.

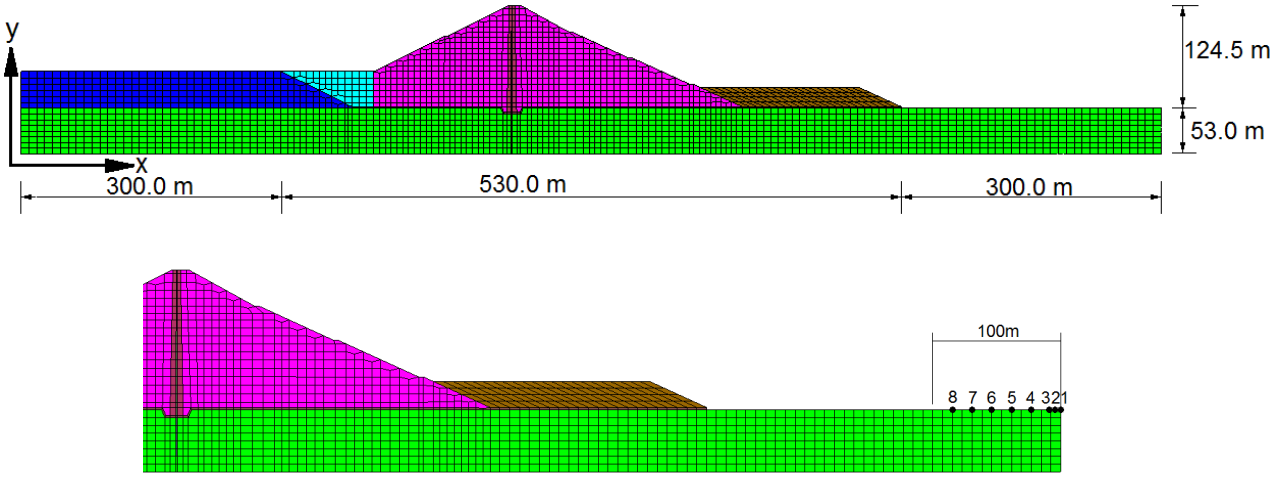
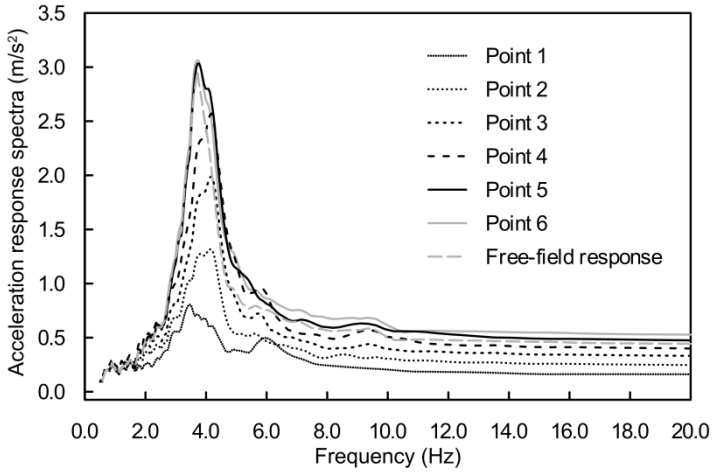
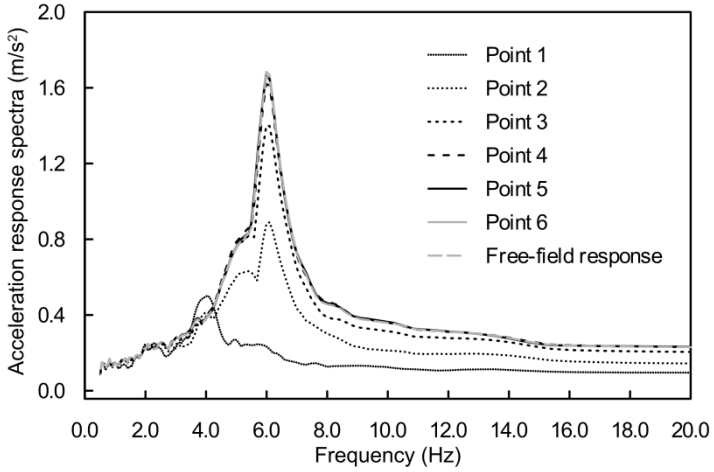


Figure 5-34: FE mesh of the Yele dam



(a): Horizontal dynamic response



(b): Vertical dynamic response

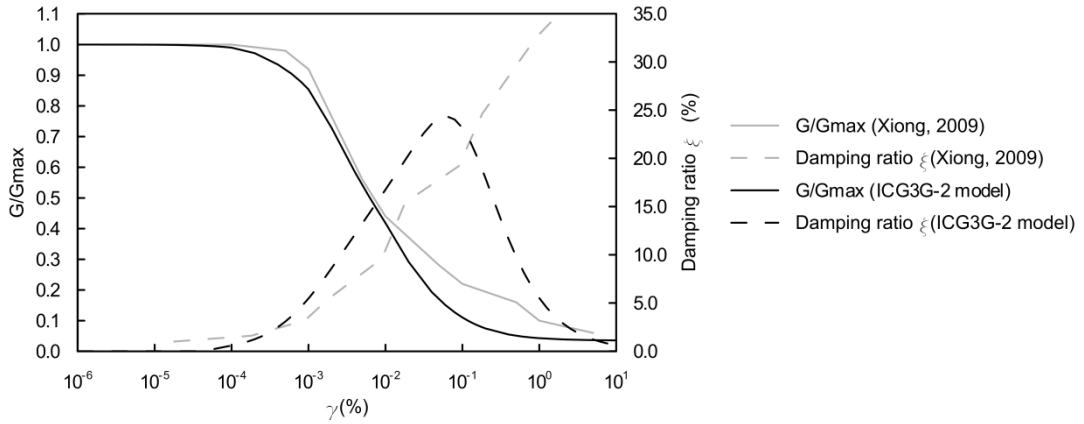
Figure 5-35: Acceleration response spectra from the parametric study for lateral boundary location

5.4.3 Calibration of constitutive models

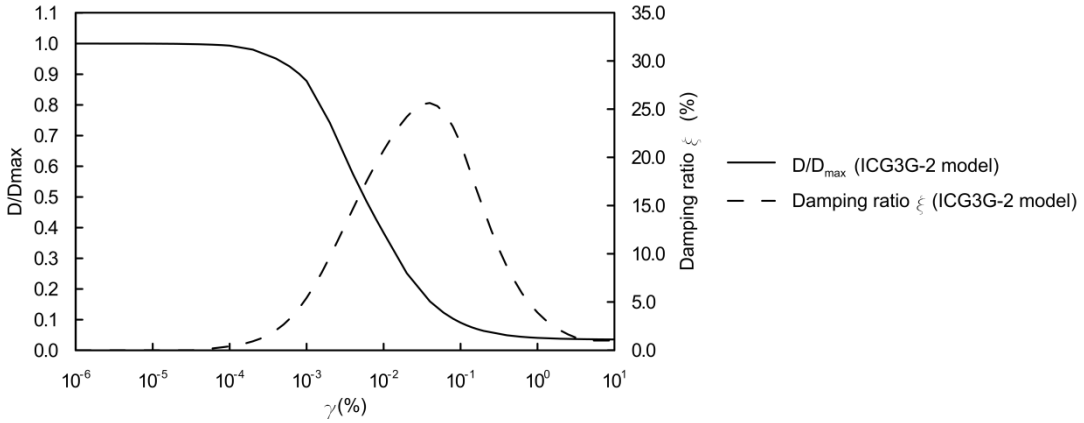
For the static and dynamic analyses of the Yele dam, a cyclic nonlinear model (ICG3S-2 model) coupled with a Mohr-Coulomb failure criterion is employed to simulate the elasto-plastic soil behaviour of dam and foundation materials. However, the asphalt concrete core and the grouting curtain are assumed to be linear elastic materials due to their large stiffness. The calibration of the ICG3S-2 model is conducted by matching the reproduced shear modulus degradation and damping curves with the reference curves, as shown in Figure 5-36 (a). However, due to the lack of laboratory data for the constrained modulus degradation and damping curves, similar model parameters are employed for the calibration related to the compressional deformation, as shown in Figure 5-36 (b). Compared to the parameters employed for the shear deformation simulation, a higher value of parameter *s* is adopted for the compressional deformation. This is based on the investigation presented in Chapter 4, where the degradation of the constrained modulus is slightly steeper than that of the shear modulus (Figure 4-61). In other words, as shown in Figure 5-36, the constrained modulus degradation simulated by the ICG3S-2 model for the Yele dam materials is more pronounced than the shear modulus degradation by adopting a slight larger value for parameter *s* than the *b* value. It should be noted that the reasons of employing the ICG3S-2 model have been explained in the previous chapter. The ICG3S-2 model can realistically simulate the material damping at very small strain levels. Furthermore, the ICG3S-2 model can independently simulate soil nonlinear behaviour in different directions, in terms of stiffness degradation and material damping, leading to more accurate simulations of multi-directional dynamic response of geotechnical structures.

Table 5-4: Parameters for the Yele dam materials by using the ICG3S-2 model

Depth (GL. meters)	**a**	**b**	**c**	**d_1**	**d_2**	**d_3**	**d_4**
0.0 ~ -100.0	7.0E-04	15.0E+00	5.0E-02	100.0E+00	2.5E-01	500.0E+00	8.3E-01
Depth (GL. meters)	**r**	**s**	**t**	**d_5**	**d_6**	**d_7**	**d_8**
0.0 ~ -100.0	7.0E-04	20.0E+00	5.0E-02	100.0E+00	2.5E-01	500.0E+00	8.3E-01



(a): Shear modulus degradation and damping curves



(b): Constrained modulus degradation and damping curves

Figure 5-36: Calibration of the ICG3S-2 model for the Yele dam materials

5.5 Static analysis of the Yele dam

The static analysis aims to simulate the static behaviour of the Yele dam before the Wenchuan earthquake by simulating a simplified geological history of the dam foundation, the dam construction process, the reservoir impounding process and the subsequent operational period. The HM coupled consolidation FE formulation is employed for the foundation materials, whereas the behaviour of the dam materials is assumed to be drained due to their high permeabilities. The material properties employed in the static analysis are listed in Table 5-1. The cyclic nonlinear model (ICG3S-2 model) coupled with the Mohr-Coulomb failure criterion is employed, where the model parameters are listed in Table 5-4.

5.5.1 Description of the static analysis

Stage 1- simulation of geological history of the dam foundation

The FE mesh of the Yele dam is shown in Figure 5-37, consisting of 2440 8-noded isoparametric quadrilateral solid elements. The static analysis starts from the geological history simulation of the asymmetric dam foundation, which is divided into two sections, a rectangular lower foundation section and a trapezoidal upper foundation section (section 1 and 2 shown in Figure 5-37). At the beginning of the static analysis, all dam sections except the lower foundation section are deactivated through an excavation process. The initial stress state of the lower foundation is defined by prescribing hydrostatic pore water pressure and static self-weight, where the coefficient of earth pressure at rest (K_0) is applied to be 0.5. The geological state of the upper foundation is simulated by constructing 6 soil layers of 7.0m thickness above the lower foundation and following a long period of consolidation process (100 years). The displacement boundary conditions for the entire static analysis are shown in Figure 5-37, where both horizontal and vertical displacements are restricted at the bottom boundary and the horizontal displacements are restricted at the lateral boundaries. Concerning the hydraulic boundary conditions employed for this stage, water flow is restricted at the bottom boundary A-B, since it is located at the bedrock surface. The pore water pressure at the far boundary B-C is prescribed as no change (i.e. Δp_f=0), which ensures the hydrostatic conditions. The pore water pressure at the top boundary C-E is prescribed as zero and is not allowed to change throughout the first stage of the analysis (i.e. Δp_f=0). Furthermore, water flow is restricted at the boundary below each under construction foundation layer. Taking boundary E-H as an example, at the construction of the first layer, water flow is restricted at this boundary, which allows the pore water pressure accumulation due to the geological simulation. Lastly, the pore water pressure at the lateral boundary G-A is gradually raised to adapt to the new hydrostatic conditions. After the construction of the upper foundation layers, the entire dam foundation experiences a long period of consolidation to enable a stable stress and seepage state before the dam construction, with the water flow being restricted at the bottom boundary and the pore water pressure at other boundaries being prescribed as no change.

Stage 2- first stage of dam construction

The first stage of the dam construction commences after the geological history simulation of the dam foundation. The construction of 10 dam material layers of 7.0m thickness are simulated in the FE analysis. After this 431-day construction stage, the dam reaches the height of 75.0m, which is the designed dead water level. Water flow is restricted at the boundary under the dam body, i.e. boundary D-E-F, since during the construction of the Yele dam, an impermeable membrane was placed under the dam body to prevent the erosion of construction materials. Furthermore, water flow is also restricted at the bottom boundary A-B and the pore water pressure at all other boundaries is prescribed as no change.

Stage 3- second stage of dam construction

In the second stage of the dam construction, additional 8 dam material layers of 7.0m thickness are constructed over 321 days, reaching the maximum dam height of 124.5m. During the same period, the reservoir is impounded up to 107.0m height, following the simplified impounding sequence scenario 1 shown in Figure 5-19. The induced hydrostatic water pressure is modelled by applying an external boundary stresses perpendicular to the upstream dam surface (boundary J-F) and upstream foundation surface (boundary F-G). The pore water pressure in the upstream dam materials, i.e. the rockfill zone, coffer dam and transition layer, is prescribed to be in equilibrium with the applied hydrostatic boundary stresses. Furthermore, water flow is restricted at the bottom boundary A-B and the pore water pressure at the boundary B-C-D is prescribed as no change. At boundary G-A, the pore water pressure is gradually raised to adapt to the new hydrostatic conditions. Water flow is restricted at the boundary D-E-F-G, to allow for the pore water pressure accumulation.

Stage 4- operational stage

After the dam construction and the reservoir impounding, the Yele dam was in operation for about three years until the Wenchuan earthquake on 12th of May, 2008. In order to simulate the seasonal water level change during this period, the reservoir level gradually drops to the dead water level (75.0m) over 683 days (illustrated in Figure 5-19 (a)). In the analysis, the prescribed boundary stresses on the upstream dam and

foundation surfaces and the pore water pressure in the upstream dam materials and at the lateral boundary G-A, are gradually decreased to adapt the new hydrostatic conditions. It should be noted that, after the dam construction, the placed membrane under the dam body was gradually water-degraded and the downstream filter layer at the boundary D-I started discharging seepage water. This ensures the dissipation of the excess pore water pressure in the dam foundation generated during the dam construction and reservoir impounding. In order to simulate this dissipation mechanism, the precipitation boundary conditions, which are explained in the next section, are employed at the boundary D-I. The pore water pressure at the boundary B-C-D is prescribed as no change. Water flow is restricted at the boundary I-E-F-G, where the pore water pressure can adapt to the new hydraulic conditions after the reservoir de-impounding. After the de-impounding process, the Yele dam experiences a 222 days of consolidation period, where the same hydraulic boundary conditions are employed as those employed in the de-impounding period, except that the pore water pressure at boundary G-A is prescribed as no change in order to ensure the new hydrostatic conditions. These applied hydraulic boundary conditions allow the dissipation of excess pore water pressure induced by reservoir level changes through boundaries B-C-D-I and G-A. Overall, the different stages of the static analysis of the Yele dam are summarised in Table 5-5.

Precipitation boundary conditions

It should be noted that the precipitation boundary condition (Potts and Zdravković, 1999) is an advanced boundary condition, which allows the dual prescription of pore water pressure value and/or water flow. At the stage 4 of the static analysis, the precipitation boundary conditions are applied at the bottom of the filter layer, in order to simulate the dissipation mechanism of excess pore water pressure generated during the dam construction and water impounding. It is specified that, if the pore pressure in the dam foundation is more compressive than those at boundary D-I, then the pore water pressure value at the boundary D-I is prescribed to be equal to zero. This allows water to flow out of the foundation, achieving excess pore water pressure dissipation. On the other hand, if the water pressure is more tensile in the dam foundation than the one at the boundary D-I, water flow is restricted from the dry materials in the downstream dam body towards the foundation.

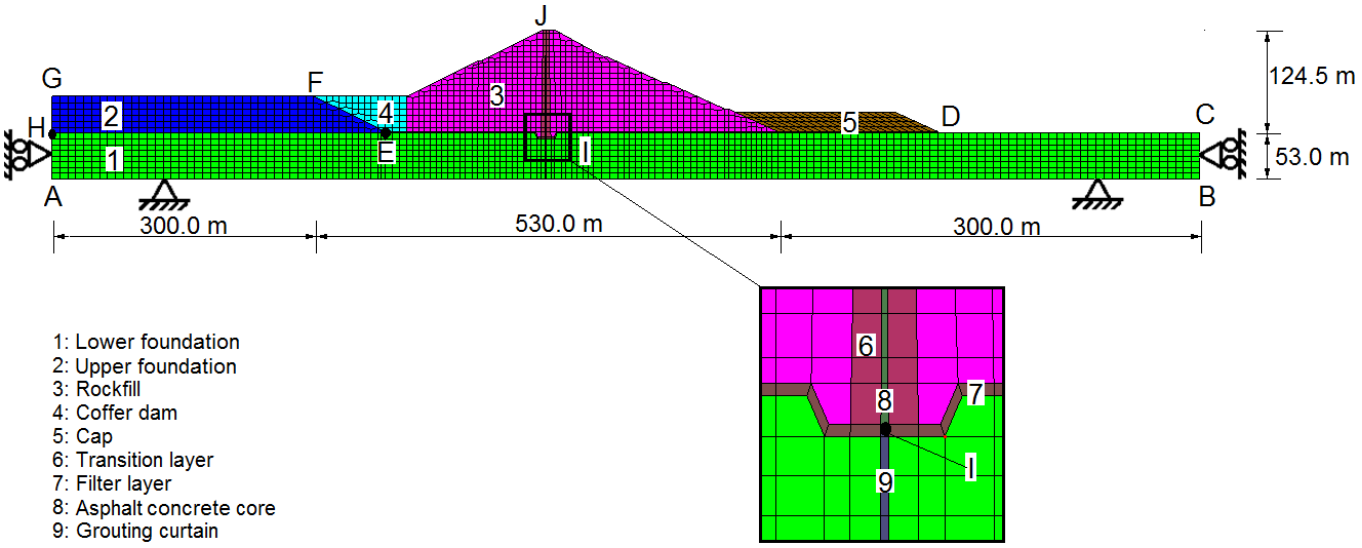


Figure 5-37: FE mesh of the Yele dam and boundary conditions for the static analysis

Table 5-5: Stages of the static analysis of the Yele dam

Stages	Duration	Increments	Dam height (m)	Stages	Duration	Increments	Reservoir level (m)
1. Simulation of geological history of dam foundation	100 years	1-60					
2. First stage of dam construction	431 days	61-160	0.0-75.0				
3. Second stage of dam construction	321 days	161-240	75.0-124.5	**Reservoir impounding**	321 days	161-240	0.0-107.0
4. Operational stage	905 days	241-293	124.5-124.5	**Reservoir de-impounding**	683 days	241-280	107.0-75.0

5.5.2 Static analysis results

The static behaviour of the Yele dam is discussed in this section. Firstly, the predicted horizontal displacement variation along the asphalt concrete core is compared with the monitored data in Figure 5-38. Results show the horizontal deformation of the concrete core at two time points, after the reservoir impounding and after the reservoir de-impounding (time points 3 and 6 respectively shown in Figure 5-24). It can be observed that due to the impounding effect, the concrete core experiences large-magnitude horizontal deformations. The maximum displacements are located at the bottom 1/3 part of the concrete core, reaching more than 400.0mm. However, after

the reservoir de-impounding in the operational stage, the horizontal deformation of the concrete core reduces about 25%, leading the maximum displacements to decrease to 300.0mm, still at the bottom 1/3 part. The decrease of the horizontal displacements can be attributed to the reduced water pressure on the upstream dam surface. In this case, the elastic deformation of the dam materials induced by the water impounding could be recovered due to the unloading condition. Furthermore, a good agreement is observed between the predicted results and the monitored data at time point 6, where the magnitude and variation of the horizontal displacements along the concrete core are reasonably simulated by the static analysis.

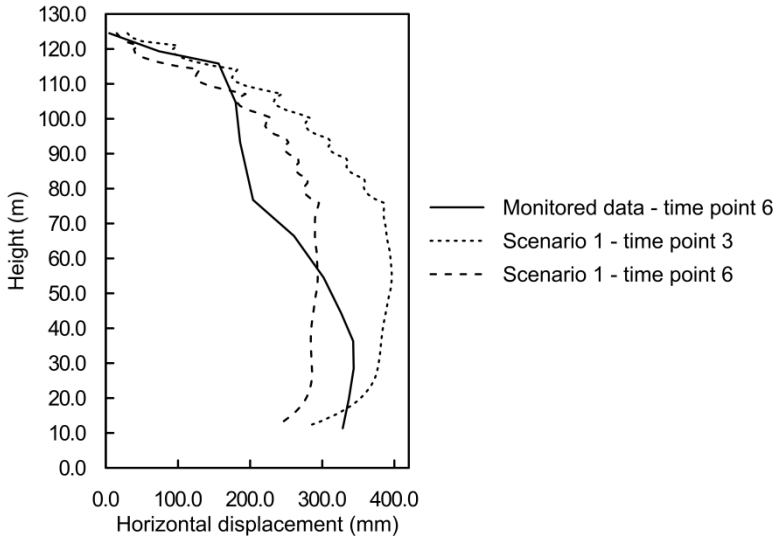


Figure 5-38: Horizontal displacement distribution along the concrete core (scenario 1)

The effects of the simulation sequence for the reservoir impounding on the static behaviour of the Yele dam are also investigated. As mentioned before, during the operation stage of the Yele dam, the reservoir experienced annual water level fluctuations due to seasonal rainfall. The reservoir water level changes are simplified into two simulation sequences, as shown in Figure 5-19. The first simulation sequence has been employed in the static analysis of the Yele dam. For the second simulation sequence, the predicted static results in terms of the horizontal displacement variation along the concrete core are compared in Figure 5-39 with the monitored data. It can be seen that the horizontal deformation of the concrete core is significantly underestimated by using the second simulation sequence. The maximum horizontal displacement is predicted to be 120.0mm, only 37.5% of the monitored one. The under-prediction is due to the incomplete simulation of the reservoir impounding, which leads to smaller water

pressure on the upstream dam surface. It should be noted that by employing the second simulation sequence, the reservoir impounding finishes before the completion of the dam construction, as shown in Figure 5-19 (b). This leads to significant underestimation of the horizontal deformations on the concrete core above the level of 100.0m. This investigation highlights the importance of employing appropriate reservoir impounding simulation sequence for the prediction of the static behaviour of rockfill dams. The highest reservoir level should be considered, in order to accurately simulate its influence on the static dam deformations. Therefore, the first impounding simulation sequence is employed in the subsequent static and dynamic analyses of the Yele dam.

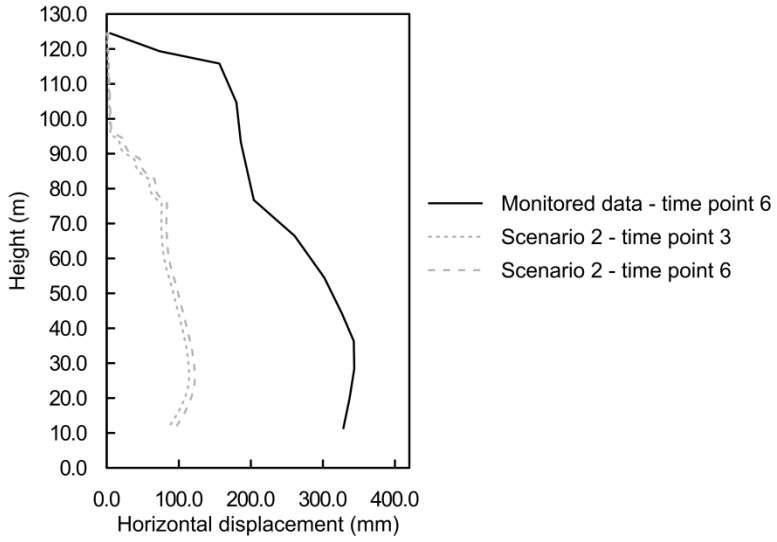


Figure 5-39: Horizontal displacement distribution along the concrete core (scenario 2)

The dam settlements at different locations on the Yele dam are predicted by the static analysis and are compared with the monitored data in Figure 5-40, i.e. the incremental settlements on the two downstream berms between the time points 4 and 6 (see Figure 5-24) and the incremental settlements on the crest between the time points 5 and 6 (see Figure 5-24). The numerical results are found to agree well with the monitored data at different locations, indicating the appropriate employment of the numerical model.

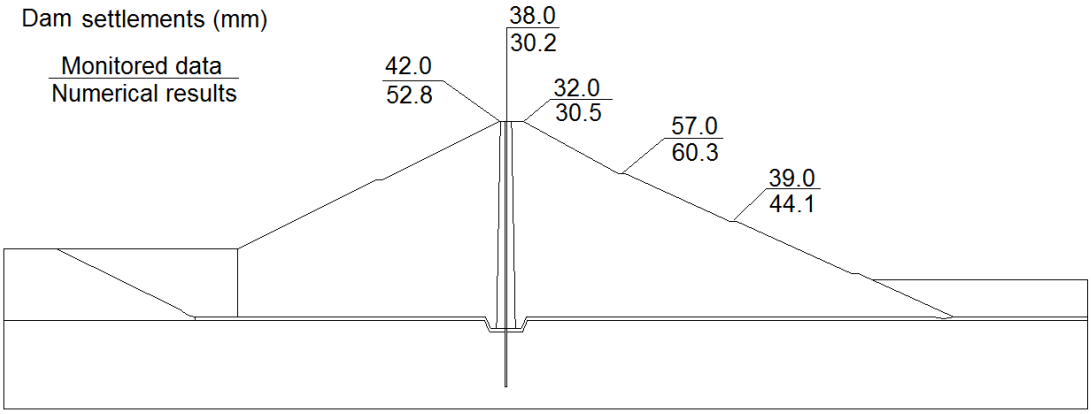
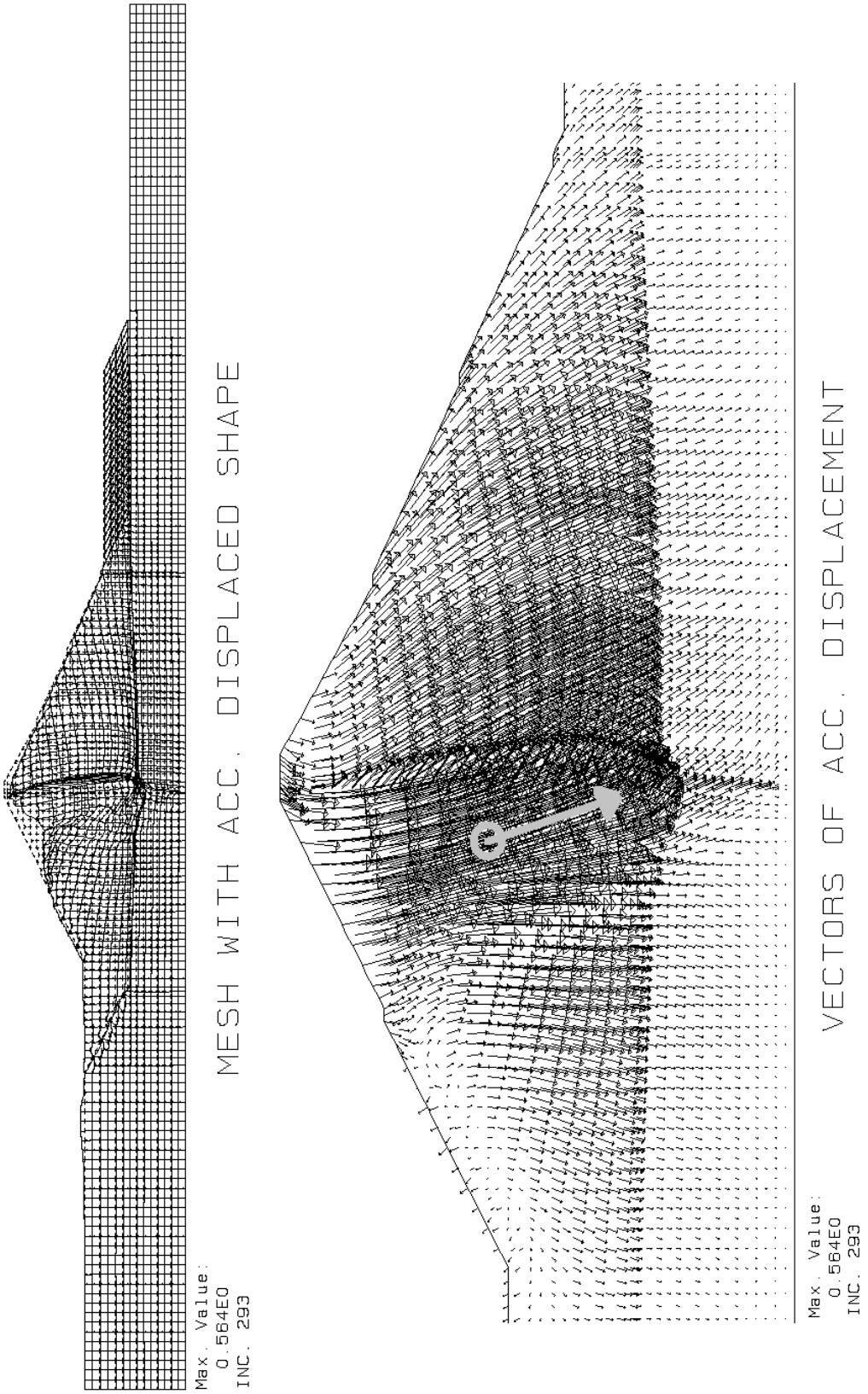


Figure 5-40: Settlements at different locations on the Yele dam

The accumulated deformed mesh and vectors of accumulated displacement of the Yele dam at the end of the static analysis are shown in Figure 5-41. It can be seen that due to the reservoir impounding, the deformation of the Yele dam is mainly downward and towards the downstream side. The maximum deformation occurs in the upstream rockfill zone, which is 0.564m and is located at the middle height of the rockfill zone and close to the core. The position and orientation of the maximum displacement are indicated by a grey vector in Figure 5-41 (b). The maximum displacement on the Yele dam is much smaller than the smallest freeboard allowance (17.5m) and it also satisfies the design standard for rockfill dams. In particular, according to the Chinese Specifications for Design of Hydraulic Structures (2000), the predicted maximum residual displacement on the dam should be less than 1.0% of the dam height, which is 1.245m for the Yele dam. Furthermore, based on the numerical results, no failure is observed on the dam. Therefore the overall deformations of the Yele dam are not significant and are well within the limit for its safe operation under static loading conditions.



(a): Accumulated deformed mesh (b): Vectors of accumulated displacement (zoomed-in)

Figure 5-41: Accumulated deformed mesh and vectors of accumulated displacement on the Yele dam before the Wenchuan earthquake (displacement scaling factor: 1:50)

The seepage pattern is presented in Figure 5-42, in terms of the compressive pore water pressure contour plots at different stages of the analysis.

In particular, Figure 5-42 (a) shows the pore water pressure contours after the long-term geological history simulation of the dam foundation, where hydrostatic conditions are achieved in the foundation before the dam construction.

Figure 5-42 (b) shows the pore water pressure contours at the time point 2, which is at the end of the first construction stage and before the reservoir impounding. During the construction process, the pore water pressure in the foundation under the dam body increases due to the applied weight of the construction materials and the assumed undrained hydraulic boundary conditions on the top of the foundation. However, the pore water pressure variation at the far boundary is not significantly affected and it remains of hydrostatic level.

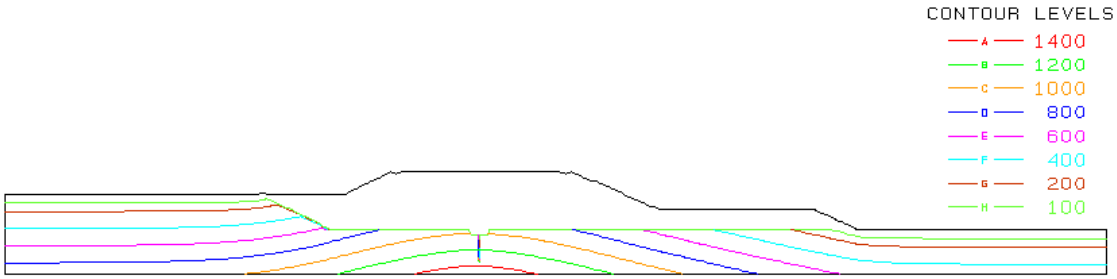
Figure 5-42 (c) shows the pore water pressure contours at the time point 3, which is after the second-stage dam construction and reservoir impounding. During the reservoir impounding process, the pore water pressure in the foundation gradually accumulates due to the dam construction and reservoir impounding. Furthermore, the pore water pressure in the upstream dam materials is raised to be in equilibrium with the increased reservoir water level.

Figure 5-42 (d) shows the pore water pressure contours at the time point 6, after the reservoir de-impounding. It can be seen that the pore water pressure in the upstream rockfill materials adapts to the new hydrostatic conditions related to the lower water level. It should be noted that the excess pore water pressure in the downstream foundation generated from the dam construction has been dissipated through the filter layer, where the precipitation boundary condition is employed for this simulation.

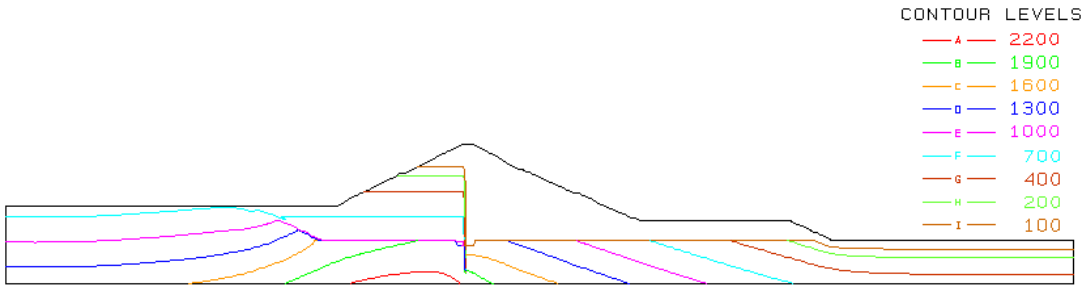
Figure 5-42 (e) shows the pore water pressure contours at the time point 7, just before the Wenchuan earthquake. It can be seen that, following a period of 222 days of consolidation, the excess pore water pressure has been gradually dissipated in the upstream foundation through seeping to the downstream side, approaching hydrostatic conditions.



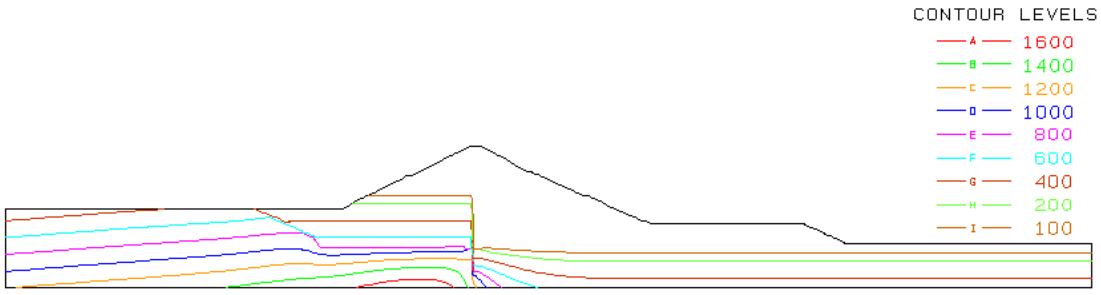
(a): Time point 1 – after foundation geological simulation



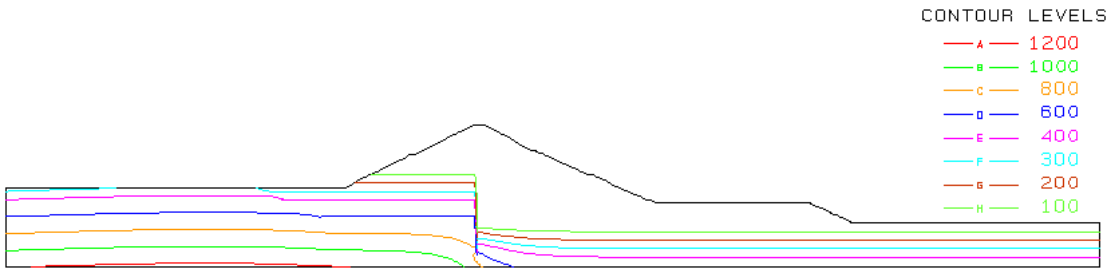
(b): Time point 2 – at the end of the first stage of dam construction



(c): Time point 3 – at the end of dam construction and reservoir impounding



(d): Time point 6 – at the end of reservoir de-impounding



(e): Time point 7 - before the Wenchuan earthquake

Figure 5-42: Contour plots of pore water pressure of the Yele dam at different stages

(Compression positive: kPa)

5.6 Dynamic analysis of the Yele dam

The seismic response of the Yele dam subjected to the Wenchuan earthquake is simulated by dynamic FE analysis using ICFEP. The initial stress state, before the Wenchuan earthquake, is reproduced by the conducted static FE analysis. The boundary conditions for the dynamic analysis are shown in Figure 5-43, where the cone boundary conditions are employed at the lateral boundaries and the recorded 2-D bedrock motion is uniformly prescribed at the bottom boundary as the input motion. The HM coupled consolidation formulation is employed for the dynamic analysis of both the dam and foundation sections. For the hydraulic boundary conditions, water flow is restricted at the bottom boundary and the pore water pressure at other external boundaries is prescribed as no change (i.e. Δp_f=0). The precipitation boundary condition is employed under the filter layer in order to simulate the dissipation mechanism of excess pore water pressure generated in the dam foundation. The time step and duration for the dynamic analysis are 0.02s and 162.0s respectively. The CH time integration method is utilised, where the employed parameters are listed in Table 5-3, which satisfy the stability conditions of the CH method under coupled formulation studied in Chapter 2. The same constitutive models, model parameters and soil properties are employed in the dynamic analysis as those for the static analysis.

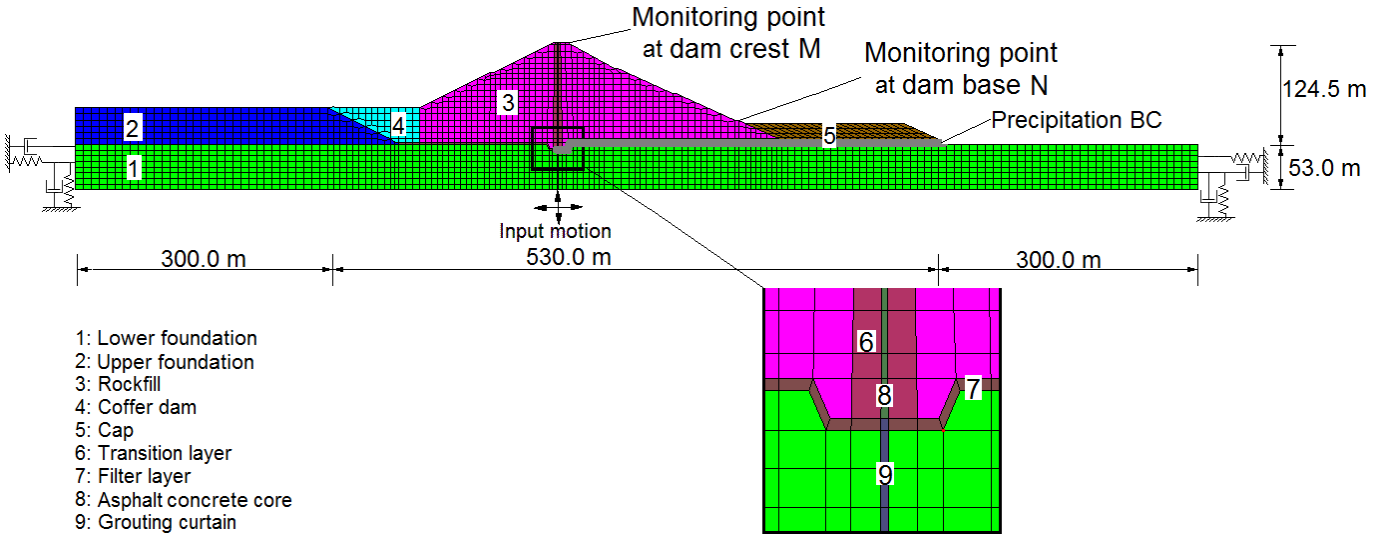
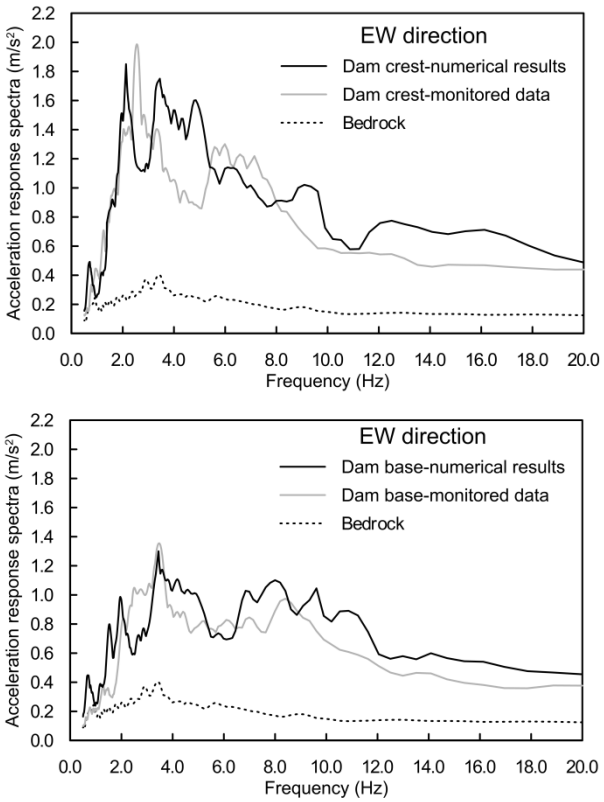


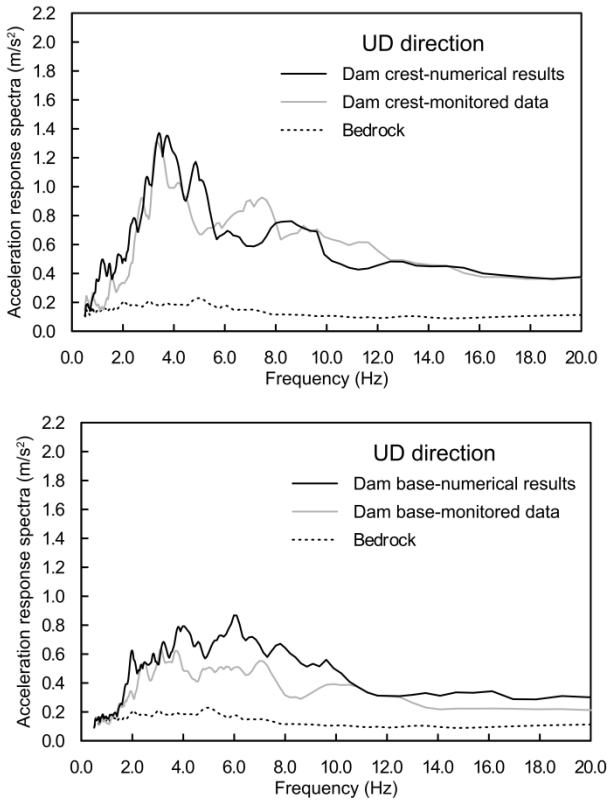
Figure 5-43: FE mesh and boundary conditions for the dynamic analysis of the Yele dam

5.6.1 Acceleration time histories and response spectra

The seismic response of the Yele dam is compared with the monitored data in Figures 5-44 and 5-45, in terms of acceleration response spectra and acceleration time histories at the two monitoring points on the dam crest and base (see Figure 5-43). Based on the comparison, it can be seen that the dynamic response of the Yele dam is appropriately predicted by the dynamic analysis. In particular, for Figure 5-44, the predicted horizontal and vertical response spectra at the dam crest and dam base match well with the monitored response, both in terms of frequency content and amplitude. Furthermore in Figure 5-45, good agreement is observed for the corresponding comparison of the two-directional acceleration time histories at the dam crest and base. Slight overestimation for the vertical response at the dam base is observed both in terms of response spectrum and acceleration time history. Based on the predicted response spectra at the dam base, this over-prediction only occurs in the frequency range of 4.0-10.0Hz. However, good agreements are observed for all other simulations and therefore the overall accuracy of the dynamic prediction is satisfactory.

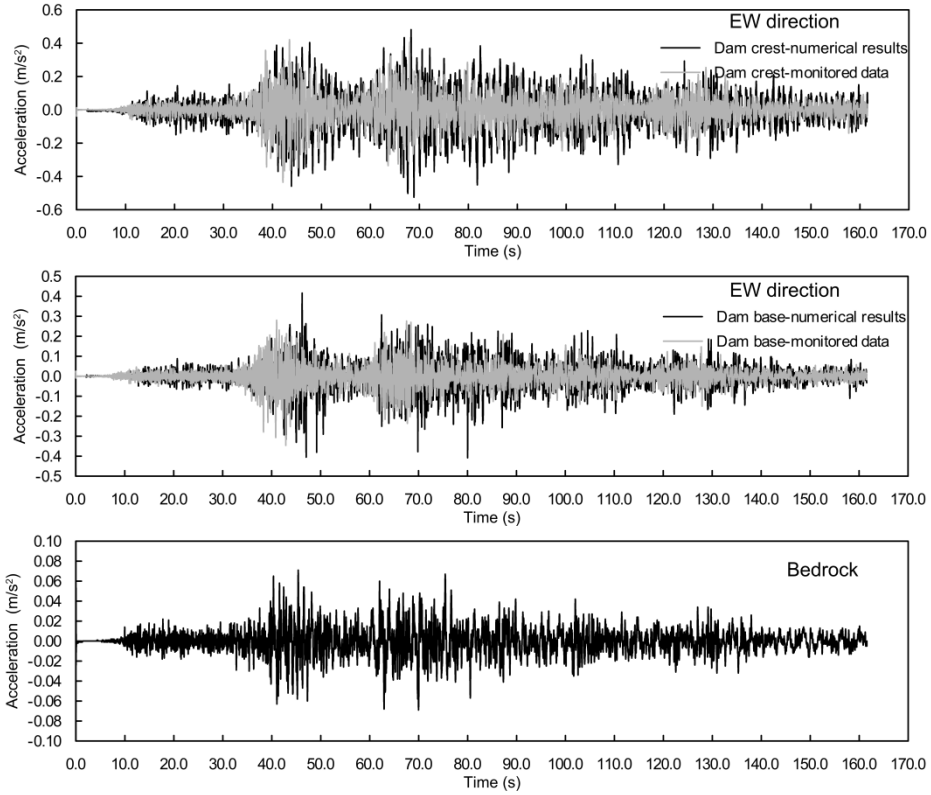


(a): Horizontal-EW direction

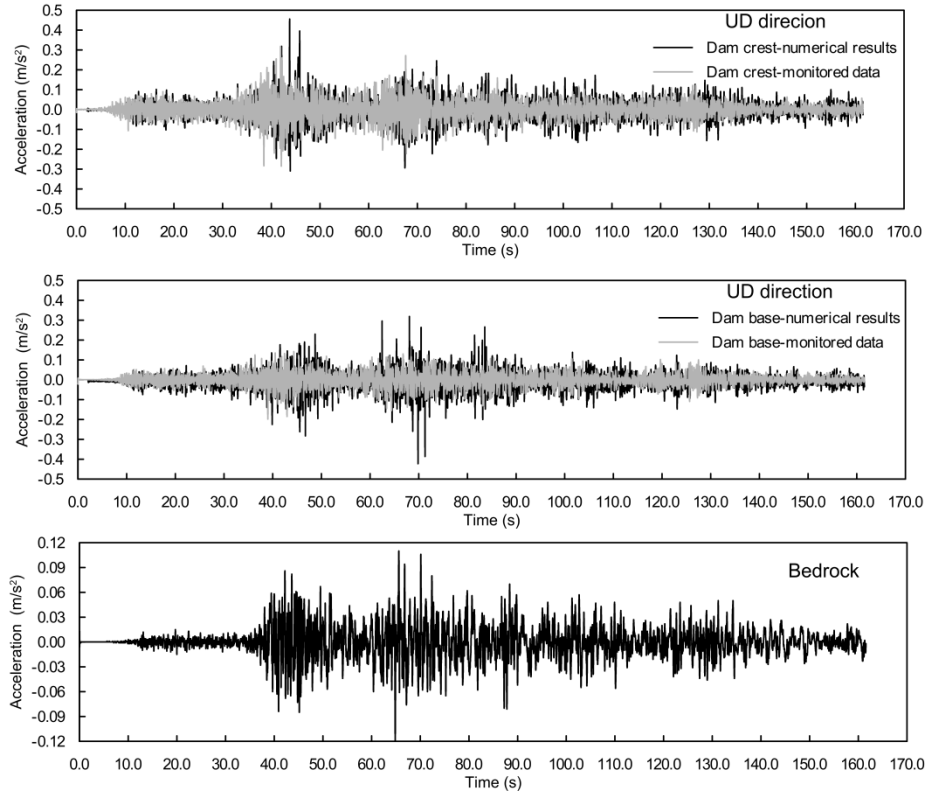


(b): Vertical-UD direction

Figure 5-44: Dynamic response of the Yele dam in two directions (acceleration response spectra)



(a): Horizontal-EW direction



(b): Vertical-UD direction

Figure 5-45: Dynamic response of the Yele dam in two directions (acceleration time histories)

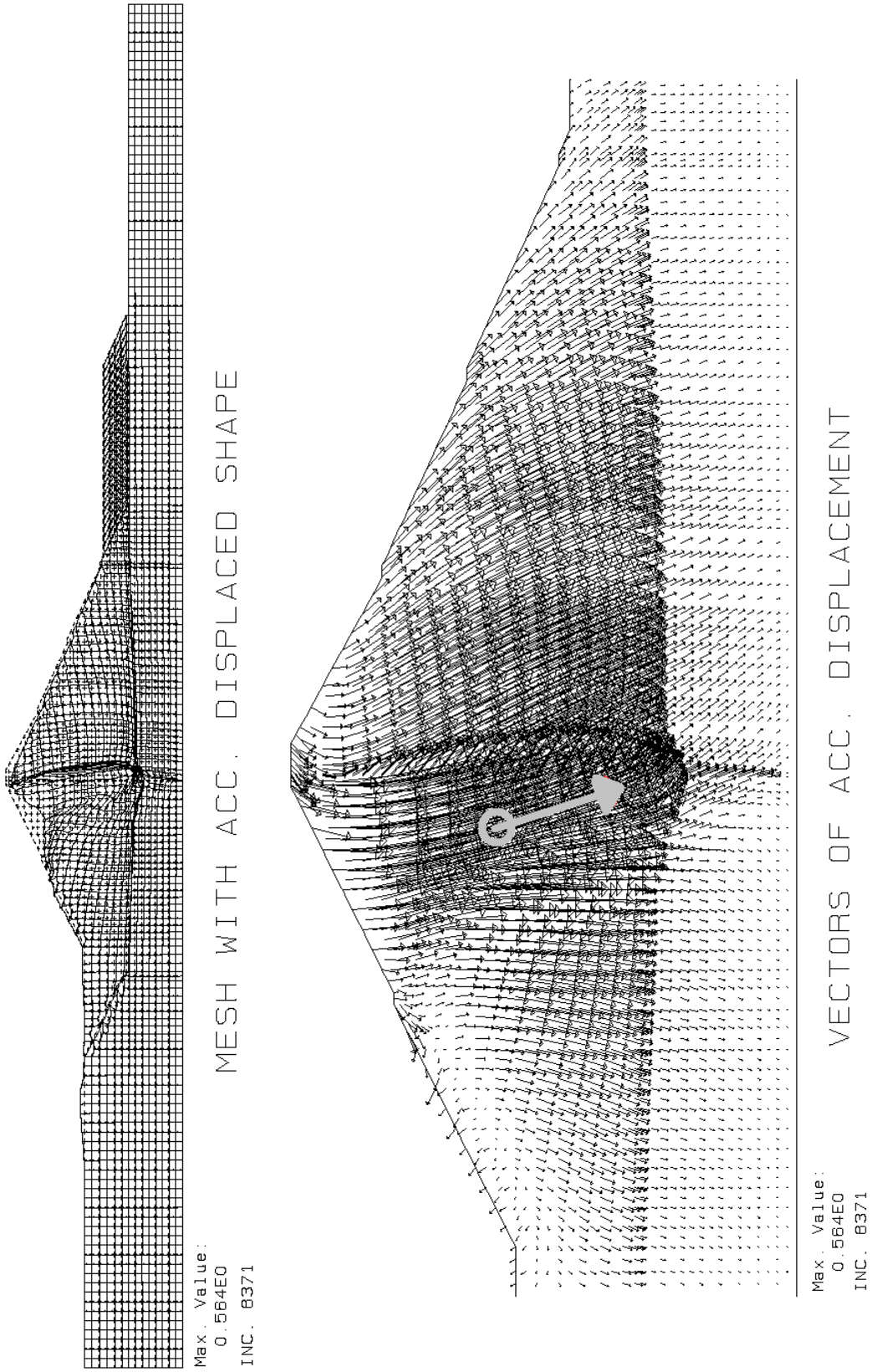
5.6.2 Seismic deformation of the Yele dam

In order to investigate the seismic deformation on the Yele dam, the accumulated deformed mesh and vectors of accumulated displacement on the Yele dam at the end of the Wenchuan earthquake are shown in Figure 5-46, which include the deformations induced by both the static and dynamic loading. It can be seen that after the Wenchuan earthquake, the deformation of the Yele dam is mainly downward and towards the downstream side, which is mainly due to the effects of the reservoir impounding. The maximum deformation occurs in the upstream rockfill zone, which is 0.564m and is located at the middle height of the rockfill zone and close to the core. The position and orientation of the maximum displacement are indicated by a grey vector in Figure 5-46 (b). Furthermore, based on the numerical results, no failure is observed on the dam after the earthquake event. It should be noted that during the Wenchuan earthquake, the reservoir water level was only at the dead water level, which was 31.5m lower than the normal water level and 48.5m below the dam crest. The predicted maximum accumulated residual settlement on the Yele dam crest is much smaller than the freeboard allowance (48.5m).

The seismically induced sub-accumulated deformed mesh and vectors of sub-accumulated displacement on the Yele dam at the end of the Wenchuan earthquake are shown in Figure 5-47, which include the deformation induced only by the dynamic loading. Based on the displaced mesh shown in Figure 5-47 (a), it is found that the final seismic deformation in the downstream part is downward and towards the upstream side, whereas the deformation in the upstream part is less significantly downward and also towards the upstream side. Based on Figure 5-47 (b), it can be seen that the maximum seismic deformation occurred on the upstream slope surface, approximately at the middle height and close to the berm. Its magnitude is 0.0744m and the position and orientation are indicated by a grey vector. Overall, the predicted maximum residual seismic deformation is less significant than the predicted static deformation and no failure is observed on the dam based on the numerical simulations. Therefore, the Yele dam is in safe-operation during and after the Wenchuan earthquake. This is also in agreement with Cao et al. (2010) and Wu et al. (2009). Based on them, the Wenchuan earthquake did not cause severe damage on the Yele dam. Only some local damage was observed, which however did not influence either the satisfactory seismic performance of the dam or the normal operation of the power plant. However, currently there is not a

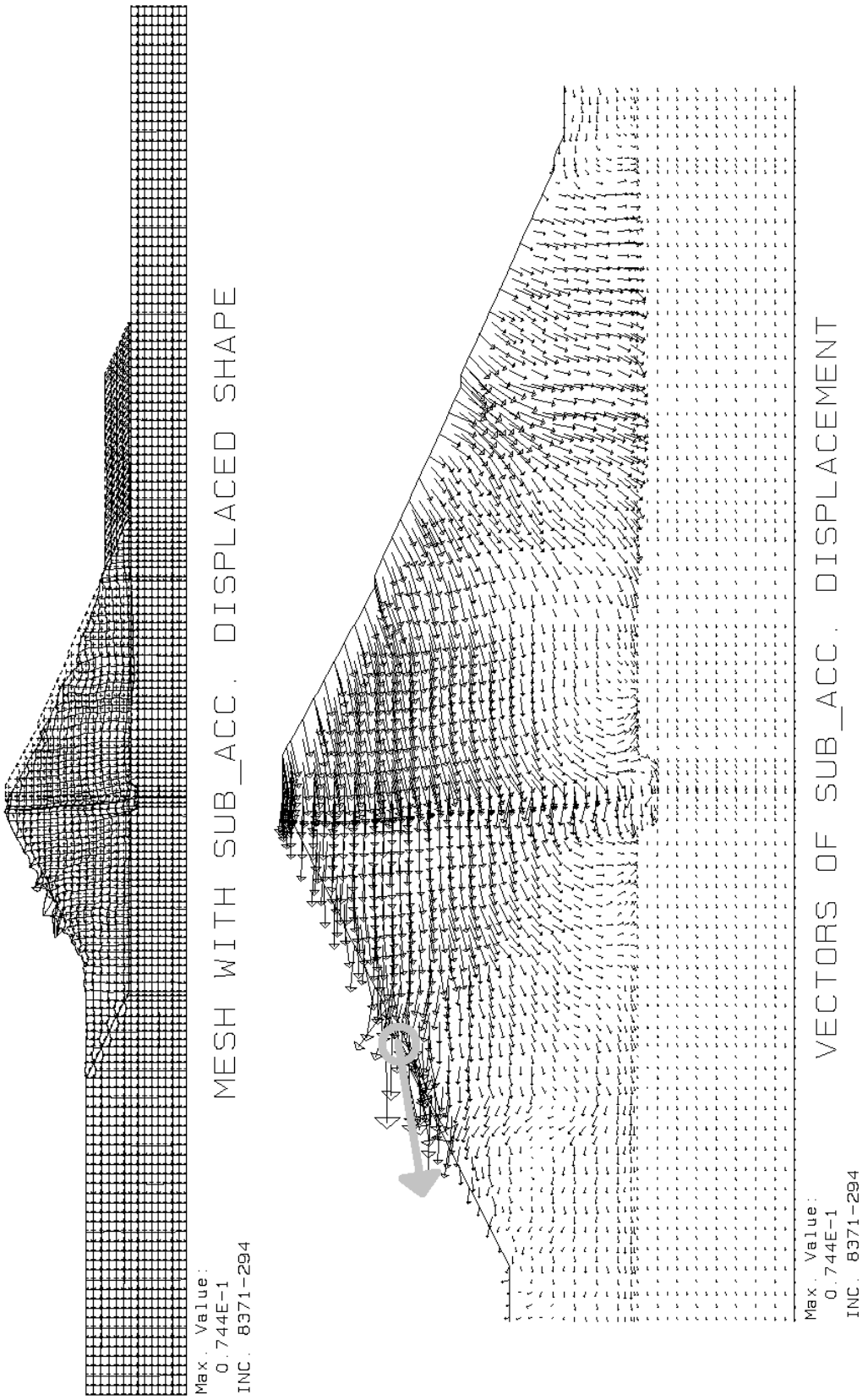
well established standard to assess the seismic safety for rockfill dams. This requires sufficient analyses of seismic observations and numerical simulations for rockfill dams, which is suggested for future research.

The seismic deformation of the Yele dam is further investigated by analysing the strain levels. The contour plots of sub-accumulated shear strain and vertical strain at the end of the Wenchuan earthquake are plotted in Figure 5-48. Based on the numerical results, higher shear strain levels are observed in the upstream slope surface, the transition layer and the filter layer. Higher vertical strain mainly concentrates on the upstream slope surface, close to the berm and in the filter layer. The material stiffness of the transition and filter layers is smaller than that of the rockfill materials, which results in the concentrated larger deformation in these two areas. Furthermore, the seismic response is usually more amplified on the surface of geotechnical structures, leading to the observed maximum strain levels on the upstream surface. This observation also agrees with the location of the maximum displacement shown in Figure 5-47 (b). Furthermore, based on the contour plots of sub-accumulated plastic shear strain and vertical strain shown in Figure 5-49, it can be observed that the seismically induced plastic deformations mainly concentrate on the upstream and downstream slope surfaces. The predicted plasticity is larger on the upstream surface than that on the downstream part, indicating the more significant permanent deformations at the upstream side.



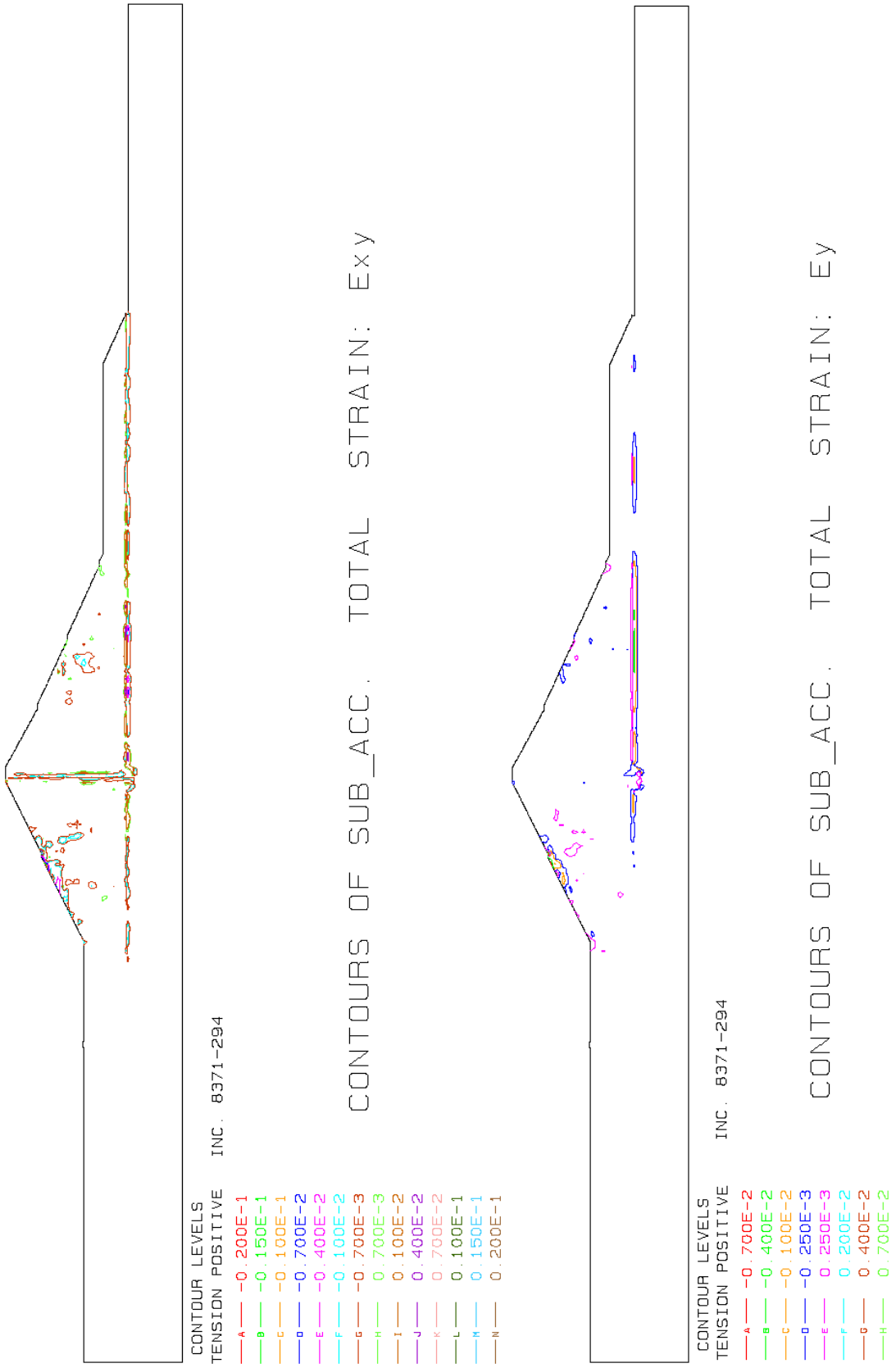
(a): Accumulated deformed mesh (b): Vectors of accumulated displacement (zoomed-in)

Figure 5-46: Accumulated deformed mesh and vectors of accumulated displacement on the Yele dam after the Wenchuan earthquake (displacement scaling factor: 1:50)



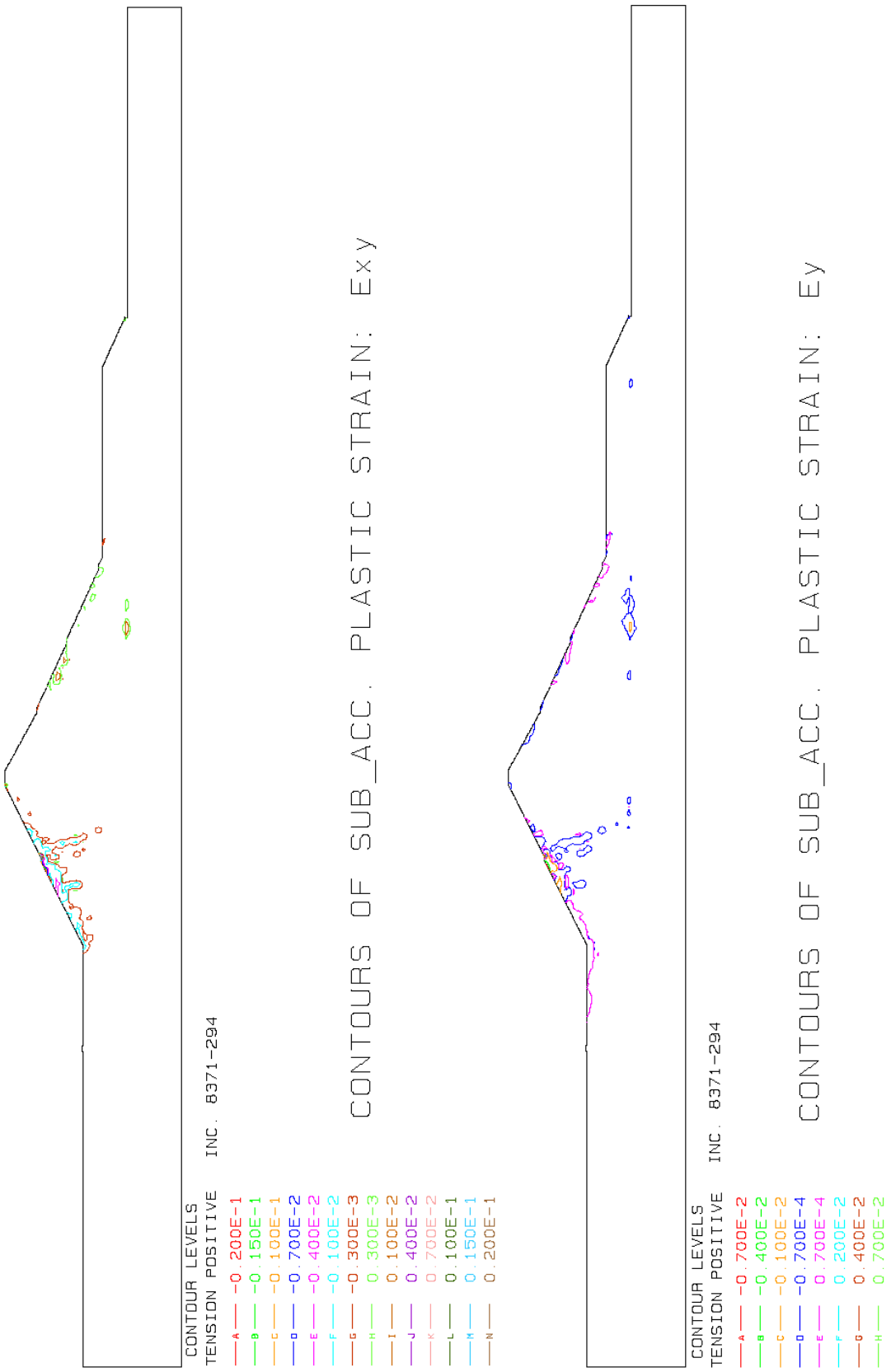
(a): Sub-accumulated deformed mesh (b): Vectors of sub-accumulated displacement (zoomed-in)

Figure 5-47: Sub-accumulated deformed mesh and vectors of sub-accumulated displacement on the Yele dam due to the Wenchuan earthquake (displacement scaling factor: 1:600)



(a): Sub-accumulated shear strain (b): Sub-accumulated vertical strain

Figure 5-48: Contours of sub-accumulated shear strain and vertical strain on the Yele dam due to the Wenchuan earthquake



(a): Sub-accumulated plastic shear strain (b): Sub-accumulated plastic vertical strain

Figure 5-49: Contours of sub-accumulated shear strain and vertical strain on the Yele dam due to the Wenchuan earthquake

5.6.3 Crest settlements

Figure 5-51 shows the sub-accumulated vertical displacement time histories due to the Wenchuan earthquake at the two monitoring points on the dam crest (point 1 and 4 in Figure 5-50). It can be seen that the vertical displacements at point 1 (downstream side) are mainly downward and the final settlement is 3.43mm. The vertical displacements at point 4 (upstream side) fluctuate in the upward and downward directions and the final settlement is 0.52mm, which is much smaller than that at point 1. This is in agreement with the observation from the sub-accumulated deformed mesh in Figure 5-47 (a), where the downstream part shows a more significant downward deformation trend than that in the upstream part. Furthermore, the predicted maximum settlement on the dam crest is smaller than the freeboard, indicating the safe-operation status of the Yele dam after the Wenchuan earthquake.

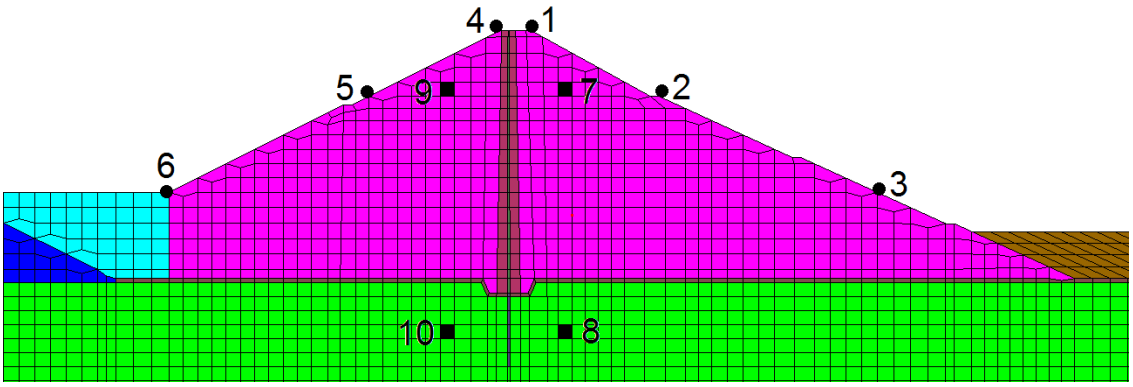


Figure 5-50: Monitoring points on the Yele dam

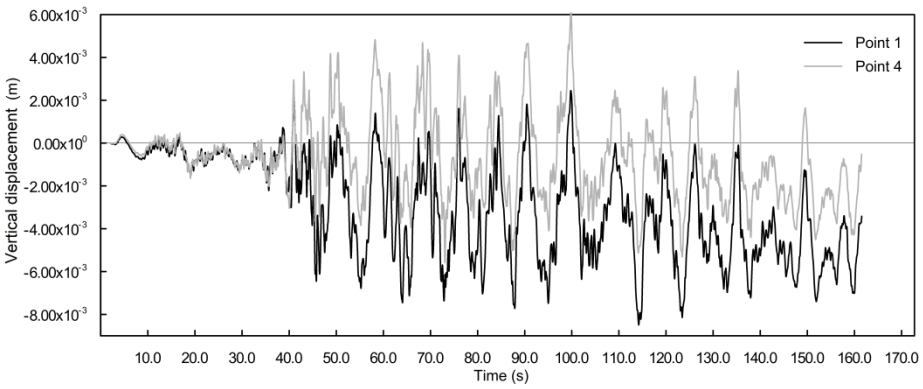
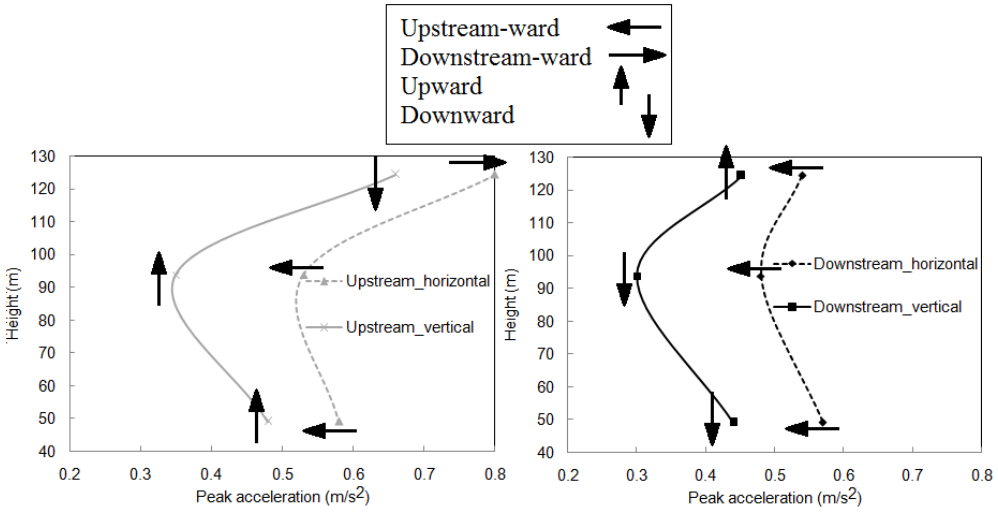


Figure 5-51: Sub-accumulated crest vertical displacement time histories at two locations on the dam crest due to the Wenchuan earthquake

5.6.4 Acceleration distributions within dam body

The acceleration time histories at six locations on the upstream and downstream slope surfaces are obtained from the dynamic FE analysis (point 1-6 in Figure 5-50). The peak accelerations at the six points are plotted against their elevation in Figure 5-52. Based on the numerical results, it can be found that from the dam base to the dam crest, the peak acceleration decreases and increases. This trend is in agreement with the seismic observation of the Yele dam subjected to a low-intensity earthquake in 2007 (Xiong et al. 2008), as shown in Figure 5-53. At the same location, the peak horizontal acceleration is larger than the peak vertical acceleration, indicating the more significant horizontal seismic response on the dam. Furthermore, the directions of the peak accelerations at the six locations are marked in Figure 5-52. It can be observed that the peak accelerations on the downstream slope are mainly downward and towards the upstream side, whereas those on the upstream slope are mostly found to be upward and towards the upstream side. This is in agreement with the observation from the sub-accumulated deformed mesh in Figure 5-47 (a), where the overall deformation of the Yele dam is towards the upstream side and the downstream part shows a more significant downward deformation trend than the upstream part. Finally, at the same elevation, the peak accelerations on the upstream slope are larger than those on the downstream slope. This observation agrees with the results of the seismic strain levels shown in Figure 5-48, where both shear and vertical strains are found to more significantly concentrate on the upstream slope.



(a): Upstream slope (point 4-6) (b): Downstream slope (point 1-3)

Figure 5-52: Peak acceleration variation on the Yele dam

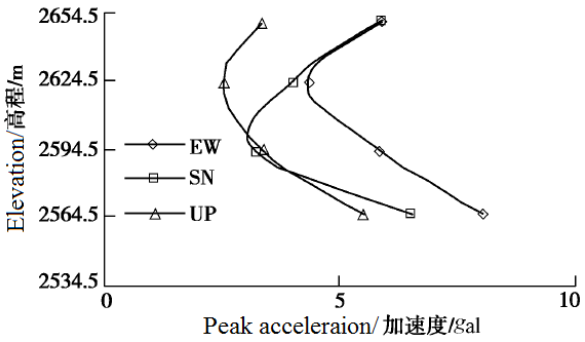


Figure 5-53: Peak acceleration variation on the largest section of the Yele dam recorded in the 23/10/2007 earthquake (after Xiong et al. (2008))

5.6.5 Safety assessment based on seismic design method

In this section, the seismic safety of the Yele dam is assessed by employing the seismic design method for embankment dams proposed by Papadimitriou et al. (2014) and Andrianopoulos et al. (2014).

Firstly, based on the geotechnical characteristics of the Yele dam and the recorded ground motion parameters, the normalised coefficient $k_{hmax}/(PGA_{crest}/g)$ is estimated for potential sliding slopes at different elevations in the dam by Equations 5-1 and 5-4. In particular, the prediction for $k_{hmax}/(PGA_{crest}/g)$ involves four successive steps, where the first three steps concentrate on estimating the PGA at the free field (step 1 in Equation 5-1), the nonlinear fundamental period of the dam vibration T_o (step 2 in Equation 5-1) and PGA at the dam crest PGA_{crest} (step 3 in Equation 5-4) respectively. In Equation 5-4, k_{hmax} is the peak seismic coefficient for a potential sliding slope during the earthquake loading, C_l, C_b, C_f and C_g are four correction parameters representing respectively the effects of the sliding mass location, the stabilising berm, the foundation material stiffness and the sliding mass geometry. Their values are all assumed to be 1.0 for this case study. z is the depth at the bottom of the slip surface from the dam crest (as illustrated in Figure 5-54), λ_d is the predominant shear wavelength in the dam body and Π is the parameter controlling the seismic amplification factor between PGA_{crest} and PGA. The estimated variations of the $k_{hmax}/(PGA_{crest}/g)$ and k_{hmax} are plotted in Figures 5-55 (a) and (b) respectively. It can be seen that, as z increases, the parameter $k_{hmax}/(PGA_{crest}/g)$ linearly decreases from 1.0 to 0.34, indicating the less significant amplification effects at the bottom part of the dam.

Secondly, in order to evaluate the dam safety, the estimated k_{hmax} values are

compared against the critical seismic coefficient k_y value of the critical sliding slope on the Yele dam (i.e. the most unstable one). This k_y value can be pseudo-statically calculated by achieving the limit equilibrium state for the critical sliding slope. The critical sliding mass is identified by the smallest factor of safety (FoS) through analysing a variety of potential sliding slopes formed by different circular slip surfaces specified by varying circle centres and radii. The Janbu's method (1957) incorporated in the soil stability analysis program (Oasys Slope 19.0) is employed for this purpose, where the geometric and material properties of the Yele dam are adopted. Furthermore, water table is assumed based on the pore water pressure pattern before the Wenchuan earthquake predicted by the static FE analysis shown in Figure 5-42 (e). The analysis profile for the Yele dam is shown in Figure 5-56 (a). It should be noted that only the upstream dam part is considered for the stability analysis since it was observed that the seismic deformation in the upstream part is more significant than that in the downstream part, as shown in Section 5.6.2.

Based on the stability analysis results, as shown in Figure 5-56 (b), the smallest FoS is observed for the sliding mass at the 1/3 bottom part (indicated by the black circular line). This sliding mass is therefore considered as the critical sliding slope for the Yele dam. By employing the trial and error method to achieve the limit equilibrium state (i.e. when FoS=1.0), the critical seismic coefficient k_y of the critical sliding slope is calculated as 0.75. It can be seen that this value is significantly larger than the estimated k_{hmax} value at the corresponding z (see Figure 5-55 (b)). This indicates that the Wenchuan earthquake loading is unlikely to induce significant slope instability or large deformation on the Yele dam, which ensures its safe operation for this level of earthquake intensity. This is also in agreement with the findings from the numerical predictions in Section 5.6.2.

It should be noted that the considerably large value of k_y is attributed to the high values of angle of shearing resistance of the rockfill materials, which are between 45-50 degrees. In order to trigger seismic movement for the critical sliding mass (i.e. reaching the limit equilibrium state), the PGA_{rock} is estimated to be 1.22g based on the design method of Papadimitriou et al. (2014).

$$\text{Step3: } \frac{\text{PGA}_{\text{crest}}}{\text{PGA}} = \begin{cases} 1+(\Pi-1)\cdot\left(\dfrac{2T_o}{T_e}\right) & \text{when } \dfrac{T_o}{T_e} \le 0.5 \\ \Pi & \text{when } 0.5 \le \dfrac{T_o}{T_e} \le 1.5 \\ \Pi\cdot\left(\dfrac{2T_o}{3T_e}\right)^{-0.7} & \text{when } \dfrac{T_o}{T_e} \ge 1.5 \end{cases} \quad 5\text{-}4$$

$$\text{where } \Pi = 2.7\left(\frac{v_b}{1000}\right)^{0.52}$$

$$\text{Step4: } \left(\frac{k_{\text{hmax}}}{\text{PGA}_{\text{crest}}/g}\right) = C_l - 1.18C_b\cdot C_f\cdot C_g\cdot\left(\frac{z}{\lambda_d}\right)$$

$$\text{where } \lambda_d = 1.3H\cdot\left(1+\frac{T_e}{T_o}\right)$$

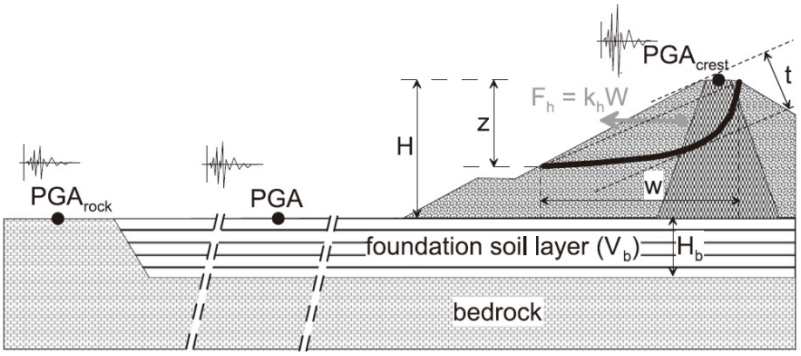


Figure 5-54: Schematic graph for the seismic design method of Papadimitriou et al. (2014)

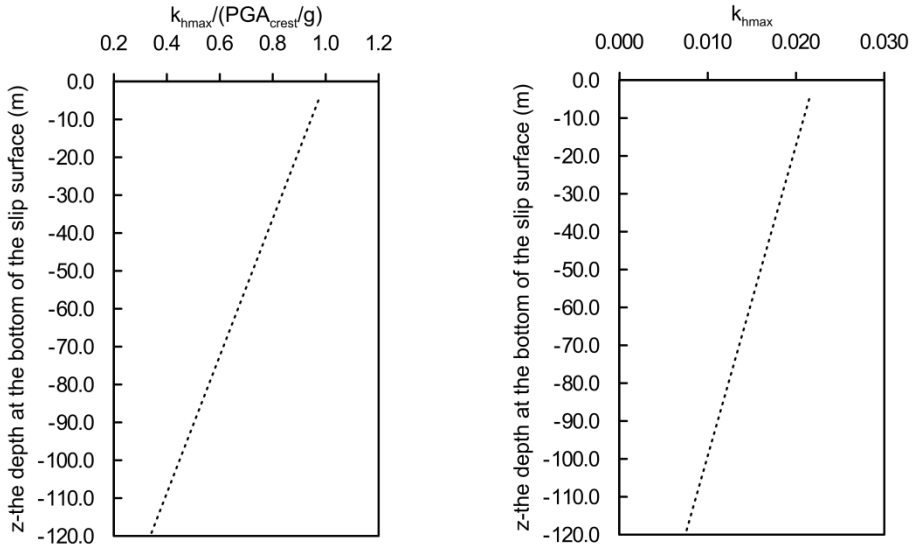
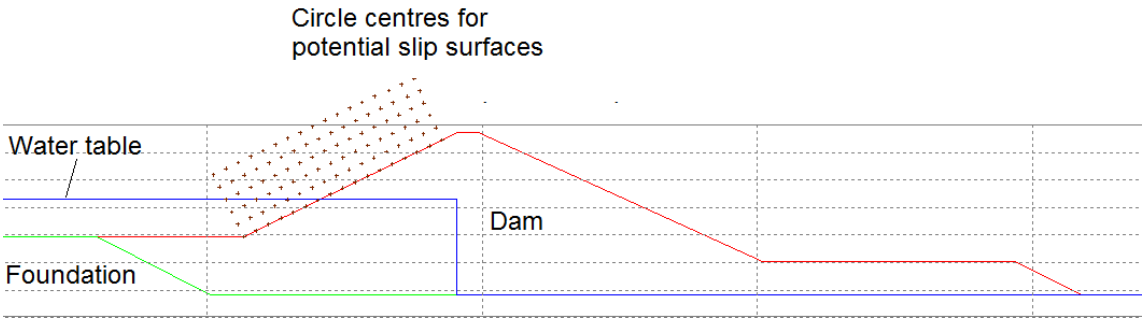
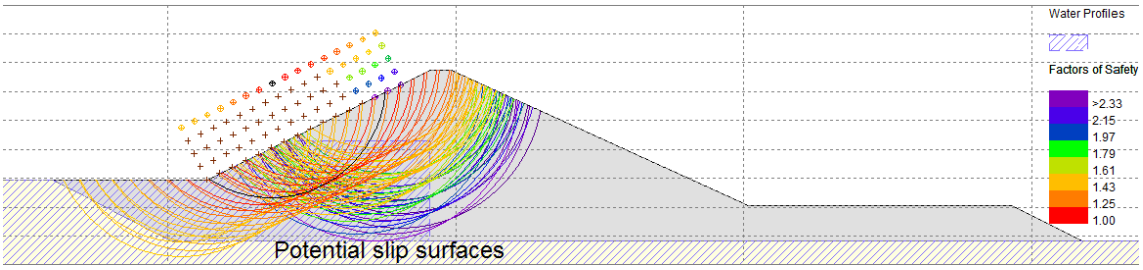


Figure 5-55: Variations of the parameter $k_{\text{hmax}}/(\text{PGA}_{\text{crest}}/g)$ and k_{hmax}



(a): Dam profile for stability analysis



(b): Stability analysis results

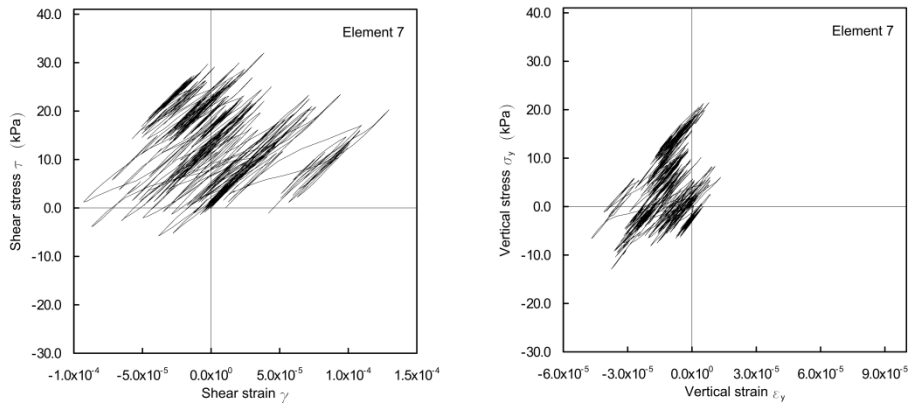
Figure 5-56: Stability analysis for the Yele dam

5.6.6 Stress-strain and pore water pressure response

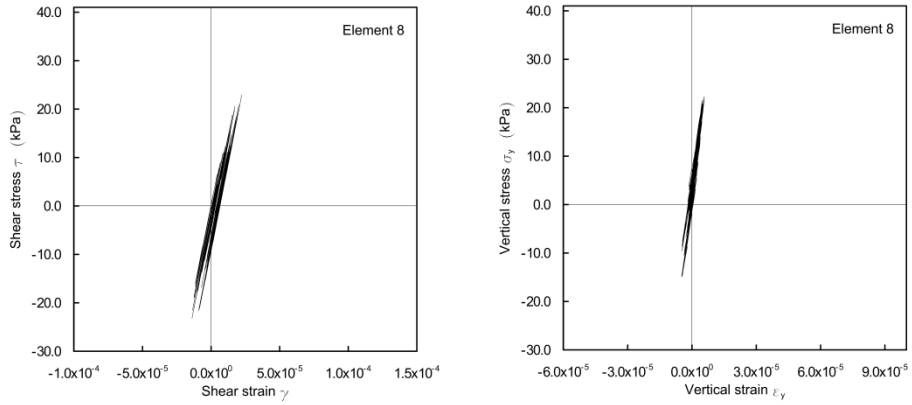
The seismic response of the Yele dam is further investigated by analysing the simulated dynamic soil behaviour. In particular, the sub-accumulated stress-strain response at an integration point of four monitoring elements due to the Wenchuan earthquake is shown in Figure 5-57. These four elements, i.e. elements 7, 8, 9 and 10 in Figure 5-50, are located in the downstream rockfill, downstream foundation, upstream rockfill and upstream foundation respectively. Based on the numerical results, it can be seen that the simulated soil behaviour in the rockfill zone is more nonlinear than that in the dam foundation. The shear and vertical strain levels in the rockfill material are larger than those in the foundation. Furthermore, it is observed that the maximum strain level for the upstream rockfill material is larger than the downstream one, both in terms of the shear and vertical strains. Simultaneously, the dynamic soil behaviour of the upstream rockfill is more nonlinear than the downstream one. This observation agrees with the results of the seismic strain levels shown in Figure 5-48, where both shear and vertical strains are found to more significantly concentrate on the upstream slope.

The sub-accumulated pore water pressure time histories at two locations on the Yele dam (element 9 and 10 in Figure 5-50) due to the Wenchuan earthquake are predicted by

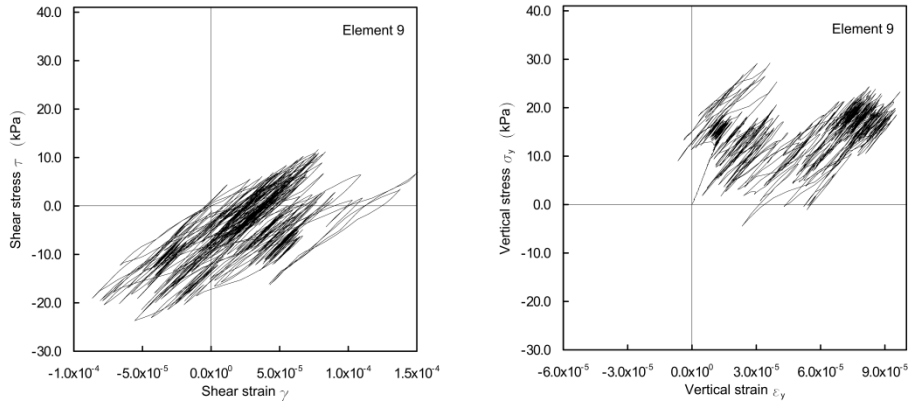
the dynamic analysis and are compared in Figure 5-58. It can be seen that excess pore water pressures accumulate more at element 9 in the upstream rockfill than that at element 10 in the dam foundation. Particularly in the first 10 seconds, compressive pore water pressures fast accumulate at element 9, whereas some minor tensive pore water pressures accumulate at element 10. It should be noted that zero plastic volumetric strains were observed at the two elements due to the earthquake loading. Therefore, the build-up of the excess pore water pressures at elements 9 and 10 is induced by other factors. By analysing the vertical acceleration time histories at the two elements in Figure 5-59, it is found that the vertical earthquake loading at element 9 shows a strong asymmetry in the first 10 seconds. In particular, the vertical acceleration values at element 9 are mainly negative (downward) at the beginning of the seismic loading, which essentially results in more significant compression deformation and compressive pore water pressure accumulation. From 10 seconds onward, the dynamic loading at element 9 becomes symmetric and no excess pore water pressure is accumulated. However, the vertical dynamic loading at element 10 at the beginning of the seismic loading shows only minor asymmetry with positive values (upward), which results in gentler build-up of tensive pore water pressure. Based on the final sub-accumulated pore water pressure contour plot in Figure 5-60, excess pore water pressure is mainly accumulated in the upstream rockfill and the foundation zone under the dam body. This indicates that the influence of the asymmetric vertical movement on excess pore pressure accumulation is only concentrated in the areas subjected to the complicated and asymmetric dam geometry. Beyond the dam heel and toe, such influence is insignificant in the homogeneous foundation layers. Lastly, the magnitude of the accumulated excess pore water pressure is relatively small compared to the total pore water pressure values. This can be seen in the final accumulated pore water pressure contour plot in Figure 5-61. It can be found that the final pore water pressure distribution is not significantly affected by the seismic loading compared to that before the Wenchuan earthquake shown in Figure 5-42 (e).



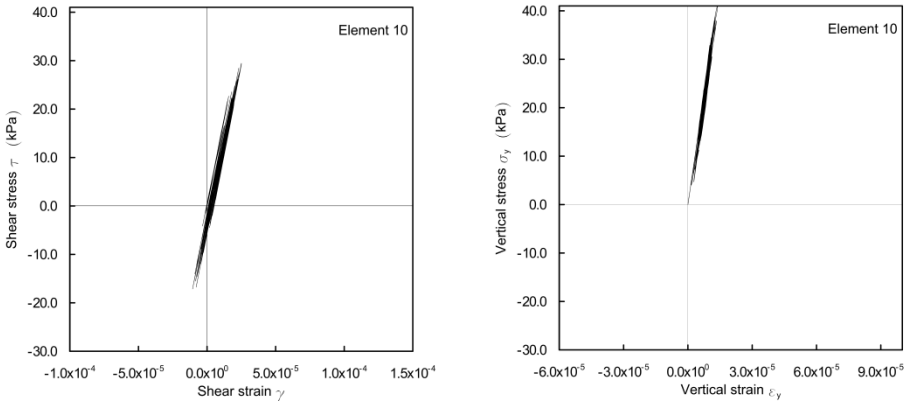
(a): Element 7



(b): Element 8



(c): Element 9



(d): Element 10

Figure 5-57: Sub-accumulated stress-stain loops at four locations on the Yele dam due to the Wenchuan earthquake

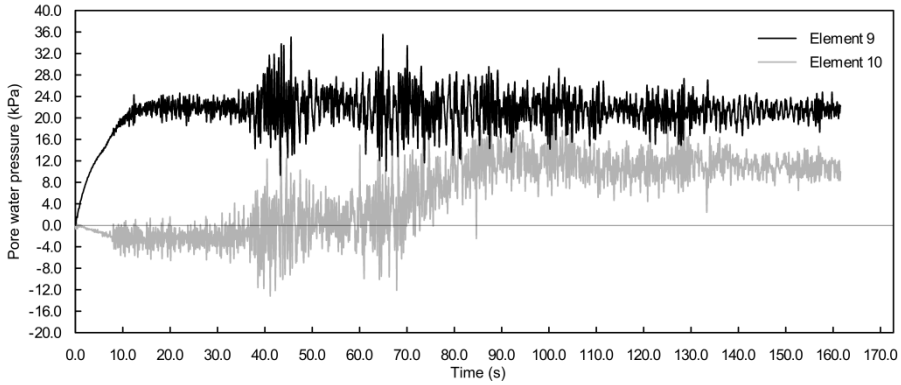


Figure 5-58: Sub-accumulated pore water pressure time histories at two locations on the Yele dam due to the Wenchuan earthquake

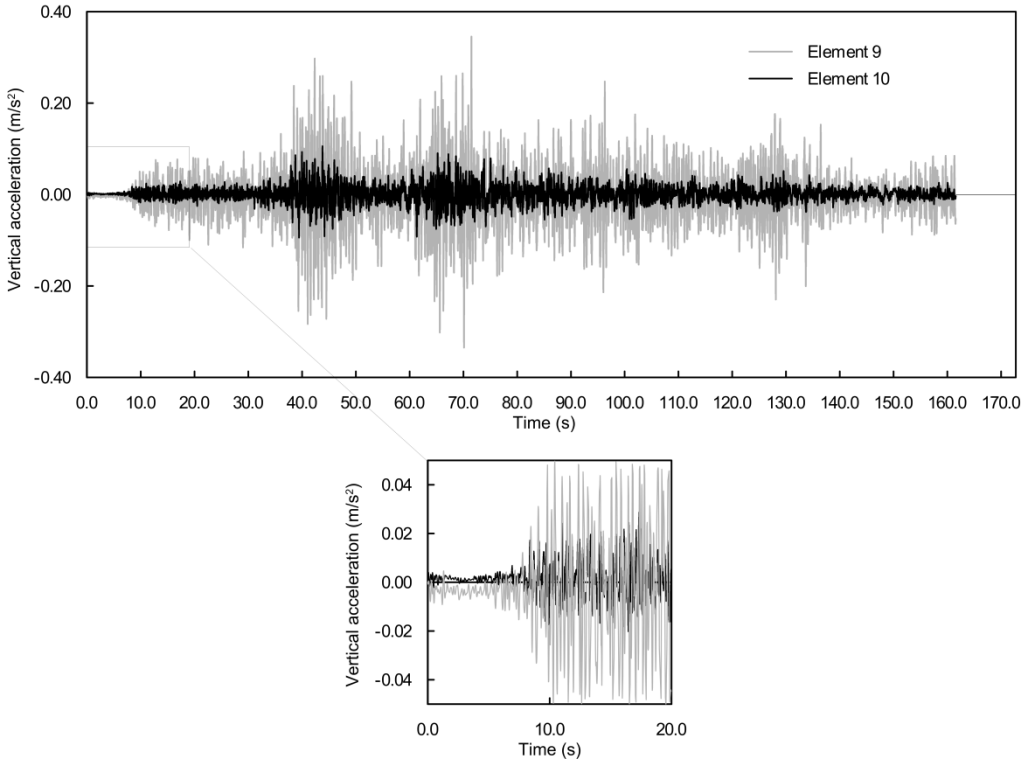


Figure 5-59: Vertical acceleration time histories at element 9 and 10



Figure 5-60: Sub-accumulated pore water pressure contour plot on the Yele dam due to the Wenchuan earthquake (Compression positive: kPa)

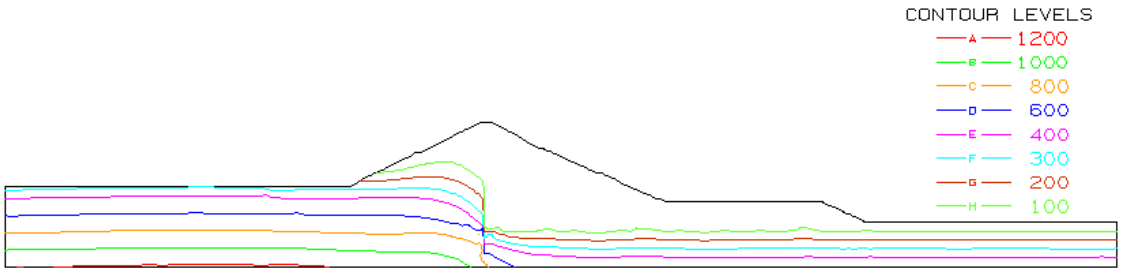


Figure 5-61: Final accumulated pore water pressure contour plot on the Yele dam after the Wenchuan earthquake (Compression positive: kPa)

5.7 Summary

In this chapter, the seismic response of a well-documented Chinese rockfill dam, the Yele dam, was investigated by employing dynamic HM coupled FE analysis. Through the conducted numerical investigation, different aspects of the numerical modelling for static and dynamic analyses of rockfill dams were validated against the available monitoring data of the Yele dam during the 2008 Wenchuan earthquake. The seismic safety of the Yele dam was assessed by analysing its dynamic behaviour predicted by FE analyses.

The numerical model of the Yele dam for the static and the dynamic analyses was firstly established, in terms of the element size, boundary location and constitutive model calibration. It was found that the vertical wave propagation was sensitive to the element dimension in the vertical direction, which needed to be parametrically defined. The cone boundary conditions were employed at the lateral boundaries of the FE mesh for the dynamic analysis. The location of the lateral boundary required further

assessment to ensure that free-field response is retained near the lateral sides of the model.

By adopting the appropriate numerical model, such as the simulation sequence, displacement and hydraulic boundary conditions and constitutive model, the static behaviour of the Yele dam under the construction, impounding and operation loading conditions was simulated. Numerical predictions were firstly compared against the static monitored data, showing satisfactory agreement in terms of the horizontal displacement variation of the core section and the settlements at different locations in the dam. It was also found that in order to accurately predict dam deformations, the actual reservoir simulation should be considered. Furthermore, the accumulated deformed mesh and vectors of accumulated displacement at the end of the static analysis showed that the overall dam deformations were not significant and were well within the limit for its safe operation under static loading conditions. Finally, the seepage pattern at different stages was reasonably predicted by the static analysis, which is helpful to better understand the static behaviour of the Yele dam.

By employing the simulated static state as the initial stress profile for the dynamic analysis, the seismic response of the Yele dam was then analysed. A good agreement was observed between the numerical results and the dynamic monitored response at two points at the dam crest and base, in terms of acceleration response spectra and time histories. Further evaluations of the seismic deformation on the Yele dam were achieved:

- The sub-accumulated deformed mesh and vectors of sub-accumulated displacement due to the earthquake loading showed a safe-operation status for the Yele dam during and after the Wenchuan earthquake. It was found that the final seismic deformation in the downstream part was downward and towards the upstream side, whereas the seismic deformation in the upstream part was less significantly downward and also towards the upstream side. Sub-accumulated shear and vertical strain levels showed that the dynamic deformation was concentrated in the upstream slope surface zone and the transition layer, due to more significant amplification effects and lower material stiffness respectively.
- The predicted sub-accumulated crest settlement time histories due to the Wenchuan earthquake further proved the safe-operation status of the Yele dam and showed a

more significant downward crest settlement at the downstream side than that at the upstream side.

- The variation of the peak acceleration on the dam surface showed that, from the dam base to the dam crest, the peak acceleration decreased and increased. This trend was in agreement with field observations at the Yele dam after a previous earthquake on 23th October, 2007. Furthermore, the results also indicated that the peak accelerations on the downstream slope were mainly downward and towards the upstream side, whereas those on the upstream slope were mostly upward and also towards the upstream side. This is in agreement with previous observations from the sub-accumulated deformed mesh.
- The seismic safety of the Yele dam was assessed by employing the seismic design method for embankment dams proposed by Papadimitriou et al. (2014) and Andrianopoulos et al. (2014). The estimated peak seismic coefficient k_{hmax} values for potential sliding slopes within the dam were found to be much smaller than the limit value of the critical seismic coefficient k_y calculated by the limit equilibrium method. This indicated that the Wenchuan earthquake loading is unlikely to induce significant slope instability or large deformation in the Yele dam, which ensures its safety operation. This is also in agreement with the findings from the numerical predictions.
- The seismic response of the dam was further investigated by analysing the simulated dynamic soil behaviour. The stress-strain response at four monitoring elements within the dam indicated more significant dynamic deformations in the upstream dam body, than those predicted in the downstream part and the foundation section.
- Finally, accumulation of excess pore water pressure was observed in the upstream rockfill, due to an asymmetric vertical movement despite the lack of volumetric plasticity in the soil response. However, this influence was only concentrated in the areas where the dam geometry is complicated. Beyond the dam heel and toe, such influence was insignificant. The magnitude of the accumulated excess pore water pressure was relatively small compared to the total pore water pressure values. The final pore water pressure distribution was not significantly affected by the seismic loading compared to the one established before the Wenchuan earthquake.

CHAPTER 6
Parametric studies of the Yele dam

6.1 Introduction

In this chapter, the effects of four critical factors on the seismic response of the Yele dam are investigated through parametric studies, i.e. the reservoir simulation method, the permeability of the materials comprising the dam body, the vertical ground motion and the reservoir water level, denoted as parametric study 1, 2, 3 and 4 respectively. The previous dynamic analysis of the Yele dam in Chapter 5 is employed as the reference study for the presented parametric investigations.

6.2 Effect of reservoir simulation

This section aims to examine the effects of the reservoir simulation on the seismic response of the Yele dam. In the previous dynamic analysis, the reservoir is simulated by employing boundary stresses on the dam and foundation surfaces. However, in this section, solid elements are used for the reservoir simulation. A similar static FE analysis is conducted to reproduce the static state of the Yele dam before the Wenchuan earthquake. The difference is that after the first stage of the dam construction, the reservoir impounding is simulated by constructing a four-layer reservoir section using solid elements (section 10 in Figure 6-1) and pore water pressure is prescribed within

the elements to satisfy the hydrostatic conditions. Since the focus of this parametric study is to investigate the effects of the reservoir simulation on the dynamic response, the reservoir impounding only follows the second simulation sequence (Figure 5-19 (b)). The reservoir is impounded to 75.0m and remains constant until the dynamic analysis. As suggested by Pelecanos (2013), a small value of shear modulus (100kPa) is employed for the water material in both static and dynamic analyses. The bulk modulus for the water material is employed as 2.2E6 kPa. The other aspects of the numerical modelling for this static analysis are the same as those employed in the reference case study. The FE mesh is shown in Figure 6-1, consisting 2644 8-noded isoparametric quadrilateral solid elements.

By employing solid elements for the reservoir simulation, the accumulated deformed mesh and vectors of accumulated displacement at the end of the static analysis are shown in Figure 6-2. Similar to the results by employing boundary stresses, due to the effects of the reservoir impounding, the dam deformation is downward and towards the downstream side, but with a smaller magnitude due to the incomplete simulation for the reservoir impounding. The maximum displacement occurs at the same place in the upstream rockfill, which is about at the middle height of the rockfill zone and close to the core. The maximum displacement value is 0.372m and its position and orientation are indicated by a grey vector in Figure 6-2 (b).

The pore water pressure distribution before the Wenchuan earthquake is predicted by the static analysis employing solid elements for the reservoir simulation and is shown in Figure 6-3. It can be seen that the pore water pressure distribution is nearly identical to that from the reference case study, which is in a steady seepage condition.

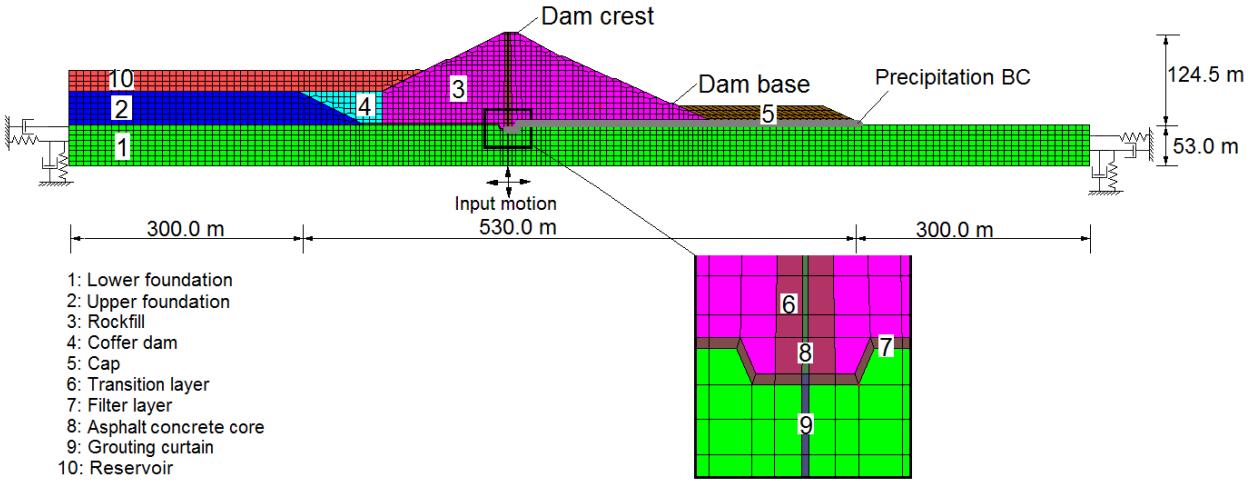
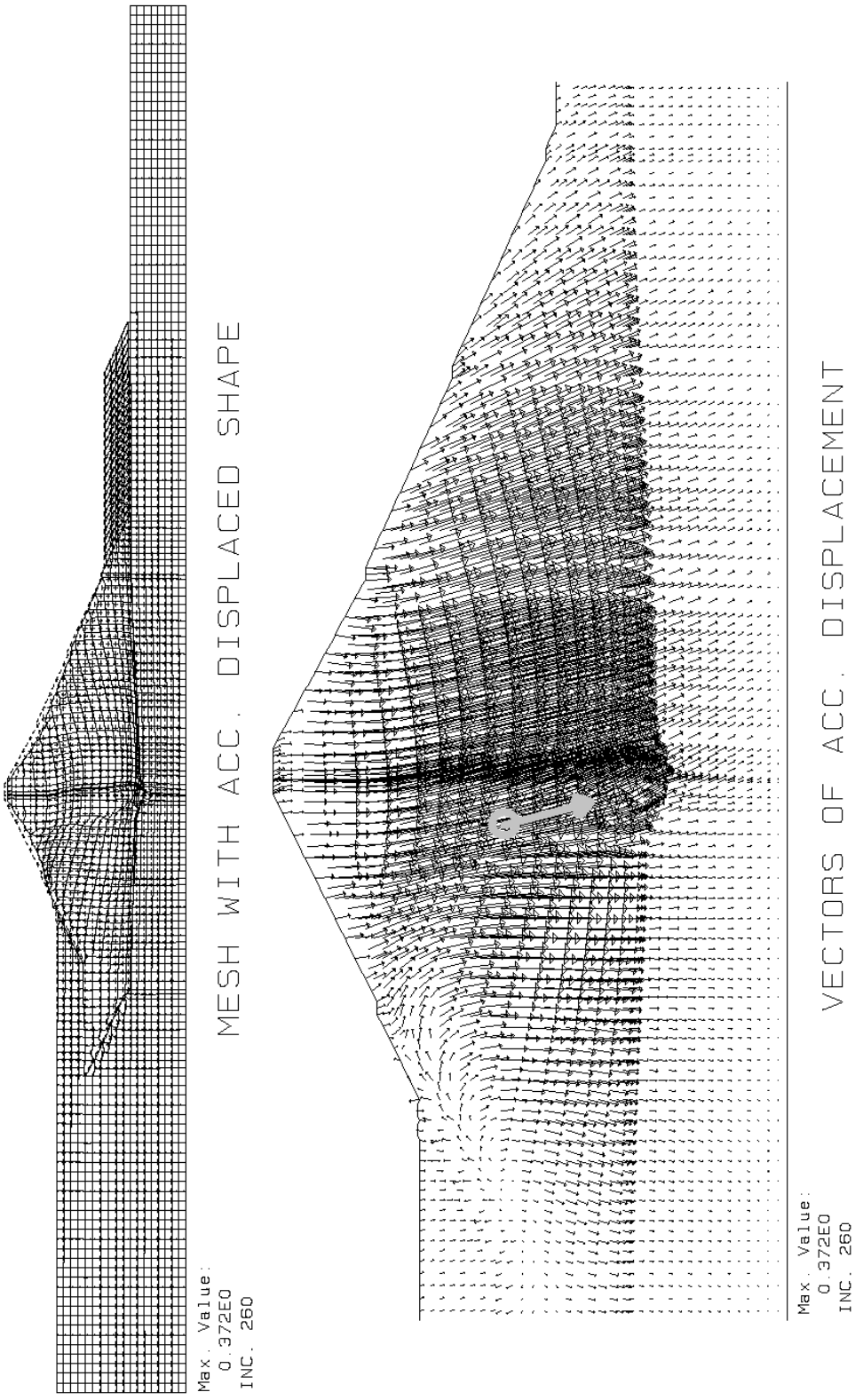


Figure 6-1: FE mesh and dynamic boundary conditions for the parametric study 1



(a): Accumulated deformed mesh (b): Vectors of accumulated displacement (zoomed-in)

Figure 6-2: Accumulated deformed mesh and vectors of accumulated displacement on the Yele dam employing solid elements for reservoir simulation before the Wenchuan earthquake (displacement scaling factor: 1:50)

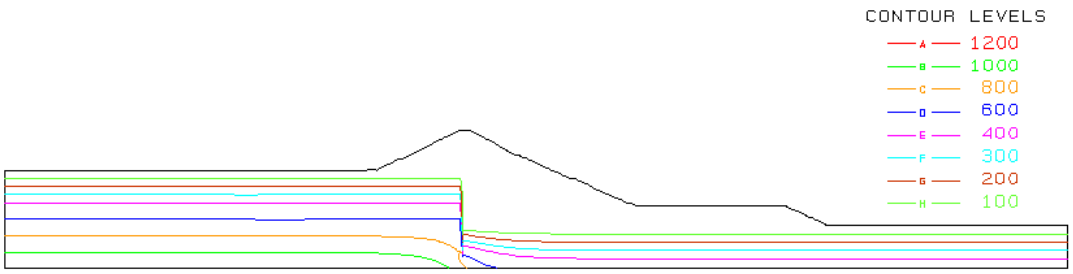


Figure 6-3: Contours of pore water pressure in the Yele dam at the end of the static analysis from the parametric study 1 (Compression positive: kPa)

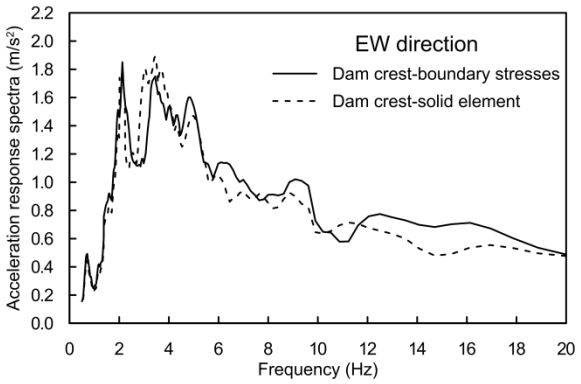
For the dynamic parametric study, the FE mesh and boundary conditions are shown in Figure 6-1. The viscous boundary conditions are extended to the lateral boundary of the reservoir, which was advised by Pelecanos (2013) and Pelecanos et al. (2013) in order to avoid wave reflections. Furthermore, 0.1% Rayleigh damping is employed to account for the material damping in the reservoir, where ω_1 and ω_2 are taken as the first and third fundamental frequencies of the reservoir section. All other aspects of the numerical model for the dynamic parametric study are the same as those employed in the previous dynamic analysis.

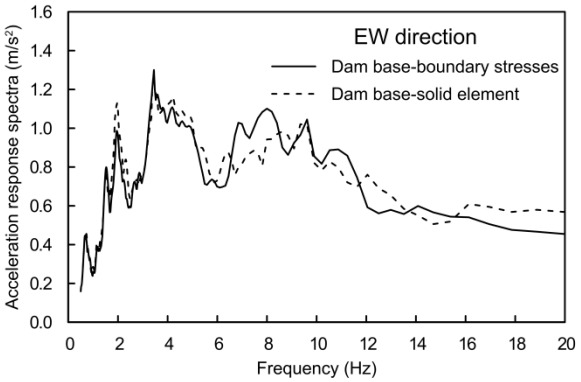
The seismic dam response is then predicted employing solid elements for the reservoir modelling in the dynamic analysis. The numerical results from the parametric study are firstly compared to the reference results in Figures 6-4 and 6-5, in terms of response spectra and acceleration time histories at the two monitoring points at the dam crest and base. Based on the comparison, it can be seen that the influence of the reservoir simulation is insignificant on the dynamic response at the dam crest and base. In particular, the response spectra in the horizontal and vertical directions at the two locations are very similarly predicted by employing the two simulation approaches. The difference is found to be negligible when exploring the comparison of acceleration time histories in Figure 6-5, where the dynamic response predicted by the two analyses is sufficiently close.

The sub-accumulated deformed mesh and vectors of sub-accumulated displacement at the end of the Wenchuan earthquake are predicted by the parametric study and are shown in Figure 6-6. The same deformation trend is observed as the reference one. The maximum displacement occurs at the same place, which is located at the middle height of the upstream slope surface, as indicated by the grey vector in Figure 6-6 (b). A slightly larger magnitude is predicted, which is 0.108m. However, the maximum

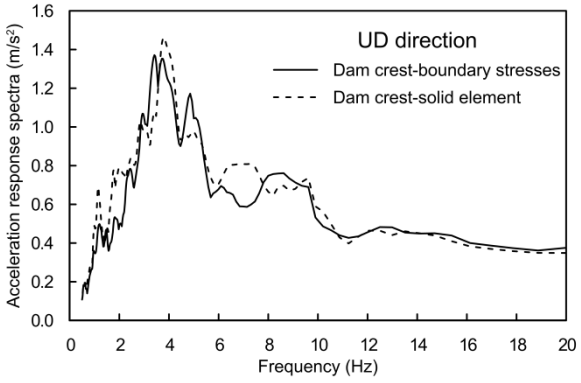
displacement only represents its local deformation, whereas the overall seismic deformation of the Yele dam is not significantly affected by the reservoir simulation compared to the results in Figure 5-47. Furthermore, large-magnitude displacements are observed in the reservoir section, as water material cannot resist shear deformations.

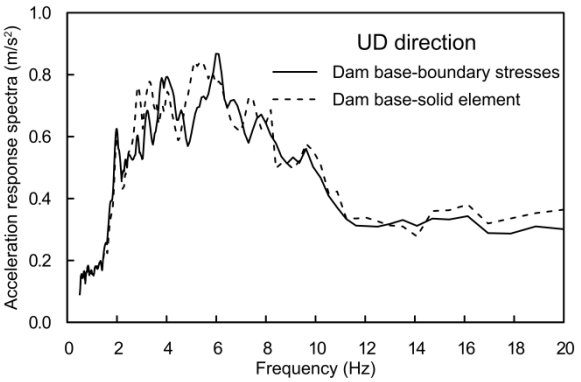
Figure 6-7 shows the comparison of sub-accumulated dam vertical displacement time histories at three locations (point 1, 4 and 6 in Figure 5-50) from analyses employing the two reservoir simulation approaches. It can be seen that the vertical displacement time histories at point 1 (the downstream crest corner) are almost identically predicted by the two analyses. However, the analysis employing solid elements predicts more significant downward settlements at point 4 (the upstream crest corner). However, this influence is only limited in the upstream crest zone, as the comparison of vertical displacement time histories at point 6 (upstream base point in Figure 5-50) is very good. The results suggest that the effects of the reservoir simulation approach and impounding sequence are reasonably insignificant for the overall dynamic response of the Yele dam subjected to the original water level. This is also in accordance with the finding from Pelecanos et al. (2013), that the dam-reservoir interaction effects are less significant for dams with inclined upstream slopes, such as earth dams, compared to dams with vertical upstream slopes.





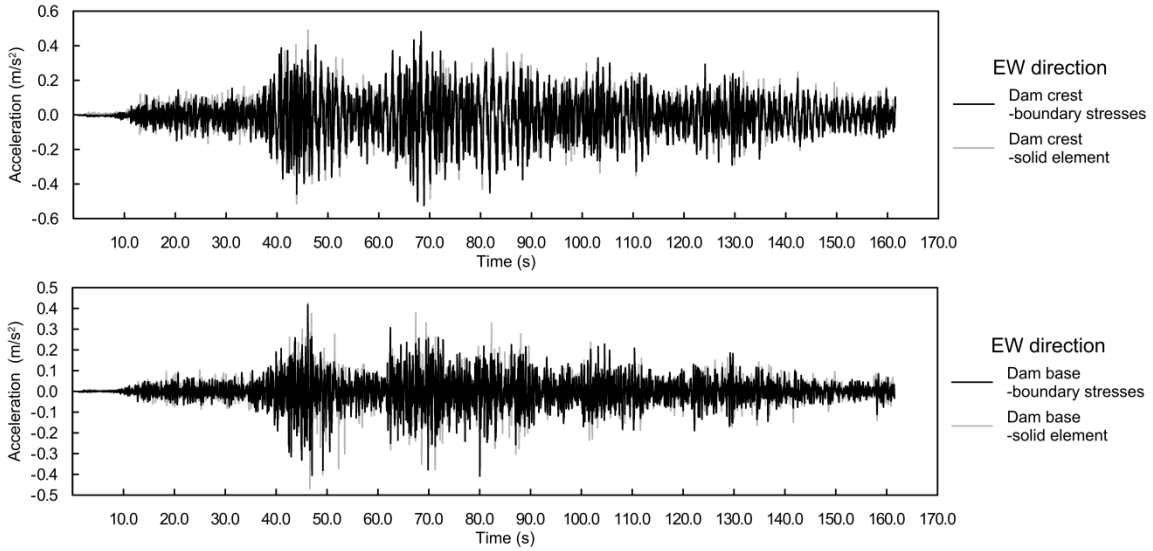
(a): Horizontal-EW direction



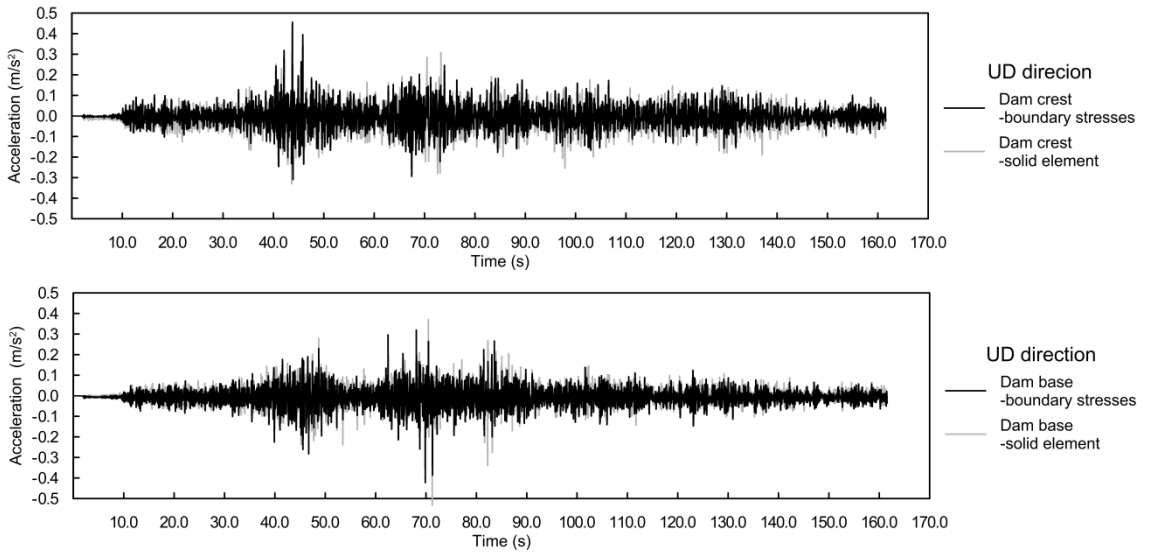


(b): Vertical-UD direction

Figure 6-4: Dynamic response of the Yele dam from the parametric study 1 (acceleration response spectra)

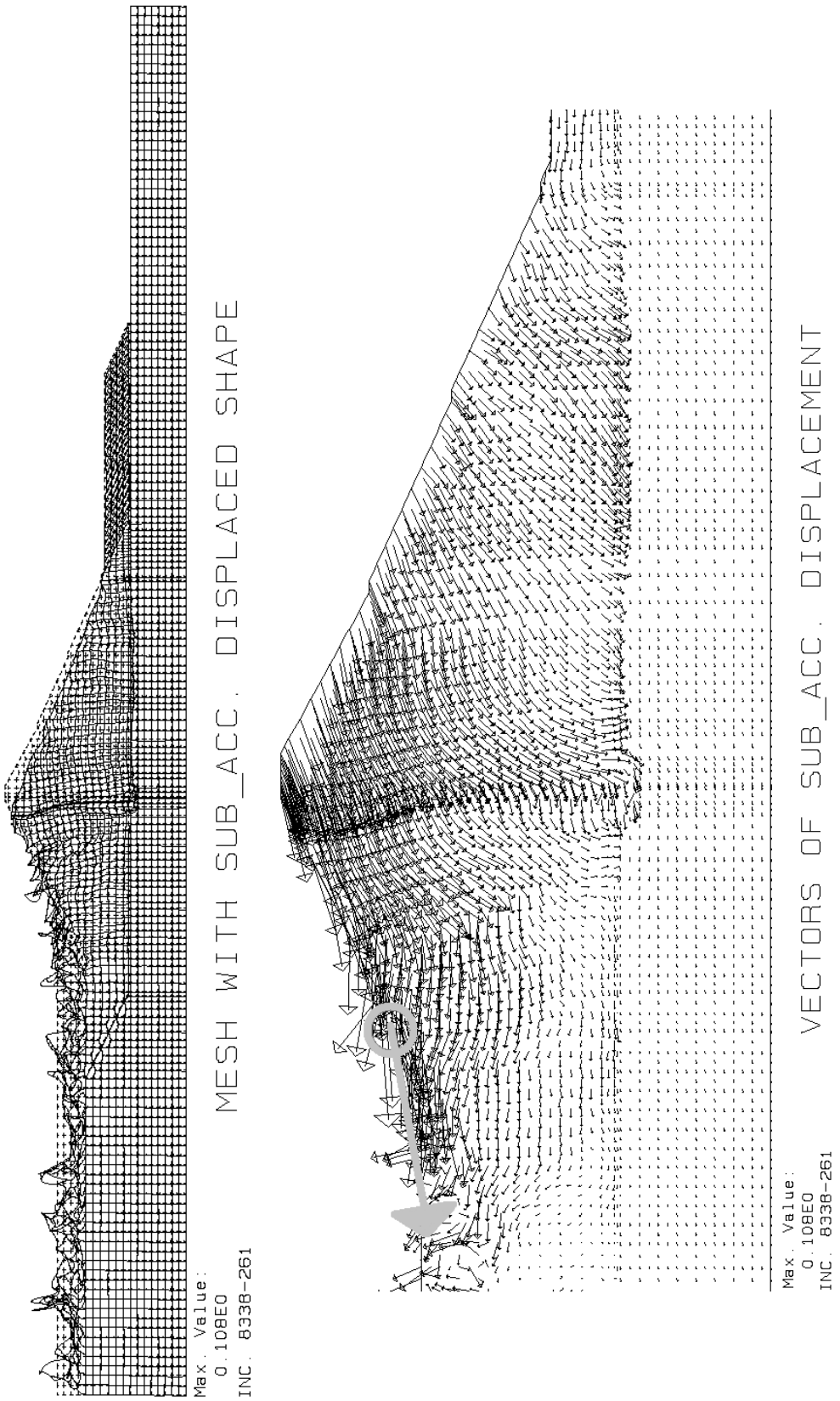


(a): Horizontal-EW direction



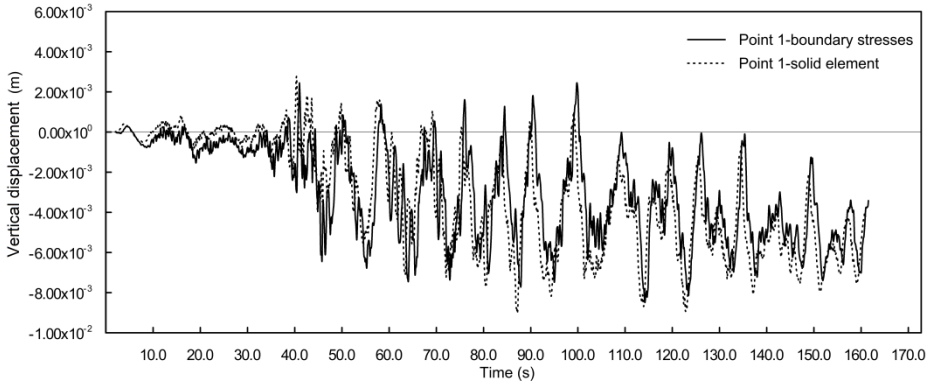
(b): Vertical-UD direction

Figure 6-5: Dynamic response of the Yele dam from the parametric study 1 (acceleration time histories)

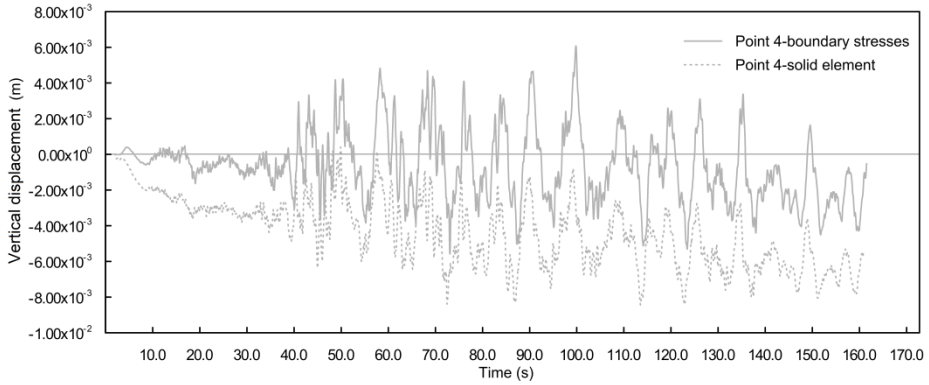


(a): Sub-accumulated deformed mesh (b): Vectors of sub-accumulated displacement (zoomed-in)

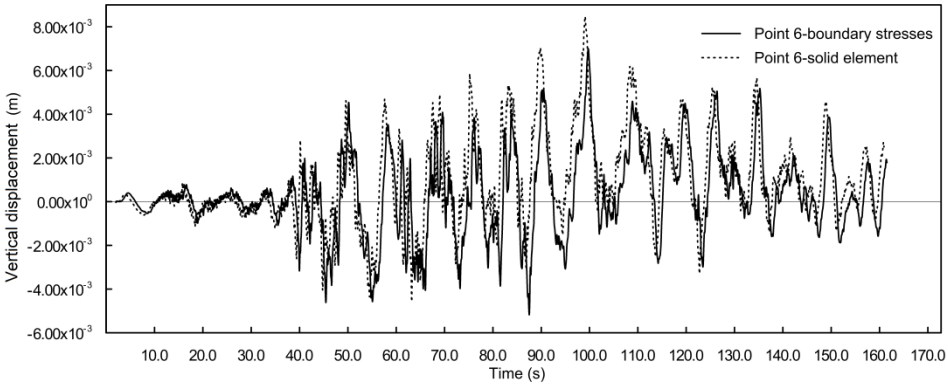
Figure 6-6: Sub-accumulated deformed mesh and vectors of sub-accumulated displacement on the Yele dam due to the Wenchuan earthquake from the parametric study 1 (displacement scaling factor: 1:600)



(a): Point 1



(b): Point 4



(c): Point 6

Figure 6-7: Sub-accumulated crest vertical displacement time histories at three locations on the Yele dam due to the Wenchuan earthquake from the parametric study 1

6.3 Effect of dam material permeabilities

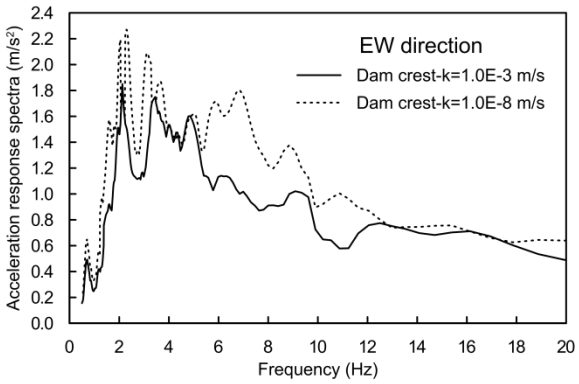
In this section, the effects of the permeabilities of materials comprising the dam body on the dynamic response of the Yele dam are investigated through the second parametric study. The previously employed soil permeabilities are listed in Table 5-1. However, in this parametric study, the permeabilities for dam materials (i.e. the rockfill, coffer dam, cap, transition layer and filter layer) are prescribed to be as low as those adopted for foundation soils, which are 1.0E-8m/s. All other aspects of the numerical model are the same as those for the reference case study.

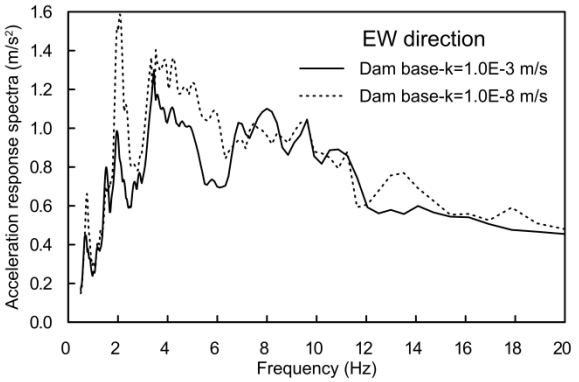
The seismic response at the dam crest and base employing the new material permeabilities is compared to the reference results in Figures 6-8 and 6-9, in terms of acceleration response spectra and acceleration time histories. It can be seen that the two-directional dynamic response is strongly affected by the soil permeabilities. Larger response is predicted when employing low permeabilities (1.0E-8m/s), both in terms of response spectra amplitudes and transient acceleration values. The differences in the vertical response are attributed to the influence of the fluid induced viscous damping discussed in Chapter 3. In particular, for low permeability soils subjected to vertical motions, less viscous damping is introduced due to the less significant interaction effect between the solid and pore fluid phases, leading to larger vertical dynamic response. However, slightly larger horizontal response is also predicted by the analysis employing the lower permeabilities, which reflects the coupling effects between the two-directional response. More specifically, the larger vertical dynamic response can result in larger vertical strain levels for dam materials. This leads to larger deviatoric strains and eventually more significant shear modulus degradation. Based on the results discussed in Chapter 4, larger shear deformation can induce larger horizontal dynamic response in the large strain range. This explanation can be confirmed by the comparison of the tangent shear modulus time histories at the integration point of element 7 in Figure 6-10. It can be observed that the shear modulus degradation for the lower permeability material is more significant due to the effects of the larger vertical response.

The seismically induced sub-accumulated deformed mesh and vectors of sub-accumulated displacement at the end of the Wenchuan earthquake employing low permeabilities are shown in Figure 6-11. The main deformation trend for the Yele dam is observed to be similar to the reference results (Figure 5-47). The seismic deformation

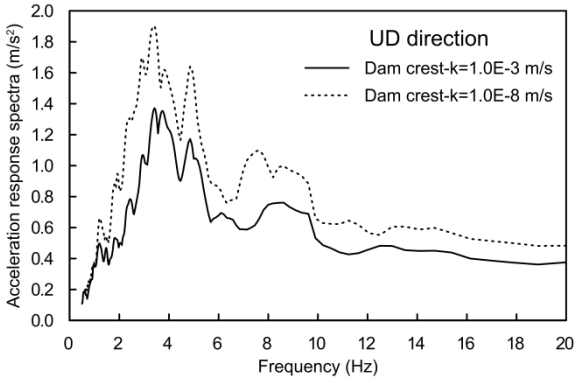
in the downstream part is downward and towards the upstream side. The vertical deformation in the upstream part exhibits slight downward and even significant upward trend close to the crest zone. A smaller maximum displacement (0.0219m) is predicted (the grey arrow in Figure 6-11 (b)), which is located in the upstream crest zone. The location of the maximum displacement is different to the one predicted by the reference study. However, the maximum displacement is only representative of the local deformation in the upstream crest zone, as the overall deformation on the Yele dam is found to be only slightly larger than the reference results, by comparing results in Figure 6-11 and in Figure 5-47.

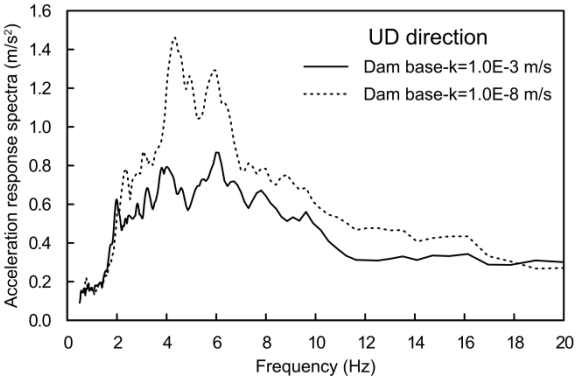
The seismic deformation of the Yele dam is further investigated by comparing the vertical displacement time histories at two crest points (points 1 and 4 in Figure 5-50) in Figure 6-12. It can be observed that, compared to the reference results, the consideration of the low permeabilities predicts more significant settlements at the downstream crest and more pronounced upward movement at the upstream crest. This observation is in agreement with the predicted sub-accumulated deformed mesh shown in Figure 6-11.





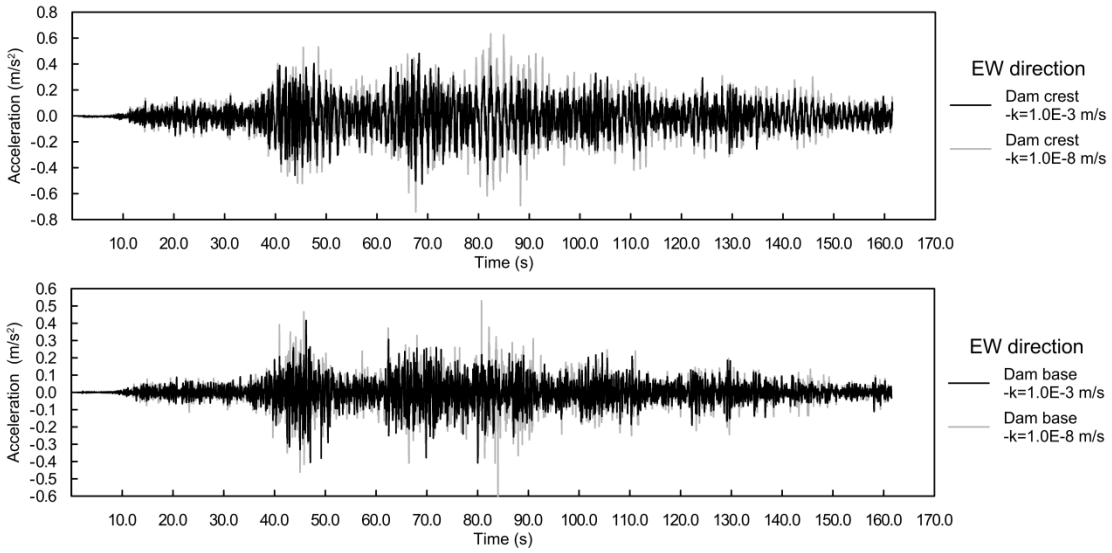
(a): Horizontal-EW direction



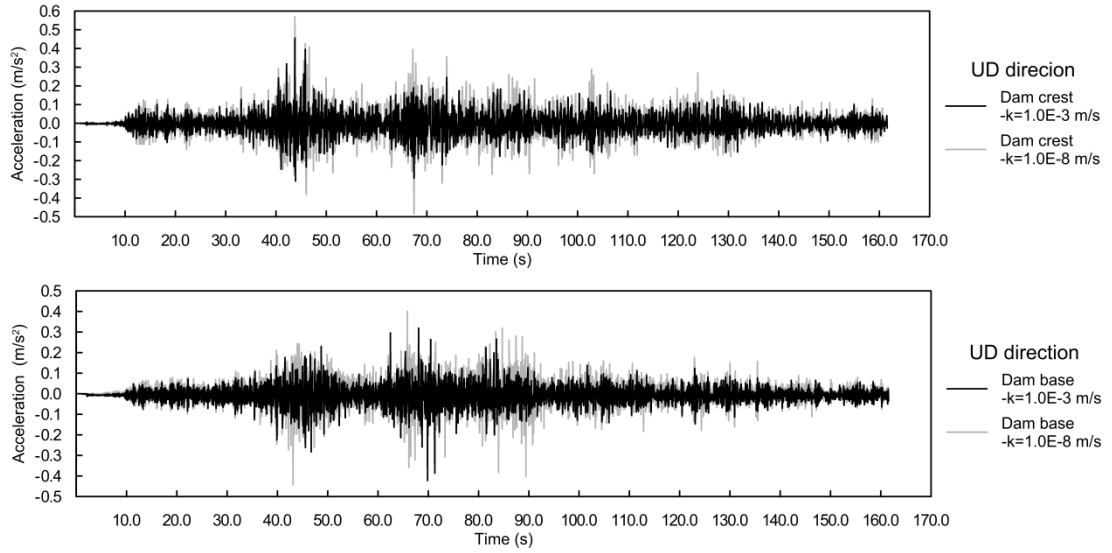


(b): Vertical-UD direction

Figure 6-8: Dynamic response of the Yele dam from the parametric study 2 (acceleration response spectra)



(a): Horizontal-EW direction



(b): Vertical-UD direction

Figure 6-9: Dynamic response of the Yele dam from the parametric study 2 (acceleration time histories)

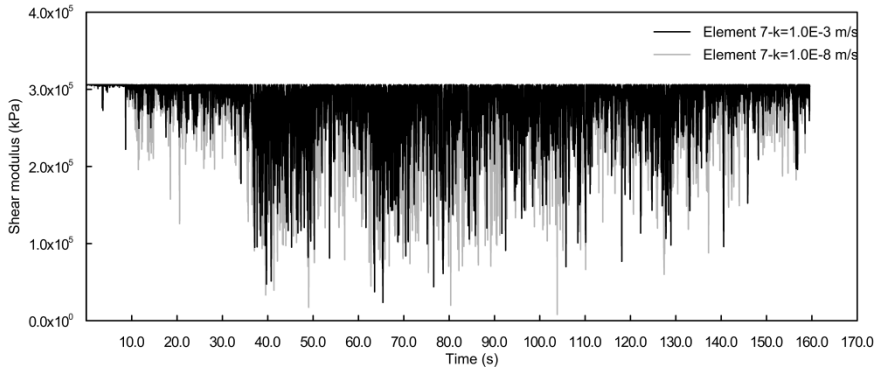
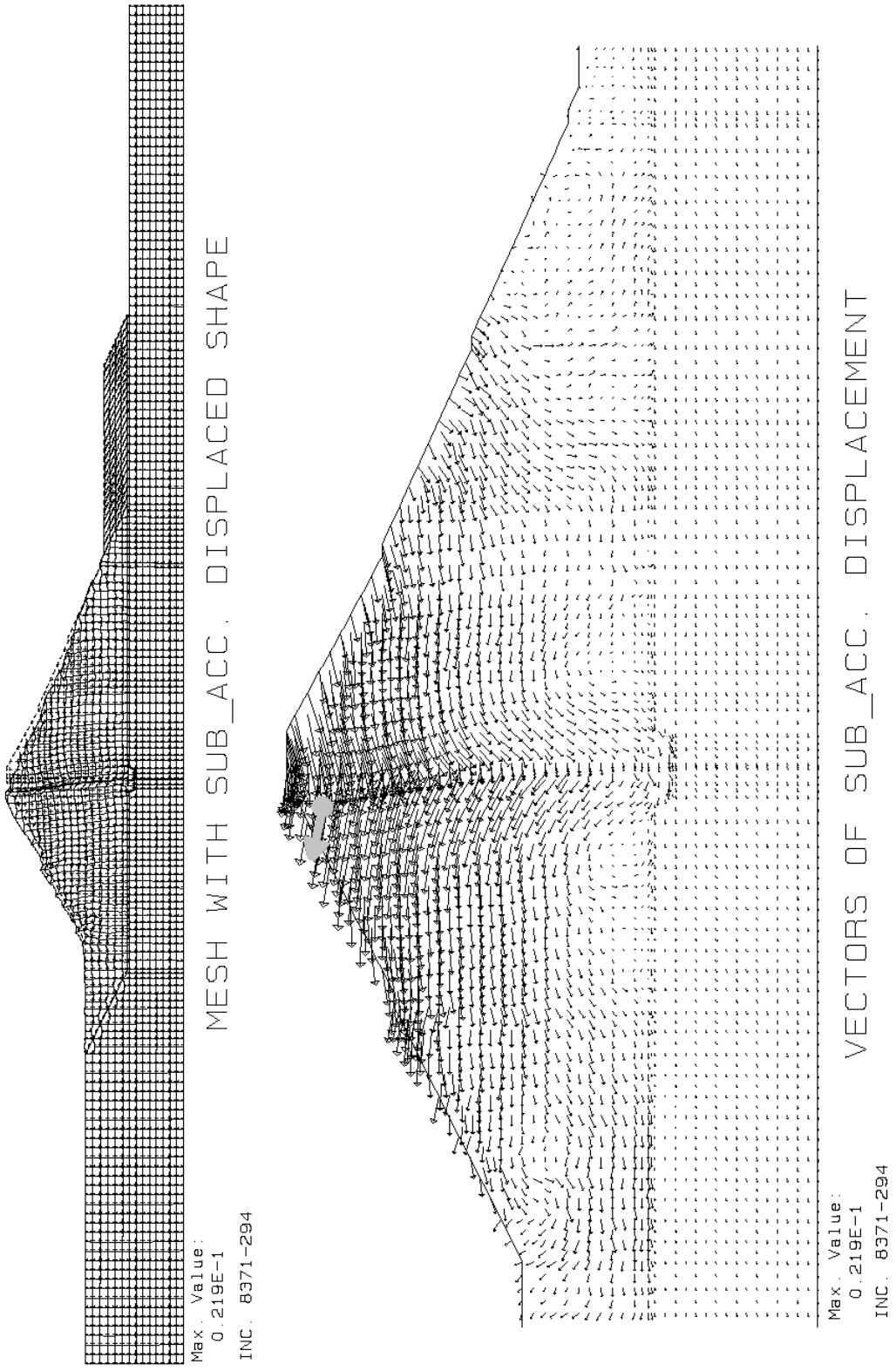
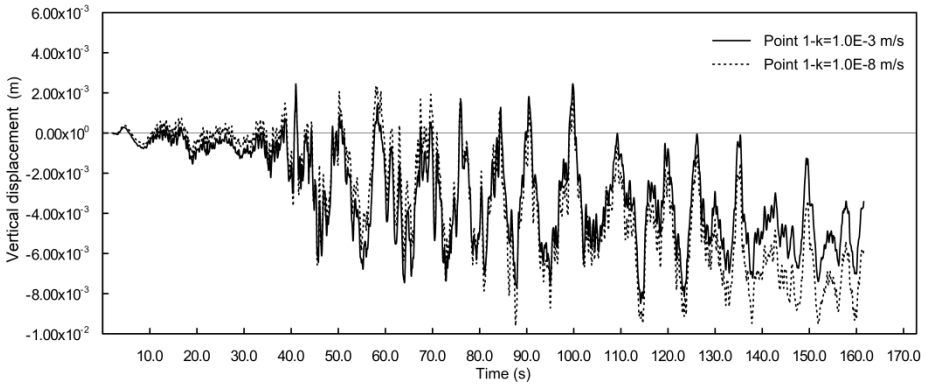


Figure 6-10: Tangent shear modulus time histories at element 7 on the Yele dam due to the Wenchuan earthquake from the parametric study 2

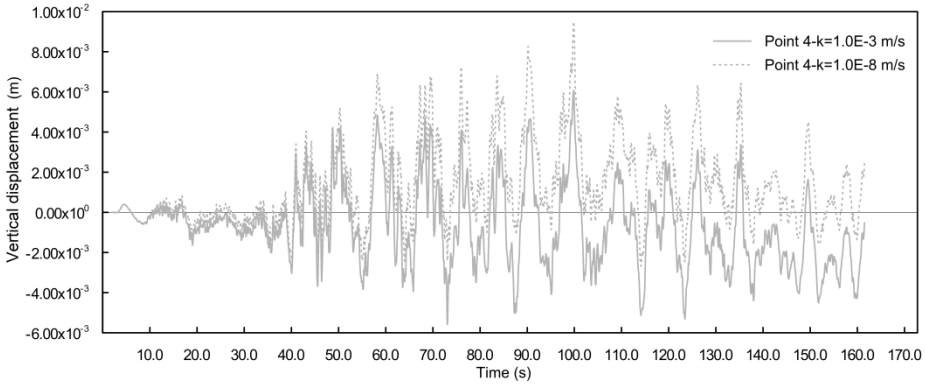


(a): Sub-accumulated deformed mesh (b): Vectors of sub-accumulated displacement (zoomed-in)

Figure 6-11: Sub-accumulated deformed mesh and vectors of sub-accumulated displacement on the Yele dam due to the Wenchuan earthquake from the parametric study 2 (displacement scaling factor: 1:600)



(a): Point 1



(b): Point 4

Figure 6-12: Sub-accumulated crest vertical displacement time histories at two locations on the Yele dam due to the Wenchuan earthquake from the parametric study 2

6.4 Effect of vertical ground motion

In this section, the effects of vertical ground motion on the dynamic response of the Yele dam are investigated through the third parametric study. For this study, only the monitored horizontal bedrock motion is imposed on the Yele dam and the vertical displacements at the bottom boundary are restricted. All other aspects of the numerical model are the same as those employed for the reference case study.

The dynamic response at the dam crest and base is predicted by the analysis only considering horizontal ground motion and is shown in Figures 6-13 and 6-14, in terms of horizontal acceleration response spectra and acceleration time histories. Compared to the reference results, the horizontal dynamic response is not found to be significantly affected by considering only the horizontal ground motion. Only in the frequency range >6.0Hz, spectral accelerations are slightly smaller, also reflected by the smaller

transient acceleration values.

However, Figure 6-15 shows the comparison of sub-accumulated crest vertical displacement time histories at points 1 and 4 (see in Figure 5-50), from analyses employing 2-D and 1-D input motions. Based on the presented results, it can be seen that by ignoring the vertical ground motion, the vertical displacement amplitudes and the stabilised values are significantly underestimated. In particular, compared to the analysis employing only the horizontal input motion, much more significant vertical displacement amplitudes are observed by employing the 2-D input motion and the predicted residual settlement values are larger due to the induced more significant plastic deformation. The predicted residual settlements by employing the 1-D input motion are approximately half of the reference results. They are believed to be generated by the plasticity induced by shear deformations. Overall, this comparison highlights the importance of considering 2-D ground motion for a more accurate simulation and evaluation of the dynamic response of rockfill dams.

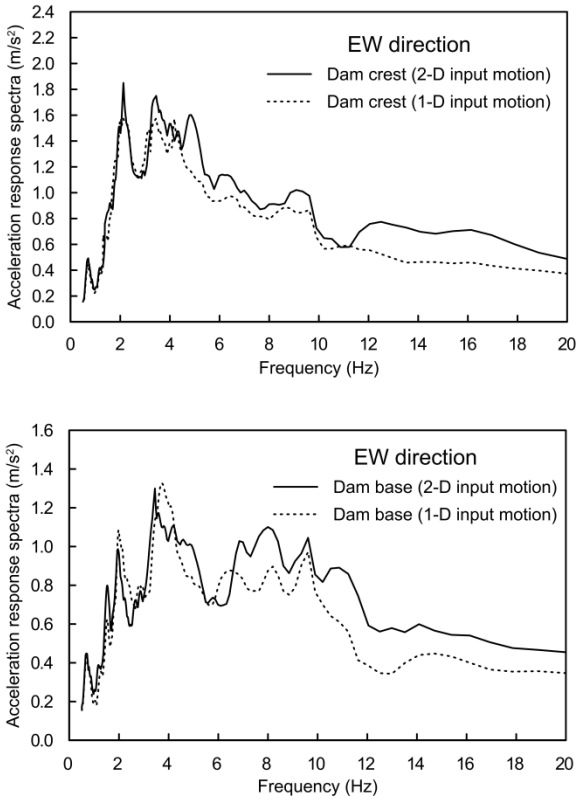


Figure 6-13: Dynamic response of the Yele dam from the parametric study 3 (acceleration response spectra)

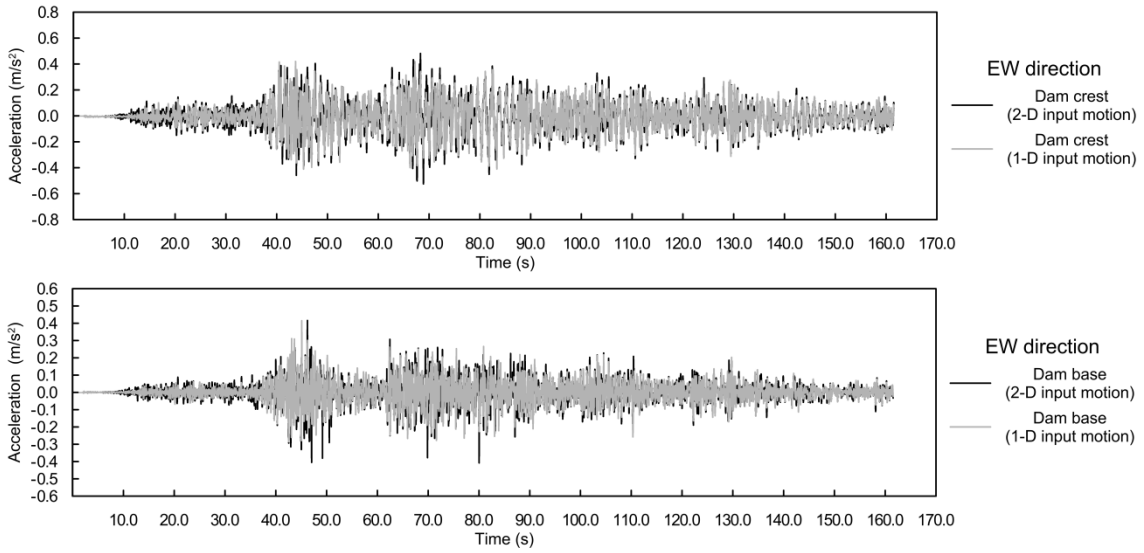
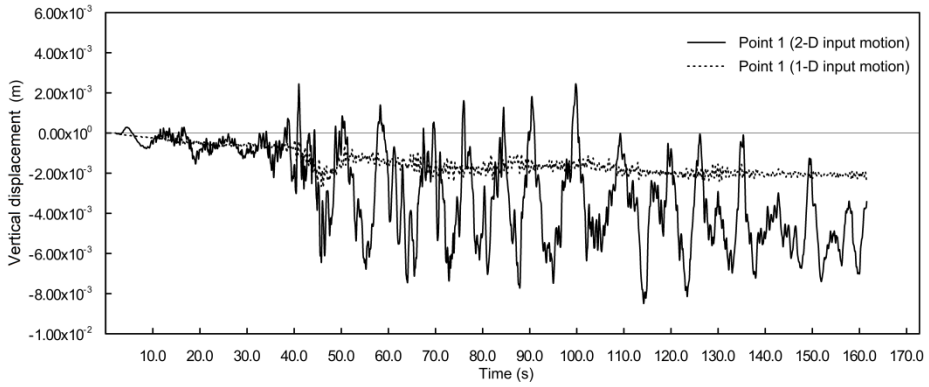
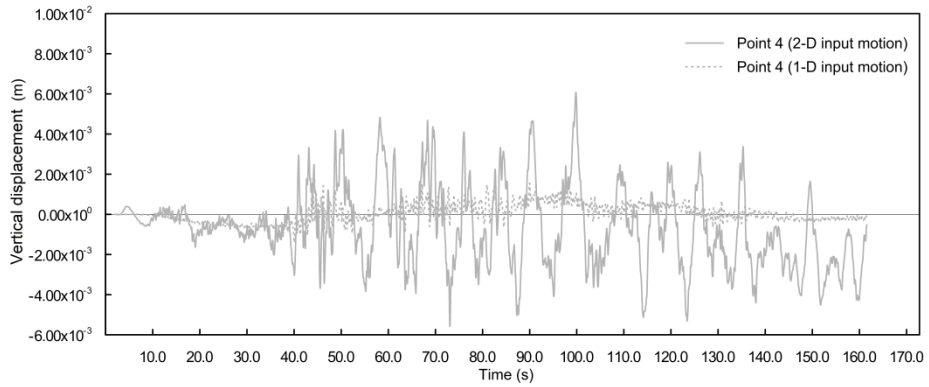


Figure 6-14: Dynamic response of the Yele dam from the parametric study 3 (acceleration time histories)



(a): Point 1



(b): Point 4

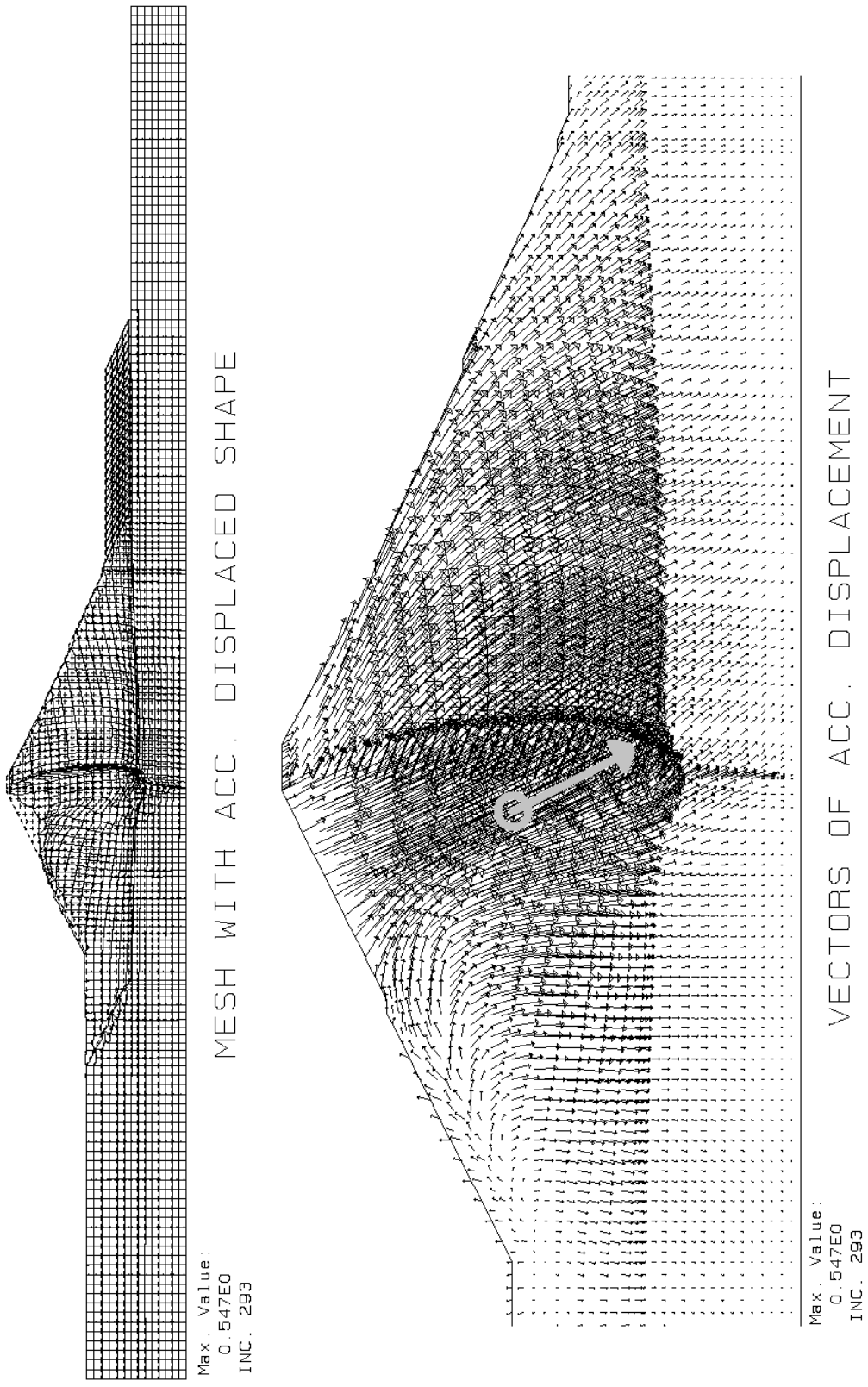
Figure 6-15: Sub-accumulated crest vertical displacement time histories at two locations on the Yele dam due to the Wenchuan earthquake from the parametric study 3

6.5 Effect of reservoir water level

Before the Wenchuan earthquake, the reservoir water level of the Yele dam decreased to the dead water level due to the insufficient rainfall in the dry season, which was 31.5m lower than the normal water level and 48.5m below the dam crest. Therefore, the seismically induced dam settlements can easier satisfy the freeboard allowance. However, this coincidence may not necessarily be a common situation for other rockfill dams subjected to earthquake events. In order to evaluate the seismic safety of rockfill dams under extreme impounding conditions, in this section, the effects of high reservoir water level on the dynamic response of the Yele dam are investigated through the fourth parametric study. A similar static FE analysis is conducted to reproduce the static state of the Yele dam before the Wenchuan earthquake, to the reference case study. The difference is that after the reservoir impounding stage, the reservoir de-impounding is not simulated in order to keep the reservoir level remain at a higher level of 107.0m.

The accumulated deformed mesh and vectors of accumulated displacement subjected to the high reservoir water level at the end of the static analysis are shown in Figure 6-16. The static deformation trend is found to be similar to the reference results, being downward and towards the downstream side due to the effect of the reservoir impounding. The maximum deformation occurs at the middle height of the rockfill zone and close to the core; the same location predicted by the reference study. The maximum displacement is 0.547m and its position and orientation are indicated by a grey vector Figure 6-16 (b). The maximum displacement is slightly smaller, which however only represents the local deformation. The overall dam deformation is larger than the reference results shown in Figure 5-41.

The seepage condition of the Yele dam before the Wenchuan earthquake is simulated by the static FE analysis subjected to the high water level and is shown in Figure 6-17, in terms of the pore water pressure contours. It can be seen that the pore water pressure distribution is reasonably simulated subjected to the high water level.



(a): Accumulated deformed mesh (b): Vectors of accumulated displacement (zoomed-in)

Figure 6-16: Accumulated deformed mesh and vectors of accumulated displacement on the Yele dam subjected to high reservoir water level before the Wenchuan earthquake (displacement scaling factor: 1:50)

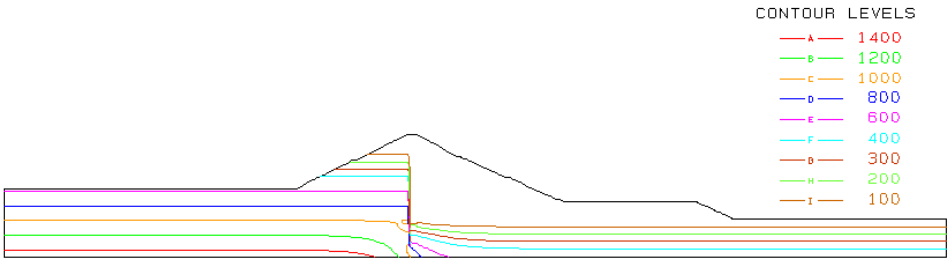


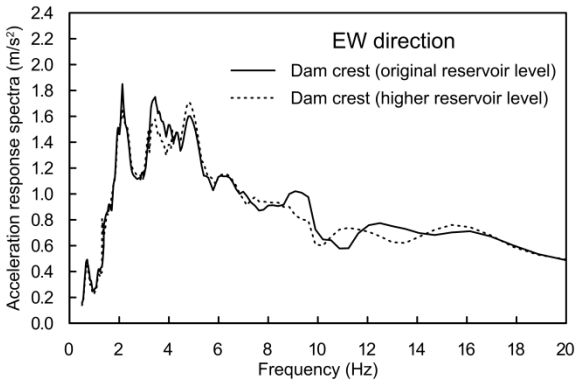
Figure 6-17: Contour lines of pore water pressure on the Yele dam subjected to high reservoir water level at the end of the static analysis (Compression positive: kPa)

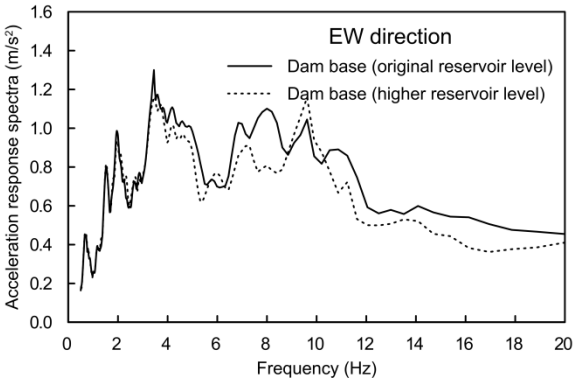
Following the static analysis considering the high reservoir level, a dynamic FE analysis is conducted, where the different aspects of the numerical model are the same as those employed in the reference case study. The predicted dynamic response at the dam crest and base subjected to the Wenchuan earthquake is firstly compared to the reference results in Figures 6-18 and 6-19, in terms of response spectra and acceleration time histories respectively. It can be seen that the two-directional dynamic response is very similarly predicted by the analyses considering two reservoir levels, both in terms of spectral and transient acceleration values. However, it is found that in the frequency range between 4.0Hz and 7.0Hz, the vertical dynamic response is slightly larger for the analysis considering the high water level.

The sub-accumulated deformed mesh and vectors of sub-accumulated displacement subjected to the high reservoir water level at the end of the Wenchuan earthquake are shown in Figure 6-20. Compared to the reference results in Figure 5-47, the seismic deformation on the Yele dam is found to be larger, where the dam body moves more significantly downward and towards the upstream side. The maximum displacement occurs at the crest, which is 0.0313m, indicated by the grey arrow in Figure 6-20 (b). This location is different to that predicted by the reference study, where the previous one occurred at the middle height of the upstream slope surface. This is due to the fact that, when subjected to the high reservoir level, the upward displacements on the upstream slope surface are constrained by the imposed boundary stresses due to the high reservoir level.

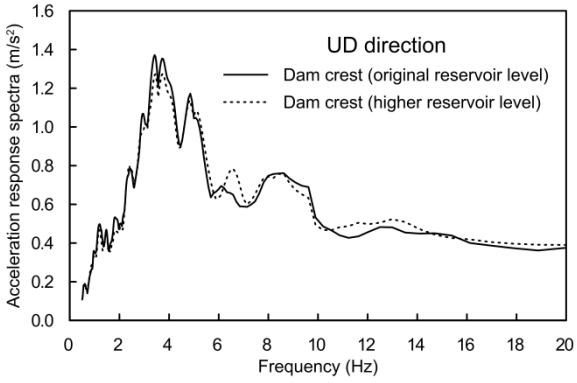
Figure 6-21 shows the comparison of sub-accumulated crest vertical displacement time histories due to the Wenchuan earthquake at points 1 and 4 (see Figure 5-50), for the analyses considering two different water levels. More significant differences are observed for the comparison of the crest settlement than for the comparison of the

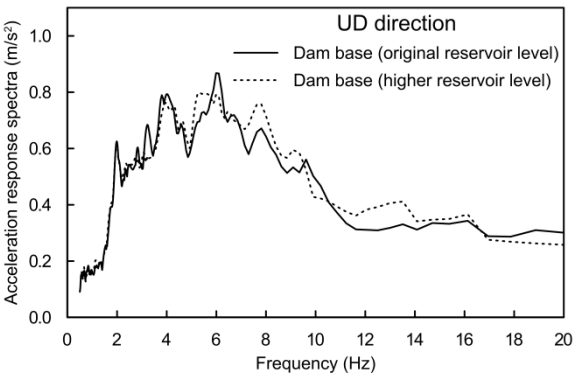
vertical spectral response (Figure 6-18 (b)). This observation is reasonable, since displacements are the second-order integration of accelerations. The predicted final crest settlements at the upstream and downstream side are 10mm and 8mm respectively, compared to the reference results of 1mm and 4mm. However, the induced crest settlements are still smaller than the free board allowance, which ensures the safe-operation of the Yele dam even subjected to the high reservoir level.





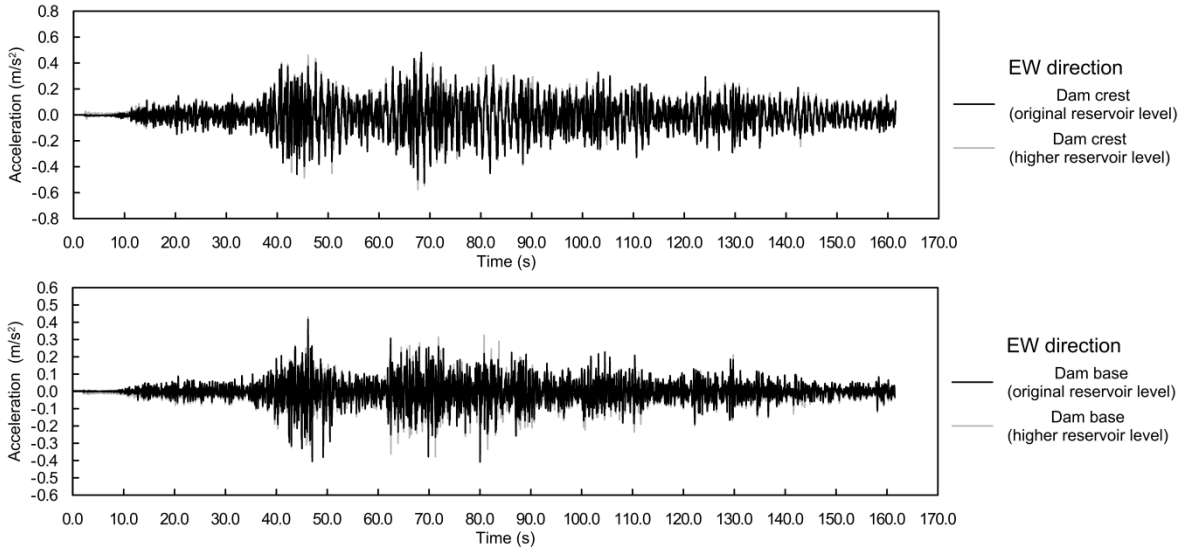
(a): Horizontal-EW direction



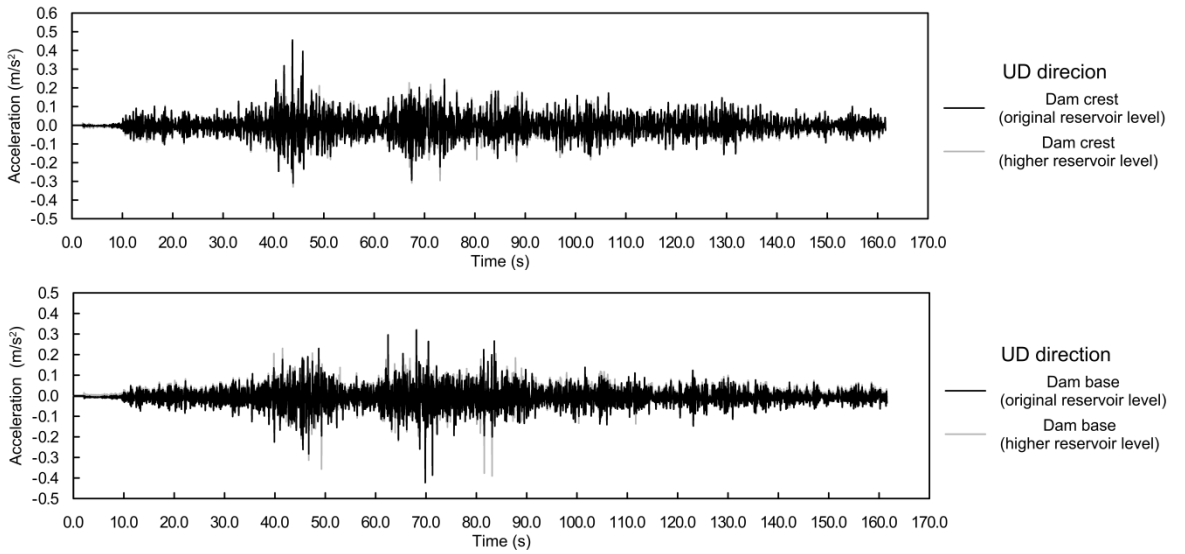


(b): Vertical-UD direction

Figure 6-18: Dynamic response of the Yele dam from the parametric study 4 (acceleration response spectra)

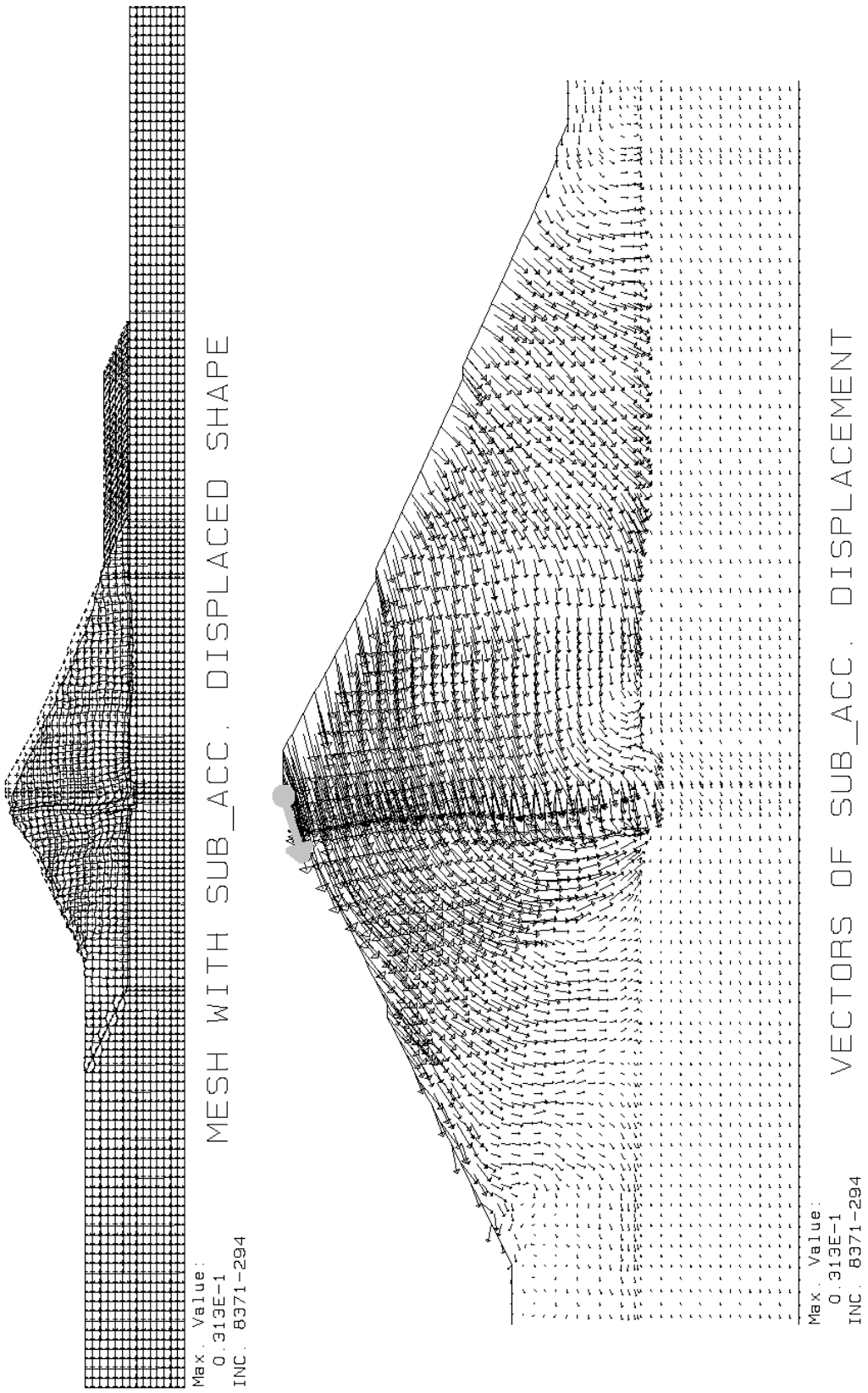


(a): Horizontal-EW direction



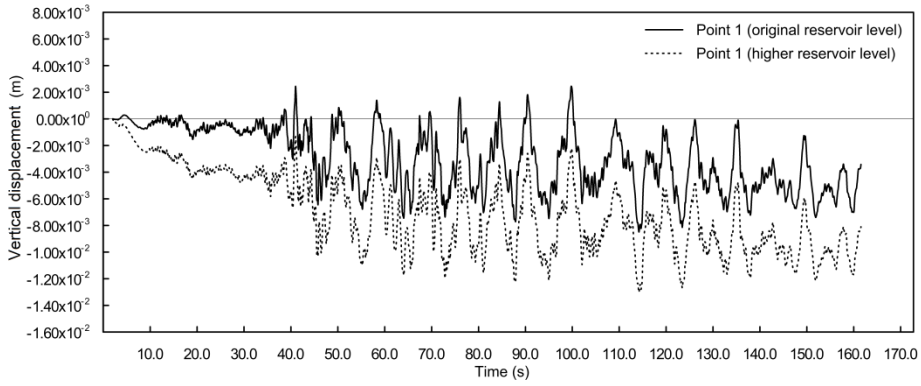
(b): Vertical-UD direction

Figure 6-19: Dynamic response of the Yele dam from the parametric study 4 (acceleration time histories)

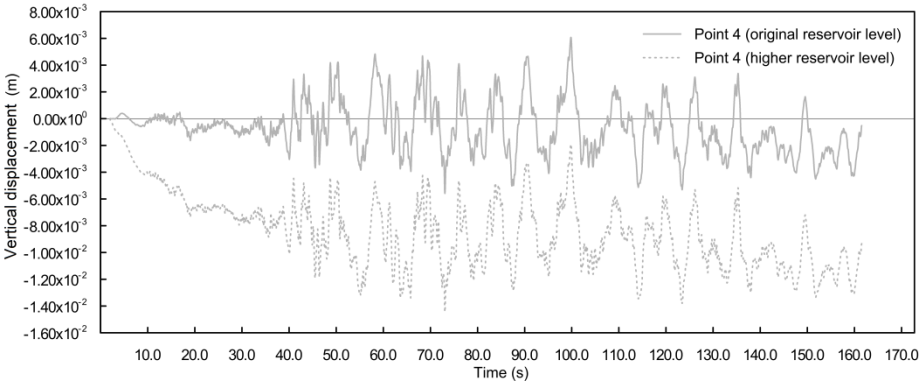


(a): Sub-accumulated deformed mesh (b): Vectors of sub-accumulated displacement (zoomed-in)

Figure 6-20: Sub-accumulated deformed mesh and vectors of sub-accumulated displacement on the Yele dam due to the Wenchuan earthquake from the parametric study 4 (displacement scaling factor: 1:600)



(a): Point 1



(b): Point 4

Figure 6-21: Sub-accumulated crest vertical displacement time histories at two locations on the Yele dam due to the Wenchuan earthquake from the parametric study 4

6.6 Summary

In this chapter, the effects of four critical factors on the seismic response of the Yele dam were investigated through parametric studies, i.e. the reservoir simulation method, permeability of materials comprising the dam body, vertical ground motion and reservoir water level.

The first parametric study examined the effects of the reservoir simulation on the dynamic response of the Yele dam. A corresponding static analysis was conducted to simulate the static state, employing solid elements for the reservoir modelling, following only a simplified impounding sequence. The predicted static behaviour showed smaller dam deformations due to the partial impounding simulation. However, the dynamic analysis suggested that the effects of the reservoir simulation method and

impounding sequence are insignificant on the overall seismic response of the Yele dam under the original water level. The parametric analysis predicted similar deformed shape and acceleration response at the dam crest, compared to the reference results.

The second parametric study indicated that the two-directional acceleration response of the Yele dam was strongly affected by the permeability of the materials comprising the dam body. In particular, by employing lower permeability for dam materials (1.0E-8 m/s), larger vertical dynamic response was induced due to less significant viscous damping effects. This in turn resulted in slightly larger horizontal dynamic response due to the coupling of the response in the two directions. Furthermore, the consideration of low permeability values resulted in more significant downward settlements and upward movement respectively at the downstream and upstream crest locations, compared to the reference results employing the high permeability values for the dam materials (1.0E-3 m/s).

The third parametric study investigated the influence of the vertical ground motion on the dynamic response of the Yele dam. The results indicated that by ignoring the vertical ground motion, the crest settlements were significantly underestimated, which highlighted the importance of employing 2-D input motion for a more accurate simulation and evaluation of the dynamic response of rockfill dams.

The fourth parametric study explored the influence of the reservoir water level on the seismic response of the Yele dam. The results showed that, although the acceleration response at the dam crest was very similarly predicted by the analyses considering two different water levels, the crest settlement was highly affected by this factor. In particular, the predicted final crest settlements at the upstream and downstream sides were 10mm and 8mm respectively, compared to the reference results of 1mm and 4mm. However, the induced crest settlements are still smaller than the free board limit, which ensures the safe-operation of the Yele dam even for higher reservoir level.

CHAPTER 7
Conclusions and recommendations

7.1 Introduction

The aim of this research was to investigate the seismic behaviour of geotechnical structures under multi-directional loading, by employing the coupled hydro-mechanical (HM) finite element (FE) method of analysis. For this purpose, four parts of work were conducted and presented in five chapters.

In order to achieve stable solutions for dynamic coupled consolidation analyses, Chapter 2 investigates the stability of the generalised-α method (CH method) for the coupled consolidation formulation following an analytical procedure. The derived stability conditions were validated by FE analyses considering a range of loading conditions and soil permeability values.

Chapter 3 explores the site response due to the vertical component of the ground motion. The vertical site response was first simulated by employing a one-phase total-stress analytical solution in frequency domain. The compressional wave propagation mechanism in saturated porous soils was further investigated by the coupled consolidation formulation accounting for the HM coupling. Finally, the coupled FE analyses explored the effects of the parameters characterising the hydraulic phase, i.e. soil permeability and soil state conditions, on the vertical site response.

Chapter 4 investigates the site response of the HINO site subjected to multi-directional ground motions employing the coupled HM formulation. This chapter presents the linear and nonlinear FE site response simulations for the HINO site subjected to two weak and one strong earthquake motions. The numerical predictions were compared against the recorded data to validate the applied numerical model in terms of the constitutive model, the use of 3-D input motion and the coupled consolidation formulation. Further parametric studies investigated the impact of the variation of the water table, the soil permeability and the 3-D input motion on the multi-directional site response.

The final objective of this thesis was to employ the developed numerical model to investigate a more complicated boundary value problem. Hence, Chapters 5 and 6 investigate the seismic response of a well-documented rockfill dam, the Yele dam, employing dynamic plane-strain FE analysis which accounts for HM coupling and nonlinear soil response. Chapter 5 presents the FE predictions for the static and dynamic behaviour of the Yele dam, under dam construction, reservoir impounding, dam operation and seismic loading conditions. Numerical predictions were compared against the static and dynamic recordings, in terms of dam settlements and acceleration time histories respectively. This allowed for a rigorous validation of the developed numerical model. Subsequently, the simulated seismic behaviour of the Yele dam was analysed and the dynamic safety was evaluated. Furthermore, Chapter 6 presents a series of parametric studies for the Yele dam. This chapter explores the effects of several critical factors on the seismic response of rockfill dams, i.e. the reservoir simulation, the permeability of materials comprising the dam body, the vertical ground motion and the reservoir water level. The influence of these factors was interpreted in terms of the dam deformed shape, acceleration time histories and settlements.

This chapter summarises the findings of the work presented in previous chapters and describes the recommendations for related future work.

7.2 Conclusions

7.2.1 The stability investigation of the CH time integration method in HM coupled formulation

In Chapter 2, the stability of the CH method for the HM coupled formulation was examined following an analytical procedure of employing the Routh-Hurwitz conditions and the unconditional stability conditions were derived. It was shown that the proposed stability conditions can simplify to the stability conditions of the CH method for the one-phase formulation (i.e. without hydraulic coupling). Furthermore, by degrading the CH method to the Newmark method, the stability conditions were in agreement with those proposed in previous stability investigations for the Newmark method based on coupled formulation. Since the CH method is a generalisation of the Newmark, HHT and WBZ methods, the proposed stability conditions are relevant for most of the commonly used time integration methods for the two-phase coupled formulation.

The analytically derived stability conditions were explored with FE analyses considering a range of loading conditions, model geometries and constitutive models. Firstly, analyses considering a 1-D linear elastic soil column subjected to a step and harmonic loads were carried out showing a good agreement between the derived stability condition and the back-calculated one with the aid of numerical analysis. This set of analyses also showed that the stability of the solution depended on the adopted soil permeability value, with the instability being more pronounced for the high permeability soil column. The next set of analyses considered the impact of numerical damping on the predicted response of a soil column subjected to impulse loading. The parametric variation of the numerical damping showed that the predicted response was significantly affected in terms of acceleration, displacement and pore water pressure. In particular, oscillations in terms of the acceleration, displacement and pore water pressure were more significantly damped as larger numerical damping was employed, but without affecting the response and finally approaching the same steady state. Finally, the stability characteristics of the CH method were investigated more stringently with an elastic and elasto-plastic analysis of a foundation subjected to dynamic loading. Satisfactory agreement was observed between the FE analysis results and the theoretical stability conditions for the linear elastic analysis. Furthermore, the investigated stability conditions with an advanced elasto-plastic constitutive model were also in agreement

with the theoretical conditions, indicating that the proposed stability conditions may be also applicable to more complicated nonlinear problems.

7.2.2 Analytical and numerical investigation of site response due to vertical ground motion

In Chapter 3, the site response due to the vertical component of the ground motion was investigated by employing analytical and numerical methods.

Firstly, a 1-D total-stress analytical solution for vertical site response was studied and compared against time domain FE analyses, for two extreme soil state conditions. It was shown that the vertical site response was significantly affected by the assumed conditions (i.e. undrained or drained), highlighting the importance of adopting a coupled consolidation formulation for simulating the vertical site response of a soil layer at any intermediate transient state (i.e. when consolidation occurs during the dynamic loading, depending on the range of soil permeability and loading duration).

Furthermore, a two-phase analytical solution for the compressional wave propagation was studied based on Biot's theory (1956a, b), showing the existence of two types of compressional waves (fast and slow waves) and indicating that their characteristics (i.e. wave dispersion and attenuation) were highly dependent on soil and dynamic parameters (i.e. the permeability, soil stiffness and loading frequency). The compressional wave propagation mechanism was then rigorously investigated by coupled FE analysis, highlighting the different dominant ranges of the two types of compressional waves in terms of soil permeability. Finally, based on the FE parametric study, the geotechnical representation of two types of compressional waves was related with different soil state conditions.

The vertical site response was further investigated with fully coupled FE analysis, considering solid-fluid interaction. The parametric studies showed that the predicted response was strongly affected by the parameters characterising the hydraulic phase, i.e. soil permeability and soil state conditions, both in terms of frequency content and amplification. In particular, a reduction of the soil constrained modulus was induced by employing higher permeability, which was depicted as a shift in the fundamental frequency of the response. Furthermore, the observed changes in the amplification function indicated the effect of viscous damping due to the interaction between the solid

and the pore fluid phases. Moreover, the quantitative investigation of the frequency content and the amplification function of the vertical site response, showed that the response was dominated by the different wave velocity and damping characteristics of two types of compressional waves affected by soil hydraulic-phase parameters. It is therefore suggested that coupled consolidation analysis is necessary to accurately simulate vertical site response at any intermediate transient state, when consolidation occurs during the dynamic loading (depending on soil permeability and loading duration).

The work presented in this chapter can also be a useful reference for simple site response analysis in the vertical direction. It was shown that the methodology adopted by the widely used program SHAKE and its modern variations can be employed for the vertical site response analysis in terms of total stresses, but only for two extreme conditions (i.e. undrained and drained conditions). If the SHAKE approach is employed for the vertical site response analysis of a soil layer at any intermediate transient state, it is suggested that appropriate amount of viscous damping needs to be employed in the analysis, additional to any considered material damping, to take into account the interaction effects between the solid and pore fluid phases. The appropriate viscous damping ratios can be decided based on the empirical curves of the investigated viscous damping ratio proposed in Section 3.5.3.

7.2.3 Numerical investigation of multi-directional site response based on KiK-net data

In Chapter 4, the multi-directional site response of the HINO site was investigated by employing the 3-D dynamic HM formulation in ICFEP. The computed results were compared with the monitored data from the KiK-net down-hole array system. The 3-D site response of the HINO site, subjected to two weak earthquake motions and the 2000 Western Tottori earthquake, was simulated by linear and nonlinear FE analyses. Different features of the numerical modelling for site response analysis, such as the constitutive models, the use of 3-D input motion and the coupled consolidation formulation, were investigated through the conducted FE simulations and parametric studies.

Firstly, the site response of the HINO site subjected to two weak motions was

simulated by linear FE analysis and the analytical solution employed by the software SHAKE. The results showed that the multi-directional site response was reasonably well simulated by both methods, when compared with the monitored response. However, the predicted site response was found to be very sensitive to the employed Rayleigh damping ratio and its associated parameters. A further investigation suggested that, in order to achieve accurate simulations for site response in all three directions, the Rayleigh damping parameters ω_1 and ω_2 should be taken as the first horizontal and vertical fundamental frequencies of the studied soil profile. Furthermore the numerical investigation revealed that the Rayleigh damping formulation is not fully compatible with the coupled consolidation formulation and this can result in the over-prediction of the vertical site response.

In order to accurately reproduce soil material damping under earthquake loading, cyclic nonlinear models were employed for the FE site response analysis of the HINO site subjected to weak earthquake motions. Three cyclic nonlinear models were utilised, which are the Logarithmic, ICG3S-1 and ICG3S-2 models. These three models distinguish by their abilities of accurately simulating material damping at very small strain levels and realistically simulating the independent shear and volumetric deformations. Numerical results showed that, in order to accurately predict the multi-directional site response, the model of the ICG3S-2 type should be used for the nonlinear FE analysis. Firstly, the ICG3S-2 model can simulate more accurately the material damping at very small strain levels. Furthermore, by employing the ICG3S-2 model, both the horizontal and the vertical site response can be accurately predicted by independently controlling the degradation of the shear and the constrained modulus.

In addition, the 3-D site response of the HINO site subjected to the 2000 Western Tottori earthquake was simulated employing the same three cyclic nonlinear models. Once more, the ICG3S-2 model showed superior performance in terms of more realistic simulation of material damping at very small strain levels and independent simulation of stiffness degradation and material damping related to the shear and compressional deformations. By employing the ICG3S-2 model, a reasonably good agreement was observed between the numerical results and the monitored site response, both in terms of acceleration time histories and response amplification spectra in the three directions. Furthermore, soil nonlinearity was observed for all three directions, but this was more significant in the soil layer above the water table due to the smaller soil constrained

modulus. The site response analysis predicted different deformation levels in the horizontal and vertical directions; the deformations were found to be in the large strain range (i.e. >0.01%-0.1%) and in the very small strain range (<0.001%) respectively as defined by Vucetic (1994). This highlighted the importance of independent optimum calibrations for the material damping related to the shear and compressional deformations at the respective relevant strain levels.

In the last part, the effects of three critical factors on the site response, i.e. the variation of water table, the soil permeability and the 3-D ground motions, were investigated through parametric studies for the selected site, where the following conclusions were reached:

– Firstly, results from linear site response analyses considering two water table locations (GL. 0.0m and GL. -10.4m) showed a significant effect of the water table depth on the vertical site response, both in terms of frequency content and amplification, while no influence was identified on the horizontal site response. This effect originates from the change of the soil constrained modulus when the water table level was varied.

– Secondly, the nonlinear site response analysis highlighted the effect of water table location on both the horizontal and vertical site response. Results showed a low-frequency shift for the fundamental frequency and smaller amplification factors for the vertical site response with lower water table. The fundamental frequency shift was attributed to the smaller constrained modulus in the soil layers above the water table and the more significant constrained modulus degradation in these layers. The smaller amplification factors were due to the larger induced material damping compared to that of the analysis involving the higher water table. Simultaneously, larger vertical strains induced larger deviatoric strains and eventually more significant shear modulus degradation. It was observed that the lower water table significantly increased the horizontal site response due to the induced large shear deformation and the stabilised material damping in the large strain range.

– Subsequently, a fully drained site response analysis was conducted, which ignored the pore fluid phase and therefore induced smaller soil constrained modulus. It was observed that larger shear and compressional deformations were induced, which resulted in more significant shear and constrained modulus degradation at all depths

than the corresponding coupled analysis. This finally led in larger site response in both horizontal and vertical directions in the large strain range.

– The effect of the water table location on the soil stiffness profile was considered for the site response analysis with the water table at the ground surface. The soil stiffness profile was adjusted by employing the empirical equation for the maximum shear modulus from Hardin and Black (1968), which accounts for the effect of effective stresses associated with the water table location. This consideration predicted larger site response compared to that employing the original soil stiffness profile, which was, however, still smaller than the one with the water table at GL. -10.4, indicating a significant influence of the water table location on site response.

– Furthermore, based on the parametric study for the soil permeability, both the horizontal and the vertical site response was found to be affected only when considerably high permeability values were assumed for the soil materials (i.e. ≥1.0E-3 m/s). Smaller vertical site response was predicted due to the introduced viscous damping generated by the solid-pore water interaction effects. The smaller vertical dynamic response resulted in smaller vertical and deviatoric strains and therefore less significant degradation for the soil constrained and shear moduli. This essentially caused slightly smaller shear deformation and horizontal site response in the large strain range.

– Finally, the analysis considering 2-D ground motions (i.e. the EW and UD directions) did not generate significant influence on the site response in the EW horizontal direction. However, in the intermediate frequency range (approximately at 4.2Hz), the amplification factors for the vertical response were underestimated by the 2-D analysis. This highlighted the role of the 3-D analysis, which can trigger additional deformations due to the interaction of the third component with other two directions. Therefore, a full 3-D analysis is suggested for more accurate predictions and comprehensive understanding for multi-directional site response analysis.

7.2.4 Static and dynamic FE analyses of the Yele dam

In Chapter 5, the seismic response of a well-documented Chinese rockfill dam, the Yele dam, was investigated by employing dynamic HM coupled FE analysis. Through the conducted numerical investigation, different aspects of the numerical modelling for

static and dynamic analyses of rockfill dams were validated against the available monitoring data of the Yele dam during the 2008 Wenchuan earthquake. The seismic safety of the Yele dam was assessed by analysing its dynamic behaviour predicted by FE analyses.

The numerical model of the Yele dam for the static and the dynamic analyses was firstly established, in terms of the element size, boundary location and constitutive model calibration. It was found that the vertical wave propagation was sensitive to the element dimension in the vertical direction, which needed to be parametrically defined. The cone boundary conditions were employed at the lateral boundaries of the FE mesh for the dynamic analysis. The location of the lateral boundary required further assessment to ensure that free-field response is retained near the lateral sides of the model.

By adopting the appropriate numerical model, such as the simulation sequence, displacement and hydraulic boundary conditions and constitutive model, the static behaviour of the Yele dam under the construction, impounding and operation loading conditions was simulated. Numerical predictions were firstly compared against the static monitored data, showing satisfactory agreement in terms of the horizontal displacement variation of the core section and the settlements at different locations in the dam. It was also found that in order to accurately predict dam deformations, the actual reservoir simulation should be considered. Furthermore, the accumulated deformed mesh and vectors of accumulated displacement at the end of the static analysis showed that the overall dam deformations were not significant and were well within the limit for its safe operation under static loading conditions. Finally, the seepage pattern at different stages was reasonably predicted by the static analysis, which is helpful to better understand the static behaviour of the Yele dam.

By employing the simulated static state as the initial stress profile for the dynamic analysis, the seismic response of the Yele dam was then analysed. A good agreement was observed between the numerical results and the dynamic monitored response at two points at the dam crest and base, in terms of acceleration response spectra and time histories. Further evaluations of the seismic deformation on the Yele dam were achieved:

- The sub-accumulated deformed mesh and vectors of sub-accumulated displacement due to the earthquake loading showed a safe-operation status for the Yele dam during and after the Wenchuan earthquake. It was found that the final seismic deformation in the downstream part was downward and towards the upstream side, whereas the seismic deformation in the upstream part was less significantly downward and also towards the upstream side. Sub-accumulated shear and vertical strain levels showed that the dynamic deformation was concentrated in the upstream slope surface zone and the transition layer, due to more significant amplification effects and lower material stiffness respectively.
- The predicted sub-accumulated crest settlement time histories due to the Wenchuan earthquake further proved the safe-operation status of the Yele dam and showed a more significant downward crest settlement at the downstream side than that at the upstream side.
- The variation of the peak acceleration on the dam surface showed that, from the dam base to the dam crest, the peak acceleration decreased and increased. This trend was in agreement with field observations at the Yele dam after a previous earthquake on 23th October, 2007. Furthermore, the results also indicated that the peak accelerations on the downstream slope were mainly downward and towards the upstream side, whereas those on the upstream slope were mostly upward and also towards the upstream side. This is in agreement with previous observations from the sub-accumulated deformed mesh.
- The seismic safety of the Yele dam was assessed by employing the seismic design method for embankment dams proposed by Papadimitriou et al. (2014) and Andrianopoulos et al. (2014). The estimated peak seismic coefficient k_{hmax} values for potential sliding slopes within the dam were found to be much smaller than the limit value of the critical seismic coefficient k_y calculated by the limit equilibrium method. This indicated that the Wenchuan earthquake loading is unlikely to induce significant slope instability or large deformation in the Yele dam, which ensures its safety operation. This is also in agreement with the findings from the numerical predictions.
- The seismic response of the dam was further investigated by analysing the simulated dynamic soil behaviour. The stress-strain response at four monitoring elements within the dam indicated more significant dynamic deformations in the upstream dam body, than those predicted in the downstream part and the foundation section.

– Finally, accumulation of excess pore water pressure was observed in the upstream rockfill, due to an asymmetric vertical movement despite the lack of volumetric plasticity in the soil response. However, this influence was only concentrated in the areas where the dam geometry is complicated. Beyond the dam heel and toe, such influence was insignificant. The magnitude of the accumulated excess pore water pressure was relatively small compared to the total pore water pressure values. The final pore water pressure distribution was not significantly affected by the seismic loading compared to the one established before the Wenchuan earthquake.

7.2.5 Parametric studies of the Yele dam

In Chapter 6, the effects of four critical factors on the seismic response of the Yele dam were investigated through parametric studies, i.e. the reservoir simulation method, permeability of materials comprising the dam body, vertical ground motion and reservoir water level.

The first parametric study examined the effects of the reservoir simulation on the dynamic response of the Yele dam. A corresponding static analysis was conducted to simulate the static state, employing solid elements for the reservoir modelling, following only a simplified impounding sequence. The predicted static behaviour showed smaller dam deformations due to the partial impounding simulation. However, the dynamic analysis suggested that the effects of the reservoir simulation method and impounding sequence are insignificant on the overall seismic response of the Yele dam under the original water level. The parametric analysis predicted similar deformed shape and acceleration response at the dam crest, compared to the reference results.

The second parametric study indicated that the two-directional acceleration response of the Yele dam was strongly affected by the permeability of the materials comprising the dam body. In particular, by employing lower permeability for dam materials (1.0E-8 m/s), larger vertical dynamic response was induced due to less significant viscous damping effects. This in turn resulted in slightly larger horizontal dynamic response due to the coupling of the response in the two directions. Furthermore, the consideration of low permeability values resulted in more significant downward settlements and upward movement respectively at the downstream and upstream crest locations, compared to the reference results employing the high permeability values for

the dam materials (1.0E-3 m/s).

The third parametric study investigated the influence of the vertical ground motion on the dynamic response of the Yele dam. The results indicated that by ignoring the vertical ground motion, the crest settlements were significantly underestimated, which highlighted the importance of employing 2-D input motion for a more accurate simulation and evaluation of the dynamic response of rockfill dams.

The fourth parametric study explored the influence of the reservoir water level on the seismic response of the Yele dam. The results showed that, although the acceleration response at the dam crest was very similarly predicted by the analyses considering two different water levels, the crest settlement was highly affected by this factor. In particular, the predicted final crest settlements at the upstream and downstream sides were 10mm and 8mm respectively, compared to the reference results of 1mm and 4mm. However, the induced crest settlements are still smaller than the free board limit, which ensures the safe-operation of the Yele dam even for higher reservoir level.

7.3 Recommendations for future work

Recommendations for related future work are proposed in this part, in order to extend and improve the current study. These are described in four sections, corresponding to the four parts of work conducted.

7.3.1 The stability investigation of the CH time integration method in HM coupled formulation

In Chapter 2, the stability conditions of the CH method were derived by employing the Routh-Hurwitz conditions. However, the stability investigation of adopting the Routh-Hurwitz conditions cannot guarantee the L-stability. A time integration method is said to be L-stable if it is A-stable and the numerical solution tends to be zero when the real part of $\lambda \Delta t$ approaches infinity, where λ is the eigenvalue of the amplification matrix and Δt is the time step (Wood, 1990). L-stability is critical for stiff systems of equations originating from FE discretisation and it can help FE analysis to dissipate the high-frequency spurious vibrations for stiff problems. For geotechnical earthquake engineering problems involving soil materials, soil stiffness is relatively low compared

to that of structure materials and therefore the A-stability is reasonably sufficient for dynamic FE analysis. However, considering the dynamic analysis of some stiff materials, such as rock and concrete, there is a need to investigate the L-stability conditions for the CH method under both the one-phase and two-phase coupled HM formulations.

7.3.2 Analytical and numerical investigation of site response due to vertical ground motion

In Chapter 3, the investigation of the compressional wave propagation mechanism in saturated porous soils demonstrated the existence of two types of compressional waves (fast and slow waves). However, for most numerical implementations or applications of dynamic boundary conditions, only one of these two types of waves is considered. For instance, the cone boundary conditions (Kellezi, 1998 & 2000) have been widely employed in numerical analysis to eliminate the wave reflection at truncated boundaries. This boundary condition applies equivalent stresses on the boundary to balance the stresses induced by the reflected waves. The applied stresses are dependent on the shear and compressional wave velocities in the tangential and normal directions respectively. However, for most applications of the viscous boundary conditions on dynamic coupled consolidation problems, only the wave velocity for the fast wave or the slow wave is considered for balancing the spurious stresses in the normal direction. This essentially indicates that the applied boundary conditions are only effective for absorbing the reflection of one type of compressional waves. It should be noted that some boundary conditions have been extended to incorporate the absorption of all three body waves propagating through saturated soils. An example can be attributed to Zerfa and Loret (2004) for a proposed viscous boundary condition for transient dynamic analysis. Therefore, it is suggested for future research to consider both the fast wave and slow wave propagation in the numerical applications of dynamic boundary conditions for geotechnical earthquake engineering problems.

7.3.3 Numerical investigation of multi-directional site response based on KiK-net data

In Chapter 4, the linear FE site response simulations of the HINO site revealed that the Rayleigh damping formulation is not fully compatible with the coupled consolidation formulation and can result in the over-prediction of the vertical site response. Therefore, there is a need to develop a compatible application of the Rayleigh damping formulation for coupled consolidation analysis.

As discussed in Chapter 4, an accurate 3-D site response simulation requires constitutive models to be calibrated based on the stiffness degradation and damping curves related to both the shear and compressional deformations. The shear modulus degradation and damping curves can be calibrated against the corresponding laboratory tests or empirical curves. However, there is currently very limited investigation on the soil nonlinear behaviour associated with compressional deformation. This leads to a lack of data for the calibration of nonlinear models which consider constrained modulus degradation and damping curves. Therefore, there is a need to investigate the vertical nonlinearity of soil materials and propose empirical curves for the soil constrained modulus degradation. This work is expected to be of importance for understanding the seismic ground response in the vertical direction and for providing reference calibration curves for nonlinear numerical analysis of geotechnical structures under multi-directional seismic loading.

7.3.4 Static, dynamic and parametric FE studies of the Yele dam

As discussed in Chapter 5, the 2008 Wenchuan earthquake caused varying-degree of damage in approximately 391 dams in Sichuan Province, China, including 4 large-scale rockfill dams (i.e. heights exceeding 100m). The damage was observed as crest settlement, concrete slab cracks, destruction of crest facilities and cracking and stripping in the overflow galleries. However, the earthquake did not induce catastrophic dam failures due to their long epicentral distance and eventually low-intensity motions at the dam sites. The seismic safety of these large-scale rockfill dams is of vital importance for millions of people in the downstream areas. Therefore, there is a need to investigate the dynamic response of rockfill dams under varying-intensity earthquake excitations, i.e. from low-intensity to high-intensity, in order to predict their potential failure

mechanisms and systematically evaluate their seismic resistance under different intensity earthquakes.

References

Aguirre, J. and Irikura, K. (1997). Nonlinearity, liquefaction, and velocity variation of soft soil layers in Port Island, Kobe, during the Hyogo-ken Nanbu earthquake. *Bulletin of the Seismological Society of America*, 87(5): 1244-1258.

Ambraseys, N. N. (1959). *The seismic stability of earth dams*. PhD thesis, Imperial College London.

Ambraseys, N. N. (1960). On the shear response of a two-dimensional truncated wedge subjected to arbitrary disturbance. *Bulletin of the Seismological Society of America*, 50(1): 45-46.

Ambraseys, N. N. and Menu, J. M. (1988). Earthquake-induced ground displacements. *Earthquake Engineering and Structural Dynamics*, 16(7): 985-1006.

Ambraseys, N. N. and Douglas, J. (2000). *Engineering seismology and earthquake engineering. reappraisal of the effect of vertical ground motions on response*. Imperial College London. ESEE Report No. 00-4.

Amorosi, A., Boldini, D. and Elia, G. (2010). Parametric study on seismic ground response by finite element modelling. *Computers and Geotechnics*, 37: 515-528.

Andrianopoulos, K. I., Papadimitriou, A. G., Bouckovalas, G. D. and Karamitros, D. K. (2014). Insight into the seismic response of earth dams with an emphasis on seismic coefficient estimation. *Computers and Geotechnics*, 55: 195-210.

Antoniou, S. and Pinho, R. (2004). *SeismoSignal: A computer program for signal processing of strong-motion data*. SeismoSoft: Technical Report 4.0.0.

Arntsen, B. and Carcione, J. M. (2001). Numerical simulation of the Biot slow wave in water-saturated Nivelsteiner Sandstone. *Geophysics*, 66(3): 890-896.

Assimaki, D. and Steidl, J. (2007). Inverse analysis of weak and strong motion downhole array data from the Mw7.0 Sanriku-Minami earthquake. *Soil Dynamics and Earthquake Engineering*, 27: 73-92.

Bardet, J. P., Ichii, K. and Lin, C. H. (2000). *EERA: A computer program for equivalent linear earthquake site response analysis of layered soils deposits*. University of Southern California, Los Angeles. Technical Report.

Bardet, J. P. and Sayed, H. (1993). Velocity and attenuation of compressional waves in nearly saturated soils. *Soil Dynamics and Earthquake Engineering*, 12(7): 391-401.

Bathe, K. J. (1996). *Finite element procedures in engineering analysis*. New Jersey: Prentice Hall.

Beresnev, I. A., Nightengale, A. M. and Silva, W. J. (2002). Properties of vertical ground motions. *Bulletin of the Seismological Society of America*, 92(8): 3152-3164.

Beresnev, I. A. and Wen, K. L. (1996). Nonlinear soil response-a reality? *Bulletin of the Seismological Society of America*, 86: 1964-1978.

Berryman, J. G. (1980). Confirmation of Biot' theory. *Applied Physics Letters*, 37(4): 382-384.

Biot, M. A. (1956a). Theory of propagation of elastic waves in a fluid saturated porous solid 1: Low-frequency range. *Journal of the Acoustical Society of America*, 28(2): 168-178.

Biot, M. A. (1956b). Theory of propagation of elastic waves in a fluid saturated porous solid 2: Higher-frequency range. *Journal of the Acoustical Society of America*, 28(2): 179-191.

Borja, R. I., Chao, H. Y., Montans, F. J. and Lin, C. H. (1999). Nonlinear ground response at Lotung LSST site. *Journal of Geotechnical and Geoenvironmental Engineering*, 125(3): 187-197.

Borja, R. I. and Wu, W. H. (1994). Vibration of foundations on incompressible soils with no elastic region. *Journal of Geotechnical and Geoenvironmental Engineering*, 120(9): 1570-1592.

Bowles, J. E. (1997). *Foundation analysis and design, 5th edition*. Peoria, Illinois: McGraw-Hill.

Boyle, F. A. and Chotiros, N. P. (1991). Experimental detection of a slow acoustic wave in sediment at shallow grazing angles. *Journal of Acoustical Society of America*, 91(5): 2615-2619.

Bozorgnia, Y. and Campbell, K. W. (2004). The vertical-to-horizontal response spectral

ratio and tentative procedures for developing simplified V/H and vertical design spectra. *Journal of Earthquake Engineering*, 8(2): 175-207.

Bradley, B. A. (2011). Near-source strong ground motions observed in the 22 February 2011 Christchurch earthquake. *Seismological Research Letters*, 82(6): 853-865.

Campbell, K. W. and Bozorgnia, Y. (2013). Updated near-source ground-motion (attenuation) relations for the horizontal and vertical components of peak ground acceleration and acceleration response spectra. *Bulletin of the Seismological Society of America*, 93(1): 314-331.

Cao, X., He, Y., Xiong, K. and Liu, B. (2010). The dynamic response of Yele dam under Wenchuan earthquake (in Chinese). *Rock and Soil Mechanics*, 31(11): 3542-3548.

Chan, A. H. C. (1988). *A unified finite element solution to static and dynamic problems of geomechanics*. PhD thesis, Swansea University.

Chan, A. H. C. (1995). *User Manual for DIANA-SWANDYNE II*. School of Engineering, University of Birmingham.

Chao, H. Y. and Borja, R. I. (1998). *Nonlinear dynamic soil-structure interaction analysis and application to Lotung problem*. JA Blume Earthquake Engineering Centre, Stanford University, Stanford, California. Technical Report.

China Earthquake Administration (2011). *Earthquake Intensity Zoning Map of China*.

Christopoulos, A. (2012). *Site response analysis for vertical ground motion.* MSc thesis, Imperial College London.

Chung, J. and Hulbert, G. M. (1993). A time integration algorithm for structural dynamics with improved numerical dissipation: the generalized-α method. *Journal of Applied Mechanics*, 60(2): 371-375.

Clough, R. W. and Chopra, A. K. (1966). Earthquake stress analysis in earth dams. *Journal of Engineering Mechanics, ASCE*, 92(EM2): 1399-1412.

Dahlquist, G. (1963). A special stability problem for linear multistep methods. *BIT*, 3: 27-43.

Dakoulas, P. and Gazetas, G. (1987). Vibration characteristics of dams in narrow canyons. *Journal of Geotechnical Engineering*, 113(8): 899-904.

Darendeli, M. B. (2001). *Development of a new family of normalised modulus reduction*

and material damping curves. PhD thesis, University of Texas at Austin.

de Boer, R., Ehlers, W. and Liu, Z. (1993). One-dimensional transient wave propagation in fluid-saturated incompressible porous media. *Archive of Applied Mechanics*, 63(1): 59-72.

Domenico, P. A. and Schwartz, F. W. (1990). *Physical and Chemical Hydrogeology*. New York: John Wiley & Sons.

Duncan, J. M. and Chang, C. (1970). Nonlinear analysis of stress and strain in soils. *Journal of the Soil Mechanics and Foundations Division, ASCE*, 96(5): 1629-1653.

Dutta, N. C. (1980). Theoretical analysis of observed second bulk compressional wave in a fluid saturated porous solid at ultrasonic frequencies. *Applied Physics Letters*, 37(10): 898-900.

Electric Power Research Institute (1993). *Guidelines for determining design basis ground motions: method and guidelines for estimating earthquake ground motion in Eastern North America*. Palo Alto, California. Report EPRI TR-102293, Vol. 1.

Elgamal, A. and He, L. (2004). Vertical earthquake ground motion records: an overview. *Journal of Earthquake Engineering*, 8(5): 663-697.

Elia, G., Chan, A. H. C., Kavvadas, M. J. and Amorosi, A. (2011). Fully coupled dynamic analysis of an earth dam. *Geotechnique*, 61(7): 549-563.

Elnashai, A. S., He, L. and Elgamal, A. (2004). Spectra for vertical earthquake ground motion. The Proceedings of *13th World Conference on Earthquake Engineering*, Vancouver, B.C., Canada, Paper No. 2309.

Elnashai, A. S. and Papazoglou, A. J. (1997). Procedure and spectra for analysis of RC structures subjected to strong vertical earthquake Loads. *Journal of Earthquake Engineering*, 1(1): 121-155.

Gazetas, G. (1987). Seismic response of earth dams, some recent developments. *Soil Dynamics and Earthquake Engineering*, 6(1): 3-47.

Gazetas, G., Debchaudhury, A. and Gasparini, D. A. (1982). Stochastic estimation of the nonlinear response of earth dams to strong earthquakes. *Soil Dynamics and Earthquake Engineering*, 1(1): 39-46.

Ghaboussi, J. and Wilson, E. L. (1973). Flow of compressible fluid in porous elastic media. *International Journal for Numerical Methods in Engineering*, 5(3): 419-442.

Gu, G. (1988). *Earthquake engineering of earth and rockfill dams (in Chinese)*. Nanjing: HoHai University Press.

Guan, F. and Moore, I. D. (1997). New techniques for modelling reservoir-dam and foundation-dam interaction. *Soil Dynamics and Earthquake Engineering*, 16(4): 285-293.

Guerreiro, P., Kontoe, S. and Taborda, D. M. G. (2012). Comparative study of stiffness reduction and damping curves. The Proceedings of *15th World Conference on Earthquake Engineering*, Lisbon, Portugal.

Gulerce, Z. and Abrahamson, N. A. (2011). Site-specific design spectra for vertical ground motion. *Earthquake Spectra*, 27: 1023-1047.

Gurevich, B., Kelder, O. and Smeulders, D. M. J. (1999). Validation of the slow compressional wave in porous media comparison of experiments and numerical simulations. *Transport in Porous Media*, 36(2): 149-160.

Hardin, B. O. and Black, W. L. (1968). Vibration modulus of normally consolidated clay. *Journal of the Soil Mechanics and Foundations Division, ASCE*, 94(SM2): 353-369.

Hardin, B. O. and Drnevich, V. P. (1972). Shear modulus and damping in soils. *Journal of the Soil Mechanics and Foundations Division, ASCE*, 98(7)

Hardy, S. (2003). *The implementation and application of dynamic finite element analysis to geotechnical problems*. PhD thesis, Imperial College London.

Haskell, N. A. (1953). The dispersion of surface waves on multilayered media. *Bulletin of the Seismological Society of America*, 43: 17-35.

Hatanaka, M. (1952). Three-dimensional consideration on the vibration of earth dams. *Journal of the Japanese Society of Civil Engineers*, 37(10): 305-312.

Hatanaka, M. (1955). *Fundamental consideration on the earthquake resistant properties of the earth dam*. Disaster Prevention Research Institute, Kyoto University. Technical Report Bulletin 11.

He, S., Hu, Y. and Liu, J. (2006). The asphalt concrete core rockfill dam in Yele hydraulic project (in Chinese). *Hydraulic stations design*, 22(2): 46-53.

Higashi, S. and Abe, S. (2002). Estimation of bedrock motions at KiK-net Hino site during the 2000 Tottori-ken Seibu earthquake based on the results of seismic reflection survey. The Proceedings of *the 11th Japan Earthquake Engineering Symposium (2002)*, Japan, 11: 461-464.

Hilber, H. M. and Hughes, T. J. R. (1978). Collocation, dissipation and overshoot for time integration schemes in structural dynamics. *Earthquake Engineering and Structural Dynamics*, 6(1): 99-117.

Hilber, H. M., Hughes, T. J. R. and Taylor, R. L. (1977). Improved numerical dissipation for time integration algorithms in structural dynamics. *Earthquake Engineering and Structural Dynamics*, 5(3): 283-292.

Huang, H. C., Huang, S. W. and Chiu, H. C. (2005). Observed evolution of linear and nonlinear effects at the Dahan downhole array, Taiwan: analysis of the September 21, 1999 M7.3 Chi-Chi earthquake sequence. *Pure and Applied Geophysics*, 162: 1-20.

Hurwitz, A. (1895). Uber die Bedingungen, unter welchen eine Gleichung nur Wurzeln mit negativen reellen Teilen bestzt. *Mathematische Annalen*, 46: 273-284.

Imazu, M. and Fukutake, K. (1986). Dynamic shear modulus and damping of gravel materials. The Proceedings of *the 21st Annual Meeting of JSSMFE*, Japan, 10: 509-512.

Ishida, K., Sato, K., Sawada, Y. and Yajima, H. (1985). *Estimation of underground structure based on earthquake observation and normalized response spectrum*. CRIEPI Report No. 385005 (in Japanese).

Ishihara, K. (1996). *Soil behaviour in earthquake geotechnics*. Oxford: Clarendon Press.

Izutani, Y. (2004). Nonlinear response of surface layers at KiK-net stations in Japan. The Proceedings of *13th World Conference on Earthquake Engineering*, Vancouver, B.C., Canada, Paper No. 2690.

Janbu, N. (1957). Earth pressures and bearing capacity calculations by generalized procedure of slices. The Proceedings of 4th International Conference Soil Mechanics and Foundation Engineering, 2: 207-212.

Joyner, W. B. and Chen, T. F. (1975). Calculation of nonlinear ground response in earthquakes. *Bulletin of the Seismological Society of America*, 65: 1315-1336.

Kaklamanos, J., Bradley, B. A., Thompson, E. M. and Baise, L. G. (2013). Critical parameters affecting bias and variability in site-response analyses using KiK-net downhole array data. *Bulletin of the Seismological Society of America*, 103(3): 1733-1749.

Kelder, O. and Smeulders, D. M. J. (1997). Observation of the Biot slow wave in water-saturated Nivelsteiner Sandstone. *Geophysics*, 62: 1794–1796.

Kellezi, L. (1998). *Dynamic soil-structure interaction transmitting boundary for transient analysis*. PhD thesis, Technical University of Denmark.

Kellezi, L. (2000). Local transmitting boundaries for transient elastic analysis. *Soil Dynamics and Earthquake Engineering*, 19: 533-547.

Kim, S. H., Kim, K. J. and Blouin, S. E. (2002). Analysis of wave propagation in saturated porous media. I. Theoretical solution. *Computer Methods in Applied Mechanics and Engineering*, 191: 4061-4073.

Kokusho, T., Aoyagi, T. and Wakunami, A. (2005). In situ soil-specific nonlinear properties back-calculated from vertical array records during 1995 Kobe earthquake. *Journal of Geotechnical and Geoenvironmental Engineering*, 131(12): 1509-1521.

Kokusho, T. and Sato, K. (2008). Surface-to-base amplification evaluated from KiK-net vertical array strong motion records. *Soil Dynamics and Earthquake Engineering*, 28: 707-716.

Kondner, R. L. and Zelasko, J. S. (1963). A hyperbolic stress-strain formulation for sands. The Proceedings of *the 2nd Pan American Conference on Soil Mechanics and Foundations Engineering*, Brazil, 1: 289-324.

Kontoe, S. (2006). *Development of time integration schemes and advanced boundary conditions for dynamic geotechnical analysis*. PhD thesis, Imperial College London.

Kontoe, S., Zdravkovic, L. and Potts, D. M. (2008a). An assessment of time integration schemes for dynamic geotechnical problems. *Computers and Geotechnics*, 35(2): 253-264.

Kontoe, S., Zdravkovic, L. and Potts, D. M. (2008b). The generalized α-algorithm for dynamic coupled consolidation problems in geotechnical engineering. The Proceedings of *12th International Conference of International Association for Computer Methods and Advances in Geomechanics (IACMAG)*: 1449-1558.

Katona, M. C. and Zienkiewicz, O. C. (1985). A unified set of single step algorithms part 3: The beta-m method, a generalization of the Newmark scheme. *International Journal for Numerical Methods in Engineering*, 21(7): 1345–1359.

Kramer, S. L. (1996). *Geotechnical earthquake engineering*. New Jersey: Prentice Hall.

Kuhlemeyer, R. L. and Lysmer, J. (1973). Finite element method accuracy for wave propagation problems. *Journal of the Soil Mechanics and Foundation Division, ASCE*, 99(SM5): 421-427.

Lacy, S. J. and Prevost, J. H. (1987). Nonlinear seismic response analysis of earth dams. *Soil Dynamics and Earthquake Engineering*, 6(1): 48-63.

LeBlanc, M. T., Stokoe, K. H., Branco, A. G. and Lee, R. C. (2012). Field determination of linear and nonlinear constrained moduli of soils using large mobile shakers. The Proceedings of *the 15th World Conference on Earthquake Engineering*, Lisbon, Portugal.

Lee, C. P., Tsai, Y. B. and Wen, K. L. (2006). Analysis of nonlinear site response using the LSST downhole accelerometer array data. *Soil Dynamics and Earthquake Engineering*, 26: 435-460.

Li, X., Han, X. and Pastor, M. (2003). An iterative stabilized fractional step algorithm for finite element analysis in saturated soil dynamics. *Computer Methods in Applied Mechanics and Engineering*, 192(35-36): 3845-3859.

Li, X. S., Shen, C. K. and Wang, Z. L. (1998). Fully coupled inelastic site response analysis for 1986 Lotung earthquake. *Journal of Geotechnical and Geoenvironmental Engineering*, 124: 560-573.

Li, X. S., Wang, Z. L. and Shen, C. K. (1992). *SUMDES, a nonlinear procedure for response analysis of horizontally-layered sites subjected to multidirectional earthquake loading*. Department of Civil Engineering, University of California, Davis, California. Technical Report.

Lollino, P., Cotecchia, F., Zdravkovic, L. and Potts, D. M. (2005). Numerical analysis

and monitoring of Pappadai dam. *Canadian Geotechnical Journal*, 42(6): 1631-1643.

Lysmer, J., Udaka, T., Tsai, C. and Seed, H. B. (1975). *FLUSH: A computer program for approximate 3-D analysis of soil-structure interaction problems*. Technical Report EERC 75-30.

Makdisi, F. I. and Seed, H. B. (1978). Simplified procedure for estimating dam and embankment earthquake-induced deformations. *Journal of the Geotechnical Engineering Division, ASCE*, 104(7): 849-867.

Masing, G. (1926). Eigenspannungen und verfestigung beim messing. The Proceedings of *the 2nd International Conference of Applied Mechanics*, Zurich, Switzerland.

Matsunami, K., Morii, T., Okamoto, Y. and Fujiwara, T. (2002). Local site amplification and damage to wooden houses in Shimoenoki, Tottori, Japan, by the 2000 Western Tottori Earthquake. *Earth Planets Space*, 54: 861-870.

Ministry of Housing and Urban-Rural Development of the People's Republic of China (2010). *China Earthquake-resistant Design Standard for Civil Engineering Structures*.

Ministry of Housing and Urban-Rural Development of the People's Republic of China (2000). *Chinese Specifications for Design of Hydraulic Structures*.

Mononobe, N., Takata, A. and Matumura, M. (1936). Seismic stability of the earth dam. *Transactions of the 2nd Congress on Large Dams, Washington D. C.*, 4: 435-444.

Mroz, Z. (1967). On the description of anisotropic work hardening. *Journal of Mechanics and Physical Solids*, 15(3): 163-175.

Muravskii, G. and Frydman, S. (1998). Site response analysis using a non-linear hysteretic model. *Soil Dynamics and Earthquake Engineering*, 17: 227-238.

Nagy, P. B., Alder, L. and Bonner, B. P. (1990). Slow wave propagation in airfilled porous materials and natural rocks. *Applied Physics Letters*, 56(25): 2504-2506.

Newmark, N. M. (1959). A method of computation for structural dynamics. *Journal of Engineering Mechanics, ASCE* 85: 67-94.

Newmark, N. M. (1965). Effects of earthquakes on dams and embankments. *Geotechnique*, 15(2): 139-160.

Okada, Y., Kasahara, K., Hori, S., Obara, K., Sekiguchi, S., Fujiwara, H. and Yamamoto, A. (2004). Recent progress of seismic observation networks in Japan -Hi-net, F-net, K-NET and KiK-net. *Earth Planets Space*, 56: 15-29.

Papadimitriou, A. G., Bouckovalas, G. D. and Andrianopoulos, K. I. (2014). Methodology for estimating seismic coefficients for performance-based design of earth dams and tall embankments. *Soil Dynamics and Earthquake Engineering*, 56: 57-73.

Papazoglou, A. J. and Elnashai, A. S. (1996). Analytical and field evidence of the damaging effect of vertical earthquake ground motion. *Earthquake Engineering and Structural Dynamics*, 25(2): 1109-1137.

Pavlenko, O. V. and Irikura, K. (2002). Nonlinearity in the response of soils in the 1995 Kobe earthquake in vertical components of records. *Soil Dynamics and Earthquake Engineering*, 22: 967-975.

Pavlenko, O. V. and Irikura, K. (2006). Nonlinear behavior of soils revealed from the records of the 2000 Tottori, Japan, earthquake at stations of the digital strong-motion network KiK-Net. *Bulletin of the Seismological Society of America*, 96(6): 2131-2145.

Pelecanos, L. (2013). *Seismic response and analysis of earth dams*. PhD thesis, Imperial College London.

Perez-Rocha, L. E. and Sanchez-Sesma, F. J. (1992). Hybrid non-linear response of soft soils. *Proceedings of the 10th World Conference of Earthquake Engineering*, 2: 973-979.

Phillips, C. and Hashash, Y. M. A. (2009). Damping formulation for nonlinear 1D site response analyses. *Soil Dynamics and Earthquake Engineering*, 29(7): 1143-1158.

Plona, T. J. (1980). Observation of a second bulk compressional wave in a porous medium at ultrasonic frequencies. *Applied Physics Letters*, 36(4): 259.

Potts, D. M. and Zdravkovic, L. (1999). *Finite element analysis in geotechnical engineering: Theory*. London: Thomas Telford.

Prevost, J. H. (1981). *DYNAFLOW: A Nonlinear Transient Finite Element Analysis Program*. Princeton University. Technical Report 81-SM-1.

Prevost, J. H., Abdel-Ghaffar, A. M. and Lacy, S. J. (1985). Nonlinear dynamic analysis of an earth dam. *Journal of Geotechnical Engineering*, 111(7): 882-897.

Puzrin, A. M. and Burland, J. B. (1996). A logarithmic stress-strain function for rocks and soils. *Geotechnique*, 46(1): 157-164.

Puzrin, A. M. and Shiran, A. (2000). Effects of the constitutive relationship on seismic response of soils. Part I. Constitutive modeling of cyclic behavior of soils. *Soil Dynamics and Earthquake Engineering*, 19(5): 305-318.

Rasolofosaon, P. N. J. (1988). Importance of interface hydraulic condition on the generation of second bulk compressional wave in porous media. *Applied Physics Letters*, 52(10): 780-782.

Rojstaczer, S., Wolf, S. and Michel, R. (1995). Permeability enhancement in the shallow crust as a cause of earthquake-induced hydrological changes. *Nature*, 373: 237-239.

Rollins, K., Evans, M., Diehl, N. and Daily, W. (1998). Shear modulus and damping relations for gravel. *Journal of Geotechnical and Geoenvironmental Engineering, ASCE*, 124(5): 396-405.

Routh, E. J. (1877). *A treatise on the stability of a given state of motion*. London: Macmillan.

Sarma, S. K. (1973). Stability analysis of embankments and slopes. *Geotechnique*, 23(3): 423-433.

Sarma, S. K. (1975). Seismic stability of earth dams and embankments. *Geotechnique*, 27(4): 743-761.

Sarma, S. K. (1979). Stability analysis of embankments and slopes. *Journal of the Geotechnical Engineering Division, ASCE*, 105(GT5): 1511-1524.

Sato, K., Kokusho, T., Matsumoto, M. and Yamada, E. (1996). Nonlinear seismic response and soil property during strong motion. *Special Issue of Soils and Foundations*: 41-52.

Schanz, M. and Pryl, D. (2004). Dynamic fundamental solutions for compressible and incompressible modeled poroelastic continua. *International Journal of Solids and Structures*, 41(15): 4047-4073.

Schnabel, P. B., Lysmer, J. and Seed, H. B. (1972). *SHAKE: A Computer Program for earthquake response analysis of horizontally layered sites*. Earthquake Engineering Research Centre, University of California, Berkeley.

Seed, H. B. (1973). *Stability of earth and rockfill dams during earthquakes. Embankment - Dam Engineering, R. Hirschfeld and S. Poulos, eds*. New York

Seed, H. B. (1979). Considerations in the earthquake-resistant design of earth and rockfill dams. *Geotechnique*, 29(3): 215-263.

Seed, H. B., Lee, K. L. and Idriss, I. M. (1969). Analysis of Sheffield dam failure. *Journal of the Soil Mechanics and Foundations Division, ASCE*, 95(SM6): 1453-1490.

Singh, R., Roy, D. and Jain, S. K. (2005). Analysis of earth dams affected by the 2001 Bhuj earthquake. *Engineering Geology*, 80(3-4): 282-291.

Smith, I. M. (1994). "An overview of numerical procedures used in VELACS project", in. *Verification of Numerical Procedures for the Numerical Analysis of Soil Liquefaction Problems*, Arulanandan & Scott (eds), Balkema, Rotterdam

Soares, D. (2008). A time-domain FEM approach based on implicit Green's functions for the dynamic analysis of porous media. *Computer Methods in Applied Mechanics and Engineering*, 197(51-52): 4645-4652.

Stara-Gazetas, E. (1986). *Method for inelastic response analysis of earth dams*. PhD thesis, Rensselaer Polytechnic Institute.

Taborda, D. M. G. (2011). *Development of constitutive models for application in soil dynamics*. PhD thesis, Imperial College London.

Taborda, D. M. G. and Zdravkovic, L. (2012). Application of a Hill-Climbing technique to the formulation of a new cyclic nonlinear elastic constitutive model. *computers and Geotechnics*, 43: 80-91.

Taborda, D. M. G., Zdravkovic, L., Kontoe, S. and Potts, D. M. (2014). Computational study on the modification of a bounding surface plasticity model for sands. *Computers and Geotechnics*, 59: 145-160.

Teng, Y. (1990). Finite element results of the slow compressional wave in a porous medium at ultrasonic frequencies. *Applied Physics Letters*, 68(8): 4335-4337.

Terzaghi, K. (1950). *Mechanics of landslides*. The Geological Survey of America. Technical Report Engineering Geology Volume.

UBC (1997). *Uniform Building Code*. International Conference of Building Officials, California.

Vardoulakis, I. and Beskos, D. E. (1986). Dynamic behavior of nearly saturated porous media. *Mechanics of Materials*, 5(1): 87-108.

Vrymoed, J. M. (1981). Dynamic FEM model of Oroville dam. *Journal of the Geotechnical Engineering Division, ASCE*, 107(GT8): 1057-1077.

Vucetic, M. (1994). Cyclic threshold shear strains in soils. *Journal of Geotechnical Engineering*, 120(12): 2208-2228.

Vucetic, M. and Dobry, R. (1991). Effect of soil plasticity on cyclic response. *Journal of Geotechnical Engineering*, 117(1): 89-107.

Wang, D., Li, T. and Zhao, L. (2008). The influence of the wetting effects on the stress deformation of asphalt concrete core rockfill dams (in Chinese). *Water Resources and Power*, 26(4): 112-115.

Wang, G. Q., Zhou, X. Y., Ma, Z. J. and Zhang, P. Z. (2001). A preliminary study on the randomness of response spectra of the 1999 Chi-Chi, Taiwan, Earthquake. *Bulletin of the Seismological Society of America*, 91(5): 1358-1369.

Wang, Z. L. (1990). *Bounding surface hypoplasticity model for granular soils and its applications*. PhD thesis, Department of Civil Engineering, University of California, Davis, California.

Wilson, R. C. and Keefer, D. K. (1985). "Predicting areal limits of earthquake-induced landsliding", in evaluating earthquake hazards in the Los Angeles region, Ziony J.I., ed. *U.S. Geological Survey, Reston, Virginia*, Professional Paper 1360: 317-345.

Wood, W. L. (1990). *Practical time-stepping schemes*. Oxford: Clarendon Press.

Wood, W. L., Bossak, M. and Zienkiewicz, O. C. (1981). An alpha modification of Newmark's method. *International Journal for Numerical Methods in Engineering*, 15(10): 1562-1566.

Wu, Y. (2005). Static and dynamic analysis of interaction effects between high rockfill

dam and deep soil foundation (in Chinese). *Bulletin of Hydropower Association of Guizhou Province*, 1(1): 343-346.

Wu, Y., Cui, H. and Teng, Z. (2009). The influence of Wenchuan earthquake on the operation safety of Yele dam (in Chinese). *Hydraulic Construction and Management*, 35(1): 45-46.

Xiong, K. (2009). *Seismic observations on Yele dam during the 2008 Wenchuan earthquake (in Chinese)*. Wuhan University. Government Report.

Xiong, K., He, Y. and Zhang, Y. (2008). Dynamic response of Yele dam under Wenchuan and Panzhihua earthquakes. *Chinese Journal of Geotechnical Engineering*, 30(10): 1575-1580.

Xu, Z. (2009). Briefly discussion on earthquake and safety (in Chinese). *China Earthquake Geology*, 3(3): 10-21.

Yang, J. and Sato, T. (2000). Interpretation of seismic vertical amplification observed at an array site. *Bulletin of the Seismological Society of America*, 90(2): 275-285.

Yang, J. and Yan, X. R. (2009a). Factors affecting site response to multi-directional earthquake loading. *Engineering Geology*, 107(3-4): 77-87.

Yang, J. and Yan, X. R. (2009b). Site response to multi-directional earthquake loading: A practical procedure. *Soil Dynamics and Earthquake Engineering*, 29(4): 710-721.

Yoshimura, C., Bielak, J., Hisada, Y. and Fernandez, A. (2003). Domain reduction method for three-dimensional earthquake modelling in localised regions, part 2: verification and applications. *Bulletin of the Seismological Society of America*, 93(2): 825-840.

Zerwer, A., Cascante, G. and Hutchinson, J. (2002). Parameter estimation in finite element simulations of Rayleigh waves. *Journal of Geotechnical and Geoenvironmental Engineering*, 128(3): 250-261.

Zhang, S. (2005). Some issues on earth dam design (in Chinese). *China Hydrology*, 4: 10-20.

Zienkiewicz, O. C., Bicanic, N. and Shen, F. Q. (1988). Earthquake input definition and the transmitting boundary condition. *Advances in Computational Nonlinear*

Mechanics, 300: 109-138.

Zienkiewicz, O. C., Chan, A. H. C., Pastor, M., Schefler, B. A. and Shiomi, T. (1999). *Computational Geomechanics with Special Reference to Earthquake Engineering*. London: John Wiley & Sons.

Zienkiewicz, O. C., Chang, C. T. and BETTESS, P. (1980b). Drained, undrained, consolidating and dynamic behaviour assumptions in soils. *Geotechnique*, 30(4): 385-395.

Zienkiewicz, O. C. and Shiomi, T. (1984). Dynamic behaviour of saturated porous media: The generalized Biot formulation and its numerical solution. *International Journal for Numerical and Analytical Methods in Geomechanics*, 8(1): 71-96.

Zienkiewicz, O. C., Wood, W. L., Hine, N. W. and Taylor, R. L. (1984). A unified set of single step algorithms. Part 1: General formulation and applications. *International Journal for Numerical Methods in Engineering*, 20(8): 1529-1552.

Zienkiewicz, O. C., Wood, W. L. and Taylor, R. L. (1980a). An alternative single-step algorithm for dynamic problems. *Earthquake Engineering and Structural Dynamics*, 8(1): 31-40.